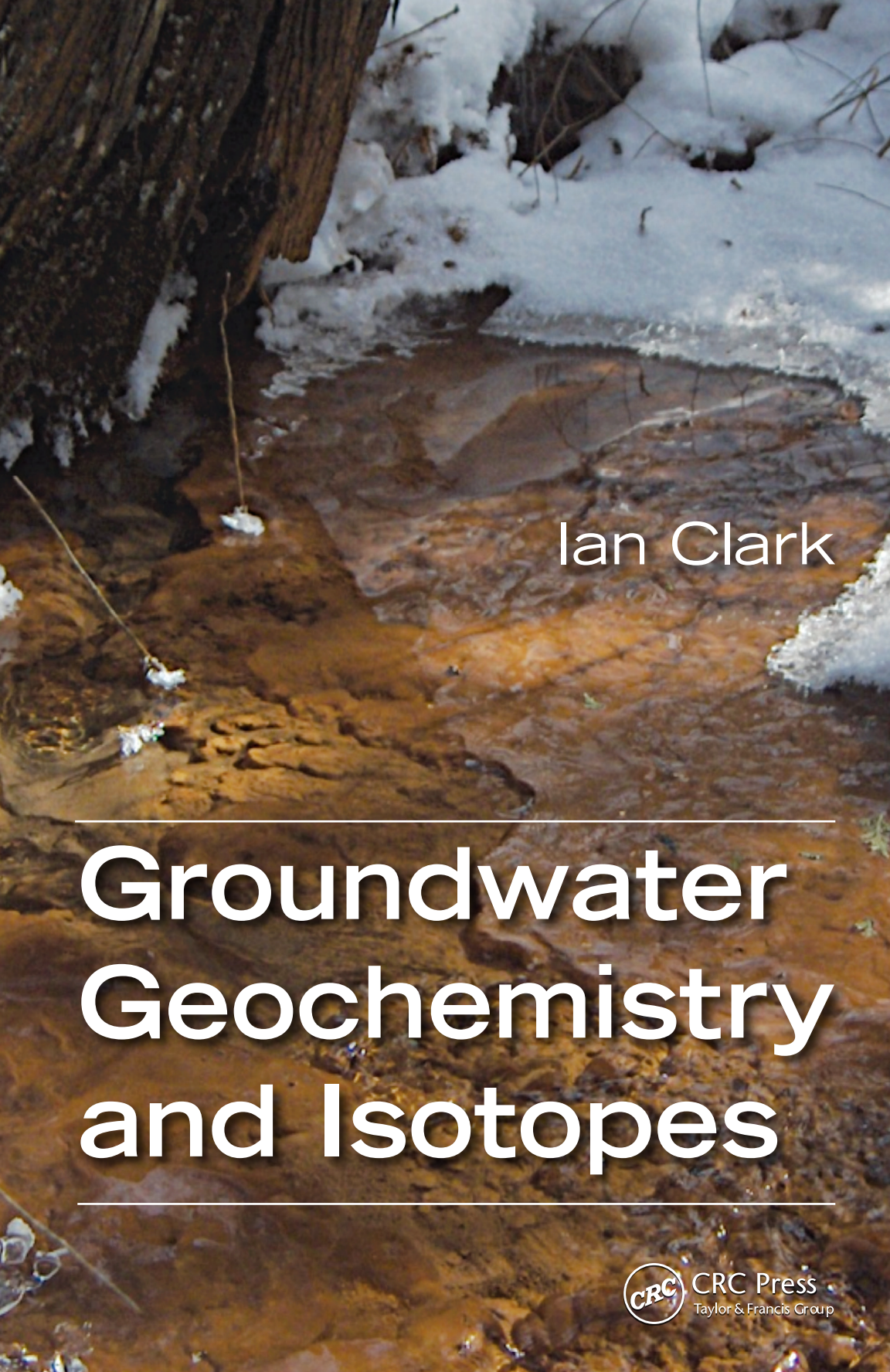
Ian Clark
Groundwater Geochemistry and Isotopes
CRC Press
Taylor & Francis Group

Groundwater Geochemistry and Isotopes

This page intentionally left blank

Groundwater Geochemistry and Isotopes

Ian Clark

CRC Press
Taylor & Francis Group
Boca Raton London New York

CRC Press is an imprint of the
Taylor & Francis Group, an **informa** business

Cover: Biogenic iron oxyhydroxides (BIOS) forming from natural ferrous iron-bearing groundwaters that discharge from an alluvial sand aquifer at the Atomic Energy of Canada research laboratories near Chalk River, Ontario, Canada. Geochemistry and isotope investigations studied their nature and capacity to attenuate radioisotopes including 129I and 90Sr (Kennedy et al. 2011; Gault et al., 2011). Photo credit: Grant Ferris.

CRC Press
Taylor & Francis Group
6000 Broken Sound Parkway NW, Suite 300
Boca Raton, FL 33487-2742

Version Date: 20150302

International Standard Book Number-13: 978-1-4665-9174-5 (eBook - PDF)

Dedication

Who could be more fortunate than those who spend their career working with young, bright people with common interests and aspirations? Whether around a campfire in the field or around a mass spectrometer in the lab, it has been my pleasure to share moments of insight and to share a laugh with many promising students and the talented people who run our labs to train them. I am grateful to you all for those moments, which have contributed greatly to this book.

This page intentionally left blank

Contents

Preface

Groundwater represents over 98 percent of terrestrial freshwater and plays a proportionally large role in terrestrial life. In soils, it helps weather minerals and releases nutrients. In plants, transpiration of soil water during photosynthesis brings the nutrients for growth. Groundwater discharge in rivers maintains base flow critical to aquatic ecosystems and overwintering habitat, even in permafrost catchments. Groundwater springs and oases were key to human migration out of arid east Africa, and since ancient times cities have been built around reliable sources of potable groundwater. Jiao (2007) describes a 5600 year old well in Zhejiang Province, China with walls and roof to protect its valuable water. The *aflaj* of Oman, horizontal conduits tunneled kilometers through sand, gravel, and rock, have drained fresh groundwater from beneath the parched landscape to water livestock and nourish gardens for millennia. Deep in the heart of Istanbul, the incredible Basilica Cistern built by the Byzantines is fed by groundwater channeled from springs hundreds of kilometers away. The early hydrogeologists who built these water supply systems had a concern for not just the source and quantity of water they could tap, but also its quality.

Today, we are approaching the limits for exploiting this resource. Potable groundwaters are threatened by industrial and urban growth in the recharge environments. Recognition has emerged over the past several decades that our groundwater resources are not infinite and must be protected. Accompanying this has been a development of geochemical and environmental isotope methods to understand the origin of groundwater, its solutes and the processes that influence groundwater quality.

Why *geochemistry*? It is the interaction of water with the minerals and organics of the geosphere that controls groundwater quality in natural and contaminated settings. Why isotopes? Stable and radioactive isotopes are natural tracers of water and solutes that complement geochemistry and provide an understanding the origin, age, and evolution of groundwater. New sampling and analytical technologies now allow us to gather abundant data at unprecedented temporal and spatial resolution. Geochemistry and isotope tools are now routinely used by professionals and students to solve hydrogeological problems. This book aims to develop a practical understanding of these complementary tools and their integration in case studies to trace the origin, age, and fate of groundwater and solutes in both natural and contaminated settings.

This page intentionally left blank

Author

Ian Clark is a professor in the Department of Earth and Environmental Sciences at the University of Ottawa. Professor Clark completed a bachelor of science degree in earth sciences and a master of science degree in hydrogeology at the University of Waterloo followed by his doctoral degree at the Université de Paris-Sud (Orsay) in isotope hydrogeology and paleoclimatology.

Since his earliest work on geothermal systems in western Canada, Dr. Clark's research has focused on the integration of geochemistry and isotopes to address questions on the origin, age, paleoclimatic context, and geochemical history of groundwater and solutes in natural and contaminated settings. He continues to be inspired by the enthusiasm of his graduate students and their research in diverse hydrogeological environments, ranging from groundwater dynamics in permafrost in the Arctic or beneath the deserts of Oman to contamination of water resources, dispersion of radionuclides in the environment, and the burial of nuclear waste.

To provide students with the most up-to-date technologies, Dr. Clark and his colleagues established just this year new facilities in the Advanced Research Complex (ARC) at Ottawa, one of Canada's leading centers for training and analysis in the geosciences. The ARC includes laboratories for geochemistry-stable isotopes, tritium, noble gases, and accelerator mass spectrometry (AMS) for radiocarbon and other radioisotopes.

Professor Clark has been involved with the International Atomic Energy Agency and the National Ground Water Association in the teaching of geochemistry and environmental isotopes in hydrology. This undergraduate textbook complements his graduate-level textbook (co-authored with Professor Peter Fritz) *Environmental Isotopes in Hydrogeology.*

This page intentionally left blank

1 Water, Rocks, Solutes, and Isotopes

THE NATURE OF WATER

Water is a substance of most intriguing characteristics. Its various states, mobility, and ability to transport solutes allows it the leading role in a host of geological processes. Deep in the earth, water lowers the melting temperature of rock to generate magma that builds the continents. As chloride-rich brine, deep crustal waters carry gold and other metals to form ore deposits. Water of the ancient oceans provided the crucible for early life to evolve, and freshwater is the basis of life in the terrestrial environment. As vapor, water provides the earth with some 30 degrees of greenhouse warming and makes the planet habitable. Yet, condensed as clouds it reflects solar radiation and regulates our climate. Its high heat capacity (4200 joules per kilogram per degree), coupled with the enthalpy of vaporization (2.4 million joules per kilogram are released during condensation), fuels hurricanes and typhoons. Crystallized as ice, it has a remarkable open-tetrahedral framework that is less dense than liquid water and so, unlike most other compounds, its solid phase is buoyant. Fortunately so, otherwise aquatic habitats could freeze to the bottom, and there would be no surface ice to regulate seasonal albedo. Even the search for life on Mars following the traces of water. All who have plunged their face into a fountain of cold, clear water to slake their thirst on a hot day, whether from a mountain spring or a garden hose, appreciate its quality for sustaining life.

In geochemistry, it is water's capacity to dissolve solids and transport solutes that makes H_2O so remarkable. The water molecule's asymmetrical charge distribution is central to this property. The two hydrogen atoms and single oxygen atom share four tetrahedrally oriented electron orbits, which give rise to a dipolar configuration. Although the overall molecule is electrically neutral, the surface charge is unevenly distributed, giving one side a net negative charge, and the other a net positive charge (Figure 1.1).

The positive and negative poles of neighboring water molecules attract to form a weak hydrogen bond that is easily broken and reformed. The result is loose clusters of molecules that are continually breaking apart and reforming. At 25°C, about 80% of the water molecules are so structured. At the boiling point, this is slightly less, and as water freezes, it becomes fully structured.

Because hydrogen bonds are weak, they easily break as water molecules evaporate to water vapor. When humidity exceeds the dew point of the air, hydrogen bonds reform and water vapor condenses—key steps in the hydrological cycle.

The dipolar nature of water provides it with some unusual properties. First, it allows H_2O molecules to attract and condense into a loosely structured liquid at Earth surface temperatures (Figure 1.2). Second, these dipolar molecules can also

orient themselves around ions, thus isolating them and holding them in solution. This makes water a good solvent, an effective chemical weathering agent, and an important medium to transport solutes. Another important property of water is how this hydrogen bond is stronger for the heavier isotopes of water. As shown in Figure 1.2, this affects reaction rates such that these isotopes are partitioned throughout the hydrological cycle and can be used to trace the origin and movement of water.

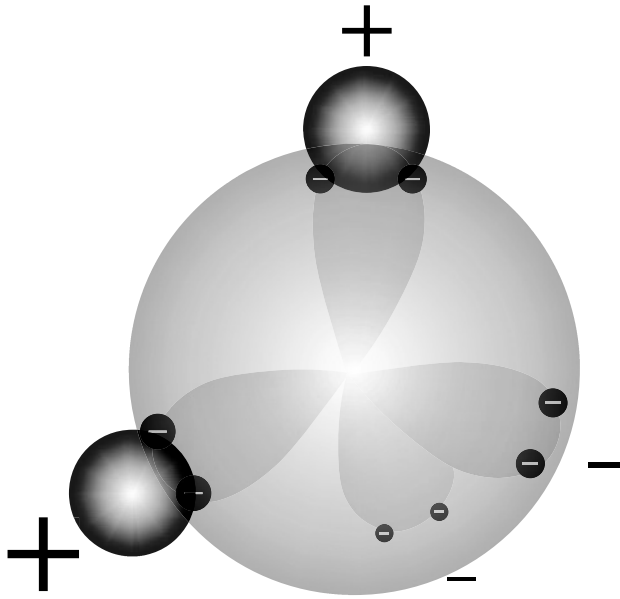

FIGURE 1.1 The dipolar molecule of H_2O with two hydrogen atoms configured within the oxygen atom at an angle of 105°.

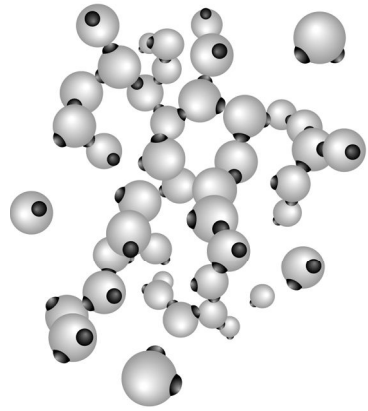

FIGURE 1.2 The tetrahedral structure of water, with clusters of water molecules held by weak hydrogen bonds generated by the polar charge distribution and with monomers that rapidly rejoin, giving structure to liquid water.

SOLUTES IN WATER

The brines of the Dead Sea in the Jordan Rift Valley are a remarkable example of water as a solvent. Held within each kilogram of clear water are more than 350 g of magnesium and sodium chloride salts. How can so much salt be dissolved in this water? The positively charged Mg^{2+} ions are surrounded by a sphere of water molecules, oriented with their negative pole toward the cation. Negative Cl^- ions are surrounded by water molecules with their positive pole oriented inward. This electrostatic interaction with water reduces the interaction between cations and anions that would otherwise allow them to bond and form minerals—an important aspect of aqueous geochemistry that begins with a look at what constitutes matter dissolved in water.

Dissolved Solids

The primary school experiment of leaving a glass of tap water by the window to dry demonstrates not only the principle of evaporation but also that the clear water contained solids, left as a residue on the walls and bottom of the glass. To say just what these solids are requires additional analyses, but they include inorganic salts formed from the major cations found in water (Ca^{2+}, Mg^{2+}, Na^+, and K^+), the complementary anions (HCO_3^-, SO_4^{2-}, and Cl^-), and any neutral or uncharged compounds like dissolved silica (H_4SiO_4), plus colloids (amorphous, small-diameter clusters of electrostatically bonded ions), and even organic matter. The inorganic components of these dissolved solids contribute to the salinity of water. Low salinity groundwaters are dominated by Ca^{2+} and HCO_3^- from mineral weathering by carbonic acid, whereas the salinity in seawater and brines is dominated by highly soluble Na^+ and Cl^-. The ranges of total dissolved solids (TDS in mg/L) as found in different water types throughout the hydrological cycle are shown in Figure 1.3.

TDS is analyzed by evaporating a filtered volume of water sample to dryness and weighing the dried precipitate, and so is expressed as milligrams per liter of solution. TDS can also be calculated by summing the mass of the dissolved ions and uncharged species that are measured in solution. However, as half of the bicarbonate, HCO_3^-, is lost as CO_2 during formation of carbonate minerals by drying, the

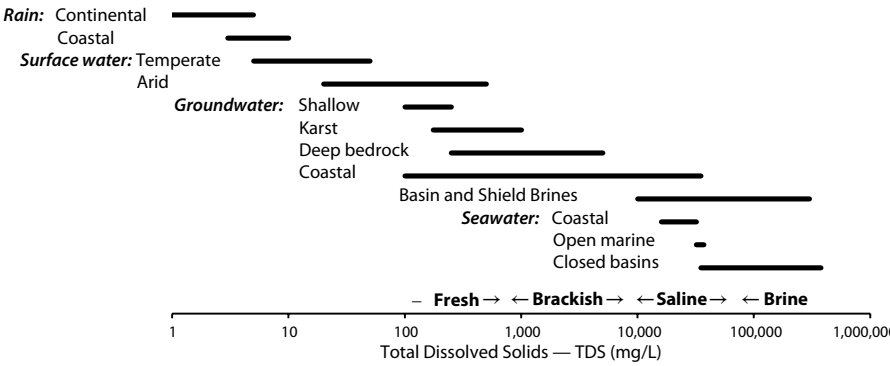

FIGURE 1.3 Typical range for total dissolved solids in different waters.

TABLE 1.1
Size Range of Solutes and Compounds in Natural Water

Species	Diameter (å)[a]		Diameter (μm)[b]
Inorganic ions	1–10		0.0001–0.001
Organic molecules	10–1,000		0.001–0.1
Viruses	~100		~0.01
	← 0.45 μm (4,500 å) →		
Colloids	10–10,000		0.001–1
Bacteria	~10,000		~1–2

[a] å—angstrom unit, where 10,000 å = 1 μm.
[b] μm—micron, 10^{-6} m.

calculated TDS should include only half the measured HCO_3^-. Table 1.1 gives the size ranges for most of the dissolved solids that are found in natural waters.

The chemistry of rainwater in nonpolluted environments is dominated by dissolved atmospheric gases, including N_2, O_2, and CO_2, plus minor contributions from soluble atmospheric compounds such as sulfuric and nitrous oxides and some Na–Cl aerosols from sea spray. Concentrations are very low (TDS less than about 10 mg/L), although this can increase 10-fold as precipitation passes through the vegetation canopy before hitting the ground.

Surface waters typically have low salinity (less than 500 mg/L TDS) comprising mainly dissolved inorganic ions and humic compounds (humic and fulvic acids) derived from soils and organic molecules from in situ biochemical processes (algae growth and decay). Groundwaters generally have higher concentrations of dissolved inorganic species as a result of interaction with aquifer minerals.

Units of Solute Concentration

Solutes are most often analyzed by spectrometric or chromatographic methods, which rely on calibration curves produced by analysis of laboratory standard solutions with a range of solute concentrations. These standards are most accurately prepared gravimetrically or volumetrically. Solute concentrations can therefore be expressed as follows:

Mass solute per mass water: milligrams of solute per kilogram H_2O (not solution) or simply the solute/water mass ratio multiplied by 1 million to give weight as parts per million (ppm). Trace elements are usually expressed as parts per billion (ppb).

Mass solute per volume solution: milligrams of solute per liter of solution (mg/L) or for trace concentrations, as micrograms per liter (μg/L).

Concentrations are often expressed as the number of moles of solute per volume or mass of water. One mole contains 6.023×10^{23} atoms or molecules with a mass equivalent to its molar mass, expressed in grams. One mole of water weighs 18 g. This gives us solute concentrations as follows:

Molality, *m*, moles of solute per kilogram of water (mol/kg)
molarity, *M*, moles of solute per liter of solution (mol/L)

Water, of course, is considered by mass (kg) or volume (L) but often forgotten is that it can be expressed in moles. In some reactions water is considered in molar units. For reference, 1 kg of water ($gfw_{H_2O} = 18$) has 1000/18 = 55.6 mol/kg. It has, therefore, 55.6 mol O per kg, and 111.1 mol H per kg.

Expressing solute concentrations as moles per kilogram of solution is the seldom used unit of *formality*. As will be seen below, mg/L and ppm are essentially equivalent concentrations for most low-salinity waters and only diverge at solute concentrations found in brackish waters and brines. For thermodynamic calculations, mole units are used. Mole concentrations are often expressed as millimoles (mmol).

Example 1.1: Molal Concentrations in Water

What are the mole concentrations of Ca^{2+} and F^- from dissolving 2 mg fluorite in 1 kg of water?

2 mg CaF_2

$gfw_{fluorite} = 40.1 + 2 \times 19 = 78.1$

2 mg/78.1gfw = 0.0256 mmol CaF_2

$CaF_2 \rightarrow Ca^{2+} + 2F^-$

$m_{Ca^{2+}} = 0.0256$ mmol/kg or 2.56×10^{-5}mol/kg. This gives 1.03 ppm Ca^{2+}.

$m_{F^-} = 2 \times 0.0256 = 0.0512$ mmol/kg or 5.12×10^{-5}mol/kg. This gives 0.97 ppm F^-.

Mass concentration units are converted to mole concentration units by dividing by the gfw of the solute, and dividing again by 1000 (for the difference between ppm [10^6] and kg [1000 g] of H_2O). For concentrations per mass of water, the result is the molal concentration (m). For this and subsequent conversions in this section, the example of Ca^{2+} with an arbitrary analytical concentration of 46 mg/L is used. At this low concentration, this can also be expressed as 46 ppm.

$$\text{ppm} = \frac{\text{mg}}{\text{kg } H_2O} \qquad 46 \text{ ppm} = \frac{46 \text{ mg } Ca^{2+}}{10^6 \text{ mg } H_2O}$$

$$\text{mg/L} = \frac{\text{mg}}{\text{L solution}} \qquad 46 \text{ mg/L} = \frac{46 \text{ mg } Ca^{2+}}{1 \text{ L } H_2O}$$

$$\text{molality, } m = \frac{\text{mol}}{\text{kg } H_2O} = \frac{\text{ppm}}{\text{gfw} \times 1000} \qquad m_{Ca^{2+}} = \frac{46}{40.1 \times 1000} = 0.00115 \text{ mol/kg}$$

Converting from concentrations per volume solution (mg/L or µg/L), the result is the molar concentration (M):

$$\text{molarity, } M = \frac{\text{mol}}{\text{L solution}} = \frac{\text{mg/L}}{\text{gfw} \times 1000} \qquad M_{Ca^{2+}} = \frac{46}{40.1 \times 1000} = 0.00115 \text{ mol/L}$$

In most reactions, it is necessary to take into account the valence (z) of the ions in solution. For example, it takes twice the concentration of Na^+ ($z = 1$) to balance with Ca^{2+} ($z = 2$) in cation exchange reactions. In this case, units of equivalents, eq, are used. In mass-based concentrations (molal) this is expressed as equivalents per million (epm) or milliequivalents (meq) per kg:

$$\text{epm} = \frac{\text{ppm}}{\text{gfw}} \times \text{z} \qquad \text{Ca}^{2+} = \frac{46\ \text{ppm}}{40.1} \times 2 = 2.3\ \text{epm}$$
$$= m \times z \times 1000 \qquad = 0.00115\ \text{mol/kg} \times 2 \times 1000 = 2.3\ \text{meq/kg}$$

For volume-based concentrations (molar) and equivalents (eq) or milliequivalents (meq):

$$\frac{\text{meq}}{L} = \frac{\text{mg/L}}{\text{gfw}} \times \text{z} \qquad \text{Ca}^{2+} = \frac{46\ \text{mg/L}}{40.1} \times 2 = 2.3\ \text{meq/L}$$
$$= M \times z \times 1000 \qquad = 0.00115\ \text{mol/L} \times 2 \times 1000 = 2.3\ \text{meq/L}$$

With low-salinity solutions (TDS less than about 10,000 mg/L), there is little difference between concentrations expressed as mg/L or ppm. Thus,

$$\text{for TDS} < \sim 10{,}000 \qquad \text{ppm} \cong \text{mg/L}$$
$$\text{and} \qquad m \cong M.$$

At higher concentrations the mass-based units (ppm and m) exceed the volumetric units (mg/L and M) due to increasing density and reduced mass of water per volume of solution. Converting between mass and volume based units is done using the difference in weight between a given volume of the solution (i.e., density, measured at 25°C) and the weight of its solutes, TDS, expressed in units of kg/L.

Consider dissolving 100 g of $CaCl_2$ salt to 1 kg (1 L) of water. The water accommodates the addition of the salt by expanding to a larger volume, nominally about 1.1 L. The solution density also increases, as the gfw of $CaCl_2$ (111.1 g/mol) is greater than that of water (18 g/mol). It also increases due to the increased structuring of water molecules into hydration shells surrounding the dissolved Ca^{2+} and Cl^-, a process which reduces to some extent the volume expansion from adding the salt. These increases in volume and density do not change the molal concentration of Cl^- or Ca^{2+}. However, they do change the molar concentration, due to the reduced mass of the solutes in 1.0 L of the now 1.1 L of solution. The increase in volume and density of a salt solution depends on the concentration and types of ions present. Small divalent cations like Mg^{2+} have a stronger effect on the solution and so have higher densities than monovalent cations like Na^+. The increased density with TDS can be seen for three different chloride brines in Figure 1.4.

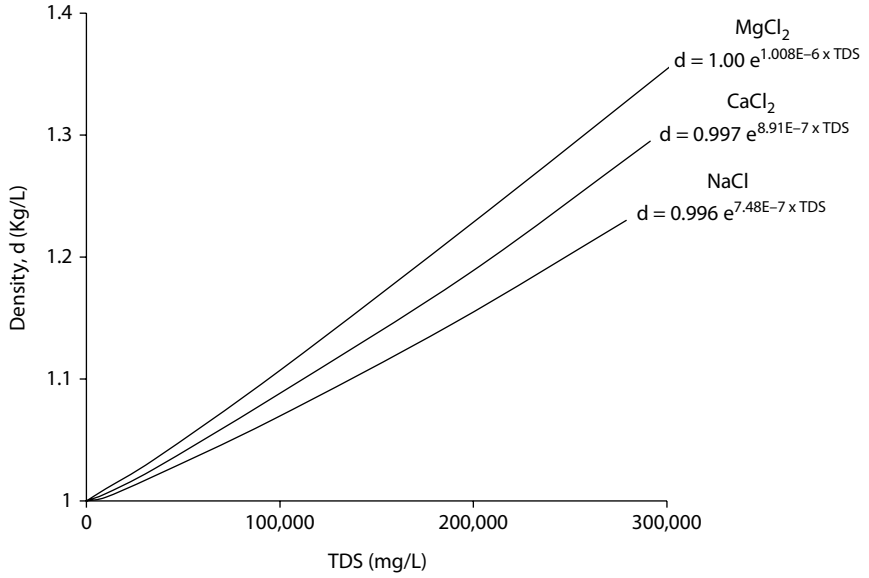

FIGURE 1.4 Change in solution density with increasing total dissolved solids for NaCl, $CaCl_2$, and $MgCl_2$ solutions.

Given the change in solution density, concentration diverges from ppm with the effect of density. The conversion from molality to molarity (ppm to mg/L) can be made with the following relationship:

$$\text{mg/L} = \text{ppm}\left[\text{density}\left(\text{kg/L}\right) - \text{TDS}\left(\text{kg/L}\right)\right]$$

$$M = m\left[\text{density}\left(\text{kg/L}\right) - \text{TDS}\left(\text{kg/L}\right)\right]$$

Example 1.2 shows the steps in converting units of concentration for solutions with high density.

Dissolved Gases

Gases are an important component of the inventory of dissolved species in water. Unlike the majority of solutes in water, which are present as ions, gases are not ionized. Some gases, such as CO_2, react with water to form other ionized and unionized species that can enhance solubility. As neutral species gases have less interaction with water and so tend to have low solubility. Gases can become dissolved in water from an adjacent gas phase, such as the atmosphere overlying surface waters and soil water in the unsaturated zone. In these cases, the concentration of gas dissolved in the water is governed by the partial pressure of that gas in the adjacent air (Table 1.2). Gases in groundwater can also be derived by geochemical reactions in the saturated zone. Gas solubility and gas–water reactions are discussed in more detail in Chapter 3.

Example 1.2: Conversion of Concentration Units

For a measured concentration of Ca^{2+} of 8500 ppm, calculate the concentration of Ca^{2+} in units of, *m*, epm, *M*, meq/L, and mg/L (gfw 40.1) in two solutions with different salinity and densities.

	Solution 1	Solution 2
Density	1.03 kg/L	1.16 kg/L
TDS	35,000 mg/L (0.035 kg/L)	240,000 mg/L (0.24 kg/L)
Ca^{2+}	8500 ppm	8500 ppm
	$m_{Ca^{2+}} = \frac{\text{ppm}}{\text{gfw} \times 1000}$	
	$m_{Ca^{2+}} = \frac{8500}{40.1 \times 1000}$	$m_{Ca^{2+}} = \frac{8500}{40.1 \times 1000}$
	$= 0.212$ mol/kg	$= 0.212$ mol/kg
	epm $Ca^{2+} = m \times z \times 1000$	
	$= 0.212 \times 2 \times 1000$	$= 0.212 \times 2 \times 1000$
	$= 424$ eq/kg	$= 424$ eq/kg
	$M_{Ca^{2+}} = m \times (\text{density} - \text{TDS})$	
	$= 0.212 \times (1.03 - 0.035)$	$= 0.212 \times (1.16 - 0.24)$
	$= 0.212$ mol/L	$= 0.195$ mol/L
	meq/L $Ca^{2+} = M \times z \times 1000$	
	$= 0.212 \times 2 \times 1000$	$= 0.195 \times 2 \times 1000$
	$= 424$ meq/L	$= 390$ meq/L
	mg/L $Ca^{2+} = M \times \text{gfw} \times 1000$	
	$= 0.212 \times 40.1 \times 1000$	$= 0.195 \times 40.1 \times 1000$
	$= 8500$ mg/L	$= 7820$ mg/L
	$\therefore$ ppm Ca^{2+} = mg/L Ca^{2+}	$\therefore$ ppm $Ca^{2+} \neq$ mg/L Ca^{2+}

TABLE 1.2
Major Atmospheric Gases and Their Equilibrium Concentration in Fresh Water at 25°C

Gas	*gfw*	Partial Pressure P(atm)	Equilibrium Concentration (ppm)
N_2	28	0.781	14.2
O_2	32	0.209	8.71
H_2O_{vapor}	18	~0.01	—
Ar	40	0.00934	0.522
CO_2	44	0.0004	0.60

Stable Isotopes

J.J. Thompson in 1913 resolved the fractional masses of the elements when he discovered that 90% of neon had mass 20, while about 10% had two additional neutrons and mass 22. Thompson's student Francis Aston began a systematic measurement of naturally occurring stable isotopes of the elements, many of which are now used along with solute concentrations in groundwater studies.

Although the chemical nature of an element is defined by its atomic number and electron configuration, its nuclear nature is defined by its neutron number. Oxygen, for example, typically has 8 protons in its nucleus, with 8 neutrons giving it a weight of 16 atomic mass units (amu). About 0.2% of oxygen nuclides carry an additional two neutrons, making ^{18}O a rare isotope of ^{16}O (Figure 1.5). While this heavier isotope behaves chemically like ^{16}O, its additional weight affects the rate at which it reacts, leading to variations in its abundance in different compounds and reservoirs of oxygen.

Stable isotope concentrations are measured as a ratio of the rare to the abundant isotope and expressed as the difference in this ratio between the sample and a known reference:

$$\delta^{18}O_{sample} = \frac{(^{18}O/^{16}O)_{sample} - (^{18}O/^{16}O)_{reference}}{(^{18}O/^{16}O)_{reference}}$$

This normalized difference between the sample and reference is then multiplied by 1000 to express the measurement in permil (‰) units:

$$\delta^{18}O_{sample} = \left(\frac{(^{18}O/^{16}O)_{sample}}{(^{18}O/^{16}O)_{VSMOW}} - 1 \right) \times 1000\ ‰\ \text{VSMOW}$$

where δ or delta indicates the difference in ratio from the standard, VSMOW (Vienna Standard Mean Ocean Water) is the standard used in this example, and ‰ is the permil notation.

A δ-value that is positive, say, $\delta^{18}O = +10‰$, signifies that the sample has 10 permil or 1% more ^{18}O than the reference, and so is *enriched* in ^{18}O. Similarly, a sample with $\delta^{18}O = -10‰$ has 10‰ or 1% less ^{18}O than VSMOW, and so is *depleted* in ^{18}O.

The routinely measured stable environmental isotopes are given in Table 1.3 along with their average natural abundance and the international references used for their measurement. The list of isotopes used in hydrology is expanding as new methods and advances in mass spectrometry are developed. Helium isotopes ($^3He/^4He$) are

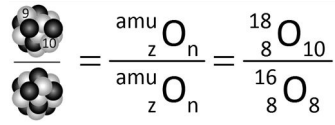

$$= \frac{^{amu}_{z}O_{n}}{^{amu}_{z}O_{n}} = \frac{^{18}_{8}O_{10}}{^{16}_{8}O_{8}}$$

FIGURE 1.5 Oxygen-18 and oxygen-16 and their mass number, amu, atomic number, *z*, and neutron number, *n*.

now often used in studies of groundwater residence time. Others, including ^{9}Li, ^{11}B, ^{37}Cl, and ^{87}Sr, are used to study weathering, sources of salinity, and contaminants.

The δ-‰ notation for stable isotope data is a derived unit of concentration that comes from the requirement to normalize measurements to a reference material for accurate measurements. However, isotope measurements could be expressed in concentration units similar to those used for solutes. For example, the $^{18}O/^{16}O$ abundance or atomic ratio in VSMOW is 0.002005 or 2005 ppm (2005 atoms of ^{18}O per million atoms of ^{16}O or 2009 atoms of ^{18}O per million oxygen atoms (^{16}O plus ^{18}O). Similarly, deuterium in VSMOW has a concentration 150 ppm. Concentrations as mass ratios rather than atomic ratios would be slightly greater than these values. Figure 1.6 adds some clarity to the conversions between δ-‰ and molar units for isotopes.

TABLE 1.3
Stable Environmental Isotopes

Isotope	Ratio	Abundance %	Reference (Abundance Ratio)	Common Sample Types
D or ^{2}H	D/H	0.015	VSMOW (1.5575×10^{-4})	H_2O, CH_4, clays
^{13}C	$^{13}C/^{12}C$	1.11	VPDB (1.1237×10^{-2})	DIC, CO_2, $CaCO_3$, CH_4, organic C
^{15}N	$^{15}N/^{14}N$	0.366	AIR N_2 (3.677×10^{-3})	NO_3^-, NH_4^+, N_2, N_2O
^{18}O	$^{18}O/^{16}O$	0.204	VSMOW (2.0052×10^{-3})	H_2O, NO_3^-, SO_4^{2-}, O_2, minerals
^{34}S	$^{34}S/^{32}S$	4.21	CDT (4.5005×10^{-2})	SO_4^{2-}, H_2S, gypsum, sulfide minerals
^{3}He	$^{3}He/^{4}He$	0.000138	AIR (1.38×10^{-6})	groundwater, minerals
^{6}Li	$^{6}Li/^{7}Li$	7.6	LSVEC (0.08215)	water, brines, minerals
^{11}B	$^{11}B/^{10}B$	80.1	NBS 951 (4.044)	water, brines, minerals
^{37}Cl	$^{37}Cl/^{35}Cl$	24.23	SMOC (0.324)	water, brines, solvents
^{87}Sr	$^{87}Sr/^{86}Sr$	7.0 and 9.8	Direct measurement	water, brines, minerals

VSMOW,Vienna Standard Mean Ocean Water; VPDB, Vienna Pee Dee Belemnite, fossil carbonate; CDT, Canon Diablo Troilite, FeS from meteorite; LSVEC, Lithium carbonate standard (Flesch et al. 1973; Coplen 2011), now also used as a carbonate standard (Coplen et al. 2006); NBS-951, Boric acid standard, also SRM 951, National Bureau of Standards; SMOC, Standard Mean Ocean Chloride.

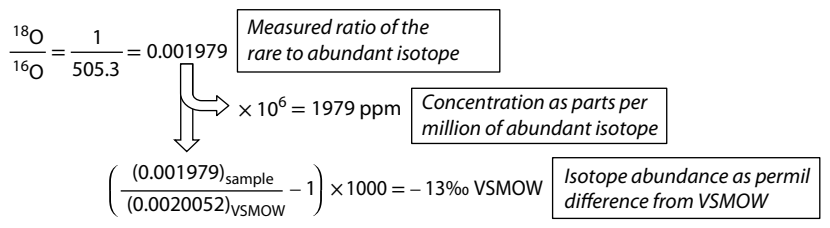

FIGURE 1.6 The concentration of stable isotopes as atomic ratio, as parts per million of the stable isotope and in δ-‰ units relative to Vienna Standard Mean Ocean Water (VSMOW) ($^{18}O/^{16}O_{VSMOW} = 0.0020052$).

Environmental Radioisotopes

The stability of a nuclide is compromised by the addition or subtraction of neutrons. For example, the addition of one neutron to ^{13}C produces the radioisotope ^{14}C with a half-life of 5730 years. Adding one neutron to deuterium produces tritium, T, with a half-life of 12.32 years. The radioisotopes are unstable nuclides that decay with time to a more stable configuration by emission of particles and gamma radiation. Although many radionuclides exist, only a few are currently of interest in hydrogeology. These include radionuclides used for dating and tracing (Table 1.4) and those of concern as radiohazards.

Abundance of radioisotopes in environmental samples can be measured and expressed by either their activity as decay events per time or, like stable isotopes, by their abundance ratio. The becquerel, Bq, is equal to one disintegration per second. This measurement is then normalized to a given sample size, using units of Bq/L for water or Bq/g for solids.

FROM ELEMENTS TO AQUIFERS

The geochemistry of water is to a very large degree controlled by the geosphere—the rocks that host the hydrological and biological processes near the earth's surface. The following is a brief introduction to the elements, minerals, and rocks important to groundwater geochemistry.

Elements and Ions

Each of the 92 natural elements from hydrogen to uranium is defined by its atomic number, z, for the number of positively charged protons (p), in the nucleus. The chemistry of the elements arises from the configuration of the electrons (e^-). In the elemental state, there are equal numbers of electrons and protons, and the atom or molecule carries a net charge of 0. The periodic table (Table 1.5) arranges the elements in rows (periods) for each electron shell, with the sequential filling of the electron shells occurring from left to right. Only with all electron orbitals filled is this outer shell stable, making the element chemically unreactive. This is the case for the six noble

TABLE 1.4
The Common Environmental Radioisotopes in Groundwater

Isotope	Half-life (years)	Decay mode	Atmospheric Ratio	Activity (Bq)	Common Sample Types
^{85}Kr	10.76	β^-	$^{85}Kr/Kr = 2.7 \times 10^{-11}$	1.5 Bq/cc_{Kr}	Dissolved Kr
T or ^{3}H	12.32	β^-	$T/H = 10^{-17}$	0.12 Bq/L	H_2O, CH_2O, H_2
^{39}Ar	269	β^-	$^{39}Ar/Ar = 8.2 \times 10^{-16}$	$1.8.10^{-6}$ Bq/cc_{Ar}	Dissolved Ar
^{14}C	5,730	β^-	$^{14}C/C = 1.18 \times 10^{-12}$	0.226 Bq/g C	DIC, DOC
^{81}Kr	229,000	EC	$^{81}Kr/Kr = 5.2 \times 10^{-13}$	$1.34.10^{-6}$ Bq/cc_{Kr}	Dissolved Kr
^{36}Cl	301,000	β^-	$^{36}Cl/Cl \sim 10^{-13}$	10^{-6} Bq/L (10 ppm Cl)	Cl^-
^{129}I	15.7×10^6	β^-	$^{129}I/I \sim 10^{-8}$	10^{-4} Bq/L (1 ppm I)	I^-, IO_4^-, CH_3I

TABLE 1.5

Periodic Table of the Elements, With Atomic Mass Units (amu), Atomic Number (*z*) and Common Redox States

IA												IIIB	IVB	VB	VI B	VIIB	VIIIB
1 1.01 **H** 0 1	IIA	z amu **H** redox															2 4.00 **He** 0
3 6.94 **Li** 1	4 9.01 **Be** 2											5 10.8 **B** 3	6 12.0 **C** −4 −2 0 4	7 14.0 **N** −3 0 3 5	8 16.0 **O** −2 0	9 19.0 **F** −1	10 20.2 **Ne** 0
11 23.0 **Na** 1	12 24.3 **Mg** 2	IIIA	IVA	VA	VIA	VIIA	← VIIIA →		IB	IIB		13 27.0 **Al** 3	14 28.1 **Si** 4	15 30.1 **P** −3 5	16 32.1 **S** −2 0 4 6	17 35.5 **Cl** −1	18 40.0 **Ar** 0
19 39.1 **K** 1	20 40.1 **Ca** 2	21 45.0 **Sc** 3	22 47.9 **Ti** 4	23 50.9 **V** 5	24 52.0 **Cr** 3 6	25 54.9 **Mn** 2 4	26 55.8 **Fe** 2 3	27 58.9 **Co** 2 3	28 58.7 **Ni** 2	29 63.5 **Cu** 1 2	30 65.4 **Zn** 2	31 69.7 **Ga** 3	32 72.6 **Ge** 4	33 74.9 **As** −3 3 5	34 79.0 **Se** −2 0 4 6	35 79.9 **Br** −1	36 83.8 **Kr** 0
37 85.5 **Rb** 1	38 87.6 **Sr** 2	39 88.9 **Y** 3	40 91.2 **Zr** 4	41 92.9 **Nb** 3 5	42 95.9 **Mo** 4 6	43 98 **Tc** 7	44 101 **Ru** 3 4	45 103 **Rh** 2 3 4	46 106 **Pd** 2 4	47 108 **Ag** 1	48 112 **Cd** 2	49 115 **In** 3	50 119 **Sn** 4,2	51 122 **Sb** 3,5	52 128 **Te** −2 0 4 6	53 127 **I** −1 7	54 131 **Xe** 0
55 133 **Cs** 1	56 137 **Ba** 2	57 139 **La** 3	72 178 **Hf** 4	73 181 **Ta** 5	74 184 **W** 4 6	75 186 **Re** 7	76 190 **Os** 3 4	77 192 **Ir** 2 4 6	78 195 **Pt** 2 4	79 197 **Au** 1 3	80 200 **Hg** 2	81 204 **Ti** 1 3	82 207 **Pb** 2	83 209 **Bi** 3 5	84 209 **Po** 2 4	85 210 **At** −1	86 222 **Rn** 0
87 223 **Fr** 1	88 226 **Ra** 2	89 227 **Ac** 3															

58 140 **Ce** 3	59 141 **Pr** 3	60 141 **Nd** 3	61 145 **Pm** 3	62 150 **Sm** 3	63 152 **Eu** 3	64 157 **Gd** 3	65 159 **Tb** 3	66 163 **Dy** 3	67 165 **Ho** 3	68 167 **Er** 3	69 169 **Tm** 3	70 173 **Yb** 3	71 175 **Lu** 3
90 232 **Th** 4	91 231 **Pa** 5	92 238 **U** 4 6	93 237 **Np** 4 5	94 244 **Pu** 4	95 243 **Am** 3	96 247 **Cm** 3	97 247 **Bk**	98 251 **Cf** 3	99 252 **Es**	100 257 **Fm**	101 258 **Md**	102 259 **No**	103 260 **Lr**

gases (He, Ne, Ar, Kr, Xe, and Rn), found on the right-hand end of each period (Table 1.5). However, the rest of the elements are left with unfilled shells and will shed or acquire electrons to stabilize their valence shells. The gain or loss of these valence electrons produces a negative or positive charge or valence. Elemental hydrogen, for example, has only one electron in its one electron shell, which it shares with another H to complete this shell at two electrons, making H_2. Alone, H sheds its sole electron to become a hydrogen ion, H^+. Elemental oxygen will acquire two additional electrons to complete its outer shell at 8, making a total of 10, with a charge of 2–. In their elemental state, two oxygen atoms share two electrons to make elemental oxygen or O_2.

Although most elements can have a variety of stable or quasi-stable oxidation states, most have only one or two common states in the environment. These are shown for each element in Table 1.5. Major groups of elements in the periodic table can be characterized by their ionization potential and common oxidation state as follows:

Alkali metals (Group IA): Li^+, Na^+, K^+, Rb^+, Cs^+, and Fr^+ always carry a charge of 1+, whether in solution or mineral phase.

Alkaline-earth metals (Group IIA): Be^{2+}, Mg^{2+}, Ca^{2+}, Sr^{2+}, Ba^{2+}, and Ra^{2+} will always be 2+, as solutes and in minerals, with Mg^{2+} and Ca^{2+} as the dominant cations in most waters and rocks.

Rock-forming elements: Al and Si. After oxygen, aluminum and silica are the most abundant elements in the crust. Al, Si, and O form the structure of feldspars, the most abundant mineral group.

Nonmetals: B, C, N, O, Si, P, S, As, Se, and Te. Elements of this group form crystalline solids in their elemental state. The most common, in aqueous and biological systems, C, N, O, P, and S, are important for their electron exchange properties. Carbon, for example, has four common states, 4–, 2–, 0, and 4+, which makes it such a key element in biological reactions.

Transition metals (Groups IIIA to IIB): Including the more common fourth-period members (Ti, V, Cr, Mn, Fe, Co, Ni, Cu, and Zn), share the characteristic of being cations with higher and usually multiple redox states. Iron, for example, is found as either Fe^{2+} or Fe^{3+}. In their elemental state, transition metals possess high electrical conductivity (EC) and metallic bonding.

Halides (Group VIIB): F^-, Cl^-, Br^-, and I^- are found mainly as anions, occurring only rarely in elemental state (e.g., Cl_2 gas in some volcanic gases) or in some organic compounds (Cl, Br, and I). The heaviest, astatine (At), is highly radioactive, with a global abundance of less than a kilogram.

Noble gases (Group VIIIB): He, Ne, Ar, Kr, Xe, and Rn have a fully filled outer shell, making them geochemically inert and so are present as gases under all conditions.

Rare earth elements (REE): lanthanum, La; plus cerium, Ce, to lutetium, Lu. The REEs (also known as the lanthanides) have such uniform geochemical characteristics (e.g., valence of 3+) that they behave as a group in geochemical processes. They are of traditional interest in magmatic and metamorphic studies. REEs are now used in low-temperature aqueous geochemistry to study weathering and transport phenomena.

Actinides: actinium, Ac; thorium, Th; protactinium, Pa; and uranium, U, are the only naturally occurring elements of the actinide series of "superheavies." None are stable. Th and U have long-lived radioisotopes with half-lives on the scale of the age of the earth. Others, like Actinium Transuranic elements, including neptunium (Np) to lawrencium (Lr), have been discovered over the past several decades. Of the naturally occurring actinides, only U is found in significant aqueous concentrations, due to its elevated solubility in the 6+ state. Thorium, by contrast, has an exceedingly low solubility in natural waters. Isotopes of Ac and Pa are generated within the ^{235}U and ^{238}U decay chains.

Distribution of Elements in the Earth's Crust

The order of abundance by weight of elements in the earth's crust is given in Table 1.6. After oxygen, silica, and aluminum, which are the principal components of silicate minerals, we see that iron is the fourth most abundant, followed by the alkali and alkaline-earth elements (Na, K, Ca, Mg). It is these four cations comprise the major cation composition of water. The low solubility of Si, Al, and Fe oxy-hydroxides limits their concentration in most natural waters. The lower crustal abundance of C, S and Cl that comprise the principal anions (HCO_3^-, SO_4^{2-}, Cl^-) is compensated by the high solubility of these species.

The distribution of elements was addressed by the pioneer of modern geochemistry, V.M. Goldschmidt, who classified the elements by their affinities to different geological environments and processes, as an extension of Mendeleev's periodic table. Based on Goldschmidt's classification, naturally occurring elements can be divided according to their affinity to native iron of the core (siderophile), silicate phases of the earth's crust (lithophile), and sulfides of base metal deposits (chalcophile). A final group includes those elements with a tendency to volatilize (atmophile). His

TABLE 1.6
Principal Elements of the Earth's Crust, by Weight

Element	Atomic Number	Crustal Abundance %	Element	Atomic Number	Crustal Abundance ppm
O	8	46.6	P	15	1050
Si	14	27.7	Mn	25	950
Al	13	8.13	F	9	625
Fe	26	5.00	Ba	56	425
Ca	20	3.63	Sr	38	375
Na	11	2.83	S	16	260
K	19	2.59	C	6	200
Mg	12	2.09	Zr	40	165
Ti	22	0.43	V	23	135
H	1	0.14	Cl	17	130

Source: Mason 1966.

divisions were based on observations of meteorites and of metallurgical processes. Some of the common and more notable elements of each division are as follows:

Siderophile elements: Fe, Co, Ni, Pt, Au, C, and P
Lithophile elements: alkalis and alkaline-earths, the halides, Mn, O, Cr, and U
Chalcophile elements: transition metals, including Cu, Zn, Ag, Cd, Hg and Pb, plus S, As, and Se
Atmophile elements: hydrogen (H_2), nitrogen (N_2), and the noble gases

Although elements have preferences of membership in one of Goldschmidt's four groups, many share characteristics with more than one. For example, Fe is the principal element of the siderophile group, yet is also chalcophylic, as pyrite (FeS_2). It is also found as an element in lithophilic, ferromagnesian-silicate minerals. Nonetheless, the classification provides general categories of elemental characteristics in geochemistry. The earth is differentiated according to Goldschmidt's classification, with a siderophilic core, a lithophilic crust, and the volatile phases of the hydrosphere and atmosphere. Chalcophile phases as sulfides are underrepresented, however, and so do not form a discrete sphere.

Rock-Forming Minerals

The principal rock-forming minerals can be classified according to a variety of subdivisions. The following is a classification from the perspective of aqueous geochemistry. Note that these minerals are ideal end-members and normally occur with minor concentrations of other elements. Calcite, for example, will always have a minor component of Mg^{2+}, which substitutes for Ca^{2+} in $CaCO_3$.

Silicates

The two most abundant elements, oxygen (–II) and silicon (+IV), coordinate to form the most abundant minerals in the crust—the silicates. Substitution of the third most abundant element, aluminum (+III), for silica, produces the aluminosilicates. These constitute over half of the minerals in the crust, and form by cooling of high temperature magma. Magma cooling and crystallization produce a series of silicate mineral types ranging from high-temperature forms, including Ca-plagioclase feldspar (anorthite) and mafic minerals rich in Fe and Mg, to lower-temperature (<300°C) minerals with Na and K. Residual silica in the melt forms quartz. The sequence of crystallization during cooling follows Bowen's reaction series, as follows.

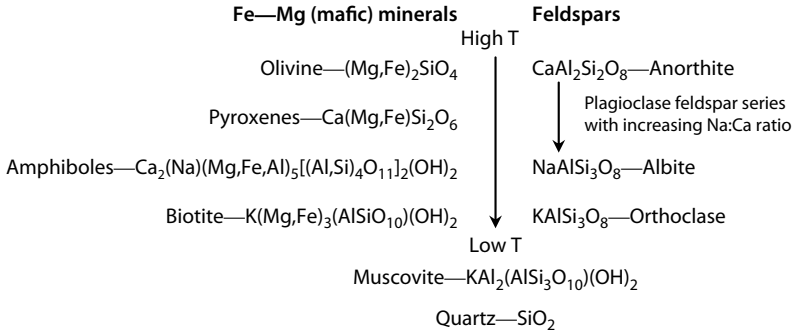

The basalt rocks of oceanic crust are composed principally of mafic minerals and Ca-rich feldspar crystallized from mantle material upwelling along mid-oceanic ridges. The metamorphic shields of most continents and cores of mountain belts are dominated by lower-temperature aluminosilicate rocks. Continental silicate terrains can also include obducted oceanic crust with mafic intrusions and volcanics. Silicates are hard, durable minerals with low solubilities and weather slowly to clay minerals.

Clay Minerals

Clay minerals form the class of minerals known for their sheet structure, the phyllosilicates. They are the weathering product of primary silicate minerals. This can be confused with the geotechnical definition, where mineral particles that are <2 μm in diameter are clay-sized. Although most clay minerals are also of clay size, many clay-sized particles may be quartz or other materials. The common feature of clay minerals is their sheet structure, which has negatively charged boundaries and faces onto which cations can be fixed and exchanged. They are of considerable importance given this affinity for cation exchange, which can affect the geochemistry of groundwater. Clay minerals carry hydroxyl groups (OH^-), derived from their origin through aqueous alteration of aluminosilicate minerals. Serpentine and chlorite are commonly produced by hydrothermal alteration of mafic minerals (olivine and pyroxene). Meteoric alteration of mafic minerals produces smectite clay, while kaolinite and illite commonly form by meteoric weathering of feldspar-rich rocks. Smectites are hydroscopic, bringing water into their inter-sheet positions, while illite and kaolinite do not. Mg, Fe, and Al substitute in the divalent sites (although Al produces a charge imbalance that must be accommodated), and Al commonly substitutes for Si in the tetrahedral sites. The principal clay mineral groups and general formulae are as follows:

Serpentine—$Mg_3Si_2O_5(OH)_4$
Chlorite—$(Mg,Fe,Al)_6(Si,Al)_4O_{10}(OH)_8$
Smectite—$Na(Al,Mg)_2Si_4O_{10}(OH)_2$
Kaolinite—$Al_2Si_2O_5(OH)_4$
Illite—$KAl_2(AlSi_3)O_{10}(OH)_2$

Carbonates

Carbonate rocks are the greatest reservoir of carbon on Earth, comprising over 100,000 times the living biomass equivalent of C. Marine limestone and dolomites can host significant aquifers and so have an impact on the geochemistry of drainage from such regions. Carbonate minerals are also common fracture-filling minerals in crystalline (silicate) or sedimentary rocks. As the carbonate minerals can be formed at low temperature, they are important to the geochemistry of natural waters. There are two principal minerals, calcite and dolomite, with higher-temperature polymorphs as well as less common carbonates. Carbonates are more soluble than silicate minerals, particularly under acidic conditions, and

so will dissolve under near-surface conditions, thus increasing fissure permeability and groundwater circulation.

Calcite—$CaCO_3$
Dolomite—$CaMg(CO_3)_2$
Siderite—$FeCO_3$
Magnesite—$MgCO_3$

Evaporites

Evaporite minerals are the highly soluble salts generally formed by the evaporation of seawater or groundwater in restricted basins. These are most commonly found in certain sedimentary rocks packaged with limestone, dolomite, or shale, formed in Paleozoic seas, although modern evaporites are still forming. An example is the precipitation of some 40 m of halite at the bottom of the Dead Sea over the past 5000 years. However, evaporite minerals may also precipitate from hydrothermal or formation fluids circulating in fractures. The following are some common evaporite minerals:

Sulfates
- Gypsum—$CaSO_4 \cdot 2H_2O$
- Anhydrite—$CaSO_4$
- Celestite—$SrSO_4$
- Mirabilite—$Na_2SO_4 \cdot 10H_2O$
- Epsomite—$MgSO_4 \cdot 7H_2O$
- Jarosite—$KFe_3(SO_4)_2(OH)_6$

Chlorides
- Halite—NaCl
- Sylvite—KCl

Carbonates
- Dolomite—$CaMg(CO_3)_2$
- Nahcolite—$NaHCO_3$
- Natron—$Na_2CO_3 \cdot 10H_2O$
- Nesquehonite—$Mg(HCO_3)(OH) \cdot 2H_2O$
- Trona—$NaHCO_3 \cdot Na_2CO_3 \cdot 2H_2O$

Nitrates
- Nitratine—$NaNO_3$
- Niter—KNO_3

Borates
- Borax—$Na_2B_4O_7 \cdot 10H_2O$
- Boracite—$Mg_3B_7O_{13}Cl$

Phosphates

Phosphate, PO_4, is a minor species in aqueous systems, yet is often the rate-limiting nutrient for photosynthetic activity. The largest reservoir of phosphorous is phosphate in apatite, an accessory mineral in many igneous rocks. Four varieties occur,

depending on the exchangeable anion. Phosphorite formations, marine precipitates of complex calcium phosphates, occur in sedimentary rocks throughout the world. Phosphate can also be complexed by iron in lakes and rivers as low-solubility ferro and ferric phosphates.

Fluorapatite—$Ca_5(PO_4)_3F$
Chlorapatite—$Ca_5(PO_4)_3Cl$
Hydroxylapatite—$Ca_5(PO_4)_3OH$
Carbonate-apatite—$Ca_{10}(PO_4)_6(CO_3)H_2O$
Strengite—$FePO_4{\cdot}2H_2O$
Variscite—$AlPO_4{\cdot}2H_2O$
Vivianite—$Fe_3(PO_4)_2{\cdot}2H_2O$

Sulfides

Sulfide (S^{2-}) is the reduced form of sulfur in the environment, usually present as hydrogen sulfide gas (H_2S) or ionized as HS^-, and is readily complexed by most transition metals. The most common sulfide mineral is pyrite, or iron sulfide. It is an uneconomical accessory mineral in many mining camps that is concentrated in mine tailings and waste rock. Pyrite is ubiquitous in organic rich sediments such as shales and some limestones. Glacial till often contains a small percentage of pyrite exposed by erosion of bedrock. Mackinawite, a more amorphous iron sulfide mineral, can form in low-temperature aqueous settings. With their capacity for oxidation, iron sulfides are important controls on redox, sulfur, and iron geochemistry in natural waters.

Pyrite—FeS_2
Mackinawite—FeS

Other sulfide minerals are the source of most base metals (Cu, Zn, Pb, Ni), which can occur in association with iron sulfide. The most abundant arsenic mineral is an iron sulfide.

Chalcopyrite—$CuFeS_2$
Sphalerite—(Zn,Fe)S
Galena—PbS
Pentlandite—$(Fe,Ni)_9S_8$
Cinnabar—HgS
Arsenopyrite—FeAsS

Oxides and Hydroxides

Oxides and hydroxides of iron and manganese form during weathering of pyrite and mafic minerals. They can form hydrated amorphous deposits on mineral or organic surfaces in soils and fractures or can crystallize to a distinct mineral phase. They can also be found as rock-forming minerals, particularly in metamorphic rocks. In soils they are particularly important as redox buffers and as a negatively charged substrate for adsorption of metals and contaminants.

Magnetite—Fe_3O_4
Hematite—Fe_2O_3
Goethite—FeO(OH)
Ferrihydrite—$Fe(OH)_3$
Pyrolusite—MnO_2
Manganite—MnO(OH)
Pyrochroite—$Mn(OH)_2$

Sediments, Rocks, Aquifers, and Aquitards

Aquifers and aquitards come in many sizes and materials, which affect the geochemistry of groundwaters. The following brief introduction provides only their principal features in the context of their effect on groundwater geochemistry. Readers unfamiliar with the principles of physical hydrogeology are referred to many textbooks covering the subject, such as Freeze and Cherry (1979), Domenico and Schwartz (1998), and Fetter (2001). Formally defined as a water-saturated geological medium capable of storing and transmitting groundwater, aquifers are commonly composed of fine- to coarse-grained porous media or are fractured and dissolution-fissured (karst) bedrock. Aquitards, by contrast, are hydrogeological units that may have high water content but do not readily transmit water. Aquitards are typically low-permeability materials such as clay-rich sediments and shales. Unconfined or phreatic aquifers are the shallowest hydrostratigraphic unit and comprise a saturated zone extending upward to the water table and an overlying unsaturated zone between the water table and ground surface. Unconfined aquifers are generally recharged by infiltration of meteoric waters through the overlying soil and unsaturated zone or by infiltration from adjacent surface water bodies. Atmospheric gases and soil CO_2 exchange with groundwaters through the unsaturated zone. Confined or artesian aquifers are overlain by lower-permeability aquitards. Recharge occurs either by flow from a region where the aquifer "outcrops" and has unconfined conditions or by leakage of groundwater from the adjacent confining aquitard.

Porous aquifers are typically unconsolidated sands and gravels, deposited by fluvial activity or glaciation, but also include sandstone and other lithified strata with intergranular porosity. The volume of pore space or porosity can be up to 20%–30%. Sand and sandstone aquifers are almost always dominated by quartz, which is the most stable of the common clastic minerals, with minor feldspar. Most other major minerals have been dissolved or altered to clays by weathering of parent materials and transport of the clastic sediments. Heavy minerals such as magnetite, zircon, and garnet can also be present. Carbonate minerals are less often present as primary grains but often present as secondary mineralization. Other secondary mineralization often includes ferrihydrite from oxidation of ferrous iron–bearing minerals. Because of the sedimentary nature of unconsolidated aquifers, they can contain buried sedimentary organic matter, which has important considerations for redox reactions in groundwater. This is particularly so for clay-rich aquitards, which typically form in lacustrine or marine settings, with significant input of sedimentary organic debris.

Fractured rock aquifers most often occur in crystalline silicate rocks including plutonic, volcanic, and metamorphic materials. Sedimentary formations such as

shales and sandstones can also be fractured, the latter often with a secondary intergranular porosity, giving such aquifers a dual porosity. Seemingly intact granites and metamorphic rocks can also have a secondary porosity as microfractures and intergranular discontinuities, although these serve more often as a source of solutes rather than significant storage of water. Movement of water and solutes through this porosity is strictly by diffusion but can be a source of salinity to groundwater moving through the open fractures. As silicate minerals have low solubility, fracture development is essentially by tectonic activity.

Although fracture density and aperture vary widely, fractured aquifers invariably have low bulk porosity (volume of fractures per volume of rock), on the order of 1%. The dominant mineralogy of fractured silicate aquifers is feldspar. Granites are composed of potassium and sodium feldspars (alkali feldspars), which are sources of low but significant concentrations Na and K in groundwaters through weathering. Rocks of intermediate to mafic composition are dominated by calcium feldspars and by increasing amounts of Mg-Fe minerals. Basalts make excellent aquifers, due to the dense fracturing from cooling joints and along flow beds, and are principally plagioclase feldspar (Ca and Na) with additional pyroxene and amphibole.

Karst aquifers are among the most exploited freshwater resources in the world. The principal mineral, calcite, is soluble under acidic conditions. This leads to a continual opening of porosity through fissure dissolution. Although dolomite is less soluble, it too provides good aquifer conditions. As groundwater recharging through soils gains carbonic acid through the dissolution of CO_2 in the soil, it is the upper limestone and dolostone surface that is most intensely fissured. Consequently, fissured limestone and dolostone aquifers are often phreatic. Karst groundwaters are dominated by Ca^{2+}, Mg^{2+}, and HCO_3^-. As carbonate aquifers are most often found within sedimentary basins, additional solutes including Na^+, Cl^-, and SO_4^{2-} may be derived from saline pore waters and minor gypsum in the carbonates and/or shaley units.

GEOCHEMICAL AND ISOTOPE ANALYSES

Water-quality analyses vary in terms of completeness, from a basic analysis of major species to a more thorough analysis including isotopes, minor and trace metals, dissolved gases, organic carbon, bacteria, contaminants, and radioactivity. Studies on watershed dynamics and water-resource management may require only a basic geochemical analysis and isotopes to determine groundwater recharge and the origin of salinity. Monitoring for drinking-water quality and detailed studies such as geochemical exploration or contaminated sites characterization would require a more comprehensive list of analytes.

More complex analyses can also be undertaken to determine the speciation or form of the dissolved component, involving filtration at different pore size and selective preservation methods. Radiological parameters may often be measured, usually as gross alpha and gross beta activity or as the activities of specific radionuclides. Radioactivity is now measured in becquerels per liter (Bq/L), where 1 Bq is one disintegration or decay-event per second. Fuels and additives (diesel, BTEX [the benzene-toluene-ethylbenzene-xylene mixture], which constitutes gasoline, and MTBE [methyl tertiary butyl ether], the oxygenate now used to replace lead), perchlorate (ClO_4^-, the

oxidant in solid rocket fuels and fireworks), halogenated carbon compounds (solvents, pesticides, herbicides), and now health-care compounds, artificial sweeteners, and manufactured biopharmaceuticals such as growth hormones can be found in groundwater and are analyzed on a selective basis for water-contamination studies.

Field and Bulk Parameters

The protocols for sampling groundwaters and measurement of field parameters are presented in Chapter 10. The following emphasizes some important points regarding the measurement of unstable parameters such as temperature, pH, and redox potential (Eh), which are, nonetheless, critical to geochemical calculations and interpretations. Examples of field measurements are given in Table 1.7.

The two most important field measurements are temperature and pH. Temperature is an important thermodynamic control on geochemical reactions and mineral solubility. pH is the negative log of the hydrogen ion activity ($pH = -\log a_{H^+}$), which is involved in most geochemical reactions. Although pH can also be measured in the lab, it is often found to change due to changes in temperature or due to degassing of CO_2. Redox potential or Eh is a bulk measurement of electron activity and responds to the dominant redox pair in solution, usually involving elements such as C, S, N, and Fe, which control their form and solubility (e.g., iron occurs as either soluble ferrous iron [Fe^{2+}], or insoluble ferric iron [Fe^{3+}]). Eh is an important parameter

TABLE 1.7
Examples of Geochemical Analyses of Water

Parameter	Rain[a]	River[b]	Groundwater[c]	Seawater	Brine[d]	Water Quality Objectives[e]
Field and bulk measurements						
T(°C)	22	9.8	21.8	—	25	15
pH	5.7	7.58	6.3	~7.0	6.5	6.5 – 8.5
Eh (mV)	380	314	–44	~400	90	—
alkalinity (meq/L)	0.005	1.02	6.31	2.3	0.24	—
EC (µS)	38	125	950	39,000	484,000	—
DO (mg O_2/L)	—	9.2	4.1	8.8	0.1	
Density (kg/L)	1.00	1.00	1.00	1.026	1.25	—
TDS measured (mg/L)	2.85	76.4	525	34,700	280,000	1000
Major ions (ppm)						
calcium—Ca^{2+}	0.62	17.4	92.8	410	73,500	—
magnesium—Mg^{2+}	0.11	3.39	31.6	1290	287	—
sodium—Na^{+}	0.2	3.06	40.5	10,760	29,800	200
potassium—K^{+}	0.01	0.72	3.9	400	272	—
bicarbonate—HCO_3^-	0.29	62	378	142	14.6	—
sulfate—SO_4^{2-}	1.4	8.47	53.7	2700	130	250
chloride—Cl^-	0.31	2.4	58.6	19,350	185,000	250

(*Continued*)

TABLE 1.7 (*Continued*)
Examples of Geochemical Analyses of Water

Parameter	Rain[a]	River[b]	Groundwater[c]	Seawater	Brine[d]	Water Quality Objectives[e]
Isotopes						
$\delta^{18}O_{H_2O}$ ‰ VSMOW	–8.2	–12.6	–5.8	0.0	–13.6	—
δD_{H_2O} ‰ VSMOW	–55	–96	–27	0	–62	—
$\delta^{13}C_{DIC}$ ‰ VPDB	—	–4.5	–12.9	+1.5	–8.0	—
$\delta^{34}S_{SO_4}$ ‰ CTD	+5.6	+6.9	–4.8	+21	+24.6	—
Nutrients (ppm)						
$\delta^{15}NNO_3$	+2.5	—	—	—	—	—
nitrite—NO_2^- as N	—	0.01	<0.01	<0.01	<0.5	1
nitrate—NO_3^- as N	0.31	0.09	<0.01	0.005–2	<0.5	10
ammonium—NH_4^+ as N	0.05	0.08	0.15	<0.1	<0.5	—
phosphate—PO_4^{3-} as P	—	0.29	0.02	<0.05	nd	—
DOC (mg-C/L)	0.05	3.6	7.8	0.3 – 2	nd	—
Minor species (ppm)						
bromide—Br^-	—	0.08	3.2	67	1336	—
fluoride—F^-	—	0.02	1.02	1.3	<1	2
silica—SiO_2	—	3.47	15.1	0.5–10	1.05	—
aluminum—Al^{3+}	—	0.08	0.11	0.001	0.08	0.2
iron—Fe_{total}	—	2.72	0.025	0.002	2.66	0.3
manganese—Mn_{total}	—	0.062	0.015	0.0002	14.1	0.05
strontium—Sr^{2+}	—	0.1	4.55	8.1	1230	—
sulfide—H_2S and HS^-	—	<0.01	0.8	<0.01	<0.01	0.05
Gas—dissolved (ppm)						
oxygen—O_2	—	9.8	18	8	<0.1	
carbon dioxide—CO_2	—	—	300	3.6	7.1	
methane—CH_4	—	—	—	<0.0005	28	
Gas—effervescent (%)						
nitrogen—N_2	—	—	75	—	2	
helium—He	—	—	<1	—	28	
methane—CH_4	—	—	<1	—	64	
carbon dioxide—CO_2	—	—	25	—	<1	

[a] Ottawa, Canada.
[b] Fraser River, British Columbia, Canada.
[c] Amman water supply well in carbonate bedrock, Mukhebeh, Jordan.
[d] Canadian Shield brine, Con Mine, 5300' level, Yellowknife, NT, Canada.
[d] U.S. Environmental Protection Agency (www.epa.gov) and Environment Canada (www.ec.gc.ca).

in biogeochemical transformations of trace metals and nutrients. Dissolved oxygen (DO) is an indication of aerobic or anaerobic redox conditions. In surface waters it can be above the concentration for air-equilibrium due to photosynthetic algae. Deeper groundwaters and groundwaters with high organic carbon contents are typically reducing and have trace to no DO.

Alkalinity and EC are more stable parameters that can be measured later. Alkalinity, discussed in Chapter 6, is a measurement of the acid-buffering potential of a solution and for most groundwaters is a measure of HCO_3^-. Alkalinity measurements are often made in the field to have a measure of the carbonate content of water when sampling for radiocarbon. Similarly, EC is an assessment of water salinity and a useful measurement in the field to help guide further sampling.

Major Ions and Isotopes

In most meteoric waters, the major cations include the alkaline-earths, Ca^{2+} and Mg^{2+}, and the alkali metals, Na^+ and K^+. These four elements are the principal cations of the primary rock-forming minerals, including the silicates (feldspars, micas, amphiboles, and pyroxenes), and the carbonates (calcite and dolomite). The major anions include the carbonate species—HCO_3^- (bicarbonate) and CO_3^{2-} (dissolved carbonate)—commonly derived from weathering by soil CO_2. Sulfate, SO_4^{2-}, is a product of weathering of sulfide minerals and evaporite beds, or from marine sources; and chloride, Cl^-, is a highly soluble ion found in crustal fluids, salt formations, and seawater.

In natural waters, these seven major geochemical species generally constitute over 95% of the TDS. They are derived from mineral weathering and mixing history of natural waters. They also have anthropogenic sources in industrial, municipal, and agricultural activities. The isotopes of water—^{18}O and D—provide complementary perspectives on the origin of the water. Routine analysis now makes these isotopes a component of many geochemical analyses. Similarly, the isotopic content of dissolved inorganic carbon, $\delta^{13}C_{DIC}$, and dissolved organic carbon, $\delta^{13}C_{DIC}$, provides a constraint on the origin of DIC, telling us then about the biogeochemical history of the water.

Minor Species, Nutrients, and Gases

A number of solutes and reactions for carbon, although not contributing significantly to TDS, are nonetheless important in aqueous geochemistry. Some very soluble elements have low aqueous concentrations due to their low crustal abundance (e.g., Li [30 ppm] or I [50 ppb]). Others have high crustal abundance but are limited by their low solubility (e.g., Fe [5%] and Al [8.13%]). Some have low abundance and low solubility (e.g., gold [2 ppb] or the REEs [< ~ 10 ppm]) and are considered to be trace elements.

Minor metals in solution include iron and manganese, which are important redox parameters in many settings. Silica, expressed analytically as SiO_2, and aluminum, Al^{3+}, are contributed from the weathering of silicate minerals. Below about pH 9, Si occurs as the neutral species $H_4SiO_4^\circ$ and so contributes to TDS but not to salinity. Strontium, Sr^{2+}, substitutes for Ca^{2+} in most minerals and so is important for

tracing sources of weathering. Strontium also has the readily measured $^{87}Sr/^{86}Sr$ isotope ratio, which provides an additional constraint on weathering and solute sources. The halide Br^- can be important for tracing sources of salinity and so is often compared with Cl^-. F^- is an important component of a water-quality analysis as it is important for tooth and bone growth but only at low concentration (less than 1 mg/L), beyond which it becomes a health hazard.

Nutrients, including nitrogen species (NO_3^-, NO_2^-, and NH_4^+), phosphate (usually present as HPO_4^{2-}), and DOC are minor constituents in most waters, found at the low ppm to ppb level. They support biogeochemical reactions in groundwaters and surface waters. NO_3^- is a contaminant in drinking water, while NH_4^+ is toxic to fish. Isotopes of these compounds provide insights on their origin and biochemical reactions.

The transition metals and heavy metals (transition metals in the fifth and sixth rows [Table 1.5]) have low crustal abundance and low solubility under oxidizing conditions and so are typically found at only trace (ppb) concentrations in waters. Many are commonly derived from human activities and so have specified water quality objectives (Table 1.8). Redox is an important solubility control that can enhance transport, as in the case of U under oxidizing conditions or Fe under reducing conditions. The analysis of trace metals depends on the objectives of the study and can vary from a select few analytes to a full scan of metals.

Many geochemical analyses include dissolved gases such as O_2, CH_4, H_2S, and CO_2 (determined from pH and alkalinity; Chapter 6), expressed as ppm, which are important in redox reactions and for tracing contamination. While dissolved oxygen is an indicator of aerobic conditions, methane is an indicator of highly anaerobic conditions. A few can be hazardous in water-supply systems. CH_4 can accumulate in household plumbing and can be a fire hazard, while H_2S is highly toxic and can be life-threatening. Very specific studies may analyze the concentration of the noble gases or of the major atmospheric gases O_2, N_2, and Ar, (expressed as ppm or as cm^3 of gas at standard pressure per cm^3 of water; Chapter 2) to reconstruct groundwater recharge conditions. Groundwaters that effervesce can provide a separate gas phase for analysis of the major gases as molar or percent fractions. Dissolved gas concentrations can also be measured, allowing thermodynamic calculations of reactions in the subsurface.

Charge Balance Error

The accuracy of a geochemical analysis can be tested by comparing the total of the negative charges in solution with the total of positive charges. The laboratory analyses are converted to equivalents or milliequivalence units (meq/L = ppm × valence/gfw) for the major and minor species. The difference between the sum of all major cations (Σcat) and anions (Σan) is then compared with the sum of all major ions to give the charge balance error:

$$\text{Charge balance error } (\%) = \frac{\Sigma\text{cat} - \Sigma\text{an}}{\Sigma\text{cat} + \Sigma\text{an}} \times 100$$

TABLE 1.8
Additional Compounds and Parameters Typically Analyzed in Water-Quality Studies and Their Maximum Acceptable Concentration (MAC) in Drinking Water, U.S. Environmental Protection Agency (www.epa.gov) and Environment Canada (www.ec.gc.ca)

Trace elements (mg/L)

Antimony—Sb	0.006[ab]	Chromium—Cr	0.1[ab]	Selenium—Se	0.01[b]
Arsenic—As	0.005[a]	Copper—Cu	1.3[ab]	Thallium—Tl	0.002[a]
Barium—Ba	1[b]	Cyanide—CN^-	0.2[ab]	Silver—Ag	0.05[b]
Boron—B	5.0[b]	Lead—Pb	0.015[a]	Uranium—U	0.02[b]
Beryllium—Be	0.004[a]	Mercury—Hg	0.001[b]	Zinc—Zn	5[ab]
Cadmium—Cd	0.005[ab]				

[a] www.epa.gov
[b] www.ec.gc.ca

Selected Manufactured Organic Pollutants (µg/L)

Atrazine[p]	3	Dioxin [i]	0.00003	Pentachlorophenol[in]	1
Benzeneh[c]	5	Ethylbenzene[hc]	700	Trichloroethylenes	5
Carbon tetrachloride	5	Chlorobenzene[in]	100	Toluene[hc]	1000
2,4–Dh	70	Lindane[h]	0.2	THMs[wc]	100
1,2–Dichloroethanes	5	PCBs[in]	0.5	Vinyl chloride[in]	2

Note: [p]pesticide, [hc]hydrocarbon, [h]herbicide, [s]solvent, [i]incineration, [in]industrial, [wc]water chlorination.

Radiological Parameters (Bq/L)

^{137}Cs	50	^{226}Ra	1	Tritium, T	7000
^{131}I	10	^{90}Sr	10	Gross alpha	0.55

Microorganisms (Colonies per 100 mL)

Total coliform	10	Fecal coliform	0
E. coli	0	*Giardia lamblia*	0

In solutions with a very low or high pH, the concentrations of H^+ or OH^- should be used in the calculation. A charge balance error of less than 5% is acceptable. When errors are greater than 5%, a major contributing species may have been overlooked or not accurately analyzed. An excess of cations may have been analyzed if samples were acidified but not filtered to remove suspended solids. Achieving a good charge balance in low-salinity waters such as surface waters is difficult due to the inherently larger percent error as concentrations approach the detection limit.

Example 1.3: Determination of Charge Balance Error for Geochemical Analyses

Determine the analysis error for these two geochemical analyses of spring waters (values in mg/L).

	pH	Ca^{2+}	Mg^{2+}	Na^{+}	K^{+}	HCO_3^-	CO_3^{2-}	SO_4^{2-}	Cl^-
Spring A	7.55	72.5	32.2	132	10.6	177	0.27	126	213
Spring B	10.40	1.91	0.12	42.5	0.20	19.2	21.1	11.7	10.1
Converting data to meq/L (e.g., Ca^{2+} in Spring A = 72.5/40.1 × 2 = 3.62 meq/L)									
Spring A	7.55	3.62	2.65	5.74	0.27	2.90	0.01	2.62	6.00
Spring B	10.40	0.10	0.01	1.85	0.01	0.31	0.70	0.24	0.28

Calculation of the analysis error is then

$$\text{Spring A charge balance error} = \frac{12.28 - 11.53}{12.28 + 11.53} \times 100 = 3.1\%$$

$$\text{Spring B charge balance error} = \frac{1.97 - 1.78}{1.97 + 1.78} \times 100 = 5.0\%$$

The error for both Spring A and Spring B are quite acceptable, although for Spring B it was necessary to consider the high pH as the high hydroxide concentration (OH^-) makes a significant contribution to the anion total. At pH 10.4, H^+ has an activity of $10^{-10.4}$. Using the dissociation constant for water by the reaction $H_2O \leftrightarrow H^+ + OH^-$, $K_{water} = 10^{-14} = a_{H^+} \times a_{OH^-}$, the OH^- activity increases at this high pH to $10^{-3.6}$ or 0.25 meq/L. When this contribution is added to the 1.53 meq/L of HCO_3^-, SO_4^{2-}, and Cl^- anions, the charge balance error reduces to an acceptable 5.0%.

PROBLEMS

1. What are the four major cations and three major anions in most natural waters? How do these compare with their crustal abundance? What are the three most abundant elements (after oxygen) and why are they not abundant in most natural waters?
2. What are the molal concentrations of Ca^{2+} and SO_4^{2-} resulting from the dissolution of 2 mg of gypsum in 1 kg of water?
3. For each of the water samples in Table 1.7, determine the concentration for Cl^- in the following units: mg/L, ppm, M, and *m*. By what percentage for each water type does Cl^- in mg/L differ from the value in ppm?
4. What is the weight of water in 1 L of the brine in Table 1.7?
5. Calculate the TDS in mg/L for the rain, river water, groundwater, seawater, and brine in Table 1.7, and compare with the measured TDS values. A correction is required for the loss of half of the HCO_3^- as CO_2. Note that for the

high-salinity waters, a correction using density is required to convert the TDS calculated in ppm to mg/L for comparison with the measured TDS values.

6. Using the density relationships in Figure 1.4, plot a diagram with ppm on the x-axis vs mg/L on the y-axis for Cl^- concentration in solutions of NaCl, $CaCl_2$ and $MgCl_2$ up to solutions with 400 g/L TDS. Which chloride salt has the greatest effect on density of the solution? Which has the greatest difference between mg/L and ppm?
7. Colloids are amorphous clusters of ions in waters with elevated salinity. Could colloids contribute to the measured solute concentrations if the water sample has been filtered with the standard 0.45 μm pore-throat filter paper?
8. Runoff water from a sulfur extraction plant has the following geochemical composition: pH = 2.3; Ca^{2+} = 25 mg/L; SO_4^{2-} = 300 mg/L. Does this analysis conform to the law of electro-neutrality?
9. Convert the following geochemical analysis into the following units by completing the following table. Report values to three significant digits only. Are the analytical errors associated with these analyses acceptable?

	Seawater					Hotspring				
T(°C)	25					50				
pH	7.13					8.05				
Density (g/cc)	1.026					1.000				
TDS	35,550					804				
	ppm	*m*	meq/kg	*M*	mg/L	ppm	*m*	meq/kg	*M*	mg/L
Ca^{2+}	410					60.3				
Na^+	10760					180				
K^+	400					7.91				
Mg^{2+}	1290					0.662				
HCO_3^-	142					50.2				
SO_4^{2-}	2700					440				
Cl^-	19350					6.13				
H_4SiO_4	5					59.4				
NO_3^- as N	2					nd				

10. What are the ion concentrations in mg/L and the TDS (mg/L) of a solution with 0.01 mmol/L NaCl, 0.005 mmol/L $CaSO_4$, and 0.05 mmol/L $CaCO_3$?
11. What are the mg/L concentrations of Ca^{2+}, SO_4^{2-}, CO_3^{2-}, and Cl^-, and TDS, in groundwater that has dissolved 1 g/L gypsum, 0.5 g calcite, and 0.05 g calcium chloride?
12. Which of these two groundwaters has the higher meq/L concentration of calcium?
    a. Groundwater with 1 g/L gypsum
    b. Groundwater with 1 g/L dolomite
13. Stable isotopes are measured as ratios of the rare isotope to the abundant isotope, and expressed as the permil difference between the measured ratio and the known ratio of an internationally recognized reference material.

What is the reference material for isotopes of water (^{18}O and D)? What are the $^{18}O/^{16}O$ and D/H ratios for this reference? Calculate the δ-‰ value for groundwater with measured $^{18}O/^{16}O$ and D/H ratios of 0.001975 and 0.000139, respectively.

14. The $^{18}O/^{16}O$ and D/H ratios for groundwater sample were measured and determined to be 0.0019851 and 0.00014391. What are their concentrations expressed as δ-‰ values and in parts per million of the abundant isotope (ppm)?
15. A sample of groundwater has measured stable isotope values of $\delta^{18}O = -6.8‰$ VSMOW and $\delta D = -44‰$ VSMOW. What are the isotope ratios ($^{18}O/^{16}O$ and D/H) for this water?
16. A rainwater sample and snow sample have $\delta^{18}O$ values of $-4.5‰$ and $-15‰$, respectively. Compare their actual isotope abundance ratios and concentrations relative to the abundant isotope.
17. Give an example of a mineral and its geochemical formula for the following:
    a. Primary aluminosilicate
    b. Carbonate
    c. Evaporite
    d. Clay
18. Name the
    a. Three most abundant elements in silicate rocks.
    b. Rock type that represents the greatest reservoir of carbon on Earth.
    c. Most ubiquitous sulfide mineral, and give its formula.
    d. Two dominant aquifer media, and describe their porosity.
19. List the four major cations in natural waters, and give two common minerals that represent a major weathering source for each.
20. For each of the five routinely analyzed light stable isotopes (D, ^{13}C, ^{15}N, ^{18}O, ^{34}S) and referring to materials introduced in this chapter, suggest three different compounds, with their chemical formula, that could be analyzed.

2 Thermodynamics of Aqueous Systems

INTRODUCTION

The geochemistry of groundwater records its recharge and weathering history as well as subsequent mixing and evolution during its time in the subsurface. The gain, transformation, and loss of solutes are controlled by the interaction of the solution with gases, organic compounds, and minerals along the flow path, according to the laws of thermodynamics controlling the transfers of energy and mass in a system.

A system that has moved to a state of minimum free energy is considered to be in thermodynamic equilibrium. Calculating the thermodynamic state of a system allows geochemists to understand what reactions have occurred and predict what reactions might take place. This approach uses the thermodynamic properties of free energy (ΔG), enthalpy (ΔH), and entropy (ΔS) for the components of a system. Thermodynamics allow geochemists to determine, for example, the solubility of metals under changing redox conditions, or the solubility of minerals. This chapter presents the basics of this approach to determining the state of equilibrium and prediction of reaction pathways.

MASS ACTION

Net transfers of mass by geochemical reactions generally proceed in a given direction until an equilibrium condition is achieved. Some reactions, such as the dissolution of high-temperature minerals like olivine or the oxidation, of pyrite, proceed in one direction only at low temperature. Others, like calcite dissolution, are reversible and proceed either forward or backward, depending on the availability of reactants and the concentrations of products. All are governed by the law of mass action.

Law of Mass Action

Geochemical reactions involve the transfer of mass between reactants as solids or solutes with given thermodynamic concentrations or *activities* (a_{reactant}) that are transformed into various products (a_{product}). From an initial condition where the system includes only reactants, the reaction proceeds in a forward direction, and products accumulate in the system:

reactants → *products*	nonequilibrium—net mass transfer from reactants to products
reactants ⇔ *products*	equilibrium reaction—no net transfer of mass

The law of mass action holds that reactions will proceed toward a state of equilibrium between reactants and products that is defined by a thermodynamic constant that is unique to that given reaction:

$$K_{\text{reaction}} = \frac{\text{activity of products}}{\text{activity of reactants}} = \frac{a_{\text{products}}}{a_{\text{reactants}}}$$

Use of a reaction constant as defined by the law of mass action provides the basis to model the interaction of all components in a system and evaluate which reactions are possible and which way they will proceed under given conditions.

The law of mass action applies to the full range of geochemical reactions and allows us to quantify a reaction based on thermodynamics—the gain and release of energy associated with the transfer of mass between reactant and product reservoirs. Low-temperature aqueous geochemistry includes the range of aqueous reactions between solids, solutes, gases, isotopes, and water. The reactants and products can be both inorganic (e.g., dissolved sulfate [SO_4^{2-}]) and organic (e.g., acetate [CH_3COOH]). Low-temperature geochemical reactions can often be abiotic, although many are mediated by bacteria, and some involve the degradation of organic substrates. There are four classes of reactions that can be considered as follows:

Dissociation reactions involve the transfer of mass through the formation and breaking of largely ionic bonds between solutes, acids, and bases.
Oxidation-reduction reactions involve the exchange of electrons between electron donor species and electron acceptors.
Gas solubility reactions are physical, rather than chemical, and consider the total and partial pressures of gases in an aqueous system.
Isotope fractionation reactions are those that partition isotopes of a compound into the reactant or product reservoir during a physical or chemical reaction.

Bonding

Transfers of mass in geochemical reactions involve the breaking and reestablishing of molecular bonds between the various ions, compounds, and charged surfaces in a system. Bonding is due to the coulomb attraction between charges. This force of attraction decreases with the square of the interatomic distance. However, too close and the repulsive force between the two positively charged nuclei exceeds the coulomb force of attraction. This interatomic distance is the bond length, as shown in Figure 2.1, and is most stable at the minimum potential energy in the molecule. Breaking the bond requires energy, usually as heat. Similarly, forming the bond releases heat to the surrounding system.

The atoms of different compounds are typically bonded by varying degrees of electron sharing, ranging from ionic, where no electrons are shared, to covalent, where the valence electrons are equally shared in the orbitals of the outer shell of both atoms. The degree of covalent bonding depends on the difference in *electronegativity* of the elements involved. Electronegativity can be considered to be the force with which an atom can attract electrons to its valence shell. Electronegativity

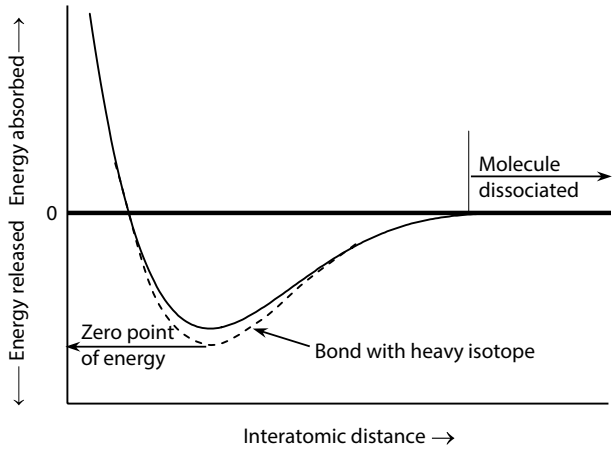

FIGURE 2.1 Potential energy gained and released according to interatomic distance between bonded atoms. The bond length is the distance at which this energy is minimized. The dashed potential energy curve is drawn for a bond that includes a heavy isotope, showing that although the bond length may be the same, the bond strength is greater.

increases toward the right side of the periodic table for elements, but decreases down the periodic table. Thus, the halides (F, Cl, Br, I) and the light nonmetals (B, C, N, O) have the highest electronegativities, while the alkalis (Li, Na, K, Rb, Cs) have the lowest.

Atoms with strongly contrasting electronegativities can share an *ionic* bond between an anion and cation by electrostatic attraction of their opposite charges. Halite (NaCl) is the most common example of ionic bonding, where Na^+ has shed its outer orbit electron, and Cl^- has gained an electron to fill its outer orbit. Ionic bonds are weak, and such minerals have higher solubilities.

Elements with similar electronegativities have greater electron sharing and form *covalent* bonds. Covalent bonds are stronger than ionic bonds, and such minerals are far less soluble. Fully covalent bonding occurs in compounds such as O_2 and N_2 and between the S atoms in pyrite (FeS_2) for example. Bonds between nonmetals with similar electronegativities also bond covalently. The silica cation Si^{4+} forms covalent bonds in tetrahedral coordination with O^{2-} ions, giving silicate minerals like quartz a low solubility.

Oxygen (O^{2-}) and many of the common nonmetal ions (C^{4+}, N^{5+}, Si^{4+}, P^{5+}, S^{6+}) have similar electronegativities, and form very stable, covalently bonded anions (CO_3^{2-}, NO_3^-, SiO_4^{4-}, PO_4^{3-}, and SO_4^{2-}). Predominantly ionic bonding with Group 1 and Group 2 cations (e.g., Na^+, K^+, Ca^{2+}, Mg^{2+}) gives the basic mineral groups discussed in Chapter 1. Nitrate compounds, like KNO_3 (saltpeter), are bonded by a single-charge ionic bond, and so the nitrate salts are among the most soluble. Similarly, ionic bonding between Ca^{2+} and SO_4^{2-} or CO_3^{2-} accounts for the relatively high solubility of gypsum and calcite.

Weak *van der Waals* forces exist between all atoms and are unrelated to charge or electronegativity. Such forces hold together the sheets of phylosilicates (micas and clays) and cause the flocculation of colloids in high-salinity solutions.

Water has one very important bond—the hydrogen bond, introduced in Chapter 1. This is the weak attractive force between polar H_2O molecules that provides the tetrahedral structure of condensed water and ice. The strength of the hydrogen bond differs for the heavy and light isotopes of water (^{18}O and D; Figure 2.1) and is responsible for the distribution of these isotopes throughout the hydrological cycle.

Equilibrium and Nonequilibrium States

The law of mass action considers a system to be in equilibrium when forward and backward reactions proceed at the same rate. Equilibrium reactions are typically written with a double arrow, ⇔, and so there is no net flux of mass from one side of the reaction to the other. For example, when halite is placed in pure water to dissolve, initially there is a net flux from the mineral to the solution. At the same time, Na^+ and Cl^- ions in solution can combine and reprecipitate on the mineral surface. The rate of this reverse reaction depends on the Na^+ and Cl^- concentrations in solution and will accelerate as dissolution proceeds. Accordingly, the flux of Na^+ and Cl^- into solution will slow down over time (Figure 2.2). At the point of equilibrium, both forward and reverse reactions will have the same rate, and there will be no net mineral dissolution. There is, however, mass flux in both directions, and this is relevant to isotope exchange between water, solutes, minerals, and gases.

A reaction that proceeds preferentially in one direction is in a nonequilibrium state, typically written with a one-way arrow, →. This is the case where reaction products are not sufficiently concentrated for significant reverse reaction. It is also the case for reactions where the reaction products are removed by some physical or chemical process, such as most redox reactions (e.g., methanogenesis by bacteria, or pyrite oxidation). Reactions can also be impeded by problems of nucleation and the activation energy required for a reaction to initiate, leading to a state of oversaturation.

Rates of reactions that involve changes of phase, such as mineral precipitation, can be impeded by the rates of diffusion between the reaction surface and the bulk reservoir. In groundwaters where the distances between particles or

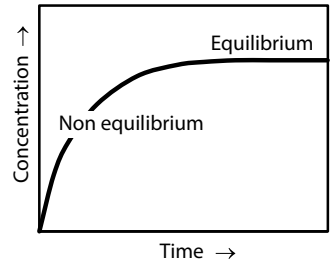

FIGURE 2.2 Kinetic and equilibrium reaction, shown schematically by the rate of increase of a solute as its salt dissolves.

fracture surfaces are short, diffusion through the bulk solution is fast and will not impede rates of reaction on the solid surfaces. However, diffusion of CO_2, for example, out of a river into the open atmosphere, may be much slower than the rates of reaction producing it in the water column, and so lake water will be overpressured and out of equilibrium with the adjacent atmosphere. Purely aqueous reactions, such as the hydration of CO_2 and dissociation of carbonic acid, are not constrained by an interface or long diffusion distances and so achieve equilibrium almost immediately.

ION ACTIVITY AND EQUILIBRIUM CONSTANTS

Calculations of mineral solubility, solute concentrations, and the geochemical forms or speciation of these solutes are based on equilibrium thermodynamics. Natural geochemical systems are dynamic and evolving and hence are seldom in complete equilibrium. Nonetheless, the state of equilibrium provides a condition to determine the direction that a geochemical system is moving, according to the law of mass action. If, for example, the concentrations of Ca^{2+} and SO_4^{2-} in groundwater are lower than at the point of gypsum ($CaSO_4{\cdot}2H_2O$) saturation, gypsum (if present) will dissolved until equilibrium is reached. Similarly, if the partial pressure of a dissolved gas is greater than its atmospheric partial pressure, it will degas until the equilibrium partial pressure is reached.

To evaluate the state of equilibrium for a given reaction, the approach is based on the activities (a) of reactants and products and the equilibrium reaction constant (K). Activities of geochemical species are their thermodynamic concentration, that is, the effective concentration that defines its ability to participate in a reaction. This differs from its analytical concentration, which is a measure of the total concentration of that species in solution.

Activities and Activity Coefficients

In aqueous solutions, ions interact electrostatically with other oppositely charged ions, allowing them to form ion complexes and minerals. The potential for reaction for a given ion increases with its concentration. However, at the same time, its potential decreases as the density of other charges in solution goes up, due to increased electrostatic interaction with the ion of interest. For example, the potential for Ca^{2+} and SO_4^{2-} in Figure 2.3 to interact in an Na^+-Cl^- solution decreases as the concentration of the Na^+-Cl^- solution increases, due to the enhanced electrostatic interactions of Ca^{2+} and SO_4^{2-} with all the additional negative and positive charges.

The increase in charge density is the *ionic strength* (I) of the solution. The effective ion concentration in solution is ion *activity* (a_i), and in most solutions is less than its true concentration or molality, m_i (mol/kg). Although ion activities have values similar to concentration, they are in fact unitless. They are related to solute concentrations through the activity coefficient, γ, which has units of inverse concentration, or kg/mol.

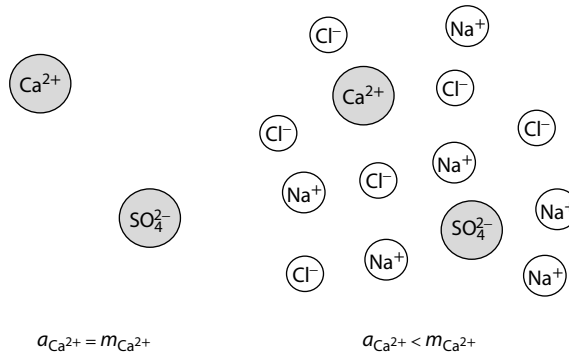

FIGURE 2.3 The activity–concentration relationship for solutes in a low-salinity (low ionic strength) solution and a high-salinity (high ionic strength solution).

$$a_i = m_i \times \gamma_i \left(\text{mol/kg} \times \text{kg/mol}\right)$$

In low-salinity water, the activity coefficient, γ, is close to 1, and so ion activities have the same numeric value as their concentration. However, as salinity increases, the activity coefficient decreases, and the ion activity become a fraction of the ion concentration (Figure 2.3). The values for γ and a decrease not only with increasing salinity, but also they are lower for ions with higher charge. Some notes on activity coefficients are as follows:

- $\gamma \approx 1$ for ions in fresh waters.
- γ and therefore a decrease with increasing salinity, but reverse to values greater than 1 for brines.
- $\gamma = 1$ for uncharged species (e.g., $H_4SiO_4^\circ$ or $H_2CO_3^\circ$) and dissolved gases.
- $\gamma_{H_2O} < 1$ for waters with high ionic strength.

The activity of an ion is reduced through electrostatic interactions with other ions in higher-salinity waters and so γ is a function of the *ionic strength* (I) of the solution (Figure 2.3). Ionic strength is calculated from the sum of the molalities of all major ions in solution times the square of their valence,

$$I = \tfrac{1}{2} \sum m_i z_i^2$$

where z is the charge of the i^{th} ion
m is the molality of the i^{th} ion

Example 2.1: Ionic Strength for Different 1 Molal Salt Solutions

What is the ionic strength of a 1 m solution of

NaCl

$$I = \tfrac{1}{2}(m_{Na^+} z^2_{Na^+} + m_{Cl^-} z^2_{Cl^-})$$
$$= \tfrac{1}{2}(1 \times 1^2 + 1 \times 1^2)$$
$$= 1$$

Na_2SO_4

$$I = \tfrac{1}{2}\left(m_{Na^+} z^2_{Na^+} + m_{SO_4^{2-}} z^2_{SO_4^{2-}}\right)$$
$$= \tfrac{1}{2}(2 \times 1^2 + 1 \times 2^2)$$
$$= 3$$

What is the ionic strength of the following groundwater?

Ca^{2+}—86 ppm	HCO_3^-—280 ppm
Mg^{2+}—33	SO_4^{2-}—120
Na^+—24	Cl^-—37
K^+—3.2	

$$I = \tfrac{1}{2}\left(4m_{Ca^{2+}} + 4m_{Mg^{2+}} + m_{Na^+} + m_{K^+} + m_{HCO_3^-} + 4m_{SO_4^{2-}} + m_{Cl^-}\right)$$
$$= \tfrac{1}{2}\left(4\left[86/40.1/1000\right] + 4\left[33/24.3/1000\right] + \ldots\right)$$
$$= 0.013$$

Debye and Hückel (1923) developed the fundamental relationship between activity coefficients and ionic strength, showing γ to be related to z and I in dilute solutions:

$$\log \gamma_i = -0.5 z_i^2 \sqrt{I} \qquad \text{Debye–Hückel limiting law for dilute solutions}$$

This model of an infinitely small charge interacting in solution breaks down in higher-salinity waters ($I > 0.01$ or >~1000 mg/L TDS [total dissolved solids]), and the hydrated radius of the ion (å in angstrom units or = 10^{-8} cm) must be taken into account with the Debye-Hückel equation, shown plotted in Figure 2.4.

$$\log \gamma_i = \frac{-0.51 z_i^2 \sqrt{I}}{1 + 0.33 \text{å}_i \sqrt{I}} \quad \text{Deby–Hückel equation for electrolytes to I = 0.1 m}$$

Values for the hydrated diameter of the common ions are as follows:

å = 2.5—NH_4^+
3.5—K^+, Cl^-
4.0—Na^+
5.0—Ca^{2+}, SO_4^{2-}, Sr^{2+}, Ba^{2+}
5.5—Mg^{2+}, HCO_3^-, CO_3^{2-}

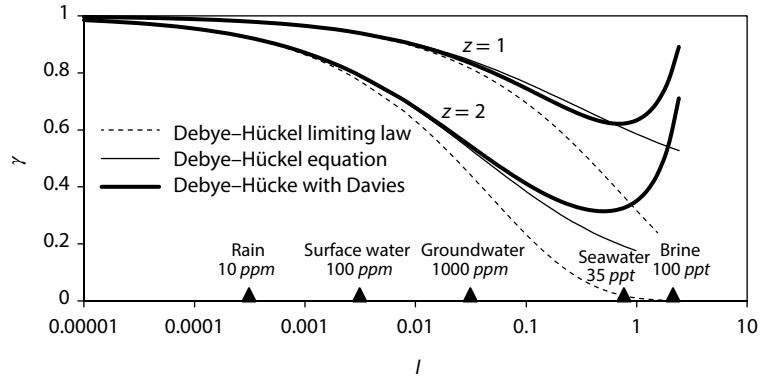

FIGURE 2.4 Activity coefficient γ for monovalent ($z = 1$) and divalent ($z = 2$) ions, as a function of ionic strength. The Debye–Hückel limiting law model is acceptable to $I \sim 0.01$, which includes waters up to a total dissolved solids of about 500 ppm. Higher ionic strength waters are more accurately modeled using the Debye–Hückel, with the Davies coefficient, up to the salinity of brine ($I > 1$). The Debye–Hückel equation requires the hydrated ionic radius, å, which in this graph was set at 5 (Ca^{2+}, SO_4^{2-}).

Davies (1962) resolved departures of the Debye–Hückel equation from measurements made for brines, with the constant (0.3I). The Debye–Hückel configured with the Davies constant is valid for solutions up to ionic strength of about 1 (i.e., about 2× seawater):

$$\log \gamma_i = \frac{-0.51\, z_i^2 \sqrt{I}}{1 + 0.33 \text{å}_i \sqrt{I}} + 0.3I \qquad \text{Debye–Hückel equation Davies constant}$$

Activity of Water and Minerals

Convention holds that the activity of solids and liquids are based on mole fraction rather than concentration. Accordingly, pure mineral phases, such as calcite ($CaCO_3$) would have an activity of 1 in thermodynamic calculations. However, substitution of ions occurs during crystal growth, producing mixtures such as strontium (Sr) replacing Ca in calcite. The resulting impure mineral will have an activity that is directly proportional to its molar percent of the solid phase. For example, if $SrCO_3$ represented 5% of the total calcite mineral, then the activity of calcite (a_{CaCO_3}) would be 0.95 rather than 1. The mole fraction for minerals and liquids is then the counterpart to the activity coefficient for solutes. In most mineral solubility calculations, only pure mineral phases are considered with activities taken to be 1.

Pure water itself has an activity of 1 (although its molality, $m_{H_2O} = 55.6$ mol/kg, is determined by dividing 1000 g by its gfw of 18). However, the activity of water also decreases with increased salinity due to the partitioning of water molecules from the open solution into ion hydration sheaths. In seawater, for example, $a_{H_2O} = 0.98$ but drops closer to 0.8 in concentrated brines.

Activities in Brines

The activities of solutes and of water in solutions of high ionic strength experience reversals that affect the solubilities of minerals and the formation of complex ions. In Figure 2.4, the activity coefficients for monovalent and divalent ions reach minimum values at ion-strength values near that of seawater. With increasing I, activity coefficients begin to increase, and, within the range of brine, become greater than 1. In conjunction with this reversal is the enhancement of ion–ion interactions, including not just binary interactions but ternary interactions as well. This leads to the creation of additional complex ions in the solution and a reduction in the activity of uncomplexed species involved in mineral precipitation reactions.

Predicting the solubility of minerals and stability of aqueous complexes becomes far more complicated than for low-salinity systems. Ion interactions in brines have been successfully modeled by calculating excess Gibbs free energy, according to Pitzer (1973). Pitzer equations are now incorporated into computer codes for evaluating speciation and mineral solubilities in brines now (Plummer et al., 1988), discussed below.

Equilibrium Reaction Constant *K*

The law of mass action holds that the activities of reactants and products in an equilibrium reaction are defined by a thermodynamic reaction constant, K, where

$$K = \frac{\text{activity of products}}{\text{activity of reactants}}$$

For example, consider (1) a generic reaction where compound AB_2 dissociates into one mole of A and 2 moles of B, and (2) the dissolution of gypsum.

$$AB_2 \Leftrightarrow A + 2B \qquad CaSO_4{\cdot}2H_2O \Leftrightarrow Ca^{2+} + SO_4^{2-} + 2H_2O$$

$$K_{AB_2} = \frac{a_A \times a_B^2}{a_{AB_2}} \qquad K = \frac{a_{Ca^{2+}} \times a_{SO_4^{2-}} \times a_{H_2O}^2}{a_{CaSO_4{\cdot}2H_2O}}$$

K is used for a variety of reactions with various designations. In all cases, it remains as the thermodynamic constant K for any reaction under equilibrium conditions, as follows:

K_{eq} The equilibrium thermodynamic reaction constant.
K_T Equilibrium thermodynamic reaction constant. Subscript T is for thermodynamic constant.
$K_{10°}$ Reaction constant for a specified temperature.
K_{sp} Solubility product, for mineral dissolution reactions.
K_1 First dissociation constant for dissociation reaction.

K_{sp} for mineral dissolution reactions provides an indication of solubility. A large value for K_{sp} indicates high activities of products in solution, whereas a small value indicates low solute activities, as contrasted by the K_{sp} values for highly soluble halite and low-solubility fluorite:

$$NaCl \Leftrightarrow Na^+ + Cl^- \qquad CaF_2 \Leftrightarrow Ca^{2+} + 2F^-$$

$$K = \frac{a_{Na^+} \times a_{Cl^-}}{a_{NaCl}} = 10^{1.58} \qquad K = \frac{a_{Ca^{2+}} \times a_{F^-}^2}{a_{CaF_2}} = 10^{-10.6}$$

For a first-order approximation, we can estimate the activity coefficients to be close to 1, which assumes that ion activity is equal to ion concentration ($a_i = m_i$). Substituting the stoichiometric relationship for these halides into the *K*-equation,

$$10^{1.58} = a_{Na^+} \times a_{Cl^-} \approx m_{Na^+} \times m_{Cl^-} \qquad 10^{-10.6} = a_{F^-}^2 \times a_{Ca^{2+}} \approx m_{F^-}^2 \times m_{Ca^{2+}}$$

$$m_{Na^+} = m_{Cl^-} \qquad m_{Ca} = \tfrac{1}{2} m_{F^-}$$

$$10^{1.58} \approx m_{Cl^-} \times m_{Cl^-} \approx m_{Cl^-}^2 \qquad 10^{-10.6} \approx m_{F^-}^2 \times m_{Ca^{2+}} \approx m_{F^-}^2 \times \tfrac{1}{2} m_{F^-}$$

$$m_{Cl^-} \approx 10^{0.79} \quad \text{or} \quad 6.17 \text{ mol/kg} \qquad m_{F^-} \approx \left(2 \times 10^{-10.6}\right)^{1/3} \approx 0.00037 \text{ mol/kg},$$

giving $Cl^- \approx 219{,}000$ ppm and $F^- \approx 7$ ppm.

Thus, a halite-saturated solution would be far more saline than water in equilibrium with fluorite. The precision of these calculations is improved by calculating the ionic strength, *I*, and then the activity coefficients, γ, as demonstrated below in Example 2.3. The actual aqueous concentrations of these ions are greater than their activities from γ and *I*.

Gibbs Free Energy and Determination of *K*

Geochemical calculations are based on equilibrium thermodynamics—the interaction of molecules under the influence of enthalpy. Geochemical reactions are governed by the changes (Δ) of energy between reactants and products, expressed as *Gibbs free energy,* Δ*G*. Reactions will tend to proceed toward a state of lower free energy, with a release of heat (heat content or enthalpy, Δ*H*, in units of kJ/mol) or an increase in disorder (entropy, Δ*S*, in units of kJ/mol·K), or some combination of both.

$$\Delta G = \Delta H - T\Delta S$$

A geochemical system having a minimum of free energy, where $\Delta G = 0$, is considered to be in thermodynamic equilibrium.

All minerals, gases, geochemical species, and the various phases of water itself have a standard (°) Gibbs free energy of formation $\Delta G°$, measured in kJ/mol. This is the change in free energy when forming one mole of the compound or ion from

its component elements in their elemental states. By convention, all elements in their elemental state (e.g., O_2, S or zero-valence metals, such as Fe°), as well as protons, H^+, and electrons, e^-, have $\Delta G° = 0$. Compounds not in their elemental state will have positive or negative $\Delta G°$ values, depending on whether they require or release energy in their formation from an elemental state. Sulfur species provide an example, as follows:

Sulfide, S^{2-}	$\Delta G°_{S^{2-}} = 85.9$ kJ/mol
Elemental sulfur, S	$\Delta G°_{S} = 0$ kJ/mol
Sulfur dioxide, SO_2	$\Delta G°_{SO_2} = -300.1$ kJ/mol
Sulfate, SO_4^{2-}	$\Delta G°_{SO_4^{2-}} = -744.0$ kJ/mol

Reduction of sulfur (valence 0) to sulfide (valence –II) requires an input of 85.9 kJ of energy per mole. By contrast, 300 kJ of energy is released per mole in converting native sulfur to SO_2 (valence +IV) or in oxidizing sulfide minerals like pyrite to SO_4^{2-} (+VI), a reaction that provides energy for *Thiobacillus thiooxidans* bacteria.

From the standard Gibbs free energies of formation for reacting compounds, we can calculate the standard Gibbs free energy of any reaction, $\Delta G_r°$ that allows determination of the equilibrium reaction constant K. The value for $\Delta G_r°$ in any reaction is equal to the sum of $\Delta G°$ for all products minus the sum of all reactants:

$$\Delta G_r^o = \Sigma \Delta G^o_{products} - \Sigma \Delta G^o_{reactants}$$

The standard Gibbs free energy of the reaction is related to the activities of the reacting components through the gas constant R (8.3143 J/mol·K or 0.0083143 kJ/mol·K) and temperature (298.16 K). Using the examples of reactions from above, the determination of K follows accordingly:

$bB + cC \Leftrightarrow dD + eE$	$CaSO_4{\cdot}2H_2O \Leftrightarrow Ca^{2+} + SO_4^{2-} + 2H_2O$
$\Delta G_r^o = -RT \ln \dfrac{a_D^d \times a_E^e}{a_B^b \times a_C^c}$	$\Delta G_r^o = -RT \ln \dfrac{a_{Ca^{2+}} \times a_{SO_4^{2-}} \times a_{H_2O}^2}{a_{CaSO_4{\cdot}2H_2O}}$
$K = \dfrac{a_D^d \times a_E^e}{a_B^b \times a_C^c}$	$K_{gypsum} = \dfrac{a_{Ca^{2+}} \times a_{SO_4^{2-}} \times a_{H_2O}^2}{a_{CaSO_4{\cdot}2H_2O}}$
$\Delta G_r^o = -RT \ln K$	$\Delta G_r^o = -RT \ln K_{gypsum}$

Substituting values for R and T and converting from natural logarithm to $\log_{10}$ give the simple relationship between the standard Gibbs free energy of reaction and the equilibrium reaction constant:

$$\log K = -\frac{\Delta G_r^o}{5.708} \quad (\Delta G \text{ in kJ/mol})$$

$$\text{or using calories, } \log K = -\frac{\Delta G_r^o}{1.364} \quad (\Delta G \text{ in kcal/mol})$$

The conversion for free energy data from calories is based on 1 J = 4.187 cal. Since ΔG°_r can be calculated from free energy data available for most geochemical species, the equilibrium constant, K, for any reaction can be determined. This calculation is shown for K_{gypsum} in Example 2.2. Values of ΔG° for a range of ions and compounds used in this and subsequent chapters are given in Table 2.1. From the calculation of K for geochemical reactions, it is then possible to calculate mineral solubility, ion activities and ion concentrations, and speciation for equilibrium conditions. Example 2.3 shows these calculations for the dissolution of gypsum.

Example 2.2: Determining the Equilibrium Reaction Constant K from ΔG° Data in Table 2.1.

Case 1: What is the solubility product K_{sp} for gypsum?

$$CaSO_4 \cdot 2H_2O \Leftrightarrow Ca^{2+} + SO_4^{2-} + 2H_2O$$

$$K_{gypsum} = \frac{a_{Ca^{2+}} \times a_{SO_4^{2-}} \times a_{H_2O}^2}{a_{gypsum}} = a_{Ca^{2+}} \times a_{SO_4^{2-}}$$

$$\Delta G_r^\circ = \Delta G^\circ_{Ca^{2+}} + \Delta G^\circ_{SO_4^{2-}} + 2\Delta G^\circ_{H_2O} - \Delta G^\circ_{gypsum}$$

$$= (-552.8) + (-744.0) + 2(-237.14) - (-1797.36)$$

$$= 26.28 \text{ kJ / mol}$$

$$\log K_{gypsum} = -\frac{\Delta G_r^\circ}{5.708}$$

$$= -\frac{26.28}{5.708} = -4.60$$

Thus, $K_{gypsum} = 10^{-4.60}$

Case 2: What is the dissociation constant of water?

$$H_2O \Leftrightarrow H^+ + OH^-$$

$$K_{H_2O} = a_{H^+} \times a_{OH^-}$$

$$\Delta G^o = 0 + (-157.2) - (-237.14)$$

$$= 79.94 \text{ kJ/mol}$$

$$\log K_{H_2O} = -\frac{\Delta G_r^\circ}{5.708}$$

$$= -\frac{79.94}{5.708}$$

$$= -14.00$$

$$K_{H_2O} = 10^{-14.00}$$

Example 2.3: Mineral Dissolution and Ion Activity

How much gypsum can be dissolved in pure water (ignoring the effects of complex species such as $CaSO_4^\circ$ or HSO_4^-)?

Step 1 Calculate the solubility product K_{sp} for gypsum from Gibb's free energy data. From Example 2.2, this was determined to be $10^{-4.60}$ at 25°C.

Step 2 Calculate the activities of Ca^{2+} and SO_4^{2-} following the dissolution of gypsum to saturation at 25°C.

From the gypsum dissolution equation above, K_{sp} is defined as:

$$K_{gypsum} = \frac{a_{Ca^{2+}} \times a_{SO_4^{2-}} \times a_{H_2O}^2}{a_{gypsum}} = 10^{-4.60}$$

$a_{gypsum} = 1$ (activities of pure solids are 1 by convention)
$a_{H_2O} = 1$ (also by convention)

$$\therefore a_{Ca^{2+}} \times a_{SO_4^{2-}} = 10^{-4.60}$$

and so $a_{Ca^{2+}} = a_{SO_4^{2-}} = \sqrt{10^{-4.60}} = 10^{-2.30} = 0.005$

Step 3 These activities are now used to calculate the concentration of Ca^{2+} and SO_4^{2-} in molality, m (mg/kg) using activity coefficients γ, calculated from ionic strength, I. This is done by iteration, calculating I, then γ, for Ca^{2+} and SO_4^{2-} and then m. I is then recalculated with the new values for $m_{Ca^{2+}}$ and $m_{SO_4^{2-}}$ and iterating until convergence on a stable value for I. The solution is simplified considering both Ca^{2+} and SO_4^{2-} have $z = 2$, and for gypsum dissolution, $m_{Ca^{2+}} = m_{SO_4^{2-}}$. As a first approximation of I, assume that $a = m$.

$$I \cong \tfrac{1}{2}\,(m_{Ca^{2+}} \times 2^2 + m_{SO_4^{2-}} \times 2^2)$$
$$\cong 0.5\,(0.005 \times 4 + 0.005 \times 4)$$
$$\cong 0.02$$

Using the Davies equation to calculate activity coefficients and the hydration radius of 5.0 for Ca^{2+} and SO_4^{2-}:

$$\log \gamma_{ca^{2+}} = \log \gamma_{SO_4^{2-}} = \frac{-0.5 \times 2^2 \sqrt{0.02}}{1 + 0.33\,(5.0)\sqrt{0.02}} + 0.3 \times 0.02 = -0.2233$$

$$\gamma_{ca^{2+}} = \gamma_{SO_4^{2-}} = 0.60$$

Then calculating molality from $m = \dfrac{a}{\gamma}$:

$$m_{Ca^{2+}} = m_{SO_4^{2-}} = \frac{a_{Ca^{2+}}}{\gamma_{Ca^{2+}}} = \frac{0.005}{0.60} = 0.0083 \text{ mol/kg}$$

Recalculating I using this new estimate of molality, then γ and m again gives

$$I \cong 0.5\,(0.0083 \times 4 + 0.0083 \times 4) = 0.033$$
$$\gamma_{Ca^{2+}} = \gamma_{SO_4^{2-}} = 0.54$$

$m_{Ca^{2+}} = m_{SO_4^{2-}} = 0.0093$ mol/kg (2nd iteration)

Repeating the calculations:

$$I \cong 0.5\ (0.0093 \times 4 + 0.0093 \times 4) = 0.037$$
$$\gamma_{Ca^{2+}} = \gamma_{SO_4^{2-}} = 0.52$$

$m_{Ca^{2+}} = m_{SO_4^{2-}} = 0.0096$ mol/kg (3rd iteration)

By the 4th iteration, these calculations have converged on a solution of 0.0096 mol/kg. Thus, 0.0096 moles or 0.0096 × 172.2 = 1.65 g of gypsum (gfw = 172.2) can be dissolved per kg of fresh water, with a final Ca^{2+} concentration of 384 ppm.

TABLE 2.1
Standard Gibbs Free Energy Data for Some Common Aqueous Species, Gases, and Minerals (kJ/mol)

Species	$\Delta G°$	Species	$\Delta G°$	Species	$\Delta G°$
Ag^+	+77.1	F^-	–281.5	MnO_2	–465.14
$Al_2Si_2O_5(OH)_{4\ kaolinite}$	–3799.7	Fe^{3+}	–8.56	$NH_{3(g)}$	–16.5
$Al(OH)_{2\ gibbsite}$	–1157.9	Fe^{2+}	–82.88	$NH_{3(aq)}$	–26.5
Ba^{2+}	–555.36	$Fe(OH)^{2+}$	–233.2	NH_4^+	–79.31
$BaCO_{3\ witherite}$	–1132.21	$Fe(OH)_2^+$	–450.5	NO_3^-	–108.74
$BaSO_{4\ barite}$	–1362.2	$Fe(OH)_3$	–648.3	NO_2^-	–32.2
$CO_{2\ (gas)}$	–394.4	$Fe(OH)_4^-$	–833.83	$N_2O_{(g)}$	104.3
H_2CO_3	–623.14	$Fe(OH)_{2\ amorphous}$	–486.5	Na^+	–262.0
HCO_3^-	–586.8	$Fe(OH)_{3\ ferrihydrite}$	–692.07	$NaAlSi_3O_{8\ albite}$	–3711.5
CO_3^{2-}	–527.9	$Fe(OH)_{3\ ferrihydrite}$	–692.07	$NaCl_{\ halite}$	–384.18
$CH_2O_{\ carbohydrate}$	–129.7	$Fe_2O_{3\ hematite}$	–742.8	HS^-	12.08
$CH_{4\ methane}$	–50.7	$FeCO_{3\ siderite}$	–673.05	S^{2-}	85.8
$CH_3COOH_{\ acetate}$	–392.52	$FeS_{2\ pyrite}$	–166.9	$H_2S_{(aq)}$	–27.83
$C_6H_{6\ benzene}$	124.5	$H_2O_{\ liquid}$	–237.14	$SO_{2(g)}$	–300.1
$(CH_3)_3COCH_{3\ MTBE}$	–236.34	$H_2O_{\ vapor}$	–228.58	SO_4^{2-}	–744.0
Ca^{2+}	–552.8	OH^-	–157.2	HSO_4^-	–755.3

Species	$\Delta G°$	Species	$\Delta G°$	Species	$\Delta G°$
$CaCO_{3\ calcite}$	–1129.07	K^+	–282.5	$SiO_{2\ quartz}$	–856.3
$CaF_{2\ fluorite}$	–1176.3	$KAlSi_3O_{8\ K\text{-}feldspar}$	–3742.9	$SiO_{2\ amorphous}$	–849.1
$CaMg(CO_3)_{2\ dolomite}$	–2161.7	$KCl_{\ sylvite}$	–408.6	H_4SiO_4	–1307.9
$CaSO_{4\ anhydrite}$	–1321.98	Mg^{2+}	–455.4	$H_3SiO_4^-$	–1251.8
$CaSO_4{\cdot}2H_2O_{\ gypsum}$	–1797.36	$Mg(OH)_{2\ brucite}$	–833.51	$H_2SiO_4^{2-}$	–1176.6
$Ca_5(PO_4)_3OH_{\ apatite}$	–6338.3	$MgCO_{3\ magnesite}$	–1012.1	Sr^{2+}	–563.83
$CaAl_2Si_2O_{5\ anorthite}$	–1310.0	Mn^{2+}	–228.1	$SrCO_{3\ strontianite}$	–1144.73
$Ca(OH)_{2\ portlandite}$	–897.5	$Mn(OH)_{2\ pyrochroite}$	–616.5	$SrSO_{4\ celestite}$	–1345.7
Cl^-	–131.2	$MnO(OH)_{\ manganite}$	–133.3		

Sources: Drever, 1997; Langmuir, 1997; Faure, 1997.
Note: This table is not exhaustive and is for use in exercises in this book. (1 kcal = 4.184 kJ).

Mineral Saturation Index

Although most solute–water reactions attain equilibrium in seconds to minutes (e.g., dissociation of carbonic acid—$H_2CO_3 \Leftrightarrow HCO_3^- + H^+$), reactions that involve different phases, such as mineral dissolution/precipitation reactions, are kinetically impeded and are seldom in equilibrium. Many may be slowly moving toward equilibrium conditions, although changes in temperature or solute concentration may alter the state of mineral saturation. A simple calculation allows geochemists to assess whether a given mineral is close to or far from equilibrium with its solubility products. This is the mineral saturation index, SI, defined as the ratio of the ion activity product (IAP) to the solubility product, K_{sp}.

$$\mathrm{SI} = \frac{\mathrm{IAP}}{K_{\mathrm{sp}}}$$

Using again the example of gypsum dissolution:

$$\mathrm{IAP}_{\mathrm{gypsum}} = a_{\mathrm{Ca}^{2+}} \times a_{\mathrm{SO}_4^{2-}}$$

$$K_{\mathrm{sp}} = 10^{-4.60}$$

$$\mathrm{SI} = \frac{a_{\mathrm{Ca}^{2+}} \times a_{\mathrm{SO}_4^{2-}}}{10^{-4.60}} \text{ or } \log \mathrm{SI} = \log a_{\mathrm{Ca}^{2+}} + \log a_{\mathrm{SO}_4^{2-}} - (-4.60)$$

The SI can then provide a qualitative assessment of the degree of saturation of any mineral for a given solution, where

SI > 1 or log SI > 0	mineral is supersaturated and can precipitate
SI = 1 or log SI = 0	mineral is in equilibrium with the solution
SI < 1 or log SI < 0	mineral is undersaturated and will dissolve if present

The greater the deviation from unity, the greater the degree of disequilibrium. As mineral saturations can vary by a few orders of magnitude, the logarithmic form (log SI) is generally used.

SI values do not take into account the conditions of mineral stability. For example, a low-salinity solution with elevated concentration of H_4SiO_4 will be supersaturated with respect to quartz at 25°C. However, quartz will never precipitate at this low temperature. A more disordered polymorph of quartz, amorphous silica, will form instead. Similarly, gypsum will not precipitate from solution at geothermal temperatures, although it may be supersaturated, as anhydrite is more stable.

The use of SI does also not take into account the slow kinetics and nucleation of many reactions. Dolomite is a mineral that is often supersaturated in carbonate waters, although it is observed only in certain high salinity environments. Clay minerals are also slow to form, due to the slow kinetics of feldspar weathering. Other, low temperature minerals such as calcite, evaporite minerals, iron sulfide (mackinawite), or hydroxides may not be kinetically impeded, and so SI is a useful indicator of their state of solubility.

Example 2.4: Determining the State of Saturation of Low Temperature Minerals

For groundwater with the following geochemical analysis, determine the saturation indices for calcite and gypsum:

T = 25°C	Na^+ = 180 ppm	HCO_3^- = 210 ppm
pH = 7.45	K^+ = 18 ppm	CO_3^{2-} = 0.37 ppm
	Ca^{2+} = 60 ppm	SO_4^{2-} = 85 ppm
	Mg^{2+} = 22 ppm	Cl^- = 280 ppm

Step 1 Determine $K_{calcite}$ and K_{gypsum}.

$$\log K_{calcite} = -\frac{\Delta G_r^\circ}{5.708}$$

$$\Delta G^\circ_{r\,calcite} = \Delta G^\circ_{Ca^{2+}} + \Delta G^\circ_{CO_3^{2-}} - \Delta G^\circ_{CaCO_3}$$

$$= (-552.8) + (-527.9) - (-1129.07)$$

$$= 48.37 \text{ kJ / mol}$$

$$\log K_{calcite} = -\frac{48.37}{5.708} = -8.47$$

log K_{gypsum} = –4.60 (from Example 2.2)

Step 2 Calculate *m*, for input species, and then calculate *I*

	Na^+	K^+	Ca^{2+}	Mg^{2+}	HCO_3^-	CO_3^{2-}	SO_4^{2-}	Cl^-
ppm	180	18	60	22	210	0.37	85	280
gfw	23	39.1	40.1	24.3	61	60	96	35.5
m	0.0078	0.00046	0.0015	0.00091	0.0041	6.22×10^{-6}	0.00089	0.0079

$$I = \tfrac{1}{2}\left(\Sigma m_i z_i^2\right) = 0.016$$

Step 3 Using *I*, calculate γ for all ions using the Debye–Hückel equation, and *a* for each

	Na^+	K^+	Ca^{2+}	Mg^{2+}	HCO_3^-	CO_3^{2-}	SO_4^{2-}	Cl^-
γ	0.87	0.87	0.61	0.62	0.89	0.62	0.61	0.87
a	0.0068	0.00040	0.00092	0.00056	0.0031	3.9×10^{-6}	0.00054	0.0069
log *a*	–2.17	–3.40	–3.04	–3.25	–2.51	–5.41	–3.27	–2.16

Step 4 Determine log $SI_{calcite}$ and log SI_{gypsum}

$$\begin{aligned}\log IAP/K_{calcite} &= \log a_{Ca^{2+}} + \log a_{CO_3^{2-}} - (-8.47)\\ &= -3.04 - 5.41 + 8.47\\ &= 0.02\\ \log IAP/K_{gyp} &= \log a_{Ca^{2+}} + \log a_{SO_3^{2-}} - (-4.60)\\ &= -3.04 - 3.27 + 4.60\\ &= -1.70\end{aligned}$$

This groundwater is essentially at equilibrium with respect to calcite but almost two orders of magnitude undersaturated with respect to gypsum. A possible scenario is that this water is dissolving gypsum and precipitating calcite through the common ion effect (Ca^{2+}).

Temperature Effect on *K*

As *K* is a function of Gibbs free energy of reaction, it will naturally vary with temperature. Adjustments to *K* for temperatures different from 25°C are made using standard enthalpy measurements for the reaction ΔH_r° and the Van't Hoff equation. The approach is based on the standard enthalpy *H* and entropy *S* of reaction (ΔH_r° in J/mol and ΔS_r° in J/mol·K) and temperature *T* (K), which relate to the standard Gibbs free energy of reaction according to

$$\Delta G_r^\circ = \Delta H_r^\circ - T\Delta S_r^\circ$$

and so

$$-RT \ln K = \Delta H_r^\circ - T\Delta S_r^\circ$$

However, to avoid inconsistencies within the various entropy and enthalpy databases, this equation is differentiated with respect to *T* and integrated over the range from 298 K (25°C) to the temperature of interest:

$$\log K_{T_2} = \log K_{298} + \frac{\Delta H_r}{2.303\,R}\left(\frac{1}{298} - \frac{1}{T_{kelvin}}\right) \qquad \text{Van't Hoff equation}$$

This integration is valid for only a limited temperature range of about ± 25°C (i.e., from 0°C to 50°C). Beyond this range, the change in enthalpy and entropy from standard values at 25°C to the new temperature must also be taken into account. Standard enthalpy of reaction data, $\Delta H°_r$, are available from the references for Gibb's free energy in Table 2.1 and are given in Table 2.2 for some common mineral dissolution reactions. The gas constant, R, in joules, is used ($R = 0.0083143$ kJ/mol/K).

Example 2.5: Calculation of K_{sp} at a New Temperature

What is the solubility of calcite at 50°C?

From Example 2.4, the solubility constant for calcite at 25°C was determined:

$$\log K_{calcite} = -8.48$$

The standard enthalpy of reaction for calcite dissolution comes from Table 2.2.

$$\Delta H^o_{\text{calcite diss.}} = -9.61$$

$$\log K_{T_2} = \log K_{298} + \frac{\Delta H^\circ_r}{2.303\ R}\left(\frac{1}{298} - \frac{1}{T_{kelvin}}\right)$$

$$= -8.48 + \frac{-9.61}{2.303\ (0.0083143)}\left(\frac{1}{298} - \frac{1}{323}\right)$$

$$= -8.61$$

This value for K_{50} is lower than K_{25}, indicating that calcite is less soluble at the higher temperature. This is so considering only the solubility constant for calcite. However, considering the increased values for the dissociation constants $K_{HCO_3^-}$ and K_{H_2O}, the overall solubility of calcite in water goes up with temperature (Figure 2.5).

TABLE 2.2
Standard Enthalpy of Reaction for Some Common Mineral Dissociation Reactions

Mineral	Dissociation reaction	$\log K_{25°C}$	ΔH°_r (kJ/mol)
Calcite	$CaCO_3 \Leftrightarrow Ca^{2+} + CO_3^{2-}$	–8.48	–9.610
Aragonite	$CaCO_3 \Leftrightarrow Ca^{2+} + CO_3^{2-}$	–8.336	–10.8324
Dolomite	$CaMg(CO_3)_2 \Leftrightarrow Ca^{2+} + Mg^{2+} + 2CO_3^{2-}$	–17.09	–39.4425
Gypsum	$CaSO_4 \cdot 2H_2O \Leftrightarrow Ca^{2+} + SO_4^{2-} + 2H_2O$	–4.58	–0.456
Anhydrite	$CaSO_4 \Leftrightarrow Ca^{2+} + SO_4^{2-}$	–4.36	–7.1478
Fluorite	$CaF_2 \Leftrightarrow Ca^{2+} + 2F^-$	–10.6	19.6042
Quartz	$SiO_2 + 2H_2O \Leftrightarrow H_4SiO_4$	–3.98	25.062
Amorphous silica	$SiO_2 + 2H_2O \Leftrightarrow H_4SiO_4$	–2.71	13.975

Source: Parkhust and Appelo 1999.

The effect of temperature varies for different minerals. The carbonates, for example, are more soluble at lower temperature, due to the increase in K_{sp} at lower temperatures. By contrast, fluorite (CaF_2) solubility increases with temperature (Figure 2.5).

ELECTRON ACTIVITY AND REDOX

Complementary to dissociation reactions controlling mineral and ion solubilities in groundwater is the exchange of electrons between reduced and oxidized (redox) species. Common examples are the oxidation of organic matter to CO_2, which then contributes to the carbonic acid activity for weathering reactions, or the reduction of ferric iron hydroxide, $Fe(OH)_{3\ ferrihydrite}$, to soluble ferrous iron, Fe^{2+}, which degrades water quality in many bedrock wells. However, unlike many mineral dissolution and precipitation reactions, redox reactions are kinetic in nature and proceed in one direction only, never really achieving a thermodynamic equilibrium.

Electron Donors, Electron Acceptors, and Redox Couples

Redox reactions involve the change of charge state of certain redox-sensitive elements by the gain or loss of electrons from the valence shell. With the exception of the noble gases, and the alkali and alkaline-earth elements, most elements have various redox states, depending on their position in the periodic table. Iron, for example, exists as a metal or in an oxidized state as ferrous iron (Fe^{2+}), or ferric iron (Fe^{3+}). All three forms exist in nature, including Fe^0 in some native iron ores and as iron meteorites. The major redox-sensitive elements and their common redox species are given in Table 2.3.

Redox reactions involve the exchange of electrons between redox species acting as electron donors and electron acceptors. In turn, the electron donor becomes a potential electron acceptor, and the electron acceptor an electron donor. Table 2.4 gives examples of redox couples in groundwater, showing the conversion of an electron donor to an electron acceptor and vice versa through the loss or gain of electrons. Each reaction in Table 2.4 is a half-cell reaction that is paired with other half-cell reaction in a complete redox reaction. The pairing of electron donors with electron acceptors must obey the rules of electrochemistry, whereby the overall reaction releases energy. Paired redox reactions are presented in Chapter 3.

Electron Activity (pe)

Earth's atmosphere, with 21% elemental oxygen, maintains an oxidized near-surface environment with an abundance of electron acceptors. It is the availability of electron donor species that limits the extent to which redox reactions can take place in

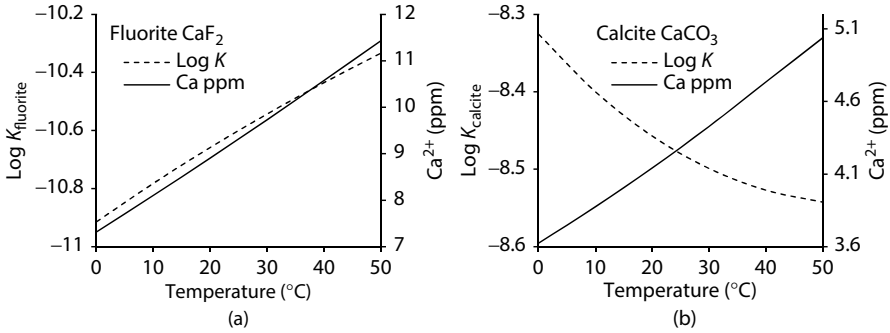

FIGURE 2.5 Change in solubility constants with temperature for fluorite (ΔH = 19.6 kJ/mol) and calcite (ΔH = –9.61 kJ/mol), showing change in (a) log $K_{calcite}$ and (b) log $K_{fluorite}$. For fluorite, Ca^{2+} increases with temperature due to the increased solubility constant, $K_{fluorite}$. For calcite, Ca^{2+} also increases with temperature, in contrast with the decreasing $K_{calcite}$. Calcite is actually more soluble at higher temperature due to an increase in the dissociation constant for bicarbonate, $K_{HCO_3^-}$, and for water, K_{H_2O}. This results in a shift in pH for calcite equilibrium that allows more calcite to dissolve at higher temperature.

TABLE 2.3
Common Forms and Oxidation States of the Important Redox-Sensitive Elements in Groundwaters

H	C	N	O	S	Mn	Fe
H_2—H^0	CO_2—C^{4+}	NO_3^-—N^{5+}	O_2—O^0	SO_4^{2}—S^{6+}	MnO_2—Mn^{4+}	$Fe(OH)_2^+$—Fe^{3+}
H^+	HCO_3—C^{4+}	NO_2^-—N^{3+}	H_2O_2—O^-	S—S^0	$HMnO_2$—Mn^{2+}	$Fe(OH)_3$—Fe^{3+}
OH—H^+	CH_2O—C^0	N_2O—N^+	H_2O—O^{2-}	FeS_2—S^-	$Mn(OH)_2$—Mn^{2+}	FeOOH—Fe^{3+}
H_2O—H^+	CH_3OH—C^{2-}	N_2—N^0	OH—O^{2-}	H_2S—S^{2-}		Fe_2O_3—Fe^{3+}
CH_2O—H^+	C_6H_6—C^-	NH_4^+—N^{3-}	CH_2O—O^{2-}	HS—S^{2-}		$Fe(OH)^+$—Fe^{2+}
C_6H_6—H^+	CH_4—C^{4-}	R–NH_3—N^{3-}	NO_3—O^{2-}	FeS—S^{2-}		$Fe(OH)_2$—Fe^{2+}

groundwaters. The abundance of electron donors is characterized by electron activity a_{e-}, or electromotive force, E.

Although free electrons do not exist in solution, we can think of electron activity in terms of the demand for electrons, which would then be provided or consumed by the complementary redox half-reaction. A high electron activity would characterize a solution with a high concentration of reduced species, such as Fe^{2+} or H_2S. Electron activity notation adopts the pH convention, and so is expressed as the negative log of the electron activity, p*e*:

$$pe = -\log a_{e-}$$

TABLE 2.4
Electron Donors, Electron Acceptors, and Redox Couples in Groundwaters

Electron Donor	Electron Acceptor	Redox Couple
$O^{2-} \leftrightarrow$	$O^0 + 2e^-$	$\underline{O_2}$
$H_2O \leftrightarrow$	$\frac{1}{2}O_2 + 2e^- + 2H^+$	H_2O
$Fe^{2+} \leftrightarrow$	$Fe^{3+} + e^-$	$\underline{Fe(OH)_3}$
$Fe^{2+} + 3H_2O \leftrightarrow$	$Fe(OH)_3 + e^- + 3H^+$	Fe^{2+}
$S^{2-} \leftrightarrow$	S^{6+}	$\underline{SO_4^{2-}}$
$H_2S + 4H_2O \leftrightarrow$	$SO_4^{2-} + 8e^- + 10H^+$	H_2S
$C^{4-} \leftrightarrow$	$C^{4+} + 8e^-$	$\underline{CO_2}$
$CH_4 + 2H_2O \leftrightarrow$	$CO_2 + 8e^- + 8H^+$	CH_4
$H^0 \leftrightarrow$	$H^+ + e^-$	$\underline{H_2O}$
$\frac{1}{2}H_2 + OH^- \leftrightarrow$	$H_2O + e^-$	H_2

Using a generic reaction and the example of iron:

$$\mathrm{Ox} + ne^- \Leftrightarrow \mathrm{Red} \qquad \mathrm{Fe}^{3+} + e^- \Leftrightarrow \mathrm{Fe}^{2+}$$

$$\Delta G_r^\circ = \Delta G_{\mathrm{Red}}^\circ - \Delta G_{\mathrm{Ox}}^\circ \qquad \Delta G_r^\circ = (-82.88) - (-8.56) = -74.32$$

$$\log K = -\frac{\Delta G_r^\circ}{2.3RT} \qquad \log K = -\frac{-74.32}{5.708} = 13.02$$

$$K = \frac{a_{\mathrm{Red}}}{a_{\mathrm{Ox}} \times a_{e^-}^{n}} \qquad K = \frac{a_{\mathrm{Fe}^{2+}}}{a_{\mathrm{Fe}^{3+}} \times a_{e^-}} = 10^{13.02}$$

$$a_{e^-} = \left(\frac{a_{\mathrm{Red}}}{a_{\mathrm{Ox}} \times K} \right)^{1/n} \qquad a_{e^-} = \frac{a_{\mathrm{Fe}^{2+}}}{a_{\mathrm{Fe}^{3+}} \times K}$$

$$\log a_{e^-} = \left(\log \frac{a_{\mathrm{Red}}}{a_{\mathrm{Ox}}} - \log K \right) \qquad \log a_{e^-} = \log \frac{a_{\mathrm{Fe}^{2+}}}{a_{\mathrm{Fe}^{3+}}} \log (10^{13.02})$$

$$pe = \frac{1}{n} \left(\log \frac{a_{\mathrm{Ox}}}{a_{\mathrm{Red}}} + \log K \right) \qquad pe = \log \frac{a_{\mathrm{Fe}^{3+}}}{a_{\mathrm{Fe}^{2+}}} + 13.02$$

For single-electron transfers, $n = 1$:

$$pe = \log \frac{a_{\mathrm{Ox}}}{a_{\mathrm{Red}}} + \log K \qquad pe = \log \frac{a_{\mathrm{Fe}^{3+}}}{a_{\mathrm{Fe}^{2+}}} + 13.02$$

Example 2.6: Calculating pe from Redox Couple Activity Ratios

What is the pe for a solution at neutral pH with a sulfate activity, $a_{SO_4^{2-}} = 10^{-2}$ (~960 ppm) and sulfide activity, $a_{H_2S_{(aq)}} = 10^{-3}$ (34 ppm)?

Write the half-reaction: $SO_4^{2-} + 8e^- \rightarrow H_2S_{(aq)}$

Balance it: $SO_4^{2-} + 8e^- + 10H^+ \rightarrow H_2S_{(aq)} + 4H_2O$

Determine *K*: $\Delta G_r^o = -27.83 + 4(-237.14) - (-744.0) = -232.39$ kJ/mol

$$\log K = -\frac{\Delta G_r^\circ}{5.708} = -\frac{-232.39}{5.708} = 40.7$$

$$K = \frac{a_{H_2S}}{a_{SO_4^{2-}} \times a_{e^-}^8 \times a_{H^+}^{10}} = 10^{40.7}$$

substituting redox species activities:

$$\log K = \log a_{H_2S} - \log a_{SO_4^{2-}} - 8 \log a_{e-} - 10 \log a_{H^+}$$

$$8 \log a_{e^-} = \log a_{H_2S} - \log a_{SO_4^{2-}} - 10 \log a_{H^+} - 40.7$$

$$= \log(0.001) - \log(0.01) - 10(-7) - 40.7$$

$$= 28.3$$

$$\log a_{e^-} = 3.54$$

$$pe = -3.54$$

Note that changing the activity of either H_2S or SO_4^{2-} has little effect on the pe, which is governed largely by the redox reaction constant, *K*. For example, increasing the activity of $H_2S_{(aq)}$, even by an order of magnitude (e.g., $a_{H_2S(aq)} = 10^{-2}$), only shifts the pe to –3.67.

Electromotive Potential (Eh)

The electron activity, p*e*, of the dominant redox couple or half-cell in water establishes the redox state of the solution. This ranges from highly oxidizing (aerobic) conditions with dissolved O_2 to reducing conditions where sulfide and methane dominate. Unlike pH, the electron activity of a solution cannot be directly measured to determine its redox state. This is because, unlike H^+ (or H_3O^+), electrons do not exist freely in the bulk solution. However, a proxy for electron activity can be measured. This is the electromotive potential of the dominant redox couple in the solution.

Electron activity, which is established by the activity ratio of given redox couple, can be measured as the electromotive potential of that redox couple or half-cell. This is done by connecting another half-cell of known electromotive potential to the solution and measuring the voltage (electrical potential) exerted by the redox couple. This is the electromotive potential, E, of the solution. Any redox half-reaction (or half-cell, e.g., SO_4^{2-}/HS^- or Fe^{3+}/Fe^{2+}) has an electromotive potential (E), which is

proportional to the activity ratio of the oxidized and reduced species in the half-cell reaction:

$$\text{Red} \Leftrightarrow \text{Ox} + ne^- \qquad \text{Fe}^{2+} \Leftrightarrow \text{Fe}^{3+} + e^-$$

$$\text{E}_{\text{half-cell}} \propto \frac{a_{\text{ox}}}{a_{\text{red}}} \qquad \text{E}_{\text{Fe}^{3+/2+}} \propto \frac{a_{\text{Fe}^{3+}}}{a_{\text{Fe}^{2+}}}$$

The standard electromotive potential of a redox half-cell, E, is related to Gibb's free energy of reaction through Faraday's constant $\mathfrak{F}$ (96.485 coulombs per mole):

$$\text{E}_{\text{half-cell}} = \frac{\Delta G^\circ_{\text{half-cell}}}{n\mathfrak{F}} \qquad \text{E}_{\text{Fe}^{3+/2+}} = \frac{-8.56 + 82.88}{96.485} = 0.77 \text{ V}$$

recalling that $\Delta G^\circ_{\text{r}} = -RT \ln K$:

$$\text{E}_{\text{half-cell}} = \text{E}_{\text{half-cell}} + \frac{RT \ln K_{\text{half-cell}}}{n\mathfrak{F}} \qquad \text{E}_{\text{Fe}^{3+/2+}} = 0.77 + \frac{RT \ln K_{\text{Fe}^{3+/2+}}}{n\mathfrak{F}}$$

$$= \text{E}_{\text{half-cell}} + \frac{0.059 \log\left(\frac{a_{\text{Ox}} \times a_{e^-}^n}{a_{\text{Red}}}\right)}{n} \qquad = 0.77 + 0.059 \log \frac{a_{\text{Fe}^{3+}} \times a_{e^-}}{a_{\text{Fe}^{2+}}}$$

If we measure E against a half-cell of known potential, its value will be the measured potential less the potential of the reference half-cell. To simplify measurements, it is the standard hydrogen electrode (SHE) against which measured potentials are expressed. The SHE is a platinum electrode connected to an acid solution with hydrogen gas bubbling through it ($P_{\text{H}_2} = 1$ atm). Both H^+ and e^- have unit activities in solution (pH = 0; pe = 0). By convention the SHE has a potential of 0 volts. Measurements against the hydrogen electrode are then Eh measurements. The half-cell reaction in the hydrogen electrode is as follows:

$$\text{H}^+ + e^- \rightarrow \tfrac{1}{2}\text{H}_2 \qquad \text{E}^\circ_{\text{SHE}} = \text{Eh} = \frac{\Delta G^\circ_{\text{r}}}{n\mathfrak{F}} = \frac{0 - (0 + 0)}{n\mathfrak{F}} = 0 \text{ V}$$

As the SHE has an electron activity of 1, when connected to the solution to measure its redox potential, the relation between measured potential and reaction constant K is simplified:

$$\text{Eh} = \text{E}^\circ_{\text{half-cell}} + \frac{0.059}{n} \log\left(\frac{a_{\text{Ox}}}{a_{\text{Red}}}\right) \qquad \text{Eh} = 0.77 - 0.059 \log \frac{a_{\text{Fe}^{3+}}}{a_{\text{Fe}^{2+}}}$$

Using the SHE to measure the electromotive potential of a solution provides a measure of the activity ratio of the redox pair. The hydrogen electrode provides a way to measure in situ redox conditions. With Eh measurements, we can determine what redox pairs are active in solution. We can also determine the solubility of other redox sensitive species and minerals and begin to predict the geochemical evolution

of waters under different scenarios, such as the addition of organic matter or a incorporation of dissolved oxygen when reduced groundwaters are discharged at surface.

Eh and pe

As a field instrument, the SHE is a rather cumbersome piece of equipment, requiring an acid solution and supply of hydrogen gas. Field measurements are made using compact electrodes that are based on metal-ion half-cell reactions. The most common is the silver–silver chloride electrode, which has a positive redox potential against the SHE:

$$Ag_{metal} + Cl^- \Leftrightarrow AgCl + e^- \qquad E^\circ_{Ag/Ag^+} = 0.202\ V$$

Measurements of E in waters are then converted to Eh using a temperature-corrected value for $E_{Ag/AgCl}$ (Table 2.5):

$$Eh = E_{measured} + E_{Ag/AgCl}$$

Unlike pH electrodes, which must be calibrated prior to use, a redox electrode responds directly to potential, and so no calibration is possible. The electrode can, however, be tested in a standard solution to assure that it is reading correctly. Zobell's solution is commonly used. This is a mixture of 3.3 m*M* potassium ferrocyanide and 3.3 m*M* potassium ferricyanide in a 0.1 *M* KCl solution. At 25°C this solution has an Eh of 0.430 V. An Ag/AgCl electrode would measure 0.228 V.

It must be remembered that an Eh measurement of a solution is a bulk measurement. The redox electrode will be responding to the dominant or most active redox pair. However, having measured Eh, it can be used in thermodynamic calculations of speciation and mineral solubility, which are based on p*e*. Using our generic case, we can relate the measured parameter Eh with the thermodynamic parameter p*e*.

$$Eh = E^\circ_{\text{half-cell}} + \frac{2.3RT}{n\Im}\log\left(\frac{a_{Ox}}{a_{Red}}\right) \qquad \text{and recalling: } E^\circ = \frac{\Delta G^\circ}{n\Im}$$

$$Eh = \frac{\Delta G^\circ}{n\Im} + \frac{0.059}{n}\log\left(\frac{a_{Ox}}{a_{Red}}\right)$$

TABLE 2.5
Standard Potentials for the Ag/AgCl Redox Electrode at Different Temperatures

T(°C)	$E_{Ag/AgCl}$	T(°C)	$E_{Ag/AgCl}$	T(°C)	$E_{Ag/AgCl}$
0	220	20	206	40	191
5	216	25	202	45	188
10	213	30	198	50	184
15	209	35	195	55	180

Substitution with $\Delta G_r^\circ = -0.059 \log K$ gives

$$\text{Eh} = -\frac{0.059 \log K}{n} + \frac{0.059}{n} \log\left(\frac{a_{\text{Ox}}}{a_{\text{Red}}}\right) = \frac{0.059}{n}\left(\log \frac{a_{\text{Ox}}}{a_{\text{Red}}} - \log K\right)$$

In this we recognize the p*e* relationship from above

$$\text{p}e = \frac{1}{n}\left(\log \frac{a_{\text{Ox}}}{a_{\text{Red}}} - \log K\right)$$

Substitution then gives the fundamental relationship between p*e* and Eh

$$\text{Eh} = 0.059\ \text{p}e$$

Redox Equilibria and Measured Eh

For acid–base reactions, the equilibrium distribution of species is related to the H^+ activity in the solution. Changing pH or the activity of one of the species results in a redistribution to a new equilibrium. This is not the case for redox reactions, where it is the activities of the redox species in solution that define Eh, as there are no free electrons. So what is the Eh of a solution with more than one redox pair? The redox electrode will typically respond to the redox pair with highest concentration. Measured Eh can be used to calculate the activities of redox pairs (e.g., SO_4^{2-} and HS^- or Fe^{3+} and Fe^{2+}), although it is more accurate to calculate p*e* from measured concentrations of these species. Take, for example, the water in Example 2.6. What would be its p*e* if there was also low but measurable dissolved oxygen—say, 0.05 ppm? The p*e* for the oxygen redox reaction can be calculated from the O_2 and H_2O redox equation:

$$\tfrac{1}{2}O_2 + 2e^- + 2H^+ \rightarrow H_2O \qquad \Delta G_r^\circ = -237.14\ \text{kJ/mol}$$

$$K = \frac{a_{H_2O}}{P_{O_2}^{1/2} \times a_{e^-}^2 \times a_{H^+}^2} = 10^{41.55}$$

$$\log K = 41.55 = \log a_{H_2O} - \tfrac{1}{2}\log P_{O_2} - 2 \log a_{e^-} - 2 \log H^+$$

$$\log a_{e^-} = \tfrac{1}{2}\log a_{H_2O} - \tfrac{1}{4}\log P_{O_2} - \log H^+ - 20.78$$

$$\text{p}e = 20.78 - \text{pH} + \tfrac{1}{4}\log P_{O_2}$$

The partial pressure, P_{O_2}, can be determined from the dissolved concentration using Henry's Law constant $K_{O_2} = 10^{-2.89}$ (mol/kg/atm; see Chapter 3, Solubility of Gases):

$$K_{O_2} = 10^{-2.89} = \frac{m_{O_2(aq)}}{P_{O_2}}$$

$$P_{O_2} = \frac{m_{O_2(aq)}}{10^{-2.89}} = \frac{0.05/32000}{0.00129} = 0.00121 = 10^{-2.92}$$

therefore:

$$\text{p}e = 20.78 - (7) + \tfrac{1}{4}(-2.92)$$
$$= 13.05$$

This p*e*, even for water that is very undersaturated with atmospheric oxygen (air-saturated water has 8.71 ppm O_2 at 25°C), is very much higher than the p*e* value of –3.54 calculated for SO_4^{2-}/H_2S equilibrium in Example 2.6. The equilibrium P_{O_2} for this water can be easily calculated:

$$pe = 20.78 - (7) + \tfrac{1}{4}\log\left(P_{O_2}\right)$$
$$-3.54 = 20.78 - (7) + \tfrac{1}{4}\log\left(P_{O_2}\right)$$
$$\log\left(P_{O_2}\right) = -69.3$$

Thus, the equilibrium concentration of O_2 in this water would be $10^{-69.3} \times 10^{-2.89} = 2.1 \times 10^{-68}$ ppm—not much oxygen, and certainly less than measured. Such disequilibrium between redox pairs is typical of many waters and can result from mixing of water from different strata in an open borehole or at a spring vent. It can also result from differences in the rates of bacterial activity which mediate most redox reactions in natural waters.

SPECIATION AND MINERAL SOLUBILITY CODES

In the sections above on activity and concentration relationships, approaches were presented to determine ion activity and mineral solubility. The iterative calculation produces an estimate of ionic strength, *I*, and calculates the activity coefficients, γ, and the activities, *a*, for dissolved species. When the solution has more than two or three components, the solution becomes much more complicated. Speciation codes manage these calculations by keeping track of all the species present, apportioning the total concentration of the element in solution (say, Ca_{total}) among all the aqueous species that contain it, and then determining the SI for all relevant minerals.

One of the earliest was WATEQ (Truesdell and Jones 1974). Such codes remain at the core of a variety of readily available geochemical packages with user-friendly data input and output interfaces. Most are available at the U.S. Geological Survey (USGS) website. The following example uses the water-quality analysis in Example 2.4 to follow the solution path used by such programs.

Example 2.7: Input and Output from PHREEQC Geochemical Program

Using the water-quality analysis from Example 2.4, determine the speciation of the major elements and solubility of all relevant minerals.

Input—Input of water-quality data including pH, temperature, and element concentrations (total dissolved concentrations). Concentration units must be specified. Alkalinity can be entered as total alkalinity, alkalinity corrected for noncarbonate species (e.g., HS^-), or as bicarbonate and/or carbonate concentration.

Species	pH	T(°C)	Ca^{2+}	Mg^{2+}	Na^{+}	K^{+}	Cl^{-}	SO_4^{2-}	HCO_3^{-}
Concentration (ppm)	7.45	25	60	22	180	18	280	85	210

In this case, minor and trace element data are not included, and the program sets their concentration to 0. Other essential data include pH and water temperature. Optional data include the redox potential measurement as Eh or with a relevant redox pair (discussed in Chapter 3). Eh is not included in this example.

Step 1—establish all the relevant reactions and their related equilibrium constant equations for standard conditions, including formation of complex species, such as:

$$H_2O \Leftrightarrow H^+ + OH^- \qquad K = a_{H^+} \times a_{OH^-} = 10^{-14}$$

$$Ca^{2+} + CO_3^{2-} \Leftrightarrow CaCO_3^o \qquad K_{CaCO_3^\circ} = \frac{a_{CaCO_3}}{a_{Ca^{2+}} \times a_{CO_3^{2-}}} = 10^{3.22}$$

$$Ca^{2+} + HCO_3^- \Leftrightarrow CaHCO_3^+ \qquad K_{CaHCO_3^+} = \frac{a_{CaHCO_3^+}}{a_{Ca^{2+}} \times a_{HCO_3^-}} = 10^{1.11}$$

$$Ca^{2+} + SO_4^{2-} \Leftrightarrow CaSO_4^o \qquad K_{CaSO_4} = \frac{a_{CaSO_4}}{a_{Ca^{2+}} \times a_{SO_4^{2-}}} = 10^{2.30}$$

$$CaCO_3 \Leftrightarrow Ca^{2+} + CO_3^{2-} \qquad K_{calcite} = a_{Ca^{2+}} \times a_{CO_3^{2-}} = 10^{-8.48}$$

$$CaSO_4 \cdot 2H_2O \Leftrightarrow Ca^{2+} + SO_4^{2-} + 2H_2O \qquad K_{gypsum} = a_{Ca^{2+}} \times a_{SO_4^{2-}} = 10^{-4.60}$$

… and so on.

Step 2—Set up mass balance equations for all input species, such as for Ca_{total}.

$$m_{Ca_{total}} = m_{Ca^{2+}} + m_{CaSO_4^\circ} + m_{CaCO_3^\circ} + m_{CaOH^+} + \cdots = 0.0015 \text{ mol/L (or 60 ppm Ca)}$$

Step 3—Use Van't Hoff Equation to determine K_{eq} for all equations at the sample temperature.

Step 4—Calculation of I using input concentrations (first estimate of I).

Step 5—Calculation of activity coefficients γ for all relevant species; that is,

$$\gamma_{Ca^{2+}}, \gamma_{SO_4^{2-}}, \gamma_{CaOH^+}, \gamma_{CaHCO_3^+} \cdots$$

Step 6—Calculate the distribution of species for all input elements, using the mass balance equations in a matrix, with an equal number of equations and unknown species activities. This distribution of species will lower the ionic strength I by the addition of neutral and singly charged species.

Step 7—Calculation of new I, which is used to calculate new activity coefficients. The code then iterates through steps 6 and 7 until the change in the calculated activities of all species is below a given threshold.

Step 8—Calculation of mineral saturation indices as a ratio of the IAP over the solubility constant:

$$\log \frac{IAP}{K_T}$$

Output: Ionic Strength = 0.0156

Charge Balance	Ionic Strength	log P_{CO_2}	CO_{2total}	a_{H_2O}
0.76%	0.016	–2.18	3.44E-03	1.000

Aqueous speciation of the input species, including molalities, activities and activity coefficients (gamma)

Species		Molality	Activity	Log Molality	Log Activity	Log γ
C(4)	3.444e-03					
	HCO_3^-	3.145e-03	2.789e-03	−2.502	−2.554	−0.052
	CO_2	2.218e-04	2.226e-04	−3.654	−3.652	0.002
	CO_3^{2-}	5.956e-06	3.687e-06	−5.225	−5.433	−0.208
Ca	1.498e-03					
	Ca^{2+}	1.382e-03	8.549e-04	−2.859	−3.068	−0.209
	$CaSO_4$	7.672e-05	7.700e-05	−4.115	−4.114	0.002
	$CaHCO_3^+$	3.430e-05	3.043e-05	−4.465	−4.517	−0.052
	$CaCO_3$	5.276e-06	5.295e-06	−5.278	−5.276	0.002
	$CaOH^+$	4.528e-09	3.997e-09	−8.344	−8.398	−0.054
	$CaHSO_4^+$	1.813e-11	1.600e-11	−10.742	−10.796	−0.054
Cl	7.905e-03					
	Cl^-	7.905e-03	6.958e-03	−2.102	−2.158	−0.055
K	4.607e-04					
	K^+	4.593e-04	4.043e-04	−3.338	−3.393	−0.055
	KSO_4^-	1.453e-06	1.282e-06	−5.838	−5.892	−0.054
	KOH	3.935e-11	3.949e-11	−10.405	−10.403	0.002
Mg	9.057e-04					
	Mg^{2+}	8.300e-04	5.183e-04	−3.081	−3.285	−0.205
	$MgSO_4$	5.465e-05	5.484e-05	−4.262	−4.261	0.002
	$MgHCO_3^+$	1.916e-05	1.692e-05	-4.718	−4.772	−0.054
	$MgCO_3$	1.817e-06	1.823e-06	−5.741	−5.739	0.002
	$MgOH^+$	6.006e-08	5.302e-08	−7.221	−7.276	−0.054
Na	7.836e-03					
	Na^+	7.807e-03	6.903e-03	−2.108	−2.161	−0.053
	$NaSO_4^-$	1.769e-05	1.562e-05	−4.752	−4.806	−0.054
	$NaHCO_3$	1.079e-05	1.083e-05	−4.967	−4.965	0.002
	$NaCO_3^-$	5.368e-07	4.739e-07	−6.270	−6.324	−0.054
	NaOH	1.280e-09	1.285e-09	−8.893	−8.891	0.002
S(6)	8.856e-04					
	SO_4^{2-}	7.351e-04	4.514e-04	−3.134	−3.345	−0.212
	HSO_4^-	1.764e-09	1.557e-09	−8.754	−8.808	−0.054

The final calculation is the SI for each relevant mineral, which is calculated from species activities and solubility constants from step 3. Not shown are the highly soluble phases such as epsomite ($MgSO_4$) or natron ($Na_2CO_3 \cdot 10H_2O$) which are highly undersaturated in this example.

Phase	log SI	log IAP	log K_T
Anhydrite [$CaSO_4$]	–2.05	–6.41	–4.36
Aragonite [$CaCO_3$]	–0.17	–8.50	–8.34
Calcite [$CaCO_3$]	–0.02	–8.50	–8.48
$CO_{2(g)}$	–2.18	–20.33	–18.15
Dolomite [$CaMg(CO_3)_2$]	–0.13	–17.22	–17.09
Gypsum [$CaSO_4 \cdot 2H_2O$]	–1.83	–6.41	–4.58
Halite [NaCl]	–5.90	–4.32	1.58

Comparing the results of the WATEQ calculations with those from the simplified hand calculations in Example 2.4 shows that for low-salinity waters, the differences are minor and due mainly to the inclusion of ion pairs (see speciation data, above), which reduce ionic strength and the activities of individual species. Simplified calculations can be carried out in a spreadsheet for low-salinity waters where ion pairs are not significant. The Debye–Hückel equation to determine activity coefficients and the equations for calculating K_{eq} at nonstandard temperature can be embedded in the spreadsheet. However, for higher-salinity waters with more solutes, computer codes are essential.

Parameter	Hand Calculations	WATEQ4F
Ionic strength I	0.016	0.016
$a_{Ca^{2+}}$	0.00092	0.00085
log $SI_{calcite}$	0.02	–0.02
log SI_{gypsum}	–1.70	–1.83

MASS TRANSFER MODELS

The thermodynamic approach of equilibrium speciation and mineral solubility codes can be expanded to include mass transfer. This allows simulating the effects of geochemical processes such as groundwater mixing, mineral dissolution and precipitation, gas exchange, cation exchange, or degassing.

Most mass transfer models are based on speciation codes, with the gain or loss of mass handled by dissolution or precipitation of minerals by gas exchange with the soil or open atmosphere. PHREEQE is one such model that allows the user to model reaction pathways and mixing, and includes effects of hydrodynamic dispersion (Parkhurst and Appelo 1999). PHRQPITZ (Plummer et al. 1988) and SOLMINEQ.88 (Kharaka et al. 1988) were written to accommodate the Pitzer (1987) equations required for speciation modeling of high-ionic-strength brines.

A second type of mass transfer model is based on net mass balance between two points along a flow path (e.g., recharge and discharge waters). NETPATH (Plummer et al. 1994) looks at the gain or loss of solutes and isotopes by geochemical processes, providing the best fit to the input data. By correctly balancing mass between two or more points, the controlling geochemical processes become better understood.

These and other geochemical codes, with input and output interfaces, are public domain and available at the USGS site http://water.usgs.gov/software/lists/geochemical.

PROBLEMS

1. Calculate the ionic strength of a 0.05 molal Na_2SO_4 solution, ignoring the effects of complex ions. What are the activities of Na^+ and of SO_4^{2-}? What would be the effect of any complex ions, such as $NaSO_4^-$, on the ionic strength and on your calculated activities of Na^+ and SO_4^{2-}?
2. Calculate the ionic strength for the waters given in Table 1.7, and plot with the measured TDS. Now use PHREEQC to determine ionic strength of these waters, taking into account complex ions ($CaSO_4^\circ$, etc.). How do the values for *I*, corrected for complex species, compare with the hand calculations and with measured TDS? What is the activity of water in the brine sample and what is its effect on ionic strength?
3. The following analysis comes from groundwater collected during a pump test for a water well drilled for a new house. Using hand calculations (and the simplified Debye-Hückel limiting law equation for this low salinity water), determine the saturation indices for calcite, dolomite and gypsum in this aquifer? (concentrations in ppm). What are their saturation indices at 50°C? Will there be a problem of mineral precipitation in the water heater?

Temperature	**5°C**	**pH**	**7.95**
Ca^{2+}	50	HCO_3^-	150
Mg^{2+}	4	CO_3^{2-}	0.37
Na^+	10	SO_4^{2-}	20
K^+	2	Cl^-	12

4. For the following groundwater analyses (concentrations in mg/L), determine the following:
   a. meq/L for all cations and anions.
   b. The charge balances. Are these acceptable analyses?
   c. The ionic strength, *I*.
   d. The activity coefficients and activities for all ions, using the extended Debye–Hückel equation.
   e. The saturation state of calcite ($K_{calcite} = 10^{-8.47}$), gypsum ($K_{gypsum} = 10^{-4.6}$), and dolomite ($K_{dolomite} = 10^{-17.1}$). Assume that the effects of complex ions are negligible.

	T	pH	Na^+	K^+	Ca^{2+}	Mg^{2+}	Sr^{2+}	HCO_3^-	CO_3^{2-}	SO_4^{2-}	Cl^-
GW1	25	7.54	205	11	33	16	0.01	380	0.61	25	111
GW2	25	7.40	120	15	380	22	0.8	150	0.10	1115	15

5. Using the data for GW2 in Question 4, calculate the solubility products, K_{sp}, for anhydrite and celestite. What are the states of saturation of these minerals?
6. Fluoride (F^-) is a contaminant in groundwater at concentrations greater than about 1 ppm. What is the concentration of F^- in groundwater that dissolves fluorite (CaF_2) to the point of saturation? Now determine the concentration of F^- when the groundwater first reaches equilibrium with gypsum then begins to dissolve fluorite. Assume activities equal molalities.
7. Write the two complementary redox half-reactions for (1) the oxidation of hydrogen (H_2) by O_2 and (2) oxidation of methane (CH_4) with O_2. Determine the Gibb's free energy for each overall reaction. Which would provide more energy to bacteria, per mole of O_2 consumed?
8. What would be the measured Eh of a solution with pH = 7 that contained equal activities of H_2S and SO_4^{2-}? (Hint: begin by finding the p*e* of the redox half-reaction for sulfate reduction.)
9. In Example 2.3, we calculated that 0.011 moles of gypsum can be dissolved in 1 kg of water. The effects of complex species were not taken into account. Using PHREEQC, determine (i) the state of saturation for gypsum in a 0.011 *m* Ca^{2+} – SO_4^{2-} solution and (ii) the moles of Ca^{2+} and SO_4^{2-} in a gypsum saturated solution. Compare the hand calculations with the PHREEQC output and account for the difference. List the complex species in solution and determine their contribution.
10. Use PHREEQC to determine the speciation for the geochemical analysis of GW1 and GW2 in question 4 above.
    a. How do the computed saturation indices for calcite, gypsum, and dolomite differ from the hand calculations in Question 4? Suggest reasons why they may differ.
    b. What are the P_{CO_2} values for GW1 and GW2? Are they greater or less than the atmospheric value (currently we have 400 ppmv CO_2)?
11. Geochemical programs are useful for demonstrating the effects of pH on carbonate solubility. For the carbonate spring water here, determine first the saturation of calcite, noting the P_{CO_2} and the carbonate activity, $a_{CO_3^{2-}}$. Now rerun the analysis with a pH that is one unit higher and again at pH one unit lower, first predicting the effect on calcite solubility and on P_{CO_2}.

T(°C)	pH	Ca^{2+} ppm	HCO_3^- ppm
15	7.70	48	150

12. Test the effects of ionic strength on mineral solubility with PHREEQC by running the calcium-bicarbonate groundwater in Question 11 (Ca^{2+} = 48 mg/L or 1.2 mmol/L and HCO_3^- = 150 mg/L or 2.46 mmol/L) with increasing concentrations of dissolved halite. Run the program with increasing ionic strength by specifying 10, 50, 100, 500, 1000 and 2000 mmol/L for Na^+ and for Cl^-. From the results, plot the log $SI_{calcite}$ values with increasing ionic strength, *I*. What happens to the saturation of calcite and why? Note as well the change in $\gamma_{Ca^{2+}}$ and $\gamma_{CO_3^{2-}}$.
13. An iron titration was performed on deep groundwater and found to contain the following concentrations of ferrous and ferric iron. Calculate the p*e* and Eh of this groundwater by hand calculations, using the dominant species for ferric iron at that pH, that is, $Fe(OH)_2^+$, then compare with the calculations made by PHREEQC, using the Fe^{3+}/Fe^{2+} redox option. Note the distribution of ferric and ferrous iron, and confirm that $Fe(OH)_2^+$ and Fe^{2+} are the dominant species.

    Run this analysis using a pH of 6.75, and compare the p*e*. Account for the difference in p*e* for the same ferric/ferrous iron ratio.

T(°C)	pH	Ca^{2+} ppm	Fe^{2+}_{total} ppm	Fe^{3+}_{total} ppm	HCO_3^- ppm
25	6.25	48	1.0	0.005	150

3 Geochemical Reactions

INTRODUCTION

The law of mass action can be observed in a range of dissociation, redox, and gas solubility reactions. The thermodynamic approach presented in Chapter 2 is useful to quantify these various reactions and to predict speciation, mineral saturation, gas partial pressures, and other geochemical insights. This chapter looks at the common mineral–solute–gas reactions in groundwater, their thermodynamic basis, and how they contribute to the geochemistry of water.

DISSOCIATION REACTIONS

A range of aqueous reactions involves the dissociation of ionic bonds and the formation and exchange of ions in solution. Although often classified as acid–base reactions, they are more than this, ranging from simple acid dissociation reactions to mineral dissolution, ion hydration, and formation of complex ions.

pH and Dissociation of Acids

The most fundamental of all aqueous geochemical reactions is the dissociation of water:

$$H_2O \Leftrightarrow H^+ + OH^-$$

This reaction proceeds rapidly in both forward and reverse directions, such that in pure water at 25°C, the activity of H^+ and OH^- is 10^{-7} (some 100 parts per billion [ppb] for H^+). Note that while it is common practice to write geochemical reactions with free protons (H^+), they typically exist in the form of H_3O^+. Changes in acidity affect the hydroxide activity through the dissociation constant for water:

$$K_{H_2O} = a_{H^+} \times a_{OH^-} = 10^{-14.0} \text{ at } 25°C$$

The pH scale for water changes with temperature. At 0°C, $K_{H_2O} = 10^{-14.9}$ and the pH is 7.45; that is, less water is dissociated. For water at 100°C, $K_{H_2O} = 10^{-13.0}$ and the pH is 6.50, indicating a higher activity for H^+ and OH^- due to greater dissociation of H_2O.

The acidity of water is the sum of the molalities of proton-donating species or acids at a given pH. Some of the major sources of acidity in water are as follows:

Carbonic acid (H_2CO_3), from dissolution of CO_2 in soils (oxidation of organics) or from geogenic sources, including mantle and metamorphic CO_2 in tectonic areas.
Sulfuric acid (H_2SO_4), from the oxidation of sulfide minerals, FeS_2 in particular in mining areas—and from the oxidation of atmospheric SO_2 from industrial sources and coal-fired power plants.
Nitric acid (HNO_3), from NO_x emissions from industrial, automotive, and power-generating sources.
Organic acids—the generation of heterogeneous humic and fulvic acids in soils as well as low-molecular-weight fatty acids, such as acetic acid (CH_3COOH).

The principal acids in natural water and their dissociation constants are given in Table 3.1. Curves showing the distribution (relative concentration) of the acid and

TABLE 3.1
Common Acids in Groundwater and Their First Dissociation Constant, in Order of Increasing Strength

Acid	First Dissociation Constant, *K*	pH at 50% Dissociated
Bisulfate (HSO_4^-)	$K_{HSO_4^-} = \frac{a_{SO_4^{2-}} \times a_{H^+}}{a_{HSO_4^-}} = 10^{-1.99}$	1.99
Phosphoric acid (H_3PO_4)	$K_{H_3PO_4} = \frac{a_{H_2PO_4^-} \times a_{H^+}}{a_{H_3PO_4}} = 10^{-2.15}$	2.15
Humic acid (HA)	$K_{HA} = \frac{a_{HA^-} \times a_{H^+}}{a_{HA}} \approx 10^{-2}$ to 10^{-4}	~2–4
Acetic acid (CH_3COOH)	$K_{CH_3COOH} = \frac{a_{CHCOO^-} \times a_{H^+}}{a_{CH_3COOH}} = 10^{-4.74}$	4.74
Carbonic acid (H_2CO_3)	$K_{H_2CO_3} = \frac{a_{HCO_3^-} \times a_{H^+}}{a_{H_2CO_3}} = 10^{-6.35}$	6.35
Hydrogen sulfide (H_2S)	$K_{H_2S} = \frac{a_{HS^-} \times a_{H^+}}{a_{H_2S}} = 10^{-6.99}$	6.99
Boric acid (H_3BO_3)	$K_{H_3BO_3} = \frac{a_{H_2BO_3^-} \times a_{H^+}}{a_{H_3BO_3}} = 10^{-9.24}$	9.24
Silicic acid (H_4SiO_4)	$K_{H_4SiO_4} = \frac{a_{H_3SiO_4^-} \times a_{H^+}}{a_{H_4SiO_4}} = 10^{-9.83}$	9.83
Bicarbonate (HCO_3^-)	$K_{HCO_3^-} = \frac{a_{CO_3^{2-}} \times a_{H^+}}{a_{HCO_3^-}} = 10^{-10.33}$	10.33

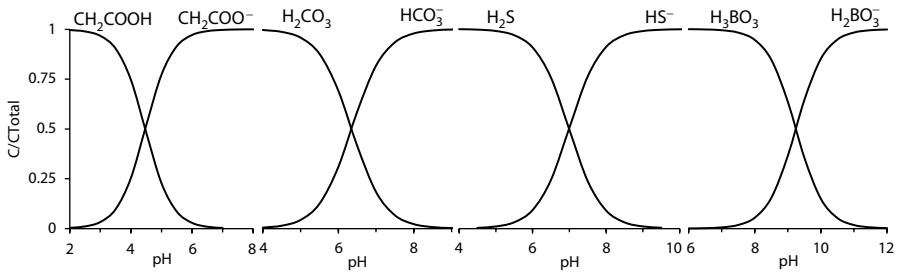

FIGURE 3.1 Relative concentration curves for the dissociation of common weak acids in groundwater.

dissociation product for selected acids (CH_2COOH, H_2CO_3, H_2S, and H_3BO_3) are given in Figure 3.1.

Note that HNO_3, HCl, and H_2SO_4 are strong acids and dissociate to nitrate, NO_3^-, chloride (Cl^-), and sulfate (SO_4^{2-}), respectively, below pH 0 (where $a_{H+} > 1$). Bisulfate, HSO_4^-, dissociates to SO_4^{2-} near pH 2. Bicarbonate, HCO_3^-, generated by the dissociation of carbonic acid, becomes the dominant dissolved carbonate species above pH 6.35. At higher pH values (>8.4), bicarbonate acts as an acid by dissociating to form dissolved carbonate CO_3^{2-} ($K_{HCO_3^-} = 10^{-10.33}$).

Phosphoric acid is found only at low concentrations in natural waters and so contributes little to acidity. Silicic and boric acids are also present in generally low concentrations. As their first dissociation constants are very low ($< 10^{-9}$), they are not dissociated in most natural waters. Thus, in the pH range of 6–8 for most natural waters, only bicarbonate, HCO_3^-, will accept or donate a proton. This makes it an important contributor to alkalinity and the natural buffering of pH.

Dissociation of Salts

The highly soluble salts, discussed in Chapter 1, are the evaporite minerals, including gypsum ($CaSO_4 \cdot 2H_2O$), halite (NaCl), and sylvite (KCl). They are commonly found in sedimentary rock sequences formed in restricted marine basins with strong evaporation. They are also common in soils from arid regions, where, at least seasonally, dry conditions provoke their precipitation from saline pore waters. Under more extreme conditions, nitrate salts, such as sodium nitrate ($NaNO_3$), can form. Such nitrates were mined in the Atacama Desert in the Andean rain shadow of Chile.

The dissociation reactions of the major salts are straight forward

$$CaSO_4 \cdot 2H_2O \Leftrightarrow Ca^{2+} + SO_4^{2-} + 2H_2O \qquad K_{gyp} = \frac{a_{Ca^{2+}} \times a_{SO_4^{2-}} \times a_{H_2O}^2}{a_{CaSO_4 \cdot 2H_2O}} = 10^{-4.60}$$

$$NaCl \Leftrightarrow Na^+ + Cl^- \qquad K_{halite} = \frac{a_{Na^+} \times a_{Cl^-}}{a_{NaCl}} = 10^{1.58}$$

Ion Hydration

The bipolar nature of water and its dissociation into hydroxide (OH^-) and hydrogen (H^+) ions make water a good solvent. Mineral dissolution and ion solubility are aided by the capacity for the polar water molecule to coordinate around ions. This is ion hydration, a fundamental reaction in water. Dissolution reactions involve the uptake of ions into solution by the hydration of the component ions. Orientation of polar H_2O molecules by ions enhances their solubility. The dissolution of a salt, such as fluorite, CaF_2, is a good example (Figure 3.2).

$$CaF_2 \Leftrightarrow Ca^{2+} + 2F^-$$

In writing this reaction for the dissolution of fluorite, the hydration role played by water is not explicitly written, but the hydration reactions and their aqueous complex can be approximated by

$$Ca^{2+} + 6H_2O \rightarrow Ca(H_2O)_6^{2+}$$
$$F^- + 6H_2O \rightarrow F(H_2O)_6^-$$

The number of water molecules fixed in a hydration sheath depends on the valence of the ion and its ionic radius. The extent of ion hydration is proportional to the ionic potential or charge to radius ratio—z/r. Smaller ions, such as Li^+ or Be^{2+}, have a higher net surface charge than K^+ and Ca^{2+} and so have more coordinated water molecules. This leads to the relationship where smaller ions have a larger hydrated radius than larger ions (shown in Table 3.2).

A consequence of hydration is the structuring of water around ions such that the number of free water molecules in the solution is reduced. In highly saline solutions, such as brines, the amount of structured water can approach and even exceed the amount of free water. This reduces the activity of free water to values less than 1, with implications for the state of saturation of minerals. This also affects the isotopic composition of the free water, which becomes depleted in ^{18}O and D, as these heavier isotopes are selectively partitioned into the hydration sheaths (Gonfiantini 1965).

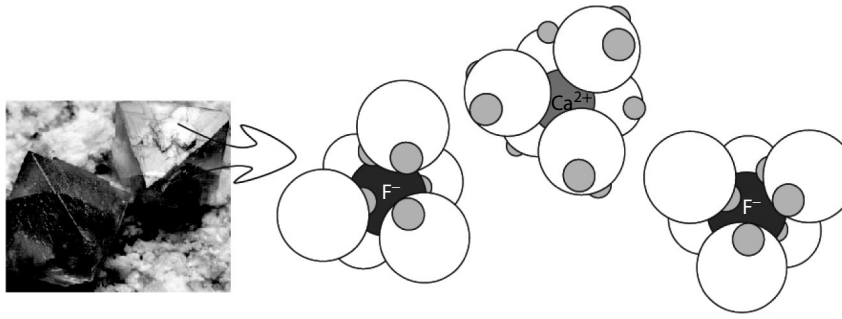

FIGURE 3.2 Dissolution of fluorite (CaF_2) and hydration of Ca^{2+} and F^-.

TABLE 3.2
Crystallographic (R_c) and Hydrated (R_h) Radii (Angstrom Units, å = 10^{-10} m) for the Alkalis and Alkaline-Earth Elements.

Element	R_c	R_h	Element	R_c	R_h
H^+	—	4.5	Be^{2+}	0.31	4.0
Li^+	0.94	3.0	Mg^{2+}	0.72	4.0
Na^+	1.17	2.0	Ca^{2+}	1.00	3.0
K^+	1.49	1.8	Sr^{2+}	1.26	2.5
Rb^+	1.63	1.3	Ba^{2+}	1.42	2.5
Cs^+	1.86	1.3	Ra^{2+}	1.48	2.5

Note: The Radius of H_2O Is 1.4 å.
Source: Shannon 1976; Parkhurst 1995.

Ion Hydrolysis

When the surface charge is extremely high, as in the case of trivalent Al^{3+} or Fe^{3+}, the strong positive charge will force the hydrated ion to shed one or more H^+ ions from its hydration sheath into the bulk solution. The result is a complex with hydroxide, OH^-, generating a new ion with lower net charge. The consequence of hydrolysis of metals dissolved in water is a decrease in pH, as hydrogen ions are expelled into solution. At the same time, the pH of the solution will affect the stability of metal hydroxide complexes in solution. The following series of hydrolysis reactions for ferric iron, Fe^{3+}, is a good example, which, through the common variable of pH, produces the ferric iron speciation diagram of Figure 3.3.

$$Fe^{3+} + H_2O \Leftrightarrow Fe(OH)^{2+} + H^+ \qquad K = \frac{a_{Fe(OH)^{2+}} \times a_{H^+}}{a_{Fe^{3+}}} = 10^{-2.19}$$

$$Fe(OH)^{2+} + H_2O \Leftrightarrow Fe(OH)_2^+ + H^+ \qquad K = \frac{a_{Fe(OH)_2^+} \times a_{H^+}}{a_{Fe(OH)^{2+}}} = 10^{-3.48}$$

$$Fe(OH)_2^+ + H_2O \Leftrightarrow Fe(OH)_3^\circ + H^+ \qquad K = \frac{a_{Fe(OH)_3^\circ} \times a_{H^+}}{a_{Fe(OH)_2^+}} = 10^{-6.89}$$

$$Fe(OH)_3^\circ + H_2O \Leftrightarrow Fe(OH)_4^- + H^+ \qquad K = \frac{a_{Fe(OH)_4^-} \times a_{H^+}}{a_{Fe(OH)_3^o}} = 10^{-9.04}$$

Aluminum, the third most abundant element in the earth's crust, is another good example of ion hydrolysis, and the effect on pH. Like ferric iron, Al^{3+} has a high surface charge, and forms a series of aluminum hydroxide species that range from uncomplexed Al^{3+} to an aluminum anion that is coordinated with four hydroxide ions ($Al(OH)_4^-$) (Figure 3.4).

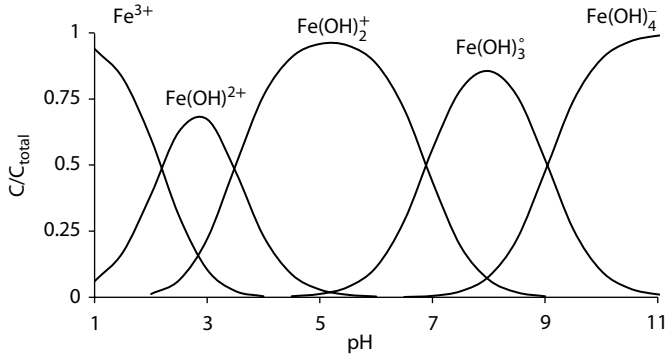

FIGURE 3.3 The distribution of iron hydroxide species with pH, given as the concentration of each species over the total dissolved iron concentration, C/C_{total}. Only at very low pH (high H^+ activity and low OH^- activity) does unhydroxylated Fe^{3+} exist in solution. Note that this graph shows only relative concentrations of ferric iron species in solution, not total concentration, which is discussed in a later chapter.

For ions with very high surface charge, hydrolysis is stronger. Silica is an example. As Si^{4+}, silicon readily coordinates with four hydroxide molecules and forms to form the stable form of dissolved silica, $H_4SiO_4^\circ$, which is stable at most pH ranges (Figure 3.5). Only at high pH does this species dissociate to the anion $H_3SiO_4^-$.

With this understanding of hydrolysis, we can predict the occurrence of hydroxide species for elements with low electromotive potential from the left side of the periodic table. Hydrolysis with the alkaline earth elements, such as Mg^{2+}, and Ca^{2+}, does not occur until hydroxide activities are very high, at pH greater than 10 (Figure 3.6). For the alkalis, Na^+ and K^+, their hydroxides, (NaOH) and (KOH), dissociate near pH 14.

Formation of Ion Pairs

In aqueous solutions, ions can have electrostatic interactions, forming ion pairs—cations joined with a ligand (the anion of an ion pair). The product is a distinct aqueous species with reduced or neutral charge. Take for example, a concentrated solution of the highly soluble salt epsomite ($MgSO_4 \cdot 7H_2O$). The high concentration of Mg^{2+} and SO_4^{2-} ions is such that a percentage will exist as the neutrally charged species $MgSO_4^\circ$. Its dissociation is defined by a reaction constant K:

$$MgSO_4^\circ \Leftrightarrow Mg^{2+} + SO_4^{2-}$$

$$K_{MgSO_4^\circ} = \frac{a_{Mg^{2+}} \times a_{SO_4^{2-}}}{a_{MgSO_4^\circ}} = 10^{-2.25}$$

From this dissociation constant, it is apparent that when $a_{SO_4^{2-}}$ is greater than $10^{-2.25}$ (or a concentration of some 900 mg/L), more Mg exists in the form of $MgSO_4^\circ$ than

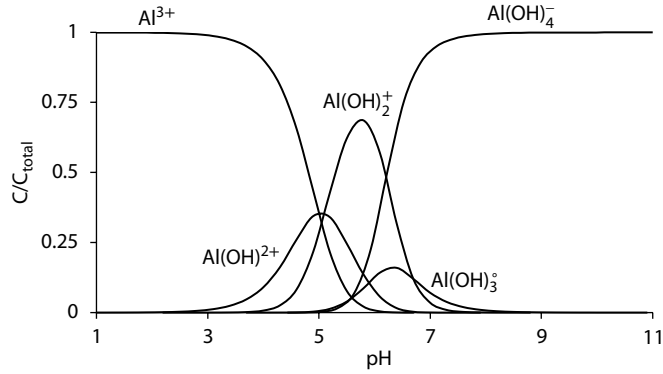

FIGURE 3.4 The distribution of aluminum hydroxide species according to pH, given as concentration relative to total dissolved Al.

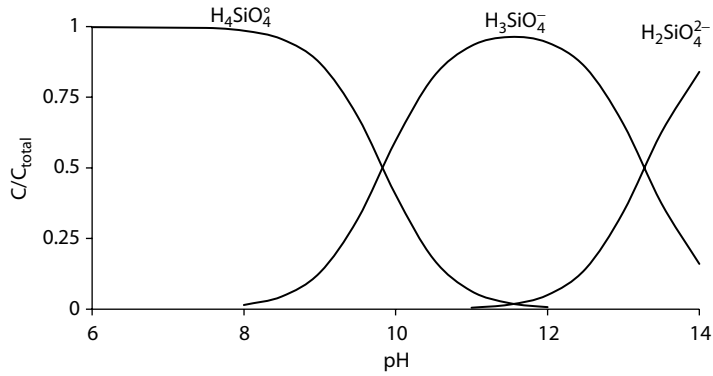

FIGURE 3.5 The silicic acid dissociation products as a function of pH. Note that silica in solution is always anionic. For the pH range of most natural waters, the unionized species, $H_4SiO_4^\circ$, is the dominant dissolved silica species and maintains a relatively low dissolved concentration. However, the dominance of the anion $H_3SiO_4^-$ at high pH greatly increases the solubility of silica in alkaline waters.

as Mg^{2+}. The dissociation constants of the principal ion pairs that form in natural waters are given in Table 3.3. These values show that the doubly charged Ca^{2+} and Mg^{2+} cations form more stable ion pairs than does monovalent Na^+.

In low-salinity solutions, the degree of ion pairing is minimal and has little effect on solute activities and the ionic strength of the solution. However, at higher ionic strength, the activities of individual ions diverge from their total (analytical) concentration due to the formation of ion pairs and ion complexes, which compete for the total amount of the ion in solution. For example, the total

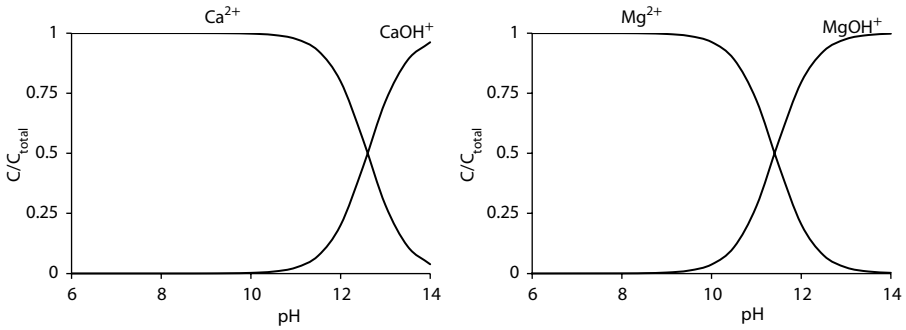

FIGURE 3.6 Hydrolysis of Ca^{2+} and Mg^{2+} occurs only at high pH. Although hydrated with six water molecules surrounding these ions in solution, they do not hydrolyze except under very alkaline conditions. Note that Mg^{2+} has a smaller diameter and higher surface charge than Ca^{2+} and so can hydrolyze at a lower pH.

TABLE 3.3
Dissociation Constants for Common Ion Pairs

Ion Pair	Log K_{diss}	Ion Pair	Log K_{diss}	Ion Pair	Log K_{diss}	Ion Pair	Log K_{diss}
$MgOH^+$	–2.21	$NaHCO_3^-$	+0.25	$NaCO_3^-$	–1.27	$NaSO_4^-$	–0.70
$CaOH^+$	–1.40	$MgHCO_3^+$	–1.07	$MgCO_3^\circ$	–2.02	$MgSO_4^\circ$	–2.25
		$CaHCO_3^+$	–1.11	$CaCO_3^\circ$	–3.23	$CaSO_4^\circ$	–2.31

concentration of Ca in high-salinity water is distributed among a number of complex ions:

$$m_{\mathrm{Ca-total}} = m_{\mathrm{Ca^{2+}}} + m_{\mathrm{CaSO_4^\circ}} + m_{\mathrm{CaOH^+}} + m_{\mathrm{CaHCO_3^+}} + m_{\mathrm{CaCO_3^\circ}} + m_{\mathrm{CaCl^+}} + \cdots$$

Determining the concentrations and activities of all relevant Ca species in a high-salinity solution requires an iterative approach calculating I and using a Ca mass balance equation together with the dissociation reaction equations γ and a for all ion pairs.

Incongruent Dissolution

The final group of dissolution reactions to be introduced is that where minerals dissolve incongruently, producing both solutes and a secondary mineral phase. Weathering of silicate minerals generally occurs incongruently. For example, feldspar weathering involves the dissolution of a primary aluminosilicate and the formation of a secondary clay mineral.

$$\mathrm{CaAl_2Si_2O_{8\ anorthite} + H_2O + 2H^+ \rightarrow Ca^{2+} + Al_2Si_2O_5(OH)_{4\ kaolinite}}$$

Clay minerals, such as kaolinite, can be further leached of their silica, producing more highly insoluble aluminum oxide and dissolved silica:

$$Al_2Si_2O_5(OH)_{4\ \text{kaolinite}} + 5H_2O \rightarrow 2Al(OH)_{3\ \text{gibbsite}} + 2H_4SiO_4^\circ$$

Another common example involves the dissolution of dolomite by Ca^{2+}-bearing waters, resulting in the precipitation of calcite:

$$Ca^{2+} + CaMg(CO_3)_{2\ \text{dolomite}} \rightarrow Mg^{2+} + 2CaCO_{3\ \text{calcite}}$$

Balancing Dissociation Reactions

Writing a geochemical reaction for mineral dissolution or precipitation begins with recognition of the basic components and their charge or valence. Most rock-forming minerals and compounds are composed of varying numbers of cations and anions, with or without water (as H_2O or OH^-). The anions define the class of mineral (recall from Chapter 1), and the cations define the mineral within that class:

$$SiO_4^{4-} \text{ — silicate} + Mg^{2+} \rightarrow Mg_2SiO_{4\ \text{olivine}}$$
$$SO_4^{2-} \text{ —sulfate} + Ca^{2+} \rightarrow CaSO_4 \cdot 2H_2O_{\text{gypsum}}$$
$$CO_3^{2-} \text{ —carbonate} + Fe^{2+} \rightarrow FeCO_{3\ \text{siderite}}$$
$$PO_4^{3-} \text{ — phosphate} + Ca^{2+} \rightarrow Ca_5(PO_4)_3OH_{\text{apatite}}$$
$$S^{2-} \text{ — sulfide} + Zn^{2+} \rightarrow ZnS_{\text{sphalerite}}$$
$$OH^- \text{ —hydroxide} + Fe^{3+} \rightarrow Fe(OH)_{3\ \text{ferrihydrite}}$$

In the case of gypsum and apatite, water and hydroxide are involved structurally in forming these minerals. Care must be taken to consider the appropriate redox state of the ions involved, as these are not necessarily apparent from the mineral formula. Iron is an example, present as either ferrous (Fe^{2+}) or ferric (Fe^{3+}) iron.

Balancing dissociation reactions requires placing the reactants and products on the left and the right sides. In straight dissolution equation, the products may not yet be established, and so the right side is blank. If the product is a secondary mineral phase, this should be written on the right side. Next write in the solutes produced or consumed by the reaction, and balance them between reactants and products. Add water or H^+ to either side as appropriate to balance oxygen and hydrogen. Finally, check that all elements and all charges are equal on both sides.

REDOX REACTIONS

Recall from Chapter 2 that redox couples act in half-cell reactions to exchange electrons from the electron donor of one couple to an electron acceptor in another. In natural and contaminated waters, a range of redox couples exist that can, depending

Example 3.1: Balancing Dissociation Reactions

Write a reaction for the dissolution of dolomite by carbonic acid.

Writing the reactants:
$CaMg(CO_3)_2 + H_2CO_3 \rightarrow$

Write their dissociation products:
$CaMg(CO_3)_2 + 2H_2CO_3 \rightarrow Ca^{2+} + Mg^{2+} + 2\ CO_3^{2-} + 2H^+ + 2HCO_3^-$

Reconcile the carbonate species into a common product:
$CaMg(CO_3)_2 + 2H_2CO_3 \rightarrow Ca^{2+} + Mg^{2+} + 4HCO_3^-$

A check on O and H shows both sides balance, and a check on charge balance shows that both sides have the same (neutral) charge.

Balance a reaction for the alteration of anorthite to kaolinite.

Reactant: $CaAl_2Si_2O_{8\ \text{anorthite}} \rightarrow$ Product: $Al_2Si_2O_5(OH)_{4\ \text{kaolinite}}$

Accounting for cations and anions liberated in the reaction:

$CaAl_2Si_2O_8 \rightarrow Ca^{2+} + Al_2Si_2O_5(OH)_4$

Balancing oxygen using water. Here the left side requires one H_2O to match the nine oxygen atoms in kaolinite:
$CaAl_2Si_2O_8 + H_2O \rightarrow Ca^{2+} + Al_2Si_2O_5(OH)_4$

Balancing H^+. An additional $2H^+$ ions are required on the left:
$CaAl_2Si_2O_8 + H_2O + 2H^+ \rightarrow Ca^{2+} + Al_2Si_2O_5(OH)_4$

A check on charge balance shows that each side has 2+ and mass is equal on both sides, and so the equation is balanced. Here we find that this reaction is acid-consuming and will cause an increase in pH, typical of weathering reactions.

Write a reaction for the dissolution of ferrihydrite with carbonic acid.

Reactants: $Fe(OH)_3 + H_2CO_3 \rightarrow$

Accounting for cations and anions: $Fe(OH)_3 + H_2CO_3 \rightarrow Fe(OH)_2^+ + HCO_3^-$

Balance oxygen with H_2O: $Fe(OH)_3 + H_2CO_3 \rightarrow Fe(OH)_2^+ + HCO_3^- + H_2O$

No H^+ needed, and the charges balance on both sides, and so the equation is correct.

on the electromotive potential of each of the couples, exchange electrons in a pair of redox half-reactions—one donating electrons and one accepting them. The overall redox reaction proceeds with an output of energy that can be exploited by bacteria and archaeans for metabolism and growth.

The occurrence of a reduced compound, such as organic matter, together with an oxidized compound such as sulfate, makes the system inherently out of equilibrium, and the redox reaction will proceed until either the electron-acceptor reservoir or the

electron-donor substrate is exhausted. For this reason, redox reactions in aqueous systems are generally unidirectional rather than forward and backward, as required for equilibrium. Such systems are very much like a charged battery, which dissipates its energy by a flow of electrons from the cathode (electron donor) to the anode (electron acceptor). To achieve thermodynamic equilibrium requires virtually complete conversion of the electron-donor or the electron-acceptor species—analogous to a flat battery. However, unlike a battery, many groundwater systems have abundant concentrations of electron acceptors but no viable electron donors, or vice versa, and so have no redox reactions taking place.

Organic matter is the most common electron donor in natural (and contaminated) systems. Elemental oxygen as an electron acceptor, supports aerobic biodegradation in soils and shallow groundwaters. This is respiration, which releases the chemical energy of carbohydrate that was stored by photosynthesis. It takes place as a pair of reactions involving an electron donor and an electron acceptor:

Electron donor $\quad CH_2O + H_2O \rightarrow CO_2 + 4e^- + 4H^+$

Electron acceptor $\quad O_2 + 4H^+ + 4e^- \rightarrow 2H_2O$

Redox pair reaction $\quad O_2 + CH_2O \rightarrow CO_2 + H_2O \quad \Delta G_r^\circ = -501.84\ \text{kJ/mol}$

Using CH_2O as a generic form of organic matter, carbon is in the 0 valence state and is oxidized to the +IV valence state as CO_2. In the reciprocal reaction, elemental oxygen is reduced to water.

Redox Couples in Groundwater

Groundwater systems are not limited to O_2 as an electron acceptor nor organic matter as an electron donor, as several other important redox couples exist, either dissolved during recharge or as minerals and gases encountered in the subsurface. Some of the more important species and oxidation state of redox-sensitive elements in groundwaters are given in Table 2.3. Common redox couples are given in Table 3.4.

Groundwaters that recharge through oxidized soils and weather mineral components in the presence of oxygen typically evolve a Ca^{2+}–HCO_3^- geochemistry under aerobic conditions with a high Eh. Groundwaters with high concentrations of organics and redox-sensitive species, however, have the potential to develop anaerobic conditions with low Eh and evolve through a series of redox reactions.

Redox Reactions in Groundwater

Given that free electrons do not normally exist in solutions, electron exchanges can only occur between two redox couples, which constitute a redox pair of two half-cell reactions. Like batteries, electron-exchange reactions in groundwater yield energy when proceeding in the forward direction but require energy to move in the reverse

TABLE 3.4
Major Redox Couples in Groundwater, Electrons Transferred (n) and Their Electromotive Potential at Neutral pH

Couple	*n*	*Eh*
		Oxidizing conditions
O_2/H_2O	2	0.81
NO_3^-/N_2	5	0.71
MnO_2/Mn^{2+}	2	0.58
$Fe(OH)_3/Fe^{2+}$	1	0.17
SO_4^{2-}/H_2S	8	–0.22
CO_2/CH_4	8	–0.24
H_2O/H_2	1	–0.41
CO_2/CH_2O	4	–0.48
		Reducing conditions

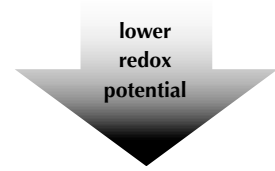

direction. The electromotive potential of the redox pair coupled in a paired reaction define in which direction it can proceed to yield energy. The rule is that the electron acceptor in a redox couple with higher Eh (higher on the scale in Table 3.4) can oxidize an electron donor from a couple with lower Eh. On the basis of the electromotive potentials given in Table 3.4, the following are examples of paired redox half-cell reactions that can proceed with a net energy yield. The electron acceptor (ea) and electron donor (ed) in each are indicated.

$$\tfrac{1}{2}O_{2(ea)} + 2Fe^{2+}_{(ed)} + 5H_2O \rightarrow 2Fe(OH)_3 + 4H^+ \quad \text{iron oxidation}$$

$$4NO^-_{3\,(ea)} + 5CH_2O_{(ed)} \rightarrow 5HCO^-_3 + 2N_2 + 2H_2O + H^+ \quad \text{denitrification}$$

$$4MnO_{2(ea)} + H_2S_{(ed)} + 6H^+ \rightarrow 4Mn^{2+} + SO^{2-}_4 + 4H_2O \quad \text{manganese reduction}$$

$$4Fe(OH)_{3(ea)} + CH_2O_{(ed)} + 7H^+ \rightarrow HCO^-_3 + 4Fe^{2+} + 10H_2O \quad \text{iron reduction}$$

$$SO^{2-}_{4\,(ea)} + CH_{4(ed)} + 2H^+ \rightarrow H_2S + CO_2 + 2H_2O \quad \text{sulfate reduction}$$

$$CO_{2(ea)} + 4H_{2(ed)} \rightarrow CH_4 + 2H_2O \quad CO_2 \text{ reduction}$$

As discussed, redox reactions are highly energetic and tend to proceed in one direction. Redox reactions in groundwater have the same energy releases associated with combustion and explosives, although the kinetics are greatly attenuated by lower concentrations and temperatures. Nonetheless, the high degree of disequilibrium found when an electron acceptor is mixed with an electron donor can be illustrated by calculating their activities under equilibrium conditions. Biodegradation of organic carbon by aerobic bacteria in shallow groundwater is shown in Example 3.2.

Example 3.2: Calculation of $\Delta G°_r$ and K_{sp} for Aerobic Respiration of Organic Carbon, CH_2O, in Groundwater

What is the equilibrium constant for oxidation of organic carbon?

The two half-cell redox reactions are as follows:

$$O_{2(ea)} + 4H^+ + 4e^- \rightarrow 2H_2O \qquad \Delta G_r^\circ = -474.3 \text{ kJ/mol}$$
$$CH_2O_{(ed)} + H_2O \rightarrow CO_2 + 4e^- + 4H^+ \qquad \Delta G_r^\circ = -27.56 \text{ kJ/mol}$$

Giving the overall redox pair reaction and free energy, $\Delta G°_r$:

$$O_2 + CH_2O \rightarrow CO_2 + H_2O \quad \text{with } \Delta G_r^\circ = (-474.3) + (-27.54)$$
$$= -501.84 \text{ kJ/mol}$$

The free energy released is significant, demonstrating this to be a highly exothermic reaction. Using $\Delta G°_r$ to calculate an equilibrium constant for this reaction:

$$\text{So,} \quad \log K_{\text{respiration}} = -\frac{-501.8}{5.708} = 87.9$$

$$\text{and } K_{\text{respiration}} = \frac{P_{CO_2}}{P_{O_2} \times a_{CH_2O}} = 10^{87.9}$$

This very high value for $K_{\text{respiration}}$ demonstrates that equilibrium between O_2 and organic matter can only exist in an environment with very high P_{CO_2}. Using the concept of saturation index from mineral saturation (ratio of the ion activity product to the equilibrium constant), typical values for a partial pressure of oxygen (0.21 atm) for organic matter (activity of 1), and a typical soil P_{CO_2} of, say, 10^{-2} atm, we can calculate the state of equilibrium for this common scenario.

$$SI = \frac{IAP}{K} = \frac{P_{CO_2}/(P_{O_2} \times a_{CH_2O})}{10^{87.9}} = \frac{10^{-2}/(0.21 \times 1)}{10^{87.9}} = 10^{-89.2}$$

From the very low index, is clear that these systems are very far from a thermodynamic equilibrium, which would require an atmosphere with a CO_2 to O_2 ratio of $10^{87.9}$.

Balancing Redox Reactions

In writing and balancing redox reactions, it is useful to write them as half-reactions first, balance the electron transfer, then add them together to balance oxygen and hydrogen. Take, for example, the oxidation of organic carbon, CH_2O, using sulfate as an electron acceptor. In this case, methane is oxidized to CO_2, and sulfate is reduced to hydrogen sulfide.

Example 3.3: Is the Oxidation of Ferrous Iron with Sulfate Possible in Groundwater?

Calculate the free energy, $\Delta G°_r$, and K for the oxidation of ferrous iron with sulfate. Is this an exothermic or endothermic reaction?

$$8Fe^{2+} + SO_4^{2-} + 20H_2O \rightarrow 8Fe(OH)_3 + H_2S + 14H^+$$

$$\Delta G_r^\circ = (-27.83) + 8(-692.07) - 20(-237.14) - (-744.0) - 8(-82.88)$$
$$= 585.45 \text{ kJ/mol}$$

$$\log K_{\text{Fe-reduction}} = -\frac{585.45}{5.708} = -102.57$$

and

$$K_{\text{Fe-reduction}} = \frac{a^8_{Fe(OH)_3} \times a_{H_2S} \times a^{14}_{H^+}}{a^8_{Fe^{2+}} \times a_{SO_4^{2-}} \times a^{20}_{H_2O}} = 10^{-102.57}$$

The answer to this question is no. From the high positive free-energy value of 585.45 kJ/mol, this is an endothermic reaction, which would require energy to proceed. The very low thermodynamic constant, K, indicates that the system is stable with sulfate and ferrous iron but not with sulfide with ferric iron. This is consistent with the position of the iron and sulfur redox couples on the electromotive potential scale in Table 3.4, as the oxidized species of a redox couple (SO_4^{2-} in this case) can only accept electrons from an electron donor that is lower, not higher, on the scale (e.g., ferrous iron).

	Oxidation	*Reduction*
	$CH_2O \rightarrow CO_2$	$SO_4^{2-} \rightarrow H_2S$
Electron accounting	$CH_2O \rightarrow CO_2 + 4e^-$	$SO_4^{2-} + 8e^- \rightarrow H_2S$
Balancing electrons	$2CH_2O \rightarrow 2CO_2 + 8e^-$	$SO_4^{2-} + 8e^- \rightarrow H_2S$
Add half-reactions	$2CH_2O + SO_4^{2-} \rightarrow 2CO_2 + H_2S$	
Balance O with H_2O	$2CH_2O + SO_4^{2-} \rightarrow 2CO_2 + H_2S + 2H_2O$	
Balance H with H^+	$2CH_2O + SO_4^{2-} + 2H^+ \rightarrow 2CO_2 + H_2S + 2H_2O$	

This reaction can be further resolved, considering that in the products, CO_2 will certainly hydrate and dissociate to produce bicarbonate, particularly considering that H^+ is being consumed on the left side:

$$2CH_2O + SO_4^{2-} + 2H^+ \rightarrow 2H_2CO_3 + H_2S$$
$$2CH_2O + SO_4^{2-} + 2H^+ \rightarrow 2HCO_3^- + H_2S + 2H^+$$
$$2CH_2O + SO_4^{2-} \rightarrow 2HCO_3^- + H_2S$$

Example 3.4: Balancing Redox Reactions

Write a reaction for the oxidation of methane to bicarbonate with sulfate.

$CH_4 + SO_4^{2-} \rightarrow HCO_3^- + H_2S$

Redox half-reactions	$CH_4 \rightarrow HCO_3^-$	$SO_4^{2-} \rightarrow H_2S$
Electron accounting	$CH_4 \rightarrow HCO_3^- + 8e^-$	$SO_4^{2-} + 8e^- \rightarrow H_2S$
Add the half-reactions	$CH_4 + SO_4^{2-} \rightarrow HCO_3^- + H_2S$	
Balance O with H_2O	$CH_4 + SO_4^{2-} \rightarrow HCO_3^- + H_2S + H_2O$	
Balance H with H^+	$CH_2 + SO_4^{2-} + H^+ \rightarrow HCO_3^- + H_2S + H_2O$	

Write a reaction for the oxidation of pyrite with atmospheric (elemental) oxygen.

$FeS_2 + O_2 \rightarrow Fe^{2+} + SO_4^{2-}$

Redox half reactions	$FeS_2 \rightarrow Fe^{2+} + 2SO_4^{2-}$	$O_2 \rightarrow 2H_2O$
Electron accounting	$FeS_2 \rightarrow Fe^{2+} + 2SO_4^{2-} + 14e^-$	$O_2 + 4e^- \rightarrow 2H_2O$
Balancing the half-reactions	$FeS_2 \rightarrow Fe^{2+} + 2SO_4^{2-} + 14e^-$	$3½O_2 + 14e^- \rightarrow 3½H_2O$
Add the half-reactions	$FeS_2 + 3½O_2 \rightarrow Fe^{2+} + 2SO_4^{2-} + 3½H_2O$	
Balance O with H_2O	$FeS_2 + 3½O_2 + H_2O \rightarrow Fe^{2+} + 2SO_4^{2-}$	
Balance H with H^+	$FeS_2 + 3½O_2 + H_2O \rightarrow Fe^{2+} + 2SO_4^{2-} + 2H^+$	

GASES IN GROUNDWATER

All groundwaters have some component of dissolved gas, which has been incorporated by dissolution from soil air during recharge with possible additions from subsurface reactions. Atmospheric O_2 plays a critical role in the oxidation of minerals, such as pyrite, or organic matter. CO_2 dissolved from soils by infiltrating groundwaters provides carbonic acid for weathering reactions. Noble gases are nonreactive and so are useful tracers, due to the dependence of their solubilities on temperature. Others are produced in the soil and in groundwater by bacterial activity, such as CO_2, CH_4, N_2, and H_2S. CO_2 generated in the soil by biodegradation is incorporated into groundwaters during infiltration and provides the acidity required for weathering. CH_4 is from anaerobic degradation of organic carbon sources and N_2 from bacterial degradation of NO_3^- (denitrification and anammox). H_2S is produced under highly reducing conditions by bacterial reduction of sulfate, usually when significant sources of organic carbon are available.

Groundwaters in deeper settings have geogenic gases. Elevated He and Ar concentrations result from the radioactive decay of U, Th, and ^{40}K. Tectonic and metamorphic zones can release abundant CO_2 to groundwaters. Providing the water depth is sufficient to maintain high confining pressure (hydrostatic pressure), solubilities can then be exceeded when groundwater circulates to surface pressure, causing effervescence. Similarly, effervescence occurs in hot springs where geothermal heating has lowered the gas solubilities, causing gas exsolution upon discharge.

Unlike ions from mineral dissolution, gases are dissolved in water as un-ionized solutes. In the recharge environment, the dissolution of gases is controlled by their partial pressure and their relative solubility. The atmospheric abundances of the major and trace gases are shown here in Figure 3.7.

Gas Partial Pressure

The concentration of an ideal gas in a free-gas phase is equal to its molar fraction, a unit-less ratio equal to the moles of the gas of interest to the moles of all the gases in the free-gas phase. The molar fraction of the major gases, N_2 and O_2 in the atmosphere, is expressed as a percent of the total gas by volume (Figure 3.7; Table 3.5). For gases of low to trace concentration, they are usually expressed

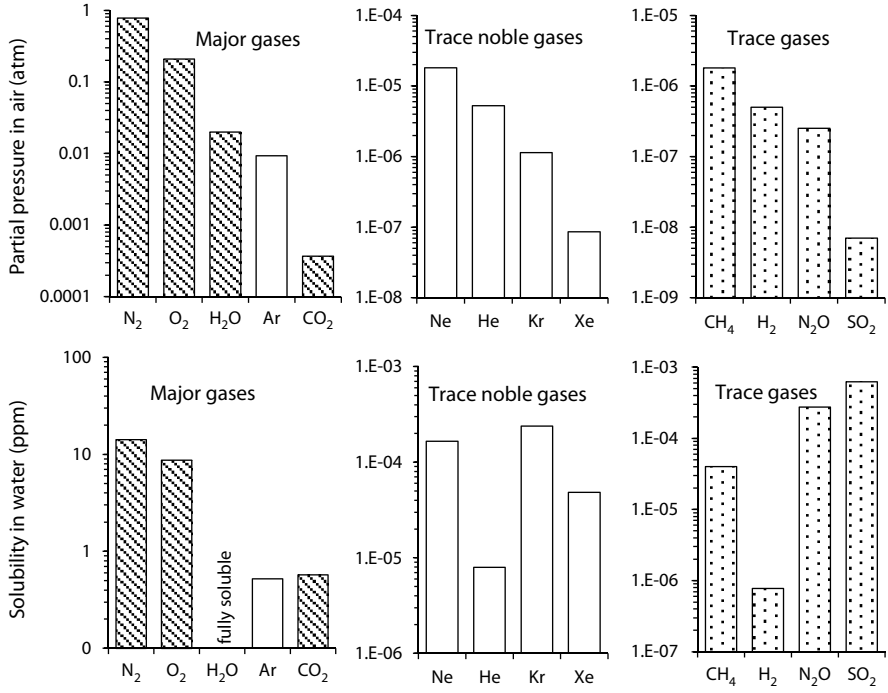

FIGURE 3.7 Partial pressure of the major, noble, and trace gases (atm) in air (above) and their solubilities (ppm) in water (below).

TABLE 3.5
Common Atmospheric Gases, Their Henry's Law Constants and Bunsen Coefficients at 25°C, and Their Aqueous Solubility When at Equilibrium with the Atmosphere

Gas	gfw	Partial Pressure *P* (atm)	Molar Fraction in Air	K_H (mol/L/atm)	Air-Equilibrated Water (ppm)	Bunsen Coefficient (cc_{STP}/cc_{H_2O}/atm)[a]	Atmospheric Equlibrium (cc_{STP}/cc_{H_2O})[a]
N_2	28	0.78084	78.10%	0.00065	14.2	0.01457	1.14E–02
O_2	32	0.209476	20.90%	0.0013	8.71	0.02914	6.10E–03
H_2O[b]	18	~0.02	~2%	—	—	—	—
Ar	39.9	0.00934	0.93 %	0.0014	0.522	0.03130	2.92E–04
CO_2	44	0.00037	380 ppmv	0.034	0.570	0.78449	2.90E–04
Ne	20.2	1.82E–05	18.2 ppmv	0.00045	1.65E–04	0.01024	1.86E–07
He	4	5.24E–06	5.24 ppmv	0.00038	7.96E–06	0.00876	4.59E–08
CH_4	16	1.80E–06	1.8 ppmv	0.0014	4.03E–05	0.03138	5.65E–08
Kr	83.8	1.14E–06	1.14 ppmv	0.0025	2.39E–04	0.05620	6.41E–08
H_2	2	5.00E–07	0.5 ppmv	0.00078	7.80E–07	0.01748	8.74E–09
N_2O	44	2.50E–07	0.25 ppmv	0.025	2.75E–04	0.56035	1.40E–07
Xe	131.3	8.60E–08	0.086 ppmv	0.0043	4.86E–05	0.09810	8.44E–09
SO_2	64	7.00E–09	0.007 ppmv	1.4	6.28E–04	31.37980	2.20E–07
H_2S	34	trace	trace	0.0001	trace	0.00224	trace

Source: Sander 2014; Smith 1983.

[a] cc gas at STP per cc water. STP = standard temperature and pressure (273.15K or 0°C and 1 atm pressure).

[b] Water vapor is the third most abundant gas in the atmosphere, but has high variability.

as parts per million by *volume* (ppmv) or parts per billion by *volume* (ppbv). This expression differs from the ppm used for solutes, which is parts per million by weight.

The partial pressure of a gas, P_{gas}, is its fractional contribution to the total gas pressure, P_{total}, and is calculated as its molar fraction (not mass fraction) multiplied by the total gas pressure:

$$P_{gas} = \frac{\text{moles}_{gas}}{\text{moles}_{total}} \times P_{total} \text{ (atm)}$$

Note that some publications express partial pressures of gases as pO_2 or pO_2, despite that small "p" represents negative log (i.e., pH, pK, and p*e*). Pressure, however, is represented by *P*, and so partial pressures should be expressed as P_{gas}. Gas pressure is commonly expressed in units of atmospheres (atm), although bars and kilopascals can also be used (1 atm = 1.01325 bar = 101.325 kPa). For example, O_2 in air has a molar fraction (or mixing ratio) of 0.209, or about 21% (Table 3.5), and at the earth's surface has a partial pressure, $P_{O_2} = 0.21$ atm. At an altitude of 10 km, where air pressure is only 0.27 atm, however, O_2 has the same molar fraction (0.209) but a partial pressure of only 0.06 atm.

Carbon dioxide has a molar fraction in air of 0.0004. Gases with such low concentrations are usually expressed as parts per million, which gives CO_2 a concentration in air of 400 ppmv. The "v" denotes that this is a volumetric concentration (molar), not a mass concentration as seen for solutes in water expressed as ppm. At 1 atm total pressure, $P_{CO_2} = 0.0004$ atm, or $10^{-3.4}$ atm.

Henry's Law for Gas Dissolution

When gas dissolves from an adjacent free-gas phase, its solubility is proportional to its partial pressure in the gas phase. In the case of gas production below the water table, gas can accumulate to the point where its concentration exceeds its solubility for the pressure (depth) conditions and then will form a free-gas phase. In both cases, the equilibrium saturation point is defined by Henry's Law, which states that the concentration of a gas dissolved in a liquid in equilibrium with an adjacent gas phase is proportional to its partial pressure in the gas phase.

The proportionality constant (K_H) for Henry's Law defines the solubility of a gas, expressed as molarity, *M*—moles of gas per liter H_2O:

$$K_{gas} = \frac{M_{gas}}{P_{gas}} \text{ Henry's Law}$$

As the partial pressure for the gas, P_{gas}, is typically in atmospheres, the units of K_{gas} are mol/L/atm. Because gases are not ionized, their activity coefficient is equal to 1 for most low-salinity waters, and so concentrations, M_{gas}, are the same as activities. For the purposes of studying solute *volatility,* such as the vapor pressure that would be exerted by a contaminant, such as benzene, in water, the inverse units of atm·L/mol are often used.

For example, the solubility of O_2 is defined by the Henry's Law constant (at 25°C):

$$K_{O_2} = 0.00126 = \frac{M_{O_2(aq)}}{P_{O_2}}$$

Air-equilibrated freshwater ($P_{O_2} = 0.21$ atm or $10^{-0.68}$) at 25°C would have dissolved oxygen (DO) concentration of $O_{2(aq)}$ equal to 0.253 mmol/kg or 8.1 ppm. Note that for aqueous concentrations, the standard mass units of ppm (mass of gas per mass of water) are used rather than volumetric units of ppmv for gases in air.

As an uncharged solute, the solubility of a gas is largely established by its mass, as seen by the positive correlation between gas solubility and gram formula weight (Figure 3.8). The Henry's constants for gas solubility are given above in Table 3.5.

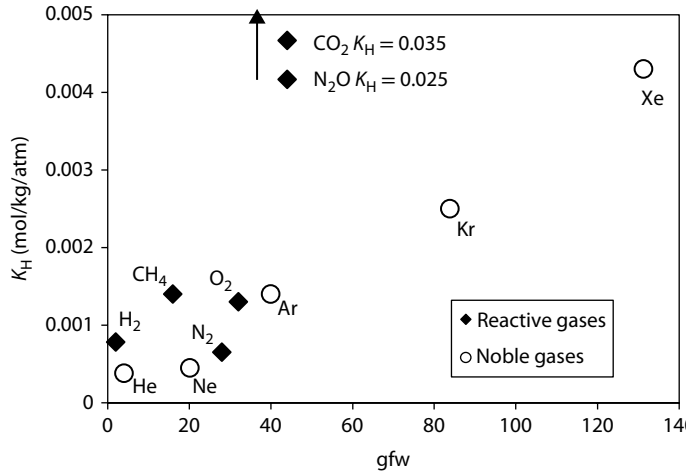

FIGURE 3.8 The solubility of common atmospheric gases according to their atomic mass (gfw) at 25°C. Note that the solubility increases with atomic mass due to the lower kinetic energy (lower diffusion) of the larger gas molecules. It also increases with reactivity in water. The most reactive gases, CO_2 and N_2O, have very high solubilities in water (high K_H values).

Example 3.5: Gas Concentrations in Air-Equilibrated Water

What are the concentrations of N_2 and CO_2 in air-equilibrated water at 25°C?

Reformulating Henry's Law and using the constants for N_2 ($K_{N_2} = 0.00065$) and CO_2 ($K_{CO_2} = 0.035$)

$$M_{N_2} = K_{N_2} \times P_{N_2}$$
$$= 0.00065 \times 0.781$$
$$= 0.000508 \text{ mol/L}$$

$$M_{CO_2} = K_{CO_2} \times P_{CO_2}$$
$$= 0.035 \times 0.0004$$
$$= 0.000014 \text{ mol/L}$$

$N_{2\ \text{dissolved}} = 14.2$ mg/L

$CO_{2\ \text{dissolved}} = 0.62$ mg/L

Partial Pressure of Dissolved Gas

The increase in pressure with depth below the water table is such that free-gas phases seldom exist in most aquifers. Nonetheless, dissolved gases still have a partial pressure. This is the equilibrium partial pressure, in atmospheres, that the gas would exert in an adjacent gas phase were it to be present. It is simply calculated from Henry's Law, using K_H for the in situ temperature and the dissolved concentration to give P_{gas}.

It is useful to express dissolved gas concentrations as partial pressures, as this allows direct comparison with their partial pressure of the original free-gas phase during recharge. If groundwater at some point of observation has a dissolved gas with a higher partial pressure than it does in the soil air, then it must have gained concentration by subsurface reactions, whereas if its concentration is lower, then some must have been lost by reaction along the flow path (Example 3.6).

Example 3.6: Partial Pressure of Gas below the Water Table

Groundwater at a depth of 10 m has a dissolved concentration of O_2 of 4.2 mg/L. How does its partial pressure compare with P_{O_2} in air?

$$O_2 = 4.2 \text{ mg/L}$$

$$= 4.2/(\text{gfw} \cdot 1000) = 4.2/32000 = 0.00013 \text{ mol/L}$$

$$K_{O_2} = \frac{M_{O_2(aq)}}{P_{O_2}} = 0.0013 \text{ mol/L/atm}$$

$$P_{O_2} = \frac{M_{O_2(aq)}}{K_{O_2}} = 0.1 \text{ atm}$$

Oxygen, O_2, in air has a partial pressure of 0.209 atm. The P_{O_2} in groundwater is 0.1 atm and so has lost over half of its DO by reaction, likely by oxidation of organics.

The partial pressure of dissolved gas in groundwater can be demonstrated with a device that uses this principle to sample dissolved gases for analysis (Gardner and Solomon 2009). A passive diffusion gas sampler is simply a copper tube sealed with a gas-permeable silicon rubber membrane that can be set at depth below the water level in a piezometer or well (Figure 3.9). Dissolved gases in the groundwater diffuse in and exchange with the original air in the sampler. When recovered after a period of a few days to equilibrate, the sampler will contain the gases dissolved in the groundwater, at concentrations equal to their respective partial pressures. The copper tube is then crimp-sealed and the sampled gases later measured for concentration and isotopes.

Gas Solubility in Volumetric Units: Bunsen Coefficient

While concentrations of gases in water can be expressed in mass units of mg/L, they can also be expressed volumetrically as a volume of gas per volume of water. This is most common with the noble gases, which are measured volumetrically. At standard

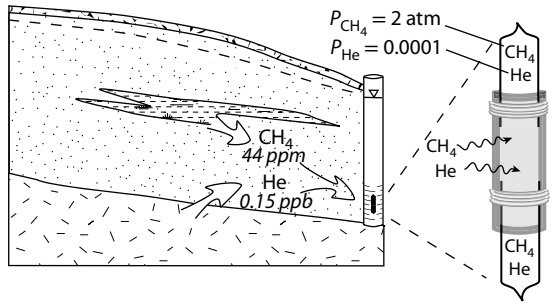

FIGURE 3.9 Dissolved gases in an aquifer sampled using a passive diffusion gas sampler using gas-permeable silicon tubing attached to air-filled copper tubes sealed at the ends to keep out water. Dissolved gases diffuse into the sampler to their respective groundwater partial pressure as established by Henry's constant for each gas.

temperature and pressure (STP = 273.16 K or 0°C and 1 atm or 101.3 kPa), one mole of gas occupies 22.414 L. This derives from the gas constant, R, and temperature, T, which define the pressure–volume relationship for a mole of an ideal gas:

$$PV = nRT \quad \text{or} \quad n = \frac{PV}{RT}$$

where n is the number of moles of the gas, P is the pressure (atm), and V is the volume (L, cm^3, or cubic cm—cc). The gas constant, R, is simply the pressure change with temperature (kelvin) for a unit volume of a mole of gas (R = 0.082058 atm L/mol/K or 8.3143 J/mol/K), and T is the absolute temperature (K). For one mole of gas at one atmosphere pressure and 273.15 K (STP), its volume $V = RT$ = 22.414 L, or 22,414 cc.

This leads to the expression of gas concentration in volumetric units, cc_{gas}, at STP per cubic centimeter of water (cc or mL). The solubility constant is the Bunsen coefficient, B. From the gas law, Bunsen coefficient is simply the Henry's Law constant multiplied by RT, derived according to:

Henry's Law constant K_H = mol/L (units = n/L_{H_2O})
and so $n = K_H \times L_{H_2O}$

Gas law $$n = \frac{PV}{RT}$$

For R = 0.082058 atm L mol^{-1} K^{-1} at STP (1 atm pressure and 273.15 K):

$$n = L_{gas}/RT$$

Equating Henry's Law with the gas law through n gives

$$L_{gas}/RT = K_H \times L_{H_2O}$$

and so for a gas partial pressure of 1 atm (i.e., a pure gas at atmospheric pressure):

$$L_{gas}/L_{H_2O} = K_H\, RT$$

Rather than liters, the convention is to use milliliters, or cc of gas, thus, for P_{gas} = 1 atm:

$$cc_{gas\text{-}STP}/cc_{H_2O} = K_H RT$$

This expression is Bunsen's coefficient (Table 3.5), which expresses the solubility of a gas per atm partial pressure.

Bunsen coefficient: $B = K_H RT$ ($cc_{STP}/cc/atm$)

Thus, the solubility of any atmospheric gas in cc_{STP}/cc_{H_2O} is equal to B_{gas} multiplied by the molar fraction of that gas in the atmosphere (e.g., 0.78 for N_2).

Example 3.7: Converting gas concentration from mass to volumetric units

What is the concentration of the dissolved O_2 in Example 3.6 expressed in volumetric units with Bundsen's coefficient?

$O_2 = 4.2$ mg/L
$= 4.2/32000 = 0.00013$ mol/L
$B_{O_2} = K_{O_2} RT = 0.0013 \times 22.414 = 0.029$ cc_{STP}/cc_{H_2O}
$O_2 = \text{mol/L} \times RT = 0.00013 \times 22.414 = 0.0029$ cc_{STP}/cc_{H_2O}

Note that air-equilibrated water would have:
$B_{O_2} \times P_{O_2} = 0.029 \times 0.21 = 0.0061$ cc_{STP}/cc_{H_2O}

So, the dissolved O_2 (DO) content of this water can be expressed as 4.2 mg/L, as 0.000131 mol/L or as 0.0029 cc_{STP}/cc_{H_2O}.

Gas Solubility with Temperature

Opening a bottle of soda demonstrates the increased solubility of gas with pressure, and drinking warm soda demonstrates the decreased solubility of gas with temperature. The Henry's Law constant for gas solubility at nonstandard temperatures is calculated from the Van't Hoff equation, as discussed in Chapter 2, using enthalpy data, $\Delta H°$ from Table 3.6 and the gas constant in joules (0.0083143 kJ/mol/K).

$$\log K_{T_2} = \log K_{298} + \frac{\Delta H_r^o}{2.303R}\left(\frac{1}{298} - \frac{1}{T_2}\right)$$

The decreased solubilities of the major atmospheric gases with increasing temperature are shown in Figure 3.10, for a partial pressure, P_{gas}, of 1 atm. The right hand chart shows their solubilities in air-equilibrated water in ppm. The temperature equations on which these graphs are based are also given. The temperature control on gas solubility during recharge allows calculation of recharge temperature for old groundwaters based on concentrations of nonreactive atmospherically-derived noble gases. Applications of this tool are presented in Chapter 8 on groundwater dating.

TABLE 3.6
Standard Enthalpy of Reaction for Some Gas Dissolution Reactions

Gas	Dissolution reaction	log $K_{25°C}$	$\Delta H°_r$ (kJ/mol)
N_2	$N_{2(g)} \Leftrightarrow N_{2(aq)}$	–3.23	–11.36
O_2	$N_{2(g)} \Leftrightarrow N_{2(aq)}$	–2.89	–15.43
Ar	$Ar_{(g)} \Leftrightarrow Ar_{(aq)}$	–2.85	–12.47
CO_2	$CO_{2(g)} \Leftrightarrow CO_{2(aq)}$	–1.47	–19.95
CH_4	$CH_{4(g)} \Leftrightarrow CH_{4(aq)}$	–2.85	–13.3

Source: Parkhurst and Appelo 1999.

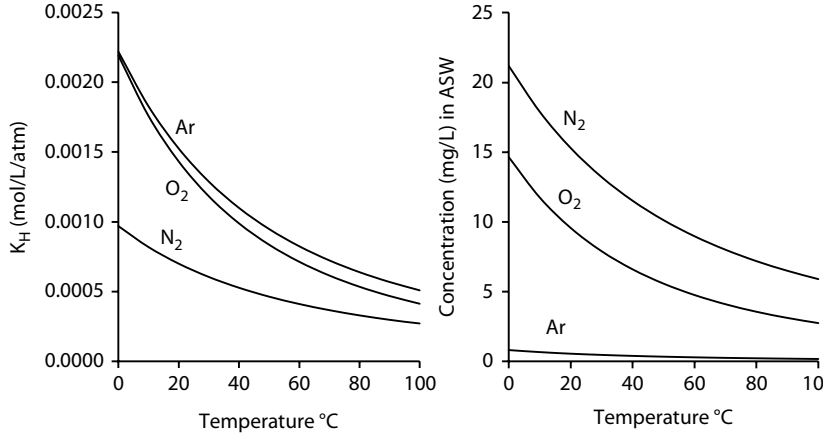

FIGURE 3.10 Left: Solubility of the major atmospheric gases with temperature (K_H for P_{gas} = 1 atm). Right: Atmospheric gas concentrations in air-saturated water (ASW) according to their respective atmospheric partial pressures, for a total atmospheric pressure of 1 atm. The following equations give the temperature-concentration relationships in the right hand chart (valid to 100°C).
N_2 (mg/L) = $-1.09 \times 10^{-5}\ T^3 + 0.003\ T^2 - 0.3437\ T + 21.13$
O_2 (mg/L) = $-1.16 \times 10^{-5}\ T^3 + 0.003\ T^2 - 0.3015\ T + 14.6$
Ar (mg/L) = $-5 \times 10^{-5}\ T^3 + 0.000142\ T^2 - 0.0152\ T + 0.8224$

Increases in temperature along the groundwater flow path will change the equilibrium solubility of dissolved gases. Geothermal waters, for example, recharge as cold groundwaters saturated with atmospheric N_2. However, as this air-saturated recharge water becomes heated, the solubility of N_2 is decreased. As the geothermal water circulates back to the low hydrostatic pressure at the surface, it will then degas N_2 at the discharge vent. For this reason, many geothermal waters effervesce.

Example 3.8: Partial Pressure of N_2 in Geothermal Waters

Groundwater recharged at 1000 m in the Coast Mountains of British Columbia, where the air pressure is 0.87 atm at an average temperature of 10°C, and circulates to some 3000 m depth before discharging in tidewater hotsprings with a temperature of 65°C and a pressure of 1 atm. What will be the partial pressure of N_2, and will it effervesce?

Using the N_2 air solubility equation in Figure 3.10, with the recharge temperature of 10°C yields a dissolved concentration for air-equilibrated water of

$$N_2 = 18.0 \text{ mg/L}$$

for 1 atm total pressure, which at 1000 m and 0.87 atm pressure would be

$$N_{2(10°C,\ 1000m)} = 18.0 \text{ x } 0.87\text{atm} = 15.6 \text{ mg/L}.$$

Atmospheric saturation of N_2 at sea level for 65°C geothermal waters would be, again using the equation in Figure 3.10

$$N_{2(65°C,0m)} = 8.5 \times 1 \text{ atm} = 8.5 \text{ mg/L}.$$

As this is less than half of the concentration that these geothermal waters gained during recharge, they will clearly degas N_2 to the atmosphere on discharge.

Gas Solubility and Pressure

Pressure plays an important role in gas solubility. Groundwater typically becomes saturated with soil air during recharge, but as groundwaters circulate more deeply, the greater pressure increases the equilibrium concentration, so that the water becomes undersaturated with its dissolved gases that is, concentrations are less than solubility for the ambient hydrostatic pressure (Figure 3.11). In the case of groundwater

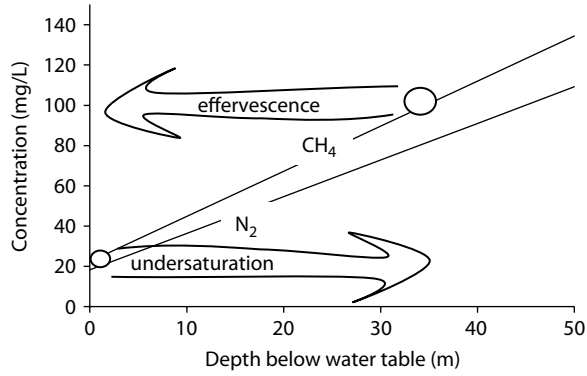

FIGURE 3.11 Gas solubility with pressure for N_2 and CH_4, at 25°C, showing linear increase in equilibrium solubility with increased pressure (pressure as depth below water table, where 10 m is 2 atm). A decrease in water pressure by pumping or discharge to a spring can cause effervescence, as shown for CH_4. By contrast, groundwater saturated with atmospheric N_2 in this example becomes undersaturated at greater depth.

recharge through an unsaturated zone in porous media and fractured rock, microbubbles of air can be entrained and carried below the water table. At higher hydrostatic pressure with depth below the water table, they then become dissolved, contributing an "excess air" component to the dissolved gas concentration. Excess air can contribute percent up to several tens of percent of the total dissolved gas concentration.

At depth during subsurface circulation, the excess hydrostatic pressure keeps the gas in solution. With the pressure drop as the groundwater discharges at surface, the dissolved gas rapidly becomes oversaturated for the temperature–pressure conditions and effervesces.

Example 3.9: Pressure and Gas Solubility

Groundwater circulating with a temperature of 10°C through a Quaternary sand aquifer encounters some methanogenic zones with high organic carbon. A well with a depth of 30 m has a methane concentration of 80 mg/L. Does a separate gas phase exist at this depth, and is there the potential for gas to accumulate in the water-distribution system?

To have a free-gas phase requires that the partial pressure of methane exceeds the confining pressure at 30 m depth, which is 3 atm pressure. Use the Van't Hoff equation with K_{CH_4} from Table 3.5 and enthalpy data, ΔH_r°, from Table 3.6 to first calculate methane solubility at 10°C:

$$\log K_{CH_{4-10°C}} = \log K_{CH_{4-25°C}} + \frac{\Delta H_r^o}{2.303\ R}\left(\frac{1}{298} - \frac{1}{273+10}\right)$$

$$= -2.85 + \frac{-13.3}{2.303 \times 0.0083143}\left(\frac{1}{298} - \frac{1}{283}\right)$$

$$= -2.73$$

$$K_{CH_{4-10°C}} = 0.00188$$

Next, use this value for K_{CH_4} at 10°C to calculate its partial pressure for the measured concentration of CH_4.

$$CH_4 = 80\ \text{mg/L}$$

$$= 80/16/1000 = 0.005\ \text{mol/L}$$

$$K_{CH_{4-10°C}} = 0.00186 = \frac{M_{CH_4}}{P_{CH_4}} = \frac{0.005}{P_{CH_4}}$$

$$P_{CH_4} = 2.7\ \text{atm}$$

This partial pressure is not greater than the confining water pressure of 30 m head, or 3 atm, and so there would not be a separate gas phase. However, pumping this water to the surface reduces the confining pressure to that of the water-distribution system, which is close to atmospheric pressure, and so methane would effervesce and collect in the plumbing. This can be predicted from the line for methane solubility with pressure in Figure 3.11, with some accommodation for the greater solubility of methane at lower temperature.

Gas Solubility and Salinity

Gases also have decreased solubility with increased salinity. The salting-out effect is well known, where addition of salt to water can cause effervescence. This has to do with the restructuring of water by solutes and the reduced activity that lowers the gas solubility for a given partial pressure. The effect is shown in Figure 3.12 for argon, as an example. Groundwaters can therefore become over saturated with dissolved atmospheric gases through increases in salinity along the flow path.

Biogenic and Geogenic Gases in the Subsurface

Below the surface, a variety of biological and abiotic reactions contribute dissolved gases to groundwater. These range from the soil environment to deep crustal settings. Soil atmospheres differ from the open atmosphere, due mainly to aerobic biodegradation and CO_2 production. This greatly increases the P_{CO_2} of groundwaters with respect to air-equilibrated water (Figure 3.13).

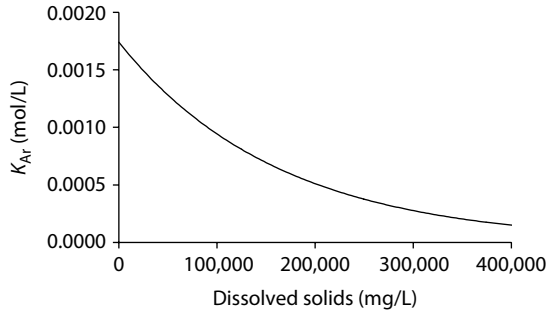

FIGURE 3.12 Effect of ionic strength on the solubility of Ar. (Modified from Kipfer et al. 1983.)

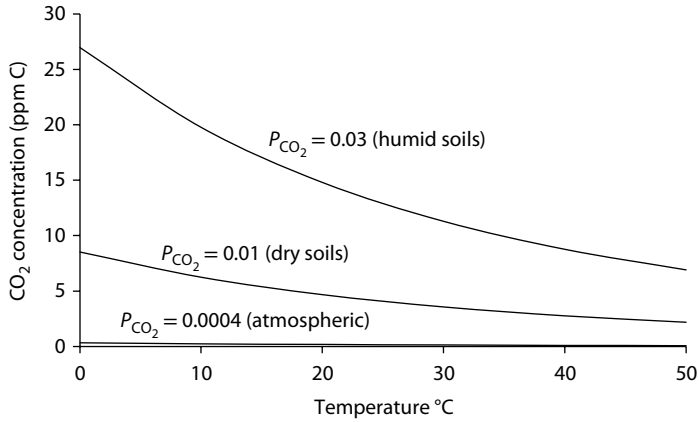

FIGURE 3.13 The solubility of CO_2 in soil water under open-system conditions, based on the temperature dependency of Henry's constant, $\log K_{CO_2} = 0.0000317\,T^2 - 0.0033\,T - 1.152$.

Below the water table, where redox conditions become anoxic, anaerobic microbial activity in the subsurface mediates biogeochemical reactions that can produce *biogenic* gases:

$$2NO_3^- + 2\tfrac{1}{2}CH_2O \rightarrow 2\tfrac{1}{2}HCO_3^- + \tfrac{1}{2}H^+ + H_2O + N_{2(aq)} \quad \text{denitrification}$$

$$CH_4 + SO_4^{2-} + 2H^+ \rightarrow CO_2 + H_2S + 2H_2O \quad \text{sulfate reduction}$$

$$CH_3COOH \rightarrow CO_2 + CH_{4(aq)} \quad \text{acetate fermentation}$$

$$CO_2 + 4H_2 \rightarrow CH_{4(aq)} + 2H_2O \quad CO_2 \text{ reduction}$$

Geogenic gases are produced by a variety of processes including radioactive decay:

$$^{238}U \rightarrow {}^{234}U + {}^{4}He \rightarrow {}^{206}Pb + 8\,{}^{4}He_{(aq)} \quad \text{alpha decay of uranium}$$

$$^{40}K \rightarrow {}^{40}Ar_{(aq)} \quad \text{beta decay of potassium}$$

Geogenic gases are also produced by high-temperature metamorphism of carbonates:

$$CaCO_3 + SiO_2 \rightarrow CaSiO_{3\ (wollastonite)} + CO_2 \quad \text{decarbonation of calcite}$$

or through mantle and crustal degasing of CO_2, He, and other volatile species.

The subsurface accumulation of dissolved biogenic and geogenic gases is greatly enhanced by the effect of pressure on solubility. Below the water table, hydrostatic pressure increases uniformly with depth. According to Henry's Law, this increases equilibrium solubility and so allows greater concentrations of gas to remain in a dissolved state. This has important implications for settings with high biogenic and geogenic gas production. Figure 3.14 shows the solubility of a selection of biogenic and geogenic gases with depth (pressure). The linear increase of saturated concentrations demonstrates the high gas concentrations that can exist in the subsurface in a

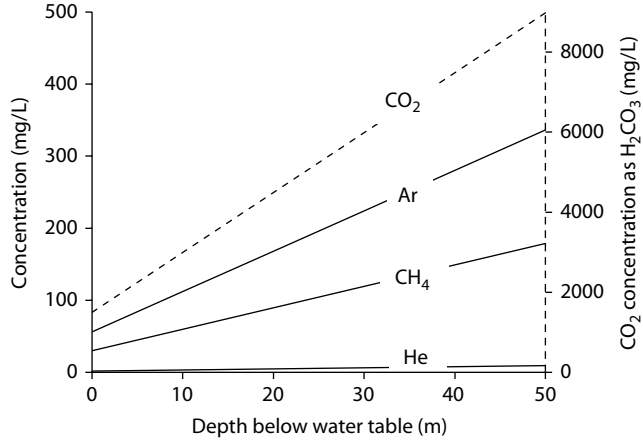

FIGURE 3.14 The solubility of the major geogenic gases that can occur in groundwaters. Equilibrium solubilities with increasing pressure (in depth below water table) at 25°C.

dissolved state. Note the very low solubility for He, which has high diffusivity and preferentially partitions into the free-gas phase.

Subsurface production can then exceed the solubility limit for a given temperature and pressure and form a free-gas phase in the aquifer. Further, the production of groundwaters with gas partial pressures greater than 1 atm can be hazardous when pumped into a water distribution system, where the lower pressure can allow buildup of a free-gas phase, commonly methane, in the plumbing.

CO_2 AND DISSOLVED INORGANIC CARBON

Aqueous reactions with inorganic carbon involve the full suite of the above reactions, including gas dissolution, hydration, acid dissociation, and mineral dissociation. Dissolved inorganic carbon (DIC) plays a central role in aqueous geochemistry and so warrants particular attention. Inorganic or mineralized carbon in its most oxidized state carries a valence of +IV. In minerals, C^{4+} coordinates covalently with three oxygen atoms as the carbonate anion (CO_3^{2-}) that forms a largely ionic bond with cations, such as Ca^{2+}. Coordinated with two oxygen atoms, it forms the stable linear CO_2 gas molecule. Dissolved in water as aqueous carbon dioxide ($CO_{2(aq)}$), this readily hydrates to form carbonic acid (H_2CO_3) and its two dissociation products, bicarbonate (HCO_3^-) and carbonate (CO_3^{2-}). Collectively, these four species comprise DIC:

$$m_{DIC} = m_{CO_2} + m_{H_2CO_3} + m_{HCO_3^-} + m_{CO_3^{2-}}$$

DIC can originate from a variety of reactions, such as:
Dissolution of CO_2 from the atmosphere or from the soil: $CO_{2(g)} \rightarrow CO_{2(aq)}$
Dissolution of calcite: $CaCO_3 + H^+ \rightarrow Ca^{2+} + HCO_3^-$
Oxidation of organics in water: $CH_2O + O_2 \rightarrow H_2CO_3$
Metamorphic reactions: $CaCO_3 + SiO_2 \rightarrow CO_2 + CaSiO_{3\ \text{wollastonite}}$

DIC is measured with a filtered sample by one of two methods. The sample can be acidified to convert all DIC species to $CO_{2(aq)}$, which is then separated by flushing with an inert gas or under vacuum and measured. The concentrations of the individual species can then be calculated from pH. Alternatively, the ionized species HCO_3^- and CO_3^{2-}, can be measured by an alkalinity titration (Chapter 10) and then used with pH to calculate the remaining DIC species. Individually, DIC species are important contributors to the acidity and buffering capacity of water as well as to the solubilities of carbonate minerals and complex ions. Their relative concentrations are governed by pH.

pH and the Distribution of Dissolved Inorganic Carbon Species

For most natural waters, it is the production of CO_2 from the degradation of plant debris in soils that contributes much of the DIC. In unsaturated, aerobic soils, CO_2 accumulates in the gas phase, sustaining high CO_2 partial pressures. The sequence of reactions begins with the dissolution and hydration of CO_2 in water to produce carbonic acid:

$$CO_{2(g)} \Leftrightarrow CO_{2(aq)} + H_2O \Leftrightarrow H_2CO_3$$

Although unhydrated $CO_{2(aq)}$ is an important species in solution, the hydration step is usually included in the overall reaction for CO_2 dissolution. By convention, all dissolved CO_2, whether hydrated or not, is taken to be in the form H_2CO_3.

Carbonic acid is a weak acid and readily dissociates to form bicarbonate and a hydrogen ion. Bicarbonate again dissociates to form carbonate. The relative distribution of DIC species is controlled by pH according to the carbonic acid dissociation reactions with their respective reaction constants:

CO_2 dissolution and hydration:

$$CO_{2(g)} + H_2O \Leftrightarrow H_2CO_3 \quad K_{CO_2} = \frac{a_{H_2CO_3}}{P_{CO_2}} = 10^{-1.47}$$

$$H_2CO_3 \Leftrightarrow H^+ + HCO_3^- \qquad K_1 = \frac{a_{HCO_3^-} \times a_{H^+}}{a_{H_2CO_3}} = 10^{-6.35}$$

$$HCO_3^- \Leftrightarrow H^+ + CO_3^{2-} \qquad K_2 = \frac{a_{CO_3^{2-}} \times a_{H^+}}{a_{HCO_3^-}} = 10^{-10.33}$$

Precipitation of calcite:

$$CaCO_3 \Leftrightarrow Ca^{2+} + CO_3^{2-} \quad K_{CaCO_3} = a_{Ca^{2+}} \times a_{CO_3^{2-}} = 10^{-8.48}$$

The concentration and distribution of DIC species is mainly controlled by P_{CO_2} and pH (a_{H^+}), which is shown by the relative concentrations of H_2CO_3, HCO_3^-, and CO_3^{2-} in Figure 3.15.

Note that K_1 and K_2 are the first and second dissociation constants for carbonic acid (i.e. $K_{H_2CO_3}$ and $K_{HCO_3^-}$). Values for these equilibrium constants are given below in Table 3.7 for different temperatures, along with their temperature equations.

From Figure 3.15, it is apparent that a decrease in pH leads to greater carbonic acid concentration as bicarbonate is converted to carbonic acid ($HCO_3^- + H^+ \rightarrow H_2CO_3$). The increased carbonic acid fraction increases the CO_2 partial pressure, P_{CO_2}, of the solution. Below the water table, this is an apparent P_{CO_2} (i.e., the CO_2 partial pressure that would be exerted if a separate gas phase existed with the water), whereas at the water table or lake surface, CO_2 would equilibrate with the atmosphere ($CO_{2(aq)} \rightarrow CO_{2(g)}$). An increase in pH has the opposite effect, shifting the relative distribution of DIC species toward the CO_3^{2-} field that favors precipitation of carbonate minerals ($CO_3^{2-} + Ca^{2+} \rightarrow CaCO_3$).

Figure 3.15 shows that over the pH range of most natural surface and groundwaters (6.5–8.5), HCO_3^- is the main DIC species, with minor carbonic acid, as $CO_{2(aq)}$ or H_2CO_3. Under acid conditions below pH 6.4, carbonic acid becomes the dominant DIC species, followed by HCO_3^-. CO_3^{2-} is present, but at trace concentrations. Only in the unusual conditions for highly alkaline waters with pH greater than 10.3 does CO_3^{2-} become the major DIC species. The relative concentrations of all DIC species can be calculated from pH. The calculations can be simplified by considering that DIC is dominated by one major and one minor carbonate species at any given pH: H_2CO_3 plus HCO_3^- below pH 8.4, and HCO_3^- plus CO_3^{2-} above pH 8.4 (Figure 3.15).

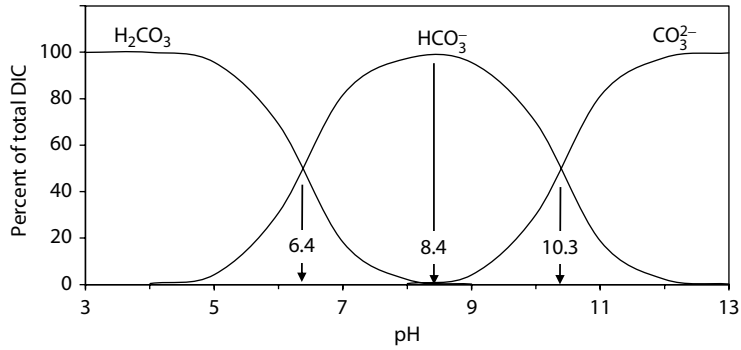

FIGURE 3.15 Relative distribution of dissolved inorganic carbon species in pure water as a function of pH, at 25°C.

The following equations allow calculation of the relative concentrations or fraction, *f*, of these species in either pH range. Note that although the third component (e.g., CO_3^{2-} at low pH or carbonic acid at high pH) is insignificant in such a mass balance calculation, it is important in thermodynamic calculations. CO_3^{2-} may contribute insignificantly to the total DIC at neutral pH, but it will have an activity that can be readily calculated from the concentration of DIC and that will play a vital role in the dissolution and precipitation of carbonate minerals. Thus, although DIC is almost entirely composed of HCO_3^- at neutral pH, it is important to calculate the concentrations of the minor DIC species, H_2CO_3 and CO_3^{2-}, for their role in CO_2 degassing and mineral precipitation reactions. The follow derives generic formulae for calculating the concentrations of DIC species from a measured DIC value. Note that these are based on the activity relationships for the DIC species and therefore include activity coefficients to determine species concentrations.

Calculating concentrations of DIC species from measured DIC (mol/kg) (note that $\gamma_{H_2CO_3} = 1$):

Acidic—below pH 8.4

$$m_{DIC} = m_{H_2CO_3} + m_{HCO_3^-}$$

$$K_1 = \frac{a_{H^+} \times a_{HCO_3^-}}{a_{H_2CO_3}}$$

$$= a_{H^+} \times \frac{m_{HCO_3^-} \times \gamma_{HCO_3^-}}{(m_{DIC} - m_{HCO_3^-})}$$

$$K_1 \times m_{DIC} = a_{H^+} \times m_{HCO_3^-} \times \gamma_{HCO_3^-} + K_1 \times m_{HCO_3^-}$$

$$m_{HCO_3^-} = \frac{K_1 \times m_{DIC}}{a_{H^+} \times \gamma_{HCO_3^-} + K_1}$$

Alkaline—above pH 8.4

$$m_{DIC} = m_{HCO_3^-} + m_{CO_3^{2-}}$$

$$K_2 = \frac{a_{H^+} \times a_{CO_3^{2-}}}{a_{HCO_3^-}}$$

$$= a_{H^+} \times \frac{m_{CO_3^{2-}} \times \gamma_{CO_3^{2-}}}{(m_{DIC} - m_{CO_3^{2-}})\gamma_{HCO_3^-}}$$

$$K_2 \times m_{DIC} \times \gamma_{HCO_3^-} = a_{H^+} \times m_{CO_3^{2-}} \times \gamma_{CO_3^{2-}} + K_2 \times m_{CO_3^{2-}} \times \gamma_{HCO_3^-}$$

$$m_{CO3^{2-}} = \frac{K_2 \times m_{DIC} \times \gamma_{HCO_3^-}}{a_{H^+} \times \gamma_{CO_3^{2-}} + K_2 \times \gamma_{HCO_3^-}}$$

Often, a geochemical analysis will include a measurement of bicarbonate, HCO_3^-, measured by an alkalinity titration (discussed in Chapter 10), rather than DIC as measured by a dissolved carbon analyzer. HCO_3^- is most often the major component of DIC and together with CO_3^{2-} participates in carbonate reactions. Calculating the distribution of the remaining DIC species from $m_{HCO_3^-}$ and pH is simply a matter of substitution into the appropriate equations for K_1 and K_2.

Example 3.10: H_2CO_3, HCO_3^- and CO_3^{2-} from Measured DIC and pH

What are the concentrations and activities of H_2CO_3, HCO_3^- and CO_3^{2-} in low ionic-strength water ($I = 0.01$) at 25°C with pH of 6.85 and measured DIC concentration of 64 ppm C?

$$\text{DIC} = 64 \text{ ppm C} = 5.33 \times 10^{-3} \text{ mol C/kg} = m_{H_2CO_3} + m_{HCO_3^-} + m_{CO_3^{2-}}$$

$$m_{DIC} = m_{H_2CO_3} + m_{HCO_3^-} = 0.0053 \text{ mol/kg}$$

$$\log \gamma_{HCO_3^-} = -0.5z^2 \sqrt{0.01}$$

$$\gamma_{HCO_3^-} = 0.89$$

$$m_{HCO_3^-} = \frac{K_1 \times m_{DIC}}{a_{H^+} \times \gamma_{HCO_3^-} + K_1} = \frac{10^{-6.35} \times 0.0053}{10^{-6.85} \times 0.89 + 10^{-6.35}} = 0.0041 \text{ mol/kg} = 250 \text{ ppm}$$

$$m_{H_2CO_3} = m_{DIC} - m_{HCO_3^-}$$
$$= 0.0053 - 0.0041$$
$$= 0.0012 \text{ mol/kg} = 74.4 \text{ ppm}$$

$$a_{HCO_3^-} = m_{HCO_3^-} \times \gamma_{HCO_3^-} = 0.0041 \times 0.89 = 0.0036$$

$$a_{CO_3^{2-}} = K_2 \times a_{HCO_3^-}/a_{H^+} = 10^{-10.33} \times 0.0036/10^{-6.85} = 10^{-5.92} = 1.21 \cdot 10^{-6}$$

$$a_{H_2CO_3} = m_{H_2CO_3} \times \gamma_{H_2CO_3} = 0.0012 \times 1.0 = 0.0012$$

$$P_{CO_2} = a_{H_2CO_3}/K_{CO_2} = 0.0012/10^{-1.47} = 10^{-1.45} \text{ or } 0.034 \text{ atm}$$

Example 3.11: Concentrations and Activities of H_2CO_3, and CO_3^{2-} from HCO_3^- and pH

What are the activities and concentrations of H_2CO_3 and CO_3^{2-} in low ionic-strength water ($I = 0.01$) at 25°C with pH of 6.85 and HCO_3^- concentration of 250 ppm?

$$m_{HCO_3^-} = \frac{\text{ppm}}{\text{gfw} \cdot 1000} = \frac{250}{61 \cdot 1000} = 0.0041 = 10^{-2.39}$$

from above, $\log \gamma = -0.5z^2\sqrt{0.05}$

$\gamma_{HCO_3^-} = 0.89$ and $\gamma_{CO_3^{2-}} = 0.63$

$a_{HCO_3^-} = m_{HCO_3^-} \times \gamma_{HCO_3^-} = 0.0041 \times 0.89 = 0.00365$

$a_{H^+} = 10^{-pH} = 10^{-6.85}$

for CO_3^{2-}:

$$K_2 = \frac{a_{CO_3^{2-}} \times a_{H^+}}{a_{HCO_3^-}} = 10^{-10.33}$$

$$a_{CO_3^{2-}} = \frac{K_2 \times a_{HCO_3^-}}{a_{H^+}} = \frac{10^{-10.33} \times 0.00365}{10^{-6.85}} = 10^{-5.91} = 1.21 \times 10^{-6}$$

$$m_{CO_3^{2-}} = a_{CO_3^{2-}} / \gamma_{CO_3^{2-}} = 1.21 \times 10^{-6} / 0.63 = 1.92 \times 10^{-6} \text{ mol/kg} = 0.12 \text{ ppm}$$

for H_2CO_3:

$$K_1 = \frac{a_{HCO_3^-} \times a_{H^+}}{a_{H_2CO_3}} = 10^{-6.35}$$

$$a_{H_2CO_3} = \frac{a_{HCO_3^-} \times a_{H^+}}{K_1} = \frac{0.00365 \times 10^{-6.85}}{10^{-6.35}} = 10^{-2.94} = 0.0012$$

$$m_{H_2CO_3} = a_{H_2CO_3} / \gamma_{H_2CO_3} = 0.0012/1 = 0.0012 \text{ mol/kg}$$

Thus, for this water, the concentration of CO_3^{2-} is an insignificant component of the total DIC reservoir. The concentration of H_2CO_3, by contrast, is over 20% of the DIC pool. The DIC concentration can be calculated as

$$\begin{aligned} \text{DIC} = m_{H_2CO_3} + m_{HCO_3^-} + m_{CO_3^{2-}} &= 0.0012 + 0.0041 + 1.3 \times 10^{-6} \\ &= 0.00240 \text{ mol/kg} \\ &= 64 \text{ ppm C (as given in Example 3.10)} \end{aligned}$$

Partial Pressure of CO_2 and Dissolved Inorganic Carbon

Any water that has a free surface (i.e., surface water or soil water in the unsaturated zone of an aquifer) will dissolve CO_2 from the adjacent gas phase according to the partial pressure of CO_2 (P_{CO_2}) present in that gas. In soils, where active aerobic decay of vegetation is producing CO_2, the P_{CO_2} of the soil air is usually between $10^{-2.5}$ and $10^{-1.5}$ atm (0.003 and 0.03 atm). In the open atmosphere, it is much lower, close to $10^{-3.4}$ atm (0.0004 atm). The concentration of carbonic acid in groundwater that is generated by dissolution of CO_2 in the soil air is governed by the Henry's Law constant, K_{CO_2}, and is proportional to the P_{CO_2} of the gas phase. At 25°C, the value for K_{CO_2} is $10^{-1.47}$ (Chapter 2 and Table 3.7). Accordingly, a partial pressure of 0.03 atm CO_2 produces some 0.001 mol/kg of H_2CO_3. This provides groundwater with the acidity required for mineral weathering.

Groundwaters below the water table (i.e., with no proximity to the free surface) may retain CO_2 acquired during recharge or may have accumulated CO_2 from subsurface reactions, such as oxidation of buried organics in the aquifer. From this concentration of H_2CO_3 (established from measurements of pH and alkalinity or DIC, as described earlier), we can calculate a value for P_{CO_2}. Although there is no separate gas phase, it represents the partial pressure of CO_2 that would be present in an adjacent gas phase to maintain the concentration of carbonic acid observed in the water. It can even be measured with a gas diffusion sampler—as shown in Figure 3.9. However, the equilibrium P_{CO_2} of water is more easily calculated from the concentration of carbonic acid, or from DIC and pH, using the thermodynamic constants from Table 3.7. The value of calculating the P_{CO_2} for groundwater is in the interpretation of its geochemical evolution.

Example 3.12: Calculating P_{CO_2} from H_2CO_3 and pH

For the water used in Examples 3.10 and 3.11 above, what is the P_{CO_2}? Starting with either DIC = 64 ppm C or HCO_3^- = 250 ppm and using the given pH of 6.85, the calculated molality and activity of carbonic acid was $m_{H_2CO_3} = 0.0012 = a_{H_2CO_3}$. The $P_{CO_2^-}$ is determined from the Henry's Law constant for CO_2 solubility:

$$CO_{2(g)} + H_2O \Leftrightarrow H_2CO_3$$

$$K_{CO_2} = \frac{a_{H_2CO_3}}{P_{CO_2}} = 10^{-1.47} = 0.034$$

$$P_{CO_2} = \frac{a_{H_2CO_3}}{K_{CO_2}} = \frac{0.0012}{0.034} = 0.035$$

$$P_{CO_2} = 0.035 = 10^{-1.5}\text{atm}$$

The resulting value is two orders of magnitude higher than the P_{CO_2} of the atmosphere ($10^{-3.4}$) and suggests equilibrium with an organic-rich soil.

TABLE 3.7
Solubility and Dissociation Constants for the Carbonate system

T(°C)	log K_{CO_2}	log $K_{H_2CO_3}$	log $K_{HCO_3^-}$	log K_{CaCO_3}
0	–1.11	–6.58	–10.62	–8.38
5	–1.19	–6.52	–10.55	–8.39
10	–1.27	–6.47	–10.49	–8.41
15	–1.34	–6.42	–10.43	–8.43
20	–1.41	–6.38	–10.38	–8.45
25	–1.47	–6.35	–10.33	–8.48
50	–1.72	–6.28	–10.16	–8.65

Equations: (T in °C)

$\log K_{CO_2} = 0.00009\,T^2 - 0.0167\,T - 1.11$

$\log K_{H_2CO_3} = -0.00013\,T^2 + 0.0125\,T - 6.58$

$\log K_{HCO_3^-} = -0.00009\,T^2 + 0.0139\,T - 10.62$

$\log K_{CaCO_3} = 0.00006\,T^2 - 0.00252\,T - 8.38$

Such calculations of P_{CO_2} are routine for geochemical interpretations. In surface waters, P_{CO_2} values may be significantly greater than atmospheric, which indicates *in situ* respiration in the water column or contributions from groundwaters recharged

through soils. In groundwaters, high P_{CO_2} values are associated with soil waters and shallow groundwaters, whereas lower values indicate weathering out of contact with soil air. Such trends are discussed further in Chapter 6 on the geochemical evolution of groundwaters.

PROBLEMS

1. Write out the reactions for the dissolution of fluorite, for the hydrolysis of Fe^{3+}, and the equation for the law of mass action for each.
2. Write balanced equations for the following aqueous reactions:
   (i) Hydration of CO_2 and dissociation of carbonic acid
   (ii) Dissolution of dolomite with dissolved CO_2
   (iii) Precipitation of ferrihydrite from waters with dissolved Fe^{3+}
   (iv) Dissolution of gypsum and precipitation of barite in a Ca^{2+}–Ba^{2+}–SO_4^{2-} solution
   (v) Oxidation of ferrous iron to ferrihydrite with nitrate.
   (vi) Incongruent dissolution of orthoclase to kaolinite.
   (vii) Dissolution of gibbsite in low pH water.
3. From the data given in Table 3.3, what would be the concentration of $CaSO_4^\circ$ in a gypsum-saturated solution at 25°C?
4. Is nitrate a functional electron acceptor for the oxidation of dissolved hydrogen sulfide? Calculate the ΔG°_r for this reaction and determine whether it is exothermic or endothermic. How does this reaction compare with the oxidation of hydrogen sulfide with O_2?
5. Provide an example of electron-donor and electron-acceptor species (redox couple) for S, N, Fe, and As, and write balanced redox half-reactions for the electron transfer.
6. Calculate the Gibbs free energy for the oxidation of organic matter (CH_2O) with nitrate. How does this compare with that for oxidation by O_2 (Example 3.2) on a per mole basis for CH_2O?
7. Write the two complementary redox half-reactions for (i) the oxidation of hydrogen (H_2) by O_2, and (ii) oxidation of methane (CH_4) with O_2. Determine the Gibb's free energy for each overall reaction. Which would provide more energy to bacteria, per mole of O_2 consumed?
8. Name the gases that are commonly found in groundwater that are: (i) essentially of an atmospheric origin, (ii) produced in the soil or groundwater by geochemical processes, and (iii) geogenic gases produced by reactions in bedrock. Note that some gases can originate from more than one of these sources.
9. How much biogenic methane can be produced (cc_{STP}/cc_{H_2O} and mol/L) at 10 m below the water table before you produce a separate gas phase (at 25°C)?
10. Figure 3.7 shows that helium has a higher atmospheric concentration than krypton but a lower concentration in air-equilibrated water. Explain this change using their Bunsen coefficients.
11. Neon, krypton, and xenon are essentially atmospherically derived gases, with only trace concentrations of some rare isotopes produced in the

geosphere. Plot the concentration of these three gases in groundwater recharge between the temperatures of 5°C and 30°C. Which shows the strongest variation with temperature as a record paleorecharge temperature?

12. A groundwater has a measured concentration of nitrogen, N_2, of 0.025 cc_{STP}/cc_{H_2O}. Its temperature is 25°C and is the same as the recharge area. Convert this concentration to ppm, and determine the amount of "excess" nitrogen above the value for equilibrium with the atmosphere. If this excess nitrogen is derived from denitrification, then how much NO_3^- would have reacted?
13. What are the concentrations and activities of carbonate, $a_{CO_3^{2-}}$, and carbonic acid, $a_{H_2CO_3}$, for low ionic-strength groundwater ($I = 0.01$) at 25°C, with pH 7.8 and bicarbonate concentration of 86 ppm as HCO_3^-? How much do they contribute to DIC?
14. Calculate the P_{CO_2} of the groundwater in Question 13 from your calculated activity of H_2CO_3. Will this groundwater degas CO_2 upon discharge? What would be the effect on pH?
15. The calcium concentration in the groundwater in Question 13 was measured to be 56.8 ppm. What is its state of calcite saturation? What will happen when this groundwater discharges?
16. What is the consequence to sampling a calcite-saturated groundwater at a low temperature of say 10°C, and then storing it at room temperature, 25°C?.

This page intentionally left blank

4 Isotope Reactions

INTRODUCTION

Complementing the geochemical reactions discussed in Chapter 3, are reactions involving the isotopes of the elements. Isotopes do not change the nature of the reaction, that is, oxygen with an additional two neutrons will still behave chemically as oxygen. They do, however, have very slightly differing free energies and therefore react at slightly different rates during physical and geochemical reactions. This partitions the heavy and light isotopes on opposite sides of the reaction. This allows isotopes to be used as tracers of water and solutes and their reactions.

The *environmental* isotopes are naturally occurring isotopes of the major elements that participate in processes at the earth's surface. In hydrology, the principal stable isotopes of interest are ^{18}O and D. Others, including ^{13}C, ^{15}N, and ^{34}S, are used to trace biogeochemical processes and the contamination of water resources. The routinely measured stable environmental isotopes are given in Table 1.3 along with their average natural abundance and the typical samples in which they are measured.

As an example, oxygen–18, or ^{18}O, is an isotope of common ^{16}O but with an abundance of only about 0.2% or 2000 ppm. Water has a second stable isotope—deuterium, D or ^{2}H, which is a hydrogen atom with one neutron and one proton, giving it a mass of 2. Deuterium has an abundance of only about 150 ppm. Water itself then can have an atomic mass of 18 (H_2O), 19 (HDO), or 20 ($H_2^{18}O$). Rare are configurations such as $HD^{18}O$ (atomic mass 21) or *heavy water* D_2O (atomic mass 20) that is concentrated and used as a neutron moderator in CanDU nuclear reactors.

Although oxygen can exist with more than 10 or fewer than 8 neutrons, these radionuclides are not stable and readily decay to other elements. Similarly, other elements can have a greater or lesser complement of neutrons, creating a host of stable and unstable or radioactive nuclides (atoms with specific number of neutrons and protons). The 92 naturally occurring elements have some 250 stable isotopes. The stable and unstable isotopes for the light elements up to atomic number 8 are shown on a neutron–proton chart in Figure 4.1.

The law of mass action applies not only for solutes in groundwaters but also for isotopes. Stable isotopes of an element behave the same chemically, and so participate in all the reactions discussed in Chapter 3. However, their slight mass difference affects bond strength such that they accumulate preferentially on one side or the other of a reaction. It is this mass-dependent partitioning or *fractionation* of isotopes that makes them good tracers of the origin and reactions of water and solutes. Radioisotopes also fractionated by their mass, but it is their decay that brings the important element of time to hydrogeology.

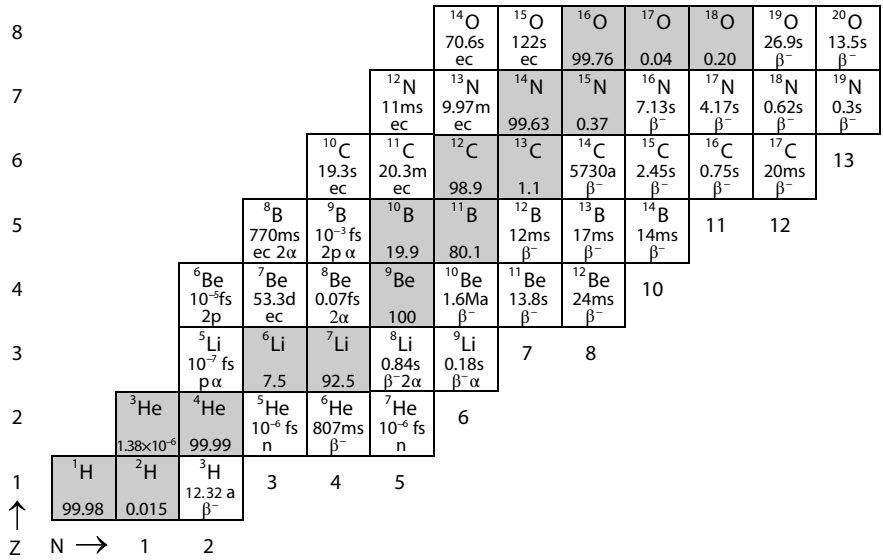

FIGURE 4.1 Light element isotopes showing percent abundances of the stable isotopes (gray fill) and half-lives of radioisotopes (s, second; m, minute; d, day; a, year) with their principal and secondary decay modes, where α = alpha emission (2p and 2n); ec, electron capture, β⁻ = electron (beta) emission; n, neutron emission; and p, proton emission. (From *Chart of the Nuclides,* 16th ed., General Electric Co. and KAPL, Inc., 2002.)

STABLE ISOTOPE FRACTIONATION AND DISTILLATION

Isotopes are a useful tool to trace the origin of water and solutes. Like geochemical components of a system, the partitioning of isotopes in the environment is facilitated by the thermodynamics of equilibrium and kinetic reactions. For most systems, their distribution is controlled by interplay of two processes, the *fractionation* of isotopes during any physical or chemical reaction, and the *distillation* of isotopes from reactant reservoir as the reaction proceeds. These two processes work together to partition isotopes into different reservoirs.

Equilibrium Fractionation

Fractionation can take place under equilibrium conditions where the distribution of isotopes is controlled by thermodynamic equilibrium with equal rates of forward and backward reaction. Equilibrium fractionation is the mass-dependent process at the level of a physical or chemical reaction that partitions isotopes on one side or the other of the reaction. It is always a difficult concept to grasp, but perhaps the analogy of building a fence from a field of stones can help. The reaction in this case is the gathering and placing of stones from the field on the fence. The fellow building the fence finds that most are regular sized, but there are some big stones (like the heavy isotope, e.g. ^{18}O). He likes these, as they make a stronger fence, and so when he

finds a bigger stone in the field, he uses it. As he works, he removes some stones and replaces them with others that fit better. His fence therefore has a higher abundance of big stones than their abundance in the field. His preference for building with bigger stones than the smaller ones is *fractionating* the heavy and light stones between the field and his fence. The fence is overall *enriched* in heavy stones compared to the reservoir of stones in the field. In a geochemical sense, the fence might be calcite and the heavy stones are carbonate molecules with $^{13}CO_3^{2-}$.

The most common equilibrium isotope fractionation reactions are those that trace water and carbon in inorganic aqueous reactions where a geochemical equilibrium is achieved. These are principally inorganic dissociation and gas-exchange reactions. A few examples are as follows:

$$H_2O_{water} \leftrightarrow H_2O_{vapor}$$
$$CaCO_3 + CO_2 + H_2O \leftrightarrow Ca^{2+} + 2HCO_3^- + H_2O$$
$$CO_{2\,gas} \leftrightarrow CO_{2\,aq}$$
$$CO_{2\,aq} + H_2O \leftrightarrow H_2CO_3 \Leftrightarrow HCO_3^- + H^+$$

The partitioning of isotopes in a physicochemical reaction is more subtle than the analogy of building a stone fence. Only slight thermodynamic differences between isotopes exist, and so the net partitioning of isotopes is very small. For example, the concentration of ^{18}O in water is about 2000 ppm and in ice is about 2006 ppm. That makes ^{18}O about 0.3% or 3‰ enriched in ice over water. We can express this as a difference in the ratio of ^{18}O to ^{16}O in the ice (2.006×10^{-3}) compared to the water (2.000×10^{-3}) giving a fractionation of 1.003. This is not much of a difference, but is measurable and reproducible.

Fractionation Factor (α)

In 1947, Harold Urey published the theoretical basis for isotope fractionation as an exchange of isotopes between molecules that are participating in a reaction. This established the equilibrium fractionation factor, α, for isotope reactions, which is essentially the equilibrium constant, *K*, presented in Chapter 2 for geochemical reactions. Just as *K* defines the equilibrium condition for mineral solubilities and solute concentrations in geochemical reactions, the fractionation factor, α, establishes the isotope ratios in components of isotope-exchange reactions. Unlike *K*, which can vary enormously (e.g., $10^{1.58}$ for dissociation of halite to $10^{-8.4}$ for the dissociation of calcite), isotope fractionation factors are for the most part very close to 1. This is because the partitioning of isotopes between compounds is very minor.

Consider the evaporation and condensation of water as an example of a physical reaction and the dissolution of CO_2 to form HCO_3^- as a geochemical reaction. As the reaction approaches equilibrium, the transfer of reactants to products is matched by the reverse reaction such that some water is evaporating to vapor and some vapor is

condensing to water, and likewise, CO_2 is dissolving and HCO_3^- is dehydrating and degassing:

$$H_2O_{water} + H_2O_{vapor} \leftrightarrow H_2O_{vapor} + H_2O_{water}$$
$$CO_2 + H_2O + HCO_3^- + H^+ \leftrightarrow HCO_3^- + H^+ + CO_2 + H_2O$$

If we consider the reactants and products as only geochemical entities, then the activity product of the reaction products will be exactly the same as the reactants, and the thermodynamic reaction constant will be 1 (using square brackets to denote thermodynamic activity):

$$K_{v-w} = \frac{[H_2O]_{vapor}[H_2O]_{water}}{[H_2O]_{water}[H_2O]_{vapor}} = 1 \qquad K_{CO_2-HCO_3^-} = \frac{[HCO_3^-][H^+][CO_2][H_2O]}{[CO_2][H_2O][HCO_3^-][H^+]} = 1$$

If we add isotopes to the reaction, there will be forward and backward exchange of isotopes until there is an equilibrium distribution with either the reactant or the product having more of the heavy isotope. In an equilibrium isotope-exchange reaction, there is no change in the geochemistry of the solution, only an exchange of isotopes:

$$H_2^{16}O_w + H_2^{18}O_v \leftrightarrow H_2^{18}O_w + H_2^{16}O_v$$
$$^{13}CO_2 + H_2O + H^{12}CO_3^- + H^+ \leftrightarrow H^{13}CO_3^- + H^+ + {}^{12}CO_2 + H_2O$$

Now the thermodynamic reaction constant becomes:

$$K_{w-v} = \frac{[H_2^{18}O]_w[H_2^{16}O]_v}{[H_2^{16}O]_w[H_2^{18}O]_v}$$
$$= \frac{[^{18}O]_w}{[^{16}O]_w} \times \frac{[^{16}O]_v}{[^{18}O]_v}$$
$$= \frac{\left(\frac{^{18}O}{^{16}O}\right)_w}{\left(\frac{^{18}O}{^{16}O}\right)_v} = \frac{R_w}{R_v}$$
$$= \alpha^{18}O_{w-v}$$

$$K_{CO_2-HCO_3^-} = \frac{[H\,^{13}CO_3^-][H^+][\,^{12}CO_2][H_2O]}{[\,^{13}CO_2][H_2O][H\,^{12}CO_3^-][H^+]}$$
$$= \frac{[^{13}C]_{HCO_3^-}[^{12}C]_{CO_2}}{[^{13}C]_{CO_2}[^{12}C]_{HCO_3^-}}$$
$$= \frac{\left(\frac{^{13}C}{^{12}C}\right)_{HCO_3^-}}{\left(\frac{^{13}C}{^{12}C}\right)_{CO_2}} = \frac{R_{HCO_3^-}}{R_{CO_2}}$$
$$= \alpha^{13}C_{HCO_3^- - CO_2}$$

The equilibrium fractionation factor, α, is simply the ratio of the isotope ratio in two reacting phases or species. Like equilibrium constants, it is usually expressed as the isotope abundance ratio in the *product* (or right side of equation) over the isotope abundance ratio in the *reactant* (left side of equation).

$$\alpha_{\text{product}-\text{reactant}} = \frac{R_{\text{product}}}{R_{\text{reactant}}} \qquad \alpha^{18}O_{w-v} = \frac{R_w}{R_v} \qquad \alpha^{13}C_{HCO_3^- - CO_2} = \frac{R_{HCO_3^-}}{R_{CO_2}}$$

From Chapter 1, the isotope abundance ratio (e.g., $^{18}O/^{16}O$) does not greatly vary in the environment, and so the fractionation factor, α, generally has a value close to 1. However, this value can be precisely measured and so is expressed with a precision of 4–5 decimal places.

Because atoms with greater mass form slightly stronger bonds, the heavier isotope is generally enriched in the more condensed phase or larger molecule. For example, the molecules of water are held together by weak hydrogen bonds. As there is slightly greater hydrogen bond strength for $H_2^{18}O–H_2O$ versus $H_2^{16}O–H_2O$ bonds, it is the ^{16}O–bonds that will be more easily broken during evaporation. The result is a lower concentration of $H_2^{18}O$ in the water vapor than in the liquid water, and so water is isotopically enriched over its vapor. Similarly, ^{18}O is more enriched in ice than in water.

Example 4.1: Expressing the Fractionation Factor in Terms of δ–‰ Values

Using the example of ^{18}O fractionation between water and vapor, express the fractionation factor, α, in terms of the $\delta^{18}O$ values of the water and vapor.

$$\delta^{18}O_{\text{water}} = \left(\frac{\left(\frac{^{18}O}{^{16}O}\right)_{\text{water}}}{\left(\frac{^{18}O}{^{16}O}\right)_{\text{VSMOW}}} - 1 \right) \times 1000$$

$$\left(\frac{^{18}O}{^{16}O}\right)_{\text{water}} = \left(\frac{^{18}O}{^{16}O}\right)_{\text{VSMOW}} \times \left(\frac{\delta^{18}O_{\text{water}}}{1000} + 1\right)$$

$$\left(\frac{^{18}O}{^{16}O}\right)_{\text{vapor}} = \left(\frac{^{18}O}{^{16}O}\right)_{\text{VSMOW}} \times \left(\frac{\delta^{18}O_{\text{vapor}}}{1000} + 1\right)$$

$$\alpha^{18}O_{\text{water-vapor}} = \frac{\left(\frac{^{18}O}{^{16}O}\right)_{\text{water}}}{\left(\frac{^{18}O}{^{16}O}\right)_{\text{vapor}}}$$

$$= \frac{\left(\frac{^{18}O}{^{16}O}\right)_{\text{VSMOW}} \times \left(\frac{\delta^{18}O_{\text{water}}}{1000} + 1\right)}{\left(\frac{^{18}O}{^{16}O}\right)_{\text{VSMOW}} \times \left(\frac{\delta^{18}O_{\text{water}}}{1000} + 1\right)}$$

$$= \frac{\delta^{18}O_{\text{water}} + 1000}{\delta^{18}O_{\text{vapor}} + 1000}$$

Enrichment Factor (ε)

Isotope geochemistry is based on the variations of isotope concentrations, expressed as δ–‰ values. To compare isotope fractionation with δ–‰ values, we can express the fractionation factor, α, in permil units, using the *enrichment factor*, ε.

$$\varepsilon = (\alpha - 1) \times 1000\ ‰$$

This is the same expression as the δ-value used to express isotope data, and so the enrichment factor can be added and subtracted with the δ-values measured in an equilibrium reaction. Recalling that R is the isotope ratio in a sample or standard, and using the example of fractionation for water evaporating to vapor:

$$\varepsilon = \left(\frac{R_{water}}{R_{vapor}} - 1 \right) \times 1000 \qquad \delta = \left(\frac{R_{sample}}{R_{standard}} - 1 \right) \times 1000$$

$$\varepsilon_{reactant-product} = \delta_{reactant} - \delta_{product}$$
$$\varepsilon_{water-vapor} = \delta_{water} - \delta_{vapor}$$

For forward and reverse reactions, the fractionation factor, α, and the enrichment factor, ε are inversed:

$$\alpha_{reactant-product} = 1/\alpha_{product-reactant} \qquad \varepsilon_{reactant-product} = -\varepsilon_{product-reactant}$$

Example 4.2: Calculating $\delta^{18}O$ of Water Vapor in Equilibrium with Water

A water sample has a $\delta^{18}O$ value of –4.5. It is in equilibrium with water vapor at 25°C. The fractionation factor at 25°C is 1.0093. What is the $\delta^{18}O$ value of the water vapor?

$$\begin{aligned}
\delta^{18}O_{water} &= -4.5 \\
\alpha^{18}O_{water\text{-}vapor} &= 1.0093 \\
\varepsilon^{18}O_{water\text{-}vapor} &= (\alpha - 1) \times 1000 \\
&= (1.0093 - 1) \times 1000 \\
&= 9.3‰ \\
\varepsilon^{18}O_{water\text{-}vapor} &= \delta^{18}O_{water} - \delta^{18}O_{vapor} \\
\delta^{18}O_{vapor} &= \delta^{18}O_{water} - \varepsilon^{18}O_{water-vapor} \\
&= -4.5 - 9.3 \\
&= -13.8‰
\end{aligned}$$

Therefore, the $\delta^{18}O$ value for the water vapor is –13.8‰. The vapor is depleted in ^{18}O by 9.3‰, which is consistent with the pattern of isotope enrichment in the more condensed phase.

Fractionation and Temperature

Isotope fractionation is a thermodynamic process and so is a function of temperature. Following from Urey's work, considerable effort has been made to establish the temperature relationship for isotope fractionation in various reactions, such as evaporation, condensation, freezing, aqueous reactions, and mineral crystallization. These relationships are important in calculations of isotope fractionation at the range of temperatures in natural systems.

At high temperature, α is very close to 1, with a departure from 1 as the temperature of reaction decreases. Fractionation factors are greatest for the low-temperature geochemical reactions in groundwaters and surface waters.

The temperature dependence of α is determined as its natural logarithm, $\ln\alpha$, and generally represented in equations of the following form:

$$\ln\alpha_{X-Y} = aT^{-2} + bT^{-1} + c$$

As α is close to 1 for most isotope reactions, $\ln\alpha$ is very close to 0, and so multiplying by 1000 fits with the ‰ convention for δ-values. Providing α is close to 1, the enrichment factor, ε, is then close to $1000\ \ln\alpha$:

$$\varepsilon = 1000\ (\alpha - 1) \cong 1000\ \ln\alpha$$

This is illustrated for water–vapor fractionation at different temperatures in Table 4.1 and Figure 4.2.

TABLE 4.1
Values for Enrichment Factors for ^{18}O and ^{2}H in Water–Vapor–Ice Reactions, Based on Equations Given Below.

T(°C)	$\varepsilon^{18}O_{w\text{-}v}$ (‰)	$\varepsilon D_{w\text{-}v}$ (‰)
Water-vapor (Majoube 1971)		
0	11.6	106
25	9.3	76
50	7.5	55
75	6.1	39
100	5.0	27
Ice-water (°C)	2.8	20.6 (O'Neil 1968)
	3.1	19.3 (Suzuoki and Kumura 1973)

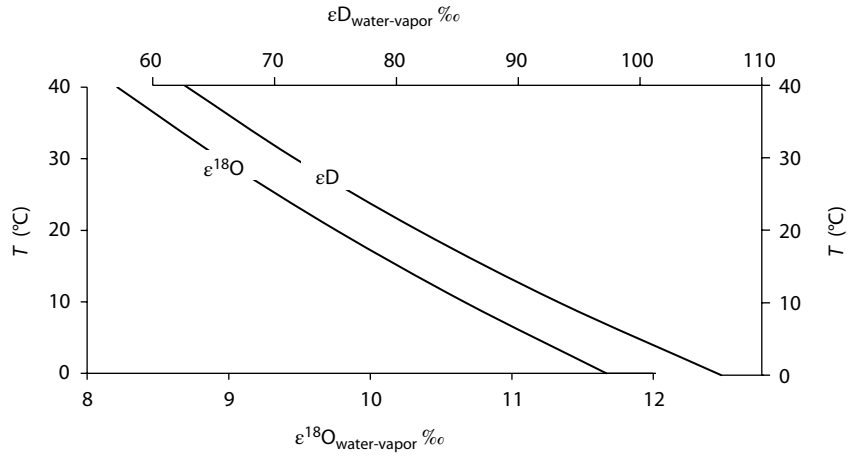

FIGURE 4.2 Temperature effect on fractionation of ^{18}O and D between water and water vapor.

Example 4.3: Temperature Effect on Fractionation

What is the $\delta^{18}O$ for rain condensing at 20°C from a vapor mass that was formed by evaporation of seawater ($\delta^{18}O$ = 0‰) at 25°C?

$$H_2O_{seawater} \leftrightarrow H_2O_{vapor}$$

$$\delta^{18}O_{seawater} = \ 0‰ \text{ VSMOW}$$

$$\varepsilon^{18}O_{vapor-water} = \delta^{18}O_{vapor} - \delta^{18}O_{seawater}$$

From Table 4.1, $\varepsilon^{18}O_{water-vapor}$ = 9.3‰ at 25°C and so the inverse, $\varepsilon^{18}O_{vapor-water}$ = –9.3‰, is calculated as shown below:

$$\delta^{18}O_{vapor} = \delta^{18}O_{seawater} + \varepsilon^{18}O_{vapor-water}$$

$$\delta^{18}O_{vapor} = 0 - 9.3$$

$$= -9.3‰.$$

The enrichment factor $\varepsilon^{18}O_{water-vapor}$ is taken from the temperature equation in Table 4.1 for 20°C.

$$H_2O_{vapor} \leftrightarrow H_2O_{rain}$$

$$\delta^{18}O_{rain} = \delta^{18}O_{vapor} + \varepsilon^{18}O_{water-vapor}$$

$$= -9.3 + 9.7$$

$$= 0.4‰.$$

For this example, evaporation and condensation were presumed to be under equilibrium conditions. While this is often the case for condensation, the formation of a vapor mass is generally more complicated, involving kinetic evaporation, mixing of different vapor sources and partial rainout.

From these data, the trend toward increasing fractionation at lower temperatures is clear. Note the much greater degree of fractionation for D than for ^{18}O between water and vapor. This is a consequence of the mass difference of D over H, which is 100%. As ^{18}O is only 12.5% heavier than ^{16}O, it will not be as strongly fractionated as D.

In this section, the isotopes of water and water vapor have been used as an example of fractionation and temperature. The same principles apply to stable isotopes in other geochemical systems, which will be introduced as tracers of geochemical evolution in natural waters. The temperature equations for the principal isotope-exchange reactions useful in groundwater work are given in Table 4.2 and a selection are shown graphically in Figure 4.3.

TABLE 4.2
Temperature and Fractionation for Some Common Isotope-Exchange Reactions (*T* in °C)

Isotope	Exchange Reaction	Temperature Equation	ε–‰ at 25°C
D	H_2O—H_2O_{vapor}	$\varepsilon D_{water-vapor} = 0.0066\,T^2 - 1.36\,T + 106$	79
	H_2O_{vapor}—H_2	$\varepsilon D_{vapor-H_2} = 0.02\,T^2 - 6.39\,T + 1395$	2485
	H_2O_{water}—H_2	$\varepsilon D_{water-H_2} = 0.026\,T^2 - 7.75\,T + 1502$	2762
	H_2O_{water}—CH_4	$\varepsilon D_{water-CH_4} = -0.0018\,T^2 + 0.64\,T + 12$	27
	H_2O_{water}—H_2S	$\varepsilon D_{water-H_2S} = 0.011\,T^2 - 3.93\,T + 949$	1358
	Gypsum—H_2O	$\varepsilon D_{water-gypsum} = 0.00008\,T^2 - 0.028\,T - 14$	–15
	Illite—H_2O	$\varepsilon D_{water-illite} = -0.0008\,T^2 + 0.4804\,T - 66.904$	–55
	Kaolinite—H_2O	$\varepsilon D_{water-kaolinite} = -0.0003\,T^2 + 0.152\,T - 35.368$	–32
^{18}O	H_2O_{water}—H_2O_{vapor}	$\varepsilon^{18}O_{water-vapor} = 0.0004\,T^2 - 0.103\,T + 11.64$	9.3
	CO_2—H_2O	$\varepsilon^{18}O_{CO_2-water} = 0.0007\,T^2 - 0.240\,T + 45.6$	41.0
	Calcite—H_2O	$\varepsilon^{18}O_{CaCO_3-water} = 0.0011\,T^2 - 0.265\,T + 34.3$	28.8
	Gypsum—H_2O	$\varepsilon^{18}O_{gypsum-water} = 0.00009\,T^2 - 0.0304\,T + 4.72$	4.0
	SO_4^{2-}—H_2O	$\varepsilon^{18}O_{SO_4-water} = 0.0011\,T^2 - 0.275\,T + 34.5$	28.7
	Illite—H_2O	$\varepsilon^{18}O_{illite-water} = 0.0004\,T^2 + 0.19\,T + 27.86$	33.1
	Kaolinite—H_2O	$\varepsilon^{18}O_{kaolinite-water} = 0.0004\,T^2 + 0.201\,T + 29.12$	34.4
	$SiO_{2(amorph)}$—H_2O	$\varepsilon^{18}O_{SiO_2-water} = 0.0014\,T^2 - 0.336\,T + 42.8$	35.9
^{13}C	H_2CO_3—$CO_{2(g)}$	$\varepsilon^{13}C_{H_2CO_3-CO_{2(g)}} = -0.000014\,T^2 + 0.0049\,T - 1.18$	–1.1
	HCO_3^-—$CO_{2(g)}$	$\varepsilon^{13}C_{HCO_3-CO_{2(g)}} = 0.00032\,T^2 - 0.124\,T + 10.87$	8.0
	CO_3^{2-}—$CO_{2(g)}$	$\varepsilon^{13}C_{CO_3-CO_{2(g)}} = 0.00033\,T^2 - 0.083\,T + 8.25$	6.4
	$CaCO_3$—HCO_3^-	$\varepsilon^{13}C_{CaCO_3-HCO_{3(g)}} = -0.0002\,T^2 + 0.056\,T - 0.39$	0.9
	$CaCO_3$—CO_2	$\varepsilon^{13}C_{CaCO_3-CO_2} = 0.0009\,T^2 - 0.184\,T + 14.4$	10.3
	CO_2—CH_4	$\varepsilon^{13}C_{CO_2-CH_4} = 0.0015\,T^2 - 0.418\,T + 77.7$	70.5
^{34}S	SO_4^{2-}—$H_2S_{(aq)}$	$\varepsilon^{34}S_{SO_4-H_2S} = 0.0019\,T^2 - 0.484\,T + 74.2$	65.4
	SO_4^{2-}—$HS^-_{(aq)}$	$\varepsilon^{34}S_{SO_4-HS} = 0.0017\,T^2 - 0.493\,T + 83.9$	75.4

Source: From data and references in Clark and Fritz 1997.

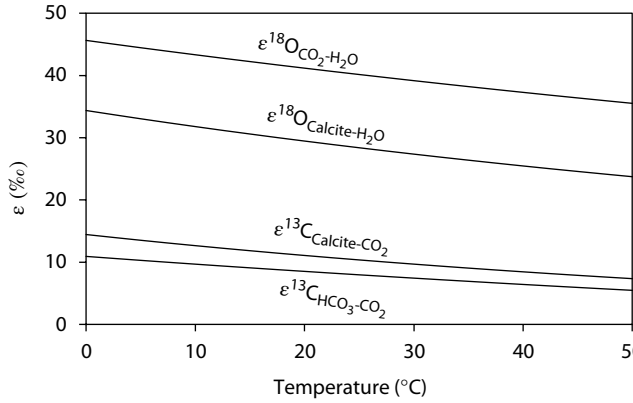

FIGURE 4.3 Variations for enrichment factors for some common isotope-exchange reactions.

Kinetic and Microbially Mediated Reactions

Physicochemical reactions are accelerated when conditions move away from equilibrium, perhaps by a change in pH or addition of a reactant. Such kinetic conditions can reduce the mass-discrimination of thermodynamic fractionation when the forward reaction greatly exceeds the backward reaction. Using the analogy of the stone fence, this would be the case where the builder works faster to complete the fence, using the nearest stones and with little to no discrimination against the small stones. An example is the precipitation of calcite from water by the sudden increase in ionic strength (addition of salt) where the calcite precipitate will have a $\delta^{13}C_{CaCO_3}$ the same as the initial $\delta^{13}C_{DIC}$.

Redox reactions are similar in that there is little to no back reaction. However, most redox reactions taking place under near-surface conditions are mediated by bacteria and archaea, which are highly selective in the isotopic bonds they choose to break. Microbes colonize a wide range of geochemical settings, from acidic mine tailings to hotsprings and hypersaline conditions, using the energy associated with the exchange of electrons between redox-sensitive elements, including carbon, sulfur, nitrogen, hydrogen, and iron. Bacteria and archaea can augment the energy they gain from such reactions by selecting preferentially the light isotopes for which bonds are easier to break, for example, ^{32}S–O rather than ^{34}S–O during sulfate reduction. For this reason, biologically mediated redox reactions are highly fractionating. Back to the analogy in the field of stones, now the fellow must clear the field and so he simply chucks stones off the field to the side. Of course he chucks only the light ones at first, as this gives him and energetic advantage. In the case of sulfate reducing bacteria, the sulfide they produce is depleted in ^{34}S relative to the SO_4^{2-}.

In microbially mediated reactions, the associated enrichment factors are not necessarily well constrained to a simple temperature–fractionation relationship. Fractionation can be affected by not only temperature but also reactant concentrations,

associated nutrient availability, concentrations of other influencing redox species, such as O_2, and the strains of microbes involved in the reactions. Some of the more common microbially mediated reactions and their associated enrichment factors include the following:

Sulfate reduction	$SO_4^{2-} + 8e^- + 8H^+ \rightarrow H_2S + 4H_2O$	$\varepsilon^{34}S_{SO_4-H_2S} \approx 20‰–30‰$
Nitrification	$NH_4^+ + 2O_2 \rightarrow NO_3^- + H_2O + 2H^+$	$\varepsilon^{15}N_{NH_4-NO_3} \approx 30‰$
Denitrification	$NO_3^- + 5e^- + 6H^+ \rightarrow ½\ N_2 + 3H_2O$	$\varepsilon^{15}N_{NO_3-N_2} \approx 15‰–20‰$
Methanogenesis	$CO_2 + 8e^- + 8H^+ \rightarrow CH_4 + 2H_2O$	$\varepsilon^{13}C_{CO_2-CH_4} \approx 60‰–80‰$

Diffusive Fractionation

Diffusion is an additional process that can fractionate isotopes and in theory can be related to the relative molecular velocity of a heavy isotope species relative to the light isotope species. It is an important process in aquitards where groundwater advection is minimal and transport is dominated by molecular diffusion in the porewaters.

The simplest case is the diffusion of gas in a vacuum, where steady-state fractionation equals the ratio of the velocities of the two isotopes, which resolves to the root of the mass ratio, which is Graham's law:

$$\alpha_{m^*-m} = \frac{\nu^*}{\nu} = \frac{\sqrt{\frac{kT}{2\pi m^*}}}{\sqrt{\frac{kT}{2\pi m}}} = \sqrt{\frac{m}{m^*}}$$

where is v, molecular velocity (cm s^{-1}); k, Boltzmann constant (1.380658×10^{-23} J/K, gas constant per molecule); m, molecular mass; and T, absolute temperature K.

Derivatives of Graham's law for diffusion through a medium such as air or water include the molecular mass of the medium. However, in groundwaters, diffusive fractionation is limited to aquitards, where low permeability brings solute transport into the domain of diffusion. Here, it is concentration gradients that determine the rate of diffusion together with the diffusion coefficient for the isotope species in water and through the porous network. Fractionation of isotopes by diffusion through aquitards is examined by the rate of diffusion of the individual isotope species (e.g., $H_2^{18}O$, HDO, or $H^{13}CO_3^-$), each with its own coefficient of diffusion. The decoupling of isotopes in this way does not allow us to represent fractionation in terms of α and ε values as shown earlier. It is a mass-dependent process like physical–chemical fractionation, but can be considered more precisely as diffusive mixing. This is presented in Chapter 5, in the section on groundwater mixing.

Quantitative (Surface) Reactions

Many geochemical reactions take place under nonequilibrium (kinetic) conditions. Mineral dissolution reactions are a good example, where there is no isotope selection during the reaction. If mineral–solution reactions take place under equilibrium conditions, with equal forward and reverse reaction rates, or during growth, isotope exchange at the mineral surface will take place. However, during net dissolution, the reaction cannot preferentially select isotopes below the surface, and is therefore quantitative. The reaction products in such quantitative reactions have the same isotope composition as the reactant material. Such reactions can be both inorganic and biologically mediated:

Pyrite oxidation	$Fe^{34}S_2 \rightarrow {}^{34}SO_4^{2-}$	$\delta^{34}S_{SO_4^{2-}} \cong \delta^{34}S_{FeS_2}$
Melting ice	$H_2^{18}O_{ice} \rightarrow H_2^{18}O_{water}$	$\delta^{18}O_{water} \cong \delta^{18}O_{ice}$
Calcite dissolution	$Ca^{13}CO_3 \rightarrow H^{13}CO_3^-$	$\delta^{13}C_{HCO_3^-} \cong \delta^{13}C_{calcite}$
Aerobic respiration	${}^{13}CH_2O \rightarrow {}^{13}CO_2$	$\delta^{13}C_{CO_2} \cong \delta^{13}C_{CH_2O}$

Note that in the case where the reactant has a high surface area, such as a melting snowpack, recrystallization of the solid reactant material can occur. In such cases, isotope exchange is associated with the recrystallization and isotope fractionation can take place.

Rayleigh Distillation of Isotopes

Isotope fractionation during a geochemical reaction acts to partition isotopes between reservoirs. Recall the fellow building his stone fence. Because he was selecting the heavy stones, the field gradually became enriched in light stones. The last stretch of the fence around this field would be built with increasing use of the light stones, until there were no stones left in the field. Isotopes behave in the same way with enrichment or depletion of isotopes in the residual reactant reservoir as it is used up.

A good example is a pond of water that is evaporating until it is dry. The fractionation between water and vapor, $\varepsilon^{18}O_{w\text{-}v}$, is 9.3‰ (Table 4.1). If the original $\delta^{18}O$ of the water is –10‰, then the vapor will initially have $\delta^{18}O = -19.3‰$. This low isotope value for the vapor product means that there is a gradual accumulation of ^{18}O in the pond as evaporation proceeds. This process is a Rayleigh distillation (Lord Rayleigh 1896), represented by the general equation

$$R_f = R_o f^{(\alpha-1)}$$

where R_f is the isotope ratio of the reactant reservoir after some reaction to some residual fraction, f. R_o is the initial isotopic ratio of the reactant reservoir when $f = 1$, and α is the fractionation factor for the reaction.

The equilibrium fractionation factor is written in the form of the product over the reactant, $\alpha_{prod\text{-}react}$, just like the mass action constant, K. A simplification of

the Rayleigh equation can be used to allow isotope ratios in δ–‰ notation and the fractionation factor in ε–‰ notation:

$$\delta_{\text{react}} = \delta_{\text{initial react}} + \varepsilon_{\text{prod-react}} \times \ln f$$
$$\delta^{18}O_{\text{water}} = \delta^{18}O_{\text{initial water}} + \varepsilon^{18}O_{\text{vapor-water}} \times \ln f$$

Plotting this relationship for the residual water in the evaporating pond gives the exponential curve in Figure 4.4. When the residual water has been reduced to a small fraction of its original volume, $\delta^{18}O$ becomes greatly enriched due to the discrimination against ^{18}O during reaction (evaporation). Evaporation is a nonequilibrium process, as it takes place under conditions of low humidity (kinetic reaction). The enrichment factors for ^{18}O and D during evaporation are greater than the equilibrium values given in Table 4.1, and become even greater with decreasing humidity.

This extreme depletion (or enrichment, depending on whether ε is positive or negative) is characteristic of Rayleigh distillation reactions. Other examples include the freezing of water in limited volumes of surface water (ponds, frost blisters), and geochemical reactions such as sulfate reduction or methanogenesis (see Chapter 7). One of the most important examples is the partitioning of ^{18}O and D through the hydrological cycle. This is essentially driven by the Rayleigh distillation of isotopes from vapor masses as they cool and rain out over the continents. This is why tropical rains are enriched in ^{18}O and D, while the rain and snow of cold-climate regions is highly depleted. Rayleigh distillation of isotopes during rain out is the process that partitions isotopes throughout the meteorological cycle and provides a versatile tracer of meteoric waters.

From isotope measurements made during a Rayleigh distillation reaction, it is then possible to calculate the enrichment factor for the reaction. Take, for example, the evaporating pond in Figure 4.4. Measurements of $\delta^{18}O$ for the residual water are

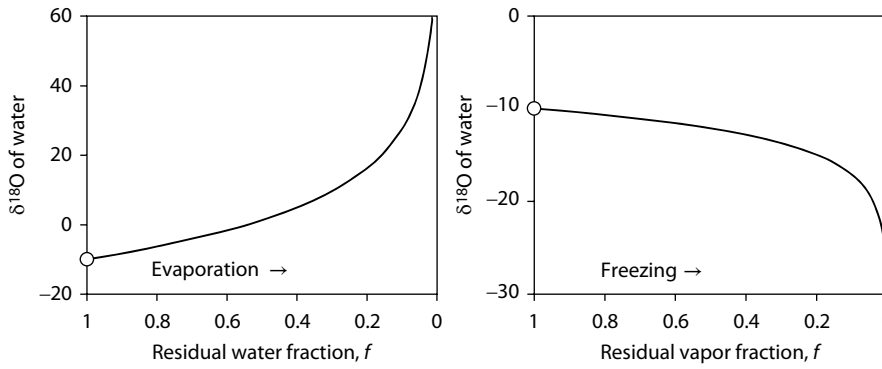

FIGURE 4.4 Rayleigh distillation for ^{18}O in water during evaporation (left) and in water during freezing (right). The initial $\delta^{18}O$ of the water is set at –10‰ for these examples. The ^{18}O preferentially partitions into the liquid phase during evaporation and so the water becomes enriched as evaporation of the pond proceeds. In contrast, ^{18}O partitions into ice during freezing and so the residual water becomes more depleted as freezing proceeds.

TABLE 4.3
Isotope Values for Evaporating Pond Water at Successive Residual Fractions of Water in the Pond at 25°C

f	$\delta^{18}O_{\text{water evaporating}}$	$\delta^{18}O_{\text{water freezing}}$
1	–10	–10
0.6	–1.7	–11.6
0.4	4.9	–12.8
0.2	16.2	–15.0
0.1	27.5	–17.1
0.05	38.9	–19.3

given in Table 4.3 for each different amount of residual water (diminishing depth of the pond). Rearranging the Rayleigh distillation equation given earlier to isolate epsilon (ε) allows calculation of the enrichment factor for the pond water:

$$\varepsilon^{18}O_{\text{vapor–water}} = (\delta^{18}O_{\text{water-}f} - \delta^{18}O_{\text{water-initial}}) / \ln f_{\text{water-}f}$$

For a simple Rayleigh distillation, $\varepsilon^{18}O_{\text{vapor–water}}$ can be calculated for any measurement made at a given residual fraction, f. In this case, the measurements give a consistent value for $\varepsilon^{18}O_{\text{vapor–water}}$ of –16.4‰, which can also be expressed as $\varepsilon^{18}O_{\text{water–vapor}}$ with a value of +16.4‰. Comparing this with values given in Table 4.1, we see that this empirical value is much greater than the theoretical values for 25°C. This can be attributed to the kinetic isotope effect that occurs during nonequilibrium evaporation, as discussed in Chapter 5.

Isotope Mass Balance Equations

Isotopes are often used to apportion the origin of solute mass in groundwater. Dissolved sulfate or DIC of differing origins will have an isotope value that reflects the relative contributions of those origins. Isotope mass balance equations are used to solve these mixing problems and are based on weighting the isotope values by solute mass or by relative fraction of the solute.

Take, for example, the $\delta^{13}C$ value of DIC that is generated by equilibration between the water and soil CO_2. Using Example 3.10, this groundwater has a pH of 7.00. At this pH, the DIC is dominantly HCO_3^- with minor H_2CO_3. The distribution of DIC between these two species is calculated in Example 3.10 to be:

$$\begin{aligned} m_{H_2CO_3} &= 0.0004 \text{ mol/kg} \\ m_{HCO_3^-} &= 0.0020 \text{ mol/kg} \\ m_{DIC} &= 0.0024 \text{ mol/kg} \end{aligned}$$

We can then calculate the relative fractions of these DIC species:

$$\begin{aligned} f_{H_2CO_3} &= 0.0004/0.0024 = 0.17 \\ f_{HCO_3^-} &= 0.0020/0.0024 = 0.83 \end{aligned}$$

As these two species are in equilibrium with soil CO_2 ($d^{13}C_{CO_2} = -20‰$), their respective isotope values will be determined by fractionation with the soil CO_2 (with values for $\varepsilon^{13}C$ from Table 4.2) and so:

$$\delta^{13}C_{H_2CO_3} = \delta^{13}C_{CO_2} + \varepsilon^{13}C_{H_2CO_3-CO_2}$$
$$\delta^{13}C_{HCO_3^-} = \delta^{13}C_{CO_2} + \varepsilon^{13}C_{HCO_3^--CO_2}$$

The isotope mass balance equation to determine the $\delta^{13}C$ of the DIC can then be made using either relative fractions of the constituent components:

$$\begin{aligned}\delta^{13}C_{DIC} &= f_{H_2CO_3} \times \delta^{13}C_{H_2CO_3} + f_{HCO_3^-} \times \delta^{13}C_{HCO_3^-} \\ &= f_{H_2CO_3} \times (\delta^{13}C_{CO_2} + \varepsilon^{13}C_{H_2CO_3-CO_2}) + f_{HCO_3^-} \times (\delta^{13}C_{CO_2} + \varepsilon^{13}C_{HCO_3^--CO_2})\end{aligned}$$

or actual concentrations:

$$\begin{aligned}\delta^{13}C_{DIC} \times m_{DIC} &= m_{H_2CO_3} \times \delta^{13}C_{H_2CO_3} + m_{HCO_3^-} \times \delta^{13}C_{HCO_3^-} \\ &= m_{H_2CO_3} \times (\delta^{13}C_{CO_2} + \varepsilon^{13}C_{H_2CO_3-CO_2}) + m_{HCO_3^-} \times (\delta^{13}C_{CO_2} + \varepsilon^{13}C_{HCO_3^--CO_2})\end{aligned}$$

Solving these equations using values for $\varepsilon^{13}C$ from Table 4.2, and the DIC species data from above, gives:

$$\delta^{13}C_{DIC} = f_{H_2CO_3} \times (\delta^{13}C_{CO_2} + \varepsilon^{13}C_{H_2CO_3-CO_2}) + f_{HCO_3^-} \times (\delta^{13}C_{CO_2} + \varepsilon^{13}C_{HCO_3^--CO_2})$$

$$\begin{aligned}&= 0.17 \times (-20 - 1.1) + 0.83 \times (-20 + 8.0) \\ &= 0.17 \times (-21.1) + 0.83 \times (-12) \\ &= -13.5‰\end{aligned}$$

$$\delta^{13}C_{DIC} \times m_{DIC} = m_{H_2CO_3} \times (\delta^{13}C_{CO_2} + \varepsilon^{13}C_{H_2CO_3-CO_2}) + m_{HCO_3^-} \times (\delta^{13}C_{CO_2} + \varepsilon^{13}C_{HCO_3^--CO_2})$$

$$\begin{aligned}&= \frac{0.0004 \times (-20 - 1.1) + 0.0020 \times (-20 + 8.0)}{0.0024} \\ &= -13.5‰\end{aligned}$$

Whether calculated with fractions or concentrations, both isotope mass balance equations give the same value. Mass balance equations are used in a range of applications from mixing calculations to the equilibrium fractionation problems. Later chapters provide examples with such mass balance equations.

RADIOISOTOPES

The addition or loss of neutrons from the stable nuclides shown in Figure 4.1 produces increasingly unstable radioisotopes, which decay to a more stable configuration, principally by emission of alpha (α) or beta (β) particles, sometimes accompanied by a photon as electromagnetic gamma, γ, radiation, from the nucleus. While nuclear radiation can be harmful to living organisms at very high levels, background levels in the environment are not harmful, and may even stimulate an important immune system response.

Radioactivity is measured as decay events per time. The original unit is the curie, Ci, which is equal to the radioactivity of 1 g of ^{226}Ra—the isotope of radium that Marie Curie isolated from the ^{238}U decay series. The Becquerel, Bq, is now used, defined as one nuclear disintegration per second (1 Ci = 3.7×10^{10} Bq).

Nuclear radiation is ionizing in that it can break apart and ionize compounds in tissue and DNA, leading to health impacts. For radiation impacts on organisms, ionizing radiation is expressed in units of absorbed radiation or Grays, where 1 Gy is 1 J/kg, but then weighted for the relative damage of the type of radiation to give equivalent doses in Sieverts, Sv. (The older unit rem is equivalent to 0.01 Sv.) Humans naturally absorb about 2–3 mSv per year, with half from inhaled radon, and the rest as a mix of radiation from space, the earth, and food. A banana has about half of a gram of K, of which 0.0117% is ^{40}K, giving off 15.6 Bq of β radioactivity. Eating one each day would give an equivalent dose of about 35 μSv/y, about 1 to 2% of the natural dose. A chest X-ray provides about 50 μSv, about the same as living by a nuclear power plant for a year (50 μSv/y) (MEXT 2012). Upper limits for emergency workers are 250 mSv/y. Ionizing radiation becomes dangerous near 1 Sv and lethal at several to tens of Sv.

Modes of Radioactive Decay

The most common decay mode is beta decay, β, which is the emission of an electron from the nucleus, converting a neutron to a proton with a translocation on the diagram in Figure 4.1 to a higher atomic number and lower neutron number (Figure 4.5). The result is an *isobaric* transformation to a nuclide of a different element, but with the same atomic mass. Similarly, decay by electron capture transforms a proton to a neutron, producing a more stable nuclide with lower atomic number but the same atomic mass. Radioisotopes of the heavy actinides, including U and Th, decay largely by emission of an alpha particle, α, which is a ^{4}He nucleus of 2n and 2p. Many of the actinides, such as ^{238}U and ^{239}Pu, can also decay by spontaneous fission into two mid-weight nuclides. The electromagnetic radiation that accompanies decay is high-energy gamma, γ, radiation from the nucleus. The intensity and wavelength of γ-radiation is characteristic for each radioisotope, and can be used in γ-counters for their identification.

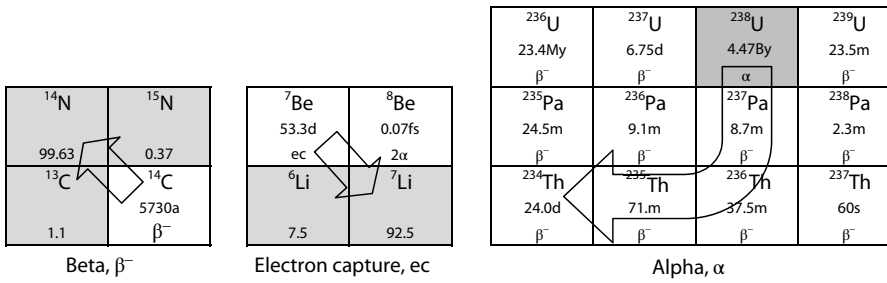

FIGURE 4.5 Principal radioactive decay schemes.

Radioactive Decay Rate, Decay Constant, and Half-Life

Radioactivity is measured in Becquerels as the number of decay events per second. Samples with a greater number of atoms of a given radioisotope will naturally have greater radioactivity. Through time, the number of atoms decreases and so does its radioactivity. This is the decay rate that is equal to the change in the number of atoms of the radioisotope per second, $\partial n/\partial t$, and so the rate of decay is proportional to the number of atoms. Each radioisotope has its unique rate of decay, represented by the decay constant, λ, which is the constant of this proportionality.

$$-\frac{\partial n}{\partial t} = \lambda n \text{ (decay/time) radioactive decay}$$

or

$$-\frac{\partial n}{n} = \lambda\, \partial t$$

Integrating gives the general form of the radioactive decay equation that determines the number of atoms after decay from an initial number, n_o, over a given period, t:

$$n_t = n_o e^{-\lambda t}$$

Taking the natural log of this exponential equation and inverting gives

$$\ln\left(\frac{n_o}{n_t}\right) = \lambda t$$

Solving the decay equation for the period of time required to decay the number of atoms, n, to half ($n_o/n_t = 2$), establishes the half-life, $T_{½}$, for a given radioisotope (Figure 4.6):

$$\ln\left(\frac{n_o}{n_t}\right) = \lambda T_{½}$$

$$\ln 2 = \lambda T_{½}$$

$$\lambda = \frac{\ln 2}{T_{½}} \left(\text{time}^{-1}\right)$$

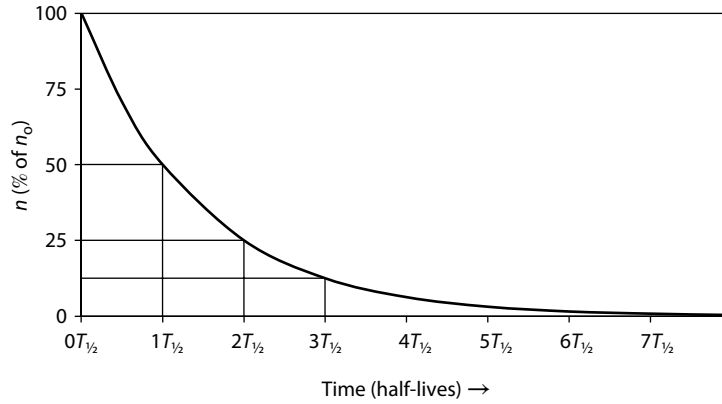

FIGURE 4.6 Radioactive decay and half-life, $T_{½}$.

Activity–Concentration Relationship

Radioisotopes, like stable isotopes, have a given concentration relative to the main (stable) isotope at a given time. Radioisotopes also have a given activity (or radioactivity), a, at that time, with units of decay events per time (i.e., Bq, or decay per second). The activity of a radioisotope is proportional to its concentration, or the number of atoms, n, of the radioisotope. The proportionality constant in this relationship is the decay constant, λ, with units of inverse time (y^{-1} or s^{-1}):

$$a = \lambda n$$

The analysis of tritium is a good example of the activity–concentration relationship. With a short half-life of 12.32 years, tritium is part of the water molecule and important for dating modern groundwater recharge. Minor amounts of T are presently released to the atmosphere by nuclear power plants, nuclear fuel reprocessing facilities, preparation of weapons-grade nuclear material, and the manufacturers of tritiated paints used in illuminating dials and tritium gas (T_2) for self-illuminating emergency signs. In radio-hazard studies of tritium emissions from nuclear activities, units of activity are used, so tritium is expressed as Bq, either per liter of water, per gram of vegetation, or per cubic meter of air. As a groundwater tracer, units of tritium concentration or tritium units, TU, are used. This is based on the molar ratio of tritium atoms to stable hydrogen atoms in a sample, T/H. In natural samples, this ratio is on the order of 10^{-18}, and so one tritium unit is equal to one T per 10^{18} H atoms:

$$\begin{aligned} 1\ \text{TU} &= 1\ \text{T per}\ 10^{18}\,\text{H} \\ &= 10^{-9}\,\text{ppb} \end{aligned}$$

The activity of tritium for this concentration can be derived using the decay constant and the activity–concentration relationship from above:

$$a_T = \lambda_T n_T$$

The decay constant, λ_T, in seconds is as follows:

$$\begin{aligned} \lambda_T &= \ln 2 / T_{½} \\ &= \ln 2/(12.32 \times 365 \times 24 \times 3600) \\ &= 1.78 \times 10^{-9}\ \text{s}^{-1} \end{aligned}$$

$$\text{and the concentration is: } n_T = 1000\ \text{g}/\,18\ \text{gfw} \times 2 = 111\ \text{mols H/L}$$

$$= 111 \times 6.02 \times 10^{23} = 6.69 \times 10^{25}\ \text{atoms/L}$$

$$\text{and so activity is: } a_T = 1.78 \times 10^{-9} \times 10^{-18} \times 6.69 \times 10^{25}$$

$$= 0.119\ \text{Bq/L}$$

Radiocarbon, with a longer half-life and as an isotope that participates in the carbon cycle, is useful for dating older groundwaters. Its activity–concentration relationship is a good contrast to that of tritium, emphasizing the difference in decay constants on activity–concentration relationships, shown here in the following example.

Example 4.4: Activity and Concentration Relationship for Radioisotopes

What are the concentrations, *n,* isotope ratios and activities, *a*, of tritium and radiocarbon in environmental samples? (note: NA = Avogadro's number)

Activity of T in water with 10 TU	Concentration of ^{14}C in Modern Carbon, MC (0.226 Bq/g C)
ratio = T/H = 10 TU/10^{18} = 10^{-17}	ratio = $^{14}C/C$
n_T = T/H × n_H atoms/L	n_{MC} = a_{MC} / λ^{14}_C
a_T = λ_T n_T Bq/L	a_{MC} = 0.226 Bq/g C
λ_T = ln2/$T_{½}$	λ^{14}_C = ln2/$T_{½}$
= ln2/12.32 y^{-1}	= ln2/5730 y^{-1}
= ln2/3.89×10^8 s^{-1}	= ln2/1.81×10^{11} s^{-1}
= 1.78×10^{-9} s^{-1}	= 3.84×10^{-12} s^{-1}
n_H = 1000 g/18 gfw × 2 × NA	n_C = 1g/12 gfw × NA
= 111 × 6.02×10^{23}	= 0.083 × 6.02×10^{23}
= 6.68×10^{25} atoms H/L	= 5.02×10^{22} atoms C/g
n_T = T/H × n_H	n_{MC} = 0.226/λ^{14}_C
= 10^{-17} × 6.68×10^{25}	= 0.226/3.84×10^{-12}
= 6.68×10^8 atoms/L	= 5.89×10^{10} atoms/g
a_T = λ_T n_T	$^{14}C/C$ = n_{MC}/ n_C
a_T = 1.78×10^{-9} × 6.68×10^7	= 5.89×10^{10}/5.02×10^{22}
= 1.19 Bq/L	= 1.17×10^{-12}

The activity of a radionuclide then depends on its half-life and its concentration. Over 900 radionuclides with half-lives longer than 1 hour have been identified. Many with long half-lives, like ^{238}U ($T_{½}$ = 4.46×10^9y), were produced during nucleosynthesis at the formation of our solar system. Others are much more radioactive and exist now because they are actively produced by natural nuclear reactions in the atmosphere and subsurface. Among the radioisotopes, only a few are readily measured and with half-lives appropriate for dating in groundwater studies (Table 1.3).

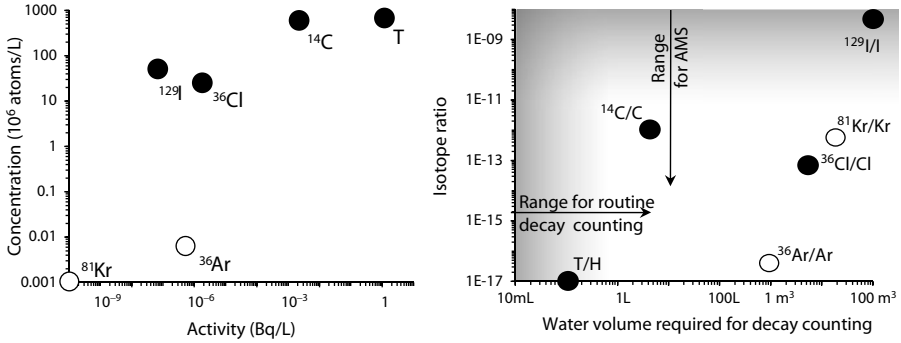

FIGURE 4.7 Left: concentration–activity relationship for the common radioisotopes present at environmental levels. Right: the ranges of analytical detection for radiometric (decay counting) and mass spectrometric (accelerator mass spectrometry, AMS) methods. Only radiocarbon has sufficient activity and high ratio for analysis by either AMS or decay counting. Note that the noble gas radioisotopes, Kr and Ar, cannot be analyzed by AMS, as they cannot be negatively charged (a requirement of AMS). However, they can now be measured by the recently developed method of laser atom trap trace analysis (Jiang et al. 2012).

The environmental concentrations and activities of the radioisotopes have bearing on how they can be analyzed. Radioisotopes with large decay constants, such as tritium, T ($\lambda = 0.056\ y^{-1}$), are routinely measured by decay counting, and in the case of tritium, to a limit of detection of 10^{-18} or better. Radioisotopes with small decay constants, such as ^{129}I ($\lambda = 4.39\times10^{-8}\ y^{-1}$) have too low a decay rate for measurement by decay counting and are routinely analyzed by accelerator mass spectrometry with atom-counting detectors. This activity–concentration relationship is shown in Figure 4.7. Applications of these isotopes in groundwater dating and tracing are discussed in Chapter 8.

Radioisotopes and Geochronology

Geochronology is based on the decay equation introduced earlier, which can be expressed as loss of the parent radioisotope from some initial number of atoms, n_{Po}:

$$n_{Pt} = n_{Po}e^{-\lambda t}$$

For the gain of the daughter isotope, n_D, this decay equation becomes:

$$n_{Dt} = n_{Po}(1 - e^{-\lambda t})$$

The exponential functions of decay and ingrowth are shown in Figure 4.8.

Groundwater dating with radioisotopes relies on the decay of atmospherically derived nuclides that accompany recharge or on the ingrowth of radiogenic nuclides produced in the subsurface. Those that are atmospherically derived are cosmogenic nuclides, produced by high-energy particles, mainly protons originating from supernovae elsewhere in the galaxy that constantly bombard our planet. Collisions with the atmosphere generate showers of secondary, lower-energy neutrons that further interact with atmospheric gases to produce a range of cosmogenic radioisotopes that

reach the surface as dry fallout or with precipitation wet fallout (Figure 4.9). The cosmogenic neutron flux can also activate nuclides such as ^{35}Cl on the earth's surface, which is *epigenic* production. These atmospheric or epigenic radioisotopes are then incorporated into groundwaters during recharge where subsequent decay from their initial value can be used as a chronometer.

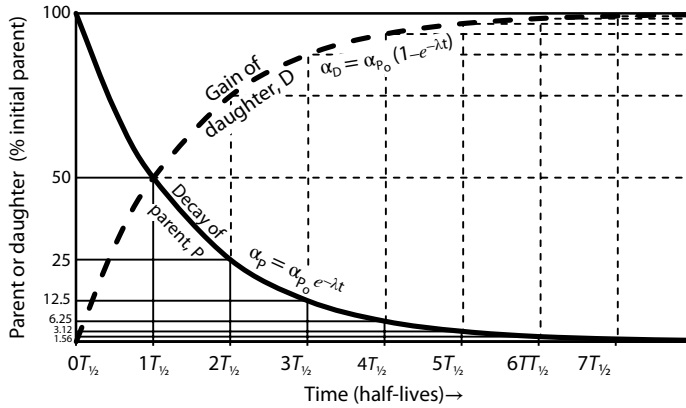

FIGURE 4.8 Radioisotope decay and half-life for loss-of-parent and for gain-of-daughter dating schemes.

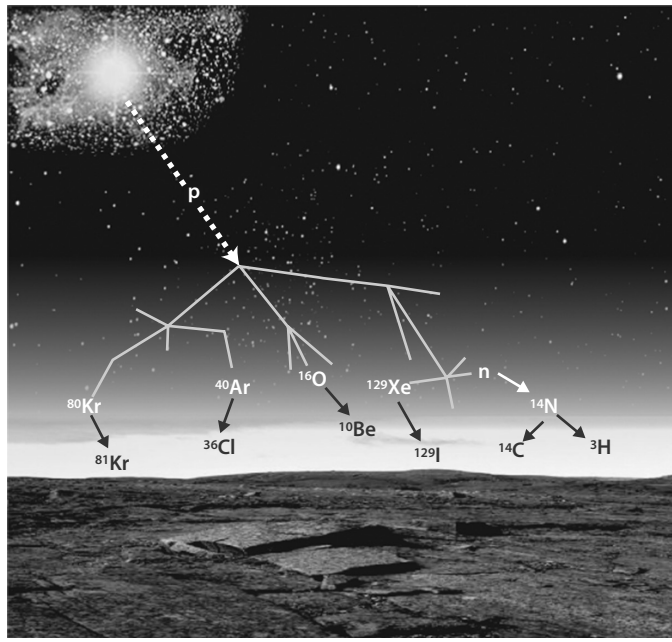

FIGURE 4.9 Production of cosmogenic nuclides in the atmosphere from the shower of secondary neutrons produced by impact of high energy particles (mainly protons) originating from supernovae in the galaxy.

Geogenic nuclides are those produced in the subsurface by the decay and spontaneous fission of uranium and other actinides present in all rocks. The range of radiogenic nuclides produced in the subsurface, which are incorporated by groundwater and can be used for chronology, was established by Andrews et al. (1989). They are generated by three principal mechanisms, which are natural U-fission, neutron-activation and radioactive decay (Figure 4.10).

Spontaneous fission (sf) of ^{238}U occurs as a very minor component of its decay scheme, but produces a range of *geogenic* nuclides. Some are radioactive themselves, such as ^{129}I, whereas others are stable, such as ^{136}Xe. Their ingrowth in groundwater can be used together with uranium concentration and its spontaneous-fission decay constant, as a measure of age. For example,

$$^{238}U \rightarrow {}^{129}I + {}^{107}Mo \quad T_{½}\,(^{238}U_{sf}) = 8.15 \times 10^{15} \text{ years} \quad T_{½}\,(^{129}I_{\beta}) = 15{,}700{,}000$$

The release of high energy α particles during the decay schemes for uranium and thorium isotopes (^{238}U, ^{235}U, and ^{232}Th) generates a secondary neutron flux through impact on light nuclei such as O, F, Na, Al, Si, and K. This secondary neutron flux impacts on other target nuclides to produce a range of geogenic nuclides through neutron-activation reactions (uptake of neutron by the target nuclide) or spallation reactions (loss of mass as protons, neutrons, or both). Two examples useful in groundwater dating are as follows:

The third class of geogenic nuclide production is by radioactive decay. Considering

$^{35}Cl + n \rightarrow {}^{36}Cl$	$T_{½}\,(^{36}Cl) = 301{,}000$ years
$^{6}Li + n \rightarrow {}^{3}He + {}^{4}He$	stable

the more than billion-year half-lives of these parent radionuclides, the production of

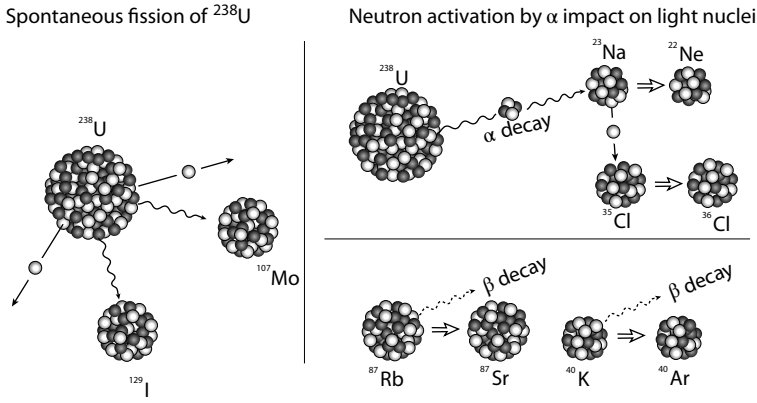

FIGURE 4.10 Radiogenic isotope production in the subsurface through spontaneous fission of ^{238}U and α decay, as well as by decay of other long-lived radioisotopes.

the stable daughter nuclides on the scale of millions of years can be calculated as linear ingrowth rates:

$^{40}K_{ec} \rightarrow {}^{40}Ar$ $\quad T_{½}(^{40}K_{ec}) = 1.28\times10^{9}$ y

^{40}Ar production $= 3.887\times10^{-14} \times [K_{\%\text{ in rock}}]$ $cc_{STP}/g/y$

$^{238}U_{\alpha} \rightarrow {}^{234}U + {}^{4}He \rightarrow \rightarrow \rightarrow {}^{206}Pb + 8\ {}^{4}He$ $\quad T_{½}(^{238}U_{\alpha}) = 4.6\times10^{9}$ y

$^{232}TH_{\alpha} \rightarrow \rightarrow \rightarrow {}^{208}Pb + 6\ {}^{4}He$ $\quad T_{½}(^{232}Th_{\alpha}) = 14.05$ By

^{4}He production $= 1.19\times10^{-13}\ [U_{ppm}] + 2.88 \times 10^{-14}\ [Th_{ppm}]$ $cc_{STP}/g/y$

PROBLEMS

1. What are the major and trace isotopes of H, C, N and O that can be measured by routine analytical methods? Give the abundance of these isotopes in nature and how they can be measured.
2. A water sample was measured by isotope ratio mass spectrometry to have a $^{18}O/^{16}O$ ratio $R = 0.00199517$ with VSMOW ($R = 0.00200520$). What is its δ-‰ value (rounded to one decimal place)?
3. A sample of water in a partially filled container has a $\delta^{18}O$ value of –7.0‰. The temperature is 25°C. What will be the $\delta^{18}O$ value of the water vapor in isotopic equilibrium with this water?
4. What are the ^{18}O fractionation factors and the ^{18}O enrichment factors for water in equilibrium with vapor at 0°C and 50°C? At which temperature will there be a greater difference between measurements of $\delta^{18}O_{water}$ and $\delta^{18}O_{vapor}$, and what are the differences?
5. Write an example of an equilibrium isotope-exchange reaction and a biologically mediated kinetic reaction involving the isotopes and associated samples in Table 1.4.
6. Give an example of a nonfractionating reaction.
7. Write the fractionation factor, $\alpha^{18}O_{water–vapor}$, in terms of the $^{18}O/^{16}O$ isotope ratio for these compounds. Using an isotope ratio of 0.00200 for water, and for vapor of 0.00198, what is the value for $\alpha^{18}O_{water–vapor}$? What are the values for $\varepsilon^{18}O_{water–vapor}$ and for $\delta^{18}O_{water}$ and $\delta^{18}O_{vapor}$ in this case (recall that $^{18}O/^{16}O$ for VSMOW is 0.0020052)?
8. The isotope fractionation factor, α, is the ratio of the isotope ratios in the two reacting compounds. The δ-value expresses the isotope ratio of a compound as a difference from that of a reference material. Express α in terms of the δ-values for the two reacting compounds in a fractionation reaction.
9. Atmospheric water vapor is seldom sampled and measured for isotopes, but assume that for a given time and place it is found to have a $\delta^{18}O$ value of –18‰. What would be the $\delta^{18}O$ value for rain that fell with a condensation temperature of 15°C?
10. Surface water from a tailings pond with sulfate concentration of 2000 ppm and $\delta^{34}S = –1.5$‰ infiltrates to groundwater that has 50 ppm sulfate with $\delta^{34}S = +20$‰. The sulfate concentration and $\delta^{34}S$ in the plume are 1025

ppm and +20‰. What is the fraction of tailings water that has mixed with the groundwater in the plume?

11. For the $\delta^{18}O$ values for residual water from freezing of the pond water in Table 4.3, calculate the enrichment factor, $\varepsilon^{18}O_{ice\text{-}water}$ for this freezing reaction.
12. The analysis of ^{18}O by gas-source isotope ratio mass spectrometry done by equilibrating the sample with CO_2 and then measuring $\delta^{18}O_{CO_2}$. The enrichment factor, $\varepsilon^{18}O_{CO_2-H_2O}$, for the exchange of ^{18}O between CO_2 and H_2O is very large: 41.5‰ at 25°C. For $\delta^{18}O_{CO_2}$ measurements of +35.5‰ and +32.1‰ VSMOW (samples A and B), what are their values for $\delta^{18}O_{H_2O}$?
13. The distribution of isotopes in nature is a function of two primary processes. One is fractionation, α, and the other is Rayleigh distillation. Give the generic Rayleigh equation relating isotope ratios, R, to α and the fraction, f, of the reactant reservoir.
14. A pond of water, with $\delta^{18}O = -10‰$, starts to evaporate to dryness. Given an enrichment factor for isotope exchange between water and vapor of $\varepsilon^{18}O_{vapor-water} = -9.3‰$, determine the isotopic composition of the pond water when it has evaporated to residual fractions $f = 0.5$, $f = 0.15$, $f = 0.05$, and $f = 0.01$. What would be the effect on your calculations if you used a kinetic enrichment factor $\varepsilon^{18}O_{vapor\text{-}water} = -13‰$)?
15. What are the ^{18}O fractionation factors and the ^{18}O enrichment factors for water in equilibrium with vapor at 0°C and 50°C? At which temperature will there be a greater difference between measurements of $\delta^{18}O_{water}$ and $\delta^{18}O_{vapor}$, and what are the differences?
16. Write out examples of parent–daughter radioisotope decay reactions involving α, β, and γ decay.
17. What are the decay constants for tritium and for ^{36}Cl based on their half-lives in years and in seconds?
18. A water sample has a tritium concentration of 0.5 TU. What is the tritium activity per L in this water? How many tritium atoms are there in 1 L of this water and what is the T/H ratio? Could this be measured by AMS?
19. Groundwater recharged near a nuclear power generating station has a tritium activity of 1500 Bq/L. What is the concentration of tritium in TU? Is this water hazardous for drinking?
20. The radiocarbon standard, percent Modern Carbon or pMC, is established at 100 pMC, which is equal to an activity of 0.226 Bq/g (Becquerels per gram C). What is the activity of a sample with 120 pMC?
21. Give two examples of (i) cosmogenic radionuclides, (ii) geogenic radionuclides, and (iii) radiogenic stable nuclides, together with their mode of formation.
22. Which thirst quencher provides the lowest dose of radioactivity: precipitation from Stuttgart, Germany, near the Neckarwestheim Nuclear Power Plants, or Gatorade?

5 Tracing the Water Cycle

INTRODUCTION

The hydrological cycle pumps over 1000 km^3 of freshwater each day to the continents, the equivalent of 2000 Niagara Falls. Of this, over 90% is transpired back to the troposphere. Most of the balance runs off over the surface or infiltrates into soils and aquifers, ultimately discharging some 75 km^3 of freshwater to the oceans each day. Surface water discharge is extensively monitored for flood control, hydroelectric generation, and water resources management. Groundwater resources are also monitored with test wells installed in major aquifers to monitor water levels, rates of recharge, and water quality. These major components of the hydrological cycle are shown in Figure 5.1.

In groundwater resource and contamination studies, questions of groundwater origin and subsurface history are important. Physical parameters such as groundwater level fluctuations when interpreted in together with rainfall and temperature data are fundamental to water resource evaluation. Isotopes provide a complementary tool for distinguishing different water sources and recharge areas. The natural isotopes ^{18}O and D are an intrinsic component of the water molecule and so are ideal tracers. They are selectively partitioned at each step of the hydrological cycle, from primary evaporation over the oceans, through condensation and precipitation to groundwater recharge and runoff back to the seas.

The principal hydrological processes that affect the distribution of isotopes through the hydrological cycle include the following:

1. Evaporation and formation of atmospheric vapor
2. Condensation and rainout with decreasing temperature
3. Reevaporation from soils and surface waters, which enriches the residual water in both isotopes
4. Mixing during recharge and groundwater flow
5. And, rarely, isotope exchange during mineral–water and gas–water reactions

The last process of isotope exchange with minerals and gases is important in only very exceptional circumstances of low water/rock or water/gas ratios. Thus, with the exception of deep geological settings (e.g., geothermal waters and brines) or highly contaminated waters (e.g., landfills), the isotope content of groundwater retains the primary meteoric signal from precipitation and recharge.

In 1961, Harmon Craig published the earliest measurements of $\delta^{18}O$ and δD for freshwaters from around the globe. His two principle observations provide the foundation of isotope hydrology.

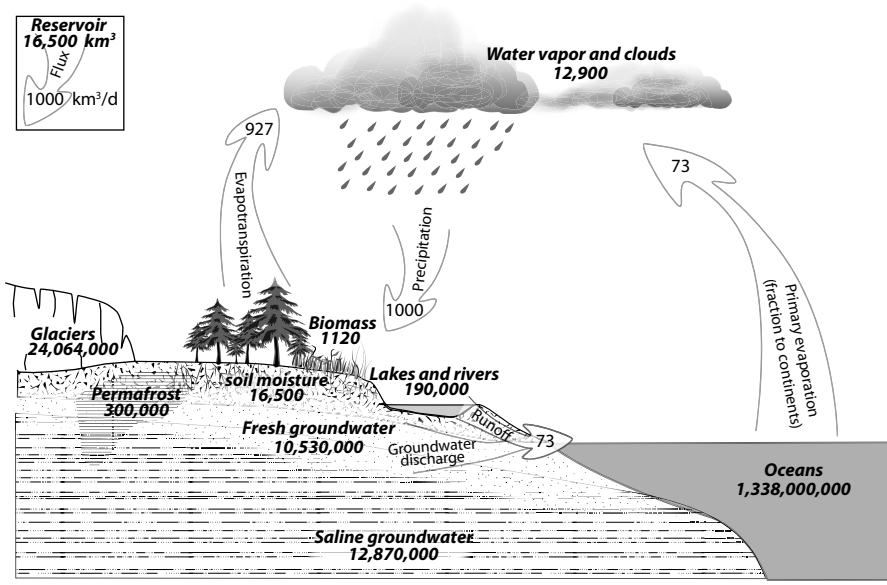

FIGURE 5.1 Components and fluxes of water in the global hydrological cycle.

1. ^{18}O and D in freshwaters are enriched in warm regions and depleted in cold regions, with a range of over 40‰ for $\delta^{18}O$ and over 300‰ for δD
2. There is a strong linear correlation between $\delta^{18}O$ and δD in meteoric waters, with a slope of 8 and deuterium intercept of 10‰

The partitioning of isotopes into warmer regions has since been well documented from precipitation stations from around the world, as shown in Figure 5.2. This apparent climatic influence on the ^{18}O and D in precipitation was quantified by Willi Dansgaard in 1964, showing that there exists a strong correlation for the mean annual values of $\delta^{18}O$ and δD with mean annual air temperature (Figure 5.3). The second observation of a strong correlation between $\delta^{18}O$ and δD provides the characteristic meteoric water lines (MWLs) for given regions that are used to determine the recharge input. These two observations are the basis of isotope hydrology.

TEMPERATURE—$\delta^{18}O$ CORRELATION IN PRECIPITATION

The global correlation observed by Dansgaard (1964) between the isotopic composition of precipitation and air temperature can be understood by examining the processes that drive condensation and precipitation. From Chapter 4, it is clear that condensation is accompanied by isotope fractionation, which for $\varepsilon^{18}O_{water-vapor}$ is 9.3‰ and for $\varepsilon D_{water-vapor}$ is 76‰ at 25°C. With this fractionation taking place as the reactant reservoir—the mass of water vapor—is converted to rain, both ^{18}O and D

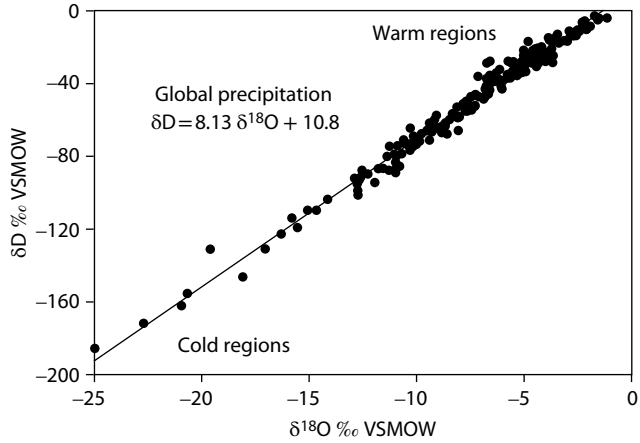

FIGURE 5.2 The $\delta^{18}O$–δD correlation for global precipitation plotted from data on the International Atomic Energy Agency GNIP database (IAEA/WMO 2013). Craig (1961) first observed this correlation in global freshwaters.

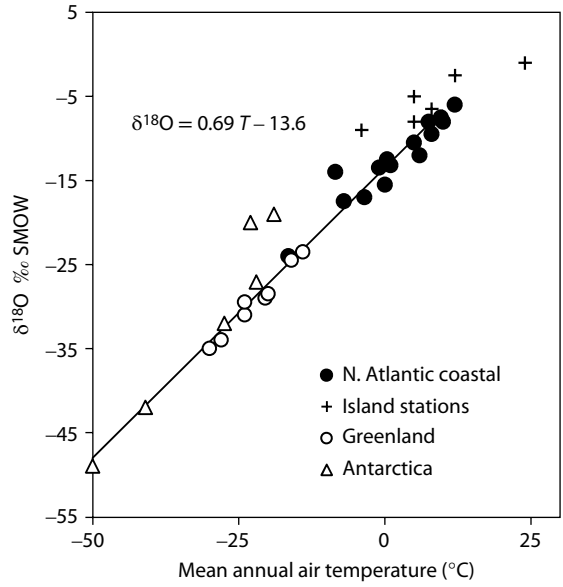

FIGURE 5.3 The global T–$\delta^{18}O$ relationship for precipitation. Temperature is mean annual surface air temperature (MAAT) at the station. For deuterium, Dansgaard found $\delta D = 5.6\ T_{MAAT} - 100‰$ SMOW (standard mean ocean water). Note that SMOW refers to the laboratory reference water used at that time. It has since run out and been replaced by VSMOW. (Modified from Dansgaard, W. 1964.)

are preferentially distilled from the vapor mass. The result is an evolution toward lighter isotopes in the residual vapor, and in successive rains, as rainout proceeds. As rainout is driven by cooling, the result is a correlation between temperature and the isotope content of precipitation.

Rainout and Rayleigh Distillation of ^{18}O

Atmospheric water vapor is generated by primary evaporation of ocean water, with contributions from evaporation from surface waters and transpiration from vegetation along the air mass trajectory. Precipitation is generated through cooling of the vapor mass. The temperature of the vapor must drop below the dew point (where humidity = 100%) for condensation to occur. Adiabatic expansion and cooling occurs as warm air rises in convective precipitation systems, orographic rainfall over topography or displacement over cold fronts. This is the process of "rainout," and it is driven by decreasing temperature.

Within the cloud, fractionation between vapor and water or vapor and ice preferentially partitions ^{18}O and D into the rain or snow, and so are distilled from the vapor phase during rainout. The vapor becomes progressively depleted in ^{18}O and D along the vapor mass trajectory. Providing no additions to the vapor mass occur, the isotope evolution will follow a Rayleigh–type distillation, as discussed in Chapter 4. As the residual vapor becomes depleted in ^{18}O and D, subsequent rains will also be progressively depleted, and so rainout evolves toward colder, isotopically depleted precipitation (Figure 5.4). The global distribution of isotopes seen above in Figures 5.2 and 5.3 is more complicated than this simplified rainout process. While Rayleigh distillation is the fundamental process partitioning ^{18}O and D into warmer regions, recycling of precipitation by continental transpiration and evaporation play important roles in the isotopic composition of atmospheric water vapor and precipitation.

The isotopic evolution of precipitation during an ideal rainout trajectory can be simulated using the Rayleigh distillation equation, modified from the simplified form given in Chapter 4 to include the isotopes of the primary vapor and the associated precipitation along the trajectory:

$$\delta^{18}O_{w(f)} = \delta^{18}O_{v(f=1)} + \varepsilon^{18}O_{w-v}\,(1 + \ln f)$$

where $\delta^{18}O_{v(f=1)}$ is the isotope value for the initial water vapor, f is the residual fraction of the vapor reservoir in the air after a certain amount of rainout, and $\delta^{18}O_{w(f)}$ is the isotopic value for the residual fraction, f. The enrichment factor $\varepsilon^{18}O_{w-v}$ is for

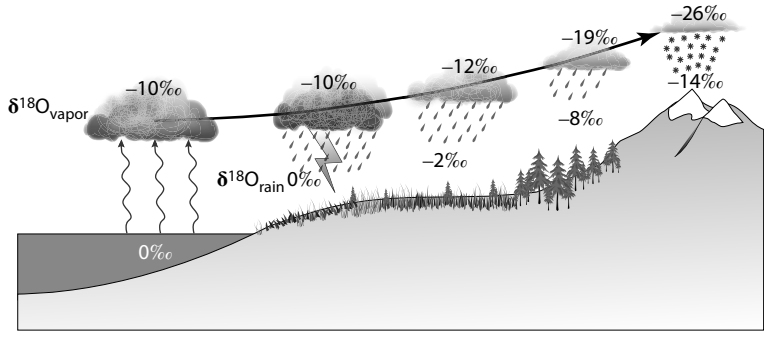

FIGURE 5.4 The evolution in the ^{18}O content of precipitation according to an ideal Rayleigh distillation during rainout. Deuterium follows a similar depletion trend.

Example 5.1: Isotopic Evolution during Rainout

A vapor mass has a $\delta^{18}O$ value of –13‰ and a temperature of 25°C as it begins to rain. What is the $\delta^{18}O$ composition of the rain at 25°C and then after cooling to 20°C and losing 30% of its mass, and then cooling to 15°C and losing 50% of its original mass?

$\delta^{18}O$ of initial rain (25°C):

$$\begin{aligned}
\delta^{18}O_{v(f=1)} &= -13‰ \\
\varepsilon^{18}O_{w-v} &= 9.3‰ \text{ at } 25°C \text{ (Table 4.2)} \\
\delta^{18}O_{rain(f=1)} &= \delta^{18}O_{v(f=1)} + \varepsilon^{18}O_{w-v} \\
&= -13 + 9.3 \\
&= -3.7‰
\end{aligned}$$

$\delta^{18}O_{rain}$ after rainout has proceeded by 30% by cooling to 20°C:

$$\begin{aligned}
\varepsilon^{18}O_{w-v} &= -11.2 \text{ at } 20°C \text{ (equation with Table 4.2)} \\
f &= 1 - 0.3 = 0.7 \\
\delta^{18}O_{w(f)} &= \delta^{18}_{o}O_{v} + \varepsilon^{18}O_{w-v}\left(1 + \ln f\right) \\
\delta^{18}O_{v(0.7)} &= -13 + 9.8\left[1 + \ln(0.7)\right] \\
&= -6.9‰
\end{aligned}$$

$\delta^{18}O_{rain}$ after rainout has proceeded to 50% of its original vapor mass by cooling to 15°C:

$$\begin{aligned}
f &= 0.5 \\
\varepsilon^{18}O_{v-w} &= -10.6 \text{ (equation with Table 4.2)} \\
\delta^{18}O_{w(f)} &= \delta^{18}_{o}O_{v} + \varepsilon^{18}O_{w-v}\left(1 + \ln f\right) \\
\delta^{18}O_{v(0.5)} &= -13 + 10.2\left[1 + \ln(0.5)\right] \\
&= -9.9‰
\end{aligned}$$

In this example, the $\delta^{18}O$ composition of the rain has evolved from –3.7‰ at the start of rainout to –6.9‰ at 30% rainout and to –9.9 at 50% rainout of the water vapor reservoir. Note that the decreased temperature actually increases the water–vapor enrichment of ^{18}O, which acts to enrich the rain as temperature decreases. However, the distillation of heavy isotopes from the vapor has a stronger effect, and results in an overall depletion at decreased residual fractions, *f*.

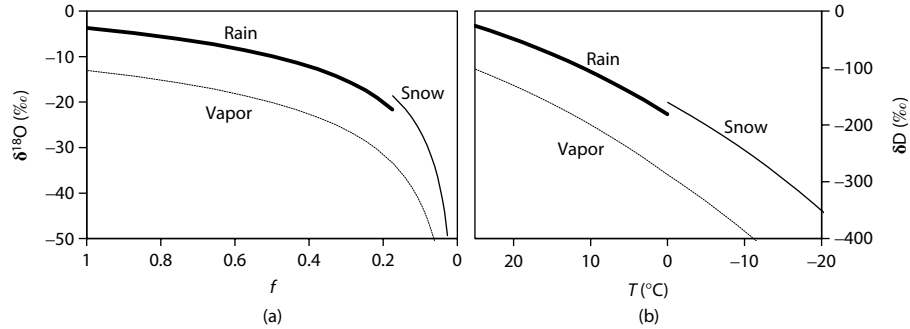

FIGURE 5.5 The evolution of $\delta^{18}O$ and δD in rain and snow during rainout. (a) Plot shows the depletion for both ^{18}O and D as the residual vapor fraction diminishes toward 0. Both isotopes follow the same depletion (but on different scales) with decreasing residual vapor fraction *f*. (b) Plot shows the ideal evolution of $\delta^{18}O$ and δD for a single vapor mass undergoing cooling, showing the co-depletion in ^{18}O and D with decreasing temperature *T*. Note the jump to higher $\delta^{18}O$ and δD at the rain-to-snow transition due to the greater fractionation between vapor and ice versus vapor and water.

equilibrium water-vapor exchange at the prevailing in-cloud temperature. At 25°C, $\varepsilon^{18}O_{w-v}$ is 9.3‰ (Table 2.7).

It is interesting to plot the isotopic evolution of precipitation during rainout, based on the simple calculations in Example 5.1. This is done in Figure 5.5, using the same initial conditions from Example 5.1. Figure 5.5a shows the isotopic evolution of rain and snow, which forms from a continually cooling vapor mass. Note the offset for precipitation when the condensation temperature drops below freezing, due to difference between water–vapor and ice–vapor fractionation at 0°C.

$\delta^{18}O$—Temperature Correlation in Global Precipitation

The partitioning of isotopes between cold and warm regions is best observed on a global map of $\delta^{18}O$ in precipitation, shown here in Figure 5.6, using mean annual precipitation data collected within the IAEA-World Meteorological Organization survey of precipitation. On this global scale, the temperature–$\delta^{18}O$ relationship is clear, with partitioning of ^{18}O into warmer, low-latitude precipitation and depletion in ^{18}O with increasing latitude. The effect of the North Atlantic Drift transporting warm ocean waters to high latitude over the British Isles and Scandinavia is also apparent, as is the upwelling of cold deep water in the eastern Pacific Ocean off the coast of Peru and Central America. Given the strong correlation observed by Craig for $\delta^{18}O$ and δD, the distribution of D in global precipitation would also be observed to partition into low latitudes and warm regions with depletions in D at high latitudes and high elevations.

The correlation between $\delta^{18}O$ and temperature observed for mean annual data can also be observed at shorter time scales. When mean monthly precipitation data for $\delta^{18}O$ (or δD) and temperature are plotted, a strong temperature–isotope correlation

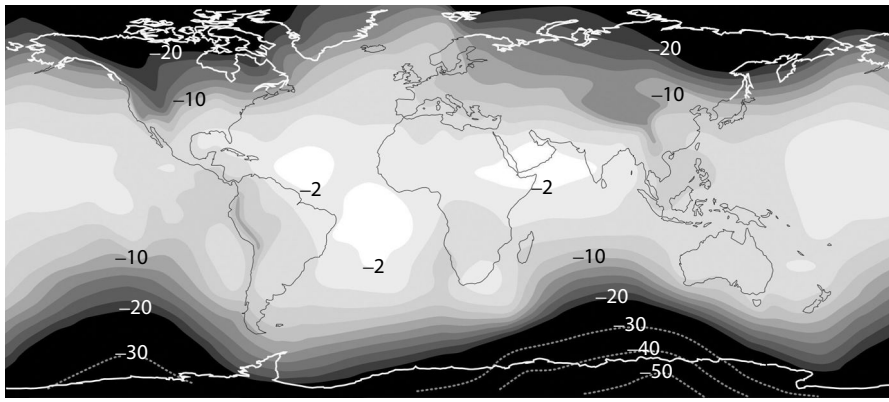

FIGURE 5.6 Global map of $\delta^{18}O$ for precipitation, based on annual averaged data from collected from International Atomic Energy Agency (IAEA) stations over the past 30 years (Rozanski et al. 1993). These long-term data are available at the IAEA Global Network for Isotopes in Precipitation program website.

is observed. The isotope data are amount-weighted in such calculations to give greater weight to isotope values for higher precipitation amounts. Amount-weighted isotope values are calculated from the measured isotope value and measured amount of precipitation for each of 1 to n precipitation events in a given month, according to the following:

$$\text{Mean monthly amount weighted } \delta_{mm} = \frac{\sum_{i=1}^{n} p_i \delta_i}{\sum_{i=1}^{n} p_i}$$

Similarly, mean annual amount weighted δ_{ma} can be calculated from mean monthly values:

$$\text{Mean annual amount weighted } \delta_{ma} = \frac{\sum_{\text{Jan}}^{\text{Dec}} p_{\text{month}} \delta_{mm}}{\sum_{\text{Jan}}^{\text{Dec}} p_{\text{month}}}$$

Figure 5.7 shows δ_{mm}–T correlations for stations from a range of latitudes. The slope of these monthly correlations for most stations are under 0.5 and considerably less than the value of 0.69 determined by Dansgaard for a broad geographical distribution. For the continental stations, a change in temperature of about 1°C changes the average $\delta^{18}O$ by about 0.3‰ to 0.5‰, or about a 2°C to 4°C change in temperature per 1‰ shift in $\delta^{18}O$. For the marine stations at Cape Grim and St. Helena, there is very little correlation with temperature. This reflects the lack of evolution in the vapor mass before rainout occurs at these stations.

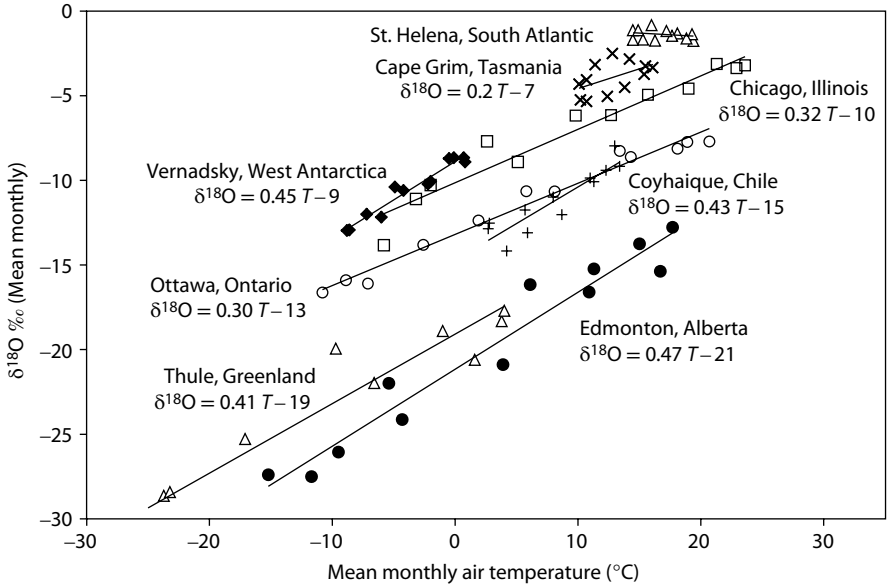

FIGURE 5.7 The correlation between mean monthly air temperature and $\delta^{18}O$ in precipitation at a selection of stations.

Non-Rayleigh Processes during Rainout

Weather seldom follows the ideal evolution presented in Figure 5.5, as most systems experience additions to their vapor content through evaporation from lakes and rivers and transpiration from vegetation over the continents. Mixing with other vapor masses in the troposphere along a rainout trajectory also occurs. Further complications come from the dynamics of many precipitation systems, with vertical transport and temperature gradients during rain events that will influence the isotopes in precipitation. For these reasons, the correlation between surface temperature and $\delta^{18}O$ (and δD) breaks down at the scale of individual rain events, and is only well correlated for mean monthly and mean annual measurements.

Aggarwal et al. (2012) have examined the rainout process using the data sets for global precipitation available through the International Atomic Energy Agency's isotope monitoring program for Global Network of Isotopes in Precipitation (GNIP, http://isohis.iaea.org). They show that the residence time of water vapor in the atmosphere has a strong effect on its isotope composition due to enhanced mixing in the upper troposphere, and that much of the signal is generated by continental sources of water vapor.

Although the generation of the observed temperature correlation is more complicated than a simple Rayleigh distillation, the empirical relationship remains critical to characterizing the recharge origin of groundwater.

METEORIC WATER LINE FOR $\delta^{18}O$ AND δD

The second observation by Craig (1961) is the strong correlation between ^{18}O and D in global freshwaters. The regression line for these data give is the "global meteoric water line" (GMWL), defined as:

$$\delta D = 8\,\delta^{18}O + 10‰$$

The regression for precipitation data (Figure 5.2) gives the same line, and so the GMWL can be used as a datum to compare the isotopic composition of surface and groundwater.

Slope of the Meteoric Water Line

The GMWL is actually an average of many local or regional MWLs, which differ from the global line due to varying climatic and geographic parameters. Local lines will differ from the global line in both slope and deuterium intercept (δD value at $\delta^{18}O = 0$). The correlation between $\delta^{18}O$ and δD is found because both isotopes are fractionated during the condensation of water vapor to form precipitation:

$$H_2O_{vapor} \rightarrow H_2O_{rain}$$

Condensation in clouds and the formation of precipitation is recognized in most cases as an equilibrium reaction and so is accompanied by equilibrium fractionation for both isotopes. The slope of 8 for this regression reflects the greater fractionation for D, which is about 8 times greater than that for ^{18}O. In fact, the ratio of the two enrichment factors is equal to the global slope, *s*, of 8 at 30°C, and increases to over 9 at 0°C. The mean slope for equilibrium fractionation would then be about 8.6, as shown in Figure 5.8.

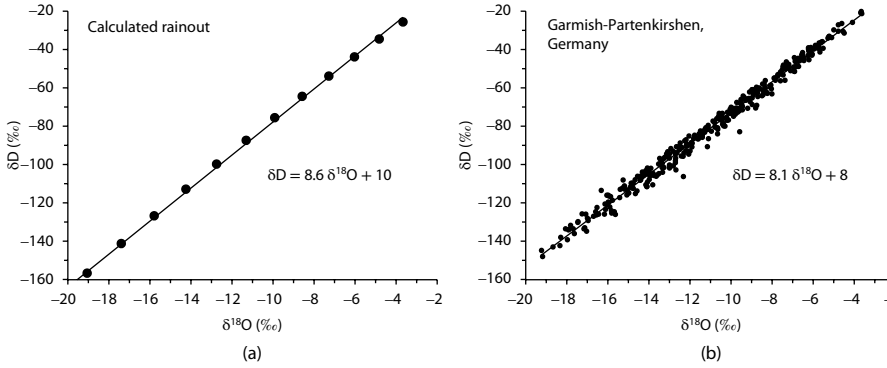

FIGURE 5.8 (a) Meteoric water line for $\delta^{18}O$ and δD in precipitation during rainout calculated using equilibrium fractionation factors, $\varepsilon^{18}O$ and εD, for water–vapor. (b) The meteoric water line for Garmish, Germany, based on precipitation data from 1978 to 2005 (From IAEA/WMO, The GNIP Database, 2013.)

$$\frac{\varepsilon D_{w\text{-}v}}{\varepsilon {}^{18}O_{w\text{-}v}} = \frac{76}{9.3} = 8.17 \text{ at } 25°C$$
$$= \frac{106}{11.6} = 9.14 \text{ at } 0°C$$

The slope from an ideal Rayleigh distillation is greater than the slope of 8 observed in meteoric waters, shown in Figure 5.8 for Garmisch-Partenkirchen, Germany, as a typical example of continental precipitation. The lower observed slope shows that the rainout process is not ideal, as it has variable contributions from mixing of vapor masses in the troposphere and from transpiration and evaporation in continental regions along a given trajectory or storm path. As different regions will have varying contributions from these different vapor sources, according to their regional geographic settings, they will then have characteristic MWLs. These will be affected in both slope and deuterium excess by a number of processes.

The slope of the MWL can also be affected by evaporation that occurs after condensation. If rain is falling through a dry air column below the cloud base, partial evaporation will impart a kinetic fractionation on the drop and give the residual rainfall a selective enrichment in ^{18}O (see Isotope Effects of Evaporation, later). Dansgaard (1964) described such evaporation of rain as the *amount effect* on the isotopic composition of precipitation. In particularly arid regions, local MWLs (LMWL) calculated using data from all the rain events are characterized by a slope that is closer to and even less than 7. Excluding the light rain events, which contribute only minimally if at all to groundwater recharge, the slope becomes closer to 8. Hughes and Crawford (2012) suggest that calculation of an LMWL should use precipitation-weighted isotope data to avoid such biases. The LMWL slope and intercept can be calculated from event-based measurements of $\delta^{18}O$, δD, and precipitation (p):

$$\text{slope, } s = \frac{\sum_{i=1}^{n} p_i {}^{18}O_i D_i - \frac{\sum_{i=1}^{n} p_i {}^{18}O_i \cdot \sum_{i=1}^{n} p_i D_i}{\sum_{i=1}^{n} p_i}}{\sum_{i=1}^{n} p_i {}^{18}O_i^2 - \frac{\left(\sum_{i=1}^{n} p_i {}^{18}O_i\right)^2}{\sum_{i=1}^{n} p_i}}$$

$$\text{intercept} = \frac{\sum_{i=1}^{n} p_i D_i - s \sum_{i=1}^{n} p_i {}^{18}O_i}{\sum_{i=1}^{n} p_i}$$

The uncertainty on the calculated LMWL can similarly be determined by weighting the precipitation isotope values by the precipitation amount. The example from Hughes and Crawford (2012) for Alice Springs, an arid site in central Australia, is shown in Figure 5.9. Here the evaporated rain samples are indicated by the enrichment in $\delta^{18}O$ for light rains less than about 20 mm. The unweighted line for these data has a slope of 6.9 reflecting evaporation whereas the amount-weighted LMWL

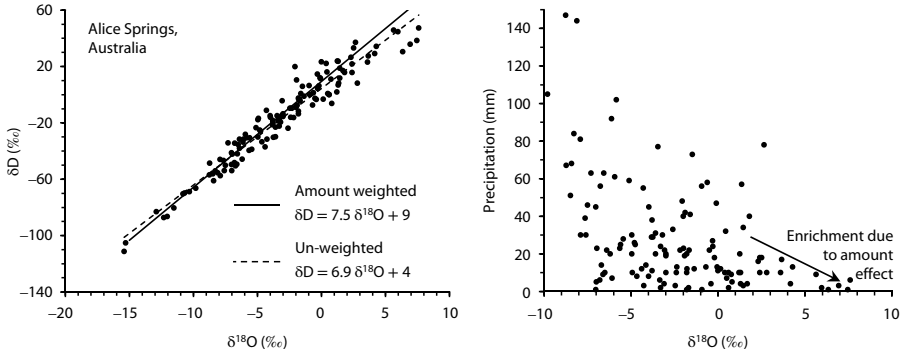

FIGURE 5.9 The isotopic composition of precipitation from Alice Springs, Australia (IAEA/WMO 2013), showing the *amount effect* first noted by Dansgaard (1964) where evaporation of low amounts of rainfall below the cloud base can enrich its isotope composition.

has a slope of 7.5, which would be more representative of the precipitation that contributes to recharge. While this is perhaps a small correction, it provides a more accurate reference line for groundwaters and to assess whether they have experienced secondary evaporation.

Deuterium Excess and the Origin of Water Vapor

The second parameter defining a MWL is the deuterium intercept. For global precipitation plotted in Figure 5.2, the $\delta^{18}O - \delta D$ line with slope 8 does not pass through the ocean water origin at 0‰ and 0‰, but rather through a deuterium intercept of +10‰. Dansgaard (1964) defined this off-set as the *deuterium excess*. Accordingly, the deuterium excess or d of precipitation is calculated from the $\delta^{18}O$ and δD for any water sample, as

$$d = \delta D - 8\ \delta^{18}O$$

For rain and snow plotting on the GMWL with slope 8, each sample has a deuterium excess, $d = 10‰$. However, this parameter can vary regionally from much less than 10‰ to over 20‰. This excess is due to kinetic evaporation (nonequilibrium) during the formation of the primary vapor mass, and it provides an additional tool to trace the origin of water.

The evaporation effect for isotopes in water is discussed more fully in the next section with respect to surface waters and groundwaters. However, it also plays a role during the formation of primary water vapor, which is a nonequilibrium or *kinetic* process that proceeds at a greater rate in the forward direction (evaporation) than the reverse (condensation). The process becomes increasingly kinetic with lower humidity. Nonequilibrium evaporation preferentially enhances fractionation of ^{18}O (with only minor enhanced fractionation of D), and so the vapor is more depleted in ^{18}O than for equilibrium conditions (Figure 5.10). As this vapor condenses to produce

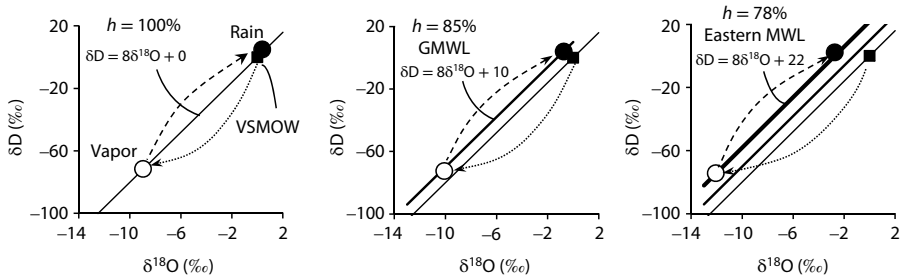

FIGURE 5.10 Deuterium excess in primary atmospheric water. Lower humidity during primary evaporation over seawater increases kinetic evaporation and generates a deuterium excess ($d = \delta D - 8\,\delta^{18}O$) in precipitation that plots on a line with slope near 8 but with a deuterium enrichment. The average deuterium excess for global freshwaters is 10‰, which is the deuterium intercept for the GMWL.

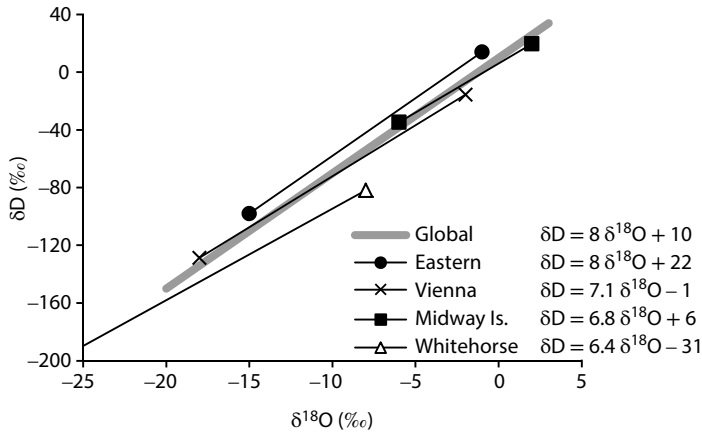

FIGURE 5.11 Local meteoric water lines for selected stations in the International Atomic Energy Agency global network for isotopes in precipitation (GNIP IAEA/WMO 2013).

rain, it does so with equilibrium fractionation for ^{18}O and D and a MWL with slope 8. The impact of kinetic evaporation is shown in Figure 5.10, where kinetic effects of lower humidity during primary evaporation results in rain with deuterium excess greater than 0‰. On average, global freshwaters are formed under conditions of about 85% humidity, and so global freshwaters plotting on the GMWL have a deuterium excess of only 10‰. An example where primary evaporation takes place with very low humidity is the eastern Mediterranean where the deuterium intercept is 22‰ (Gat and Carmi 1970).

Because of differences in the origin of water vapor and rainout along the trajectory from its source, any given region will have its own characteristic MWL (Figure 5.11). This is a datum with which the surface and groundwater in that region can be compared. The case study in Example 5.2 shows the difference in deuterium excess associated with different storm systems, and illustrates the value of establishing the local water line for groundwater recharge studies.

The IAEA maintains a global network for isotopes in precipitation (GNIP, www.iaea.org/water) with stations from all around the globe. These data include mean monthly values for $\delta^{18}O$ and δD together with precipitation amounts, temperature, and other meteorological data and are available for download. This provides local or regional precipitation data to produce LMWLs for groundwater studies. In any study of isotope hydrology, it is useful to use precipitation data that best represent the study area. In the absence of regional or local precipitation data, the GMWL is often substituted. However, this can bring uncertainty, particularly in arid and high latitude regions.

Example 5.2: Deuterium Excess and Origin of Rain

In a study by Cruz-San Julian et al. (1992) on the origin of rain responsible for groundwater recharge in southeastern Spain, deuterium excess proved to be a diagnostic tool in distinguishing between two major meteorological systems. High-pressure systems over the Azores drive a strong NW circulation bringing cold vapor masses in from the north Atlantic over the country, with a MWL close to the global line. The second evolves from low pressure systems over the Gulf of Cadiz to the west of the Straits of Gibralter, bringing moisture from the Mediterranean (Figure 5.12). Precipitation originating from the north Atlantic is characterized by a deuterium excess similar to the global value of 10‰, while stronger evaporation in the warmer Mediterranean translates into greater kinetic fractionation and deuterium excess value of 22‰. Groundwaters have a deuterium excess in the range of 10‰ to 14‰, indicating north Atlantic storms to be the dominant source of recharge.

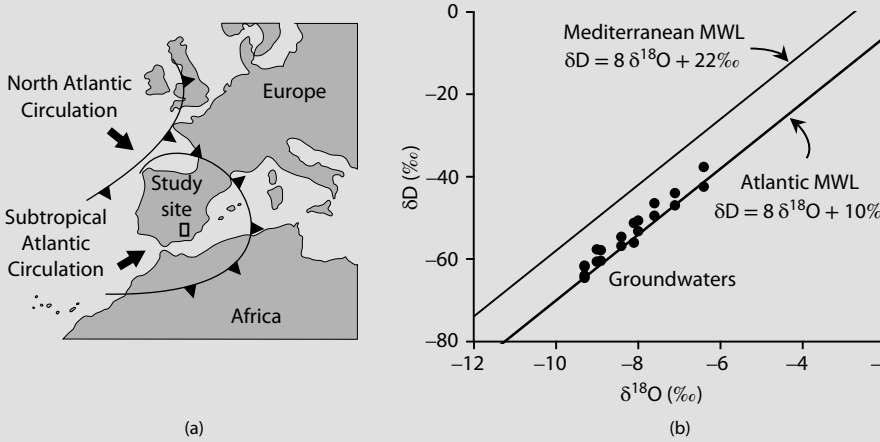

FIGURE 5.12 Source of water vapor for precipitation recharging groundwaters in Mediterranean Spain. (a) Recharge region and the two principal origins of water vapor. (b) Strong deuterium excess in the precipitation from the Mediterranean (d = 22‰) and from the Atlantic (d = 10‰). Despite proximity to the Mediterranean coast, groundwaters are largely recharged by cyclonic activity in the Atlantic arriving from the northwest (After Cruz-San Julian et al. 1992.)

TEMPERATURE EFFECTS IN PRECIPITATION

The very strong correlation between decreasing temperature and isotope depletion in precipitation observed on a global scale is manifested at the regional to local scale, where temperature gradients occur. Spatially, this can be observed at the continental scale to the watershed scale, and temporally at the scale of seasonal change to millennial-scale climate change. All are important in establishing the $\delta^{18}O$ and δD signature of precipitation which can then be used to trace the origin of groundwater.

Continental Effect

The proximity to marine waters exerts a control on the isotope composition of precipitation as vapor masses move inland. Continentality is expressed by Conrad's index, which is a function of the amplitude of the seasonal temperature range, and increases with distance from the coast, and latitude. Stations with increased continentality have lower $\delta^{18}O$ and δD values for mean annual precipitation. Continentality is associated with greater mixing with isotopically more depleted vapor masses in the upper troposphere.

The continental effect can be observed in Figure 5.6 as gradients in $\delta^{18}O$, for example, northwestward from the Gulf of Mexico in North America, or moving eastward through Europe from Atlantic coastal stations. It is often manifested in the isotope composition of rivers draining from continental scale basins, which will have a depleted signature relative to local precipitation in the downstream regions.

Altitude Effect

The effect of topography can also be observed in Figure 5.6, with depletions observed over the Rocky Mountains in western North America, over the Tibetan Plateau and in the Andes of South America. This is attributed to the decrease in temperature with elevation, which drives rainout and distillation of isotopes during orographic precipitation. This is also observed at the catchment-scale and is an important tool to identify the recharge elevation of groundwater. Tropospheric temperatures decrease by about 0.6°C per 100-m rise in altitude (the tropospheric lapse rate). From Figure 5.2, precipitation should then experience depletion in ^{18}O of about 0.4‰ per 100-m rise in altitude. In fact, the $\delta^{18}O$ of precipitation decreases by 0.15‰ to 0.5‰ per 100-m rise in altitude, whereas δD decreases by between 1‰ and 4‰.

Precipitation for catchment in the maritime piedmont of the Italian Alps was sampled at different elevations, providing the good correlation observed in Figure 5.13. In this case, the altitude effect was –0.31‰ for $\delta^{18}O$ per 100-m rise. For Mont Blanc (Moser and Stichler 1970), the gradient was a much steeper –0.5‰ for $\delta^{18}O$, based on their measured –4‰ for δD per 100-m rise. Warmer regions tend to have lower temperature gradients, and so the altitude effect is generally less than –0.2‰ for $\delta^{18}O$ per 100-m rise.

Lower elevation catchments with relief contrasts as low as a few hundred meters also demonstrate an altitude effect for ^{18}O and D, based on long-term weighted averages of precipitation. This is worthwhile to monitor in a study site given that groundwater recharge itself is often a long-term weighted average of precipitation in the recharge area. Accordingly, recharge elevations can even be distinguished in low-relief catchments.

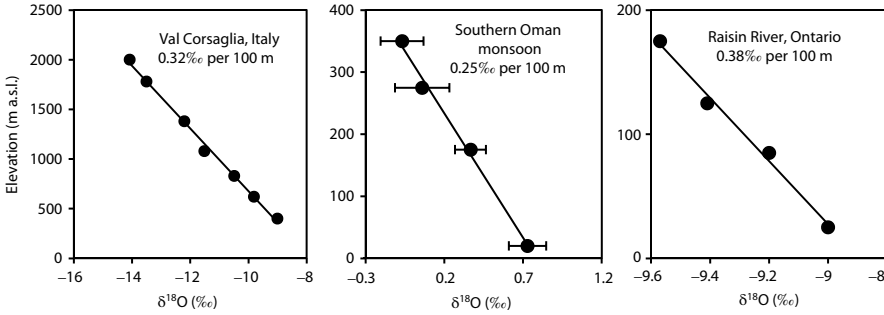

FIGURE 5.13 The altitude effect for $\delta^{18}O$ in precipitation at three sites. Val Corsaglia, a high-altitude site in the Italian Alps sampled during October, 1974 (Bortolami 1978), the summer monsoon in the Dhofar Mountains of Southern Oman monitored weekly over the 1985 monsoon period (Clark et al. 1987), and a low relief agricultural catchment in Eastern Ontario monitored over a 15-month period (amount-weighted, Suchy 2008). The studies for the Oman and the Raisin River sites demonstrate that the depletion trend with elevation is apparent even for low-relief catchments, providing multiple events or long-term monitoring data that are collected.

Example 5.3: Recharge of Coastal Groundwaters in Chile

The northern coast of Chile hosts alluvial sand and gravel aquifers bounded inland by the Coastal Mountains up to 2000 m above sea level, rising to over 4000 m in the Andes some 150 km further to the east. However, the coast receives an average of only some 100 mm of rain annually, mostly as infrequent El Niño events followed by years of drought, and as fog (occult precipitation) in the uplands. Groundwater discharge from this coastal aquifer sustains coastal wetlands in this arid environment. Squeo et al. (2006) collected local rainfall and fog precipitation in an isotope study to determine the relative contributions of local precipitation and drainage from the mountains to the coastal aquifer system.

The $\delta^{18}O$ and δD data for the region are plotted in Figure 5.14, showing the isotopic composition of precipitation and the distinct signatures for the groundwaters sampled in the three well fields. The LMWL characterizing coastal precipitation in the study area ($\delta D = 7.7\ \delta^{18}O + 9.6$) is close to the global meteoric line. However, groundwater from the three alluvial aquifer wells defines a meteoric waterline with a similar slope but lower deuterium intercept. They are also isotopically depleted with respect to local precipitation, with northernmost groundwater being most enriched and the southernmost groundwater near the Elqui River being the most depleted.

These data illustrate the elevation effect, with recharge dominantly at higher elevations and with a different MWL than the local rain. The even more enriched fog waters show no evidence of contributing to recharge. Given a typical $\delta^{18}O$-elevation gradient of –0.25‰ per 100 m rise, the 8‰ depletion for the Elqui

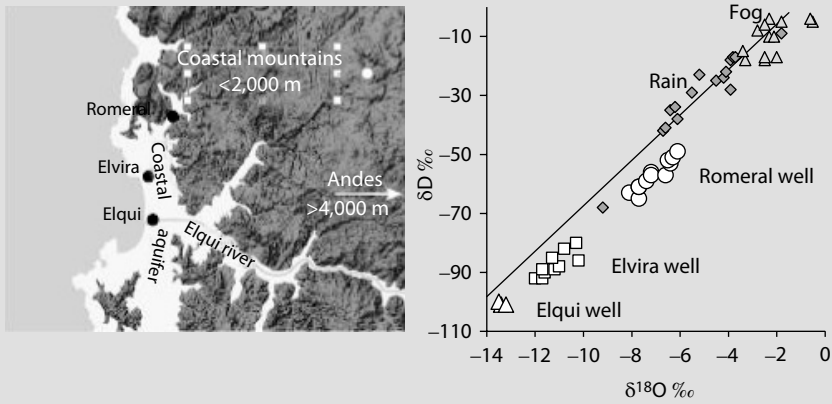

FIGURE 5.14 Coastal aquifer recharge in an arid region of northcentral Chile. (After Squeo et al. 2006.) Fog was sampled with 1 m high interceptors. Strong isotope depletion in Elvira well indicates recharge from precipitation in the Andes, while the Romeral well is recharged in the lower elevation Coastal Mountains.

River aquifer (Elqui well = –13‰) relative to local rain (–5‰) would be recharged at an average elevation some 3200 m higher, which is beyond the range of the coastal mountains and within the elevation range of the Andes to the east. The 2‰ depletion for the Romeral groundwater (–7‰) relative to local rain suggests recharge at about 800 m higher elevation in the local Coast Mountains. The Elivira well groundwater (–10 to –12‰) apparently has contributions from both the Coastal Mountains and the Andes.

This is not to say that local rain, although infrequent, does not recharge this coastal aquifer. The authors detailed time-series data show that the Romeral well responds to exceptional local precipitation events, such as the 1997 El Niño, which was associated with both an increase in water level and a shift in $\delta^{18}O$ and δD toward the isotopically enriched rain.

Seasonal Effects in Continental Precipitation

For temperate and continental regions, a principal control on the isotopic composition of precipitation is the seasonal change in temperature and consequently in the $\delta^{18}O$ and δD of precipitation. These seasonal variations in $\delta^{18}O$ and δD give us an important tool to determine watershed response to precipitation, mean residence time of water in drainage basins, and to monitor groundwater recharge.

Figure 5.15 shows the seasonal variation for $\delta^{18}O$ for stations from Antarctica to northern Greenland. The greatest seasonal change is observed for sites with high continentality and high latitude (e.g., Edmonton and Thule). Marine (St. Helena) and coastal sites (Cape Grim) show the least amount of seasonal variation.

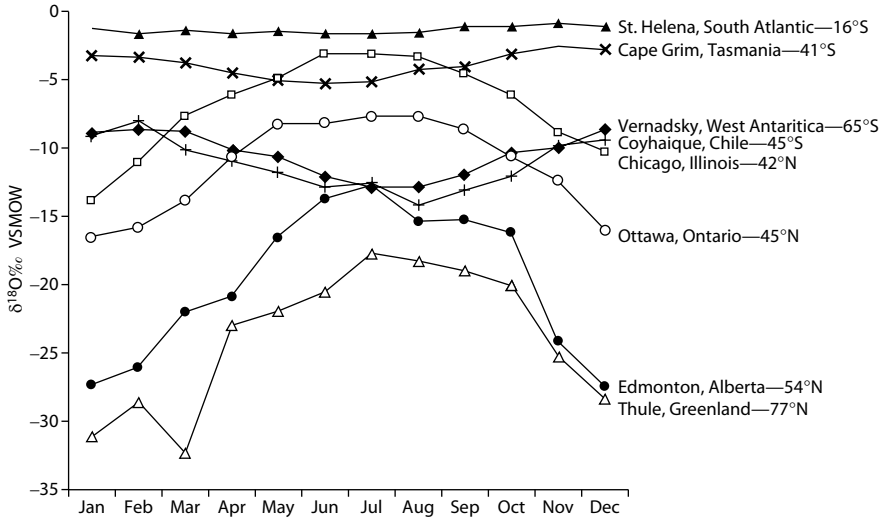

FIGURE 5.15 The seasonal variation in $\delta^{18}O$ in precipitation at stations from low to high latitude in the northern and southern hemispheres. Data are for monthly averages. Note the lack of seasonal effect for the oceanic station—St. Helena, an atoll in the south Atlantic Ocean, and the subdued seasonal effect for the two coastal stations at Cape Grim, Tasmania, and Vernadsky, a Russian research station near the tip of the West Antarctic peninsula. Strong seasonality imparts a high amplitude variation for ^{18}O in precipitation at the inland stations—Chicago, Ottawa, and Edmonton.

Example 5.4: Seasonal Discharge from a Small Permafrost Watershed

Seasonal hydrograph separation is a useful approach to understanding the contributions of groundwater to discharge from a watershed. This is particularly interesting in permafrost watersheds where groundwater recharge and flow is difficult to assess. Figure 5.16 shows the weekly monitoring of discharge and $\delta^{18}O$ for a watershed near Whitehorse, Yukon Territory, which is situated within the zone of discontinuous permafrost.

The monitoring results show clearly the seasonal signal in discharge, with the spring freshet beginning with a strongly depleted signal of snowmelt in the watershed, followed by summer precipitation that contributes to discharge. The earliest sample from April was taken prior to melting, and so represents groundwater baseflow. The enriched signal indicates that groundwaters in this permafrost basin are recharged mainly by summer precipitation with little contribution from snowmelt.

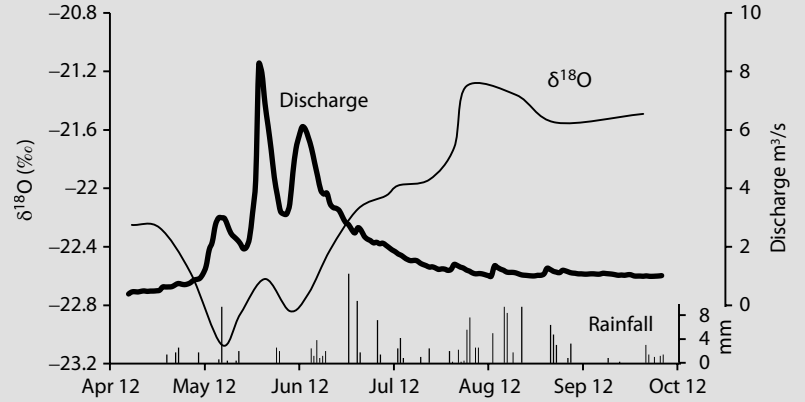

FIGURE 5.16 Flow rate and $\delta^{18}O$ for Wolf Creek basin discharge from spring snowmelt through to the beginning of freeze-up in October 2012. (Data from Li, T. 2013.)

Example 5.5: Seasonal versus Mean Annual Precipitation

The seasonal effect can be used to identify the source of water for geotechnical purpose such as seasonal inflows to a mine, a construction site, or basements. This example follows from a flooded basement during spring thaw. Pooling snowmelt draining in through a cracked foundation was a potential source of the floodwater. Another was the plumbing to the outside tap which had potentially frozen over the winter and split and was now leaking into the basement with the spring temperatures. Remediation required either removing the drywall to repair the plumbing or dig into the foundation to seal a crack. It was resolved with three $\delta^{18}O$ measurements. The results (Figure 5.17) indicate that a plumbing rather than foundation repair was required.

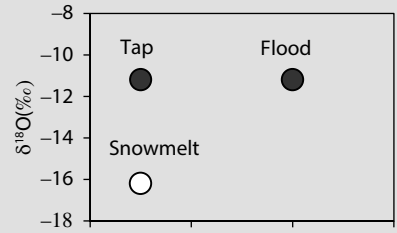

FIGURE 5.17 $\delta^{18}O$ versus δD of water in a flooded basement, showing the source of floodwater to be a broken water pipe in the wall.

Paleoclimate Effects

Climate change can be recorded by the stable isotope contents of precipitation. Measurements in precipitation over the past 30 years show strong T–$\delta^{18}O$ correlations but with amplitudes on the order of 1‰ to 2‰ and 1°C to 2°C (Rozanski et al. 1993). Longer precipitation records are archived in glacier ice cores. The $\delta^{18}O$ and δD variations in these cores provide a remarkable record of temperature change that now extends back over some 650,000 years (Figure 5.18).

Other sources of such climate records are found in the steady accumulation of speleothem from groundwater, where the ^{18}O in calcite ($CaCO_3$) can be used to reconstruct the $\delta^{18}O$ of the groundwater that formed the deposit. One of the most interesting such records is that from Devil's Hole, Nevada, where regional groundwaters discharging through an open fault have lined the wall with up to a meter of carbonate. Profiles of $\delta^{18}O$ along cores from this speleothem provided a 500,000-year record of climate that records the timing and duration of glacial periods (Winograd et al. 1992) (Figure 5.18).

Groundwaters recharged during these glacial events, or by meltwater at the end of continental glaciation hold an isotope record of the event noted by a depletion in ^{18}O and D (e.g., Clark et al. 2000; Grasby and Chen 2005). One of the earliest recognition of such recharge comes from Siegel and Mandle (1984), in Example 5.6.

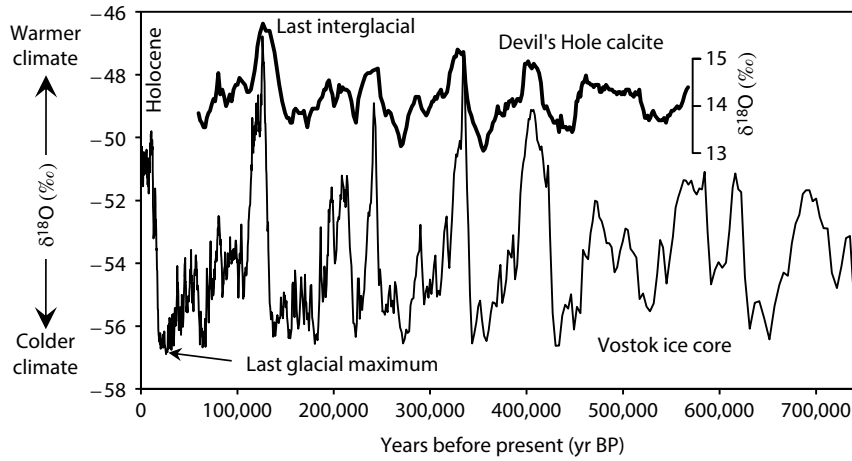

FIGURE 5.18 Change in climate temperature as recorded by the $\delta^{18}O$ in glacier ice from Vostok Station, Antarctica (Data from EPICA 2004) and in calcite precipitated from regional groundwaters at the Devil's Hole springs, Nevada (data from Winograd et al., 1992). Periods characterized by depleted values for $\delta^{18}O$ correspond with glaciations. Peaks of enriched ^{18}O values document the warmer climates of the interglacial periods.

Melting of the Laurentide Ice Sheet during climate improvement at the end of the Pleistocene some 12,000 years ago was a dramatic hydrological and morphological event impacting most of the northern North American landscape. Remnants of the meltwater event are found today in the subsurface where the steep hydraulic gradients along the margin of the ablating ice sheet caused deep circulation of glacial meltwater through bedrock aquifers. With the decayed gradients in these aquifers following retreat of the ice, glacial meltwater remained in place with little subsequent flushing (Example 5.6).

Example 5.6 Pleistocene Glacial Meltwater Recharge

Siegel and Mandle (1984) provide an example for groundwaters recharged by glacial meltwater in the well-developed Cambrian–Ordovician sandstone aquifer, which outcrops east of Lake Michigan. The $\delta^{18}O$ values follow a gradient from enriched values in the outcrop area to the north to values less than –17‰ in the south, highlighting the major infiltration pathways (Figure 5.19). The associated isotope plot for these groundwaters show a marked depletion in both ^{18}O and D relative to modern, tritium-bearing groundwaters in the region.

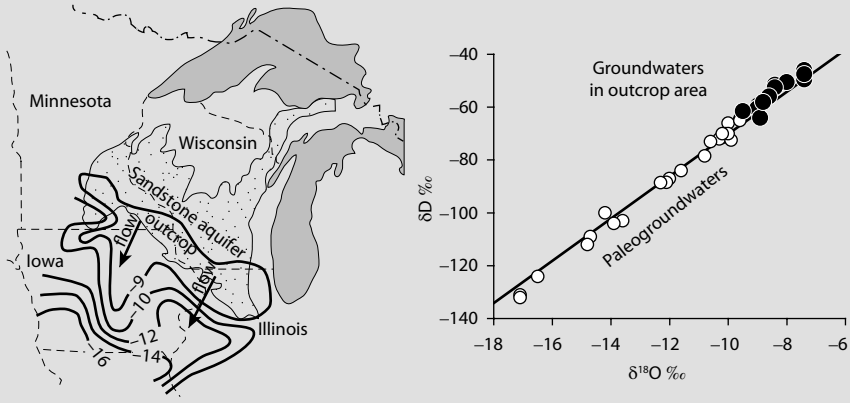

FIGURE 5.19 Glacial meltwater recharged into the Cambrian–Ordovician sandstone aquifer where it outcrops in the northern United States (After Siegel and Mandle 1984). Groundwaters are a mixture of modern precipitation ($\delta^{18}O > -9‰$) and glacial meltwater ($\delta^{18}O$ to –16‰).

High latitude regions have experienced considerable fluctuations in temperature since Pleistocene time, including the cold conditions of the last glacial maximum some 20,000 years ago, the early Holocene warming with extensive permafrost degradation,the late Holocene cooling culminating in the Little Ice Age of 1400 to 1800, and followed by twentieth century warming. Much of this history is recorded by the massive ice and interstitial ice found in the subsurface in permafrost regions, and can be observed in thaw slumps that occur when permafrost becomes exposed at the surface (Example 5.7). Stable isotopes are one of the tools used to understand the origin of ice in permafrost and reconstruct the Quaternary history at high latitudes.

Example 5.7: Origin of Buried Ice in Permafrost

Sites on the Peel Plateau in the Northwest Territories of the Canadian Arctic have been studied by Lacelle et al. (2004) and by Kokelj et al. (2013) where massive retrogressive thaw slumps have exposed permafrost faces up to 30 m in height. The stable isotopes show three different ice origins, including massive ice and contemporaneous ice wedge ice developed under cold climate conditions near the glacial maximum. These Pleistocene ice bodies contrast with the icy diamicton (glacial till), which has stable isotope values identical to modern local runoff. The interstitial ice in the diamicton originates as recharge during the warmer Holocene when the permafrost surface had degraded to a considerably depth and allowed Holocene precipitation to circulate. Climate cooling and permafrost aggradation since this time froze the diamicton.

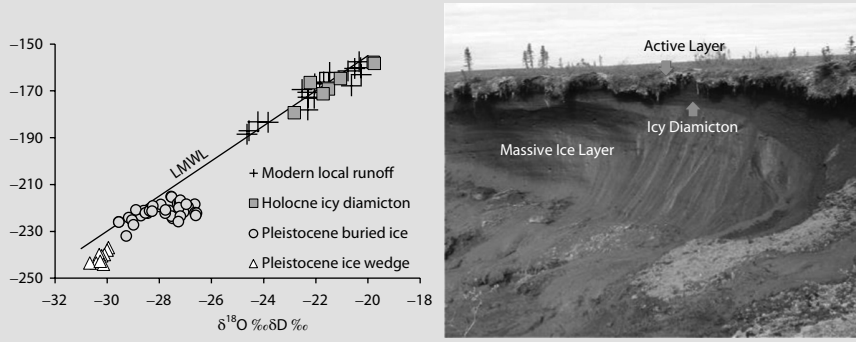

FIGURE 5.20 Distinctions in ^{18}O for ice of different origins in a retrogressive thaw slump, northern Northwest Territories, Canada. The icy diamicton holds precipitation recharged during the warm early Holocene when the active layer melted to over 2 m depth. The buried ice formations have cold-climate Pleistocene precipitation that remains trapped in the permafrost.

GROUNDWATER RECHARGE

The translation of the isotope signal in precipitation into groundwater is an important step in the use of stable isotopes as tracers of groundwater origin. Although the various temperature-dependent processes of rainout distribute isotopes in precipitation over a wide range, this range is highly attenuated as precipitation enters the subsurface. The seasonality of precipitation plays a role in this, where groundwater may be recharged only at certain times of the year. Hydrodynamic dispersion also plays a role. The effect is such that while the $\delta^{18}O$ content of precipitation may vary over 8‰, in groundwater the variation will usually be less than 1‰.

Seasonality of Recharge

The isotopic composition of groundwater can be traced to that of precipitation in the recharge area. Typically, the weighted mean annual value of $\delta^{18}O$ and δD in precipitation is considered to represent the isotopic signature of groundwater. A good example is in tropical regions with strong seasonal bias in the amount of precipitation (Figure 5.21). Using the mean monthly value to represent groundwater would overly

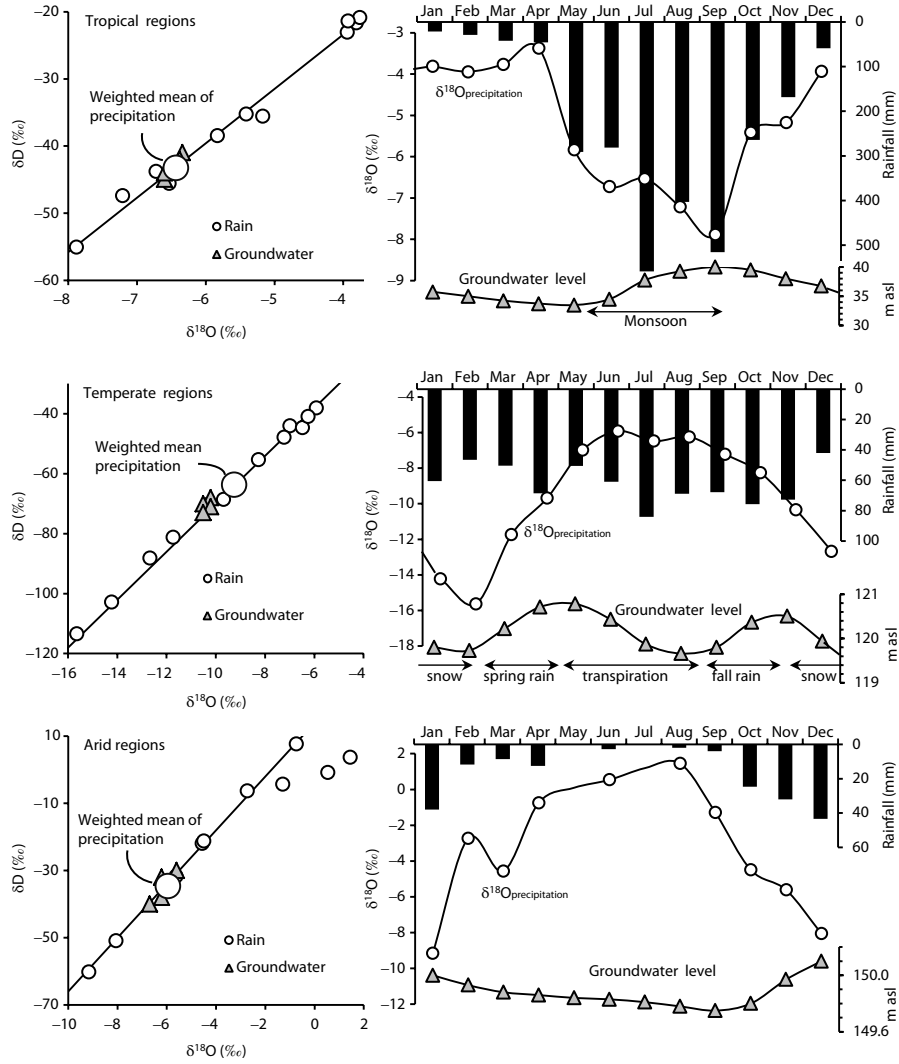

FIGURE 5.21 The seasonal timing of precipitation and transfer of the isotope signal into groundwater for characteristic sites in tropical (Manila), temperate (Ottawa), and arid (Sana'a) regions. Isotopes in precipitation are weighted mean monthly values. Typical groundwater levels shown (IAEA/WMO 2013).

bias toward the isotopically enriched dry months, whereas using the weighted mean of monthly precipitation gives a value that is more representative of groundwater.

In temperate climates, the combined effects of winter snow accumulation and transpiration during the summer months restrict groundwater recharge to the spring and fall periods (Figure 5.21). Although the $\delta^{18}O$ and δD in precipitation during these transition seasons approximate that of mean annual precipitation, there can be deviations of a few permil. In these climates, the weighted mean annual isotopic composition of precipitation is often enriched over local groundwater.

In arid regions, groundwater recharge is largely biased toward the large precipitation events (Figure 5.21). As light rains contribute little to the weighted mean of precipitation, the isotopic composition of groundwater is well represented by the weighted mean annual or long term weighted value for precipitation.

Dispersion during Recharge

At the micro-scale, groundwater flow through a porous medium or fracture is mixed by hydrodynamic dispersion due to the differences in porewater velocity and pathways within connected porosity. This is characterized for a porous medium as its dispersivity, α, in units of length (m), where the coefficient of hydrodynamic dispersion, D, is a function of the medium's dispersivity and its average linear groundwater velocity, v, plus molecular or effective diffusion, D_e:

$$D = \alpha v + D_e$$

Molecular diffusion only becomes relevant at very low groundwater velocities, and so is an important mechanism for groundwater mixing in aquitards, discussed below.

In recharge environments, the effect of dispersivity is the attenuation of seasonal and event scale variations in isotopes and geochemistry. The shallow groundwater in most phreatic aquifers has an age distribution reflecting contributions from several months to several years of precipitation, increasing to years and decades in confined systems. The effect of this mixture of groundwaters of different age is an increased attenuation or damping of the event-scale to seasonal-scale variability of isotopes in precipitation. Long-term monitoring of $\delta^{18}O$ or δD in groundwaters at increasing depths and distances along the flow system shows the convergence on a long-term mean value (Figure 5.22). This temporal variation in $\delta^{18}O$ is shown schematically in Figure 5.23 for monitoring in a water table well and in a confined aquifer well.

Temporal-scale monitoring by repeat sampling at selected sites provides insights on the sensitivity of the groundwater system to recharge frequency and drought. Although considerable damping of event-scale to seasonal isotope variability in precipitation occurs in the unsaturated zone, groundwater near the water table may still fluctuate within 1 to 2 permil for $\delta^{18}O$ (Figure 5.23). This is particularly so where macroporosity from root zones and worm holes can short-circuit recharge to the water table, and highlights the uncertainty of characterizing groundwater with one sample on one sampling campaign. It also provides indications of contaminant potential from surface activities. Groundwaters with little to no variability are typically considered to be part of larger, deeper flow systems that are more resilient to temporal variations in recharge than shallow systems showing greater correlation with the temporal signal in precipitation.

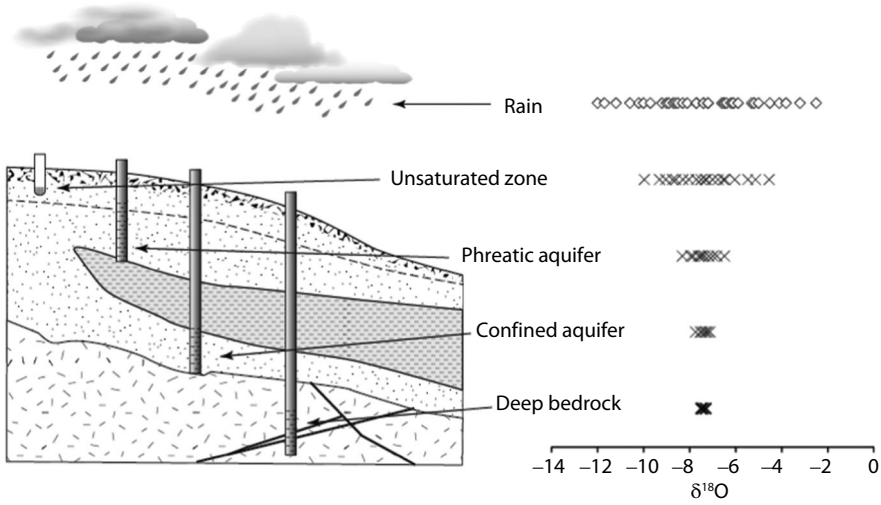

FIGURE 5.22 Attenuation of seasonal $\delta^{18}O$ in precipitation by hydrodynamic dispersion in phreatic and confined aquifers.

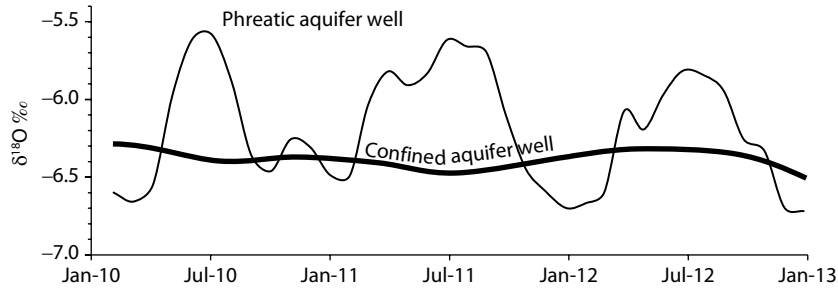

FIGURE 5.23 Temporal-scale monitoring for $\delta^{18}O$ in a water-table well in a phreatic aquifer and a deeper well in a confined aquifer (schematic). Seasonal and event scale recharge is moderately damped in the phreatic aquifer and fully damped in the confined aquifer.

Spatial-scale monitoring of groundwaters in aquifer systems, unlike temporal-scale monitoring, provides insights on the heterogeneity of recharge over the extent of the aquifer outcrop. Figure 5.24 gives example data sets for spatial-scale monitoring of phreatic and confined aquifers in humid and arid regions. The wide range of data in the phreatic aquifer represents not only the temporal variability of each sampling point as observed in Figure 5.23 but also any elevation contrasts for the origin of recharge within the catchment. This variability is attenuated in the confined aquifer by dispersion. In arid regions, phreatic groundwaters may also show evidence of evaporation, which typically accompanies recharge of lower-intensity precipitation events or partial evaporation during surface flow and infiltration, and can be characterized by a local evaporation line.

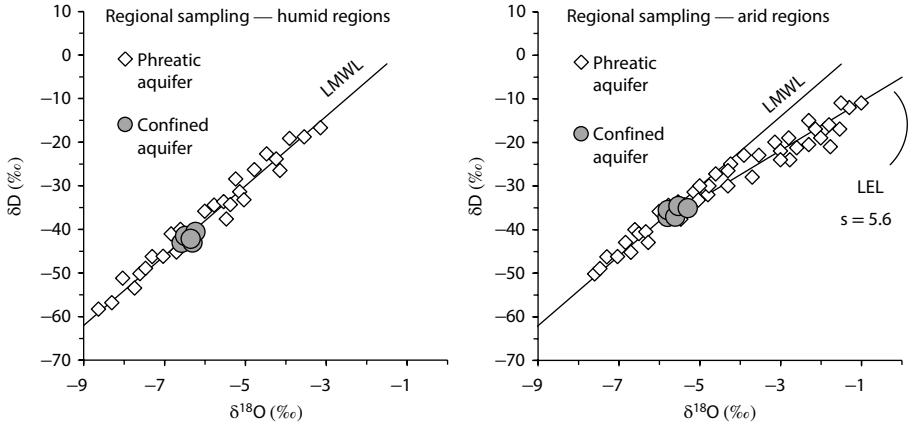

FIGURE 5.24 Spatial-scale monitoring of groundwater resources.

ISOTOPE EFFECTS OF EVAPORATION

Although the $\delta^{18}O$–δD signal of precipitation is generally transferred to groundwater with some fidelity, it can be modified in the recharge environment by evaporation which imparts an isotopic enrichment on the residual water. This can occur during rainfall for minor precipitation events or during overland flow prior to infiltration. Rivers and lakes will experience some evaporation which can be transferred to groundwaters if they are a recharge source. Evaporation from the unsaturated zone and ultimately from the water table can also occur. The loss of water by transpiration, in contrast to evaporation, does not fractionate ^{18}O and D. The isotope effect of evaporation is the preferential loss of ^{16}O and ^{1}H in the vapor fraction (recall that $\varepsilon^{18}O_{\text{vapor-water}}$ is about –10‰). However, evaporation under conditions of lower humidity, nonequilibrium, or *kinetic* effects imparts an additional fractionation. As these kinetic effects are disproportionally greater for ^{18}O, the result is a characteristic deviation from the LMWL for evaporated waters.

Kinetic evaporation effects are due to the differences in the velocities of the three isotope species: $H_2{}^{16}O$ (mass 18), $HD^{16}O$ (mass 19) and $H_2{}^{18}O$ (mass 20), as they diffuse through the air column from the boundary layer of water-saturated air overlying the evaporating water (Figure 5.25). Enhanced evaporative loss of ^{16}O and H results in accumulation of ^{18}O and D in the residual water.

Evaporative enrichment is greater for $\delta^{18}O$ than for δD, with the result that evaporated waters fall off the MWL on a $\delta^{18}O$–δD diagram, and plot along a distinct *evaporation line* typically less than 6 (Figure 5.26). If evaporation is minor, then little to no effect will be observed in the residual water. If the water loss is more than a few percent, the result is a positive shift in the $\delta^{18}O$ and δD composition of the residual water away from a position on the local MWL. Kinetic evaporation typically occurs during overland flow in arid landscapes as observed for groundwaters in such regions (Figure 5.26), in lakes and reservoirs, and from bare soils during infiltration. It can also occur for light rains falling through warm air column, noted by Dansgaard (1964) as the *amount* effect.

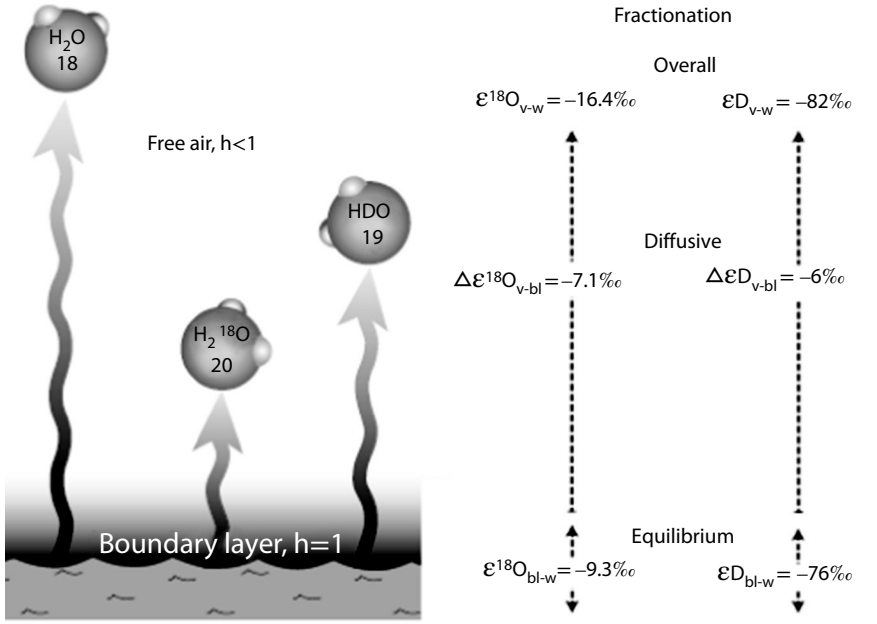

FIGURE 5.25 Kinetic fractionation during non-equilibrium evaporation of water, due to enhanced diffusion of H_2O (mass 18) relative to HDO (mass 19) and $H_2{}^{18}O$ (mass 20) from the boundary layer to open air. Diffusion of $H_2{}^{18}O$ is lower than for HDO due to the greater mass effect, and so there is enhanced accumulation of ^{18}O in the residual water. The greater kinetic fractionation for ^{18}O reduces the $\varepsilon D/\varepsilon^{18}O$ ratio from 8 for equilibrium fractionation to a value closer to 5.

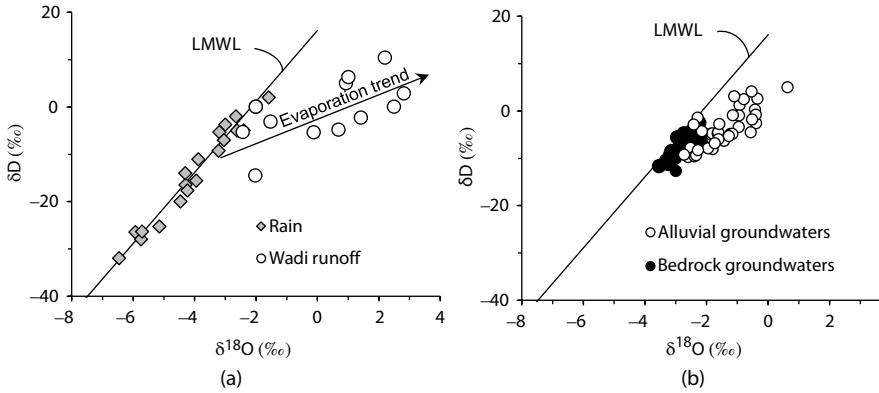

FIGURE 5.26 Evaporation effect observed in surface flow (drainage channels or wadis in arid areas) (a) following precipitation and (b) groundwater, for a catchment in the arid country of Oman. Both ^{18}O and D become enriched in water by evaporation during overland flow in the wadi channels. This evaporative signature is retained during infiltration into the alluvial aquifers along the wadi channels. Bedrock aquifers are recharged by direct infiltration during major storm events, with minimal evaporation during recharge.

Evaporation of water produces an enrichment trend for both $\delta^{18}O$ and δD according to a Rayleigh distillation, like rainout above in Figure 5.5. Figure 5.27 shows this exponential enrichment for ^{18}O and D as the residual water fraction f approaches 0. In a plot of $\delta^{18}O$ and δD, evaporated waters form a positive trend that deviates from the MWL with prefer ^{18}O enrichment (Figure 5.27). Evaporative slopes vary between about 4 and 7, depending on the relative humidity.

The reason for this deviation is found in the kinetic fractionation factors for ^{18}O and D. Gonfiantini (1986) determined empirical relationships for the kinetic enrichment factor, $\Delta\varepsilon_{water-vapor}$ based on humidity that is used to determine the isotopic fractionation between water and vapor during nonequilibrium evaporation from surface waters:

$$\Delta\varepsilon^{18}O_{water-vapor} = 14.2(1-h)$$
$$\Delta\varepsilon D_{water-vapor} = 12.5(1-h)$$

These kinetic enrichment factors add to the equilibrium enrichment factors to give overall enrichment:

$$\delta^{18}O_{water} - \delta^{18}O_{vapor} = \varepsilon^{18}O_{water-vapor} + \Delta\varepsilon^{18}O_{water-vapor}$$

$$\text{and } \delta D_{water} - \delta D_{vapor} = \varepsilon D_{water-vapor} + \Delta\varepsilon D_{water-vapor}$$

From these two equations, the additional enrichment in the water is greater for ^{18}O than for D, which imparts the deviation from the MWL along an evaporation line with lower slope. The influence of humidity h is such that under drier conditions, the slope of the evaporation trend is lower. This can be seen from the ratios of the combined D/^{18}O enrichment factors calculated here for different values of humidity (Table 5.1 and Figure 5.28).

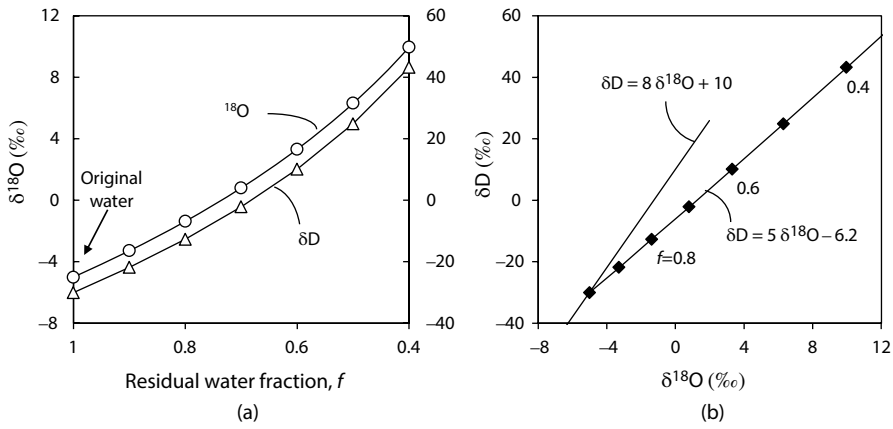

FIGURE 5.27 The isotopic effect of evaporation on water. (a) Diagram shows the Rayleigh enrichment of ^{18}O and D as the residual fraction of water f approaches 0, for humidity of 50% and at 25°C. (b) Diagram shows the combined evaporation effect for $\delta^{18}O$ and δD as f approaches 0.

Groundwaters may have an evaporated signal due to evaporation of surface waters prior to infiltration, but can also undergo evaporation of soil moisture from the unsaturated zone. In this case, the evaporation effect is even stronger and results in an isotope shift along a line with much lower slope than for surface water evaporation due to the long diffusional distance through the upper dry soil column (Allison 1982).

TABLE 5.1
Evaporative Enrichment Factors for $\Delta\varepsilon D$ and $\Delta\varepsilon^{18}O$ for Varying Values of Humidity, Using the Relationships from Gonfiantini (1986)

Humidity	1	0.8	0.5	0.2
$\Delta\varepsilon D_{water-vapor}$	0	3	6	10
$\Delta\varepsilon^{18}O_{water-vapor}$	0	2.8	7.1	11.4
$\varepsilon D + \Delta\varepsilon D$	76	79	82	85
$\varepsilon^{18}O + \Delta\varepsilon^{18}O$	9.3	12.9	16.4	19.2
$\dfrac{\varepsilon D + \Delta\varepsilon D}{\varepsilon^{18}O + \Delta\varepsilon^{18}O}$	8.2	6.5	5.0	4.2

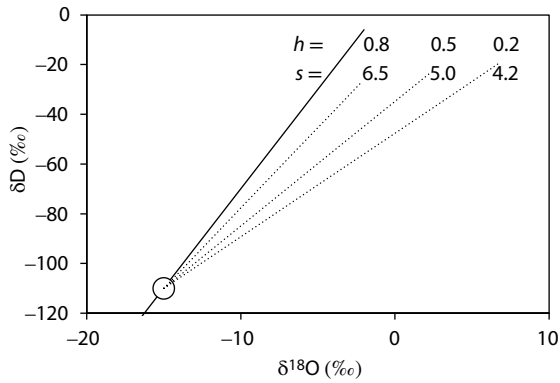

FIGURE 5.28 Evaporation lines for varying humidity. The slope is defined by the $\dfrac{\varepsilon D + \Delta\varepsilon D}{\varepsilon^{18}O + \Delta\varepsilon^{18}O}$ ratio, which decreases with lower humidity.

Example 5.8: Calculating Water Lost by Evaporation from a Surface Water Body

The evolution of $\delta^{18}O$ and δD in water retained by a desert dam on a dry river course in an arid region has been monitored to assess losses to evaporation prior to infiltration. As wind mixing of the water column is efficient, the data are representative of the full water column, which have $T = 25°C$. What is the evaporative loss as a fraction of the original water volume and what is the percent infiltration?

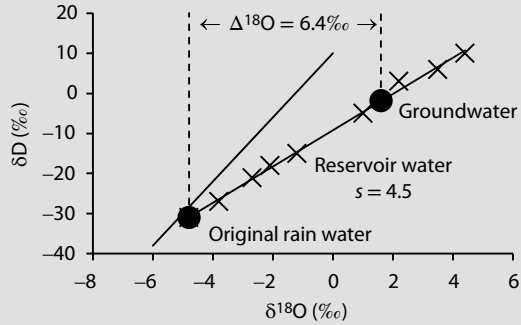

FIGURE 5.29 Plot of $\delta^{18}O$–δD for surface waters in a scenario for evaporation from a desert dam reservoir.

Figure 5.29 shows that these waters have evaporated with a $\delta^{18}O$–δD slope of 4.5. From the above data for slope versus humidity, this correlates with a humidity of 50%.

The kinetic enrichment factor for ^{18}O is determined using the empirical relationship introduced above, and the equilibrium enrichment factor $\varepsilon^{18}O_{w-v}$ = 9.3‰ (expressing enrichment factor as product–reactant):

$$\begin{aligned}\delta^{18}O_w - \delta^{18}O_v &= \varepsilon^{18}O_{w-v} + \Delta\varepsilon^{18}O_{w-v} - 14.2\ (1-h)\\ &= 9.3 + 14.2(1-0.5)\\ &= 16.4\ ‰\end{aligned}$$

The overall enrichment for ^{18}O under these conditions is 16.4‰ as water-vapor. The Rayleigh equation requires the enrichment as product-reactant or vapor-water, so the enrichment factor is then –16.4‰. The fraction water loss is calculated from the difference between the initial and final ^{18}O content of the reservoir water ($\delta^{18}O_{final} - \delta^{18}O_{initial}$ = 6.4‰, from diagram) using the simplified Rayleigh equation as follows:

$$\begin{aligned}\delta^{18}O_{final} - \delta^{18}O_{initial} = 6.4‰ &= -\left(\varepsilon^{18}O_{w-v} + \Delta\varepsilon^{18}O_{w-v}\right) \times \ln f = 6.4‰\\ 6.4 &= -16.4 \times \ln f\\ \ln f &= -0.39\\ f &= 0.68\end{aligned}$$

This gives a residual water fraction f of 0.68 and so an evaporative loss of 32%. Thus, only 68‰ of the original water volume in the reservoir has infiltrated to the aquifer. Note that this solution is a first-order approximation. A more accurate analysis requires consideration of the isotope value for the ambient water vapor in the atmosphere, as this back-exchanges with the reservoir water during evaporation.

Example 5.9: Evaporated Signal as a Tracer

An urban woodland in southern Ontario features a small recreational lake. However, there was concern that an adjacent municipal water well would induce recharge from the lake, adversely affecting lake levels (Figure 5.30). This example of groundwater–surface water interaction was tested by monitoring stable isotopes during an extended-duration pumping test. In Figure 5.30 the lake waters plot near $\delta^{18}O$ of –8‰ with an evaporated ($\delta^{18}O$ enriched) signature. If the pumping well was inducing significant recharge from the lake, this would be observed in the isotopic composition of the pumped groundwater. On a $\delta^{18}O$ versus δD diagram, this would appear as a straight mixing line from the pumping water toward the lake water.

The groundwaters sampled from the pumping well fall with the range for the average for precipitation in this area of –9.5‰ to –10‰ (Fritz et al. 1987). However, the lake water is enriched in ^{18}O with a relative depletion in deuterium typical of evaporation in surface waters, providing a good tracer of lake water influence during the pumping test. Over the duration of the pumping test, the isotopes in the pumping water do not track toward the isotope signature of the lake waters, and so there is no induced recharge to the well from the lake. The pumping well water actually tracks away from the surface water source likely showing some heterogeneity in isotopic composition typical of unconfined aquifers which may preserve some seasonal effects in recharge.

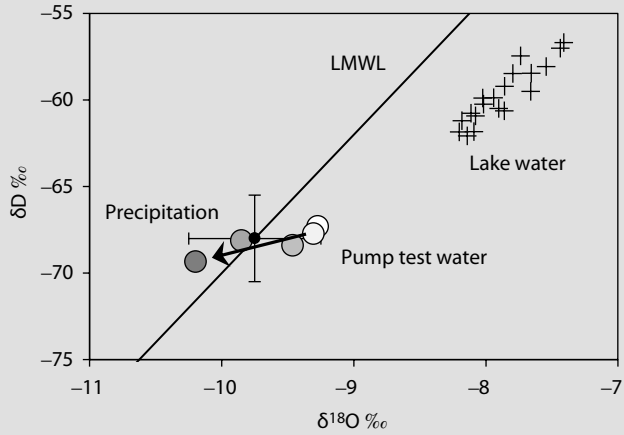

FIGURE 5.30 Water supply well pumping from an aquifer beneath a recreational lake in Ontario. The potential impact on water level from extended pumping was evaluated with a 2-month pumping test. The evaporated signature in the lake water contrasts with that of the pumped water at the outset of the pumping test (white disc). The isotope composition of the pumping water evolves over the course of the pump test (increasingly grey discs), but away from the lake water, indicating no contribution of lake water to the well.

Although groundwater losses by evaporation from bare soil can be significant in arid regions, vegetative cover minimizes evaporation. However, forested landscapes and grasslands transpire groundwaters at even greater rates. About

1000 times more H_2O is transpired from leaves than the CO_2 that is fixed during photosynthesis. A single acacia tree can transpire up to a cubic meter of water per day. However, this transpired water is taken up by the roots in a quantitative manner without fractionation. Such losses of soil water by transpiration leaves no isotopic signature on the residual water, although the process does increase soil water salinity. This is useful in attributing water losses to evaporation and transpiration. Both result in increased salinity, but only evaporation will enrich the soil water in ^{18}O and D.

The kinetic fractionation with evaporation coupled with nonfractionating loss of water by transpiration is important at the watershed scale for calculations of basin water balance. Such calculations have been made for some of the world's largest drainage basin to break out the transpiration component which is a measure of plant growth and primary productivity.

Example 5.10: Evaporation and Transpiration in Drainage Basin Water Balance

Two contrasting examples of evaporation and transpiration from regional watersheds are the Fly River Basin in tropical New Guinea and the South Saskatchewan in the northern Great Plains region of North America (Ferguson and Veizer 2007).

In the tropical Fly River basin, the amount of discharge is about 62% of rainfall, whereas for the South Saskatchewan it is only 14% (Figure 5.31). The difference between precipitation and discharge, assuming no change in storage (ΔS, groundwater, surface reservoirs) is considered to be evapotranspiration, ET.

$$P = R + ET + \Delta S$$

Transpiration, corrected for evaporative loss from soils and surface waters, is a measure of primary productivity. Evaporation can be resolved from ET with isotopes, which become enriched in basin discharge and fall on a region's characteristic evaporation slope on a plot of $\delta^{18}O$ and δD. Measurements of discharge from the two basins show that the drier South Saskatchewan watershed has considerable loss by evaporation while the Fly River of New Guinea experiences very little (Figure 5.32). This is quantified by stable isotopes according to the relationship for evaporation from a system with inflow and outflow at steady state:

$$E_v = P \times \frac{(\delta_P - \delta_D)(1 - h + \Delta\varepsilon)}{(\delta_D + 1)(\Delta\varepsilon + \varepsilon / \alpha) + h(\delta_v - \delta_D)}$$

where the δ-values are for $\delta^{18}O$ or δD of precipitation (δ_P), basin discharge (δ_D), and vapor (δ_v), h is fractional humidity, $\Delta\varepsilon$ is the kinetic enrichment factor as above, derived from Gonfiantini (1986), ε is the equilibrium water–vapor enrichment factor for the local temperature, and α is the water–vapor fractionation factor (Table 4.1; $\varepsilon = (\alpha - 1)1000$).

Figure 5.32 shows that the drainage from the South Saskatchewan watershed is very evaporated, falling on a line with slope 4.3, whereas for the Fly River watershed it is much closer to the local precipitation line. Figure 5.31 shows the relative contributions of evaporation and transpiration for these watersheds, resolved using the above formula and the isotope data in Figure 5.32. The results show that the much drier South Saskatchewan watershed in the Great Plains is a water-limited watershed, losing about 9% of precipitation to evaporation, but using over 50% of precipitation for primary productivity as transpiration. By contrast, the wet, tropical Fly River watershed loses only 5% to evaporation and less than 20% is used for plant growth. Here, primary productivity is limited by available sunlight due to cloudiness during the monsoon season (Ferguson and Veizer 2007).

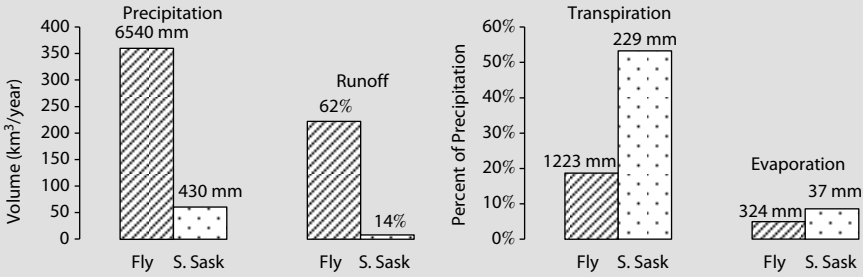

FIGURE 5.31 Basin normalized precipitation, discharge, transpiration and evaporation from a tropical watershed (Upper Fly River basin, New Guinea) and a temperate watershed (South Saskatchewan River Basin, Great Plains of North America). (Data from Ferguson and Veizer 2007.)

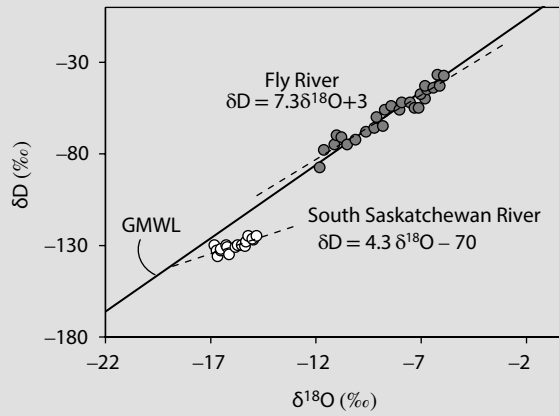

FIGURE 5.32 Stable isotopes of drainage from the South Saskatchewan River in the northern Great Plains of North America (50°N) and from the Fly River draining a tropical watershed in New Guinea (4°S), showing strong evaporation for the South Saskatchewan River, and only minor evaporative loss for the Fly River. (Data from Ferguson and Veizer 2007.)

MULTICOMPONENT GROUNDWATER MIXING

The geochemistry and isotopes of groundwater and surface water vary both spatially and over time due to mixing of waters of different origins and geochemical facies. Calculating mixing proportions provides an understanding of water origin and solute transport in natural and contaminated waters.

Mixing of water occurs at all stages of groundwater flow, from the attenuation of seasonal inputs in the recharge area, to the mixing of deep and shallow flow paths in the discharge area. Diffusion of isotopes and solutes through aquitards is a mixing process, and mixing also occurs in wells with screens or intakes that bridge two or more inflows of geochemically distinct groundwater.

Mixing is calculated from the concentrations of conservative species such as Cl^-, $\delta^{18}O$, and δD provided their concentrations are known for the different mixing end-members. Other tracers, such as Ca^{2+} and Na^+ or HCO_3^-, SO_4^{2-} and their isotopes are less reliable due to non-conservative exchange or redox reactions.

Two-Component Mixing

In aquifers and surface waters, mixing is spatially variable, with a range of tracer concentrations occurring in the zone of mixing. Resolving mixed waters into the proportions of composite end-members follows a simple mass balance equation, where the sum of the end-member contributions, expressed as fractions, f, is equal to 1.

$$\text{Two end-members: } f_A + f_B = 1 \quad \text{Three end-members: } f_A + f_B + f_C = 1$$

Solving these mass balance equations with two or three unknowns requires an additional equation or two, using either one or two conservative solutes or isotopes. Consider the case of water from a geothermal well in an area of hotsprings with springs of different temperatures and local cold groundwaters as shown in Figure 5.33. Mixing between cold shallow groundwaters and the rising geothermal fluid is evident based on the range in geochemistry and temperature. Figure 5.33

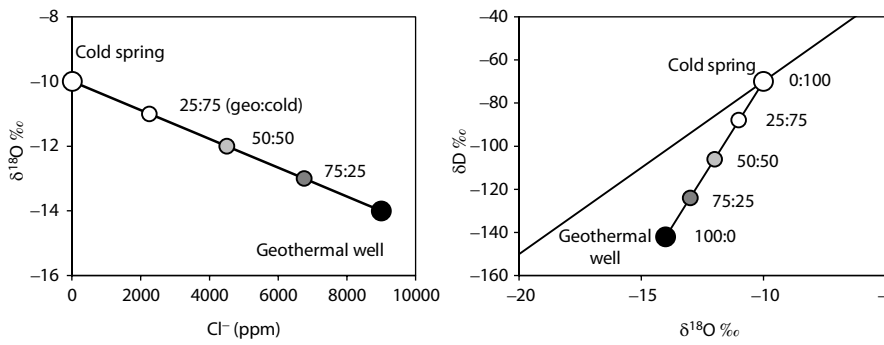

FIGURE 5.33 Two-component mixing trends for conservative species. Cl^-, $\delta^{18}O$ and δD are independent parameters and mixing follows a linear relationship. Mixing proportions can be determined directly from either axis.

shows graphically this mixing using either ^{18}O or Cl^- as a tracer. The relative fractions of these two end-members in each spring are calculated as:

$$f_{geo} + f_{cold} = 1 = \text{hotspring(hs)}$$
$$\delta^{18}O_{hs} = f_{geo}\,\delta^{18}O_{geo} + f_{cold}\,\delta^{18}O_{cold}$$

Substituting and rearranging

$$f_{geo} = 1 - f_{cold}$$
$$\delta^{18}O_{hs} = f_{geo}\,\delta^{18}O_{geo} + f_{cold}\,\delta^{18}O_{cold}$$
$$\delta^{18}O_{hs} = \left(1 - f_{cold}\right)\delta^{18}O_{geo} + f_{cold}\,\delta^{18}O_{cold}$$

and so

$$f_{cold} = \frac{\delta^{18}O_{hs} - \delta^{18}O_{geo}}{\delta^{18}O_{cold} - \delta^{18}O_{geo}}$$

For the hotspring with the greatest geothermal component in Figure 5.33, this gives:

$$f_{cold} = \frac{(-13) - (-14)}{(-10) - (14)} = 0.25$$

and

$$f_{geo} = 0.75$$

In this case, hotspring 1 has 25% cold groundwater and 75% geothermal water. The same calculations using Cl^- produce the same results. However, less conservative tracers such as HCO_3^- could produce different mixing fractions due to changes in their concentration by reaction. Nonconservative reaction is observed by a deviation from the mixing trend line.

Another practical example of groundwater mixing is that of surface water infiltration and mixing with groundwater. Well fields are often designed to intercept surface water infiltration to augment water supplies. The efficiency of the system can be monitored with stable isotopes providing the surface water source and the groundwater source have well-defined and distinctive isotope signatures. This is shown schematically in Figure 5.34, using the example of binary mixing in wells that induce infiltration from surface waters.

As above, the percent mixing in a given sample is based on the end-member isotope or geochemical tracer values weighted by their mixing fractions, *f*:

$$\delta_{spl} = \delta_a f_a + \delta_b\left(1 - f_a\right)$$

and

$$f_a = \frac{\delta_{spl} - \delta_b}{\delta_a - \delta_b}$$

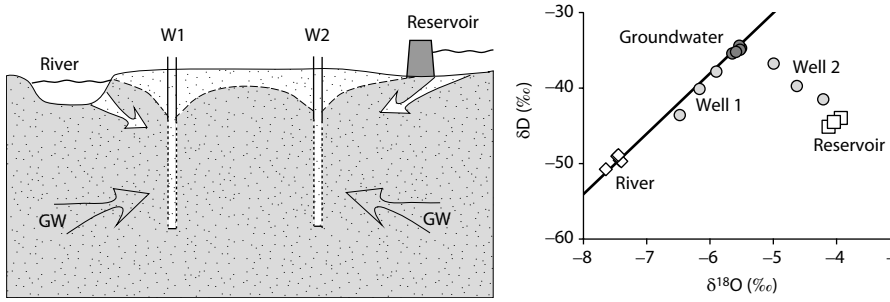

FIGURE 5.34 Infiltration of surface waters to an aquifer supplying groundwater to water supply wells. River waters typically are more depleted in ^{18}O and D than locally derived groundwater as they originate higher in the catchment (elevation effect) and further inland (continental effect). Surface water reservoirs, whether dam-impounded or natural lakes often have an enriched isotope signal due to evaporation. In this schematic example, the fraction of well water from infiltration of river water and from reservoir water pumped from wells 1 and 2 can be determined from their isotope values, each as a two component mixing problem.

In this case, the river and reservoir end-members have some variability. The uncertainty of mixing calculations is a function of the uncertainty in the value for the end-member components and the permil difference between the mixed water and a given end-member. It can be calculated from the isotope values for the end-members, a and b, and the mixed sample value, (δ_S, δ_a, and δ_b) and the standard deviation, σ, for each end-member value based on the number of replicates made (σ_a and σ_b). The uncertainty of the mixing fraction ($f_a \pm$ uncertainty) is calculated with the following equation:

$$f_a \pm \left[f_a \times \left(\left\{ \frac{1}{(\delta_a - \delta_b)^2} \right\}^2 \times \sigma_{spl}^2 + \left\{ \frac{(\delta_b - \delta_{spl})}{(\delta_a - \delta_b)^2} \right\}^2 \times \sigma_a^2 + \left\{ \frac{(\delta_{spl} - \delta_a)}{(\delta_a - \delta_b)^2} \right\}^2 \times \sigma_b^2 \right)^{\frac{1}{2}} \right]$$

Mixing with Solute Isotope and Concentration

The isotope of a solute, such as $\delta^{34}S_{SO_4^{2-}}$ or $\delta^{13}C_{DIC}$, can also be used to calculate mixing. However, the trend for mixing of two waters follows a curve due to the difference in the concentration of the solute in the two end-members (Figure 5.35). The following solute mass balance and isotope mass balance equations for a hotspring in Figure 5.33 is an example for this trend (where *m* is concentration, in this case for ppm SO_4^{2-} and δ the isotope of the solute, in this case is $\delta^{34}S_{SO_4^{2-}}$):

mixing fractions expressed as f_{geo}

$$1 = f_{geo} + f_{cold}$$
$$f_{geo} = 1 - f_{cold}$$

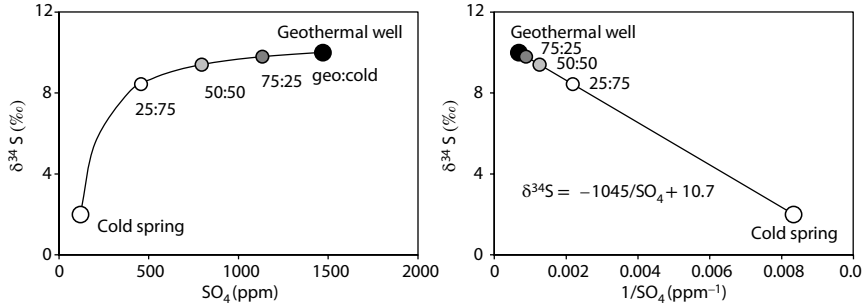

FIGURE 5.35 Two-component mixing trend for a solute and an isotope of the solute. In this case, the mix follows a hyperbolic curve. Plotted as the inverse of the solute concentration produces a straight-line relationship, which can be used as a test for binary mixing.

and isotope mass balance equation with substitution and expressing as f_{cold}

$$\delta_{\text{hs}}\, m_{\text{hs}} = f_{\text{geo}}\ \delta_{\text{geo}}\, m_{\text{geo}} + f_{\text{cold}}\, \delta_{\text{cold}}\, m_{\text{cold}}$$

$$\delta_{\text{hs}}\, m_{\text{hs}} = (1 - f_{\text{cold}})\, \delta_{\text{geo}}\, m_{\text{geo}} + f_{\text{cold}}\, \delta_{\text{cold}}\, m_{\text{cold}}$$

$$f_{\text{cold}} = \frac{\delta_{\text{hs}}\, m_{\text{hs}} - \delta_{\text{geo}}\, m_{\text{geo}}}{\delta_{\text{cold}}\, m_{\text{cold}} - \delta_{\text{geo}}\, m_{\text{geo}}}$$

This allows calculation of the end-member mixing components of a given sample, here for a hotspring in Figure 5.35.

Binary mixing of two waters can be readily identified by plotting two conservative tracers as in Figure 5.33, but is less obvious when plotting a solute concentration against its isotope, as in Figure 5.35, due to the hyperbolic trend. Plotting the isotope value against the inverse solute concentration ($1/SO_4$ in this example) resolves this, producing a straight line (Figure 5.35).

Three-Component Mixing

It is often the case that a third end-member contributes to mixing. Calculating the mixing fractions will require a second conservative parameter to solve the mixing equations. Near the hotsprings in the case above, three additional springs are found near tidewater. In these springs, a third mixing component is suspected—seawater. Plotting this new end-member and the new springs on a two-component graph shows that they fall within the mixing envelope defined by binary mixing between pairs of end-members (Figure 5.36). Samples that fall outside of this envelope indicate either nonconservative behavior (reaction) in the subsurface, or that the end-member compositions are not correctly defined.

The mixing fractions shown visually in Figure 5.36 can be calculated from solute and isotope mass balance equations. The mixing envelope produced using $\delta^{18}O$–Cl^- provides a better distribution of mixing end-members than for $\delta^{18}O$–δD, and is a better choice for these calculations. For three-component mixing, three mass balance equations are needed. The first is a simple mass balance of the fractions of

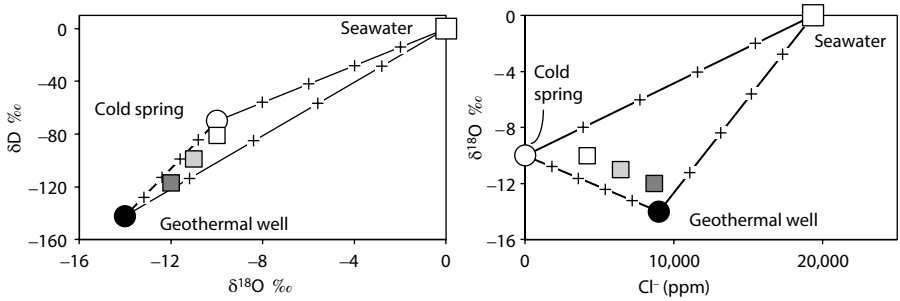

FIGURE 5.36 Three end-member mixing diagrams showing the mixing envelope within which conservatively mixed samples will plot. Note that the use of $\delta^{18}O$–Cl^- produces a better (broader) mixing envelop than the $\delta^{18}O$–δD due to better separation of the end-member values. The boundary lines are binary mixing lines between two end-members, with crosses plotted at 20% mixing increments. The shaded squares are the hot springs with 25%, 50%, and 75% geothermal water, 15%, 40%, and 65% cold groundwater and each with 10% seawater.

end-member waters (geo, cold, and sea) in the sample. The second and third are mass balance equations for $\delta^{18}O$ and for Cl^- concentration.

$$f_{hs} = 1 = f_{geo} + f_{cold} + f_{sea}$$
$$Cl_{hs} = f_{geo}Cl_{geo} + f_{cold}Cl_{cold} + f_{sea}Cl_{sea}$$
$$\delta^{18}O_{hs} = f_{geo}\delta^{18}O_{geo} + f_{cold}\delta^{18}O_{cold} + f_{sea}\delta^{18}O_{sea}$$

Through rearrangement of the first equation to express it in terms of f_{geo} and then f_{cold}, followed by substitution into the second and third equations, we can determine the fraction contributions of f_{geo} and f_{cold} from the known values for the two parameters (Cl and $\delta^{18}O$) in the three end-members and in the hotspring.

$$f_{geo} = \frac{Cl_{hs} - Cl_{cold} - f_{sea}(Cl_{sea} - Cl_{cold})}{Cl_{geo} - Cl_{cold}}$$
$$f_{cold} = \frac{\delta^{18}O_{hs} - \delta^{18}O_{geo} - f_{sea}(\delta^{18}O_{sea} - \delta^{18}O_{geo})}{\delta^{18}O_{cold} - \delta^{18}O_{geo}}$$
$$f_{sea} = 1 - f_{geo} - f_{cold}$$

Using two parameters where one is a dependent parameter, such as SO_4^{2-} and $\delta^{34}S_{SO_4}$ again requires an isotope mass balance equation that gives hyperbolic mixing lines (again using *m* for solute concentration and δ for the isotope of the solute for end-members "geo, cold and sea") the mixing components of the sample hotspring are determined as:

Establishing the fraction, solute and isotope mass balance equations:

$$1 = f_{geo} + f_{cold} + f_{sea}$$
$$m_{hs} = f_{geo}\,m_{geo} + f_{cold}\,m_{cold} + f_{sea}\,m_{sea}$$
$$\delta_{hs}\,m_{hs} = f_{sea}\,\delta_{sea}\,m_{sea} + f_{geo}\,\delta_{geo}\,m_{geo} + f_{cold}\,\delta_{cold}\,m_{cold}$$

then substituting $f_{cold} = 1 - f_{geo} - f_{sea}$ and $f_{geo} = 1 - f_{cold} - f_{sea}$ in the solute and isotope mass balance equations and rearranging to give three equations to solve for the mixing end-members:

$$f_{geo} = \frac{m_{hs} - m_{cold} - f_{sea}(m_{sea} - m_{cold})}{m_{geo} - m_{cold}}$$

$$f_{cold} = \frac{\delta_{hs} m_{hs} - \delta_{geo} m_{geo} - f_{sea}(\delta_{sea} m_{sea} - \delta_{geo} m_{geo})}{\delta_{cold} m_{cold} - \delta_{geo} m_{geo}}$$

$$f_{sea} = 1 - f_{geo} - f_{cold}$$

The mixing envelope using these tracers for the hotsprings above is shown in Figure 5.37. Providing all parameters are conservative in the subsurface, they will provide the same values for the f_{geo} and f_{cold} mixing fractions. The seawater end-member, f_{sea}, is calculated by iteratively solving the three equations. On a spreadsheet program, a goal-seek function is useful for this exercise.

Isotopes are commonly used in mass balance equations as they can be measured with high precision. Using $\delta^{18}O_{H_2O}$ or δD_{H_2O} provides a parameter that, unlike a solute, truly tracks the water. Using a dependent parameter such as $\delta^{34}S_{SO_4}$, $\delta^{13}C_{DIC}$, or even $\delta^{15}N_{NH_3}$, for example, allows calculations using one species only. This helps identify nonconservative behavior, as both parameters will change with reaction, and move samples outside the mixing envelope.

These mixing calculations are the basis of hydrograph separation (Figure 5.38), where contributions to basin discharge can be resolved as a two- or three-component mixing problem. Hydrograph separations can be done by solving these mixing equations using the measured parameters in stream discharge at discrete times. In most cases this can be done with some confidence, given that groundwater baseflow is generally geochemically and isotopically distinct from the storm or snowmelt events that contribute to surface flow. Greater uncertainty arises when there is seasonal or spatial variability in the mixing end-members.

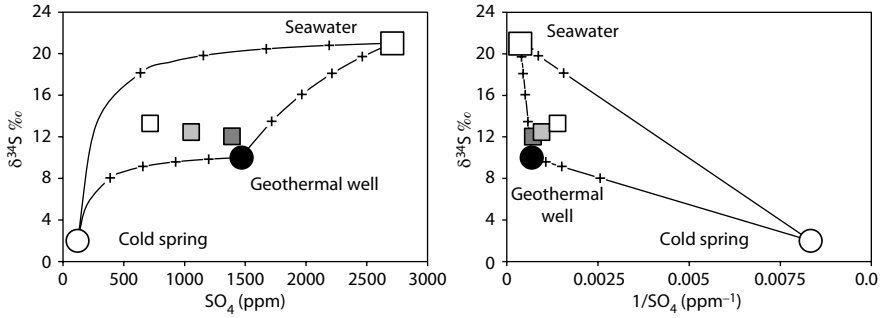

FIGURE 5.37 Mixing envelope for the hot spring data using a dependent parameter, $\delta^{34}S$ with SO_4^{2-} concentration. Expressing SO_4^{2-} as inverse concentration produces straight mixing lines, which are diagnostic for conservative mixing.

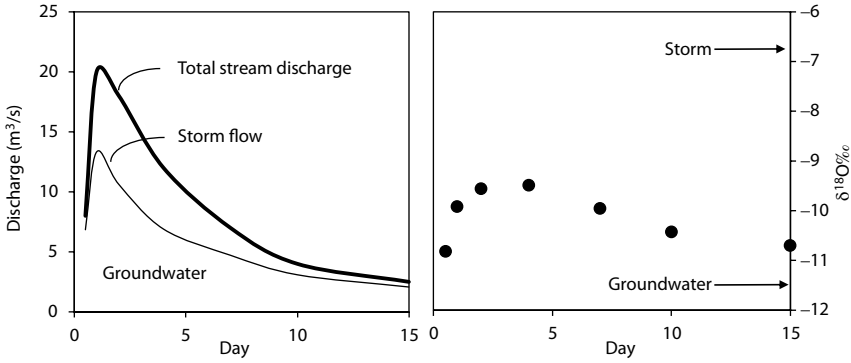

FIGURE 5.38 Storm hydrograph separation resolved as a two-component mixing system using $\delta^{18}O$.

Diffusive Mixing in Aquitards

Understanding the movement of groundwater through aquitards is critical where such units are used as barriers to contaminant migration and the protection of water resources from waste storage and subsurface disposal. This is the case for surface waste management facilities such as sanitary landfills, for fracking activities and for the siting of geological repositories for nuclear waste. Isotopes are important to identify aquitards where diffusive transport dominates over advective transport.

Diffusive transport is represented by Fick's Law, which characterizes the diffusive flux of a solute through a low permeability material:

$$J = -D_e \frac{\partial C}{\partial x}$$

In the case of isotope diffusion, J is the flux of the isotope (i.e., mol/m^2), C is the isotope concentration (mol/m^3), x is the diffusion distance (m) and D_e is the effective diffusion coefficient for the isotopic species in that medium (m^2/s). For diffusion in aquitards, D_e is equal to the free-water diffusion coefficient, D, for the species, multiplied by dimensionless parameters that characterize the porosity and tortuosity of the porous medium. Although D is known for a wide range of solutes and isotopes in water, D_e must be determined for the particular aquitard materials under investigation.

Hendry and Wassenaar (1999) present a 180 m isotope profile for porewaters in clay-rich sediments in southern Saskatchewan. The aquitard comprises 80 m of clay till deposited by the Pleistocene Laurentide Ice Sheet overlying 76 m of Cretaceous marine clay. Looking here at the upper 50 m of their profile, δD in porewaters extracted from the clay till shows a smooth profile from modern values of –130‰ (136 ppm in H_2O) at surface to a glacial meltwater value of –180‰ (127 ppm) at 40 m depth in the till (Figure 5.39).

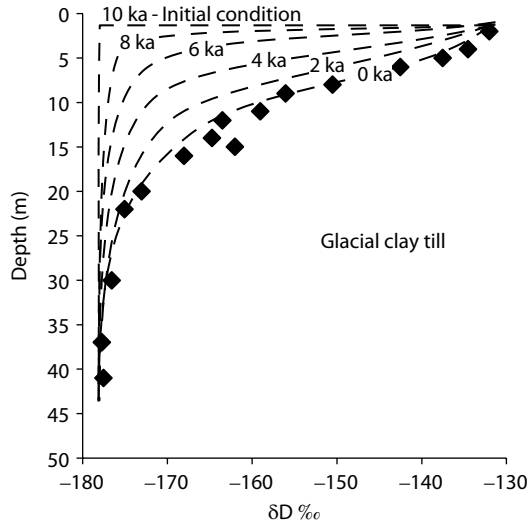

FIGURE 5.39 Diffusion profile for deuterium in porewaters from clay till in southern Saskatchewan. (Data from Hendry and Wassenaar 1999.)

The use of a one-dimensional advective-diffusion model shows that the upper profile (0–40 m) developed since the glacier retreated 10,000 years ago when modern HDO began diffusing downward into the D-depleted glacial meltwaters in the till (Hendry and Wassenaar 1999). Shown in Figure 5.39 are the stages for the porewater isotope profile as it evolved by diffusion from an initial condition with glacial meltwater in the till to the profile observed today. A minor advective flux is apparent from the downward flexure in the measured profile near the surface.

ROCK–WATER–GAS INTERACTION

The use of stable isotopes to trace groundwaters from their recharge origin as precipitation is based on a preservation of the meteoric signal during its subsurface flow. In this way, recharge at different elevations, different seasons, or different climates can be recognized. However, under certain circumstances, the isotope composition of groundwater can be modified by exchange reactions in the subsurface (Figure 5.40). Such exchange can only take place through a geochemical reaction, such as mineral alteration reactions or gas production reactions. Such reactions, as seen in Chapters 2 and 3, typically involve solute concentrations at the parts per million level (millimolar), whereas the "concentration" of water is 55.6 mol/kg. Therefore, the impact of an isotope exchange reaction taking place at the millimolar scale on the isotope composition of the water itself will be negligible unless the reaction proceeds between a small volume of water and a large volume of rock or gas. This is the case for groundwaters in settings with very low water to rock ratios such as deep crystalline rocks and geothermal settings, or in settings with very high gas production.

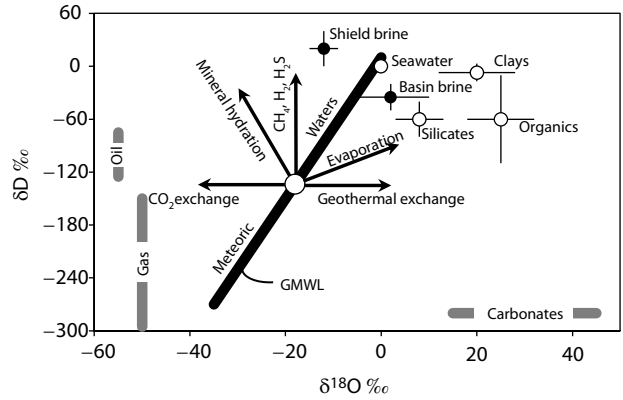

FIGURE 5.40 $\delta^{18}O$ and δD ranges for major crustal reservoirs and principal subsurface exchange mechanisms for the modification of the isotopic composition of meiteoric waters. (Sources of data: Savin and Epstein 1970; Craig 1963; Clayton et al. 1966; Feurdean et al. 1997; Clark and Fritz 1997; Pearson 1987; Edwards et al. 1985; Gori et al. 2013.)

Mineral Hydration and Shield Brines

Hypersaline Ca–Na–Cl brines, with salinities often exceeding 200 g Cl^-, have been observed at depths greater than about 500 m in most shield environments. Interest in these deep crustal settings for siting deep geological repositories generated considerable research on the origin and age of these fluids. The salinity was attributed to various possible sources from leaching of fluid inclusions to concentration through radiolysis of water. Geochemical and isotopic evidence now supports an origin through infiltration of dense, evaporatively enriched Paleozoic seawater (Bottomley et al. 1994; Greene et al. 2008). However, their unusual deuterium enrichment is such that they all plot above the MWL. The example of the brines from 1600-m depth in the Con Mine, Yellowknife, shows the strong enrichment together with the mixing line with the shallowly circulating meteoric waters (Figure 5.41). Considerable debate has ensued over the origin and age of these groundwaters, and how they have gained their salinity. Reardon and Fritz (1979) attributed the unusual isotopic composition of shield brines to evolution during hydration of primary silicates under closed system conditions.

Partitioning of ^{18}O differs from D during hydration reactions. The enrichment factors in Table 4.2 for kaolinite, for example, shows an enrichment in the $\delta^{18}O$ of the clay relative to the water ($\varepsilon^{18}O_{\text{kaolinite–water}} = 34‰$) at 25°C. By contrast, it is depleted in deuterium over water ($\varepsilon D_{\text{kaolinite–water}} = -32‰$). This reversal in fractionation is similarly observed for gypsum (Table 4.2) and occurs during reactions such as alteration of albite or hydration of anhydrite:

$$CaAl_2Si_2O_{8\ \text{anorthite}} + 3H_2O \rightarrow Ca^{2+} + Al_2Si_2O_5(OH)_{4\ \text{kaolinite}} + 2OH^-$$
$$CaSO_{4\ \text{anhydrite}} + 2H_2O \rightarrow CaSO_4 \cdot 2H_2O_{\text{gypsum}}$$

Under conditions of low water to rock ratios, the residual water hosting such reactions becomes measurably depleted in ^{18}O but enriched in D, such that these waters

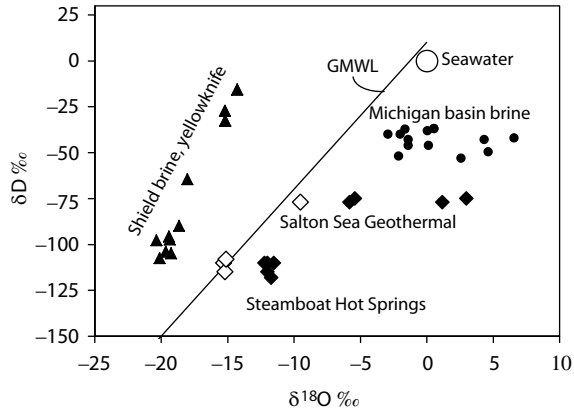

FIGURE 5.41 Isotope exchange at low water–rock ratios: shield brine exchange with crystalline rock (Con Mine, Yellowknife; Douglas et al. 2000; filled triangles), basin brine in shale and carbonate rock (Michigan Basin, filled circles; Clayton et al. 1966) and geothermal exchange for geothermal waters in silicate (Steamboat) and carbonate (Salton Sea) reservoir rocks. (Craig 1963; local cold waters—open diamonds, geothermal waters—filled diamonds.)

plot above the MWL with a strong deuterium excess (Figure 5.40, and for the shield brines in Figure 5.41).

Isotope exchange with minerals

The strong ^{18}O enrichment by Craig (1963) for geothermal waters (Figure 5.41) is a good example of isotope exchange between water and minerals. As noted above, key to a measurable shift in the isotope value of meteoric waters is a net mass exchange on the same scale as the mass of water; that is some tens of moles of reaction per kilogram of water. This can occur where a limited mass of water is in contact with a large volume of rock, generally achieved through fracture flow. However, reaction at elevated temperature is critical, as this lowers the degree of isotope fractionation between the water and mineral. Two important exchange reactions in geothermal systems would be with calcite and with silica. The enrichment factor (Table 4.2) for ^{18}O between water and calcite decreases from $e^{18}O = 28‰$ at 25°C to 19‰ at 150°C and for silica from 35‰ at 25°C to 23‰ at 150°C. With a small water reservoir reacting with a large mineral reservoir, the isotope value of the water will shift towards that of the mineral, rather than the reverse case for systems with high water to rock ratios.

The net result is enrichment of ^{18}O for local meteoric waters circulating through geothermal reservoirs. The two examples in Figure 5.41 show moderate enrichment for the Steamboat Hot Springs hosted by granodiorite rock and considerably more enrichment for the Salton Sea geothermal waters which circulate through carbonate rocks.

The $\delta^{18}O$ enrichment in basin brines has a more complicated history, as they begin as evaporated seawaters that infiltrate the sedimentary basin strata (Clayton et al. 1966). They begin with an ^{18}O-enriched evaporation signature which can then be further modified by mineral exchange and alteration reactions at elevated

temperatures (Harper 1995). At low water to rock ratios this results in positive isotope excursions. Such brines are considered to have residence times on the order of hundreds of millions of years (Clark et al. 2013).

Gas Exchange Reactions

Under circumstances where substantial production of gas takes place in the subsurface, isotope partitioning with the gas can impart a measureable enrichment or depletion on the residual water phase. This could potentially occur for ^{18}O during the migration of CO_2 from deep injection wells for carbon storage and sequestration, or for D with high production of methane in landfills (see Chapter 9). As for rock–water interaction, the water to gas ratio must be low and so implies a free-gas phase migrating through. The following example illustrates the process and the molar volumes required for a measurable shift.

Example 5.11: Shift in $\delta^{18}O$ by Exchange With CO_2

Injection of supercritical CO_2 into deep aquifers is proposed for sequestration of CO_2 from power plants. In addition to the challenges of separating the CO_2 from the N_2 air stream and transporting to a suitable injection site, monitoring is required to see that there are no losses to shallow groundwaters. This example shows the amount of CO_2 that is required to exchange with (migrate through) a given groundwater to impart a measurable shift on the water. The problem is simplified as a mass balance; weighting the moles of reacting H_2O and CO_2 with their initial values ($\delta^{18}O_{in}$). For H_2O this is $\delta^{18}O$ in the groundwater, say –10‰ and for the CO_2 which is produced by combustion with air this is 23‰. The mass balance is then reformulated such that isotope equilibrium ($\varepsilon^{18}O_{CO_2-H_2O}$) is maintained between the CO_2 and H_2O to yield final values ($\delta^{18}O_{fin}$):

$$m_{H_2O}\delta^{18}O_{H_2O_{in}} + 2m_{CO_2}\delta^{18}O_{CO_{2in}} = m_{H_2O}\delta^{18}O_{H_2O_{fin}} + 2m_{CO_2}\delta^{18}O_{CO_{2fin}}$$

$$\delta^{18}O_{CO_{2fin}} = \delta^{18}O_{H_2O_{fin}} + \varepsilon^{18}O_{CO_2-H_2O}$$

$$m_{H_2O}\delta^{18}O_{H_2O_{in}} + 2m_{CO_2}\delta^{18}O_{CO_{2in}} = m_{H_2O}\delta^{18}O_{H_2O_{fin}} + 2m_{CO_2}\left(\delta^{18}O_{H_2O_{final}} + \varepsilon^{18}O_{CO_2-H_2O}\right)$$

$$\delta^{18}O_{H_2O_{final}} = \frac{m_{H_2O}\delta^{18}O_{H_2O_{in}}\, 2m_{CO_2}\delta^{18}O_{CO_{2in}} - 2m_{CO_2}(\delta^{18}O_{H_2O_{fin}} + \varepsilon^{18}O_{CO_2-H_2O})}{(m_{H_2O} + 2m_{CO_2})}$$

Using: $m_{H_2O} = 55.6$ mol/kgw

$$\delta^{18}O_{H_2O_{in}} = -10‰$$

$$\delta^{18}O_{CO_{2in}} = 23‰$$

$$\varepsilon^{18}O_{CO_2-H_2O} = 41‰ \text{ (Table 4.2)}$$

This allows solving this mass balance equation for any selected value for m_{CO_2} (note that $2m_{CO_2}$ is used as it has two oxygen atoms to contribute to the exchange

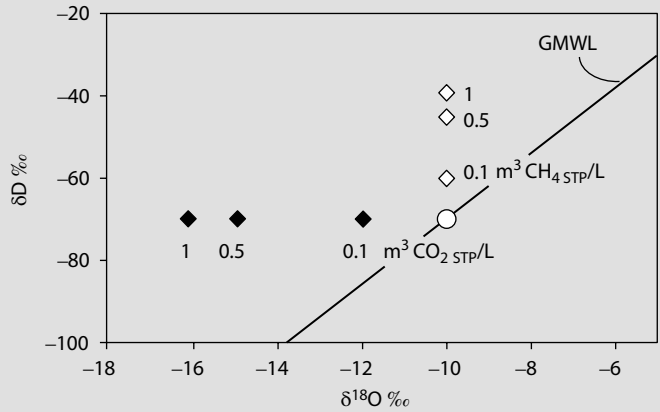

FIGURE 5.42 The shift in $\delta^{18}O$ of groundwater due to exchange with CO_2 and for δD from methanogenesis. Volumes of CO_2 and CH_4 are calculated for STP. At depth, hydrostatic pressure would reduce the volume of gas as a separate phase, and increase its solubility.

reaction). Recall that at standard temperature and pressure (STP), one mole of a gas is equivalent to 22.4 L. Solving this equation for a range of values for m_{CO_2} produces the shifts in $\delta^{18}O_{H_2O}$ observed in Figure 5.42. In this figure, the amounts of CO_2 equilibrating with the groundwater are converted from moles to m^3 using the gas law (1 mole = 22.4 L at STP).

As seen in this example, a considerable amount of CO_2 gas is required to produce a measurable shift in $\delta^{18}O_{H_2O}$. For this reason, such modifications of the isotope content of groundwater are seldom observed. Similarly, during methanogenesis there is a significant fractionation between the methane and water. However, to impart a measurable positive shift on the water, similar volumes of CH_4 would be required. This is observed in landfill leachates, which infiltrate the waste pile under unsaturated conditions, allowing high reaction rates in low volumes of water. However, examples of such shifts due to gas production in natural groundwaters are rare.

PROBLEMS

1. Plot the enrichment factors for ^{18}O and D for the temperature range of 0°C–50°C and note that fractionation is enhanced at lower temperature. Which isotope is most strongly fractionated and why? If fractionation is enhanced at lower temperature, why is precipitation in cold regions depleted in ^{18}O and D?
2. From the GNIP site, download the monthly stable isotope data from 1995 to 2000 for (1) a low latitude site and (2) a high latitude site. Plot them on a $\delta^{18}O$ versus δD diagram and produce an LMWL for each site. Compare their range, slope, and deuterium-intercept. Average the $\delta^{18}O$ data for each

month and plot for each month of the year. Compare the seasonal effect for these two sites.

3. Using the equilibrium fractionation equations in Chapter 4 and the moisture content of water-saturated air for different temperatures given here, calculate the step-wise evolution of $\delta^{18}O$ and δD in rain from a continually cooling vapor mass with $\delta^{18}O = -11‰$ and $\delta D = -73‰$

T (°C)	Water Content (g/m³)
25	24.5
20	17.3
15	12.2
10	8.6
5	6.1
0	4.3

4. The following data were acquired from a precipitation station and groundwaters in a semiarid region where an aeolian sand aquifer overlies fissured limestone bedrock that outcrops in local karst landscape. Plot these data and discuss what these measurements record about recharge mechanisms for these two groundwaters.

$\delta^{18}O_{rain}$	δD_{rain}	$\delta^{18}O_{sand\ gw}$	$\delta D_{sand\ gw}$	$\delta^{18}O_{karst\ gw}$	$\delta D_{karst\ gw}$
−9.3	−58	−5.1	−34	−7.3	−44
−8.8	−55	−4.6	−32	−7.2	−43
−8.8	−55	−2.9	−25	−7.5	−42
−7.2	−42	−4.2	−30	−7.3	−43
−5.9	−31	−4.0	−30	−7.5	−46
−5.5	−32	−3.8	−26	−7.4	−45
−5.9	−34	−5.9	−40		
−6.2	−36	−5.2	−35		
−7.5	−44	−4.0	−30		
−7.7	−48				
−8.6	−54				
−6.7	−37				
−6.7	−40				

5. The Fraser River Delta has extensive alluvial sediments forming a thick phreatic aquifer with semiconfined zones at depth. The following data were measured in a piezometer nest situated in a residential area in Maple Ridge (49°14′N; 122°33.7′W) that relies on groundwater wells for domestic water. The mean annual $\delta^{18}O$ for local precipitation is –10‰. Nearby Fraser River water is –17‰. Considering the Fraser to be a source of $\delta^{18}O$-depleted groundwater in this aquifer, what is the mixing ratio of river infiltration to rain infiltration?

Depth(m)	$\delta^{18}O$
5	−10
30	−10.5
100	−12.5

6. The following data were measured for groundwater in a sand aquifer beneath an agricultural field in a region that receives 460 mm of precipitation annually. Precipitation has an average of 8 mg/L Cl^-. The enrichment of Cl^- in the groundwaters indicates some loss of recharge water during infiltration. Is this due to evaporation from the soil or transpiration by crops? Calculate the fraction of water lost, and the annual recharge rate (mm/y). Comment on the seasonality of any water loss.

$\delta^{18}O$	δ^2H	Cl^-	$\delta^{18}O$	δ^2H	Cl^-
Rainwater			**Groundwater**		
−11.9	−76	11	−8.7	−55	38
−6.6	−40	6	−9.4	−60	42
−12.3	−80	10	−8.8	−57	39
−9.5	−61	9	−9.1	−57	27
−7.1	−48	6	−9.1	−58	53
−7.4	−46	5	−9.8	−63	52
−8.1	−52	8	−9.7	−61	41
−8.4	−58	9	−8.7	−55	22
−8.4	−53	5	−8.6	−54	24
−8.9	−52	4	−9.1	−57	26
−11.5	−75	12	−9.2	−58	22
−10.5	−70	11	−8.9	−57	30

7. Groundwater is being pumped from a fully screened well that includes an upper unconfined sand and a fractured bedrock zone overlain by clay till. Seasonal monitoring of $\delta^{18}O$ for the well water and for two piezometers completed in the sand and the bedrock are given here. Calculate the percent mixing of the two sources of groundwater in the well for each month of monitoring.

	Jan	April	Jul	Oct
Shallow sand	−12	−10	−8	−10
Deep bedrock	−13	−13	−13	−13
Well	−12.9	−11.8	−12	−12.1

8. A munitions factory has been discharging nitrate to a shallow aquifer adjacent to an organic agricultural field that uses only manure as fertilizer. Regional nitrate contributions from natural sources also exist. The deep aquifer has nitrate concentrations that exceed the 10 mg-N/L drinking water standard. Who is contributing nitrate to the deep aquifer nitrate problem and what are their fractional contributions of water and of nitrate?

	NO_3^-	$\delta^{15}N$
Munitions	39	2
Agriculture	12	8
Regional	1	9
Aquifer	11	4

9. Groundwater at an ambient temperature of 25°C with initial values of $\delta^{18}O = -10‰$ and $\delta D = -70‰$ penetrates an aquitard rich in anhydrite.

$$2H_2O + CaSO_4 \rightarrow CaSO_4 \cdot 2H_2O$$

Using a Rayleigh distillation, plot the trend in $\delta^{18}O$ and δD as the water reacts to form gypsum, losing up to 50% of its mass to form the hydration waters.

This page intentionally left blank

6 CO_2 and Weathering

INTRODUCTION

Carbon is the fourth most abundant element in the universe, although in the crust of the earth it drops to 17th place, with an abundance of only 200 ppm. Nonetheless, biological cycling of carbon through cell building and energy transformations leaves its geochemical imprint throughout the hydrosphere. Its range of redox states gives it remarkable versatility to build organic compounds and to store energy. From a geochemical perspective, both inorganic and organic carbon are important. Inorganic or mineralized carbon includes CO_2 and its hydrated forms (H_2CO_3, HCO_3^-, and CO_3^{2-}). Organic carbon includes primary forms, such as carbohydrate (CH_2O), the main building block of terrestrial and marine biomass, and more evolved complexes, such as humic substances and hydrocarbons. In groundwaters, both dissolved organic carbon (DOC) and CO_2 as dissolved inorganic carbon (DIC) play fundamental roles in weathering reactions and the geochemical evolution of groundwater.

CO_2 AND THE CARBON CYCLE

While most carbon on the earth resides as inorganic C in carbonates and graphite in the crust (Figure 6.1), the active cycling of carbon takes place in the atmosphere and hydrosphere. The atmosphere now holds approximately 800 gigatons (Gt) of carbon (800 billion metric tons) as CO_2, with a much smaller 4 GtC present as methane and other carbon gases. The CO_2 partial pressure in 2014, $P_{CO_2(atm)}$, is 0.0004 atm ($10^{-3.40}$ atm) or about 400 ppmv. This has been increasing by about 2 ppm/year over the past decade.

Carbon Reservoirs and Fluxes

Terrestrial forests and grasslands annually sequester 122 GtC or 17% of atmospheric CO_2 through gross primary production (GPP). Living terrestrial biomass amounts to over 650 GtC. Another 1500 GtC exists as labile organic carbon in soils (SOC), which is available for bacterial respiration in soils, which returns most of this CO_2 back to the atmosphere. Both GPP and terrestrial biomass are increasing in a response to increased CO_2 fertilization, particularly in the boreal forests (Hyvönen et al. 2007) and agricultural areas (Erda et al. 2005). The net flux between CO_2 uptake by GPP and return to the atmosphere by respiration is therefore an important control of atmospheric CO_2 concentrations. Changes in soil temperature and humidity are responsible for much of the year-to-year variability in atmospheric CO_2 (Sarmiento and Gruber 2002; Jones et al. 2003). Humlum et al. (2013) show this net flux to

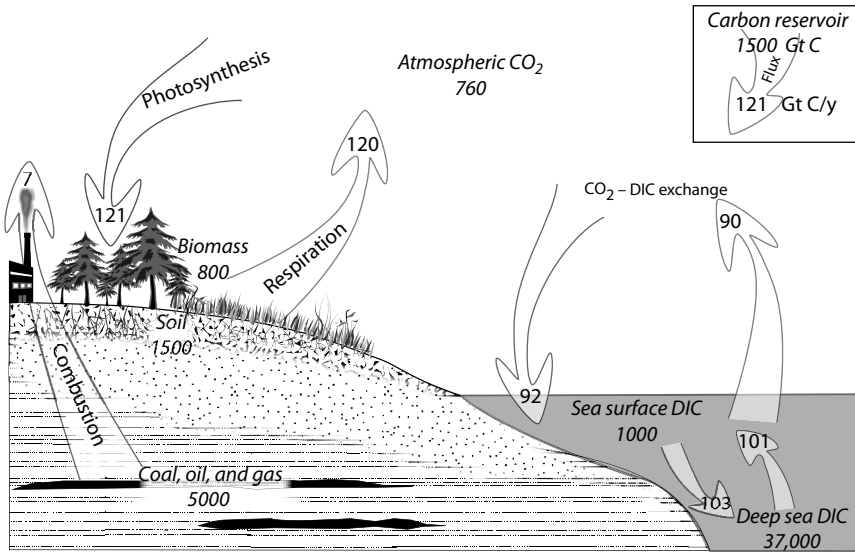

FIGURE 6.1 The carbon cycle with major carbon reservoirs and fluxes of carbon. Values in GtC (gigatons or billion tons carbon) for reservoirs and GtC/y for fluxes. (Sources of data: U.S. Department of Energy; IPCC, 2007.)

be correlated with temperature with a slight lag, suggesting that temperature may be responsible for some of the twentieth-century rise in atmospheric CO_2. This is certainly known to be the case on a seasonal basis, as the seasonal variations in photosynthesis and respiration affect the monthly concentrations of atmospheric CO_2, giving life to the idea of Gaia—the breathing Earth (Figure 6.2).

Marine ecosystems also represent a significant reservoir of carbon. Sea surface waters have approximately 28 ppm of DIC present mostly as HCO_3^-. From Henry's constant for CO_2 ($K_{CO_2} = 0.0339$ at 25°C), marine waters are near equilibrium with atmospheric P_{CO_2}. The shallow oceans hold 900–1000 GtC, mostly as DIC with about 3 GtC as algae and DOC. Exchange of CO_2 with the atmosphere amounts to approximately 90 GtC annually or about 10% of the shallow ocean reservoir. The deep ocean holds about 38,000 Gt of carbon that exchanges only slowly with the shallow ocean carbon pool, on centennial time scales.

Geological controls on carbon cycling include terrestrial volcanic degasing about 0.2 GtC of mantle CO_2 to the atmosphere each year. A similar amount is removed by continental weathering and drains through aquifers to the oceans as DIC. Although minor with respect to biological cycling of carbon, this flux is important from the perspective of groundwater geochemistry.

Considering both the terrestrial and the marine fluxes of CO_2, over one quarter of the atmospheric CO_2 (about 210 GtC) is exchanged annually, giving CO_2 a residence time of only a few years in the atmosphere. To this combined flux, the combustion of fossil fuels and production of cement add about 6 GtC per year or 3%. The short residence time for atmospheric CO_2 means that this anthropogenic contribution is

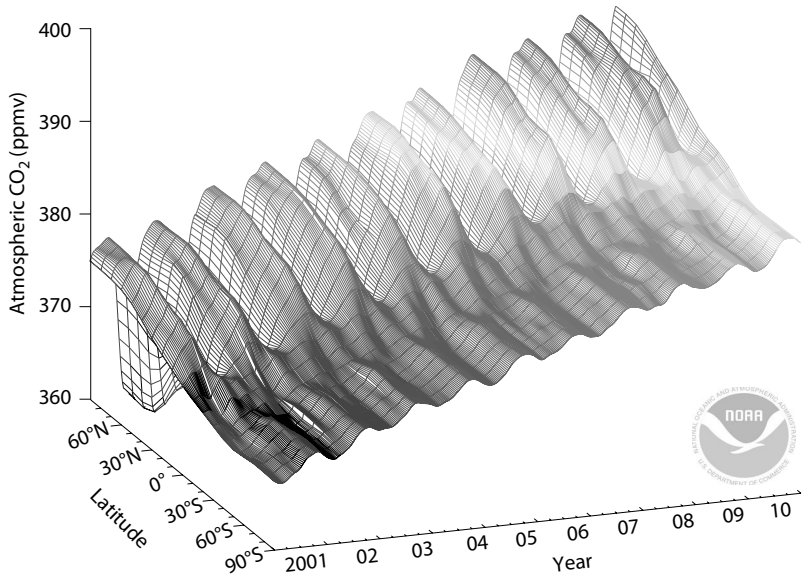

FIGURE 6.2 Spatial and temporal variations in atmospheric CO_2 concentrations due to annual variations in photosynthesis and respiration. The strong latitudinal effect reflects the greater participation of the northern boreal forests and disproportionate continental land mass in the northern hemisphere. The overall increase reflects contributions from fossil fuels, land use change, and respiration. (From NOAA 2014.)

mixing with the combined reservoirs of atmospheric, soil, and shallow marine carbon, approximately 4100 GtC or about 0.1% annually. For this reason, the annual increase in atmospheric CO_2 of about 1.7 ppmv or 0.4% is less than the 0.8% increase calculated from simple mixing of 6 GtC with the 800 Gt atmospheric CO_2.

$\delta^{13}C$ and ^{14}C in the Carbon Cycle

Tracing the carbon cycle globally and in groundwaters is greatly aided by the use of carbon isotopes, including stable ^{13}C and radiocarbon, ^{14}C. Fractionation of ^{13}C during organic and inorganic transformations partitions this isotope among various carbon reservoirs (Table 6.1). These isotopes then become important tracers of carbon reactions and fluxes between reservoirs, and for past reconstructions of reservoir sizes. The range for $\delta^{13}C$ in the major carbon reservoirs is shown in Figure 6.3.

Ice cores and early atmospheric monitoring shows that $\delta^{13}C_{CO_2\text{-atm}}$ was close to about –6.4‰ VPDB during preindustrial times. Atmospheric CO_2 today has a $\delta^{13}C$ value of about –8.3‰ and is gradually decreasing, mainly due to inputs of ^{13}C-depleted CO_2 from fossil fuel combustion and by enhanced soil respiration.

Photosynthesis is a highly fractionating process that discriminates against ^{13}C during transformation of CO_2 to carbohydrate, CH_2O. Most plants follow Calvin or C_3 photosynthetic pathway, which involves an inefficient step of CO_2 respiration

TABLE 6.1
Crustal Reservoirs of Carbon, in Gigatons (10^9 Metric Tons) and Their Average $\delta^{13}C$ and ^{14}C Composition

Reservoir	Form	Mass (GtC)	$\delta^{13}C$ (‰)	^{14}C (pMC)
Atmosphere	CO_2	800	–8	104
Atmosphere	CH4	4	–47	122
Living biomass	CH_2O	800	–27	100
Soil biomass	CH_2O	1500	–27	95
Shallow marine	DIC	918	0	110
Shallow marine	DOC	3	–30	110
Deep marine	DIC	38,000	0	75
Carbonate rocks	$Ca(Mg)CO_3$	100,000,000	0	0
Coal	C	910	–27	0
Oil and bitumen	C_6H_{6x}	2,600	–33	0
Gas (recoverable)	CH_4	230	–45	0
Gas hydrates	$CH_4 \cdot 6H_2O$	500–2,500	–45	0

Note: ^{14}C activities greater than 100 pMC represent residual ^{14}C produced by atmospheric tests of thermonuclear weapons.

Source: Data sources include U.S. Department of Energy; IPCC 2007.

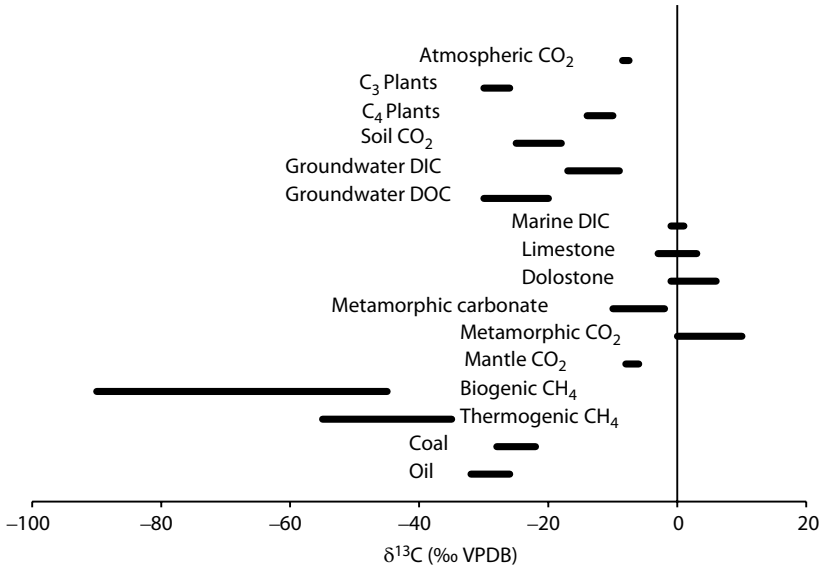

FIGURE 6.3 Ranges of $\delta^{13}C$ for major terrestrial reservoirs of organic and inorganic carbon. The VPDB standard for ^{13}C is a synthesized calcite powder prepared by the International Atomic Energy Agency in Vienna, and closely represents the original PDB standard from a fossil belemnite from the Pee Dee Formation in South Carolina.

from the plant. As a result, the $\delta^{13}C$ of C_3 plants is much lower than that of atmospheric CO_2, with a fractionation of close to 20‰ ($\varepsilon^{13}C_{CH_2O\text{-}CO_2} \approx -20‰$). The C_3 pathway is used by almost 95% of plants, including most terrestrial trees and shrubs as well as marine plants and algae. Carbon fixed by terrestrial C_3 plants has $\delta^{13}C$ values of about –27‰ (O'Leary 1988).

In response to declining atmospheric CO_2 concentrations during the past 15 million years, a more efficient photosynthetic pathway evolved. Hatch-Slack or C_4 photosynthetic cycle accelerates the fixation of CO_2 by reducing respiration, resulting in lower fractionation ($\varepsilon^{13}C_{CH_2O\text{-}CO_2} \approx -6‰$) and $\delta^{13}C$ values between about –10‰ and –14‰. C_4 plants include various tropical grasses. For geochemists, the contrast in $\delta^{13}C$ between C_3 and C_4 vegetation provides a useful tracer for DIC, particularly in agricultural areas cropped with C_4 plants:

C_3 crops: wheat, rice, barley, oats, rye, tobacco, sugar beets, dry beans, soybeans, sunflowers, ground nuts, bluegrass and most lawn grasses, and fescue
C_4 crops: corn (maize), sugar cane, sorghum (millet), prairie and dryland grasses

Marine organic carbon is accompanied by a greater fractionation during photosynthesis, and so has $\delta^{13}C$ values closer to –30‰. The degradation of marine organic carbon during diagenesis and hydrocarbon formation produces enriched CO_2 as a by-product, and so oil and gas have additional depletion in ^{13}C.

SOIL CO_2 AND WEATHERING

The chemical weathering of carbonate and silicate minerals is greatly aided by acidity. The solubility of most minerals in pure water is very low. Carbonate minerals, such as calcite or dolomite, have low dissociation constants ($K_{cal} = 10^{-8.48}$ and $K_{dol} = 10^{-17.09}$) and simple dissociation reactions, producing Ca^{2+} and Mg^{2+}, and CO_3^{2-} allows dissolution of only a few ppm. However, addition of acid greatly enhances carbonate dissolution. Weathering of aluminosilicate minerals, such as feldspars, follows hydrolysis reactions that consume hydrogen ions and raises pH. The addition of acid therefore increases the solubility of such minerals, and so greatly accelerates weathering.

In natural soils, the acidity required for weathering is principally generated by oxidation of organics to generate carbonic acid (H_2CO_3) produced from hydration of CO_2. The atmosphere contains about 400 ppmv of CO_2, whereas CO_2 from respiration of SOC reaches 3,000–10,000 ppmv. In Precambrian and early Paleozoic times, the atmosphere hosted CO_2 at concentrations over an order of magnitude higher than today, which supported geochemical weathering before the arrival of terrestrial plants and soils. With the development of the terrestrial biosphere and reduction of atmospheric CO_2 concentrations, continental weathering became constrained to the soil horizon overlying bedrock.

Open and Closed System Weathering

The action of weathering by carbonic acid is greatly enhanced when the carbonic acid can be replenished as it is consumed. This is the case for unsaturated soils and

fractures, where mineral weathering takes place in the soil water with open contact with CO_2-rich soil air. As carbonic acid in the soil water is consumed by weathering, it is replenished by CO_2 from the soil air. This is weathering under *open system conditions.*

In the saturated zone below the water table, groundwater is not in direct contact with the soil atmosphere. As carbonic acid is consumed by weathering, it is not replenished. Here, weathering reactions are more limited and take place under *closed system conditions*. Closed system conditions exist in recharge areas characterized by rapid infiltration, where percolation to the water table occurs before minerals are encountered and weathering can begin. Conditions evolve rapidly toward high pH values and reduced water–rock interaction. By contrast, weathering is more aggressive under open system conditions, resulting in higher concentrations of solutes, and is increased with residence time for water in unsaturated soils.

Soil P_{CO_2} and Carbonic Acid in the Recharge Environment

Respiration of fixed or reduced carbon by aerobic bacteria for metabolism and cell construction is strongly exothermic and produces high P_{CO_2} typical of soils:

$$O_2 + CH_2O \rightarrow CO_2 + H_2O \quad \text{with } \Delta G_r^\circ = -501.8 \text{ kJ/mol}$$

A product of respiration is the humification of soil, with the accumulation of less labile and more refractory compounds collectively referred to as humic substances (Figure 6.4). These include 10,000-plus Da (Dalton, unified atomic mass units or u) humic acids and their lighter-weight fulvic acids, which are complex aromatic carbon structures with OH and COOH functional groups. They dissociate near pH 2–4, making them weak acids. Also produced are lighter-weight and more labile organic acids, such as acetic (CH_3COOH), carboxylic ($C_2O_2[OH]_2$), formic (HCOOH), and lactic (CH_3CH [OH] COOH) acids, all with pK values from 3 to 5, and so they contribute acidity under slightly acid to alkaline pH conditions. These organic acids, however, are rapidly consumed by aerobic bacteria and converted to CO_2.

The aerobic decay of vegetation can generate P_{CO_2} levels generally between $10^{-2.5}$ and $10^{-1.5}$ atm (0.003–0.03 atm), whereas in the open atmosphere, it is much lower ($10^{-3.40}$ or 0.0004 atm). The concentration of carbonic acid in groundwater is established by the Henry's Law constant, K_{CO_2}, which is $10^{-1.47}$ or 0.0339 mol/kg at 25°C. So, for a partial pressure of 0.03 atm CO_2 recharging groundwaters would gain 0.001 mol/kg of carbonic acid for mineral weathering.

The P_{CO_2} of water can be calculated from pH and DIC (Chapter 2), as can DIC species and pH of recharging groundwater be determined from P_{CO_2}. This is an important calculation to determine the initial carbonic acid concentration and pH of water equilibrating with the open air or with different soil atmospheres (Figure 6.5).

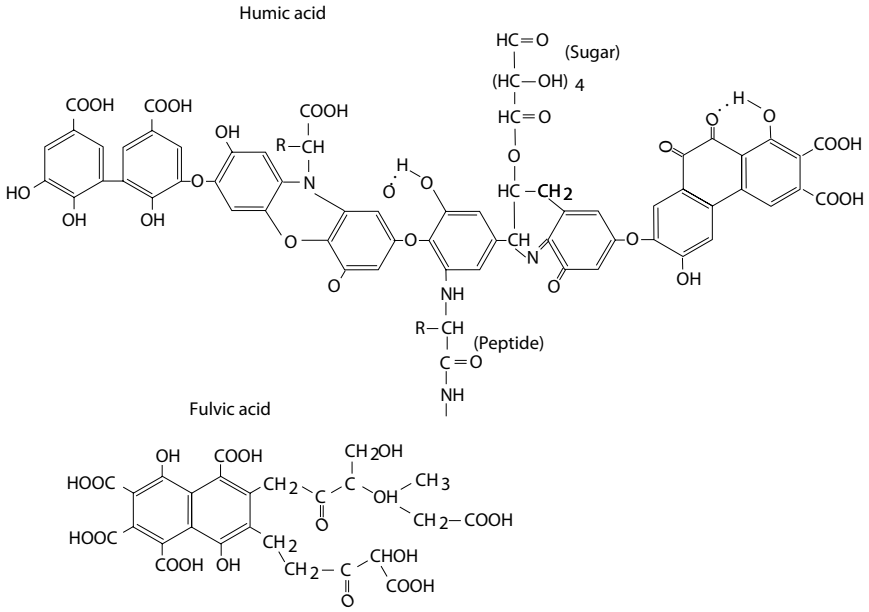

FIGURE 6.4 Typical structure of humic and fulvic acids. (Modified from Stevenson, 1985; Buffle, 1977.)

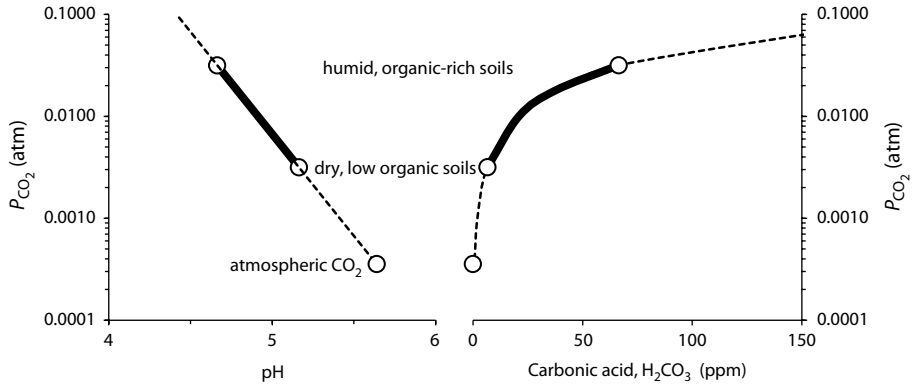

FIGURE 6.5 pH and carbonic acid for groundwater in equilibrium with varying soil P_{CO_2}.

Soil Acidity from Sulfide, Organic Nitrogen, and Fe^{2+} Oxidation in Soils

In addition to CO_2, the degradation of organics also releases organic sulfur and nitrogen, both of which are generally found in fixed or reduced states in organic compounds. Mineralization of these elements to compounds such as sulfide (H_2S) and ammonia (NH_4^+) makes them available for oxidation in aerobic reactions generally mediated by bacteria.

Example 6.1: pH and DIC of Water with Externally Fixed P_{CO_2}

What are the pH and concentrations of the DIC species H_2CO_3, HCO_3^-, and CO_3^{2-} for water in equilibrium with atmospheric CO_2 at 10°C?

$$P_{CO_2\,\text{atmosphere}} = 10^{-3.40}$$

$$\text{Carbonic acid activity}: K_{CO_2} = \frac{a_{H_2CO_3}}{P_{CO_2}} = 10^{-1.27}$$

$$a_{H_2CO_3} = 10^{-1.27} \times 10^{-3.40} = 10^{-4.67}$$

Carbonic acid dissociates to HCO_3^- and H^+, although the extent of dissociation depends on the pH, which changes as H_2CO_3 dissociates. A solution to this iteration is based on the observation that dissociation of H_2CO_3 should produce equal concentrations of HCO_3^- and H^+ (neglecting the minor initial 10^{-7} mol/kg H^+ in pure water). The pH and HCO_3^- activity from the dissociation of carbonic acid is then calculated from

$$K_1 = \frac{a_{HCO_3^-} \times a_{H^+}}{a_{H_2CO_3}} = 10^{-6.47}$$

$$a_{HCO_3^-} \times a_{H^+} = 10^{-6.47} \times 10^{-4.67} = 10^{-11.14}$$

$$a_{HCO_3^-} = a_{H^+} = \sqrt{10^{-11.14}}$$

$$= 10^{-5.57}$$

and so

$$\text{pH} = 5.57$$

The activity of CO_3^{2-} will always be equal to K_2, given that, by definition, $a_{HCO_3^-} = a_{H^+}$:

$$K_2 = \frac{a_{CO_3^{2-}} \times a_{H^+}}{a_{HCO_3^-}} = 10^{-10.49}$$

$$a_{CO_3^{2-}} = \frac{10^{-10.49} \times 10^{-5.57}}{10^{-5.57}} = 10^{-10.49}$$

Thus, water in equilibrium with atmospheric CO_2 will have a pH of 5.61. The concentrations of DIC species can be calculated assuming that activities equal molalities:

$$m_{H_2CO_3} = 10^{-4.67}\,\text{mol/kg} = 0.26\ \text{ppm C}$$

$$m_{HCO_3^-} = 10^{-5.57}\,\text{mol/kg} = 0.03\ \text{ppm C}$$

$$m_{CO_3^{2-}} = 10^{-10.49}\,\text{mol/kg} = < 0.01\ \text{ppm C}$$

$$m_{DIC} = 10^{-4.62}\,\text{mol/kg} = 0.29\ \text{ppm C}$$

The dissolution of CO_2 is an acidic reaction, yielding a low pH, minor HCO_3^- activity, and very little CO_3^{2-}.

What are the pH, $a_{H_2CO_3}$ and $a_{HCO_3^-}$ for water in equilibrium with soil air with $P_{CO_2} = 10^{-2}$?

$$a_{H_2CO_3} = 10^{-1.27} \times 10^{-2}$$
$$= 10^{-3.27}$$
$$a_{HCO_3^-} \times a_{H^+} = 10^{-6.47} \times 10^{-3.27} = 10^{-9.74}$$
$$a_{HCO_3^-} = a_{H^+} = \sqrt{10^{-9.74}}$$
$$= 10^{-4.87}$$

so
$$pH = 4.87$$

and assuming $a_{HCO_3^-} \approx m_{HCO_3^-}$:

$$m_{DIC} = (10^{-3.27} + 10^{-4.87}) = 0.00055 \text{ mol/kg} = 6.6 \text{ ppm C}$$

Thus, water in equilibrium with soil CO_2, which typically has P_{CO_2} of one to two orders of magnitude greater than that of air, will have a lower pH and higher DIC (13.1 ppm C). The pH–P_{CO_2} correlation is defined by the dissociation constant for carbonic acid, and is shown graphically in Figure 6.6.

$$H_2S + 2O_2 \rightarrow SO_4^{2-} + 2H^+ \qquad \text{sulfuric acid from sulfide oxidation}$$
$$NH_4^+ + 2O_2 \rightarrow NO_3^- + H_2O + 2H^+ \qquad \text{nitric acid from nitrification}$$

Bedrock is also a source of reduced compounds that release acidity through oxidation. Sulfide minerals, such as pyrite, are often found in shales, limestones, and igneous rocks, and can be a component of unconsolidated tills. As soils develop, these minerals become exposed and oxidized by bacteria. Ferrous iron (Fe^{2+}) present in pyrite as well as in a host of ferromagnesian silicates, such as olivine (Fe_2SiO_4) and pyroxene ($FeSi_2O_5$) is released by weathering and provides an additional source of acidity through oxidation. Precipitation of ferric iron hydroxide ($Fe[OH]_3$) in soils and on outcrops is evidence for this source of acidity.

$$FeS_2 + 3\tfrac{1}{2}O_2 + H_2O \rightarrow Fe^{2+} + 2SO_4^{2-} + 2H^+ \qquad \text{sulfuric acid from pyrite oxidation}$$
$$Fe^{2+} + \tfrac{1}{4}O_2 + 2\tfrac{1}{2}H_2O \rightarrow Fe(OH)_3^\circ + 2H^+ \qquad \text{ferrous iron oxidation and hydration}$$

CARBONATE WEATHERING

Weathering of carbonate rocks proceeds more rapidly than weathering of silicate rocks. Carbonate minerals are ubiquitous, not just as limestone and dolomite formations, but as secondary phases filling fractures in aluminosilicate rocks, and as cements and crusts in soils. Carbonate dissolution, whether in sedimentary rocks or in fractures within crystalline rocks, generates porosity and facilitates groundwater advection.

Carbonate bedrock, limestone and dolomite, are important aquifers and figure highly in the supply of groundwater to wells and surface water bodies. Despite a low relative abundance less than 0.1% of the lithosphere, their high rate of weathering allows that carbonates have the dominant effect on watershed geochemistry. The high Ca^{2+} and Mg^{2+} bicarbonate content of hard water is due to the weathering of carbonate rocks. Even in crystalline terrains, weathering of carbonate minerals lining fractures can dominate over silicate weathering (Leybourne and Goodfellow 2010). Two principal reactions dominate—calcite and dolomite dissolution.

$$CaCO_3 + H_2CO_3 \rightarrow Ca^{2+} + 2HCO_3^-$$
$$CaMg(CO_3)_2 + 2H_2CO_3 \rightarrow Ca^{2+} + Mg^{2+} + 4HCO_3^-$$

The extent of mineralization is a function of the P_{CO_2} of soils in the recharge area and the degree of openness of the system during weathering.

Open System Carbonate Weathering

Much of carbonate weathering occurs under open system conditions where the reservoir of soil CO_2 and organics replenish the carbonic acid consumed by mineral dissolution. Contact with soil CO_2 maintains a constant P_{CO_2} and so a constant concentration of carbonic acid. As carbonate weathering proceeds under these conditions, the system reaches calcite saturation with no further net dissolution (Figure 6.6). This contrasts with carbonate dissolution under closed system conditions where the limited CO_2 gained during infiltration through the soil precludes extensive weathering. Here, the P_{CO_2} will evolve to very low values with correspondingly high pH, often without achieving calcite saturation, as shown in Figure 6.6.

The amount of carbonate dissolved under open system conditions is ultimately controlled by partial pressure of the soil CO_2. The concentration of Ca^{2+} as well as the DIC and pH of the groundwater can be easily calculated using the basic equations that control DIC speciation, and shows the importance of open system weathering.

Closed System Carbonate Weathering

Once groundwaters have infiltrated through the unsaturated zone and below the water table, the access to soil CO_2 is restricted by diffusion through the water column. Without replenishment of soil CO_2, the carbonic acid concentration decreases as weathering proceeds. The degree of mineral weathering is then limited to the amount of CO_2 dissolved during recharge through the unsaturated soil zone. As this carbonic acid is consumed, P_{CO_2} decreases, pH increases, and weathering is greatly diminished.

The dissolution of calcite under closed system conditions follows a more complicated pathway than for open system conditions because the P_{CO_2} and carbonic acid concentration decrease as the system moves toward equilibrium. A unique solution exists for a given initial P_{CO_2}, and can be determined from the DIC reaction equations used earlier plus equations of electroneutrality and mass balance. A simple

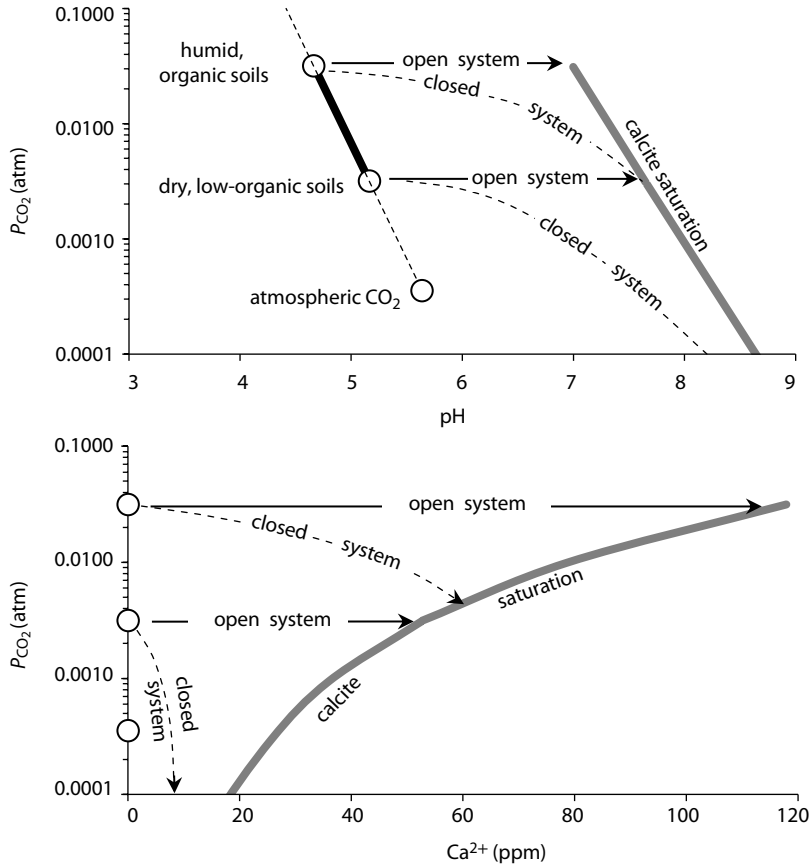

FIGURE 6.6 Evolution of pH and groundwater P_{CO_2} during mineral weathering, starting at the point of equilibration with soil CO_2 and proceeding to the point of calcite saturation. Mineral weathering under both open system (in contact with soil air) and closed system (below water table out of contact with soil air) consumes acid and raises pH to the point of carbonate saturation. However, only under closed system conditions does the P_{CO_2} of the groundwater evolve to lower levels, as carbonic acid is consumed.

calculation can be made if we assume that the mass of calcite dissolved is approximated by the concentration of carbonic acid dissolved during recharge. For high initial P_{CO_2} conditions, the groundwater may reach calcite saturation before the carbonic acid is fully consumed. Figures 6.6 and 6.7 illustrate the enhanced weathering potential of open system conditions over closed system conditions for various soil P_{CO_2} conditions.

WEATHERING IN SILICATE TERRAINS

Crystallization of magma and high-temperature metamorphism produces feldspars, which represent the most abundant mineral group in the crust. The feldspars include anorthite ($CaAl_2Si_2O_8$) and the alkali feldspars, albite ($NaAlSi_3O_8$) and orthoclase

Example 6.2: Carbonate Dissolution under Open System Conditions

How much calcite can be dissolved by water in an open system with P_{CO_2} of 0.01 (10^{-2}) and at a temperature of 10°C?

Under open system conditions, the carbonic acid activity remains constant under conditions of fixed P_{CO_2}

$$K_{CO_2} = \frac{a_{H_2CO_3}}{P_{CO_2}} = 10^{-1.27}$$

$$\begin{aligned} a_{H_2CO_3} &= K_{CO_2} \times P_{CO_2} \\ &= 10^{-1.27} \times 10^{-2} \\ &= 10^{-3.27} \\ &= 0.000537 \end{aligned}$$

Carbonic acid dissociates to give equal concentrations of HCO_3^- and H^+ (Examples 4.6 and 6.1). However, as calcite begins to dissolve, CO_3^{2-} is converted to HCO_3^- by reaction with H^+. This causes more H_2CO_3 to dissociate and more CO_2 to diffuse into solution. The following are the relevant reactions at the point of calcite saturation, with their reaction constant given for 10°C (Table 3.7):

$$\begin{aligned} CO_2 + H_2O &\Leftrightarrow H_2CO_3 & K_{CO_2} &= 10^{-1.27} \\ H_2CO_3 &\Leftrightarrow H^+ + HCO_3^- & K_1 &= 10^{-6.47} \\ HCO_3^- &\Leftrightarrow H^+ + CO_3^{2-} & K_2 &= 10^{-10.49} \\ CaCO_3 &\Leftrightarrow Ca^{2+} + CO_3^{2-} & K_{cal} &= 10^{-8.41} \end{aligned}$$

Under open system conditions, the fixed parameters include $P_{CO_2} = 10^{-2}$ atm and $a_{H_2CO_3} = 10^{-3.27}$. Unknown parameters include H^+, HCO_3^-, CO_3^{2-}, and Ca^{2+}, which indicates the amount of calcite dissolved. Solving for these unknowns begins with the basic equations for DIC speciation and calcite dissolution 7. By substitution and rearrangement, they can be expressed in terms of a_{H^+}:

$$a_{HCO_3^-} = \frac{K_1 \times a_{H_2CO_3}}{a_{H^+}} = \frac{10^{-6.47} \times 10^{-3.27}}{a_{H^+}} = \frac{10^{-9.74}}{a_{H^+}}$$

$$a_{CO_3^{2-}} = \frac{K_2 \times a_{HCO_3^-}}{a_{H^+}} = \frac{10^{-10.49} \times \dfrac{10^{-9.74}}{a_{H^+}}}{a_{H^+}} = \frac{10^{-20.23}}{a_{H^+}^2}$$

$$a_{Ca^{2+}} = \frac{K_{calcite}}{a_{CO_3^{2-}}} = \frac{10^{-8.41}}{10^{-20.23} / a_{H^+}^2} = 10^{11.82} \times a_{H^+}^2$$

A fourth equation is required to solve for four unknown parameters. As the solution must be electrically neutral, the charge balance equation can be used:

$$2m_{Ca^{2+}} + m_{H^+} = m_{HCO_3^-} + 2m_{CO_3^{2-}} + m_{OH^-}$$

Considering that for circumneutral systems like this, H^+, OH^-, and CO_3^{2-} will have very low concentrations compared to Ca^{2+} and HCO_3^- (as demonstrated by the equation for calcite dissolution: $CaCO_3 + H_2CO_3 \rightarrow Ca^{2+} + 2HCO_3^-$), the charge balance equation can be simplified to:

$$2m_{Ca^{2+}} = m_{HCO_3^-}$$

Substituting into the charge balance equation for $m_{Ca^{2+}}$ and $m_{HCO_3^-}$ solves for H^+:

$$2 \times 10^{11.82} \times a_{H^+}^2 = \frac{10^{-9.74}}{a_{H^+}}$$
$$10^{-3pH} = 10^{-21.86}$$
$$pH = 7.29$$

With pH, the activity of all other components can be solved. With no correction for *a* to *m*, this gives a Ca^{2+} concentration of

$$m_{Ca^{2+}} = 10^{11.82} \times a_{H^+}^2 = 10^{11.82} \times 10^{-14.58} = 10^{-2.76} = 0.00174 \text{ mol/kg}$$
$$= 69.7 \text{ ppm}$$

and $$m_{HCO_3^-} = \frac{10^{-9.74}}{a_{H^+}} = \frac{10^{-9.74}}{10^{-7.29}} = 0.00355 \text{ mol/kg}$$
$$= 216 \text{ ppm}$$

From these molalities, ionic strength can be calculated by iteration, as was done for gypsum solubility in Example 2.3. The result is a greater amount of Ca^{2+} (95 ppm) and HCO_3^- (234 ppm) in solution. This amounts to a total of 234 mg of calcite dissolved per liter of groundwater under open system conditions with a soil CO_2 concentration of 10^{-2} or 1%. If the P_{CO_2} is greater, for example, $10^{-1.5}$ (3.2% CO_2), the final pH is lower (6.95) and the amount of calcite dissolved increases to 300 ppm.

$[KAlSi_3O_8]$ (see Chapter 1, Silicates). Silicate terrains also include varying amounts of high-temperature ferromagnesian minerals, including olivine ($[Fe,Mg]_2SiO_4$) and pyroxene ($Ca[Mg,Fe]Si_2O_6$), amphibole ($KCa_2[Mg,Fe,Al]_5[(Al,Si)_4O_{11}]_{22}[OH]_2$), and biotite ($[Mg,Fe)_3[AlSiO_{10}][OH]_2$), plus muscovite ($KAl_2[AlSi_3O_{10}][OH]_2$) and quartz ($SiO_2$).

Weathering of these high-temperature minerals releases cations and silica while forming an array of more stable aluminosilicate clay minerals. All silicate alteration reactions are acid consuming and greatest under open system conditions in soils with high P_{CO_2} and carbonic acid. Equilibrium, however, is rarely attained. Only at high pH and high cation activities do thermodynamics favor precipitation of feldspars or other primary silicate minerals at low temperature.

Example 6.3: Calcite Dissolution under Closed System Conditions

How much calcite can be dissolved under closed system conditions with an initial P_{CO_2} of 0.01 and at a temperature of 10°C?

With this initial condition, the concentrations of the DIC species

$$P_{CO_2} = 0.01$$
$$K_{CO_2} = 10^{-1.27}$$
$$a_{H_2CO_3} = P_{CO_2} \times K_{CO_2} = 10^{-1.27} \times 10^{-2}$$
$$= 10^{-3.27}$$

As $\gamma_{H_2CO_3} = 1$ for neutral species,

$$m_{H_2CO_3} = a_{H_2CO_3}$$
$$= 10^{-3.27}$$
$$= 0.00054 \text{ mol/kg}$$

This is the initial concentration of acid available for calcite dissolution according to the reaction

$$H_2CO_3 + CaCO_3 \rightarrow Ca^{2+} + 2\ HCO_3^-$$

and so a maximum of 0.00054 mol/kg or 54 ppm $CaCO_3$ can be dissolved as an approximation. Less will be dissolved for higher initial carbonic acid concentrations as calcite saturation is reached before all the carbonic acid is consumed. A more accurate calculation of closed system calcite dissolution based on calcite solubility, including the final pH, is presented in the solution to Problem 8.

In this case, the 54 ppm of calcite is considerably less than the 234 ppm that can be dissolved under open system conditions in Example 6.2, and underlines the importance of open system versus closed system weathering.

Silicate Weathering Reactions

Aluminosilicate weathering releases cations into solution, according to incongruent dissolution reactions, where the primary minerals, such as feldspars, are altered to more stable clay minerals:

$$NaAlSi_3O_{8\ \text{albite}} + 4.5H_2O + H_2CO_3 \rightarrow Na^+ + HCO_3^- + \tfrac{1}{2}Al_2Si_2O_5(OH)_{4\ \text{kaolinite}} + 2H_4SiO_4^\circ$$

$$CaAl_2Si_2O_{8\ \text{anorthite}} + H_2O + 2H_2CO_3 \rightarrow Ca^{2+} + 2HCO_3^- + Al_2Si_2O_5(OH)_{4\ \text{kaolinite}}$$

Acid is essential to silicate hydrolysis reactions, as the product clays are hydrated with OH^-. Silica is released into solution by the weathering of the alkali feldspars (albite and orthoclase) although not by the weathering of anorthite, in which an extra Al^{3+} replaces one Si^{4+} to maintain the charge balance with divalent Ca^{2+}.

The alteration of these high-temperature feldspars and formation of low-temperature clay minerals (incongruent dissolution) is such that equilibrium with primary mineral phases is seldom reached. In the near-surface environment where water circulation is relatively rapid, weathering will continue as long as there

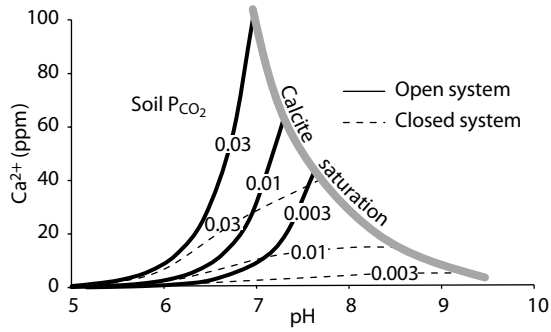

FIGURE 6.7 The evolution of pH and Ca^{2+} (a measure of calcite dissolution) as groundwater dissolves calcite under open and closed system conditions, for varying initial P_{CO_2} conditions. The continual access to soil CO_2 under open system conditions allows considerably more calcite to be dissolved than for closed system conditions.

is a source of acidity to drive the reactions. For the alkali feldspars, the concentrations of Na^+ and K^+ can be used as an indication of the extent of weathering, as there are few mineralogical controls on their concentrations. For anorthite, Ca^{2+} concentrations are generally limited by calcite saturation.

Weathering of the ferromagnesian silicates, such as pyroxene and olivine, can proceed congruently, with release of silica and either Fe^{2+} or Mg^{2+} to solution:

$$CaMgSi_2O_{6\ \text{pyroxene}} + 4H^+ + 2H_2O \rightarrow Ca^{2+} + Mg^{2+} + 2H_4SiO_4^\circ$$
$$MgFeSiO_{4\ \text{olivine}} + 4H^+ \rightarrow Mg^{2+} + Fe^{2+} + H_4SiO_4^\circ$$

As these minerals contain no aluminum, clay minerals, such as kaolinite, do not form, although under conditions of low water/rock ratios serpentinization proceeds ($[Mg,Fe]_3Si_2O_5[OH]_4$). Later-crystallizing (lower temperature) ferromagnesian silicates containing aluminum, such as biotite, can weather to form aluminosilicate clays.

$$KMg_3\left(AlSi_3O_{10}\right)(OH)_{2\ \text{biotite}} + 7H^+ + \tfrac{1}{2}H_2O \rightarrow$$
$$K^+ + 3Mg^{2+} + 2H_4SiO_4^\circ + \tfrac{1}{2}Al_2Si_2O_5(OH)_{4\,\text{kaolinite}}$$

Controls on Silicate Weathering

In the low salinity, freshwater settings that characterize most groundwaters, the controls on silicate weathering are generally limited to the amount of available acid. This is unlike open system carbonate weathering, where a calcite solubility limit is met, at which point the pH and concentrations of Ca^{2+} and HCO_3^- become stable. However, where divalent cations are released by silicate weathering, Ca^{2+}, Mg^{2+}, and Fe^{2+} carbonate minerals can form and limit the buildup of these cations and HCO_3^-.

$$CaAl_2Si_2O_{8\,\text{anorthite}} + H_2O + H_2CO_3 \rightarrow Al_2Si_2O_5(OH)_{4\,\text{kaolinite}} + CaCO_3$$
$$CaMgSi_2O_{6\ \text{pyroxene}} + 2H_2CO_3 + 2H_2O \rightarrow 2H_4SiO_4^\circ + CaMg(CO_3)_2$$

The weathering of anorthite to the point of calcite precipitation under open and closed conditions is shown in Figure 6.8. This is incongruent dissolution, and although it does not limit the dissolution of the primary silicate minerals being weathered, it does limit the ionic strength of the groundwater as weathering proceeds.

As $a_{H_4SiO_4^\circ}$ increases through the weathering of silicate minerals, quartz solubility is readily exceeded. The solubility of silicic acid is ultimately limited by amorphous silica gel ($H_4SiO_{4\,am}$), which can precipitate at low temperature. Over time, this phase can recrystallize into more stable opal ($SiO_2 \cdot n[H_2O]$), a hydrated form ($n < 1$) with little to no crystallinity. Opal can also be directly precipitated from solution, for example, in plant cells as phytoliths, which can be analyzed for $\delta^{18}O$ as a climate indicator (Webb and Longstaffe 2000). With increased temperature and time, amorphous to poorly crystalline silica forms transform to chalcedony (SiO_2)—a microcrystalline form of quartz. The solubility of quartz and its polymorphs, however, are very much temperature dependent (Figure 6.8). The solubility curves for chalcedony and quartz are useful to reconstruct geothermal temperatures (greater than 100°C). A further control on amorphous silica solubility is pH. Silicic acid dissociates above pH 9 (Figure 3.5), which greatly increases its solubility. Figure 6.8 (right) shows this effect, where the solubility of amorphous silica increases from less than 200 ppm in neutral pH waters to very high levels near pH 10.

Although amorphous silica has high solubility, values seldom exceed about 50 ppm, and are more commonly in the range of 10–30 ppm. This is due to the low rate of silicate mineral weathering, particularly under closed system conditions as well as sorption.

Differentiating between silicate and carbonate weathering can be approached using ion ratios. From the reactions presented earlier, the production of alkali elements, in particular Na^+, can be an indicator of feldspar weathering. However, it must be corrected for chloride salinity by subtracting the moles of Na^+ that are supported by Cl^- derived from marine and halite sources. Gaillardet et al. (1999) show that the weathering in carbonate watersheds produces runoff that is enriched in the alkali earths over the alkali catios, with Ca/Na molar ratios greater than 10. In contrast, feldspar weathering yields higher alkali cations, and so the Ca/Na ratio

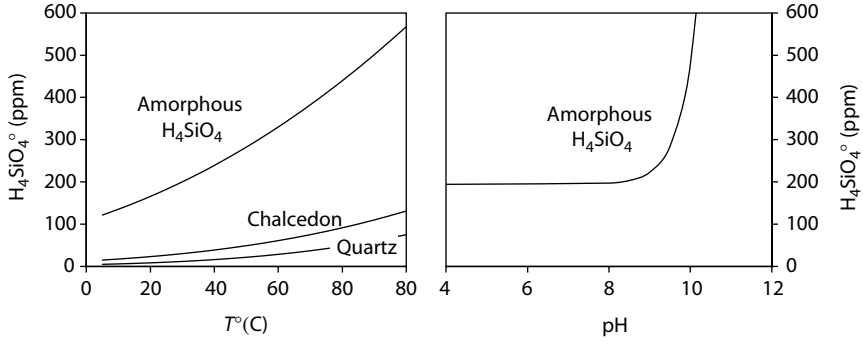

FIGURE 6.8 Solubility of quartz (SiO_2) and its polymorphs with temperature (left) and pH (at 25°C, right).

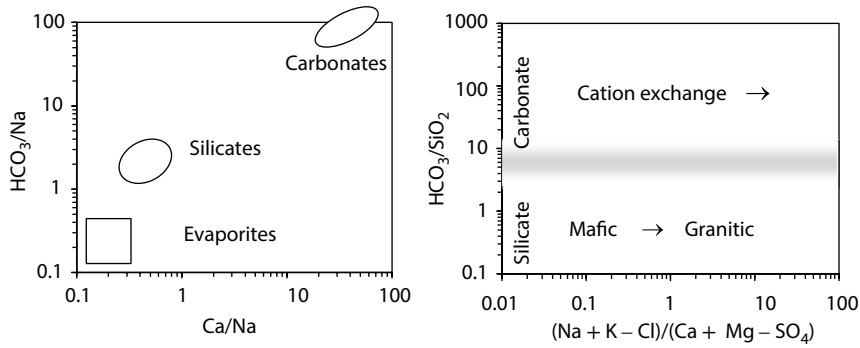

FIGURE 6.9 Molar ratios in runoff as indicators of silicate versus carbonate weathering. (Modified from Gaillardet, 1999.) Chloride and sulfate corrections are made to account for evaporite contributions in the right-hand chart.

is generally less than 1 (Figure 6.9). Bicarbonate provides an additional constraint when normalized to Na, with strong enrichment of the HCO_3/Na ratio in drainage from carbonate terrains but with ratios closer to 1 in silicate terrains. Silica provides an additional constraint. Plotting the ratio of bicarbonate to silicate provides further distinction of carbonate and silicate weathering fields (Figure 6.9).

Closed System Silicate Weathering and pH

The acidity available for weathering in silicate terrains is largely determined by the P_{CO_2} conditions that exist in the recharge area. Organic acids and oxidation of sulfide minerals may also contribute H^+ ions. The slow rates of silicate weathering are such that much may take place under closed system conditions below the water table. If no subsurface sources of CO_2 (e.g., oxidation of methane, metamorphic CO_2) or other acids (e.g., H_2SO_4 from oxidation of pyrite) are available, then P_{CO_2} will drop to very low levels and pH will increase to values as high as 10 or higher. An example of such a case comes from the Ahouset geothermal spring on the Pacific Coast of southern Canada (Example 6.4).

WEATHERING AND ^{13}C OF DISSOLVED INORGANIC CARBON

Understanding the source of DIC and weathering reactions becomes important in tracing groundwater recharge and mixing. It is also important for tracing biodegradation of organic contaminants, and in applications of ^{14}C for dating groundwater and tracing carbon. Stable ^{13}C is used for such studies, as has characteristic concentrations in different carbon pools and fractionates during reaction.

$\delta^{13}C_{DIC}$ in the Recharge Environment

Carbon isotopes are useful for tracing the carbon cycle and evolution of DIC in waters. Atmospheric CO_2 in recharge waters is soon masked by the much greater

Example 6.4: Weathering in Silicate Terrains

The Ahouset geothermal waters discharge from a quartz diorite (quartz [SiO_2] and albite [$NaAlSi_3O_8$]) pluton on the west coast of Vancouver Island. The temperature is 23°C, about 10°C above the average annual temperature, indicating a depth of circulation of at least 500 m with a geothermal gradient of about 2°C per 100 m depth. Can weathering of the quartz diorite pluton produce the following geochemistry of this spring?

Ahouset geothermal water, T = 23°C pH = 10.05.

	HCO_3^-	CO_3^{2-}	SO_4^{2-}	Cl^-	Ca^{2+}	Mg^{2+}	Na^+	K^+	Si_{total}
ppm	15.8	8.24	11.7	10.1	1.91	0.12	32.6	0.18	9.01
mmol/kg	0.259	0.137	0.12	0.29	0.048	0.005	1.42	0.0051	0.30

The very high pH, Na^+ as the major cation and elevated SiO_2 suggest extensive closed system weathering of albite in the host silicate rocks. The absence of significant Ca^{2+} precludes dissolution of calcite that can occur in fractures within silicate rocks. Note that the high sodium is not fully supported by Cl^-, which may come from marine aerosols (sea spray) in this coastal setting. Most of the Na^+ is then rock-derived. A correction for marine Na^+ ($m_{Na^+}/m_{Cl^-} = 0.86$) can be made by subtracting the amount supported by Cl^- from the measured Na^+ (1.42 – 0.86 × 0.29 = 1.17 mmol/kg).

The reaction constant for alteration of $NaAlSi_3O_{8\ albite}$ to $Al_2Si_2O_5(OH)_{4\ kaolinite}$ from above is determined from values for $\Delta G°$ (Table 2.5):

$$\begin{aligned}\Delta G_r^\circ &= 2\Delta G^\circ_{Na^+} + \Delta G^\circ_{Al_2Si_2O_5(OH)_4} + 4\Delta G^\circ_{H_4SiO_4} - 2\Delta G^\circ_{NaAlSi_3O_8} - 9\Delta G^\circ_{H_2O}\\ &= 2(-262.0) + (-3799.7) + 4(-1307.9) - 2(-3711.5) - 9(-237.14)\\ &= 1.96\end{aligned}$$

$$\log K = -\frac{\Delta G_r^\circ}{5.708} = \frac{1.96}{5.708} = -0.34$$

$$K = 10^{-0.34} = \frac{a^2_{Na^+} \times a^4_{H_4SiO_4}}{a^2_{H^+}}$$

This relationship defines the activities of Na^+, silicic acid, and pH for equilibrium between albite and kaolinite, showing an inverse relationship between H^+ consumed by weathering and Na^+ produced by weathering. Rewriting it in logarithmic format and using the Na^+/H^+ ratio as an index of the extent of weathering allow the reaction of albite to kaolinite to be plotted on a mineral stability diagram (Figure 6.10).

$$\log \frac{a_{Na^+}}{a_{H^+}} = -\ 2\ \log a_{H_4SiO_4} - 0.17$$

This equation defines the boundary between albite and kaolinite. In the recharge area at low pH (high a_{H^+}) and low Na^+ concentration, kaolinite is the stable phase. Above this line, at high pH and high Na^+ activity, albite is thermodynamically stable and further weathering reaction will essentially end. Small open circles in

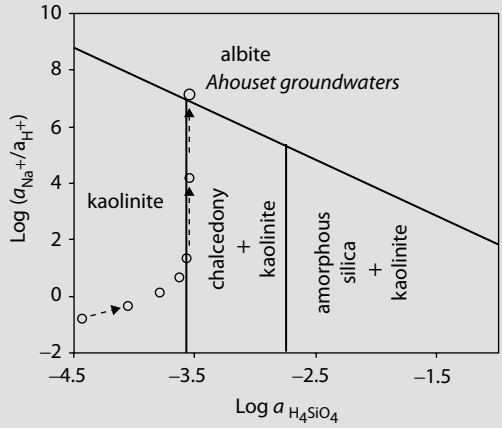

FIGURE 6.10 Mineral stability diagram for Na^+ and silicic acid with pH, showing the path for weathering of albite.

Figure 6.10 show the geochemical evolution during albite weathering from the initial condition, with an increase in the activities of both Na^+ and silicic acid and an increase in pH.

The Ahouset waters are plotted on this diagram to show the extent of albite weathering. The activity of Na^+ is determined using its concentration (32.6 ppm), corrected earlier for Cl^- supported Na^+ from seawater (Na^+_{rock} = 26.7 ppm) and the ionic strength (I = 0.0017), giving $a_{Na^+_{rock}} = 0.0011$.

$$\text{pH} = 10.05$$

$$a_{H^+} = 10^{-10.05} = 8.91 \times 10^{-11}$$

$$I = 0.0017$$

$$\gamma_{Na^+} = 0.957$$

$$a_{Na^+_{rock}} = (26.7/23000) \times 0.957 = 0.0011$$

$$\log(a_{Na^+_{rock}}/a_{H^+}) = \log(0.0011/8.91\times10^{-11}) = 7.09$$

$$a_{H_4SiO_4} = 0.000113$$

$a_{H_4SiO_4} = 0.000113$ (using the first dissociation constant of H_4SiO_4 $K_1 = 10^{-9.71}$)

These water plots on the line for albite–kaolinite equilibrium indicate that weathering in this system has proceeded to the full extent for the given initial conditions.

reservoir of CO_2 found in soils. As the high CO_2 in soils is generated by degradation of biomass, its $\delta^{13}C$ is much more negative and close to the ranges for C_3 and C_4 vegetation shown in Figure 6.3. Soil CO_2, however, has a slightly modified value, due to the outward diffusion from high P_{CO_2} in soils. As ^{12}C is more diffusive, this imparts a slight enrichment on the remaining soil CO_2 (Cerling et al. 1991). In most C_3 landscapes, the soil CO_2 has $\delta^{13}C$ in the range of –20 to –23‰.

During dissolution and hydration of soil CO_2, ^{13}C is preferentially partitioned into the DIC species, with greater ^{13}C enrichment in HCO_3^- and CO_3^{2-}. The $\delta^{13}C$ of DIC is in fact a composite of the enrichment factors between CO_2 in the soil and the DIC species, weighted of course by their relative abundance. The ^{13}C content of the dissolved CO_2 ($\delta^{13}C_{CO_2(aq)}$) is about 1‰ lower than that of the soil CO_2 ($\delta^{13}C_{CO_2(g)}$), while $\delta^{13}C_{HCO_3^-}$ is about 9‰ greater than $CO_{2(g)}$. As the relative abundance of these DIC species is controlled by pH, the value for $\delta^{13}C_{DIC}$ is then a function of pH, as long as the recharge waters are in contact with soil CO_2 (open system conditions). This is illustrated in Figure 6.11, which shows the enrichment in ^{13}C of DIC as the pH rises and the DIC becomes increasingly dominated by HCO_3^- rather than H_2CO_3. The actual values for these enrichment factors, $\varepsilon^{13}C_{HCO_3^- - CO_2}$, for example, are given in Table 6.2.

The precise value for $\delta^{13}C_{DIC}$ will depend on pH, which controls the ratio of $CO_{2(aq)}$ to HCO_3^-. Temperature also plays a role, as it affects the HCO_3^-–$CO_{2(g)}$ enrichment factor ($\varepsilon^{13}C_{HCO_3^- - CO_{2(g)}}$). Values for the $\delta^{13}C$ of DIC during recharge at different temperatures and pH are given in Table 6.2, calculated according to the isotope mass balance equation:

$$\delta^{13}C_{DIC} = \left(\frac{m_{HCO_3^-}}{m_{DIC}}\right) \times (\delta^{13}C_{CO_2} + \varepsilon^{13}C_{H_2CO_3 - CO_2}) + \left(\frac{m_{HCO_3^-}}{m_{DIC}}\right) \times (\delta^{13}C_{CO_2} + \varepsilon^{13}C_{HCO_3^- - CO_2})$$

If the pH of the soil water is below about 6.4, the DIC is composed mainly of $CO_{2(aq)}$, and so $\delta^{13}C_{DIC}$ will be close to the $\delta^{13}C_{CO_2(g)}$. At greater pH values, it is mainly HCO_3^-, and so $\delta^{13}C_{DIC}$ will be closer to $\delta^{13}C_{CO_2(g)} + 10‰$.

Below, this effect of pH on $\delta^{13}C_{DIC}$ during recharge becomes a useful tool to distinguish open versus closed system weathering in carbonate and silicate terrains. DIC and $\delta^{13}C_{DIC}$ in groundwater evolve to higher values as weathering proceeds. Controls on this evolution include whether open or closed system conditions prevail, and whether the parent material is silicate or carbonate. Each weathering scenario will support a different evolution for DIC and $\delta^{13}C_{DIC}$.

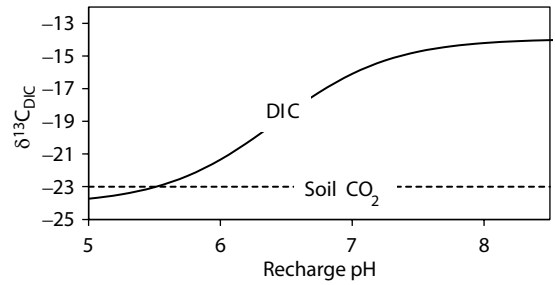

FIGURE 6.11 Effect of recharge pH on the $\delta^{13}C$ of dissolved inorganic carbon (DIC) in equilibrium with soil CO_2 (open system conditions). Calculated for case where $\delta^{13}C$ of soil CO_2 is –23‰ at 15°C.

TABLE 6.2
$\delta^{13}C_{DIC}$ of Recharge Water in Equilibrium with Soil CO_2 a 10°C for Different pH Values

pH	$\frac{HCO_3^-}{H_2CO_3}$	$\delta^{13}C_{soil\ CO_2}$	$\varepsilon_{H_2CO_3^*-CO_2}$	$\varepsilon_{HCO_3^--CO_2}$	$\delta^{13}C_{DIC}$
5.5	0.11	–20	–1.1	9.7	–20.0
6.5	1.1	–20	–1.1	9.7	–15.5
7.5	11.0	–20	–1.1	9.7	–11.2

From Table 4.2:

$$\varepsilon^{13}C_{H_2CO_3^*-CO_{2(g)}} = -0.000014 \times T^2 + 0.0049 \times T - 1.18$$

$$\varepsilon^{13}C_{HCO_3^--CO_{2(g)}} = 0.00032 \times T^2 - 0.124 \times T + 10.87$$

$$\varepsilon^{13}C_{CO_3^{2-}-CO_{2(g)}} = 0.00033 \times T^2 - 0.083 \times T + 8.25$$

$\delta^{13}C$ and Carbonate Weathering

The $\delta^{13}C$ value of groundwater DIC evolves during open and closed system weathering of carbonates. This serves as a baseline for evaluating whether subsequent reactions have taken place in the subsurface. If weathering reactions take place under open system conditions during recharge in carbonate terrains, the $\delta^{13}C$ of the DIC is often controlled by exchange with the soil CO_2 and the pH. In this case, as the recharge water dissolves calcite with a $\delta^{13}C$ value of, say, 0‰, exchange between the DIC and the reservoir of soil CO_2 maintains $\delta^{13}C_{DIC}$ in equilibrium with $\delta^{13}C_{CO_2}$. Accordingly, the final $\delta^{13}C_{DIC}$ after weathering reactions can be determined from Table 6.2 and Figure 6.11. As soil water moves relatively quickly toward equilibrium with calcite during open system recharge, groundwaters recharged under such conditions have generally achieved calcite saturation at a circumneutral pH. The final $\delta^{13}C_{DIC}$ is then enriched by about $\varepsilon^{13}C_{DIC\text{-}CO_2} = 10‰$, depending on temperature (Figure 6.11). For open system recharge through soils with $\delta^{13}C_{CO_2}$ of –20 to –23‰, values for $\delta^{13}C_{DIC}$ will be –10 to –13‰.

Open system	CO_2 – DIC exchange	$CO_2 + H_2O \leftrightarrow HCO_3^- + H^+$
	^{13}C fractionation	$\delta^{13}C_{CO_2} + \varepsilon^{13}C_{DIC-CO_2} \rightarrow \delta^{13}C_{DIC}$
		$-20‰ \quad + \quad 10‰ \quad \rightarrow -10‰$

If carbonate weathering takes place under closed system conditions, exchange with soil CO_2 cannot occur, and so the initial $\delta^{13}C_{DIC}$ value will increase as ^{13}C-enriched DIC is gained from bedrock. According to the stoichiometry of the carbonate dissolution reaction, this results in a 50% dilution with the aquifer carbonate. Unfortunately, the result is close to that of open system dissolution with equilibrium exchange:

Closed system	Carbonate dissolution	$H_2CO_3 + CaCO_3 \rightarrow Ca^{2+} + 2HCO_3^-$
	^{13}C mixing	$\delta^{13}C_{CO_2} + \delta^{13}C_{CaCO_3} \rightarrow \delta^{13}C_{DIC}$
		$-20‰ \quad + \quad 0‰ \quad \rightarrow -10‰$

This will happen not only in limestone aquifers but also in silicate aquifers where calcite may be present as fracture minerals (secondary metamorphic or hydrothermal calcite), or as carbonate grains, cobbles, or cement in clastic aquifers. Most marine carbonates have $\delta^{13}C \approx 0 \pm 1‰$ VPDB. Carbonate minerals in igneous and metamorphic rocks have $\delta^{13}C$ values of 0 to –10‰.

While the open system weathering dissolves considerably more carbonate than closed system, the final $\delta^{13}C$ of the DIC is ambiguous. This is observed in Figure 6.12, where the left diagram shows the final HCO_3^- concentration following open and closed system weathering of carbonate for different CO_2 concentrations in the soil atmosphere. Note that the examples shown fall on the line for open system carbonate weathering, which is by far the dominant recharge scenario and leads to the highest concentrations of HCO_3^- (and of course for Ca^{2+} and Mg^{2+}). However, for these same conditions, the right-hand chart shows that $\delta^{13}C$ is similar for either recharge scenario. Unlike stable ^{13}C, radiocarbon, discussed later, is unambiguous. Under open system conditions, equilibrium exchange with the soil CO_2 maintains an activity of $^{14}C_{DIC}$ near 100 pMC, whereas under closed system conditions, the acquired soil $^{14}CO_2$ is diluted to about 50 pMC with old, usually marine DIC that is ^{14}C-free.

The following example calculates the final $\delta^{13}C$ of the DIC after the dissolution of limestone to the point of calcite saturation.

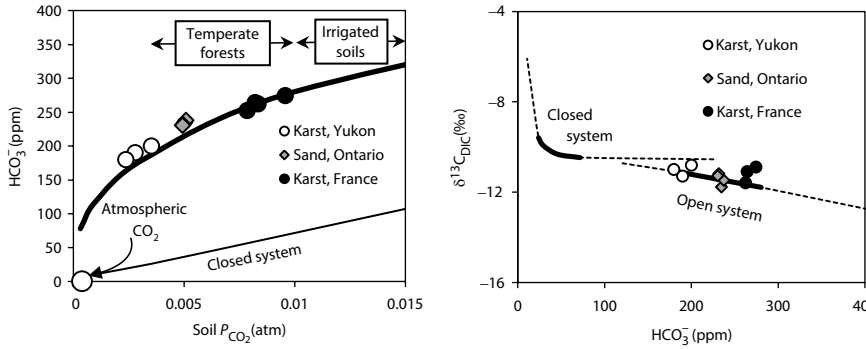

FIGURE 6.12 HCO_3^- and $\delta^{13}C_{DIC}$ following carbonate weathering under open and closed system conditions. Karst, Yukon (Utting et al. 2012); Sand, Ontario (Reardon et al. 1979); Karst, France (Emblanch et al. 2003).

Example 6.5: $\delta^{13}C_{DIC}$ Following Limestone Dissolution

What is the final $\delta^{13}C$ value of DIC after dissolving marine limestone under open system conditions, assuming an initial P_{CO_2} of 0.01 (10^{-2}), $\delta^{13}C_{soil\ CO_2} = –20‰$, and temperature = 10°C?

If recharge occurs under open system conditions, then the final $\delta^{13}C_{DIC}$ is determined by the final pH and the fractionation of ^{13}C between the soil CO_2 and DIC species (H_2CO_3 and HCO_3^-) at that pH. From Example 6.2, the pH was 7.29 for calcite dissolution under open system conditions with $P_{CO_2} = 0.01$.

First, we need the relative proportions of H_2CO_3 and HCO_3^-. From Example 6.2, the carbonic acid concentration (and activity for a neutral species) was 0.000537 mol/kg and for bicarbonate it was 0.00355 mol/kg. At a pH below 8.4, these are the two dominant DIC species, so the total DIC would be 0.004087 mol/kg.

The mole fraction of each DIC species is then as follows:

$$f_{H_2CO_3} = 0.000537 / 0.004087 = 0.13$$
$$f_{HCO_3^-} = 0.00355 / 0.004087 = 0.87$$

Then using an isotope mass balance equation and $\varepsilon^{13}C$ values from Table 6.2:

$$\begin{aligned}\delta^{13}C_{DIC} &= f_{H_2CO_3}\left(\delta^{13}C_{CO_2} + \varepsilon_{H_2CO_3-CO_2}\right) + f_{HCO_3^-}\left(\delta^{13}C_{CO_2} + \varepsilon_{HCO_3^--CO_2}\right)\\ &= 0.13(-20 - 1.1) + 0.87(-20 + 9.7)\\ &= -11.8‰\end{aligned}$$

Now what would this value be if calcite dissolution takes place under closed system conditions?

In the closed system case, the final $\delta^{13}C_{DIC}$ is a mixture of the initial $\delta^{13}C_{DIC}$ established in the soil before dissolving any calcite, and the amount of calcite dissolved in the aquifer. In Example 6.3, the initial $m_{H_2CO_3}$ was 0.00054 mol/kg, with an equivalent number of moles of calcite dissolved. From Example 6.1, this carbonic acid was partially dissociated to HCO_3^- with a concentration of $10^{-4.87}$ or 0.0000137 mol/kg, giving a total initial DIC of 0.00055 mol/kg. The $\delta^{13}C$ value for the final DIC is apportioned by the relative concentrations of H_2CO_3 and HCO_3^- in the recharge water plus the carbonate dissolved (which is approximately equal to the concentration of carbonic acid, 0.0054 mol/kg).

Using a isotope mass balance equation weighted with concentrations rather than fractions of the components:

$$\delta^{13}C_{DIC} \times m_{DIC} = m_{H_2CO_3} \times \left(\delta^{13}C_{CO_2} + \varepsilon_{H_2CO_3-CO_2}\right) + m_{HCO_3^-} \times \left(\delta^{13}C_{CO_2} + \varepsilon_{HCO_3^--CO_2}\right) + m_{CaCO_3} \times \left(\delta^{13}C_{CaCO_3}\right)$$

$$\begin{aligned}\delta^{13}C_{DIC} &= \frac{0.00054 \times (-20 - 1.1) + 0.0000136 \times (-20 + 9.7) + 0.00054 \times (0)}{0.00054 + 0.0000137 + 0.00054}\\ &= -10.7‰\end{aligned}$$

In both cases, the DIC after carbonate weathering is more enriched in ^{13}C than the initial DIC. As well, the final values for $\delta^{13}C$ of the DIC are very similar (–11.8‰ and –10.7‰). However, the enrichment under closed system conditions is due to mixing with the initial DIC from the soil and the DIC from calcite dissolution, which can be observed in the ^{14}C of the DIC, which will be diluted to near 50 pMC from the 100 pMC value typically found in soil CO_2.

Evolution of $\delta^{13}C_{DIC}$ in Silicate Aquifers

The change in $\delta^{13}C$ during weathering in silicate terrain is less complicated than in carbonate aquifers, as the only source of carbon is the soil CO_2, providing no carbonate fracture minerals are involved. As a consequence, the only controlling factor is the pH at the point that the recharge waters enter closed system conditions. After this point, the $\delta^{13}C_{DIC}$ will not change, even as the pH continues to increase, providing no

subsurface sources of carbonate are encountered. Figure 6.13 shows the evolution of $\delta^{13}C_{DIC}$ for both open and closed system weathering in silicate bedrock.

The pH under open system weathering of silicate minerals is controlled by the P_{CO_2} in the unsaturated zone and so controls the distribution of HCO_3^- and H_2CO_3, which in turn controls $\delta^{13}C_{DIC}$ in isotopic equilibrium with soil CO_2.

$\delta^{13}C$ of Dissolved Inorganic Carbon in Surface Waters

Rivers and lakes fed by shallow groundwaters and runoff through soils will have DIC with $\delta^{13}C$ that has evolved under mostly open system conditions (Figure 6.12).

Subsequent exchange with atmospheric CO_2 ($P_{CO_2} = 10^{-3.4}$; $\delta^{13}C = -7.5‰$) will attenuate the P_{CO_2} in the water column and increase the $\delta^{13}C_{DIC}$. In lakes with residence times that exceed a few years, the $\delta^{13}C_{DIC}$ will approach an equilibrium value, which depends on pH and temperature.

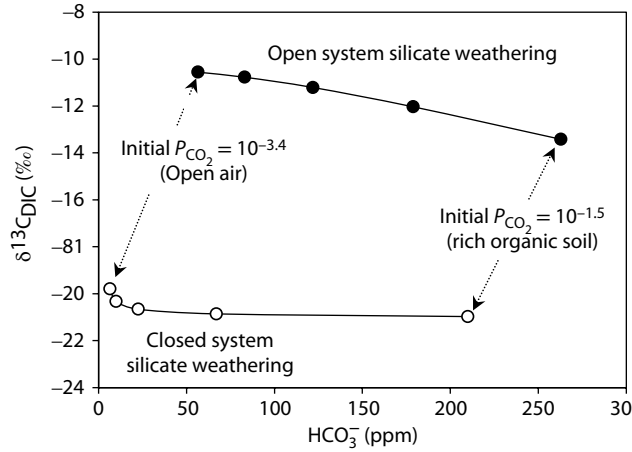

FIGURE 6.13 $\delta^{13}C$ of dissolved inorganic carbon during open and closed system silicate weathering, for $\delta^{13}C$ of soil CO_2 of –20‰ and at 10°C. Note that in both cases, the $\delta^{13}C$ value is controlled by equilibrium exchange with the soil CO_2 according to the enrichment factors, $\varepsilon^{13}C_{H_2CO_3-CO_2}$ and $\varepsilon^{13}C_{HCO_3^--CO_2}$.

Example 6.6: $\delta^{13}C$ of Surface Water Dissolved Inorganic Carbon in Equilibrium with Atmospheric CO_2

The $\delta^{13}C_{DIC}$ of surface water from Lake Ontario (T = 15°C, pH = 7, $m_{HCO_3^-}$ = 0.0008 mol/kg) was found to be –1‰. Is this due to exchange with atmospheric CO_2 or from DIC in the drainage from the watershed?

From Table 6.2, the enrichment factors for ^{13}C during $CO_{2(g)}$—DIC exchange are

$$\varepsilon^{13}C_{HCO_3^--CO_{2(g)}} = 9.1‰$$

$$\varepsilon^{13}C_{H_2CO_3-CO_{2(g)}} = -1.1‰$$

DIC speciation at pH 7 is

$$f_{HCO_3^-} = \frac{K_1}{K_1 + 10^{-pH}} = \frac{10^{-6.42}}{10^{-6.42} + 10^{-7}} = 0.79$$

$$f_{H_2CO_3} = 1 - f_{HCO_3^-} = 0.21$$

Substituting the molar fractions into the isotope mass balance equation:

$$\begin{aligned}\delta^{13}C_{DIC} &= f_{HCO_3^-}\left(\delta^{13}C_{CO_2} + \varepsilon^{13}C_{HCO_3^- - CO_2}\right) + f_{H_2CO_3}\left(\delta^{13}C_{CO_2} + \varepsilon^{13}C_{H_2CO_3 - CO_2}\right)\\ &= 0.79\,(-7.5 + 9.1) + 0.21\,(-7.5 - 1.1)\\ &= -0.5‰\end{aligned}$$

It would seem that exchange with atmospheric CO_2 is the main control on carbonate alkalinity.

The P_{CO_2} of the water is also very close to the atmospheric value ($10^{-3.4}$, using the calculations in Example 3.12), supporting the $\delta^{13}C$ data in concluding that CO_2 exchange with the atmosphere controls the alkalinity, rather than other processes, such as oxidation of DOC in the water column or excessive photosynthesis.

This is particularly important in rivers and springs, which are typically oversaturated with CO_2 compared with the atmosphere. The P_{CO_2} of rivers and springs is typically an order of magnitude or more above atmospheric P_{CO_2}. This engenders a rapid degassing, which favors ^{12}C and imparts an enrichment in ^{13}C in the DIC (Lee et al. 2013).

In rare situations, CO_2 underpressuring can occur. During periods of intense photosynthetic activity, algae and macrophytes in the water column consume more HCO_3^- than can be replenished by oxidation of organics or diffusion from the air. In such situations, the P_{CO_2} in the water column may be considerably lower than atmospheric equilibrium, and the DIC is highly depleted in ^{13}C due to kinetic effects of CO_2 diffusion from the air under nonequilibrium conditions.

Radiocarbon as a Tracer of Dissolved Inorganic Carbon

In addition to ^{13}C, radiocarbon can provide an additional constraint on the origin and evolution of DIC. The high activity of ^{14}C in the living biosphere is also present in soil CO_2. However, any material of geologic age (limestones, metamorphic CO_2, fossil fuel, bitumen, coal, etc.) will have long ago lost ^{14}C through radioactive decay (Table 6.1). Vegetation formed within the past 4 decades will have values greater than 100 pMC (up to ~150 pMC) due to contributions from atmospheric testing of thermonuclear weapons in the 1960s. Today, atmospheric CO_2 has ^{14}C contents close to 110 pMC. This adds an additional ^{14}C signature for the sources of DIC.

Considering the recharge scenarios for groundwaters in carbonate terrains presented earlier, ^{14}C provides a useful constraint on the origin of the DIC. In the case of open system recharge, the exchange of CO_2 between the DIC and soil atmosphere during carbonate weathering will impart the ^{14}C activity of the soil CO_2 on the DIC, maintaining $a^{14}C_{DIC}$ at 100 pMC or greater.

By contrast, groundwaters that dissolve carbonate under closed system conditions will derive a significant amount of DIC from ^{14}C-free sources. From Example 6.5, half of the DIC comes from subsurface calcite. Accordingly, DIC that evolved during closed system weathering today will have $a^{14}C_{DIC} \sim 50$ pMC. These systematics are discussed in Chapter 9 considering tracing fugitive gases, such as CO_2 and CH_4, from CO_2 sequestration and shale fracking activities.

Strontium Isotopes as Tracers of Weathering

The weathering of carbonate rocks and silicate rocks can be distinguished not only on the basis of DIC and its isotopes, but also by the use of strontium isotopes. As a divalent alkaline earth element, Sr^{2+} substitutes for Ca^{2+} in carbonates, sulfates, feldspars, and other rock-forming minerals. However, its $^{87}Sr/^{86}Sr$ ratio varies greatly based on the potassium content of the rock. Potassium-bearing rocks also contain the alkali element rubidium, Rb^+, which can substitute for K^+. The radioisotope ^{87}Rb decays to ^{87}Sr and over time enriches the $^{87}Sr/^{86}Sr$ ratio in K-bearing rocks.

$$^{87}Rb \rightarrow {}^{87}Sr + \beta^- \qquad T_{1/2} = 47.5 \text{ billion years}$$

The primordial $^{87}Sr/^{86}Sr$ ratio that existed at the time of nucleosynthesis some 5 billion years ago was 0.699, as derived from meteorites. Contributions from the decay of primordial ^{87}Rb have increased this ratio over the life of the earth. Alkaline rocks, such as granites with abundant potassium, K^+, will also have abundant Rb^+ and so will have greater $^{87}Sr/^{86}Sr$ ratios than will have more basic Ca^{2+} settings, such as basalts. In contrast, marine carbonates and seawater itself have relatively low $^{87}Sr/^{86}Sr$ ratios due to contributions from weathering of K-poor basalts along mid-oceanic ridges. The seawater $^{87}Sr/^{86}Sr$ curve through Phanerozoic time (Veizer 1989) is an important datum for tracing Sr and Ca in groundwaters, and is discussed in Chapter 9 as a tool for tracing sources of salinity.

Marine carbonates then have a $^{87}Sr/^{86}Sr$ ratio between about 0.707 and the modern seawater value of 0.709. In contrast, crystalline terrains are typically much more enriched, with $^{87}Sr/^{86}Sr$ ratios of 0.71 and higher. Accordingly, the $^{87}Sr/^{86}Sr$ of Sr^{2+} is a good indicator of the terrain through which groundwater has recharged and weathering took place (Figure 6.14).

WEATHERING AND ALKALINITY

The consumption of acidity during mineral weathering results in the production of alkalinity (alk)—a measure of the anions in water that can buffer pH during the addition of acid. As carbonic acid is the dominant weathering agent in most natural groundwaters, carbonate alkalinity is the principal buffering agent. Alkaline species, such as HCO_3^-, are capable of associating with H^+, providing an acid buffering capacity in water. This is important, for example, in mitigating acidification in waters that receive acid runoff or acid rain. The major anions that provide this acid-buffering

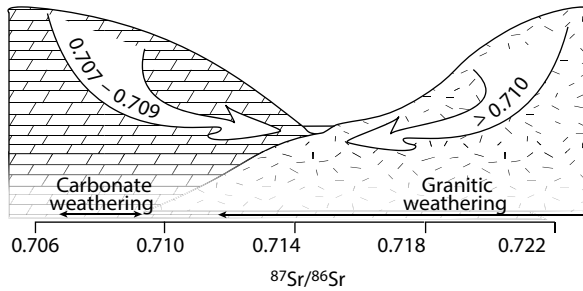

FIGURE 6.14 Strontium isotope ratios in groundwaters from weathering of carbonate terrain and crystalline (granitic) terrain.

capacity are HCO_3^- and CO_3^{2-}, with minor contributions in some groundwaters from dissociated weak acids, including hydrogen sulphide (HS^-), borate ($H_2BO_3^-$), silicate ($H_3SiO_4^-$), and even hydroxide (OH^-). In rare geochemical settings, the salts of some bases, such as the evaporite mineral nahcolite ($NaHCO_3$) or portlandite ($Ca[OH]_2$), provide considerable alkalinity.

Carbonate Alkalinity

Alkalinity is the sum of the concentrations of all acid-consuming species and is expressed in units of equivalents. At high pH, the anions of dissolved silica ($H_3SiO_4^-$) and boron ($H_2BO_3^-$) contribute to alkalinity. At neutral pH, HS^- will as well. For most waters, total alkalinity (alk_T) is represented by the following:

$$\text{Total alkalinity, } \text{alk}_T = m_{HCO_3^-} + 2m_{CO_3^{2-}} + m_{H_3SiO_4^-} + m_{HS^-} + m_{H_2BO_3^-} + m_{OH^-} - m_{H^+}$$

Carbonate alkalinity is the sum of the carbonate species alone:

$$\text{Carbonate alkalinity, } \text{alk}_C = m_{HCO_3^-} + 2m_{CO_3^{2-}}$$

As carbonic acid is consumed by weathering, the pH increases, as do the concentrations of HCO_3^- and CO_3^{2-}, the components of carbonate alkalinity. In most waters, the species that contributes the most to alkalinity is bicarbonate, by conversion to carbonic acid, H_2CO_3:

$$H_2CO_3 \Leftrightarrow HCO_3^- + H^+$$

In most waters, the carbonate alkalinity is very close to the total alkalinity due to the normally low concentration of the other alkaline species. However, measurements of total alkalinity should be corrected for the presence of other contributing species:

$$\text{alk}_C = \text{alk}_T - m_{H_3SiO_4^-} - m_{HS^-} - m_{H_2BO_3^-} - m_{OH^-}$$

Carbonate alkalinity is a component of DIC, and a measurement of either DIC or carbonate alkalinity can be used to determine the distribution of DIC species in waters below pH 9 (at higher pH CO_3^{2-} begins to contribute to alkalinity).

$$\text{DIC} = \text{alk}_C + m_{H_2CO_3}$$

Earlier, the carbonate species were shown to be measured as DIC, usually by acidification of the sample and measuring the liberated CO_2. Alkalinity provides a second method to measure the DIC species. This is done by titration with acid and measuring the pH response to determine the concentration of the alkaline species, HCO_3^- and CO_3^{2-}. Both DIC and alk_C measurements can be used with pH to calculate the distribution of DIC species. Alkalinity titrations are a routine analysis for the measurement of HCO_3^- (and CO_3^{2-} in high pH waters) that can be used in place of DIC measurements. They have the advantage of being easily done in the field, and are described in more detail in Chapter 10.

Example 6.7: Carbonate Alkalinity in Near-Neutral pH Waters

Determine the carbonate alkalinity and concentrations of DIC species for circumneutral karst spring water waters with the following geochemical composition:

Karst spring $T = 10°C$ pH = 7.95 alk_T = 1.92 meq/kg

	SO_4^{2-}	Cl^-	HS^-	Ca^{2+}	Mg^{2+}	Na^+	K^+	Si_{total}
ppm	6.2	4.6	1.2	35	2.8	4.3	0.18	2.8
mmol/kg	0.063	0.014	0.036	0.87	0.12	0.17	0.0046	0.10

The first step is to calculate the distribution of H_2CO_3, HCO_3^-, and CO_3^{2-}. In Example 3.10, this distribution was calculated from measured DIC and pH. Now, it is the measured carbonate alkalinity and pH that will provide the distribution of carbonate species.

In near-neutral pH, the only significant contributor to carbonate alkalinity is HCO_3^-. Recall from above that below pH 8.4, it is HCO_3^- and H_2CO_3 that contribute to DIC. CO_3^{2-} is of course present in these waters, but not at a concentration that contributes significantly to alkalinity or DIC. Even at very low concentration, CO_3^{2-} plays a key role in the solubility of carbonate minerals. Its activity can be determined from $m_{HCO_3^-}$, using K_2 and pH (Chapter 3), or here, using measured carbonate alkalinity. For ease of calculations, *a* and *m* are taken as equivalents. It is also important to use the dissociation constants, K_1 and K_2, for the field temperature (from Table 3.7).

$$\begin{aligned}\text{alk}_C &= \text{alk}_T - m_{HS^-} = 1.92 - 0.036 \\ &= 1.88 \text{ meq/kg}\end{aligned}$$

Using alkalinity formulas

$(\text{alk}_C = m_{HCO_3^-} + 2m_{CO_3^{2-}})$

$$m_{CO_3^{2-}} = \frac{\text{alk} \times K_2}{(2 \times K_2 + 10^{-\text{pH}})}$$

$$= \frac{0.00188 \times 10^{-10.49}}{2 \times 10^{-10.49} + 10^{-7.95}}$$

$$= 5.39 \times 10^{-6} \text{mol/kg}$$

$$= 0.065 \text{ ppm C}$$

$$m_{HCO_3^-} = \frac{\text{alk} \times 10^{-\text{pH}}}{(2 \times K_2 + 10^{-\text{pH}})}$$

$$= 0.00187 \text{ mol/kg}$$

$$= 22.4 \text{ ppm C}$$

Using dissociation equations

$(\text{alk}_C = m_{HCO_3^-})$

$$m_{CO_3^{2-}} = \frac{m_{HCO_3^-} \times K_2}{K_{H^+}}$$

$$= \frac{0.00188 \times 10^{-10.49}}{10^{-7.95}}$$

$$= 5.42 \times 10^{-6} \text{mol/kg}$$

$$= 0.065 \text{ ppm C}$$

$$m_{HCO_3^-} = \text{alk}_C$$

$$= 0.00188 \text{ mol/kg}$$

$$= 22.6 \text{ ppm C}$$

$$m_{H_2CO_3} = \frac{\text{alk} \times 2 \times 10^{-2\text{pH}}}{K_1(K_2 + 2 \times 10^{-\text{pH}})}$$

$$= \frac{0.00188 \times 2 \times 10^{-15.9}}{10^{-6.46}(10^{-10.49} + 2 \times 10^{-7.95})}$$

$$= 6.07 \times 10^{-5} \text{mol/kg}$$

$$= 0.73 \text{ ppm C}$$

$$m_{H_2CO_3} = \frac{m_{HCO_3^-} \times m_{H^+}}{K_1}$$

$$= \frac{0.00188 \times 10^{-7.95}}{10^{-6.46}}$$

$$= 6.08 \times 10^{-5} \text{mol/kg}$$

$$= 0.73 \text{ ppm C}$$

$$m_{DIC} = m_{H_2CO_3} + m_{HCO_3^-} + m_{CO_3^{2-}}$$

$$= 0.00194 \text{ mol/kg}$$

$$= 23.2 \text{ ppm C}$$

$$m_{DIC} = m_{H_2CO_3} + m_{HCO_3^-} + m_{CO_3^{2-}}$$

$$= 0.00195$$

$$= 23.4 \text{ ppm C}$$

Either calculation gives acceptably similar results. For this groundwater with high pH and alkalinity, it is bicarbonate that dominates the DIC. The error in using the simplification that $\text{alk}_C = m_{HCO_3^-}$ is negligible, but becomes greater for higher pH waters, where $m_{CO_3^{2-}}$ becomes a significant component of alk_C.

Alkalinity in High pH Waters

Recall that HS^- contributes to alkalinity in neutral pH waters, while $H_2BO_3^-$, $H_3SiO_4^-$, and CO_3^{2-} contribute in higher (>9) pH waters. In hyperalkaline waters (pH > 10), hydroxide (OH^-) becomes an important contributor to alkalinity. The Ahouset geothermal spring provides a good example to illustrate total alkalinity and carbonate alkalinity in high pH waters.

Example 6.8: Carbonate Alkalinity in High pH Waters

Calculate total alkalinity and carbonate alkalinity for the high-pH Ahouset geothermal waters.

The geochemistry of these thermal waters is given above in Example 6.4 as an example of silicate weathering. The unusually high pH of 10.05 is close to 10.33, where CO_3^{2-} and HCO_3^- have the same activity, and so the DIC must include a significant component of CO_3^{2-}. Further, the pH is greater than the first dissociation constant for silicic acid (pH 9.83, Table 2.1), and so most of the dissolved silica is in the form of the anion $H_3SiO_4^-$. Another potential contribution to alkalinity at this high pH will be hydroxide, OH^-, which has an activity of $10^{-(14-pH)}$, thus $10^{-3.95}$ or 0.000112. As there is no measured $H_2BO_3^-$ or HS^-, their contributions must be considered negligible.

The measured titration curve is shown in Figure 6.15. Also shown are titration curves calculated for individual acid-buffering species. These, of course, cannot be individually measured, and are plotted here to show the relative contribution of each species to total alkalinity. The total alkalinity titration curve includes two steep sections, near pH 10 and between pH 6 and 7, which represent maxima in buffering potential. Buffering near pH 10 occurs as CO_3^{2-} consumes H^+ by conversion to HCO_3^-. However, at this high pH, both $H_3SiO_4^-$ and OH^- will contribute to buffering:

$$CO_3^{2-} + H^+ \rightarrow HCO_3^- \qquad \text{maximum at pH 10.33}$$
$$H_3SiO_4^- + H^+ \rightarrow H_4SiO_4 \qquad \text{maximum at pH 9.83}$$
$$OH^- + H^+ \rightarrow H_2O \qquad \text{increases above pH 10}$$

The titration curve flattens through an unbuffered zone near pH 8, at which point the three reactions above are essentially complete and no H^+-consuming reactions occur. Below pH 8, buffering increases as HCO_3^- takes up H^+ through conversion to H_2CO_3:

$$HCO_3^- + H^+ \rightarrow H_2CO_3 \qquad \text{maximum at pH 6.4}$$

The titration end point for total alkalinity is found at the inflection point near pH 4.5, where HCO_3^- buffering is complete. Total alkalinity is determined from the amount of acid added at this point. Total alkalinity is calculated as follows:

$$\text{alk}_T\,(\text{eq/kg}) = \frac{V_{\text{acid}}\ (\text{mL}) \times N_{\text{acid}}\ (\text{eq/kg})}{V_{\text{sample}}\ (\text{mL})}$$
$$= \frac{0.052 \times 1.6}{100}$$
$$= 0.00083 \text{ eq/kg or } 0.83 \text{ meq/kg}$$

Total carbonate alkalinity is determined by correcting total alkalinity for $H_3SiO_4^-$ and OH^-. The concentration of $H_3SiO_4^-$ at pH 10.05 is calculated by rearranging

the Si mass balance equation and substituting it into the silicic acid dissociation equation:

Silica alkalinity: Total Si $= 3 \times 10^{-4}$ mol/kg $= m_{H_3SiO_4^-} + m_{H_4SiO_4}$

$$K_{H_4SiO_4} = 10^{-9.83} = 1.48 \times 10^{-10} = \frac{a_{H_3SiO_4^-} \times a_{H^+}}{a_{H_4SiO_4}}$$

$$a_{H^+} = 10^{-10.05} = 8.91 \times 10^{-11}$$

at low ionic strength $a \approx m$, through substitution and rearrangement:

$$m_{H_3SiO_4} = \frac{K_{H_4SiO_4}\left(m_{Si-total}\right)}{K_{H_4SiO_4} + 10^{-pH}} = \frac{1.48 \times 10^{-10} \times \left(3 \times 10^{-4}\right)}{1.48 \times 10^{-10} + 10^{-10.05}}$$
$$= 0.00019 \text{ eq/kg}$$

Hydroxide alkalinity: $m_{OH^-} = 10^{-(14-pH)}$
$= 10^{-3.95}$mol/kg
$= 0.00011$ eq/kg

Carbonate alkalinity: $\text{alk}_C = m_{HCO_3^-} + 2m_{CO_3^{2-}}$
$= \text{alk}_T - m_{H_3SiO_4^-} - m_{OH^-}$
$= 0.00083 - 0.00019 - 0.00011$
$= 0.00053$ eq/kg

The distribution of carbonate species are calculated from pH and alkalinity using their temperature-dependent dissociation constants.

$$m_{H_2CO_3} = \frac{\text{alk}_C \times 10^{-2pH}}{K_1(2 \times K_2 + 10^{-pH})} \qquad m_{HCO_3^-} = \frac{\text{alk}_C \times 10^{-pH}}{2 \times K_2 + 10^{-pH}} \qquad m_{CO_3^{2-}} = \frac{\text{alk}_C \times K_2}{2 \times K_2 + 10^{-pH}}$$

$$= \frac{0.00053 \times 10^{-20.10}}{10^{-6.35}(2 \times 10^{-10.33} + 10^{-10.05})} \qquad = \frac{0.00053 \times 10^{-10.05}}{2 \times 10^{-10.33} + 10^{-10.05}} \qquad = \frac{0.00053 \times 10^{-10.33}}{2 \times 10^{-10.33} + 10^{-10.05}}$$

$= 5.16 \times 10^{-8}$mol/kg $= 0.000259$ mol/kg $= 0.000136$ mol/kg

$= 0.0004$ ppm C $= 3.10$ ppm C $= 1.63$ ppm C

$$m_{DIC} = m_{H_2CO_3} + m_{HCO_3^-} + m_{CO_3^{2-}}$$
$$= 0.0004 + 3.10 + 1.63$$
$$= 4.73 \text{ ppm}$$

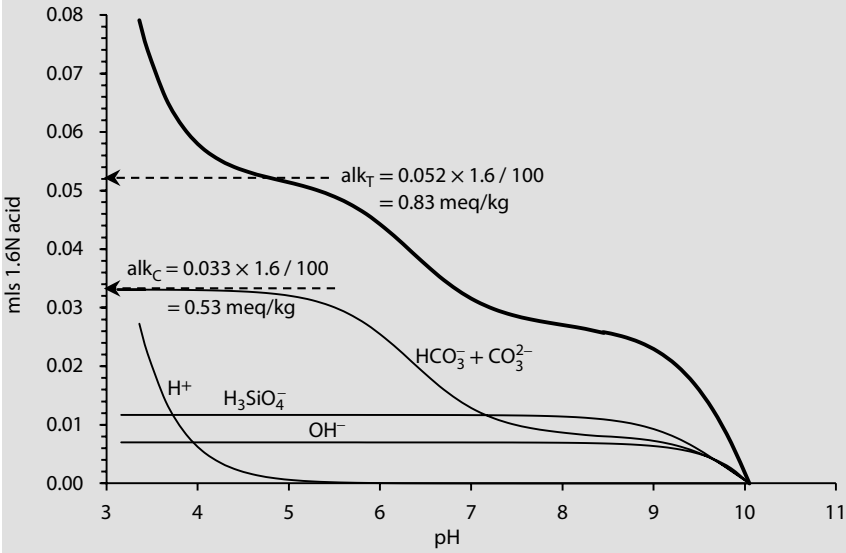

FIGURE 6.15 Alkalinity titration curve for a sample of water from the Ahouset geothermal spring in western Canada ($T = 23°C$, pH 10.05). Alkalinity titrations are discussed in Chapter 10. A 100 mL sample was titrated with 1.6 N sulfuric acid. The total alkalinity titration curve can be seen to be a composite of curves for all acid-buffering species. This water has 0.83 meq/kg total alkalinity.

Most alkalinity titrations are much simpler than this example because the pH of most natural waters is below pH 8.5. In neutral pH waters, HCO_3^- is the only significant alkaline species. There is no contribution from CO_3^{2-}, or from B or Si anions, and only dissolved sulfide, HS^-, may contribute to alkalinity (Figure 3.1).

P_{CO_2} and Alkalinity

The relationship between P_{CO_2} and DIC, discussed in Chapter 2, relates to carbonate alkalinity through the distribution of DIC species. As groundwater below the water

Example 6.9: Calculating P_{CO_2} from pH and Carbonate Alkalinity

What is the P_{CO_2} for the karst water sample in Example 6.7?

The P_{CO_2} can be calculated either from the carbonic acid concentration with pH or directly from alkalinity and pH if carbonic acid has not yet been calculated. Using carbonic acid, H_2CO_3, P_{CO_2} is calculated directly from the Henry's Law constant for CO_2 solubility. Using only alkalinity and pH, a general equation can be used. The results are essentially identical:

Karst spring : $T = 10°C$, pH = 7.95, $alk_C = 1.88$ meq/kg $(0.00188$ eq/kg$)$,
$m_{H_2CO_3} = 6.07 \times 10^{-5}$ mol/kg

$$P_{CO_2} = \frac{alk \times 10^{-2pH}}{K_1(K_2 + 10^{-pH}) \times K_{CO_2}} \qquad K_{CO_2} = \frac{a_{H_2CO_3}}{P_{CO_2}}$$

$$= \frac{0.00188 \times 10^{-15.9}}{10^{-6.46} \times (10^{-10.49} + 10^{-7.95}) \times 10^{-1.19}} \qquad P_{CO_2} = \frac{6.07 \times 10^{-5}}{10^{-1.19}}$$

$= 0.00094$ atm $\qquad = 0.00094$ atm

$\log P_{CO_2} = -3.03 \qquad \log P_{CO_2} = -3.03$

For this karst spring water, closed system carbonate weathering has lowered the P_{CO_2} to $10^{-3.02}$ from an initially higher value gained during recharge through soil (P_{CO_2} typically between $10^{-2.5}$ and $10^{-1.5}$).

table (i.e., with no additional CO_2) consumes carbonic acid through mineral weathering, P_{CO_2} drops and carbonate alkalinity increases. Alkalinity measurements are often made instead of DIC measurements to determine DIC species, and can be used in calculations of P_{CO_2} and calcite saturation.

Extreme Alkalinity: High pH versus High P_{CO_2}—a Tale of Two Travertines

The following two case studies are remarkably different examples of extremely high alkalinity in natural groundwaters. The groundwaters in these two different settings have almost identical alkalinities of 40 meq/kg. They are also both rapidly depositing extensive formations of calcite travertine. However, the origin of these two waters and their geochemistry could not be more different. The differentiating feature of these two systems is their P_{CO_2}.

I—the hyperalkaline groundwaters of Maqarin, Jordan (Khoury et al. 1992; Clark et al. 1993). Unusual groundwaters discharge in northern Jordan with a pH of 12.5. They flow from a metamorphic zone where bituminous limestone had spontaneously combusted during the Pleistocene, similar to burning coal seams. This natural combustion calcined the calcite at some 1000°C, producing minerals found in cement clinker, including Ca and Si oxides. Groundwaters recirculating through these zones hydrate the oxides to soluble alkaline minerals, such as portlandite ($Ca[OH]_2$) ($K = 10^{-5.19}$), becoming calcium hydroxide waters, Ca^{2+}–OH^-, with an equilibrium pH of 12.5.

$$CaCO_3 \rightarrow CaO + CO_2$$
$$CaO + H_2O \rightarrow Ca(OH)_2$$
$$Ca(OH)_2 \rightarrow Ca^{2+} + 2\,OH^- \qquad K_{Ca(OH)_2} = 10^{-5.19} = a_{Ca^{2+}} \times a^2_{OH^-}$$
$$a_{Ca^{2+}} \cong \tfrac{1}{2} a_{OH^-}$$
$$10^{-5.19} = \tfrac{1}{2} a_{OH^-} \times a^2_{OH^-} = \tfrac{1}{2} a^3_{OH^-}$$
$$a_{OH^-} = 10^{-1.63}$$
$$pH = 14 - 1.63 = 12.4$$

The springs discharge along seepage faces and into adits excavated for the Jordanian–Syrian Dam on the Yarmouk River, forming extensive travertines, stalactites, and stalagmites over periods of months rather than the thousands of years typically required for speleothem growth (Figure 6.16).

The geochemical analysis for this water is

Maqarin hyperalkaline spring water				***T* = 25°C**		**pH = 12.5**		**alk_T = 39.5 meq/kg**	
	OH^-	**SO_4^{2-}**	**Cl^-**	**CO_3^{2-}**	**Ca^{2+}**	**Mg^{2+}**	**Na^+**	**K^+**	**H_4SiO_4**
ppm	537	1670	6.6	1.2	1120	<0.2	193	770	<0.01
mmol/kg	39.5	17.4	1.29	0.02	27.9	<0.01	8.39	19.7	<0.001

In this case, the carbonate alkalinity (0.04 meq/kg) is too low to be measured by alkalinity titration, and was measured by acidification under vacuum during extraction for $\delta^{13}C_{DIC}$ analysis. No significant HCO_3^- is present at the pH.

FIGURE 6.16 The Maqarin, Jordan, hyperalkaline spring travertine. Uptake of atmospheric CO_2 by these Ca-OH waters causes $CaCO_3$ supersaturation and formation of travertine. Inset shows meter-tall stalagmites growing from drips of these hyperalkaline groundwaters in the roof of this adit.

$$m_{CO_3^{2-}} = 2\times10^{-5}\,\text{mol/kg}$$

$$\text{alk}_C = 2\times m_{CO_3^{2-}} = 0.04\ \text{meq/kg or}\ 4\times10^{-5}\,\text{eq/kg}$$

$$m_{HCO_3^-} = \frac{m_{CO_3^{2-}}\times10^{-\text{pH}}}{K_2} = \frac{2\times10^{-5}\times10^{-12.5}}{10^{-10.32}} = 1.32\times10^{-7}$$

$$m_{H_2CO_3} = \frac{m_{HCO_3^-}\times10^{-\text{pH}}}{K_1} = \frac{1.32\times10^{-7}\times10^{-12.5}}{10^{-6.34}} = 9.14\times10^{-14}$$

$$P_{CO_2} = \frac{a_{H_2CO_3}}{K_{CO_2}} = \frac{9.14\times10^{-14}}{10^{-1.48}}$$

$$= 2.76\times10^{-12} = 10^{-11.56}$$

$$\log P_{CO_2} = -11.56$$

Note that the measured alkalinity of this water is extremely high (39.5 meq/kg), while the carbonate alkalinity (0.02 meq/kg) is extremely low. This is entirely due to hydroxide (OH^-), which is responsible for the high pH. The carbonate alkalinity is very low due to calcite saturation (note the high Ca^{2+} activity). In this pH range, DIC consists of only CO_3^{2-}. With the high Ca^{2+} from $Ca(OH)_2$ dissolution in the subsurface, calcite saturation at high pH is readily attained with low DIC.

When these waters discharge at the surface, their P_{CO_2} ($10^{-11.56}$) is far from equilibrium with the P_{CO_2} of the open atmosphere ($10^{-3.40}$), which is almost 1 billion times greater. This provokes a rapid uptake of atmospheric CO_2, which is quickly converted to CO_3^{2-}. Calcite becomes highly supersaturated and rapidly precipitates, forming extensive travertine according to the following reaction:

$$Ca^{2+} + 2OH^- + CO_{2(atm)} \rightarrow CaCO_3 + H_2O$$

The result is the rapid precipitation of calcite on the seepage faces where these springs discharge and on the ceiling and floors of the adits where they intersect the metamorphosed zones.

The $\delta^{13}C$ of this travertine is also very unusual. Measurements show that the calcite has $\delta^{13}C < -25‰$. Equilibrium with atmospheric CO_2 should normally produce calcite with $\delta^{13}C$ according to the following equation:

$$\delta^{13}C_{\text{calcite}} = \delta^{13}C_{CO_2(atm)} + \varepsilon^{13}C_{CaCO_3-CO_2}$$

$$= -7.5 + 10.4$$

$$= +2.9‰$$

Such depletions are rarely observed in travertines, and are attributed to kinetic effects during the reaction of $CO_{2(aq)}$ with OH^- in hyperalkaline $Ca–OH^-$ waters (Clark et al. 1992). Under such circumstances, the formation of $^{12}C–O$ bonds requires less energy and so are favored over $^{13}C–O$ bonds when there is no back-reaction (a requirement of equilibrium).

II—The Taweh hot springs from the Mount Edziza volcanic complex (Clark et al. 1989). Like the Maqarin high-pH groundwaters, the Taweh groundwaters have a very high alkalinity of 40.2 meq/kg. However, with the low pH of only 6.59, their alkalinity is essentially from bicarbonate. They discharge on the flank of a recently active (Holocene) volcano, where the hot magma at depth is decomposing limestone to wollastonite and producing metamorphic CO_2 according to:

$$CaCO_{3\,\text{calcite}} + SiO_{2\,\text{quartz}} \rightarrow CaSiO_{3\,\text{wollastonite}} + CO_2$$

The springs are spectacular, with river-sculpted, ochre and green algae-colored formations (Figure 6.9) and football fields of travertine draping hill slopes. This is commonly observed in tectonically active areas. The geochemical analysis for this water is as follows:

Taweh hot spring, Mount Edziza, British Clumbia			T = 45.9°C		pH = 6.59		alk_T = 40.2 meq/kg	
	HCO_3^-	SO_4^{2-}	Cl^-	Na^+	K^+	Ca^{2+}	Mg^{2+}	H_4SiO_4
ppm	2455	1.78	61.2	529	62	171	136	230
mmol/kg	40.2	0.02	1.72	23.0	1.59	4.27	5.60	3.83

Given the low pH of 6.59, the only two DIC species of significance are HCO_3^- and H_2CO_3 (Figure 3.13). Bicarbonate can be considered equal to total alkalinity, as there are no other contributors at this low pH. Carbonic acid and P_{CO_2} are calculated using the temperature equations for K_1 and K_{CO_2} in Table 3.7. While the more complex alkalinity formulas used in Example 6.9 can be applied here, the low pH allows direct calculation from the carbonic acid dissociation and CO_2 dissolution equations:

$$m_{HCO_3^-} = \text{alk}_C = 40.2 \text{ meq/kg}$$

$$K_1 = \frac{a_{HCO_3^-} \times a_{H^+}}{a_{H_2CO_3}} \approx \frac{m_{HCO_3^-} \times m_{H^+}}{m_{H_2CO_3}}$$

$$m_{H_2CO_3} = \frac{m_{HCO_3^-} \times m_{H^+}}{K_1} = \frac{0.0402 \times 10^{-6.59}}{10^{-6.26}}$$

$$= 0.0188 \text{ mol/kg} = 18.8 \text{ meq/kg}$$

$$P_{CO_2} = \frac{a_{H_2CO_3}}{K_{CO_2}} = \frac{0.0188}{10^{-1.69}}$$

$$= 0.94 = 10^{-0.03}$$

$$\log P_{CO_2} = -0.03$$

In this case, the high carbonate alkalinity and the low pH place the DIC speciation close to the carbonic acid field, resulting in a P_{CO_2} value that is close to 1 atmosphere pressure. In fact, these springs are bubbling gas, which is 95% CO_2 (inset in Figure 6.17). Although the high P_{CO_2} and low pH are the inverse of the Jordan hyperalkaline groundwaters, the Edziza thermal waters are also oversaturated with respect to calcite. In this case, calcite supersaturation is due to CO_2 degassing. As the P_{CO_2} is 2500 times greater than the atmospheric value of $10^{-3.4}$, CO_2 rapidly bubbles

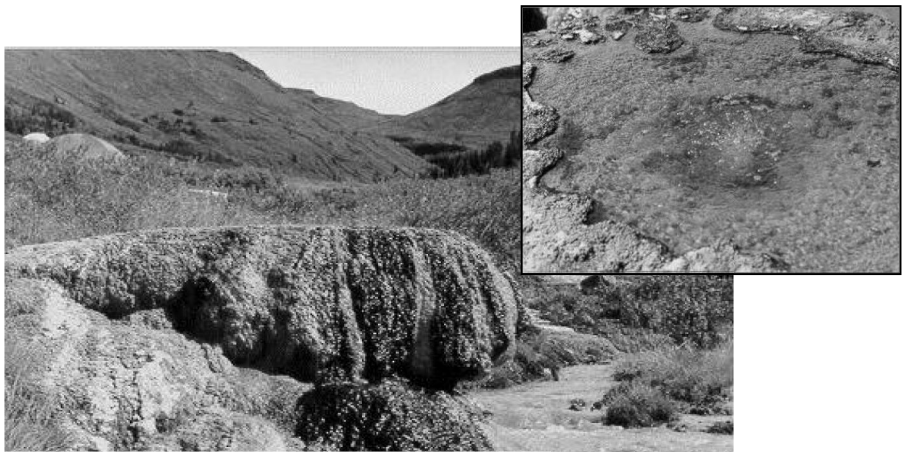

FIGURE 6.17 The Taweh hotspring at Mount Edziza, British Columbia, where CO_2 degassing at spring vent (inset photo) causes calcite to precipitate from these Ca-HCO_3 waters, forming the extensive travertine.

out following discharge. This lowers the carbonic acid concentration and raises the pH according to the following reaction:

$$HCO_3^- + H^+ \rightarrow H_2CO_3 \rightarrow CO_2\uparrow + H_2O$$

DIC speciation shifts out of the carbonic acid field and into the bicarbonate and carbonate fields, increasing $a_{CO_3^{2-}}$ and calcite saturation. This follows the overall reaction:

$$Ca^{2+} + 2HCO_3^- \rightarrow CO_2\uparrow + H_2O + Ca^{2+} + CO_3^{2-} \rightarrow CO_2\uparrow + H_2O + CaCO_3$$

The DIC in these waters is very high:

$$\begin{aligned} DIC &= m_{HCO_3^-} + m_{H_2CO_3} \\ &= 40.2 + 18.8 \\ &= 59.0 \text{ meq/kg or } 708 \text{ ppm C} \end{aligned}$$

This accounts for the extensive travertine forming at this site. While the alkalinity at Edziza is essentially the same as at Maqarin (40 meq/kg), their DIC values are remarkably different, with only 0.24 ppm C for the high pH groundwaters in Jordan. Like the Jordan hyperalkaline waters, the thermal waters are rapidly precipitating travertine, although it is due to CO_2 outgassing rather than uptake of atmospheric CO_2.

The $\delta^{13}C$ of the DIC from the Taweh hot spring, measured to be –1.2‰, is diagnostic of its origin. This value is in the range for marine limestone. Mantle-derived CO_2 associated with many volcanoes usually has $\delta^{13}C$ values in the range of –7‰. In this case, the higher $\delta^{13}C$ value, combined with the high overpressuring of CO_2, indicates subsurface decarbonation of marine limestones through contact metamorphism. The DIC in these waters is also ^{14}C-free.

The result is a carbonic acid solution with high P_{CO_2} capable of extensive mineral weathering during its migration to surface. The weathering potential of this carbonic acid solution is evident in the geochemistry shown earlier, with high base cations (Ca^{2+}, Mg^{2+}, Na^{+}, K^{+}) and silica from extensive weathering.

ADVANCED CHEMICAL WEATHERING: SAPROLITES AND LATERITES

Terrestrial landscapes are dominated by silicate and aluminosilicate minerals, from the metamorphic shield terrains at the core of the continents to the extensive flood basalts and plutonic rocks in igneous terrains. Continental-scale weathering of feldspar in silicate landscapes is the primary sink for atmospheric CO_2 on geological time scales, as observed for the alteration of anorthite and alkali feldspars to clay:

$$CaAl_2Si_2O_{8\,\text{anorthite}} + H_2O + 2H_2CO_3 \rightarrow Ca^{2+} + 2HCO_3^- + Al_2Si_2O_5(OH)_{4\,\text{kaolinite}}$$

However, silicate weathering does not necessarily stop at this point, as weathering under humid tropical climates leads to further leaching of silica. The result is the formation of highly insoluble aluminum hydroxide, gibbsite.

$$Al_2Si_2O_5(OH)_{4\,\text{kaolinite}} + 7H_2O \rightarrow 2Al(OH)_{3\,\text{gibbsite}} + H^+ + 2H_4SiO_4^\circ$$

Extensive weathering of ferromagnesian minerals, such as pyroxene, leads to the formation of iron hydroxide:

$$Fe_2Si_2O_{6\,\text{pyroxene}} + 2H_2O + 4H_2CO_3 \rightarrow 2Fe^{2+} + 4HCO_3^- + 2H_4SiO_4^\circ$$
$$2Fe^{2+} + \tfrac{1}{2}O_2 + 5H_2O \rightarrow 2Fe(OH)_{3\,\text{ferrihydrite}} + 4H^+$$

Such alteration of feldspars and mineral dissolution weathers silicate bedrock to a residual mantle of saprolite—the clay and iron hydroxide weathering products. Saprolites are typically found in lower-latitude regions with substantial seasonal precipitation, which favors growth of vegetation and high soil P_{CO_2}.

From the weathering reactions mentioned previously, the groundwaters typically draining these profiles carry a Ca^{2+}–HCO_3^- to Na^{+}–HCO_3^- facies (K^{+} from orthoclase feldspar weathering is preferentially exchanged onto clays) with dissolved silica. The weathering of the Deccan Trap basalts in western and northern India is a good example. These basalts date to the late Cretaceous, and their impact on the global environment has been suggested to have contributed to the Cretaceous-Tertiary mass extinction event (Self et al. 2006). Extensive weathering over millions of years in the monsoon climate of western India has produced deep accumulations of laterites overlying the flood basalts.

The major oxide geochemistry of the basalts is presented in the column chart in Figure 6.18, showing the basalts to be dominated by the calcic aluminosilicate feldspars (Si and Al with Ca) with significant ferromagnesian minerals (Fe and Mg). However, the drainage from weathering of these formations has a Ca-HCO_3 geochemical facies, with high dissolved Si and the soluble base cations (Ca^{2+}, Mg^{2+},

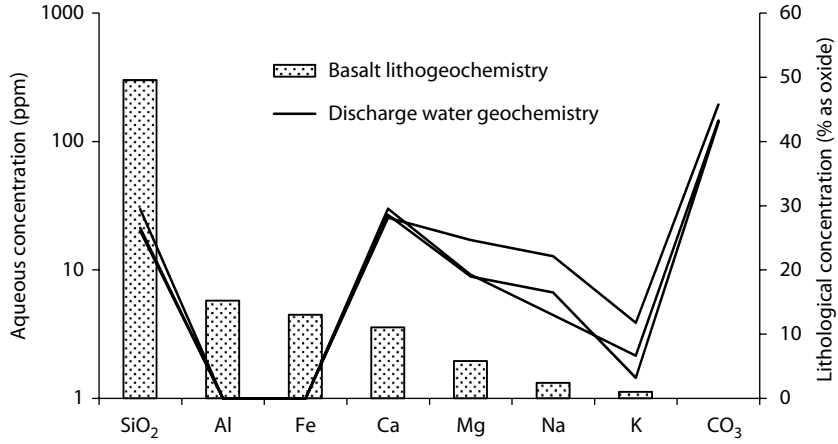

FIGURE 6.18 Geochemistry of drainage from laterite development on basalt, from the Deccan Traps volcanics in the Western Ghats of India. Lithogeochemistry of the basalts is from Cox and Hawkesworth (1985), and aqueous geochemistry of discharge waters from the region is from Das et al. (2005).

Na^+, and K^+). The high bicarbonate concentration is generated by the open system weathering of the basalts with carbonic acid incorporated from these tropical soils with high P_{CO_2}. Neither Fe nor Al is significant in drainage from these rocks, due to the very low solubility of Fe and Al hydroxides, as shown in Chapter 3.

Given extensive time and little mechanical erosion characteristic of the highly vegetated landscape, the leaching of base cations and silica enriches the regolith in iron and aluminum hydroxides. Under the seasonal monsoon climate with an extensive dry season, these hydroxides stabilize to oxides and oxi-hydroxides. Thus, the mineralogy of these laterite formations is dominated by iron oxides and hydroxides including ferrihydrite ($Fe[OH]_3$), goethite (FeOOH), hematite (Fe_2O_3) with bauxite ores of gibbsite ($Al[OH]_3$), and diaspora (AlOOH).

The extensive weathering of bedrock, typified by the Deccan basalts in Figure 6.18, then preferentially removes silica due to its higher solubility compared with iron and aluminum. This is shown in Figure 6.19, where the solubility of the principle controlling phases for Si, Fe, and Al are shown over the pH range of most natural waters. Over millions of years of weathering, laterites become increasingly dominated by Fe and Al oxy-hydroxide minerals. Given that the solubility of gibbsite is even lower than ferric iron hydroxide, over time the aluminum-to-iron ratio in laterites increases, generating bauxite ore suitable for aluminum smelting.

The high iron content of many tropical laterites, or ferricretes that often cap plateaux as mesa landscapes, are considered to also have a redox step in their formation, implying that the iron is not all generated by relative enrichment by leaching of silicates. Rather, regional additions by transport as ferrous iron under reducing conditions are thought to add iron to such profiles (Brown et al. 2003). This is an important consideration in the studies of landscape evolution where the accumulated ferric oxy-hydroxides are used as a measure of chemical weathering.

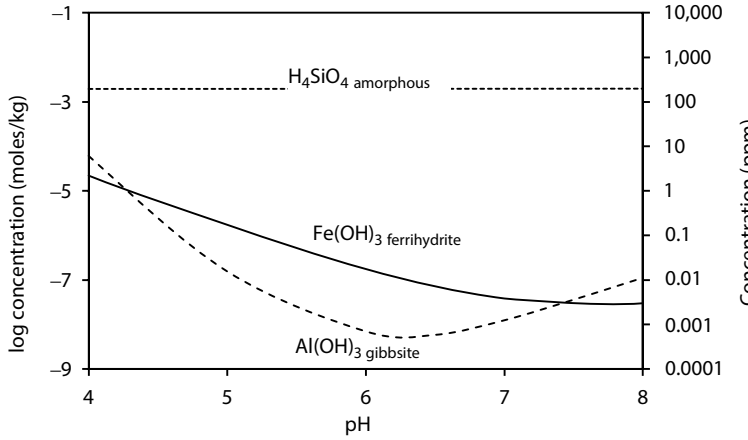

FIGURE 6.19 Solubility of the three most abundant elements of silicate rocks (after oxygen). The higher solubility of silica from feldspar and clay weathering removes this from the accumulating saprolite, leaving behind the highly insoluble ferric iron and aluminum hydroxides as laterite formations capping the weathered igneous and metamorphic parent rocks.

PROBLEMS

1. What are the activities of dissolved carbonate, $a_{CO_3^{2-}}$, and carbonic acid, $a_{H_2CO_3}$, for 25°C water with pH 7.8 and bicarbonate concentration of 86 ppm as HCO_3^-? Assume that the bicarbonate activity is equal to its molality. How much do they contribute to DIC?
2. A shallow groundwater has a pH of 6.4 and a measured carbonate alkalinity of 1 meq/kg. What are the activities of the DIC species, and what is the P_{CO_2} of this water? As there are no other solute concentrations given to calculate I, it can be assumed that activities = concentrations.
3. What is the pH of a groundwater in equilibrium with a soil atmosphere that has $P_{CO_2} = 10^{-1.8}$? The groundwater temperature is 25°C. Determine the distribution of carbonate species (i.e., $m_{H_2CO_3}$, $m_{HCO_3^-}$ and $m_{CO_3^{2-}}$).
4. Account for the ~8‰ depletion in $\delta^{13}C$ of atmospheric CO_2 in comparison with marine DIC.
5. Determine the pH of soil water (25°C) in equilibrium with a soil air having P_{CO_2} of $10^{-1.75}$.
6. The soil air in Problem 5 has a $\delta^{13}C$ value of –23‰ VPDB. What will be the $\delta^{13}C$ of DIC in soil water?
7. How many parts per million calcite (ppm $CaCO_3$) will be dissolved during open system weathering of limestone in a soil with $P_{CO_2} = 10^{-2}$, and what is the final pH? Assume activities equal molalities.
8. How much calcite can be dissolved under closed system conditions with an initial P_{CO_2} of $10^{-1.5}$?
9. The Ahouset spring waters in Example 6.5 are a good case study for the non-carbonate contributions to alkalinity. The alkalinity titration in Figure 6.15, after correction for OH^- and $H_3SiO_4^-$, provides total carbonate alkalinity,

which includes both HCO_3^- and CO_3^{2-}. From this titration, calculate the concentration of CO_3^{2-}. Using CO_3^{2-} *activity*, what would be the concentration of Ca^{2+} for calcite equilibrium?

10. What is the P_{CO_2} of the Ahouset spring water? Will this water degas CO_2 upon discharge?
11. Calculate the $\delta^{13}C$ of the $CO_{2(g)}$ in equilibrium with a lake whose DIC (2.1 ppm) has a $\delta^{13}C = -1.5‰$ and a pH of 6.8 at 15°C. Determine the appropriate enrichment factors from equations in Table 6.2 (or Table 4.2). What is a likely source of this CO_2?
12. The DIC sample from the spring in Problem 2 has a measured $\delta^{13}C$ value of –19.5‰ VPDB. What would be the $\delta^{13}C$ value for a $CO_{2(g)}$ gas phase in equilibrium with this water?
13. The high pH groundwaters from Maqarin have no detectable Mg^{2+}. Determine the solubility constant for brucite ($Mg[OH]_2$) and calculate the equilibrium concentration of Mg^{2+} at this pH.
14. Calculate the calcite saturation indices for the Maqarin and the Mount Edziza spring waters from Example 6.10.
15. Describe, with relevant reactions, how recharge waters in soil developed on basalt bedrock can precipitate calcite. Note that basalts are mafic rocks dominated by calcium-rich feldspars (anorthite).
16. These three wells were installed along a flow system in a confined basalt aquifer. In the outcrop region, the soil P_{CO_2} was measured at $10^{-1.6}$ with $\delta^{13}C_{CO_2} = -23‰$. The DOC in BC1 was identified as humic and fulvic acids with $\delta^{13}C_{CH_2O} = -26‰$. Concentrations are in ppm.
    a. Calculate the P_{CO_2} for each well and compare with the recharge area. Is this open or closed system weathering? Explain the trends for Ca^{2+} and Na^+.
    b. Write out the likely weathering reactions along the flow path.
    c. Write out any reactions involved in the evolution of redox along the flow path.
    d. Do a mass balance calculation for the total of DIC and DOC to account for their changes along the flow path. Explain the evolution of $\delta^{13}C_{DIC}$.

	ED1	ED2	ED3
pH	6.8	7.8	8.8
T	10	15	18
Ca^{2+}	6.8	8.8	10.1
Mg^{2+}	1.1	1.3	1.3
Na^+	5.3	7.3	8.6
K^+	1.2	1.6	1.7
SiO_2	12.5	18.1	21.7
HCO_3^-	23.9	41.1	51.2
SO_4^{2-}	12.8	6	0.1
HS^-	0	2.3	4.4
Cl^-	1.2	1.4	1.3
DOC (ppm C)	3.2	1.5	0
$\delta^{13}C_{DIC}$	–15.8	–17.9	–19.2

17. The following analyses (in ppm) were made for groundwater sampled from successively greater depths in a carbonate aquifer overlain by tundra vegetation. The soil has $P_{CO_2} = 10^{-1.8}$ but is saturated at a shallow depth. The DOC was identified as soil-derived humic material. Write out a series of equations to describe the evolution of the carbonate system in this aquifer. How does calcite saturation and the P_{CO_2} of this system evolve? Account for the evolution in $\delta^{13}C$ in these groundwaters. What would you predict for the $\delta^{13}C$ of the methane observed in these groundwaters?

	FR1	FR2	FR3	FR4
pH	8.05	7.85	7.50	7.42
T	5.1	5.1	5.1	5.1
Eh (mV)	325	–175	–213	–207
Ca^{2+}	31	48	61	68
Mg^{2+}	1.9	1.8	2.1	1.7
Na^{+}	2.4	3.2	1.8	2.9
HCO_3^-	108	163	199	223
SO_4^{2-}	<0.5	<0.5	<0.5	<0.5
Cl^-	3	2	4	3
DOC (ppm C)	44	28	12	2
CH_4	0	21	43	56
$\delta^{13}C_{DIC}$	–13.7	–2.1	3.1	5.2

18. Weathering experiment. Select two rock types: granite and limestone. Crush the granite to powder and the limestone to sand-sized granules and weigh out 50 g each. Add 400 mL distilled water to a 500 mL volumetric flask. Bubble a gas mixture of 5% CO_2 in air through each of the flasks, and record the stable pH. Now add the measured amounts of crushed rock to each flask, allowing the gas supply in each to mix the water and sediment in the flask. Record pH and take water samples with a syringe and plastic tubing on the following schedule: 1 minute, 5 minutes, 15 minutes, 2 hours, evening day 1, morning day 2, morning day 3, evening day 4, and morning day 7. For each sample, take 10 mL and filter into a sample tube (labeled with experiment number, day, and time) and cap for analysis by ICP-AES or MP-AES. With the final sample, do an alkalinity titration to determine HCO_3^-.
    a. Calculate the initial pH of the solution after equilibrating with the gas mixture and compare to the measured pH. Use your measured pH to calculate a more precise fraction of CO_2 for the tank mixture..
    b. Plot the geochemical results for the experiments and comment on the degree of equilibrium achieved in each. Which cation best represents the weathering of the limestone and the granite?

c. Comment on the sources of the major cations in each experiment and account for their concentrations based on the minerals in these rock types.
d. Predict the concentration of Ca^{2+} in the limestone weathering solution. How does this compare with the final value?
e. Now calculate the state of saturation for calcite and for the major silicate minerals (amorphous H_4SiO_4 etc.).

This page intentionally left blank

7 Geochemical Evolution

INTRODUCTION

Beyond the weathering environment, natural groundwater geochemistry evolves through a range of processes including cation exchange, dissolution of salts, and mixing with other groundwaters and brines. Soils and the shallow subsurface are environments that are typically leached of the more soluble minerals, leaving mineral alteration products, including clays and iron oxyhydroxides. Higher salinity groundwaters are typically encountered in deeper geological settings or in arid and coastal regions. Older and more slowly circulating groundwaters develop more complicated subsurface histories through rock–water interaction in these deeper settings. Unraveling the geochemical evolution of such groundwaters is important not only for water quality concerns but also for investigations of contaminant transport and assessment of such sites for waste isolation.

ION EXCHANGE SURFACES IN AQUIFERS

The effect of surface reactions on groundwater geochemistry can be considered from two perspectives. One is the alteration of the major cation composition of the water by *cation exchange* with the surface of solids in the aquifer. The second involves the *adsorption* of trace metals and trace organics from solution onto a solid surface and *desorption* from a surface into solution. Sorption and exchange reactions are enhanced by the reactivity of solid surfaces. It follows that materials with the smallest grain size, such as clays, have the highest surface area and so are the most reactive in sorption and exchange processes. Similarly, noncrystalline solids, such as amorphous ferric iron oxyhydroxides, colloidal particles, and organic matter, possess high electrostatic charges on their surfaces.

Clay Minerals

Clay minerals are classified by their structure and chemistry, both of which affect their capacity to exchange cations with surface and groundwaters. Structurally, they comprise alumino silicate sheets in tetrahedral layers—sheets of Si^{4+} coordinated with O^{2-} in a tetrahedron structure—and octahedral layers—layers of Al^{3+} coordinated with O^{2-} (the gibbsite [$Al(OH)_3$] layer) (Figure 7.1). During the weathering of ferromagnesian minerals (olivine, pyroxene, and amphibole), Al^{3+} is replaced by Mg^{2+} (the brucite [$Mg(OH)_2$] layer). Oxygen atoms in the octahedral layer coordinate with Si^{4+} in the tetrahedral layer, bonding them into two (oct–tet) or three (tet–oct–tet) layer sheets. The sheets are joined by weak van der Waals' bonds into a single crystal.

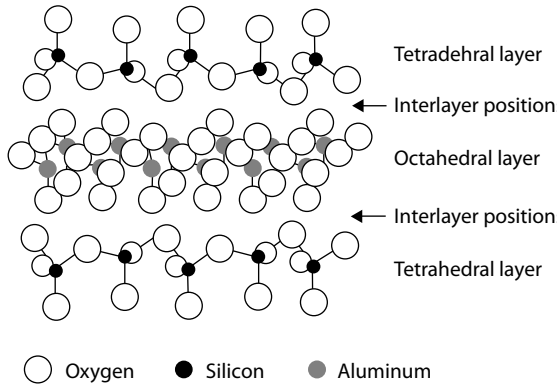

FIGURE 7.1 Tetrahedral and octahedral layers of clay minerals.

Common clays from the three principal groups and their basic chemical formula include the following, with their general chemical formula showing common substitutions (Mg, Fe, and Al) and *interlayer* cations in italics.

- Kaolinite ($Al_2Si_2O_5[OH]_4$)—a two-layer clay that forms in humid climates from acid weathering of granites. Note that kaolinite has no interlayer positions, which limits its ion exchange capacity to surface charge sites. Other two layer clays include serpentine, in which a brucite layer replaces the gibbsite layer.
- Smectite ($[Na,Ca_{0.5}][Mg,Fe,Al]_2Si_4O_{10}[OH]_2$)—three-layer clays that form from weathering of mafic (Fe-, Mg-, and Ca-rich, K-poor rocks). These clays, and particularly the Na-montmorillonite variety, swell from the uptake of water to satisfy excess negative charges when Na and Ca are leached from interlayer positions. This gives the smectite clays a high cation exchange capacity (CEC). Other common three-layer clays include pyrophyllite (the pure three-layer clay with no substitutions), talc (brucite replacing gibbsite), and chlorite (three-layer units with brucite layers, often Fe-rich).
- Illite ($K[Fe,Mg,Al]_2[AlSi_3]O_{10}[OH]_2$)—also a three-layer clay that forms from weathering of potassic rocks. Unlike smectites, the interlayer ion, K^+, is firmly positioned and stabilizes the structure, and so reduces its CEC.

Variations occur due to substitutions for Si and Al. For example, Fe^{2+} and Mg^{2+} can replace Al^{3+}, although this leaves a net negative charge for the layer. Similarly, Al^{3+} can replace Si^{4+} in the tetrahedral layer, again leaving a charge imbalance. Further, the oxygen atoms on the surface of individual clay crystals and on their edges maintain a net negative charge. The negative charges from substitutions within the layers can be satisfied by cations that fill *interlayer* positions. The surface negative charges can be balanced by adsorbing cations from pore waters.

Because hydrogen ions, H^+, can adsorb and desorb from surface charge sites, the pH of the pore waters affects the net surface charge of a clay mineral, and thus its

exchange capacity. The charge of the surface oxygen atom in a Si–O layer will vary, depending on pH:

$$\begin{aligned} &Si - OH_2^+ && pH < \sim 2 \\ &Si - OH && pH \sim 2 - 3 \\ &Si - O^- && pH > \sim 3 \end{aligned}$$

The pH at which a surface has an overall charge of zero is known as its point of zero charge (PZC). The high CECs for which silica clay minerals are known comes from the low PZC of Si, which allows a negative surface charge at pH values above about 3. For the iron oxides and hydroxides, the PZC occurs in the pH range of about 5–9, and so has a negative surface charge only at neutral to elevated pH. Gibbsite, $Al(OH)_3$, has an even higher PZC, at pH 9.

Clay minerals occur on the fracture surfaces in primary silicate rocks, where weathering occurs. Clays also develop through weathering of clastic material, such as feldspar-rich sands and glacial till. Alternatively, clay minerals can be allochthonous, transported and deposited with coarser-grained sediment as a clayey sand or till. Shaley laminations present in limestone and sandstone aquifers, and fractured, weathered shale sequences are also geological settings where circulating meteoric waters can experience ion exchange reactions with clay minerals.

Humic Substances

Humic substances are the principal organic component of soils, and develop through the biodegradation of vegetation. They are heterogeneous, high-molecular-weight C–O–H–(N, S) compounds that are soluble only at higher pH and give the dark brown color to soils and wetland waters. Humic acids are soluble above pH 2, whereas humin is the refractory component, which is strongly adsorbed to soil minerals and insoluble at all pHs.

Structurally, humic substances are three-dimensional networks of aromatic rings that are fringed with various functional groups including carboxyl (−COOH) and phenol (−OH). These groups can shed their H^+, providing negative sites for other cations in the pore waters (Figure 7.2).

Iron and Manganese Oxyhydroxides

The third principal type solid substrate for sorption reactions is iron oxyhydroxide or ferrihydrite, which is essentially amorphous and hydrated ferric iron oxide. Crystalline forms include goethite and limonite. Iron and manganese are released by the weathering of mafic minerals such as biotite, amphiboles, and pyroxenes or by oxidation of sulfides such as pyrite. Under oxidizing conditions and neutral pH, iron occurs as $Fe(OH)_3$ and is highly insoluble (see Chapter 3). Similarly, manganese is soluble only under reducing or acidic conditions. In soils and aquifers, amorphous forms dominate as coatings on mineral grains and partially filling porosity.

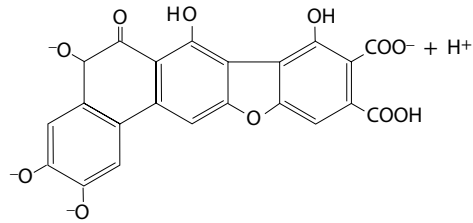

FIGURE 7.2 Schematic of a component of humic matter showing negatively charged exchange sites, which can be occupied by H^+ in low pH waters, by major cations from solution, or trace metals.

Oxygen atoms on ferrihydrite surfaces give a negative surface charge. Although protons can configure with them to form a surface hydroxide, there is increasing competition for these sites under neutral to high pH. As a result, such amorphous and semicrystalline solids represent excellent substrates for cation exchange and adsorption of trace metals.

Colloids

Colloids are small (<10 μm), noncrystalline particles of mineral or organic composition dispersed in water. In most natural waters, mineral colloids are typically hydroxides of Si, Fe, Mn, or Al. Their small size and high surface area combined with their noncrystalline structure give them a very high, negative surface charge. In fresh waters, electrostatic repulsion precludes flocculation, whereas in saline waters such as seawater, this effect is suppressed and colloids will flocculate and settle out of solution. In waters where colloids remain in suspension, they can be transported by advection.

Dissolved organic compounds in natural waters can also form colloids. Tea-colored waters are typically rich in humic colloids and demonstrate the characteristic of colloids to absorb and disperse certain wavelengths of light. The high negative charge found on the edges of many dissolved organic compounds allows these colloids adsorption and complexation properties similar to their inorganic counterparts.

Their high negative surface charge allows the adsorption of heavy metals and other contaminants onto their surfaces. Thus, the total amount of lead, for example, which could be held in solution by adsorption onto colloids, can far exceed its concentration as, say, Pb^{2+} or as a lead complex such as lead hydroxide, $PbOH^+$. As colloids can be carried advectively in surface waters and groundwaters, this provides a mechanism for contaminant transport.

Zeolites

Zeolites are a low-temperature form of tectosilicates (like feldspars) with an open crystal structure formed by silica tetrahedrons linked corner to corner. They occur as a product of weathering of volcanic rocks and feldspar-rich sediments under conditions of high pH and high salinity. Their porous structure allows the incorporation of considerable amounts of hydration water. Charge deficiencies are caused by

replacement of Si^{4+} with Al^{3+}. This allows incorporation of cations such as Ca^{2+} or Na^{+} during zeolite formation according to weathering reactions such as the following:

$$NaAlSi_3O_{8\ albite} + 3H_2O \rightarrow NaAlSi_3O_8{\cdot}H_2O_{analcime} + H_4SiO_4$$

$$CaAl_2Si_2O_{8\ anorthite} + 2H_2SiO_4 \rightarrow CaAl_2Si_4O_{12}{\cdot}4H_2O_{laumontite}$$

Both unbalanced charge deficiencies and the high surface area of these minerals make them excellent substrates for cation exchange. Combined with their open water-filled lattice, zeolites are important industrial minerals used as molecular sieves to purify waters and gases.

CATION EXCHANGE

Surface reactivity is largely generated by hydroxyl ions coordinated with Si, Al, or Fe cations, which gives a negative electrostatic potential on the surface. This electropotential can be satisfied by sorption of protons. However, as ionic strength is increased, so too is the competition for these exchange sites by other cations in solution. Because protons and cations are held only by weak electrostatic attraction, they can be displaced by other cations in solution, which may have a greater electrostatic charge or simply a higher concentration. This is the basis of cation exchange, a process that can alter the cation geochemistry of groundwater. A Ca-HCO_3 groundwater, for example, can evolve to a Na-HCO_3 groundwater through cation exchange on clays.

The Double Layer

The most versatile model for cation exchange involves a double layer of cations electrostatically bound to the clay surface (Figure 7.3). The electrostatic potential is

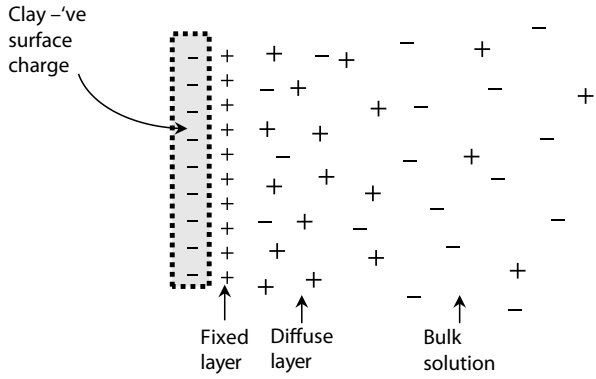

FIGURE 7.3 Double-layer model of the negative charge distribution on a clay mineral and cations attached at exchange sites.

greatest along the negatively charged surface, and maintains a *fixed* layer of cations. Outward from the fixed layer, the electrostatic potential decreases, creating a *diffuse* layer characterized by a cation excess over anions that diminishes with distance. Cations within the diffuse layer are free to move, as their electrostatic attraction is considerably less than in the fixed layer.

Ions in both layers can exchange with the adjacent solution, although cations in the diffuse layer can be expected to exchange more readily than those in the fixed layer. However, under steady-state conditions, an equilibrium is established between the solution and the surface that governs the concentration of adsorbed cations according to their concentration in solution.

Selectivity Coefficient

The exchange of a cation in solution with another adsorbed to a clay surface can be represented by the following reaction:

$$\text{Clay}_A + B^+ \Leftrightarrow \text{Clay}_B + A^+ \qquad 2\text{Na-clay} + Ca^{2+} \Leftrightarrow \text{Ca-clay} + 2Na^+$$

The reaction constant is known as the selectivity coefficient:

$$K_{A-B} = \frac{[\text{Clay}_A] \times [B^+]}{[\text{Clay}_B] \times [A^+]} \qquad K_{Na-Ca} = \frac{[\text{Clay}_{Na}]^2 \times [Ca^{2+}]}{[\text{Clay}_{Ca}] \times [Na^+]^2}$$

The activities of the dissolved cations are determined from ionic strength and activity coefficients. The adsorbed cation activities are most easily considered by their molar fraction of the total clay surface, hence the following:

$$[\text{Clay}_A] = \frac{\text{moles } A^+ \text{ on clay}}{\text{moles } A^+ + B^+ \text{ on clay}} \qquad [\text{Clay}_{Na}] = \frac{\text{moles } Na^+ \text{ on clay}}{\text{moles } Na^+ + Ca^{2+} \text{ on clay}}$$

In high ionic strength groundwaters where monovalent Na^+ tends to dominate (i.e., seawater), more Na^+ will reside on clay exchange sites. Displacement with a lower salinity Ca^{2+}-dominated groundwater will produce a new equilibrium with more Ca^{2+} on the clays. The distribution is then governed by the selectivity coefficient determined for this system.

Each cation has its own selectivity or tendency for sorption onto a charged surface. This characteristic relates to the surface charge of the cation, and the stability of its hydration sheath, which reduces its electrostatic interaction. Divalent cations have a greater tendency for exchange onto surfaces than monovalent ions. Cations with smaller hydrated radii (Table 2.1) are also more readily adsorbed. Without considering their concentration in solution, the orders of selectivity for adsorption of the major alkaline earth and alkali metals are as follows:

$$\textit{more soluble} \rightarrow$$
$$Ba^{2+} > Sr^{2+} > Ca^{2+} > Mg^{2+}$$
$$Cs^+ > Rb^+ > K^+ > Na^+ > Li^+$$
$$\leftarrow \textit{more sorption}$$

Although the selectivity coefficient can be determined for any cation exchange reaction, it is less of a constant than an empirical value incorporating the heterogeneities of the surface in question and the bulk ion geochemistry and ionic strength of the solution. Thus, the exchange of Na^+ and Ca^{2+}, for example, between solution and a clay surface will be affected also by other cations in solution and by the ionic strength of the solution.

Cation Exchange Capacity

The capacity for clay or other solid substrates to exchange cations with the solution is an important characteristic with respect to the geochemical evolution of groundwater. Relatively inert media, such as quartz sand or fractured crystalline rock, offer little in the way of exchange sites for reaction with the solution. However, the presence of clays or ferrihydrite coatings on quartz and feldspar grains greatly increases their CEC. Measuring CEC is important in soil studies where the conversion of Ca-clays to Na-clays can adversely affect permeability and drainage. It can also be important in water quality studies where cation exchange can affect the concentrations of potential contaminants such as fluoride.

The CEC of a soil represents the number of exchange sites per unit dry weight of sample. It is measured by saturating the sample's exchange sites with a 1 molar ammonium acetate solution at pH 7 and analyzing the release of NH_4^+ following equilibration with a (usually) Na^+ solution. CEC is expressed as meq/100 g dry sample. It provides an indication of the potential for exchange and sorption.

Of the principal clay groups identified above, smectites have the highest CEC, with values between 50 and 150 meq/100 g (Figure 7.4). Montmorillonite is a good example of a smectite clay with particularly high CEC, due to leaching of Na from interlayer positions. By contrast, K^+ is retained in interlayer positions of illite clays, reducing their CEC to less than 50 meq/100 g. Kaolinites have tightly spaced layers with no interlayer cations, and so have low CEC, generally less than 10 meq/100 g.

The CEC of ferric iron oxyhydroxides (ferrihydrite) is even greater than that of smectite clays, with values often exceeding 500 to 600 meq/100 g. However, this is the case only at neutral to high pH. As pH becomes more acidic, H^+ competes for exchange sites. Below ~ pH 4, ferrihydrite becomes increasingly soluble, and it retains no capacity for cation exchange. Similarly, zeolites and humic substances have high CECs in the range of 200 to 700 meq/100 g.

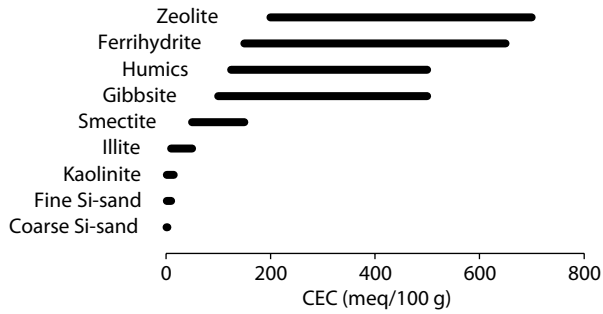

FIGURE 7.4 Ranges of cation exchange capacity for different aquifer materials at neutral pH.

Cation Exchange Disequilibrium

Groundwater evolution by cation exchange is a geochemical response to a disequilibrium between the groundwater geochemistry and the exchange medium. The example of road salt contamination is useful. Take the case where groundwater recharge takes place through a shallow glacial till with interstitial clay as a product of weathering. Groundwater in the till will likely have a Ca–HCO_3 geochemical facies, produced through dissolution of carbonates and feldspars. Over time, clays in the till will become loaded with Ca^{2+}. One spring, the excessive use of road salt has caused a plume of Na–Cl water to infiltrate the till. The Na^+-rich solution is no longer in equilibrium with the Ca-clays, and Na^+ begins to displace Ca^{2+} from the exchange sites. The spring groundwater moving through the till begins to evolve from a Na–Cl water to a Ca–Cl water. If Na–Cl waters continue to infiltrate through the till, they will eventually reestablish an equilibrium with the clays, converting them from Ca-clays to Na-clays. At this point, the groundwaters discharging below the till will evolve from a Ca–Cl water back to a Na–Cl water. If the original Ca–HCO_3 groundwaters reestablish in the recharge zone, then the deeper groundwater will evolve toward a Na–HCO_3 facies as Ca^{2+} replaces Na^+ on the clays, and eventually back to a Ca–HCO_3 water. Key to this process, however, is the transient geochemical condition in the recharge environment, which generated nonequilibrium conditions, and the evolution back to equilibrium.

Nonequilibrium conditions are also generated by a change in groundwater flow paths through new material. Examples include erosion and uplift, allowing groundwater circulation through deeper bedrock horizons, and the reestablishment of groundwater flow through previously inundated (marine) sediments.

Natural Groundwater Softening

The process of natural water softening, such as observed in the Tertiary shales of northern New Brunswick (Boyle and Chagnon 1995), is a common example of cation exchange. Here, the gradual erosion and exposure of marine units has allowed Ca–HCO_3 groundwaters to circulate more deeply and exchange with the Na-clays of these sediments. The natural water softening process is as follows:

$$2\text{Na-clay} + Ca^{2+} \rightarrow \text{Ca-clay} + 2Na^+$$

Here, shallow groundwaters have a Ca–HCO_3 geochemical facies and recharge to the deep bedrock aquifer used by the local population. As these groundwaters penetrate the deeper reservoir of Na-clays, the waters are naturally softened by exchange of Ca^{2+} from the shallow groundwaters, transforming these waters to a Na–HCO_3 facies (Figure 7.5). The reduction of Ca^{2+} activity has also reduced the saturation index for calcite, allowing dissolution of this mineral and an increase in HCO_3^-.

Although softened water is generally considered an attribute for domestic water supplies, in this case it has caused a serious water quality issue. Fluorite, CaF_2, is common in sediments, and has low solubility in most groundwaters maintained by

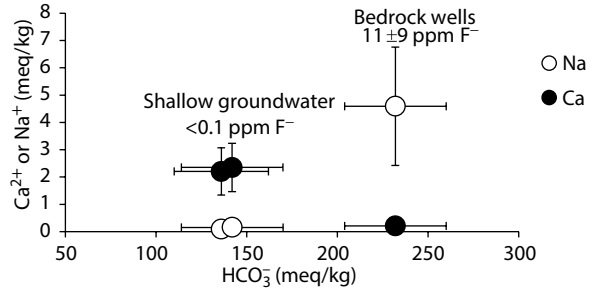

FIGURE 7.5 Natural water softening in deep groundwaters in Gaspé, Quebec (Data from Boyle and Chagnon 1995). Decreased Ca^{2+} in the deep groundwaters has allowed dissolution of fluorite, CaF_2. Consequently, the high F^- in these groundwaters has caused cases of skeletal fluorosis in the local population.

elevated Ca^{2+}. As Ca^{2+} is removed from solution by exchange onto the clays, fluorite can dissolve, adding F^- to the groundwaters. The drinking water limit for F^- is set at 2 ppm. Dental fluorosis can occur above this level, with risk of skeletal fluorosis above about 5 to 10 ppm.

SORPTION

The exchange of solutes between reactive surfaces and the bulk solution is an important process for the retardation of contaminant migration during advective groundwater flow. Like cation exchange processes, the amount exchanged or *sorbed* onto the solid surface is proportional to the amount in solution. However, as sorption reactions are considered for trace solutes rather than the exchange of major cations with the solution, they are modeled with a distribution coefficient rather than an exchange selectivity coefficient.

Distribution Coefficient, K_d, and the Sorption Isotherm

The simplest model for the movement of a reactive solute through an aquifer is that of reversible sorption. Here, the amount of the solute sorbed onto the surface is proportional to its concentration in solution; the higher its concentration, the greater the mass sorbed onto the surface. This is expressed by a distribution coefficient or K_d, which relates the mass of the solute sorbed onto the surface to that in solution:

$$K_d = \frac{\text{mass sorbed}}{\text{mass dissolved}} = \frac{\mu g/g}{\mu g/mL} = \frac{S}{C_{eq}} \quad (mL/g),$$

giving units of volume per mass, or mL/g in this case. Distribution coefficients depend not only on the chemical characteristics of the solute or contaminant but also on the aquifer medium. In particular, the CEC, solid organic fraction, types of minerals, presence of iron oxyhydroxides, and so forth all affect the distribution coefficient that controls sorption.

Given the range of controlling factors, the K_d value for a given groundwater–aquifer combination is empirically measured. This is done by batch tests, whereby a water sample with given concentration of the solute is mixed with a given mass of the medium. The difference between the solute concentration before mixing ($C_{initial}$ in, say, mg/L) and after equilibrium is established (C_{eq}) yields the mass sorbed, S, per mass of sediment.

$$S = \frac{(C_{initial} - C_{eq}) \times (L_{solution})}{\text{g sediment}} = \frac{\text{mg}}{\text{g}}$$

Comparison of the sorbed mass, S, with the equilibrium concentration (C_{final}) gives the distribution coefficient for that concentration at the batch reaction temperature for the test sediment.

$$S = K_d C_{eq}$$

Conducting batch tests for a range of concentrations yields the sorption isotherm for that solution–sediment system (Figure 7.6). For these linear isotherms, K_d is the slope of the S versus C relationship. If a solute is conservative, such as Cl^-, then there is no sorption onto the solid surface and the sorption isotherm sits on the abscissa. For increasingly reactive solutes, the isotherm becomes increasingly steep. In the example for Sr^{2+} and NH_4^+ in Figure 7.6, strontium is more reactive than ammonium.

Nonlinear Sorption Isotherm

For higher concentrations of reactive solutes and for highly reactive solutes, the linear sorption isotherm becomes inadequate, and nonlinear representations are required for modeling reactive transport. In the case of ammonium, higher concentrations would lead to a saturation of the available exchange sites on the aquifer medium, and the K_d decreases (Figure 7.7). At this point, the retardation factor decreases and the solute behaves in a more conservative fashion, with a transport velocity approaching that of the groundwater.

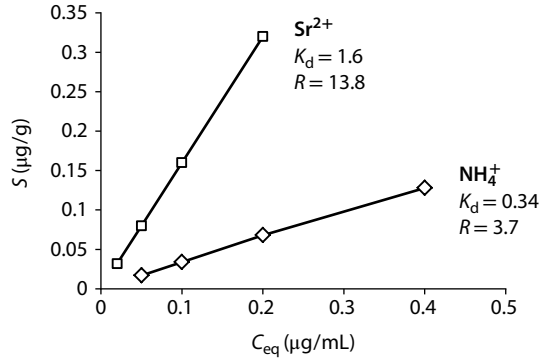

FIGURE 7.6 Sorption isotherms for two reactive solutes. Sr^{2+} sorption onto a medium-to-fine grain quartz sand aquifer was investigated by Lee et al. (1998) to remediate a ^{90}Sr plume. Böhlke et al. (2006) investigated NH_4^+ sorption onto glacial outwash sand aquifer.

Sorption and Retardation

The effect of sorption on solute transport in advective groundwater flow is to retard its movement along the flow path. Figure 7.8 shows the retardation of ammonium in groundwater by sorption onto the aquifer medium, where the NH_4^+ plume moves slowly relative to the movement of a non-sorbing solute, Cl^-. The degree of retardation is affected by the available surface area for sorption, which is a function of both porosity, θ, and sediment bulk density, ρ (g/cm^3). The relative velocity of a nonconservative solute or contaminant that is sorbed by equilibrium exchange with the medium is characterized by its retardation factor, R (unitless).

$$R = 1 + \frac{\rho}{\theta} \times K_d$$

$$\text{and so } R = \frac{v_{gw}}{v_c}$$

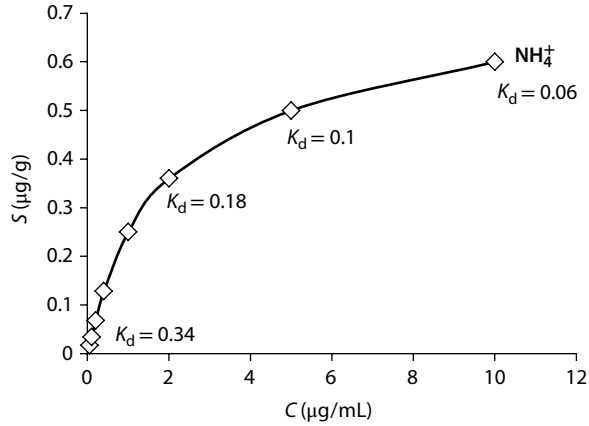

FIGURE 7.7 Sorption isotherm for ammonium at higher concentrations. Increased saturation of exchange sites leads to a reduction in the distribution coefficient, K_d, leading to reduced retardation and more conservative transport.

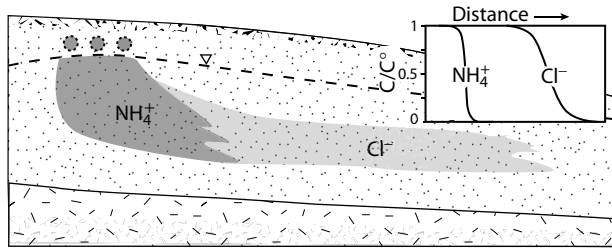

FIGURE 7.8 Relative velocity of a sorbed ammonium plume and a conservative chloride plume from a septic tile field. The sorption of ammonium slows its movement to a fraction of the average linear groundwater velocity.

where v_{gw} is the average linear groundwater velocity, and v_c is the retarded solute velocity. Conservative solutes then have a retardation factor of $R = 1$, while reactive solute with $R > 1$ moves more slowly that the groundwater.

Sorption and Solid Organic Carbon

Un-ionized, non-polar compounds such as hydrocarbons and chlorinated solvents do not sorb onto charged surfaces. However, they can sorb onto organic substrates in an aquifer, which can retard their transport. Nonpolar compounds are soluble in organic substrates, and so partition onto these phases as a plume that migrates through the aquifer. Further, the availability of negatively charged sites on complex organic compounds fosters chelation of multivalence cations, such as the transition metals. Chelating compounds have multiple charge sites to complex metals and remove them from solution. In the case of waters with high dissolved organic carbon (DOC), chelation with such compounds can increase the transport of metals.

Characterizing the sorption capacity of a soil for a given organic compound or metal then requires some assessment of its organic content and its affinity for sorption. This is represented for most compounds of interest as the partition coefficient for that compound in water relative to a fatty alcohol, octanol ($CH_3(CH_2)_7OH$). This is the octanol–water partition coefficient, K_{O-W}. Depending on the degree of polarity, an organic contaminant will preferably partition into the organic liquid, octanol, or into water. This partitioning function, in conjunction with the fraction of organic carbon in the aquifer, can define how the organic contaminant will sorb onto the aquifer. The coefficient, K_d, defining the distribution of that compound between the soil or aquifer with a given organic carbon fraction, f_{OC}, and groundwater is defined as follows:

$$K_d = K_{O-W} \times f_{OC}$$

From this relationship, sorption and retardation increases for organic molecules with higher K_{O-W} in aquifers with more organic carbon.

REDOX EVOLUTION IN GROUNDWATERS

The change in redox conditions during flow from the oxidizing conditions in the recharge environment to reducing conditions represents a second evolution pathway for groundwater geochemistry. In natural and contaminated settings, a range of redox reactions can occur, depending on the availability of both electron donors, such as organic carbon or sulfides, and electron acceptors, including elemental oxygen, nitrate, ferrihydrite, and sulfate. Redox evolution can follow a number of paths, but all lead toward conditions of high electron activity (low p*e* or Eh), where reduced species, such as ferrous iron, sulfide, methane, and even hydrogen gas, are produced.

In most cases, redox evolution is driven by an excess of organic carbon, whether transported with groundwater from the recharge environment, or gained in the subsurface from buried organics, such as peat in Quaternary sediments, hydrocarbons from marine sediments, or from contaminated settings such as landfills. Other electron donors, such as sulfides, ammonium, and hydrogen, exist in certain geological settings, which can also drive redox evolution.

The redox sequence takes place at electromotive potentials between the oxidizing conditions dominated by the O_2/H_2O redox couple and very reducing conditions where H_2O/H_2 dominates. These two redox couples define the p*e*–pH stability field for water.

p*e*–pH Stability Field for Water

Water will only be stable under a range of p*e* and pH conditions, within which aqueous redox reactions will be required to take place. The upper stability field for water is defined by the redox half-cell reaction for elemental oxygen conversion to water, as follows:

$$\tfrac{1}{2}O_2 + 2e^- + 2H^+ \rightarrow H_2O \qquad \Delta G_r^\circ = -237.14 \text{ kJ/mol}$$

The lower limit for the stability field for water is established by the redox couple with which water is reduced to hydrogen gas, H_2.

$$H_2O + e^- \rightarrow \tfrac{1}{2}H_2 + OH^- \qquad \Delta G_r^\circ = 79.9 \text{ kJ/mol}$$

The water stability field can be calculated from the Gibb's free energy of these two reactions.

$$\tfrac{1}{2}O_2 + 2e^- + 2H^+ \rightarrow H_2O \quad \Delta G_r^\circ = -237.14 \text{ kJ/mol}$$

$$K = \frac{a_{H_2O}}{P_{O_2}^{1/2} \times a_{e^-}^2 \times a_{H^+}^2} = 10^{41.55}$$

$$\log K = 41.55 = \log a_{H_2O} - \tfrac{1}{2}\log P_{O_2} - 2 \log a_{e^-} - 2 \log a_{H^+}$$

$$\log a_{e^-} = \tfrac{1}{2}\log a_{H_2O} - \tfrac{1}{4}\log P_{O_2} - \log a_{H^+} - 20.78$$

$$pe = 20.78 - pH + \tfrac{1}{2}\log P_{O_2}$$

This equation defines the p*e*–pH conditions for the stability of water for a given P_{O_2}. Plotted on a p*e*–pH diagram for a P_{O_2} of 1 atm, this line divides the lower p*e* zone, where water is stable, from the high p*e* zone, where H_2O is oxidized to O_2.

The lower stability limit for water is defined by the reduction of water to elemental hydrogen, which can also be written as the simple reduction of H^+, as follows:

$$H_2O + e^- \rightarrow \tfrac{1}{2} H_2 + OH^- \qquad H^+ + e^- \rightarrow \tfrac{1}{2} H_2$$

$$\Delta G_r^\circ = -14 \text{ kJ/mol} \qquad \Delta G_r^\circ = 0 \text{ kJ/mol}$$

$$K = \frac{P_{H_2}^{1/2} \times a_{OH^-}}{a_{H_2O} \times a_{e^-}} = 10^{-14} \qquad K = \frac{P_{H_2}^{1/2}}{a_{H^+} \times a_{e^-}} = 1$$

$$-14 = \tfrac{1}{2} \log P_{H_2} + \log a_{OH^-} - \log a_{e^-} \qquad 0 = \tfrac{1}{2} \log P_{H_2} - \log a_{H^+} - \log a_{e^-}$$

$$pe = -14 - \tfrac{1}{2} \log P_{H_2} - \left(-14 - \log a_{H^+}\right) \qquad pe = \tfrac{1}{2} \log P_{H_2} + \log a_{H^+}$$

$$= -\tfrac{1}{2} \log P_{H_2} - \text{pH} \qquad = -\tfrac{1}{2} \log P_{H_2} - \text{pH}$$

For near-surface conditions with P_{H_2} or P_{O_2} of 1 atm, where O_2 and H_2 gas bubbles would occur in shallow waters, these relationships defining the stability field for water become as follows:

$$pe = 20.78 - \text{pH} \qquad \text{For } O_2/H_2O$$

$$pe = -\text{pH} \qquad \text{For } H_2O/H_2$$

Using the electromotive scale, where Eh = 0.059 p*e*, gives us the following:

$$\text{Eh} = 1.23 - 0.059 \text{ pH} \qquad \text{For } O_2/H_2O$$

$$\text{Eh} = -0.059 \text{ pH} \qquad \text{For } H_2O/H_2$$

Plotted in Figure 7.9, these relationships define the H_2O stability field. At electron activities greater than those along this line (more negative p*e*), the H^+ in H_2O is reduced to H_2 gas. This reaction is hydroxide-generating and can in fact take place in natural waters. The hyperalkaline springs in the Sultanate of Oman are an example

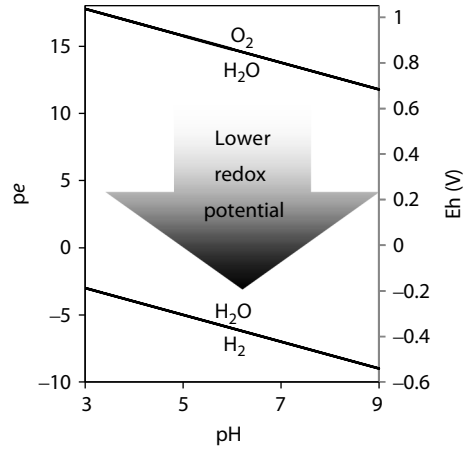

FIGURE 7.9 p*e*–pH diagram showing the stability field of water.

(Fritz et al. 1992), where natural groundwaters with pH 11.6 are discharging H_2 gas produced by low-temperature serpentinization of ultramafic rocks.

In all cases, redox evolution follows a sequence of redox reactions (often referred to as the tower or chain of redox reactions) arranged according to the electromotive potential of the electron acceptor. Considering only the major electron acceptors typically found in groundwaters, the sequence is as follows:

Aerobic oxidation	$O_2 \rightarrow H_2O$
Denitrification	$NO_3^- \rightarrow N_2$
Manganese reduction	$MnO_2 \rightarrow Mn^{2+}$
Iron reduction	$Fe(OH)_3 \rightarrow Fe^{2+}$
Sulfate reduction	$SO_4^{2-} \rightarrow H_2S$
Methanogenesis	$CO_2 \rightarrow CH_4$
Hydrogen reduction	$H_2O \rightarrow H_2$

This sequence of redox reactions takes place within the p*e*–pH stability field for water. As an electron acceptor with a higher electromotive potential is depleted, the p*e* of the system drops to that of next available redox couple. In most cases bacteria mediate these reactions. Those involved in reactions at lower p*e* (and lower energy) are less competitive for available substrate (usually organic carbon) unless the electron acceptor at the step above is depleted. Accordingly, each successive redox reaction takes place at decreasing Eh or p*e*. These are not only p*e*-dependent reactions but also pH dependent. Plotting each of these redox half-reactions on a p*e*–pH diagram shows the evolution of redox conditions in natural waters (Figure 7.10). The equilibrium redox line at each step is constructed from Gibb's free energy data, as demonstrated in the following sections.

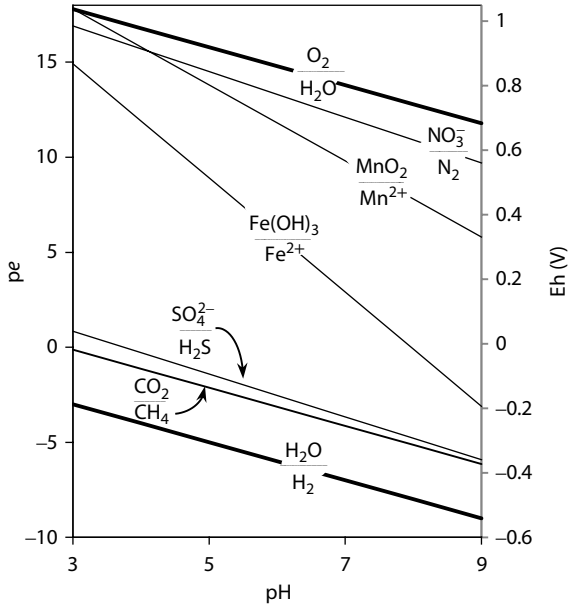

FIGURE 7.10 p*e*–pH diagram for principal redox buffering pairs in water.

O_2/H_2O: Aerobic Degradation of Organic Carbon

The first step along the sequence of redox reactions is the aerobic oxidation of organic carbon. The reaction is highly energetic, and so aerobic bacteria out-compete those operating with electron acceptors at lower electromotive potential.

Respiration $CH_2O + O_2 \rightarrow CO_2 + H_2O \qquad \Delta G_r^\circ = -501.84$ kJ/mol

The redox half-cell reaction is the same as the upper stability boundary for water, given above. Respiration is the dominant reaction returning biomass from primary production back to CO_2. It also proceeds below the water table, to the point where dissolved oxygen is depleted. This O_2 depletion is observed in the vadose zone of fine sand in northern Alberta, where vertical profiles of CO_2 and O_2 concentrations in the soil atmosphere were measured (Birkham et al. 2007). In Figure 7.11, the profiles of these gases show a downward increase in respiration, which is confirmed by the enrichment trend in $\delta^{18}O$ of the O_2 due to fractionation by microbial activity.

NO_3/N_2: Denitrification

Nitrate is one of the most soluble anions, and its removal from surface and groundwaters is mainly achieved by bacterial reduction to elemental nitrogen, N_2 — the process of denitrification. In this reaction, an electron donor, such as organic carbon, is oxidized. The resulting release of energy is significant and so is mediated by bacteria.

Denitrification $\quad CH_2O + \frac{4}{5}NO_3^- + \frac{4}{5}H^+ \rightarrow \frac{2}{5}N_2 + CO_2 + \frac{7}{5}H_2O$

$\Delta G_r^\circ = -509.7$ kJ/mol

The stability field for the redox pair NO_3^-/N_2 can be determined following the same approach used for the stability of water (Figure 7.10):

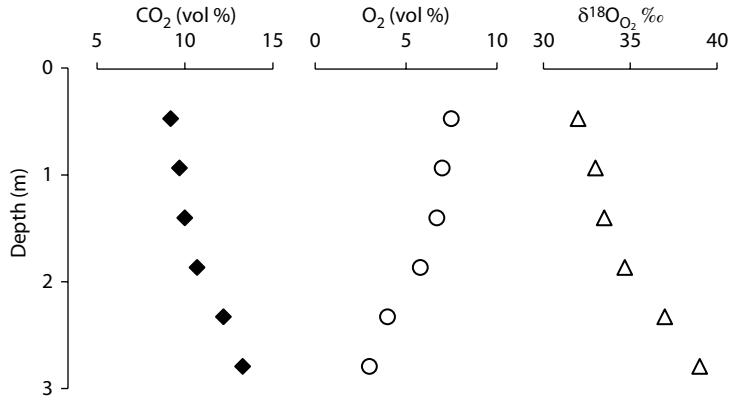

FIGURE 7.11 Profiles for CO_2, O_2, and $\delta^{18}O_{O_2}$ in unsaturated sand, showing the downward increase in CO_2 and decrease in O_2 consistent with aerobic degradation of organic carbon (modified from Birkham et al. 2007). The increase in $\delta^{18}O_{O_2}$ demonstrates reactive loss of O_2 where the aerobic bacteria discriminate against ^{18}O during respiration, leaving the residual O_2 enriched in ^{18}O.

$$NO_3^- + 5e^- + 6H^+ \Leftrightarrow \tfrac{1}{2}N_2 + 3H_2O \quad \Delta G_r^\circ = -602.68 \text{ kJ/mol}$$

$$K = \frac{P_{N_2}^{1/2} \times a_{H_2O}^3}{a_{NO_3^-} \times a_{e^-}^5 \times a_{H^+}^6} = 10^{105.6}$$

$$105.6 = \tfrac{1}{2}\log P_{N_2} - \log a_{NO_3^-} - 5 \log a_{e^-} - 6 \log a_{H^+}$$

Using $P_{N_2} = 0.8$ atm and defining nitrate activity with the drinking water limit of 10 ppm N ($a_{NO_3^-} = m_{NO_3^-} = 10^{-3.15}$ mol/kg) this produces the line for denitrification shown in Figure 7.10:

$$pe = 20.5 - \tfrac{6}{5}pH$$

Denitrification is evident from the enrichment in both $\delta^{15}N$ and $\delta^{18}O$ in the residual nitrate (Figure 7.12). Denitrifying bacterial produce ^{15}N-depleted N_2, leaving the residual nitrate enriched. As the nitrate is consumed, the isotope enrichment for both ^{15}N and ^{18}O follows a Rayleigh distillation (Figure 7.12). The organic carbon substrate is transformed to inorganic carbon, contributing ^{13}C-depleted carbon to the dissolved inorganic carbon (DIC) reservoir.

MnO_2/Mn^{2+}: Manganese Reduction

Like iron, manganese is a transition element commonly found in natural systems as either insoluble Mn^{4+} as pyrolusite (MnO_2) or highly soluble Mn^{2+}. The manganese oxide pyrolusite (MnO_2) is the common mineral form, found as a cement or heavy mineral in clastic aquifers.

Manganese reduction $\quad CH_2O + 2MnO_2 + 4H^+ \rightarrow CO_2 + 2Mn^{2+} + 3H_2O$

$$\Delta G_r^\circ = -502.05 \text{ kJ/mol}$$

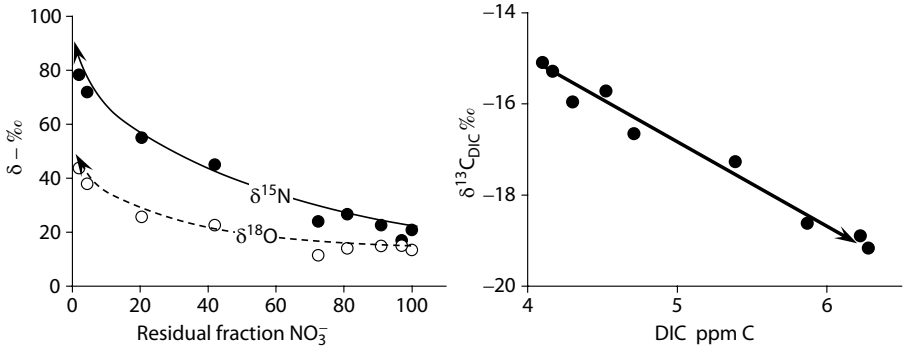

FIGURE 7.12 Left: enrichment in $\delta^{15}N$ and $\delta^{18}O$ for residual nitrate during denitrification, following a Rayleigh distillation trend toward very enriched residual nitrate. Right: depletion in $\delta^{13}C$ of DIC during denitrification due to contributions to total DIC from oxidation of organics. (Modified from Suchy 2008.)

The reduction half-cell reaction is as follows:

$$MnO_2 + 2e^- + 4H^+ \Leftrightarrow Mn^{2+} + 2H_2O \qquad \Delta G_r^\circ = -237.45$$

$$K = \frac{a_{Mn^{2+}} \times a_{H_2O}^2}{a_{MnO_2} \times a_{e^-}^2 \times a_{H^+}^4} = 10^{41.6}$$

$$\log K = 41.6 = \log a_{Mn^{2+}} - 2\log a_{e^-} - 4\log a_{H^+}$$

$$pe = 20.8 - \tfrac{1}{2}\log a_{Mn^{2+}} - 2\,pH$$

and fixing the dissolved Mn^{2+} concentration to the drinking water limit of 0.05 ppm (10^{-6} molal), this provides the line plotted for Mn^{2+} in Figure 7.10

$$pe = 23.8 - 2\,pH$$

$Fe(OH)_3/Fe^{2+}$: Iron Reduction and Solubility

Iron is the crust's fourth most abundant element, yet is rarely found in surface or groundwaters at concentrations over 1 ppm. Sources of Fe in soils and aquifers include the weathering of common mafic silicates, such as amphiboles and pyroxenes, as well as iron sulfides (pyrite) and oxides (magnetite). Its solubility in groundwater is controlled mainly by redox and pH.

Under the oxidizing conditions of most near-surface weathering environments, Fe concentrations are limited by the low solubility of ferric oxyhydroxide minerals. Amorphous and poorly structured forms have the general formula of $Fe(OH)_3$ and are known as limonite or ferrihydrite. Through burial and heating, water is lost and crystalline forms develop, including goethite (FeOOH) and hematite (Fe_2O_3). These forms of ferric iron present as grain and fracture coatings represent an electron acceptor with relatively high electromotive potential that is very important in the redox evolution of groundwaters.

The energy released per mole of CH_2O oxidized by iron reduction is substantial:

$$CH_2O + 4Fe(OH)_3 + 8H^+ \rightarrow CO_2 + 4Fe^{2+} + 11H_2O \qquad \Delta G_r^\circ = -436.48 \text{ kJ/mol}$$

$$Fe(OH)_3 + e^- + 3H^+ \Leftrightarrow Fe^{2+} + 3H_2O \qquad \Delta G_r^\circ = -102.23 \text{ kJ/mol}$$

$$K = \frac{a_{Fe^{2+}} \times a_{H_2O}^3}{a_{Fe(OH)_3} \times a_{e^-} \times a_{H^+}^3} = 10^{17.9}$$

$$17.9 = \log a_{Fe^{2+}} - \log a_{e^-} - 3\log a_{H^+}$$

$$pe = 17.9 - \log a_{Fe^{2+}} - 3pH$$

To plot this line on a p*e*–pH diagram, set the activity of ferrous iron at 10^{-6} mol/L. This gives us the following line in Figure 7.10 defining the boundary between the Fe^{2+} and the $Fe(OH)_3$ stability fields:

$$pe = 23.9 - 3pH$$

Chapelle and Lovley (1992) present an example of iron reduction based on the availability of ferrihydrite and organic carbon in the aquifer is the coastal aquifer in South Carolina. This confined sandy aquifer contains sedimentary organic carbon with ferrihydrite coatings on the sand grains over a 45 km stretch along the groundwater flow path. Dissolved iron concentrations up to 3 ppm have degraded the quality of these groundwaters that supply a number of local communities. The authors show the redox potential of groundwaters to evolve from aerobic conditions in the recharge area to iron reduction through the ferrihydrite zone and into sulfate reduction in the ferrihydrite-free zone (Figure 7.13). These reactions are driven by the sedimentary organic carbon substrate in the aquifer and support a community of iron reducers within the high iron zone. Beyond the ferrihydrite zone, the redox conditions drop to that of sulfate reduction, using sulfate that has diffused into the groundwater from confining beds. Here, reduction of sulfate to hydrogen sulfide (discussed in following section) sequesters the ferrous iron produce up-gradient and precipitates it as iron sulfide, mackinawite (FeS).

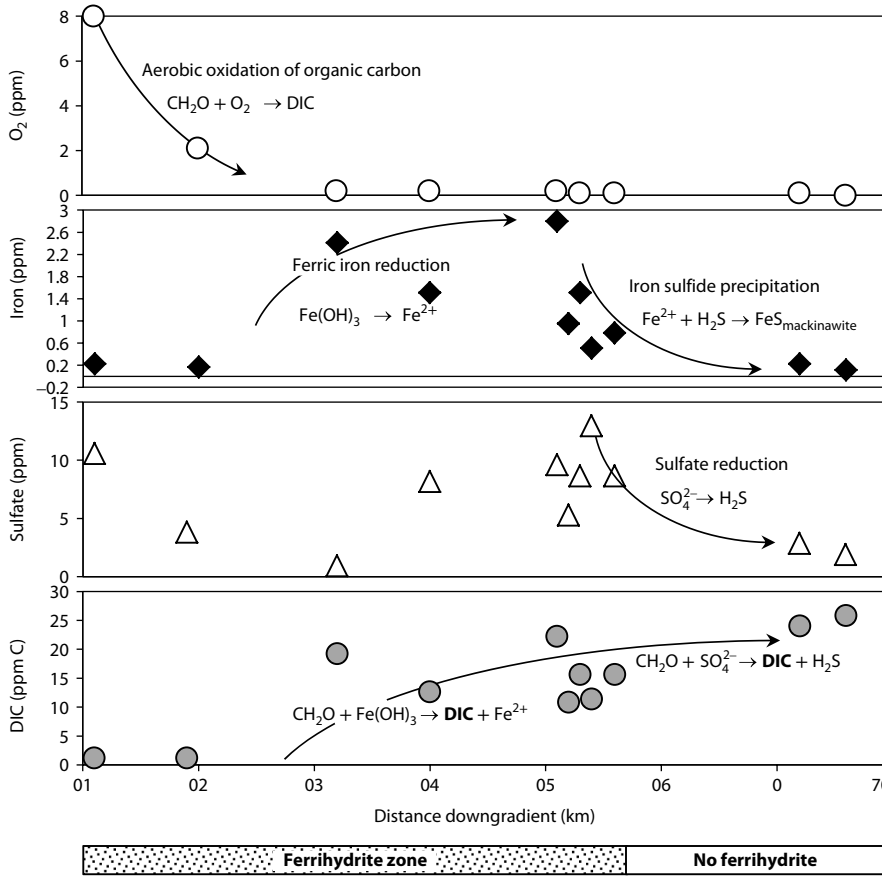

FIGURE 7.13 Redox evolution along groundwater flow path in sand aquifer with 2% to 5% organic carbon and ferric iron oxyhydroxide coatings (Chapelle and Lovley 1992).

This study illustrates the enhanced solubility of iron under reducing conditions. However, both ferrous and ferric iron have constraints on their solubility due to the control of pH on the stability of iron hydroxides species and hydroxide minerals like ferrihydrite. Ferrihydrite precipitates are common in aquifers, as almost all soils will have some ferrihydrite coatings on mineral grains from the weathering of iron-bearing minerals under oxidizing conditions. The following calculations determine the concentration of the main dissolve ferric hydroxide species in equilibrium with $Fe(OH)_{3\ ferrihydrite}$:

$$Fe(OH)_{3\ ferrihydrite} \Leftrightarrow Fe(OH)_3^\circ \qquad K = 10^{-7.67}$$
$$\log a_{Fe(OH)_3^\circ} = -7.67$$

$$Fe(OH)_{3\ ferrihydrite} + H^+ \Leftrightarrow Fe(OH)_2^+ + H_2O \qquad K = \frac{a_{Fe(OH)_2^+}}{10^{-pH}} = 10^{-0.78}$$
$$\log a_{Fe(OH)^{2+}} = -0.78 - pH$$

$$Fe(OH)_{3\ ferrihydrite} + 2H^+ \Leftrightarrow Fe(OH)^{2+} + 2H_2O \qquad K = \frac{a_{Fe(OH)^{2+}}}{10^{-2pH}} = 10^{2.70}$$
$$\log a_{Fe(OH)^{2+}} = 2.70 - pH$$

$$Fe(OH)_{3\ ferrihydrite} + 3H^+ \Leftrightarrow Fe^{3+} + 3H_2O \qquad K = \frac{a_{Fe^{3+}}}{10^{-3pH}} = 10^{4.89}$$
$$\log a_{Fe^{3+}} = 4.89 - 3pH$$

$$Fe(OH)_{3\ ferrihydrite} + H_2O \Leftrightarrow Fe(OH)_4^- + H^+ \qquad K = a_{Fe(OH)_4^-} \times 10^{-pH} = 10^{-16.71}$$
$$\log a_{Fe(OH)_4^-} = -16.71 + pH$$

Plotted on a diagram of pH versus dissolved iron concentration, these lines give the concentration of each ferric hydroxide species in equilibrium with ferrihydrite. The sum of these individual concentrations gives the total ferric iron concentration in solution under oxidizing conditions (Figure 7.14). Clearly, in oxidizing waters at circumneutral pH, iron has a very low solubility.

We can carry out similar calculations to see Fe solubility under reducing conditions (Figure 7.14). In this case, the solid phase is $Fe(OH)_2$, which dissociates under neutral pH conditions to produce dissolved Fe^{2+}. Under very alkaline conditions, the anion $HFeO_2^-$ becomes stable and increases Fe solubility.

$$Fe(OH)_2 + 2H^+ \Leftrightarrow Fe^{2+} + 2H_2O \qquad K = a_{Fe^{2+}} \times 10^{2pH} = 10^{12.38}$$
$$\log a_{Fe^{2+}} = 12.38 - 2pH$$
$$Fe(OH)_2 \Leftrightarrow HFeO_2^- + H^+ \qquad K = a_{HFeO_2^-} \times 10^{-pH} = 10^{-18.83}$$
$$\log a_{HFeO_2^-} = -18.83 + pH$$

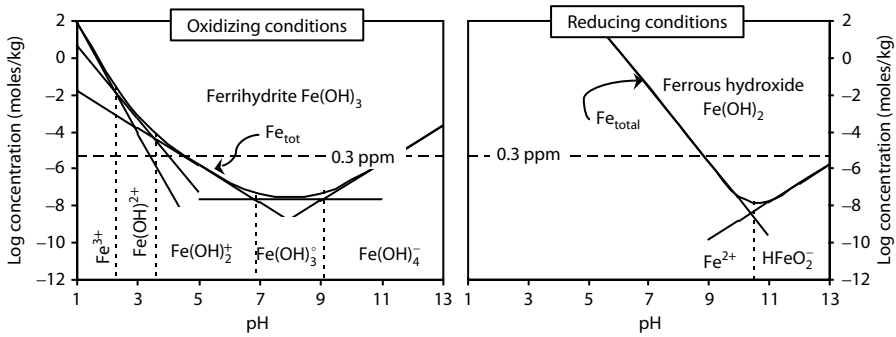

FIGURE 7.14 Solubility of ferric iron (left diagram) and ferrous iron according to pH. The WHO water quality objective of 0.3 ppm for total dissolved iron is shown.

Figure 7.14 shows that the solubility of Fe^{2+} hydroxide is much greater than Fe^{3+} hydroxide (ferrihydrite) over the pH range of most natural waters. In fact, at pH 7, the concentration of Fe^{2+} can exceed 1000 ppm. Ferrihydrite ($Fe[OH]_3$) maintains iron solubility below the drinking water standard of 0.3 ppm over a wide pH range from below pH 5 to above pH 11. Only under acidic conditions or highly alkaline conditions, well beyond the range for most groundwaters, will ferric iron become soluble. In contrast, ferrous iron has high solubility over the pH range of most groundwaters. Only above pH 9 does ferrous iron have low solubility as $Fe(OH)_2$, referred to as green rust, which is a strong reducing agent for electron acceptors with higher electromotive potential (MnO_2, NO_3^-).

This is important for the attenuation of heavy metals and other contaminants, which are strongly sorbed onto the highly charged surface of ferrihydrite (see cover photo). However, under anoxic conditions, reduction of ferrihydrite to ferrous iron not only solubilizes iron, but also releases all the sorbed metals and other compounds into solution. This is an important consideration for contaminant transport under reducing conditions.

Beyond the high pH control on reduced iron as ferrous iron hydroxide, both sulfide and carbonate place important limits on Fe^{2+} solubility. In the presence of high DIC, ferrous iron will precipitate as the carbonate phase, siderite [$FeCO_3$]. Like calcite, siderite precipitation is favored at high pH where CO_3^{2-} is the dominant DIC species, and so Fe^{2+} solubility decreases with increasing pH in groundwaters with high DIC (Figure 7.15).

Hydrogen sulfide in groundwater wells is associated with the familiar black FeS precipitate that encrusts the pump and well casing. In the absence of O_2, steel will oxidize to Fe^{2+} by reducing H^+ to H_2. In the presence of H_2S and HS^- from sulfate reduction (below), the Fe^{2+} will precipitate to as amorphous ferrous iron sulfide or mackinawite [FeS]. Crystalline forms such as pyrrhotite (FeS) and pyrite (FeS_2) are thermodynamically more stable, but require time and higher temperature to form, and so are not controlling phases in near surface geochemical environments.

To see how effective amorphous FeS_{am} is at limiting Fe^{2+} concentrations in water, let us presume that a groundwater with excess organic carbon has reduced ferrihydrate ($Fe(OH)_3$) in the subsurface and is now reducing sulfate. Sulfate reduction is

an acid-consuming reaction and so the pH will generally be above 7, making HS^- the dominant species. The following mineral dissociation reaction will control the solubility of Fe^{2+} and HS^-:

$$FeS + H^+ \Leftrightarrow Fe^{2+} + HS^- \qquad K_{FeS_{am}} = \frac{a_{Fe^{2+}} \times a_{HS^-}}{a_{H^+}} = 10^{-3.92}$$

$$\log a_{Fe^{2+}} = -3.92 - \log a_{HS^-} - \text{pH}$$

As with siderite, the activity of HS^- must be specified to determine FeS_{am} solubility with pH. For this example, let us set the concentration of HS^- at 10 ppm (3.03×10^{-4} or $10^{-3.5}$ mol/kg) and use the simplification that $a = m$.

The results of this calculation, plotted in Figure 7.15, show that at a reasonable level of HS^-, FeS is a highly limiting Fe phase. In this example, Fe^{2+} is below 0.3 ppm at all pH values above 5. Note that FeS has much lower solubility than siderite. Thus, in the presence of dissolved sulfide, siderite will be dissolved and the Fe^{2+} reprecipitated as FeS.

SO_4/H_2S: Sulfate Reduction

The reduction of sulfate to sulfide is one of the most common redox buffers, owing to the high solubility and variety of sources of SO_4^{2-} in natural waters. In marine sediments, the high sulfate content in seawater provides a large reservoir of this electron acceptor, giving it an important role in diagenetic reactions involving sedimentary organic carbon. Sulfate can be found as gypsum deposits in fractures or in evaporitic horizons. It can be derived from oxidation of pyrite if present within the oxidizing zone of aquifers. Sulfate also is supplied by high-salinity brines found in deep crystalline settings and deep sedimentary basins.

Sulfate reduction is a common reaction that is mediated by a group of bacteria referred to simply as sulfate reducing bacteria or SRBs. They can operate on very different organic substrates ranging from fixed organic carbon (oxidation state of 0, e.g., CH_2O) source's such as peat and soil organics, to reduced organic carbon (oxidation

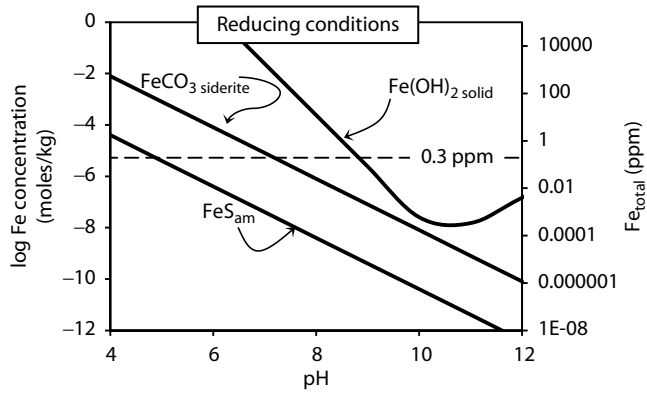

FIGURE 7.15 Solubility of iron under reducing conditions (Fe^{2+}) in the presence of HCO_3^- (200 ppm) and in the presence of hydrogen sulfide (10 ppm).

state of –IV), including petroleum, bituminous solids, and methane. Sulfate reduction involves an 8 electron transfer, from S^{6+} to S^{2-}.

$$\textit{Sulfate reduction}\quad 2CH_2O + SO_4^{2-} \rightarrow H_2S + 2HCO_3^- \quad \Delta G_r^\circ = -197.9$$

The sulfate reduction half reaction can be written as follows:

$$SO_4^{2-} + 8e^- + 10H^+ \rightarrow H_2S + 4H_2O \qquad \Delta G_r^\circ = -232.26 \text{ kJ/mol}$$

$$K = 10^{40.7} = \frac{a_{H_2S} \times a_{H_2O}^4}{a_{SO_4^{2-}} \times a_{e^-}^8 \times a_{H^+}^{10}}$$

$$40.7 = \log a_{H_2S} - \log a_{SO_4^{2-}} - 8 \log a_{e^-} - 10 \log a_{H^+}$$

$$pe = 5.09 + \tfrac{1}{8}\log\left(\frac{a_{SO_4^{2-}}}{a_{H_2S}}\right) - \tfrac{5}{4}pH$$

When the two redox species are both dissolved, the stability line is generally drawn for the case where they have equal concentrations, and so their activity ratio is 1.

$$pe = 5.09 - pH$$

In this case, less energy is released per mole of CH_2O and the reaction has a lower equilibrium constant. Clearly, sulfate reduction will take place only when the more favored reaction—O_2 respiration—is precluded by anaerobic conditions.

The sulfide product of sulfate reduction, as either H_2S or HS^- at pH>7, is toxic to most organisms. Hydrogen sulfide has a high solubility unless there are metals present in solution to form sulfides, such as FeS ($K_{FeS} = 10^{-3.92}$), PbS ($K_{PbS} = 10^{-12.8}$), or ZnS ($K_{ZnS} = 10^{-9.05}$).

Sulfate reduction, like denitrification, is accompanied by enrichment of ^{34}S and ^{18}O in the residual SO_4^{2-} in the groundwater. Bacteria preferentially reduced the isotopically light SO_4^{2-} to H_2S, leaving behind the ^{34}S- and ^{18}O-enriched SO_4^{2-} in the residual sulfate reservoir (Figure 7.16). A strong enrichment in $\delta^{34}S_{SO_4^{2-}}$ and $\delta^{18}O_{SO_4^{2-}}$ is a clear sign that SRBs are at work.

The enrichment for ^{18}O during sulfate reduction is less dramatic, due to exchange with ^{18}O of the water. Although sulfate is unwilling to exchange its oxygen with water at low temperatures, during microbially mediated sulfate reduction, such exchange can take place (Fritz et al. 1989). For this reason, the Rayleigh enrichment seen in Figure 7.16 is less for ^{18}O than for ^{34}S.

CO_2/CH_4: Methanogenesis

The last of the redox reactions that can occur in this scenario of redox evolution driven by excess organic carbon is that of methanogenesis. This is in fact a complicated series of complementary reactions whereby the organic carbon itself plays the opposing roles of electron acceptor and electron donor. This involves the formation of intermediary organic carbon species with varying associated free energies.

Methanogenic reactions offer little energy to the bacteria and archaea that catalyze them, as much is left behind, stored as chemical energy in CH_4. Nonetheless, in

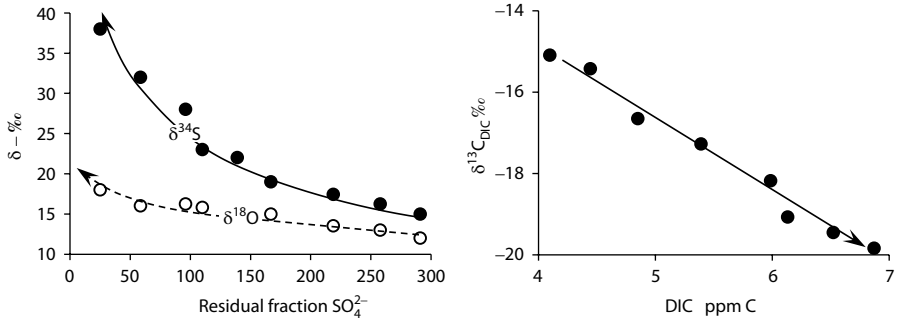

FIGURE 7.16 Sulfate reduction trend observed for $\delta^{34}S$ and $\delta^{18}O$ in the residual sulfate in artesian groundwaters from Oman. These groundwaters have several ppm H_2S. Gypsum in the Cretaceous aquifer is the source of sulfate.

the absence of the foregoing electron acceptors, from O_2 to SO_4^{2-}, microbial methanogenesis is viable and ubiquitous. Virtually all water-saturated environments host the microbial community capable of methanogenesis, including wetlands, tundra, landfills, and in foregut ungulates. Various fermentative bacteria degrade the complex organic carbohydrates (starch, cellulose, etc.) to simpler fatty acids, with by products including acetate CH_3COOH, CO_2 and H_2.

$$C_6H_{12}O_6 \rightarrow CH_3CH_2CH_2COOH + 2CO_2 + 2H_2$$

Acetogenic bacteria thrive on fatty acid products to produce acetate and additional CO_2 and H_2:

$$CH_3CH_2CH_2COOH + 2H_2O \rightarrow 2CH_3COOH + 2H_2$$

Complementary archaeal reactions can then produce methane by either acetoclastic reaction or reduction of CO_2 with H_2 (Klass 1984):

Acetate fermentation	$CH_3COOH \rightarrow CH_4 + CO_2$	$\Delta G_r^\circ = -48.64$ kJ/mol
CO_2 reduction	$CO_2 + 4H_2 \rightarrow CH_4 + 2H_2O$	$\Delta G_r^\circ = -130.58$ kJ/mol

The overall reaction can be written simply as the oxidation and reduction of different forms of carbohydrate:

Methanogenesis	$2CH_2O \rightarrow CH_4 + CO_2$	$\Delta G_r^\circ = -316.28$ kJ/mol

Writing this as a redox half-reaction with electrons on the left side, as conventionally expressed:

$$CO_2 + 8e^- + 8H^+ \rightarrow CH_4 + 2\,H_2O \qquad \Delta G_r^\circ = -130.58 \text{ kJ/mol}$$

$$K = \frac{P_{CH_4} \times a_{H_2O}^2}{P_{CO_2} \times a_{e^-}^8 \times a_{H^+}^8} = 10^{22.9}$$

$$\log K = \log P_{CH_4} - \log P_{CO_2} - 8 \log a_{e^-} - 8 \log a_{H^+} = 22.9$$
$$pe = 2.86 + \log P_{CH_4} + \log P_{CO_2} - pH$$

Creating the stability line for atmospheric conditions where P_{CO_2} and $P_{CH_4} = 1$ gives the following equation:

$$pe = 2.86 - pH$$

Biogenic methane occurs naturally in many Quaternary aquifers with buried organics of Holocene age. It can also migrate into groundwaters with leachates from unlined landfills. However, deeper-sourced methane of thermocatalytic origin can also migrate upward into shallow aquifers. Water supplies tapping such groundwaters can accumulate free methane, which presents an explosion hazard. The expanding development of shallow gas and shale gas increases this risk through losses from leaking well casings or by fracturing of the shale caps that normally protect the shallow groundwaters (Osborn et al. 2011).

Distinguishing the origin of methane in shallow groundwaters between natural biogenic sources and fugitive gas from deeper thermocatalytic sources is critical for mitigation. The difference in the isotopic composition of these distinct sources can be used to discern whether deeper gas has migrated into shallow aquifers and wells.

Microbial methanogenesis is highly fractionating for ^{13}C. Archaea are highly selective due to the low energy yield of the reaction with organic carbon, with an enrichment factor $\varepsilon^{13}C_{CH_4\text{-}CH_2O}$ of −30‰ to −60‰. The result is a strong depletion for microbial methane, with values typically less than −60‰ and as low as −90‰ (Figure 7.17 A). This distinguishes biogenic methane from thermogenic methane, which has only a modest depletion in $\delta^{13}C$ values of the methane due to fractionation at much higher temperatures.

DIC in methanogenic groundwaters is typically more enriched than the usual range of −15 to −10‰, with values often as high as +5‰ and higher. Although values up to −1 and 0‰ can be explained by exchange with marine limestones in old groundwaters, values above 0‰ can usually be attributed to bacterial methanogenesis by CO_2 reduction (above) where the DIC substrate experiences a Rayleigh distillation during methanogenesis, with $^{12}C_{DIC}$ preferentially selected by the bacteria for reduction with H_2 to methane, leaving the residual DIC enriched in ^{13}C. This strong enrichment in the residual DIC can be preserved in calcite cements and nodules, and used to indicate a methanogenic environment during formation (Dimitrakopoulos and Muehlenbachs 1987; Clark et al. 2004).

The $\delta^{13}C$ of DIC associated with thermogenic methane generally has values up to only 0‰ due to exchange with carbonate minerals in the reservoir, and is useful when used with $\delta^{13}C_{CH_4}$ to distinguish methane sources (Figure 7.17 B). The most diagnostic combination of isotopes is that of $\delta^{13}C$ with ^{14}C of the methane. Biogenic methane typically has a measurable radiocarbon activity due to production from buried organic carbon in surficial sediment (Quaternary) aquifers (Figure 7.17 C). Thermogenic CH_4 is generated from ancient marine organic carbon and is ^{14}C-free. Radiocarbon is becoming an important tool to unambiguously identify fugitive methane from deep production zones in shallow groundwaters.

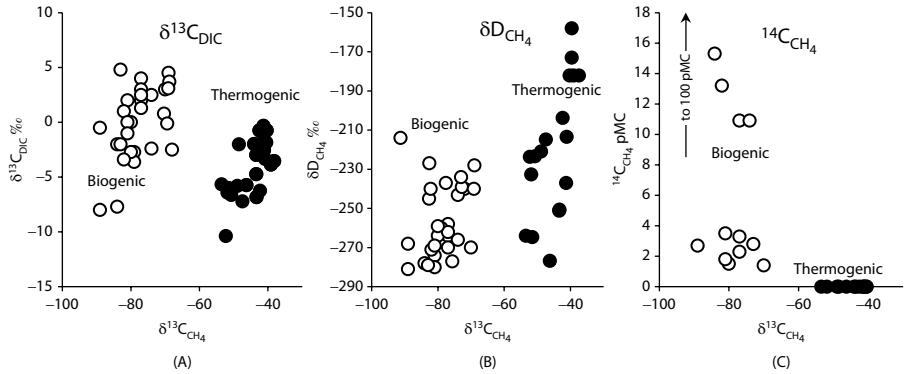

FIGURE 7.17 The $\delta^{13}C$ of CH_4 plotted with (A) $\delta^{13}C_{DIC}$, (B) δD_{CH_4}, and (C) ^{14}C for biogenic methanogenesis in fresh water (Data from Aravena et al. 1995; Coleman et al. 1988) and for thermogenic methane in sedimentary basins. (Data from Barker, and Pollock, 1984.)

H_2O/H_2 — Reduction of water

The lowest electromotive potential achieved in the redox evolution in groundwaters is the lower stability limit for water itself where hydrogen gas is generated. While the chain of reactions that occur during the degradation of organic carbon can produce hydrogen along the way, this is rapidly consumed by methanogenic archaea operating at a higher electromotive potential. The production of H_2 from the reduction of water is not associated with degradation of organics. Rather, it relies on electron donors with lower electromotive potential than carbon. Zero-valence iron is one potential electron donor, and is discussed in Chapter 9 for its role in reductive dehalogenation of contaminants like trichloroethylene. In fact, there are few naturally-occurring electron donors that exist below the electromotive potential of the H_2O/H_2 redox couple:

$$H_2O + e^- \rightarrow \tfrac{1}{2}H_2 + OH^- \qquad \Delta G_r^\circ = -14 \text{ kJ/mol}$$

Where: $pe = -pH$ for 1 atm H_2

and $Eh = -0.059\ pH$ (Figure 7.10).

A remarkable example of this reaction is found in Oman, where hyperalkaline springs up to pH 12 are bubbling hydrogen gas. These springs occur in the ultramafic sequence of the Semail Ophiolite, the world's best exposure of oceanic crust obducted onto the Arabian plate in late Cretaceous time. Extensive closed-system alteration or *serpentinization* of olivine and pyroxene by the deeply circulating groundwaters produces hydroxide minerals including serpentine ($Mg_3Si_2O_5[OH]_4$), brucite ($Mg[OH]_2$) and ferrous iron hydroxide ($Fe[OH]_2$) according to:

$$5Mg_2SiO_{4\ ol} + Fe_2SiO_{4\ px} + 9H_2O \rightarrow 3Mg_3Si_2O_5(OH)_{4\ serpentine} + Mg(OH)_2 + 2Fe(OH)_2$$

The hyperarid environment in Oman limits groundwater circulation with the result that the highly soluble brucite and ferrous iron hydroxide push the pH of these waters to such high levels (Barnes and O'Neil 1978; Neal and Stanger, 1983; Table 7.1).

TABLE 7.1
Geochemistry of the Oman hyperalkaline springs (Nizwa-Jill spring, in meq/kg)

pH	T°C	Na^+	K^+	Ca^{2+}	Mg^{2+}	Cl^-	SO_4^{2-}	OH^-	alk_c
12.1	25	16.2	0.23	3.21	0.06	11.8	0.09	7.49	0.0

Source: (Neal and Stanger, 1983)

The high pH of these groundwaters has an interesting effect on the redox conditions. Inspecting Figure 7.10, we observe the steep slope of the ferric/ferrous iron line ($Fe(OH)_3^\circ/Fe^{2+}$) which approaches the H_2O/H_2 line at high pH. The equation for the iron line, given in the section above on iron reduction, can be equated with the hydrogen line, showing that they intersect near pH 12.

$$pe = 23.9 - 3pH \qquad \textit{iron reduction}$$
$$pe = -pH \qquad \textit{hydrogen reduction}$$
$$-pH = 23.9 - 3pH$$
$$23.9 = 2pH$$
$$pH = 11.95$$

This means that above pH 11.95, ferrous iron is a favorable electron donor for the reduction of water to H_2. This occurs in Oman according to the two half-cell reactions:

$$2Fe(OH)_2 + 2OH^- \rightarrow 2Fe(OH)_3 + 2e^-$$
$$2H_2O + 2e^- \rightarrow H_2 + 2OH^-$$

which give the overall redox reaction:

$$2Fe(OH)_2 + 2H_2O \rightarrow 2Fe(OH)_3 + H_2$$

The high hydrostatic pressure at depth allows the hydrogen gas to accumulate. It then bubbles from solution in the discharge area with the loss of hydrostatic pressure. The hyperalkaline waters are also depositing thick accumulations of white calcite. The very low carbonate content (carbonate alkalinity, alk_c is less than detection; Table 7.1) and at high pH means that the P_{CO_2} of these waters is less than 10^{-12} atm. Like the Jordan hyperalkaline groundwaters in Figure 6.17, this contrasts with surface conditions ($P_{CO_2} = 10^{-3.4}$ atm), causing the rapid uptake of atmospheric CO_2 and triggering extreme oversaturation for calcite. Issuing from the dry, unvegetated ultramafic rocks, the natural blue pools of Oman are a remarkable site.

SALINITY IN GROUNDWATER

As seen in the preceding chapter on weathering, the weathering of carbonates and silicates does not contribute significantly to the salinization of groundwater. With high soil P_{CO2} and open system conditions, total dissolved solid (TDS) may approach perhaps two to three hundred parts per million, whereas groundwaters in formations with evaporite minerals may carry over two to three hundred thousand ppm of dissolved solids (Figure 7.18). The geochemistry of high salinity groundwaters provides insights to the source of solutes and the groundwater flow history.

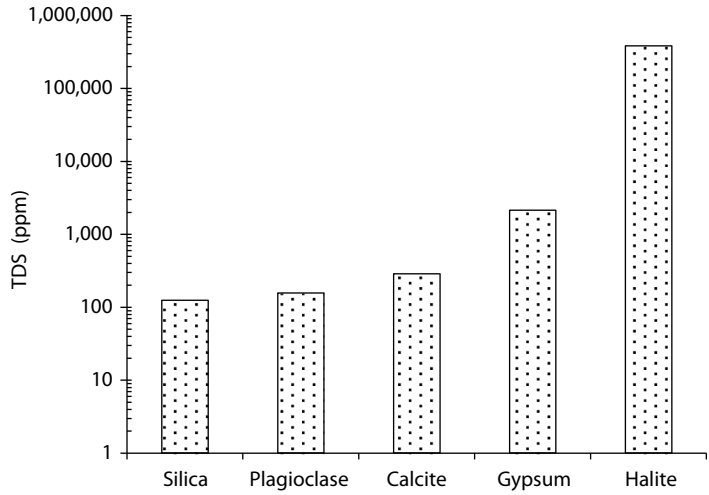

FIGURE 7.18 TDS from solubility of silicates, carbonates, sulfates, and halides, with P_{CO_2} of 0.01 atm.

Salinity in groundwater is typically present as chloride salinity, as this is the most soluble of the common anions. Groundwaters saturated with gypsum, for example, have a TDS of only 1300 ppm as Ca–SO_4 (example 2 and 3 in Chapter 2; Figure 7.18), whereas groundwaters saturated with halite will have a TDS of over 300,000 ppm as Na–Cl. Other chloride minerals, such as $CaCl_2$ and hydrous magnesium chlorides, are even more soluble.

There is a very general correlation between groundwater depth and salinity, and with the dominant geochemical facies. Chebotarev (1955) was one of the earliest geochemists to publish on the evolution of groundwater geochemical facies from shallow meteoric weathering to deep crustal fluids, based on over 6000 geochemical analyses from basins around the world. The Chebotarev sequence considers three spheres for the *metamorphism* or evolution of groundwater geochemistry, from the shallow zone of active flushing with low salinity HCO_3-type waters, through SO_4-type waters in zones of limited flushing and transitional salinity, to Cl-type waters in stagnant, high-salinity strata. His use of the three principle anions in natural waters relates to the solubilities of carbonates, sulfates, and chlorides as salts of the four abundant base metal cations, Ca^{2+}, Mg^{2+}, Na^{+} and K^{+}, that dominate in natural waters.

The Chebotarev sequence is a demonstration of the relative solubility of the carbonates, sulfates and halides, but does not fully address the origin of salinity in groundwater. Beyond the zone of weathering, a variety of processes can be considered. The major sources of salinity in groundwater range from natural processes, including accumulation of sea spray in coastal areas that mixes with deep bedrock brines, to salt contamination from road salting and wastewater infiltration. Salinity in groundwater represents a considerable problem in many regions where freshwater resources may be limited or where salinization of groundwaters has increased over time due to anthropogenic impacts. The geochemical and isotopic tools to trace the sources of salinity are discussed in Chapter 9.

GRAPHICAL PRESENTATION OF GEOCHEMICAL EVOLUTION

Graphs of geochemical data can be considered for the case where the major ions and geochemical facies are to be presented for the purpose of distinguishing the different water types encountered in a study. In this case, there can be six or more species to be represented. On the other hand, scatter plots showing, for example, correlation of Ca^{2+} with SO_4^{2-}, or Na^+ with Cl^-, are useful to demonstrate trends that would indicate the origin of salinity or give evidence of a process.

The principal geochemical facies are based upon the relative concentrations of the major cations and anions. The major cations include the alkali metals—Na^+ and minor K^+, and the alkaline earth metals—Ca^{2+} and Mg^{2+}. The major anions include HCO_3^-, SO_4^{2-}, and Cl^-. For ease of presenting these different graphical approaches, the following data set was selected (Table 7.2), which is a series of geochemical analyses from a watershed in which three water types are mixing.

Piper Diagram

One of the most well-known diagrams for presenting the principal geochemical components of waters is with the trilinear Piper plot (Piper 1944). The diagram comprises two base triangular plots and one diamond (Figure 7.19). The triangles present the molar percent for the three principal anions—HCO_3^-, SO_4^{2-}, and Cl^-, and for the three principal cations—Na^+(plus K^+), Ca^{2+}, and Mg^{2+} for a given sample. The upward projection of these two points along lines parallel to the sides of the

TABLE 7.2
Monitoring Data for Drainage from a Spring-fed Catchment (meq/kg)

Sample	Discharge (m^3/s)	TDS (mg/L)	Ca^{2+}	Mg^{2+}	Na^++K^+	HCO_3^-	SO_4^{2-}	Cl^-
Chloride spring		2869	2.7	1.84	45.6	4.41	4.76	35.1
Sulfate springs		170	2.3	0.21	0.04	1.95	0.01	0.02
Carbonate springs		287	2.5	1.37	0.33	1.28	2.8	0.007
River water								
January	1.8	2607	2.7	1.8	41.1	4.1	4.5	31.6
February	1.6	2791	2.7	1.8	44.2	4.3	4.7	34.0
March	2.0	2341	2.6	1.6	36.5	3.9	4.1	28.1
April	4.0	1308	2.6	1.4	18.4	2.6	3.3	14.0
May	151.7	203	2.3	0.3	0.5	1.9	0.2	0.4
June	52.5	274	2.4	0.5	1.5	1.9	0.7	1.1
July	19.9	421	2.4	0.7	3.8	1.9	1.2	2.8
August	10.6	622	2.4	0.9	7.0	2.1	1.8	5.3
September	6.4	903	2.5	1.2	11.6	2.2	2.6	8.8
October	2.9	1689	2.6	1.5	25.2	3.1	3.5	19.3
November	2.1	2218	2.6	1.7	34.3	3.7	4.1	26.3
December	1.9	2476	2.7	1.8	41.1	4.1	4.5	31.6

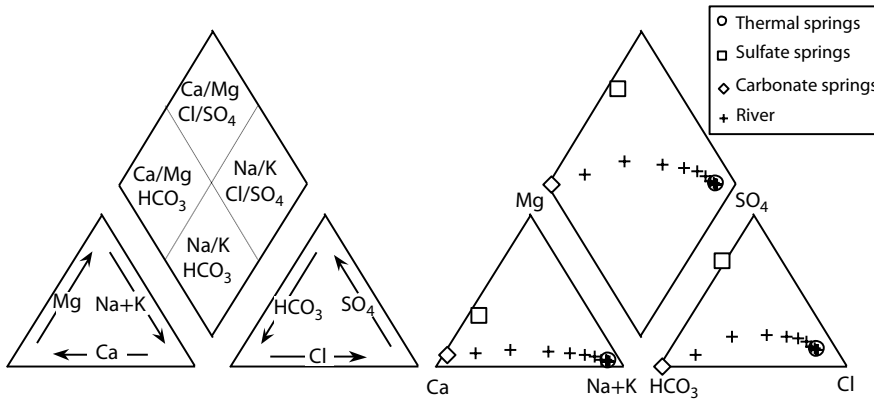

FIGURE 7.19 Piper trilinear diagram showing geochemical facies, (left) and with data from Table 7.2 (right).

diagram intersects at a point in the quadrant of the diamond, representing one of four geochemical facies:

- Ca/Mg–HCO_3—typical bicarbonate groundwater from near-surface mineral weathering
- Na/K–HCO_3—*softened* bicarbonate water, where alkalis replace alkaline earth metals
- Ca/Mg–SO_4/Cl—saline water, dominated by alkaline earth metals
- Na/K–SO_4/Cl—sodium-dominated saline water

Plotting points on a Piper diagram first involves converting analytical data (mg/L or ppm) to milliequivalents (divide by gfw and multiply by charge) then converting to percent of total anions and cations. For example:

Anions: $HCO_3^- = 4.41/(4.41 + 4.76 + 35.1) \times 100 = 10.0\%$

$$SO_4^{2-} = 4.76/(4.41 + 4.76 + 35.1) \times 100 = 10.8\%$$

$$Cl^- = 35.1/(4.41 + 4.76 + 35.1) \times 100 = 79.2\%$$

Quantitative Diagrams

Although Piper diagrams serve the purpose of distinguishing different geochemical facies on the same plot, salinity (TDS) data can only be presented inelegantly according to symbol size or shape. Stiff diagrams offer a visual presentation of both geochemical facies and salinity by means of a polygon. The shape is used to emphasize the dominant anion and cation components, while the width of the plot is proportional to concentration in milliequivalents. A further advantage of Stiff diagrams is that they can be placed on a map for spatial presentation of geochemical data. Figure 7.20 presents the three springs used in the above example.

Like the Stiff diagram, other representations can be used to show both geochemical facies and total salinity. These include circular or pie diagrams (Figure 7.21) and simple line graphs (Figure 7.22).

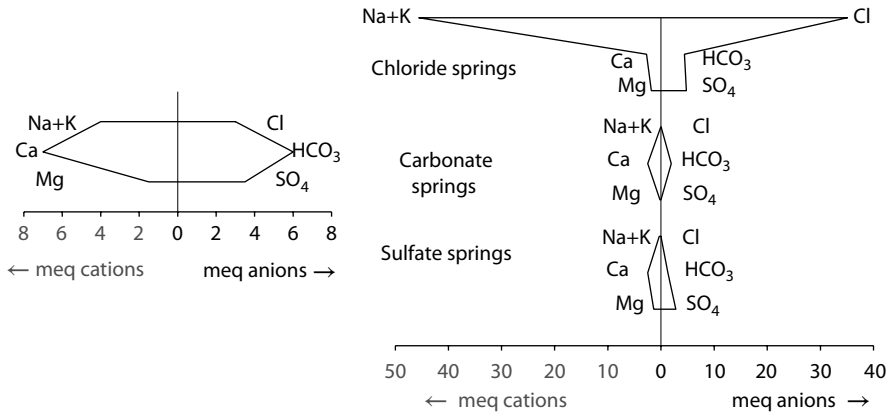

FIGURE 7.20 Stiff diagrams for a typical Ca-HCO_3 groundwater (left) and for the three groundwater sources in Table 7.2.

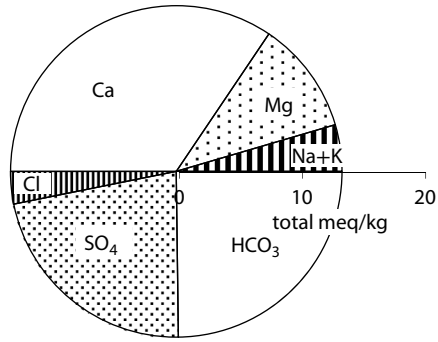

FIGURE 7.21 Pie diagram of geochemical facies.

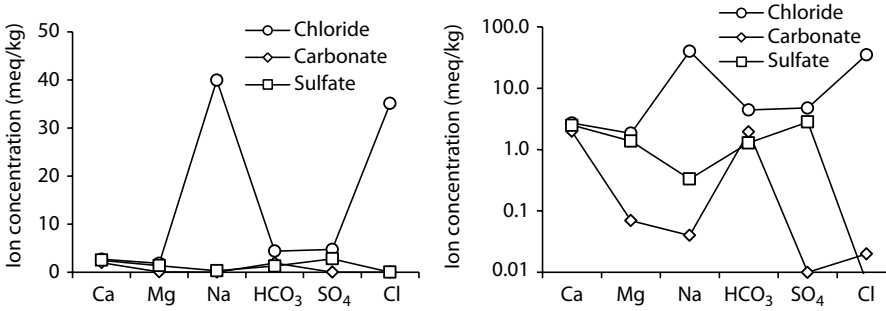

FIGURE 7.22 Normal and semilogarithmic Schoeller diagrams for spring waters in Table 7.2.

PROBLEMS

1. The following data were produced from batch tests to test the sorption of Sr^{2+} on a clay till. For the experiment, 100 g of clay till was used with 1 L water with different initial concentrations of Sr^{2+}. Calculate the amount of Sr^{2+} sorbed from the initial and final concentration data and plot the isotherm. Describe the isotherm that you plotted and calculate K_d for each batch step. What is the retardation factor at low Sr^{2+} concentrations and at high Sr^{2+} concentrations?

C_{final} (mg/L)	0.095	0.188	0.378	0.76
$C_{initial}$ (mg/L)	0.1	0.2	0.4	0.8

2. Write the two redox half reactions that define the upper and lower stability limits for water and give the their values for ΔG_r° and K.
3. Write the two redox half-reactions for the oxidation of methane with sulfate and with ferrihydrite ($Fe[OH]_3$) and determine the Gibb's free energy for each overall reaction. Which is more favorable?
4. A groundwater was sampled from a confined aquifer. The temperature was measured at 25°C, and the water had a pH of 8.15 and Eh of −0.27 V. The geochemical analysis for this water is as follows (in mg/L):

Ca^{2+}	Mg^{2+}	Na^+	K^+	Fe^{2+}	HCO_3^-	Cl^-	SO_4^{2-}	HS^-	DOC
68.71	0.34	95	5.7	<0.001	31.0	2.34	300	4.1	6.8

   Calculate an Eh for this water from the sulfate/sulfide redox couple (do not forget to use activities). What is the calculated p*e* for this water? How does your calculated Eh compare with the measured Eh? Write the geochemical reaction that is buffering redox. Note that this water contains no detectable ferrous iron. What solid phase would be limiting its concentration, and what should be the equilibrium concentration of Fe^{2+}?
5. The oxidation of ammonium by O_2 is an important reaction in soils and surface waters that releases NO_3^- to the environment. Write a redox equation for the oxidation of ammonium ($\Delta G^\circ_{NH_4^+} = -79.31$ kJ/mol) to nitrate, and determine the p*e*–pH relationship that defines the equilibrium for this redox pair at an ion activity ratio of 1 (i.e., for $a_{NO_3^-}/a_{NH_4^+} = 1$).
6. Under hyperalkaline conditions, ferrous iron oxidation to ferric iron can proceed by the reduction of water to H_2. This can be shown by calculating the redox potential for Fe^{3+}/Fe^{2+} and for H_2O/H_2 at pH 12. Which has the higher redox potential? Write an equation for this overall reaction.
7. The fractionation for deuterium between water and hydrogen gas in the Oman hyperalkaline groundwaters (section H_2O/H_2 — Reduction of Water) was used to determine the temperature of H_2 production. Using the equation for this reaction in Table 4.2, calculate the temperature for the serpentinization reaction.

8. Plot the evolution of $\delta^{15}N_{NO_3^-}$ during denitrification, using an initial nitrate concentration of 20 mg-N/L and $\varepsilon^{15}N_{NO_3\text{-}N_2}$ of 20‰. What is the value for $\delta^{15}N_{NO_3^-}$ at a residual nitrate concentration of 2 ppm N?
9. What are some potential sources of SO_4^{2-} and Cl^- in groundwaters? What about HCO_3^-?
10. Figure 7.14 and associated equations show the speciation of ferric and ferrous iron. Write redox equations for equilibrium between the various ferric iron species (Fe^{3+}, $Fe[OH]^{2+}$, $Fe[OH]_2^+$, $Fe[OH]_3^\circ$, and $Fe[OH]_4^-$) and their neighboring ferrous iron species (Fe^{2+} and $HFeO_2^-$) for the pH range of 1–13. Plot these on a p*e*–pH diagram, assuming the total dissolved Fe concentration to be 10^{-8}.
11. Graphically present the data for the groundwaters in Chapter 6, problem 16 and problem 17. How are these differentiated, and which best delineates the differences between these silicate and carbonate weathering terrains?

This page intentionally left blank

8 Groundwater Dating

INTRODUCTION

Of the considerable amount of groundwater recharge that occurs on a daily basis, most circulates rapidly to surface water drainage systems such that storm hydrographs respond closely with precipitation. Alluvial aquifers along drainage channels or shallow bedrock aquifers can respond rapidly to recharge and have groundwater with mean residence times on the order of months to a few years (Figure 8.1). Only a small fraction recharges to groundwater systems with much longer circulation times. Deeper and confined aquifers host groundwaters that may circulate over hundreds to thousands of years. Others may retain groundwaters recharged under climate conditions different from current and host *fossil* groundwaters that are not being recharged today.

Determining the mean subsurface residence time or *age* of groundwater is important for several reasons. Groundwater age translates roughly to circulation and renewability, which is critical for water resource planning. Groundwater resources identified as being modern are regularly recharged and can be sustainably developed, whereas exploiting fossil groundwaters is essentially mining the resource. The age of groundwater relates also to its vulnerability to contamination. Modern groundwaters will have more direct pathways from the surface, facilitating infiltration of contaminants from surface activities in the recharge area. Old groundwaters are isolated from the surface and perhaps less vulnerable to anthropogenic contamination.

GROUNDWATER *AGE* AND MEAN RESIDENCE TIME

Groundwater recharge occurs in most cases by infiltration of precipitation and runoff through soils, alluvial sediments and bedrock surfaces into the subsurface. It may move slowly through an unsaturated zone, or directly to the water table through macroporosity. In any case, some of the water will take a longer pathway through the pores and fissures, whereas some will take a more direct route. This process of hydrodynamic dispersion mixes waters having recharged at different times from different precipitation events. The difference in time may only be days for soil waters in the first several centimeters. In the unsaturated zone and just below the water table, a given volume may integrate groundwaters recharged over a span of weeks to months. Deeper in the aquifer, the groundwater will include components recharge over a greater range of months to years. At each point, the groundwater will have a mean age and a range of ages.

Approaches to determining the mean subsurface residence time of groundwater, the time since recharge, fall into two groups.

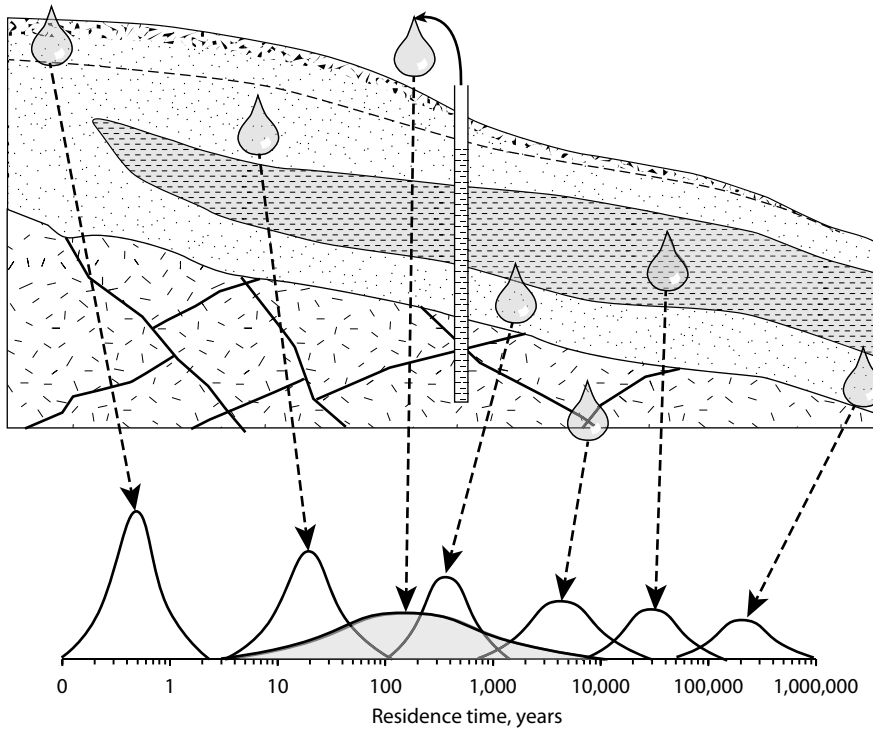

FIGURE 8.1 Ranges in subsurface residence time typical for groundwaters at different points along flow paths. Residence time, or age, increases with distance and isolation from the recharge area. The range in age also increases, due to dispersion, hydrodynamic mixing, and diffusion. Vertical scale on curves represent relative age distribution for groundwater at that point. Peak represents the mean age of groundwater.

1. Anthropogenic activities have contributed several tracers with a time-varying atmospheric history, which are transferred to the subsurface during recharge. Their concentration in groundwater relative to the atmospheric scenario can be used to constrain the time of recharge.
2. Naturally occurring radionuclides produced by cosmic rays in the atmosphere and radiogenic isotopes produced from nuclear reactions in the subsurface provide measurements of time that can be used to date groundwaters.

The selection of techniques depends on the anticipated age range of the groundwater flow system, as well as the need for resolution in refining the age calculation. All methods have constraints, whether from a sampling and analytical perspective or from an interpretive perspective. The use of two or more methods provides some measure of assurance when the results converge on an estimate of mean groundwater age. Figure 8.2 shows the typical effective age range for various methods, with details given in Table 8.1. Phillips and Castro (2003) provide a detailed overview of many of these methods. Note that many are nonroutine and experimental, and so their use is often restricted to research studies.

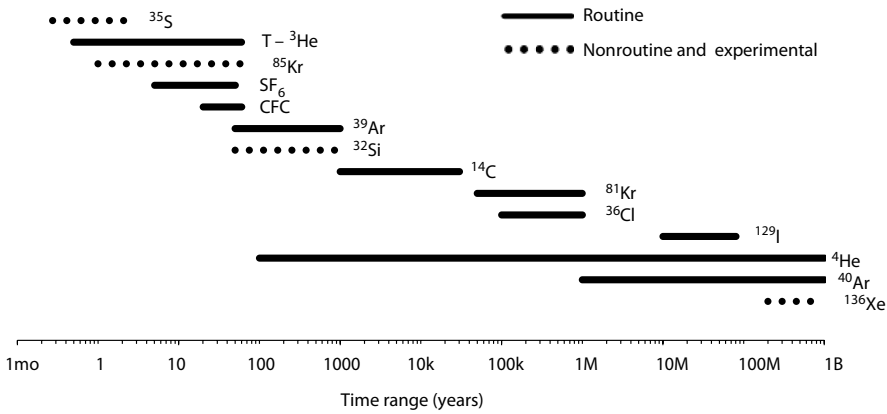

FIGURE 8.2 Age range for routine, nonroutine, and experimental radioisotopes and anthropogenic gases in groundwater dating.

TABLE 8.1
Tracers for Age Dating Groundwaters

Tracer	Half-Life	Troposphere Half-Time	Source (Target Nuclide)	Atmospheric Concentration
Modern Groundwaters				
^{35}S	87.5 d	<1 y	Cosmogenic (^{40}Ar)	Steady state
Tritium, T	12.32 y	~1 y	Thermonuclear bomb tests	5800 TU in 1963 rain
T–^{3}He	12.32 y		Cosmogenic (^{14}N)	5–15 TU
^{85}Kr	10.76 y		U-fission, fuel reprocessing	1.8 Bq/m^3, increasing
SF_6	Stable	3200 y	Electrical insulator emissions	7 pptv, increasing
CFC	Stable	100–200 y	Refrigerant emissions, aerosols	CFC-12: 538 ppt in 2000
Sub-Modern Groundwaters				
^{39}Ar	269 y		Cosmogenic (^{40}Ar)	16.7 mBq/m^3
^{32}Si	~172 y	<1 y	Cosmogenic (^{40}Ar)	2 atoms/m^2/s
Old Groundwaters/Brines				
^{14}C	5730 y	~4 y	Cosmogenic (^{14}N)	100 pMC, 0.226 Bq/g C
^{81}Kr	229,000 y		Cosmogenic (^{80}Kr)	1.8 μBq/m^3
^{36}Cl	301,000 y	<1 y	Cosmogenic (^{35}Cl)	<50 atoms/m^2/s
			Subsurface, (^{35}Cl)	$^{36}Cl/Cl > 500\times10^{-15}$
^{129}I	15.8 My	<1 y	Cosmogenic (^{129}Xe)	100,000 atoms/L
			Subsurface (^{238}U sp. fission)	$<500\times10^{6}$ atoms/L
^{4}He	Stable		Subsurface (U and Th α-decay)	5.24×10^{-6} ppmv
^{40}Ar	Stable		Subsurface (^{40}K)	0.93%
^{136}Xe	Stable		Subsurface (^{238}U sp. fission)	8.9% of Xe_{atm}

ANTHROPOGENIC TRACERS OF MODERN GROUNDWATER

Emissions of certain anthropogenic components to the atmosphere provide useful tracers of recent groundwater recharge. Where the atmospheric concentration follows a documented ingrowth function, this can be used to constrain age through measurement of the tracer in groundwater and comparison with its atmospheric history. Two principal modern tracers fall into this category: SF_6 and ^{85}Kr. Complications arise when the tracer concentration levels off or declines, which can reduce age resolution or generate ambiguities. Tracers in this group include chlorofluorocarbons (CFCs) and thermonuclear bomb tritium.

Tritium was the first such tracer used, which had increasing atmospheric concentrations generated through the atmospheric testing of thermonuclear devices, or hydrogen fusion bombs, and culminated in the well-known 1963 tritium peak in precipitation. The implementation of the U.S.–USSR atmospheric Test Ban Treaty in 1964 ended most atmospheric testing and reversed the trend for tritium in precipitation. The use of tritium in groundwater age dating remains a routine method, enhanced more recently by combining T with its daughter, ^{3}He, to resolve groundwater ages independently of the complicated tritium input function. This is discussed later.

Chlorofluorocarbons and SF_6

Chlorofluorocarbon compounds (CFCs), used in air conditioners and as aerosol propellants since the 1940s, have steadily accumulated in the atmosphere. With their increasing atmospheric concentrations and conservative behavior in aerobic groundwaters, CFCs became an important tool for dating (IAEA 2006). Following discovery of their role in the photochemical degradation of stratospheric ozone, the 1989 Montreal Protocol greatly reduced global emissions such that atmospheric concentrations leveled off in the 1990s and are now declining (Figure 8.3). Like tritium, this has now introduced ambiguity into the interpretation of CFC ages. Other complications include their temperature-dependent solubilities, elevation, and effect of salinity. Warner and Weiss (1985) determined their solubilities, with Henry's Constants of 0.0127 and 0.0035 mol/L/atm for CFC-11 and CFC-12, respectively, at 20°C, but varying by almost an order of magnitude between 0°C and 40°C.

The ambiguity from declining atmospheric CFC signals is not found for the use of SF_6. This nontoxic, inert gas is used as an insulator in electrical equipment, such as high-voltage supplies. It has been accumulating in the atmosphere since the 1950s, with an ingrowth function that has remained essentially linear over the past two decades (Darling et al. 2012). SF_6 has an even lower atmospheric concentration and lower Henry's constant (0.00024 at 25°C), such that aqueous concentrations are less than about 3 fmol/L (3×10^{-15} mol/L). There is evidence, however, that the atmospheric concentrations reconstructed at the hemispheric scale are exceeded in the regions around major urban centers, requiring special consideration of the input function used in such areas (Santella et al. 2008). Despite these constraints on the input function and measurement, SF_6 has become a complementary tracer to CFCs and is now routinely analyzed by many laboratories.

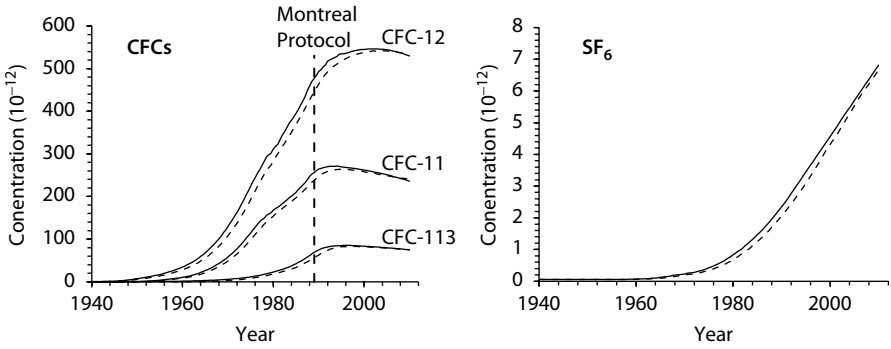

FIGURE 8.3 Atmospheric concentrations of CFCs and SF_6 in northern hemisphere (solid lines) and southern hemisphere (dashed lines). (Data from water.usgs.gov/lab/software/air_curve/.) The air-equilibrated water concentrations depend on water temperature. For low-salinity waters, the temperature-dependent values Henry's constant can be calculated from the following equations (T in degree Celsius) based on data in IAEA (2006) for CFCs and in Sander (1999) for SF_6:

$$K_{\text{CFC-11}} = -6.22 \times 10^{-7} T^3 + 6.15 \times 10^{-5} T^2 - 2.27 \times 10^{-3} T + 3.85 \times 10^{-2}$$

$$K_{\text{CFC-12}} = -1.28 \times 10^{-7} T^3 + 1.30 \times 10^{-5} T^2 - 5.03 \times 10^{-4} T + 9.37 \times 10^{-3}$$

$$K_{\text{CFC-113}} = -2.28 \times 10^{-7} T^3 + 2.21 \times 10^{-5} T^2 - 7.95 \times 10^{-4} T + 1.25 \times 10^{-2}$$

$$K_{\text{SF}_6} = -1.95 \times 10^{-9} T^3 + 2.60 \times 10^{-7} T^2 - 1.57 \times 10^{-5} T + 5.01 \times 10^{-4}$$

Example 8:1 Dating Groundwater with CFC Concentrations

What is the concentration of CFC-12 in groundwaters at 20°C recharged in the year 2000, following the Montreal Protocol ban?

From Figure 8.3, the atmospheric mixing ratio of CFC-12 is 550 pptv or 5.50×10^{-10}. Assuming an atmospheric pressure of 1 atm and using the temperature equation for CFC-12 in Figure 8.3 Henry's constant of 0.0035 mol/L/atm, this gives the aqueous concentration, according to Henry's Law:

$$K_{\text{gas}} = \frac{m_{\text{gas}}}{P_{\text{gas}}}$$

$$K_{\text{CFC-12}} = 0.0035 = \frac{m_{\text{CFC-12}}}{P_{\text{CFC-12}}} = \frac{m_{\text{CFC-12}}}{5.50 \times 10^{-10}}$$

$$m_{\text{CFC-12}} = 1.9 \times 10^{-12} \text{mol/L}$$

Given that their atmospheric concentrations are lower in the past, air contamination during sampling is a great risk. For this reason, rigorous field and laboratory protocols are required (Darling et al. 2012).

Like SF_6, the radionuclide ^{85}Kr released from nuclear fuel reprocessing has a steadily increasing atmospheric concentration. Unlike SF_6, it decays, with a half-life of 10.76 years, by β emission to common ^{85}Rb. Back-extrapolation from a measured value along a decay line to the input function provides an unambiguous age that can be quite accurate. However, its use is not routine due to the large samples required (thousands of liters) to strip enough gas for radiometric counting, and the potential for atmospheric contamination.

The use of the dissolved concentration of atmospheric gases, such as CFCs, SF_6, and ^{85}Kr, has an additional complication from the physical incorporation of microbubbles of air during recharge at the water table. Entrained with the influx of groundwater following a recharge, this excess air can add a significant fraction of gas, which is then dissolved as the groundwater recharges to higher pressures below the water table. This can be corrected for using the solubility and concentration of a gas with a known and stable concentration, such as Ne, Ar, or N_2.

Thermonuclear Tritium and the 1963 Peak

The first test of fission for a nuclear weapon was the *Trinity* plutonium device detonated on July 16, 1945. Six years later, hydrogen fusion was demonstrated on May 9, 1951, with the fission device code-named *George*, which fused a small core of deuterium to helium. On November 1, 1952, the first thermonuclear bomb, *Ivy Mike*, was tested. The 10.4 megaton explosion obliterated the Enewatak Atoll in the Marshall Islands of the western Pacific Ocean, generating a fireball over 3 miles wide with a rate of neutron production calculated to be greater than that of a supernova. The ensuing decade of American and Soviet atmospheric tests ended in 1962 with a final release of over 140 megatons of energy. The 1963 Soviet–American atmospheric test-ban treaty brought subsequent testing of nuclear weapons underground. The neutron flux associated with these thermonuclear tests activated ^{14}N and other nuclides in the atmosphere, producing tritium as well as ^{14}C, ^{36}Cl, and other radionuclides.

The Soviet tests were conducted in eastern Kazakhstan at about 50°N, and the American tests in the Marshall Islands of the eastern Pacific Ocean at 12°N. The resulting spike of tritium in precipitation was over 5000 TU in the northern hemisphere in the spring of 1963 (Figure 8.4). Levels in the southern hemisphere were much lower and lagged northern hemisphere precipitation by a few years (Figure 8.5). The 1963 tritium peak remains a well-defined feature in ice caps (Figure 8.6) where it is attenuated only by decay.

Very few measurements exist of natural, prebomb tritium in precipitation. Precipitation near Ottawa had about 10 to 15 TU before 1951, as determined from archived samples and vintage wines bottled in the 1940s (Brown 1961).

The 1963 peak became a useful time horizon used in many hydrogeological studies to determine recharge and flow velocities, such as the case for the vertically recharged groundwaters in the Sturgeon Falls deltaic sand aquifer (Robertson and Cherry 1989; Figure 8.6). While the 1963 peak has been flushed from most groundwater systems, residual bomb tritium may remain although highly attenuated by

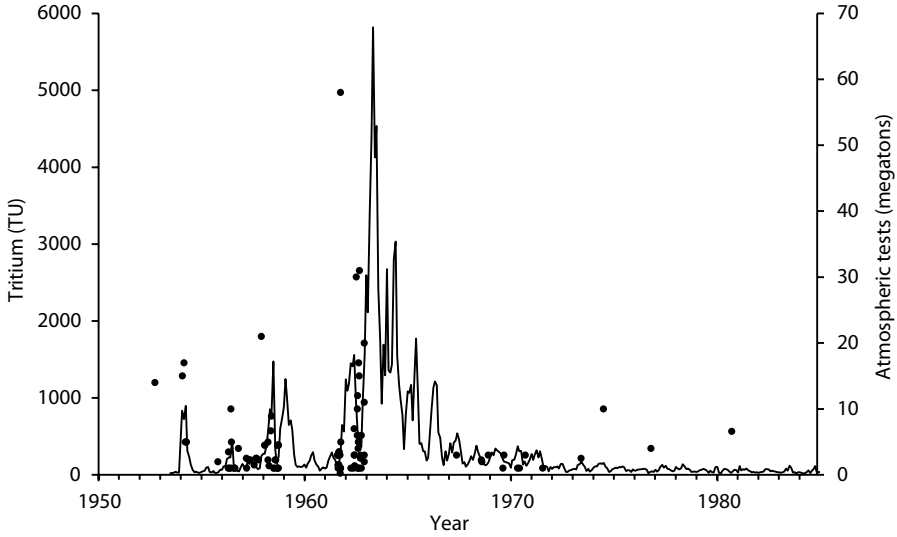

FIGURE 8.4 The production of anthropogenic tritium as a consequence of atmospheric testing of thermonuclear (hydrogen-fusion) weapons. The Ottawa record is the longest continuously monitored tritium record for precipitation, begun in 1951 by Dr. Bob Brown, a radiochemist with Atomic Energy of Canada Limited, Chalk River, Ontario, and maintained by the Environmental Isotope Laboratory, University of Waterloo, Ontario, available through IAEA/WMO (2013). The limited test-ban treaty of 1963 between the USSR and United States began an era of recovery to background levels. Annual leaks of tritium from the stratosphere to the troposphere occur each spring with the northward shift of the Hadley cells and the jet stream.

dispersion and decay. Where identified, the 1963 peak has been used for calculation of groundwater flow velocity and recharge rates.

Calculating groundwater age by simple decay is complicated by the varying input function and requires that there has been no significant hydrodynamic dispersion (i.e., piston flow). The calculation uses the decay equation where the measured tritium concentration T_t after some time, t, is equal to the initial concentration, T_0 multiplied by the exponential decay function:

$$T_t = T_0 e^{-\lambda t}$$

From above, the decay constant, λ, is equal to ln2 divided by the half-life, $T_{½}$. Using tritium's half-life of 12.32 years, this equation can be rewritten:

$$t = -17.77 \ln \frac{T_t}{T_0}$$

This equation is visually represented by the decay curves in Figure 8.7, which decrease by 5.6% per year. Back-extrapolation to the input function theoretically

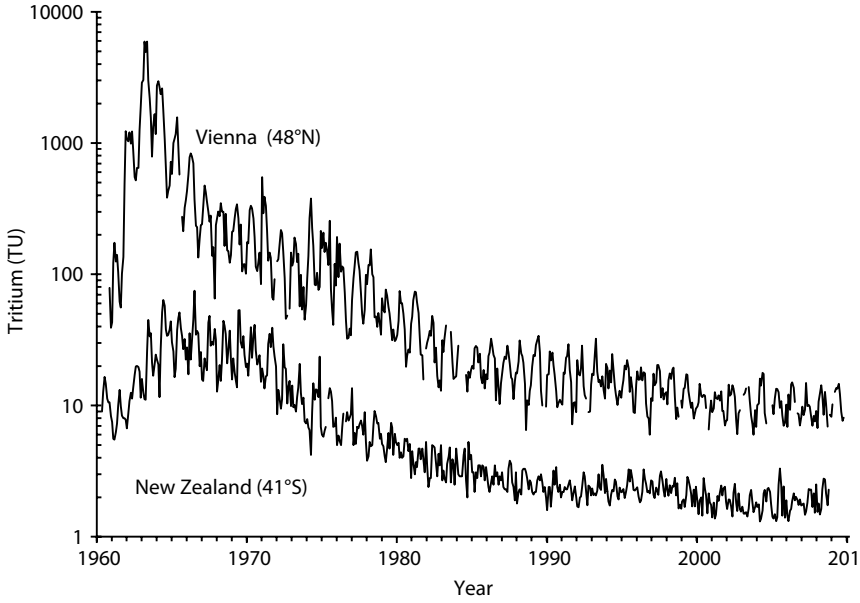

FIGURE 8.5 Magnitude and attenuation of the 1963 thermonuclear tritium peak in northern and southern hemisphere precipitation. The high production from Soviet tests in Kazakhstan by the American tests in the Marshal Islands is seen in the high fallout for the northern latitudes shown for Vienna, Austria. Transfers to the southern hemisphere represented by New Zealand are attenuated by a factor of over 10. Both hemispheres have essentially recovered to natural production levels by the year 2000.

provides a determination of age. The problem is that groundwaters recharged at any time since about 1972 have tritium that is decaying at the same rate of decline as the input function, precluding the use of such a simple decay model (Figure 8.7). Simple decay also fails to capture the reduction in tritium by dispersive mixing. More realistic are lumped parameter models that combine cumulative tritium input over specified period with dispersion, mixing, and decay (Maloszewski and Zuber 1982, 1996). Doney et al. (1992) parameterize the bomb contribution to annual precipitation globally to determine atmospheric scenarios for bomb tritium at specific locations. The USGS has developed this approach into an accessible Excel-based program, Tracer LPM, to model tritium and other atmospheric tracers of groundwater age (Jurgens et al. 2012).

As the 1963 tritium spike recedes into the past, its use as a time horizon for dating groundwaters diminishes. Hydrogeologists now rely on measurement of the daughter ^{3}He, discussed later, which provides an age estimate that is independent of the input concentration of tritium and so is not compromised by its complicated atmospheric scenario.

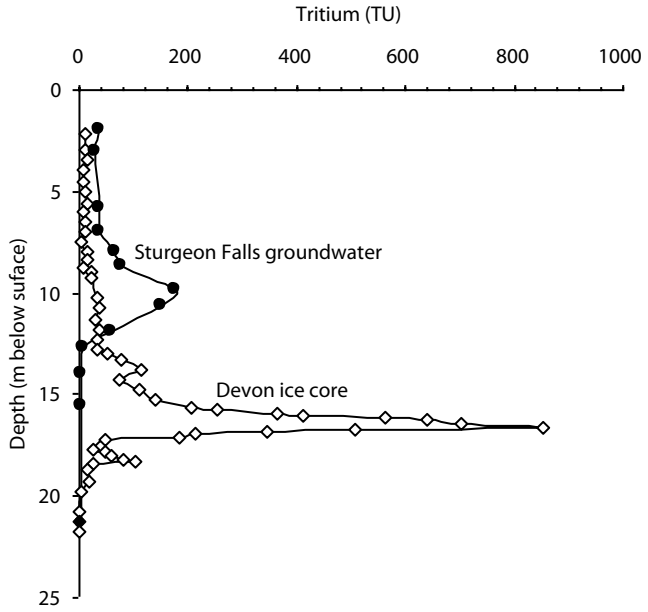

FIGURE 8.6 Preservation of the 1963 bomb peak in precipitation measured in an ice core collected in 1998 from Devon Island Ice Cap (Clark et al. 2007), and in downward-moving groundwater sampled in a sandy aquifer near Sturgeon Falls, Ontario (Robertson and Cherry 1989; Renaud et al. 2005). Note the highly attenuated peak in the groundwater due to hydrodynamic dispersion and decay, whereas the glacier ice experiences only decay.

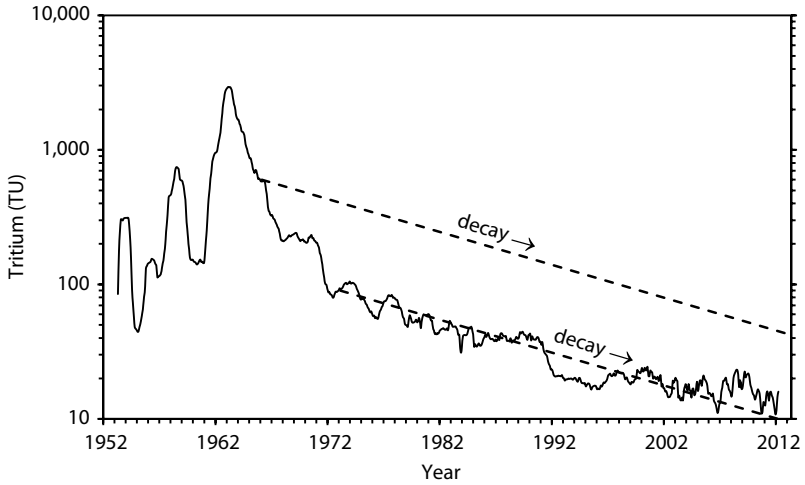

FIGURE 8.7 Tritium concentrations in composite monthly precipitation from Ottawa, Canada. Dashed lines represent radioactive decay. Tritium decay in groundwaters recharged after about 1972 follows the atmospheric scenario, and so T_0 is ambiguous, requiring exponential decay models (Jurgens et al. 2012) with mixing and dispersion.

Anthropogenic ^{85}Kr

The reprocessing of spent nuclear fuel to recover uranium and plutonium and remove fission products releases radioisotopes of noble gases to the atmosphere. The short-lived noble gases, including ^{133}Xe ($T_{½}$ = 5 days) and ^{37}Ar ($T_{½}$ = 35 days), readily decay to stable nuclides. However, the longer-lived krypton fission product, ^{85}Kr ($T_{½}$ = 10.76 years), has been steadily accumulating in the atmosphere (Figure 8.8). Unlike thermonuclear tritium, the ^{85}Kr signal is not decreasing. As a noble gas, it therefore provides a geochemically conservative tracer of modern recharge. Unfortunately, the low concentrations at which it is found in recharge precludes this interesting tracer from routine application for dating groundwaters.

In a study of groundwaters in an aquifer of pyroclastic material in the Kumamoto volcanic region of Japan, Momoshima et al. (2011) use ^{85}Kr to date groundwater from two sites along the hydrodynamic flow path. Their method is based on scintillation counting required recovery of gas from over 5 m^3 (5000 L) of groundwater. Contamination from the atmosphere is a concern for such tracers, requiring closed system extraction methods in the field. Measurements are made on the total krypton separated from the extracted gases in the groundwater and expressed as the ^{85}Kr activity in Bq normalized to the total stable Kr extracted. These were then simply compared to the decay-corrected ^{85}Kr/Kr atmospheric scenario (Figure 8.8) to give groundwater ages of 8.2 ± 0.7 years and 20.7 ± 0.6 years at the respective sites, which compared favorably with tritium and hydrodynamic ages.

Recently, new atom-counting techniques using laser trapping and cooling of Kr (Atom Trap Trace Analysis; Sturchio et al. 2004; Jiang et al. 2012) has reduced the sample requirement from over 200 µL of Kr to less than 0.5 µL STP. This greatly reduces the amount of groundwater from which the Kr sample must be stripped from solution.

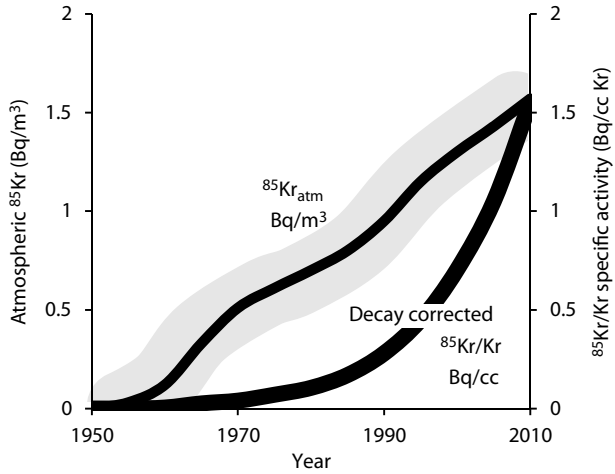

FIGURE 8.8 Global atmospheric ^{85}Kr compiled by Momoshima et al. (2011), gray represents variability from nuclear reprocessing activities. The ^{85}Kr/Kr specific activity ratio in the atmosphere, corrected for decay to 2010 for comparison with ^{85}Kr/Kr in groundwater.

Example 8.2 Calculating Sample Size for Kr Isotope Analysis

How much water is required to extract sufficient Kr for an isotope analysis by scintillation counting and by laser trap methods?

Kr Atmospheric partial pressure (Table 3.5)	1.14×10^{-6} atm	
Bundsen's coefficient of Kr solubility	0.0562 cc_{STP}/cc_{H_2O}/atm	
Kr solubility in recharge (at 25°C)	$1.14 \times 10^{-6} \times 0.0562 = 6.41 \times 10^{-8}$ cc_{STP}/cc_{H_2O}	
	Scintillation	*Laser Trapping*
Krypton required (μL STP)	200	0.5
(cc STP)	0.2	0.0005
Volume of water required (cc)	$0.2/6.41 \times 10^{-8}$ = 3,120,000	$0.0005/6.41 \times 10^{-8}$ = 7,800
Volume of water required (L)	3,120	7.8

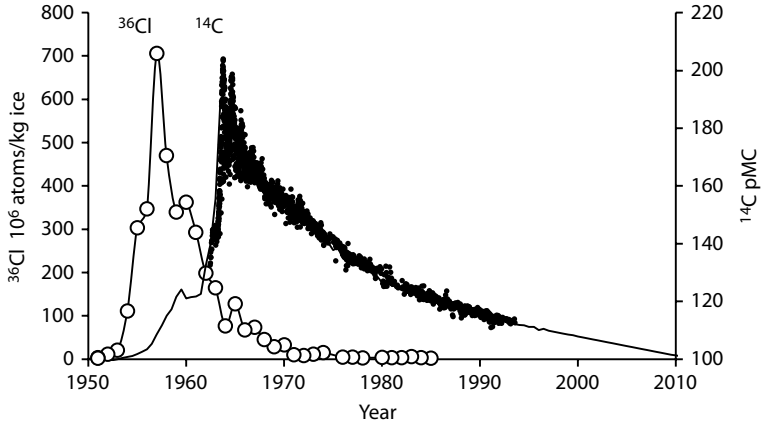

FIGURE 8.9 Anthropogenic ^{36}Cl and ^{14}C in the atmosphere following thermonuclear bomb testing. The ^{36}Cl peak follows detonations at sea between 1954 and 1958, as observed in fallout recovered from the Dye-3 ice core from Greenland (Synal et al. 1990). The thermonuclear radiocarbon record (Nydal and Lövseth 1983; with data before 1962 and after 1980 from Jurgens et al. 2012) is similar to that of bomb tritium peak, as both are from neutron activation of atmospheric ^{14}N.

Thermonuclear ^{14}C and ^{36}Cl

The testing of nuclear devices during the 1950s and 1960s generated more than a peak in tritium in the atmosphere. The levels of ^{14}C in atmospheric CO_2 and ^{36}Cl in atmospheric Cl also increased considerably above their natural abundance levels. Early in the era of thermonuclear weapons testing, ship borne devices were detonated at sea, resulting in the neutron activation of ^{35}Cl in seawater and subsequent injection into the upper atmosphere by the ensuing fireball. Synal et al. (1990) recovered the atmospheric fallout pattern over this period in an ice core from the Greenland ice sheet near the Dye-3 site (Figure 8.9).

The natural background for atmospheric ^{14}C in CO_2 was close to 100 pMC (percent Modern Carbon) or 0.226 Bq/g C. The high neutron flux from atmospheric testing of thermonuclear weapons activated ^{14}N to produce ^{14}C, raising $^{14}CO_2$ activities to over 200 pMC (Figure 8.9). This has subsequently been attenuation by exchange with the oceans although thermonuclear radiocarbon persists in the biosphere, such that most vegetation and shallow soil carbon have ^{14}C activities above 100 pMC.

Like tritium, both ^{36}Cl and ^{14}C can serve as useful tracers of modern groundwater recharge, although their atmospheric concentrations have recovered to natural production levels. Thermonuclear radiochloride, as a conservative solute, has largely been flushed from aquifers. By contrast, biomass that grew during the past decades retains these high radiocarbon activities and so serves as a useful tracer of carbon. Examples include dissolved inorganic carbon (DIC) and dissolved organic carbon (DOC) from landfill leachate impacting groundwaters, in which elevated ^{14}C in these compounds can serve as tracers (Hackley et al. 1996).

TRITIUM–^{3}He DATING

The tritium peak from atmospheric testing of thermonuclear weapons proved to be a valuable time horizon for dating modern waters during the latter half of the twentieth century. This peak has now been attenuated through decay or has been flushed from most aquifers. Global monitoring shows tritium concentrations in rainfall to have stabilized at natural background levels for over two decades. Nonetheless, new developments in low-detection analysis coupled with the added precision of tritium–helium dating allow the continued use of tritium dating based on background signals.

The presence of tritium in groundwater, at its most fundamental level of interpretation, is an indication that the groundwater contains at least some component of modern recharge. Modern recharge is taken to be younger than the onset of thermonuclear bomb tests. Today, this gives a time constraint of some 50 years. However, different scenarios for groundwater flow and discharge will greatly affect the concentration of tritium at the point of recharge. Groundwater mixing, particularly at the discharge zone in spring vents or in open boreholes, greatly affects the range of groundwater ages.

Natural Production of Tritium in the Atmosphere

Cosmogenic or natural tritium production occurs in the upper atmosphere from the bombardment of nitrogen by the flux of secondary neutrons in the atmosphere generated by cosmic radiation, following the reaction

$$^{14}N + {}^{1}n \rightarrow {}^{12}C + T$$

The tritium thus formed combines with stratospheric oxygen and hydroxyl ions to form water

$$T^+ + OH^- \rightarrow HTO,$$

and enters the troposphere through mixing at the tropopause. This flux is not great, providing about 5 to 20 TU (5 to 20 parts per 10^{18}).

The cosmic ray flux and tritium production varies with geomagnetic latitude with elevated production at higher latitudes. This latitudinal variability and the effect of dilution by coastal water vapor from the tritium-free oceans cause some variability in the distribution of global tritium in precipitation. Precipitation monitoring at a number of stations world wide by the International Atomic Energy Agency's Global Network for Isotopes in Precipitation (GNIP) provides freely accessible data. Figure 8.10 shows trends for a selection of stations over a range of latitudes and continents. Most stations show stabilization over the past decade, indicating that they have recovered from the era of thermonuclear bomb testing and have returned to natural atmospheric production levels.

An annual spring peak of tritium is seen in most records due to seasonal transfers from the stratosphere, where it is produced, to the troposphere, where it enters the hydrological cycle. The latitudinal variability in production and the effect of proximity to the oceans are evident in Figure 8.10. The low latitude oceanic station Quezon City at 15°N in the Philippines has stabilized at tritium values less than 2 TU, whereas a high latitude, inland station such as Krakow, Poland (50°N), is at 10 TU. Stations near centers of nuclear activity, such as Ottawa, Canada, may have occasional contributions from local sources that raise values above the natural background. In contrast, stations remote from nuclear activities, such as Kaitoke, New Zealand, and Halley Bay, Antarctica, have more harmonic signals that suggest an influence of solar cycle 24 on tritium production by attenuation of cosmic radiation during increased solar activity. Elevated tritium is apparent at these stations during the solar minima in 1995 and 2009, and lower values correlate with the solar maximum near the year 2000.

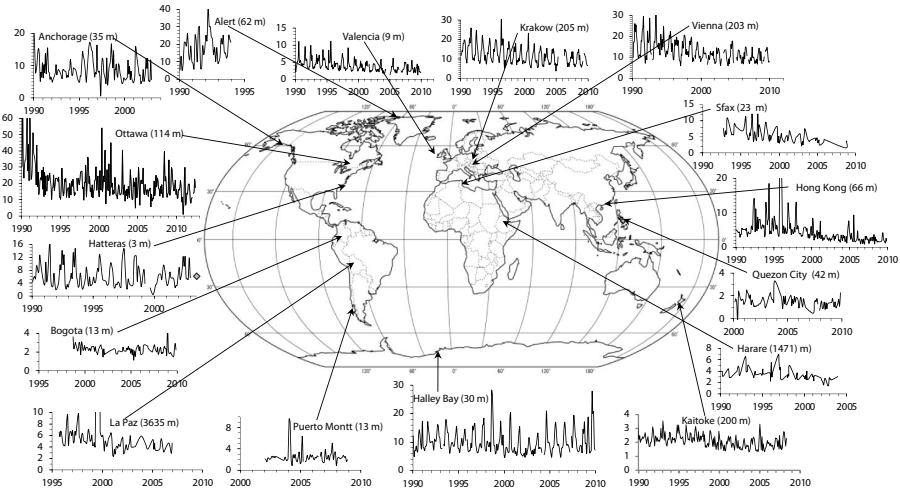

FIGURE 8.10 Trends for global tritium in precipitation since 1990. (Data from IAEA/WMO, The GNIP Database, 2013. Accessible at: http://www.iaea.org/water.) High latitude and high elevation as well as distance from coastal waters contribute to increased natural tritium production.

Unlike other radionuclides like ^{129}I and ^{36}Cl, subsurface production of tritium is generally negligible. It is produced through the fission of ^{6}Li from the neutron flux present in all U-bearing rocks (Figure 4.10) according to

$$^{6}Li + n \rightarrow {}^{3}H + \alpha$$

However, tritium's short half-life allows insufficient time for any measurable accumulation except in high U-bearing granite or in uranium ore zones. Andrews et al. (1989), for example, calculate a concentration of less than 1 TU from subsurface production in the Stripa granite in Sweden, which has a high uranium content of 44 ppm.

Dating Groundwaters with T–^{3}He

Groundwater age can be calculated for any tritium-bearing groundwater from the exponential decay equation,

$$T_t = T_0 e^{-\lambda t}$$

providing that the groundwater has followed a simple piston flow and the initial tritium concentration at time of recharge, T_0, is known (Figure 8.10). However, recharge may involve the integration of precipitation with variable tritium concentrations over a substantial period. Consider the two wells in Figure 8.11. The phreatic

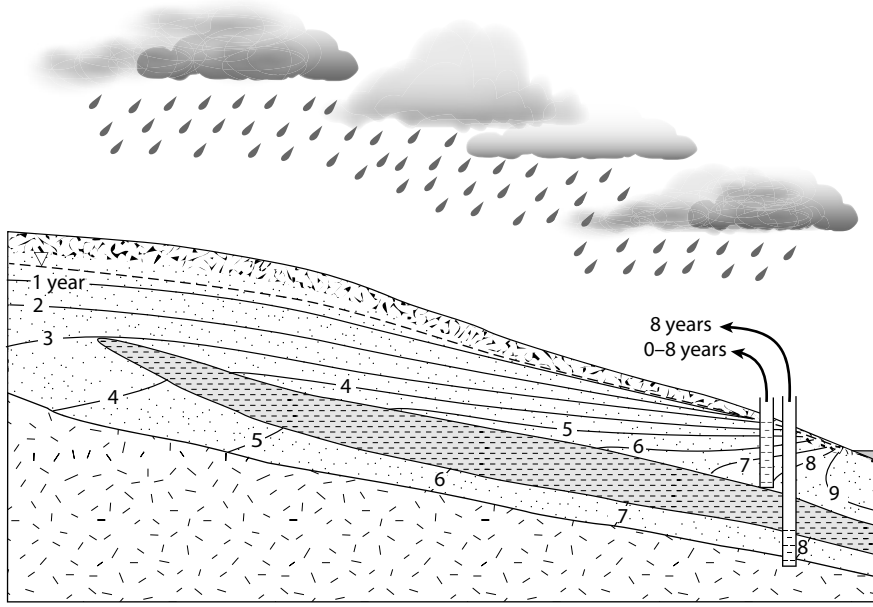

FIGURE 8.11 Schematic of groundwater age for exponential mixing in a phreatic aquifer and piston-flow in a confined aquifer. Note that the simple piston-flow hydrodynamic dispersion would broaden the range of ages in the sample. Groundwater sampled from the well in the phreatic aquifer has recharge along its length and so integrates precipitation over a longer period of time, giving a broader range of ages, whereas the confined aquifer well samples groundwater recharged over a well-constrained period of time.

aquifer gains recharge along its full length, such that groundwater sampled down gradient integrates a greater range of ages than the groundwater in the confined aquifer. Groundwater comprising recharge over a greater range of years has greater the uncertainty on the initial tritium input, T_0, and so greater error on its age from the exponential decay equation.

Initial tritium is poorly known in most groundwater systems due to seasonal, interannual, and spatial variability. However, knowledge of T_0 is not required if the accumulated daughter, tritigenic ^{3}He, is also measured in the groundwater at the time of sampling. Measuring tritigenic ^{3}He can allow much more precise age calculations, often with resolution to months. An increasing number of noble gas laboratories are now available to provide measurements of ^{3}He in groundwater to complement enriched tritium measurements for this now routine dating scheme.

The T–^{3}He dating method combines the two exponential functions for loss of parent and gain of daughter shown in Figure 4.8.

Loss of initial tritium	$T_t = T_0 e^{-\lambda t}$
Gain of tritigenic ^{3}He	$^3He_t = T_0(1 - e^{-\lambda t})$

By rearranging the tritium decay equation and substituting into the ^{3}He ingrowth equation, the input concentration of tritium T_0 is removed, and time, t, can be calculated from the measured tritium and ^{3}He concentrations:

$$^3He_t = T_t(e^{\lambda t} - 1)$$

The measured helium concentration, ^3He_t, is expressed in TU (1 ^{3}He per 10^{18} H). It must also be corrected for atmospheric ^{3}He that accompanies the groundwater during recharge. The atmospheric ^{3}He includes both a dissolved component and an excess air component that can be entrained as microbubbles during recharge. Atmospheric He has a partial pressure of 5.24×10^{-6} and a dissolved concentration that ranges from 5.0×10^{-8} cc_{STP}/cc_{H_2O} at 0°C to 4.58×10^{-8} cc_{STP}/cc_{H_2O} at 30°C (Figure 8.12) and has a ^{3}He/^{4}He ratio in air-equilibrated water of 1.36×10^{-6}. This ratio is slightly less than the atmospheric ratio of 1.38×10^{-6} due to fractionation during dissolution, which favors ^{4}He in water. Note that the abundance of ^{3}He is only 1.38 ppm, and so measurements of total helium are essentially a measurement of ^{4}He. In calculations below, ^{4}He is taken to be total helium for solubility considerations, and ^{3}He concentrations are then determined by multiplying He (cc_{STP}/cc_{H_2O}) by the ^{3}He/^{4}He ratio.

$$^3He\left(cc_{STP}/cc_{H_2O}\right) = He\left(cc_{STP}/cc_{H_2O}\right) \times {}^3He/{}^4He$$

Contributions of ^{3}He from excess air are normally determined by the excess Ne in the sample, for which its solubility is less sensitive to temperature than for He. If Ne is not measured, the dissolved plus excess air components can be calculated from the measurement of total He.

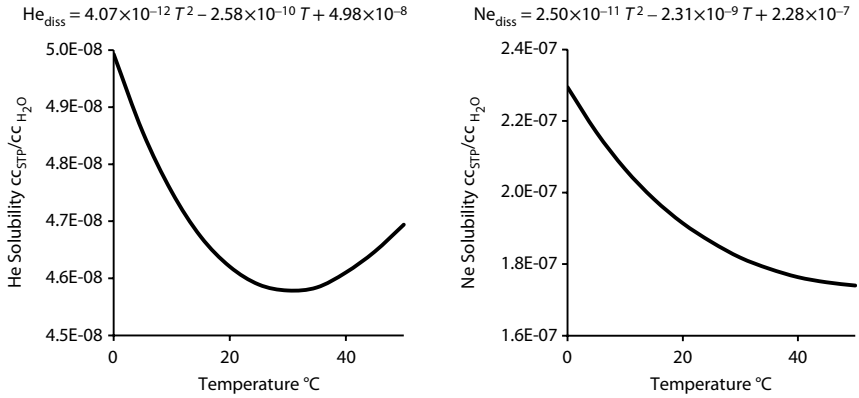

FIGURE 8.12 Solubility of atmospheric helium and neon in fresh water at different temperatures. Equations use temperature in degrees Celsius.

Example 8.3 Correcting ^{3}He for Dissolved Atmospheric He and Excess Air

What is the tritigenic ^{3}He content in groundwater that has been sampled and analyzed for both He and Ne? Note that the measured temperature of shallow groundwater in low-relief areas can be taken as the temperature in the recharge environment.

1. Measurements
   Total He = 7.75×10^{-8} cc_{STP}/cc_{H_2O}
   Total Ne = 3.11×10^{-7} cc_{STP}/cc_{H_2O}
   $^3He/^4He = 1.86 \times 10^{-6}$
   Temperature = 10°C
2. Calculate excess air and excess He from air, He_{excess}.
   From the temperature–solubility equations in Figure 8.12, the concentrations of atmospheric He and Ne would be as follows:

$$He_{diss} = 4.76 \times 10^{-8}\, cc_{STP}/cc_{H_2O}$$
$$Ne_{diss} = 2.07 \times 10^{-7}\, cc_{STP}/cc_{H_2O}$$

   The helium acquired from excess air is calculated from excess neon, as the difference between the measured neon concentration, Ne_{meas} and neon in air-equilibrated water, Ne_{aew}, as follows:

$$Ne_{excess} = Ne_{meas} - Ne_{aew}$$
$$= 3.11\times10^{-7} - 2.07\times10^{-7} = 1.04\times10^{-7}\, cc_{STP}/cc_{H_2O}$$
$$He_{excess} = Ne_{excess} \times He/Ne_{air}$$
$$= 1.04\times10^{-7}\left(5.24\times10^{-6}/1.82\times10^{-5}\right)$$
$$= 2.99\times10^{-8}\, cc_{STP}/cc_{H_2O}$$

3. He isotope ratios in air and in air-equilibrated water (known):

$$^3He/^4He_{air} = 1.38 \times 10^{-6}$$
$$^3He/^4He_{aew} = 1.36 \times 10^{-6}$$

4. Calculate total ^3He:

$$\begin{aligned} ^3He_{total} &= He_{meas} \times {}^3He/{}^4He_{meas} \\ &= 7.75 \times 10^{-8} \times 1.86 \times 10^{-6} \\ &= 1.44 \times 10^{-13} \end{aligned}$$

5. Calculate tritigenic ^3He:

$$\begin{aligned} ^3He_{trit} &= {}^3He_{total} - \left(He_{aew} \times {}^3He/{}^4He_{aew}\right) - \left(He_{excess} \times {}^3He/{}^4He_{air}\right) \\ &= 1.44 \times 10^{-13} - \left(4.76 \times 10^{-8} \times 1.36 \times 10^{-6}\right) - \left(2.99 \times 10^{-8} \times 1.38 \times 10^{-6}\right) \\ &= 3.8 \times 10^{-14}\, cc_{STP}/cc_{H_2O} \end{aligned}$$

The total ^3He measured in this groundwater was 1.44×10^{-13} cc_{STP}/cc_{H_2O}, of which 3.8×10^{-14} cc_{STP}/cc_{H_2O} or about 26% was produced by decay of tritium in the subsurface.

Note that the same calculation can be made without Ne, by using the solubility of He in water at the recharge temperature, in this case at 10°C. This is done by calculating excess He_{excess} at step 2:

Using the temperature–solubility equation for He in Figure 8.12, the concentration of atmospheric He dissolved at recharge would be

$$He_{aew} = 4.76 \times 10^{-8}\, cc_{STP}/cc_{H_2O}$$

And the He from excess air is then calculated:

$$He_{excess} = 7.75 \times 10^{-8} - 4.76 \times 10^{-8} = 2.99 \times 10^{-8}\, cc_{STP}/cc_{H_2O}$$

The calculation of tritigenic $^3He_{trit}$ then continues through steps 3, 4, and 5, above.

The measured value of ^3He, corrected for atmospheric ^3He, represents ^3He ingrown from ^3H decay, and is then used in the dating equation: $^3He_t = T_t\,(e^{\lambda t} - 1)$ and reconfigured to calculate time, t:

$$t = 17.77 \times \ln\left(1 + \left[{}^3He_t\right]/\left[T_t\right]\right)$$

where $[^3He_t]/[T_t]$ is the concentration ratio of these two isotopes expressed in tritium units. To make this age calculation, the corrected ^3He concentration in volumetric units of cc of ^3He at STP per cc water must be converted to equivalent tritium units, or atoms $^3He_{trit}$ per 10^{18} atoms of H. This is done with the gas law and the moles of H in a cubic centimeter of water. Making this conversion and then calculating age is demonstrated in Example 8.4.

Example 8.4: Calculating the T–^{3}He Age for Groundwater

What is the calculated age of groundwater in a shallow sandy aquifer that has been sampled for T and ^{3}He? In this case, the ^{3}He has been corrected for atmospheric He from recharge as shown in Example 8.3.

Measurements

Tritium, T = 4.7 TU

Tritigenic $^3He = 3.8 \times 10^{-14}$ cc_{STP}/cc_{H_2O}

To use the ^{3}He/T—age relationship above, the measured ^{3}He concentration in units of cc_{STP} per cc_{H_2O} needs to be converted to tritium units, that is, the number of ^{3}He atoms per 10^{18} atoms of H.

$$\begin{aligned} {}^3He &= 3.8 \times 10^{-14} cc_{STP}/cc_{H_2O} \times mol/cc_{STP} \\ &= 3.8 \times 10^{-14} \times 1/22{,}414 \\ &= 1.70 \times 10^{-18} mol/cc_{H_2O} \\ H &= 1g/18\ g/mol \times 2 = 0.111\ mol/cc_{H_2O} \\ &\quad (\text{given that } 1\ cc_{H_2O} = 1g) \end{aligned}$$

So:

$$\begin{aligned} {}^3He/H &= 1.70 \times 10^{-18}/0.111 = 1.53 \times 10^{-17} \\ &= 1.53 \times 10^{-17} \times 10^{18} \\ &= 15.3\ TU \end{aligned}$$

allowing calculation of age, *t*:

$$\begin{aligned} 15.3 &= 4.7\ (e^{\lambda t} - 1) \\ t &= 17.77 \times \ln\left(1 + \left[{}^3He_t\right]/\left[T_t\right]\right) \\ &= 17.77 \times \ln(1 + 15.3/4.7) \\ &= 25.7\ \text{years} \end{aligned}$$

The tritium–helium dating method has a couple of caveats that must be considered. The above calculations in Examples 8.3 and 8.4 are based on the assumption that there is no loss of ^{3}He from shallow groundwater to the phreatic zone and atmosphere. This is unlikely if flow is sufficiently deep below the water table and out-diffusion to the atmosphere does not occur. Loss of ^{3}He produces a bias to erroneously young groundwater ages. This may be the case for groundwaters less than a couple of meters below the water table.

Also, groundwaters that are deep and close to crystalline bedrock may gain geogenic helium, which brings with it geogenic ^{3}He, producing erroneously old ages. Helium-4 is produced in the subsurface by alpha decay of uranium and thorium, and ^{3}He is produced by fission of ^{6}Li. Both U and Li are enriched in granitic environments. The most common decay chain is that from ^{238}U to ^{206}Pb, with the production of 8 α particles, which are simply ^{4}He atoms.

$$^{238}U \rightarrow {}^{206}Pb + 8\,{}^{4}He$$
$$^{235}U \rightarrow {}^{207}Pb + 7\,{}^{4}He$$
$$^{232}Th \rightarrow {}^{208}Pb + 6\,{}^{4}He$$

Fission of ^{6}Li occurs with the secondary neutron flux in the subsurface from spontaneous fission of ^{238}U and impact of α particles on light nuclei (Figure 4.10):

$$^{6}Li + n \rightarrow {}^{4}He + {}^{3}He_{geo}$$

The contribution of $^{3}He_{geo}$ to groundwater can be determined by calculating any helium in excess of the excess air component from recharge as determined with Ne (Example 8.3), and the $^{3}He/^{4}He$ ratio for geogenic helium. This ratio is generally taken to be 2×10^{-8} for shield terrains, given the greater production of He from alpha decay than from lithium fission (Bottomley et al. 1984).

$$He_{geo} = He_{meas} - He_{diss} - He_{Ne-excess}$$
$$^{3}He_{geo} = He_{geo} \times {}^{3}He/{}^{4}He_{geo}$$

A good case study using T–^{3}He to determine groundwater ages is the site of a trichloroethylene (TCE) plume at Valcartier, Quebec (Murphy et al. 2010). Groundwater ages were required to determine velocity of the TCE plume to wells and river water down-gradient from the source. The aquifer is composed of up to 10 to 20 m of clean glaciofluvial outwash sands overlying a silt aquitard with underlying proglacial sands and gravels. The bedrock is granite gneiss of the Canadian Shield.

The measured ^{3}He concentrations together with the geogenic ^{3}He calculated from the Ne and ^{4}He concentrations are given in Table 8.2. The T–^{3}He ages, corrected for atmospheric helium incorporated during recharge and geogenic contributions in the subsurface, show consistent increases with depth and along the flow path (Figure 8.13). Groundwaters at the down-gradient end of the aquifer have mean ages of roughly 30 years with little vertical variation, reflecting upward flow and mixing over basal topography. These ages were used to constrain aquifer parameters in the particle tracking model (Figure 8.13).

TABLE 8.2
Tritium and Helium Concentrations with Calculated T–^{3}He Ages for Groundwaters from a Glaciofluvial Outwash Aquifer in Valcartier, Quebec.

Piezometer nest P-125-126 (Figure 8.13)

Piezometer depth (m)	3.08	6.11	11.68	24.56
T (°C)	15.5	15.5	15.5	15.5
Tritium (TU)	14.1	13.5	12.7	11.7
$He_{measured}$ (cc_{STP}/cc_{H_2O})	8.80E–08	9.17E–08	8.31E–08	1.30E–07
$^3He/^4He_{measured}$	1.17E–06	1.41E–06	1.45E–06	8.96E–07
$^3He_{measured}$ (cc_{STP}/cc_{H_2O})	1.27E–13	1.31E–13	1.21E–13	1.26E–13
$^{20}Ne_{measured}$ (cc_{STP}/cc_{H_2O})	3.54E–07	3.44E–07	2.88E–07	2.77E–07
$^{20}Ne_{excess\ air}$ (cc_{STP}/cc_{H_2O})	1.37E–07	1.27E–07	7.09E–08	5.99E–08
$^4He_{air\ equilibrated}$ (cc_{STP}/cc_{H_2O})	4.68E–08	4.68E–08	4.68E–08	4.68E–08
$^3He_{air\ equilibrated}$ (cc_{STP}/cc_{H_2O})	6.36E–14	6.36E–14	6.36E–14	6.36E–14
$^4He_{excess\ air}$ (cc_{STP}/cc_{H_2O})	3.94E–08	3.65E–08	2.04E–08	1.73E–08
$^3He_{excess\ air}$ (cc_{STP}/cc_{H_2O})	6.19E–14	5.79E–14	3.57E–14	3.13E–14
$^4He_{geogenic}$ (cc_{STP}/cc_{H_2O})	1.66E–08	3.88E–09	1.06E–08	7.11E–08
$^3He_{geogenic}$ (cc_{STP}/cc_{H_2O})	3.33E–16	7.75E–17	2.12E–16	1.42E–15
$^3He_{tritogenic}$ (cc_{STP}/cc_{H_2O})	1.15E–15	9.38E–15	2.15E–14	2.97E–14
$^3He_{tritogenic}$ TU	0.46	3.77	8.65	11.9
Age (years)	0.6	4.4	9.2	12.5

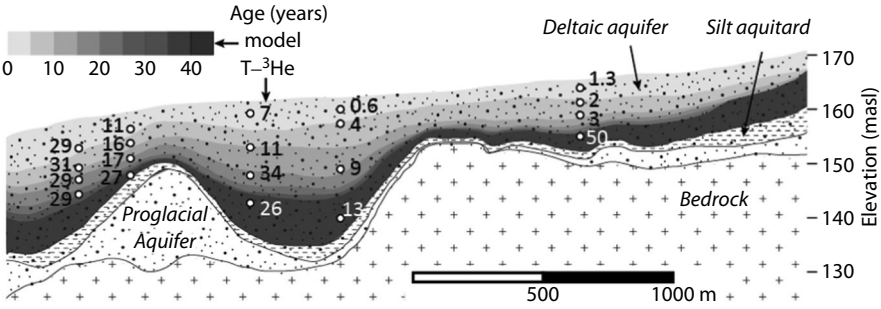

FIGURE 8.13 Cross-section of a glaciofluvial sand aquifer contaminated by TCE in Valcartier, Quebec. Sampling points of groundwater samples were taken in vertical profiles at five locations along the flow path, with T–^{3}He ages in comparison with particle track ages. (After Murphy et al. 2010.)

DATING SUBMODERN GROUNDWATERS

Anthropogenic tracers and natural tritium provide very good coverage for dating groundwaters recharged in the past five to six decades. Radiocarbon, discussed in the following section, remains the most useful dating tool for groundwaters recharged during the Holocene and late Pleistocene. However, uncertainties in estimating the initial ^{14}C activity restrict applications to groundwaters older than about 1000 years.

Few radionuclides have half-lives that are appropriate for dating the submodern range of about 50 to 1000 years before present.

Argon-39

Argon-39 is an atmospherically produced radioisotope with a half-life of 269 years, is not reactive in the subsurface, and so is a good tool for estimating groundwater age in the submodern range. Atmospheric production of ^{39}Ar is by neutron impingement on stable ^{40}Ar. It decays to stable ^{39}K by beta emission:

$$^{40}Ar + n \rightarrow {}^{39}Ar + 2n$$
$$^{39}Ar \rightarrow {}^{39}K + \beta$$

The atmospheric production and decay maintains an atmospheric abundance ratio for $^{39}Ar/^{40}Ar$ of 8.2×10^{-16} or 0.0018 Bq per L Ar at STP (Benneti et al. 2007). However, subsurface production can contribute to this through the activation of ^{39}K by neutrons that are continually generated by α particles from U and Th decay impinging on light nuclei:

$$^{39}K + n \rightarrow {}^{39}Ar + p$$

Loosli and Oeschger (1980) suggest that high production in granitic terrain and K-rich sediments can generate up to fourfold increases over atmospheric ^{39}Ar. In contrast, production in K and U/Th poor aquifers, such as carbonates, would have much less impact on calculated ages.

Until recently, a handicap was the great volumes of water that were required to be stripped of Ar, out of contact with the modern atmosphere, for a radiometric analysis (Loosli et al. 2000). Atmospheric production of ^{39}Ar maintains an activity of 0.016 Bq/m^3 in air. Dissolved in water using the Bunsen coefficient of 0.0313 cc_{STP}/cc_{H_2O} for Ar gives an activity of ^{39}Ar in air-equilibrated water of 5.25×10^{-7} Bq/L. This amounts to only about 6000 atoms of ^{39}Ar per liter, requiring extraction from several cubic meters of water for measurement by decay counting (Loosli and Oeschger 1980). A new method for counting atoms rather than decay events has greatly reduced the required sample size. Atom trap trace analysis (ATTA) using a laser trap and atom counting requires the argon stripped from only a few liters of water for reliable measurement (Welte et al. 2010, Jiang et al. 2011; Reichel et al. 2013). This greatly expands the use of the method for the important submodern groundwater age range.

Reichel et al. (2013) report the first ^{39}Ar dating of groundwater by ATTA, using membrane separation of gas from groundwater in the field followed by cryogenic separation of Ar in the laboratory. This was carried out on confined groundwaters from the upper Rhine Graben of southwestern Germany, yielding a subsurface residence time of 360 ± 68 years, which matched with hydrodynamic models for groundwater flow in this highly exploited aquifer.

The subsurface production of ^{39}Ar in environments with high ^{39}K and high secondary neutron flux from alpha decay of U and Th remains an obstacle to dating the submodern range. However, like other geogenic radionuclides, such as ^{129}I and ^{36}Cl,

dating by ingrowth toward secular equilibrium can be used to extend its useful dating range (Yokochi et al. 2012; Lu et al. 2013).

Silicon-32

Silicon-32, with a half-life of about 170 years, is less promising as a tool to date groundwaters. It is produced by cosmic ray spallation of ^{40}Ar (n – 2α) with an average rate of only two atoms per m^2 per second in the atmosphere, followed by wet or dry fallout to the surface. It has a low activity in recharge waters of less than about 0.0001 Bq/L, which complicates analysis. More restricting for routine use is its high reactivity in soils, where most is lost through exchange with stable silica on minerals in soils (Morgenstern 2000). This dilution in the subsurface combined with uncertainties with the atmospheric input as required for calculating the decay period make ^{32}Si a poorly constrained geochronometer for groundwaters.

Helium-4

Accumulation of geogenic ^4He is a geochronometer that can be applicable over a wide range of time (Figure 8.2). Uncertainties arise from its high diffusivity, which can add helium from deep crustal sources into shallower aquifers (Marty et al. 1993). However, if diffusive fluxes in and out can be constrained, then in situ production from U and Th concentrations can provide reasonable estimates of groundwater age. This method is described in detail later for old groundwaters.

The youngest ages possible by this method are limited by the uncertainty in resolving geogenic production in excess of atmospheric ^4He that is incorporated during recharge. This correction is generally made on the basis of atmospheric Ne concentrations, as required for T–He dating (above). Given sufficiently high U and Th concentrations in the aquifer, the ingrowth of geogenic ^4He can be used to date groundwaters that are a few hundred to a few thousand years old, which fall within the important submodern age range.

RADIOCARBON DATING OLD GROUNDWATER

Tritium-free groundwaters are considered to be greater than about 50 years old. In the submodern range of 50 to about 1000 years, groundwater ages must largely be assessed by hydrodynamic modeling until sampling and analysis of ^{39}Ar becomes more accessible. Beyond about 1000 years, radiocarbon remains the most useful and routine approach to date old groundwaters. Its 5730 year half-life is well suited to dating groundwater recharge during the Holocene and late Pleistocene, a period with significant variations in climate associated with the melting of continental ice sheets in high-latitude regions and shifting pluvial regimes at lower latitudes.

Atmospheric $^{14}CO_2$, with an activity of 0.226 Bq/g of C or 100 pMC, mixes with living biomass through photosynthesis, as well as with meteoric waters and oceans (and carbonates precipitated from such waters), giving these carbon reservoirs a modern ^{14}C activity. Once isolated from exchange with atmospheric $^{14}CO_2$, subsequent decay provides a precise chronometer for any carbon compound derived from atmospheric CO_2 since the late Pleistocene.

Groundwater dating is based on radiocarbon incorporated from the soil during recharge in the soil. This includes DIC from soil $^{14}CO_2$ but also can include DOC derived from the degradation of biomass. The challenge in radiocarbon dating groundwater is in distinguishing the modern component of dissolved carbon that accompanied groundwater recharge from that gained through geochemical reactions in the subsurface. Despite this complication, radiocarbon remains the foremost method for dating groundwaters that are tritium-free and considered old. Its range is appropriate for many aquifers hosting important freshwater supplies. The uncertainty on the age estimates can be within the range required for hydrodynamic interpretations of groundwater recharge, movement, and resource evaluation. Further, sampling is straightforward with minimal risk of atmospheric contamination and, with recent developments in accelerator mass spectrometry (AMS), analysis is rapid and inexpensive.

Atmospheric Production of ^{14}C in the Atmosphere

Cosmic radiation, as discussed in Chapter 4, produces ^{14}C in the upper atmosphere by neutron activation of atmospheric nitrogen:

$$^{14}N + n \rightarrow {}^{14}C + p$$

Oxidized to $^{14}CO_2$, radiocarbon mixes in the troposphere, where it cycles into the marine system as DIC and into terrestrial vegetation by photosynthesis. Surface production of radiocarbon from neutron impact on ^{17}O can be used for surface dating (Gosse et al. 2006), but has negligible contribution to ^{14}C in groundwater (Andrews et al. 1989).

Radioactive decay of ^{14}C produces stable ^{14}N, which is indistinguishable from atmospheric and subsurface nitrogen, and so the dating method is based on the loss of the parent, according to the decay equation rearranged to yield time:

$$t = -8267 \times \ln\left(\frac{a_t\,{}^{14}C}{a_0\,{}^{14}C}\right)$$

This equation assumes that the initial concentration of the parent is known and that the system is closed to subsequent gains or losses of the parent, except through radioactive decay. The usual expression of ^{14}C activity is as a percent of the initial ^{14}C activity ($a_0^{14}C$), that is, pMC (discussed in Chapter 1).

The ^{14}C activity of modern carbon, $a_0^{14}C$, has not been constant in the past, with fluctuations of up to 10% during the Holocene and 20% to 30% in the late Pleistocene (Figure 8.14). These are attributed to secular variations in the heliomagnetosphere from solar activity and changes in the geomagnetosphere, both of which attenuate the cosmic ray flux and therefore the production of ^{14}C (Solanki et al. 2004). For the precise age dating possible with organic compounds (wood, bone, organics) the deviation of $a_0^{14}C$ from 100 pMC is incorporated into radiocarbon ages modeled with

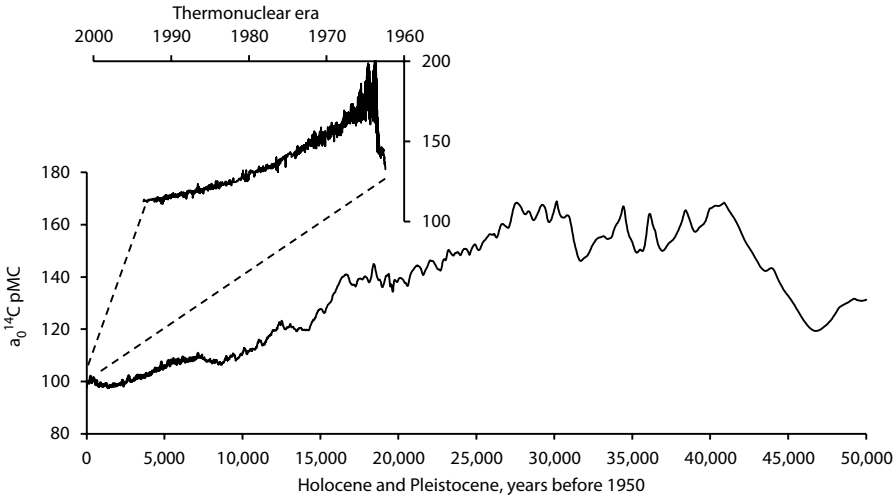

FIGURE 8.14 Atmospheric ^{14}C activity during Holocene and late Pleistocene (Data from Bayari 2002), based on tree rings and shallow marine corals, based on their U/Th age. Variations that are related to changes in solar output. The strong decrease from ca. 30,000 years BP to present is related to changes in the earth's geomagnetic field.

internationally recognized calibration programs, such as InterCal09 (Reimer et al. 2009), with dating possible to beyond 50,000 years BP.

For groundwater dating, the effective range is much shorter, up to about 25,000 or 30,000 years, due to carbonate geochemical reactions that dilute the soil-derived ^{14}C and limit precision.

^{14}C in the Recharge Environment

Aerobic respiration from the degradation of vegetation combined with root respiration in the rhizosphere maintains a large reservoir of $^{14}CO_2$ in the soil zone with modern ^{14}C activity and $\delta^{13}C = -25‰$. This is dissolved by infiltrating precipitation, generating carbonic acid for weathering, as discussed in Chapter 6. The concentration of CO_2 that is incorporated during recharge depends on the geochemistry of the recharge environment: the temperature, the pH of the water, the partial pressure of CO_2, and the weathering reactions that take place in the unsaturated zone. Consequently, as groundwaters recharge through soils, they gain levels of ^{14}C-active DIC that are much higher than that provided by direct dissolution of atmospheric CO_2. However, as weathering reactions proceed, there is potential to dilute this ^{14}C-active DIC and produce artificially old ages. If open system conditions prevail during carbonate weathering, then the DIC maintains a modern ^{14}C activity. However, if carbonate dissolution takes place under closed system conditions, $a^{14}C_{DIC}$ will be closer to 50 pMC due to

the dilution with ^{14}C-free carbonate from the marine limestone matrix or fracture minerals:

Closed system conditions

$$^{14}CO_2 + H_2O + CaCO_3 \rightarrow Ca^{2+} + H^{14}CO_3^- + HCO_3^- \qquad a^{14}C_{DIC} = 50 \text{ pMC}$$

Open system conditions

$$^{14}CO_2 + H_2O + CaCO_3 \Leftrightarrow Ca^{2+} + H^{14}CO_3^- + HCO_3^-$$

$$^{14}CO_2 + HCO_3^- \Leftrightarrow CO_2 + H^{14}CO_3^- \qquad \text{exchange with soil } ^{14}C_{DIC}$$

$$^{14}CO_2 + H_2O + CaCO_3 \Leftrightarrow Ca^{2+} + 2\,H^{14}CO_3^- \qquad a^{14}C_{DIC} = 100 \text{ pMC}$$

The degree of openness of the system during mineral weathering then controls the initial activity of the DIC. As seen in Chapter 6, open system conditions often prevail, and so groundwaters recharge with 100 pMC. This is not always the case; for example, in karstic regions rapid recharge can minimize the exchange with soil DIC, and so $a^{14}C_{DIC}$ is less than 100 pMC. The impact of this loss is an apparent age of the groundwaters that is greater than their true age, and must be corrected by the determination of a radiocarbon dilution factor, q, which represents the fractional reduction of $a^{14}C$ to some value less than 100 pMC.

$q = 1$	no dilution of ^{14}C by reaction
$q = 0.75$ to 1	minor dilution of initial ^{14}C from closed system exchange
$q = 0.5$ to 0.75	closed system carbonate weathering and exchange
$q < 0.5$	extensive carbonate exchange, possible sulfate reduction

The correction for dilution of $^{14}C_{DIC}$ is applied to the modern radiocarbon activity of the soil CO_2 at the time of recharge, $a_0^{14}C$, multiplied by the dilution factor:

$$a^{14}C_{corr} = q \times a_0^{14}C$$

and the dilution-corrected decay equation after some period of decay, t:

$$a_t^{14}C = q \times a_0^{14}C \times e^{-\lambda t}$$

$$\text{or } t = -8267 \times \ln\left(\frac{a_t^{14}C}{q \times a_0^{14}C}\right)$$

Determining the recharge conditions and subsequent geochemical reactions that have taken place for a groundwater that is now perhaps thousands of years old is a challenging task. If the climate has not changed and it is simply a long-flow path, then analyzing the DIC of young (tritium-bearing) groundwaters in the

Example 8.5 Radiocarbon Dilution Factor and Age Correction

Groundwater recharged following closed system weathering, which diluted the initial radiocarbon activity to 50%, as in the reaction above. The DIC fraction was found to have a radiocarbon activity, $a^{14}C_{DIC}$, of 25 pMC. Calculate its apparent age, and then determine the radiocarbon dilution factor and its corrected age.

Apparent age: $t = -8267 \times \ln\left(\frac{a_t{}^{14}C}{a_0{}^{14}C}\right)$

$= -8267 \times \ln\left(\frac{25}{100}\right)$

$= 11{,}460$ years

Closed system dilution reaction: $^{14}CO_2 + H_2O + CaCO_3 \rightarrow Ca^{2+} + H^{14}CO_3^- + HCO_3^-$

Dilution factor, $q = 0.5$

Corrected age: $t = -8267 \times \ln\left(\frac{a_t{}^{14}C}{q \times a_0{}^{14}C}\right)$

$= -8267 \times \ln\left(\frac{25}{0.5 \times 100}\right)$

$= 5730$ years

recharge area can help. Many approaches and models have been developed over the past decades to calculate q for various groundwaters and reactive losses of ^{14}C (Pearson 1965; Pearson and Hanshaw 1970; Fontes and Garnier 1979; Plummer et al. 1994). Most are based on the use of geochemical parameters and ^{13}C of DIC. The basic approaches that can be used for the principle geochemical processes are summarized here.

Determining q from $^{14}C_{DIC}$ in the Recharge Area

In aquifer systems with well-defined recharge areas, sampling groundwaters in the recharge zone that contain tritium can provide an indication of the ^{14}C dilution before decay. From such studies, the dilutions measured in typical recharge areas have been characterized (Vogel 1970). For karst systems, where recharge can be rapid and minimizes exchange between DIC and the soil CO_2, q will be close to 0.7. For recharge though porous media with carbonate and carbonate-rich soils, q will be greater than 0.9, and so dilution is almost negligible. In some crystalline rocks with no sources of carbonate in the recharge area or along the flow path (i.e., no carbonate fracture minerals) then q will be equal to 1, and no ^{14}C dilution is considered.

It is valuable to measure $a^{14}C_{DIC}$ in tritium-bearing groundwaters in the recharge area. Assuming that the recharge conditions were similar in the past, and ignoring the slight fractionation in ^{14}C between soil CO_2 and DIC (about 0.2%), then the initial radiocarbon content can be estimated from the relationship:

$$q = \frac{a^{14}C_{DIC}}{a^{14}C_{soil}}$$

This approach was taken in Jordan (Bajjali et al. 1997), where $a^{14}C_{soil}$ was measured at 114 ±6 pMC, and tritium-bearing groundwaters in the recharge area had $a^{14}C_{DIC} = 73$ pMC. The ^{14}C dilution by carbonate dissolution before decay is then calculated as

$$q = \frac{a^{14}C_{DIC}}{a^{14}C_{soil}} = \frac{73}{114} = 0.64$$

In this case, the recharge in this system has evolved under essentially closed system conditions. Corrections for this dilution of $^{14}C_{DIC}$ cannot always be made by these measurements in the recharge area. In many cases, other tracers of dilution, including ^{13}C, are used, as discussed in the following section.

Carbonate Dissolution and Matrix Exchange

Carbonate dissolution under closed system conditions beyond the recharge environment is not the only geochemical process that can dilute the initial ^{14}C activity of DIC. Dilution of ^{14}C due to the exchange of carbonate between the host rocks and DIC, *matrix exchange*, can also occur and must be considered. The actual ^{14}C dilution is usually much larger (and thus the *q*-factors lower) in older systems than in young ones due to longer time periods for exchange reactions with the host carbonate phases. In the case where the carbonate matrix is marine, it will typically have a $\delta^{13}C$ value close to 0‰. The exchange of carbon isotopes between the DIC and carbonate minerals in the aquifer matrix is often considered as a cause for $\delta^{13}C_{DIC}$ enrichment and ^{14}C dilution. Groundwaters that are essentially at equilibrium with calcite will exchange carbonate across the mineral–solution interface, where Ca^{2+} and CO_3^{2-} are in a continual process of equilibrium dissolution/reprecipitation exchange with $CaCO_3$. This results in ^{14}C loss according to

$$CaCO_3 + H^{14}CO_3^- \rightarrow Ca^{14}CO_3 + HCO_3^-$$

Similarly, ^{14}C losses to the matrix can occur due to the incongruent dissolution of dolomite.

$$Ca^{2+} + H^{14}CO_3^- + CaMg(CO_3)_2 \rightarrow 2Ca^{14}CO_3 + Mg^{2+} + HCO_3^-$$

In both cases, the addition of ^{14}C-free DIC from the aquifer matrix can be traced with stable ^{13}C, which has a characteristic value for both DIC from recharge ($\delta^{13}C_{rech}$ with ^{14}C-bearing DIC) and DIC from the rock ($\delta^{13}C_{rock}$ with ^{14}C-free DIC). The greater the degree of contribution from the rock through exchange or dolomite alteration,

the more the groundwater $\delta^{13}C_{DIC}$ will evolve toward $\delta^{13}C_{rock}$. Pearson (1965) and Pearson and Hanshaw (1970) were the earliest to recognize the elegance of this tracer of dilution, calculated as

$$q = \frac{\delta^{13}C_{DIC} - \delta^{13}C_{rock}}{\delta^{13}C_{rech} - \delta^{13}C_{rock}}$$

where: $\delta^{13}C_{DIC}$ = measured ^{13}C in groundwater
$\delta^{13}C_{rech}$ = $\delta^{13}C$ of the DIC following open system weathering (usually close to –12‰)
$\delta^{13}C_{rock}$ = $\delta^{13}C$ of the calcite being dissolved (usually close to 0‰)

This is a versatile algorithm because it provides a simple and linear correction for the dilution of $^{14}C_{DIC}$ after the initial carbonate weathering in the recharge environment. However, it assumes that the only dilution of the DIC pool originates from the carbonate rock encountered along the flow path. If this is a fractured crystalline system, then these might be hydrothermal or other types of fracture carbonate minerals. Providing their $\delta^{13}C$ values can be determined, this algorithm still applies.

This formulation of q accounts also for DIC derived from incongruent dissolution of dolomite. In such terrains, the ^{14}C dilution can also be calculated from the gain in Mg^{2+} beyond the recharge environment. This is useful in the case where a series of dilution factors are determined for different reactions along the flow path. The increase in $m_{Mg^{2+}}$ beyond the recharge area, expressed as excess Mg^{2+}, reflects this additional dilution:

$$m_{Mg_{excess}} = m_{Mg_{meas}} - m_{Mg_{rech}}$$

The dilution factor for this process takes into account the fact that two moles of carbonate ions are exchanged for each mole of Mg^{2+} in dolomite, and is approximated by

$$q_{dol} = \frac{m_{DIC}}{m_{DIC} + 2m_{Mg\ excess}}$$

Example 8.6: Correcting for ^{14}C Dilution from Matrix Exchange Using $\delta^{13}C_{DIC}$

Groundwaters were sampled at discrete depths for radiocarbon dating, from boreholes in the upper 200 m of Paleozoic bedrock, on the eastern margin of the Michigan Basin in Southern Ontario (Intera 2011). The bedrock comprises dolostones, which host some karst horizons. Measured radiocarbon activities range from 16 to 22 pMC, but $\delta^{13}C_{DIC}$ values are quite enriched, with values up to –2.28‰ (Table 8.3).

The uncorrected radiocarbon ages for these samples suggest that they were recharged during the late Pleistocene when the region was still glaciated. However, the enrichments of ^{13}C in these groundwaters indicate significant exchange with the dolostones, which have $\delta^{13}C_{rock}$ near 4‰. Radiocarbon dilution factors, q, are

calculated using a value for $\delta^{13}C_{rech}$ = –12‰ for the DIC at the time of recharge and $\delta^{13}C_{rock}$ = 4‰ for the dolostones, e.g.:

$$q = \frac{\delta^{13}C_{DIC} - \delta^{13}C_{rock}}{\delta^{13}C_{rech} - \delta^{13}C_{rock}} = \frac{-2.28 - 4}{-12 - 4} = 0.39$$

Table 8.3 gives the dilution factors for these groundwaters and their dilution-corrected radiocarbon ages, showing recharge during the Holocene when the region was ice free. Figure 8.15 shows that these groundwaters are depleted in ^{18}O, and so are a mixture of late Pleistocene glacial meltwater ($\delta^{18}O$ –20 to –30‰) and Holocene meteoric waters. In regions that were ice covered at the last glacial maximum, high hydrostatic pressures at the base of the melting ice front generated circulation to hundreds of meters depth (e.g. Figure 5.19) (Siegel and Mandle 1984; Clark et al. 2000). Today it is common to have meltwater in aquifers that are not actively flushed with modern recharge.

TABLE 8.3
Carbon Isotopes and ^{14}C Age Correction for Groundwaters in Carbonate Strata from Southern Ontario

Depth (m)	$a^{14}C_{DIC}$ (pMC)	Age Uncorrected (Years BP)	$\delta^{13}C$ DIC	$\delta^{13}C$ Rock	q	Age Corrected (Years BP)	$\delta^{18}O$
32	21.0	12,900	–2.28	4	0.39	5,100	–13.9
68	22.2	12,500	–2.44	4	0.40	4,900	–14.2
69	16.5	14,900	–2.89	4	0.43	7,900	–14.3
158	19.2	13,700	–4.63	4	0.54	8,500	–16.4
179	22.3	12,400	–2.72	4	0.42	5,200	–14.3

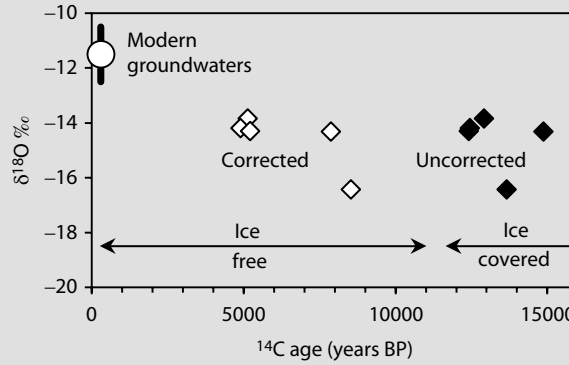

FIGURE 8.15 Corrected and uncorrected ^{14}C ages with $\delta^{18}O$, showing the corrected ages indicating recharge dominantly in the Holocene, but with a component of recharge from Pleistocene meltwater. (Modified from Intera 2011.)

A more sophisticated correction model was developed by Fontes and Garnier (1979; 1981), which uses major ion geochemistry to assess the contribution of ^{14}C-free matrix carbonate, and isotope mass balance to apportion $^{14}C_{DIC}$ from open system and closed system weathering. In their model, the total of matrix-derived carbonate is calculated from major ions:

$$m_{carb} = m_{Ca^{2+}} + m_{Mg^{2+}} - m_{SO_4^{2-}} + \tfrac{1}{2}\left(m_{Na^+} + m_{K^+} - m_{Cl^-}\right)$$

This accounts for carbonate dissolution based on Ca^{2+} and Mg^{2+}, with a correction for evaporite dissolution ($m_{SO_4^{2-}}$) and cation exchange ($m_{Na^+} + m_{K^+}$, with a correction for Na^+ from salt, m_{Cl^-}). This DIC is then apportioned into two components—that which has exchanged with the soil CO_2 (^{14}C active) in an open system and that which has exchanged with the carbonate matrix (considered to be ^{14}C-dead) under closed system conditions. The fraction of this DIC that has exchanged with soil CO_2 in an open system (m_{exch}) is calculated from the following mass–balance relationship:

$$m_{exch} = \frac{\delta^{13}C_{DIC\ meas} \times m_{DIC\ meas} - \delta^{13}C_{carb} \times m_{carb} - \delta^{13}C_{soil} \times \left(m_{DIC\ meas} - m_{carb}\right)}{\delta^{13}C_{soil} - \varepsilon^{13}C_{CO_2\text{-}CaCO_3} - \delta^{13}C_{carb}}$$

The dilution factor is calculated as:

$$q_{F\text{-}G} = \frac{m_{DIC\ meas} - m_{carb} + m_{exch}}{m_{DIC\ meas}}$$

The dilution factor, q, is then based on the geochemistry with weighting from ^{13}C of the different DIC components, although there remains inherent uncertainty of the $\delta^{13}C$ of the recharge DIC that the modeler must prescribe according to pH and $\varepsilon^{13}C_{CO_2\text{-}DIC}$ during open system weathering.

Dissolved Inorganic Carbon from Organic Carbon

In addition to carbonate minerals, solid organic carbon in aquifers can contribute to the dilution of the soil-derived $^{14}C_{DIC}$. Aquifers may contain organic carbon both as buried plant debris, such as peat horizons in unconsolidated sand and gravel aquifers, coal beds in sandstone and shale horizons, and residual bitumen and kerogen in marine rocks, such as limestone and dolostone. Under reducing conditions, bacteria will oxidize these organic substrates, typically using sulfate or ferrihydrite as an electron acceptor. In the absence of such electron donors, DIC can be generated through fermentative and methanogenic reactions.

Marine sediments often retain a small percentage of sedimentary organic carbon following diagenesis. DIC derived from organics encountered within marine rocks are ^{14}C-free and a dilution to the soil-derived DI^{14}C. Unconsolidated aquifers, such as glaciofluvial outwash sands deposited during deglaciation in late Pleistocene

or Holocene, may contain organic carbon with measurable ^{14}C. The ^{14}C activity of DIC generated from such sources must then be taken into account in any correction model (Aravena et al. 1995).

The contribution of organic carbon to the DIC pool is evident from $\delta^{13}C_{DIC}$, which is generally around –27‰ for terrestrial organics, and closer to –30‰ for marine organics. However, with the enrichment of ^{13}C that accompanies carbonate reactions (above), this tool is not always quantitative, and therefore a second parameter must be used.

In the case of sulfate reduction, the dissolved H_2S (or HS^- at pH above 7) concentration can be used as a measure of DIC from oxidation of organics. Sulfate is not uncommon in many aquifers. It may be supplied by marine aerosols that accumulate in the recharge environment. It can be found as residual brine or seawater sulfate, or come from gypsum dissolution in the subsurface. Oxidation of pyrite in the recharge zone is another source of SO_4^{2-}.

The production of DIC during sulfate reduction depends on the type of organic involved. Oxidation of buried terrestrial plant debris (e.g., peat) in which the carbon has an overall redox state near 0 (fixed carbon) would follow a reaction such as the following:

$$2CH_2O + SO_4^{2-} \rightarrow H_2S + 2HCO_3^-,$$

where 1 mole of H_2S would signify the contribution of 2 moles of DIC. The dilution factor, q_{H_2S}, can be calculated as

$$q_{H_2S} = \frac{m_{DIC}}{m_{DIC} + 2m_{H_2S}}$$

If a reduced carbon substrate is used (C redox state of –IV for methane), the reaction will be

$$CH_4 + SO_4^{2-} \rightarrow HS^- + HCO_3^- + H_2O$$

where one mole of H_2S follows from the production of one mole of DIC. In this case, the dilution factor for the process of sulfate reduction alone can be expressed as

$$q_{H_2S} = \frac{m_{DIC}}{m_{DIC} + m_{H_2S}}$$

In these equations, H_2S represents the sum of both H_2S and HS^- sulfide species.

Sulfate reduction affects not only $^{14}C_{DIC}$ but also $\delta^{13}C_{DIC}$ due to the addition of ^{13}C-depleted DIC from the organics, for which $\delta^{13}C_{org}$ is generally about –25‰ to –30‰. The ^{13}C content of the final DIC after carbonate dissolution and sulfate reduction can be calculated from

$$\delta^{13}C_{DIC} = \frac{\delta^{13}C_{DIC\text{-}rech} \times m_{DIC\ rech} + \delta^{13}C_{org} \times m_{H_2S}}{m_{DIC\ rech} + m_{H_2S}}$$

The calculated values for $\delta^{13}C_{DIC}$ should match closely with values for $\delta^{13}C_{DIC}$ measured for the sample. If not, other geochemical processes, such as sulfide precipitation or additional CO_2 reactions, may have occurred.

Example 8.7: Correcting for Sulfate Reduction

Correct the radiocarbon age of thermal springs from western Canada for sulfate reduction.

The Hotsprings Cove thermal springs are found near tidewater on the west coast of Vancouver Island, onshore from the Cascadia subduction zone, in faulted quartz diorite of Mesozoic-aged West Coast mountains. The geochemistry of these hot springs indicate a low-salinity (515 ppm total dissolved solids [TDS]) water typically of circulation through silicate rocks. The Na-Cl facies is likely marine in origin.

The waters are reducing, with a low measured Eh (–0.25 V) and measurable sulfide. They are at saturation with calcite (log SI_{cal} = 0.2) and have a low P_{CO_2} of $10^{-3.89}$, suggesting closed system weathering. Eh calculated from the measured concentrations of SO_4^{2-} and HS^- (the dominant sulfide phase at this high pH) is the same as the measured Eh, showing that sulfate reduction is buffering the redox state of these waters. The source of the sulfate was established to be Mesozoic marine sulfate based on its $\delta^{34}S$ value (see Figure 9.40). This was corrected for SO_4^{2-} loss (and fractionation) from sulfate reduction to HS^- by a simple isotope mass balance.

$$\delta^{34}S_{total} = \left[\left(\delta^{34}S_{SO_4^{2-}} \times m_{SO_4^{2-}}\right) + \left(\delta^{34}S_{HS^-} \times m_{HS^-}\right)\right] / \left(m_{SO_4^{2-}} + m_{HS^-}\right)$$
$$= +17.6‰$$

The thermal waters have stable isotope contents that indicate recharge on the upper reaches of the local mountains. They are tritium-free and so have taken more than 50 years to circulate from the recharge area. The radiocarbon activity of the DIC is only 18.4 pMC, which give an apparent age of 14,000 years before present (14 ka BP). This is unreasonable, given that the region was covered by the Cordilleran Ice Sheet at that time. The measured HS^- concentration of 6.83 ppm suggests that the DIC might be diluted by organic carbon that has been oxidized by sulfate reduction. The depleted value measured for $\delta^{13}C_{DIC}$ (–24.0‰) is more negative than the value for open system recharge in crystalline terrain of about –17‰ (Chapter 6). This indicates an input of DIC from organic carbon. A radiocarbon correction can be made using the HS^- concentration. We can assume that the source of organic carbon is old, perhaps related to the source of Mesozoic marine sulfate, and so free of ^{14}C.

Converting the concentrations of DIC and HS^- to molar values, the radiocarbon dilution factor, *q*, is then calculated as follows:

$$q = m_{DIC\ measured} / \left(m_{DIC\ measured} + 2 \times m_{HS-measured}\right)$$
$$= 0.31 / \left(0.31 + 2 \times 0.21\right)$$
$$= 0.42$$

This correction factor attributes an amount of DIC equal to twice the moles of HS^- added to the water (the denominator in this formula). Some DIC has been lost by calcite precipitation, as sulfate reduction is an alkaline reaction, and we observe that the waters are slightly oversaturated with calcite ($\log SI_{cal} = 0.20$; Table 8.4).

TABLE 8.4
Geochemistry and Isotope Data for the Hotsprings Cove Geothermal Waters. Concentrations in ppm

T(°C)	51.3	Na^+	149	Tritium (TU)	1.0 ±0.8
pH	8.71	K^+	2.00	DIC ppm C	7.92
Eh (V)	–0.25	Ca^{2+}	22.7	$\delta^{13}C_{DIC}$	–24.0
HCO_3^-	18.0	Mg^{2+}	0.08	$a^{14}C$ (pMC)	18.4 ±0.22
CO_3^{2-}	0.64	SiO_2	50.1	$\delta^{34}S_{SO_4^{2-}}$	30.3‰
SO_4^{2-}	31.1	$\log SI_{cal}$	0.20	$\delta^{34}S_{HS^-}$	3.12‰
HS^-	6.83	$\log SI_{anh}$	–2.29	$\delta^{18}O_{SO_4^{2-}}$	9.84‰
Cl^-	224	$\log P_{CO_2}$	–3.89	$\delta^{34}S_{total}$	17.62‰

This dilution factor is also close to that which can be calculated from $\delta^{13}C$, based on a shift by the addition of ^{13}C-depleted DIC from the organic carbon. Using the correction developed by Pearson (1965) shown earlier, but substituting DIC dilution from organic carbon (~ –29‰) for that of carbonate rock:

$$q = \frac{\delta^{13}C_{DIC} - \delta^{13}C_{organic\ C}}{\delta^{13}C_{rech} - \delta^{13}C_{organic\ C}}$$
$$= \frac{-24 - (-29)}{-17 - (-29)}$$
$$= 0.42$$

giving a corrected age of

$$t = -8267 \times \ln\left(\frac{18.4}{0.42 \times 100}\right)$$
$$= 6800 \text{ years}$$

This age is now more realistic, indicating recharge within the Holocene when the ice sheet had retreated from the region.

DIC from buried or sedimentary organic carbon in the aquifer can also be contributed to groundwaters by microbial methanogenesis. The series of fermentative reactions (anoxic degradation of higher-weight organic compounds) that precede the production of CH_4 produce considerable amounts of DIC (see Chapter 6):

$$\underset{}{C_6H_{12}O_6} + \underset{}{2H_2O} \xrightarrow{\textit{fermentation}} \underset{}{2CH_3COOH} + \underset{}{2CO_2} + \underset{}{4H_2} \xrightarrow{\textit{methanogenesis}} \underset{}{3CH_4} + \underset{}{3CO_2} + \underset{}{2H_2O}$$

The DIC resulting from this complex series of biological reactions dilutes the ^{14}C-active DIC that accompanied groundwater recharge. Correction is complicated and not simply traced with $\delta^{13}C$ as was done for carbonate reactions. This is due to the fractionation for ^{13}C in this overall reaction. From the precursor carbohydrate with $\delta^{13}C$ of around –27‰, the ^{13}C is selectively partitioned into the DIC while the methane is enriched in ^{12}C. The overall fractionation in these reactions, $\varepsilon^{13}C_{CO_2\text{-}CH_4}$, is on the order of 50‰ to 70‰, leaving the DIC in such waters with $\delta^{13}C_{DIC}$ values much greater than the –10‰ to –15‰ for soil-derived DIC, and often up to +10‰ or higher (see Figure 6.18).

Developing an algorithm based on methane concentrations to correct for these effects requires the assumption that CH_4 is retained in the groundwater sampled and that DIC has not been affected by carbonate exchange unless otherwise corrected. If the source of organic carbon is ^{14}C-free, then a correction factor calculated as follows may approximate the ^{14}C dilution from methanogenesis:

$$q_{CH_4} = \frac{m_{DIC\,meas} - 2m_{CH_4}}{m_{DIC\,meas}}$$

A more comprehensive approach to correcting for the various carbon reactions in methanogenic groundwaters involves geochemical programs to calculate their effect on DIC as well as on $\delta^{13}C_{DIC}$ and $a^{14}C_{DIC}$.

Example 8.8 Radiocarbon Age Corrections in Methanogenic Groundwaters

Aravena et al. (1995) undertake radiocarbon dating for the methanogenic groundwaters of the Alliston aquifer, a regional aquifer of glaciofluvial outwash sediments in southern Onterio, Canada, confined above by late Pleistocene clay till. Elevated DOC concentrations between 5 and 20 ppm C are generating on average about 3 mmol/kg methane concentrations (Table 8.5). This represents over 2 atm partial pressure ($K_{CH_4} = 0.0014 = m_{CH_4}/P_{CH_4}$, and so $P_{CH_4} = 0.003/0.0014 = 2.1$ atm) held in solution by the hydrostatic head in the aquifer (>20 m or 2 atm pressure). When pumped by local groundwater users, such methane degases in the water distribution system and presents an explosion hazard.

TABLE 8.5
Concentrations, $\delta^{13}C$ and $a^{14}C$ of Methanogenic Groundwaters in the Alliston Aquifer, Ontario

Well	DOC	DIC	$\delta^{13}C_{DIC}$	CH_4	$\delta^{13}C_{CH_4}$	$a^{14}C$	Apparent age	q	Age NETPATH
	ppm C	ppm C	‰	mmol/kg	‰	pMC	ka BP		ka BP
OV7	7.4	67.2	2.0	2.08	–84	3.6	28.4	0.23	15
OV15	18	85.2	1.3	3.55	–77	4.7	23.4	0.15	9
OV23	15	85.6	–2.7	2.75	–73	2.0	31.2	0.17	18
OV34	7.1	46.8	–8	0.94	–86	2.6	31.1	0.19	16

On the basis of this ^{13}C enrichment observed for the DIC (Table 8.5), the source of the methane was identified using $\delta^{13}C_{CH_4}$ and δD_{CH_4} as in situ biogenic production and not thermocatalytic methane from the bedrock (see the section on methane in groundwater, Chapter 10).

Uncorrected radiocarbon activities gave apparent ages between 23,000 and 31,000 years before present. Again, unrealistic, considering that this coincides with the period that the region was covered by 3000 m of Laurentide glacier ice. Moreover, it was the meltwater and sediment outwash during ablation of this ice sheet that created the aquifer. Corrections for contributions to the DIC pool by methanogenesis were made using the USGS geochemical mass balance program NETPATH (Plummer et al. 1994). The results of NETPATH modeling show that methanogenesis has diluted the ^{14}C-active DIC derived from the soil by about five times, giving a dilution factor, q, of about 0.2. Using this factor calculates corrected ages of 9,000–18,000 years, which place recharge at some point following deglaciation, when the region was largely ice-free.

Incorporation of Geogenic CO_2

Deeply circulating groundwaters along plate margins or in volcanic settings may often have elevated P_{CO_2} values due to the incorporation of geogenic CO_2. This can be mantle-derived CO_2, which has a $\delta^{13}C$ value of about –6‰. An example of this input is the Mount Meager geothermal waters (Clark et al. 1982), which have 150 ppm DIC with $\delta^{13}C = -6.3$ and pH of 6.85. The spring waters have tritium and so have a recently recharged component, but the radiocarbon activity, $a^{14}C$, is only 0.2 pMC.

Another geogenic source of CO_2 is from the thermal metamorphism of limestone by magma. In the presence of silica, the decarbonation of $CaCO_3$ occurs as low as 300°C, with the formation of wollastonite:

$$CaCO_3 + SiO_2 \rightarrow CaSiO_3 + CO_2$$

Such CO_2 is similar to or enriched above the carbonate precursor. This is the case for the Mount Edziza geothermal waters (Example 6.12) that have a $\delta^{13}C_{DIC}$ value of –1.2‰ and no measurable ^{14}C (Clark et al. 1989).

In both these cases, any radiocarbon incorporated from recharge through soils has been highly diluted by geogenic CO_2, precluding any potential to be used to date such waters.

^{14}C Dating with Dissolved Organic Carbon

Radiocarbon dating with soil-derived DOC holds some advantage over DIC. It is not affected by carbonate dissolution or exchange as is DIC, and losses by oxidation along the flow path will not significantly affect the radiocarbon content of DOC, just the overall concentration of DOC. There are, however, serious limitations to its application. As seen for the Alliston aquifer above, subsurface contributions to DOC in groundwater exist and would dilute the soil-derived component used for dating. Although corrections for subsurface DOC can be made (Aravena and Wassenaar 1993), this requires knowledge of the $a^{14}C$ of the buried organic carbon. Typically only the fulvic acid component can be reliably traced to an origin in the soil, and so detailed characterization and column separation (with XAD-8® resin) of the DOC fractions are required. Other components of the DOC pool are of uncertain origin and cannot be used.

STABLE ISOTOPES AND NOBLE GASES IN PALEOGROUNDWATERS

Complementary tools that aid in the identification of old groundwaters include stable isotopes and noble gases as indicators of recharge during past climates (cool vs. warm, pluvial vs. arid). These do not provide quantitative measurements of subsurface residence time, but do provide useful constraints on age as well as providing valuable paleoclimate information.

Stable Isotopes and Paleogroundwaters

The distillation of ^{18}O and D during rainout partitions these isotopes according to temperature. This has been exploited as a tool to trace groundwaters of different origin (Chapter 5). The temperature–isotope relationship is also a fundamental tool in paleoclimatology, where the $\delta^{18}O$ and δD in climate records, such as ice cores and speleothem, are used to reconstruct past temperatures. Figure 5.4 depicts the evolution of an atmospheric vapor mass as it cools and rains out. The outcome of this process is a depletion of stable isotopes as the system moves to cooler regions, and hence there exists a strong correlation between cooler climate regions and lower stable isotope values in precipitation.

Old groundwaters recharged under a different climate regime in the past will then preserve the isotopic signature of that regime. Comparison of the isotope content of old groundwaters with modern groundwaters from a given region provides an indication of the climate shift. For groundwaters recharged during the late Pleistocene to Holocene, this is related to climate shifts from the last glacial maximum at around 21 ka to the current interglacial climate from the early Holocene to present. This is manifested in the stable isotope contents of groundwater in two ways. One is the incorporation of meltwater from the massive continental ice sheets, typically observed in higher-latitude aquifers outcropping along the margin of the ablating ice as it retreated over the landscape. The other is from the recharge of cooler Pleistocene precipitation, which is typically observed in groundwaters from nonglaciated regions at lower latitude.

The old groundwaters sampled in the Alliston aquifer (Example 8.8) have $\delta^{18}O$ and δD values that are anomalously depleted with respect to modern shallow (tritium-bearing) groundwaters in the area (Figure 8.16). This isotopically depleted component is attributed to glacial meltwater recharged during deglaciation in the area in the late Pleistocene. Glacial meltwater recharge is also shown in Figure 5.19, for the example of groundwaters in northern Illinois.

The recharge of groundwaters under differing climate conditions in the past, as opposed to meltwater from Pleistocene ice sheets, is recorded by the stable isotopes of old groundwaters from many nonglaciated regions (Figure 8.17). Differences in comparison with modern recharge from such regions reflect the change in climate. Shifts can arise due to changes in temperature, which affect both $\delta^{18}O$ and δD. Changes in humidity in the vapor source region can be manifested by changes in deuterium excess, *d*. Observation of such changes is an indication that the groundwaters are old, and can often be correlated with paleoclimate reconstructions.

Noble Gas Recharge Temperatures

While changes in regional paleoclimates are recorded by depletion in $\delta^{18}O$ and δD values of old groundwater, cooler local recharge temperatures are recorded by noble gas concentrations. This is based on their increase in solubility with decreasing temperature. Other atmospheric gases, such as O_2 and N_2 have a similar solubility–temperature relationship, but are reactive and so may be lost or gained along the flow path. This is not the case for the atmospheric noble gases. However, only two, Kr and Xe, reliably record recharge temperatures, as both have significant change in concentration with temperature. Helium and argon concentrations in groundwater can have geogenic contributions through radioactive decay (^4He from alpha decay in the U and Th decay series and ^{40}Ar from beta decay of ^{40}K) and so can gain concentrations along the flow path. Ne is the least sensitive to temperature of the three strictly atmospheric noble gases, and is used to correct for excess air gained during

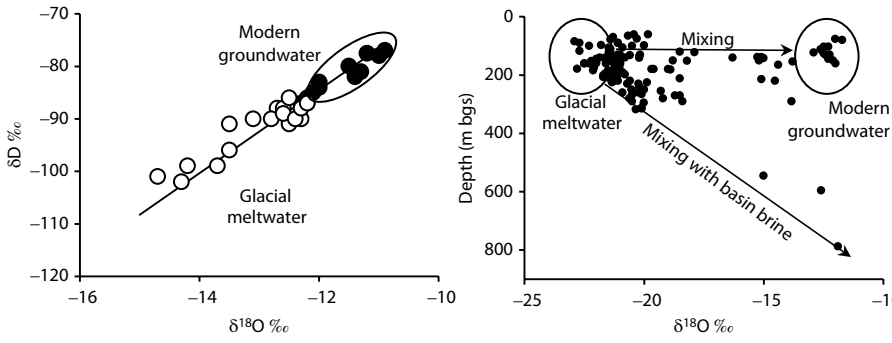

FIGURE 8.16 Stable isotope depletion in paleogroundwaters with glacial water recharge. Left: Late Pleistocene and early Holocene groundwaters in the Alliston aquifer, southern Ontario (After Aravena et al. 1995). Right: Late Pleistocene glacial meltwaters in the Paleozoic aquifers of the Baltic Basin (Finland through the Balkan states to Moscow), mixing with shallow modern groundwater and with deeper sedimentary basin brine (Modified from Raidlaa et al., 2009.)

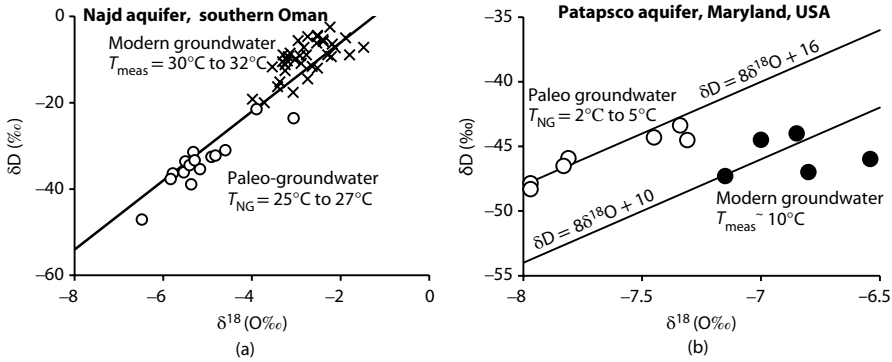

FIGURE 8.17 Stable isotope signature of paleogroundwaters recharged under past climates. (a) the Najd paleogroundwaters with modern groundwaters from the interior. (After Clark et al., 1987) (b) Paleorecharge during past glacial maxima (low sea level) in the northern flow path upper Patapsco aquifer flowing under Chesapeake Bay, Maryland. Drier and cooler climate (noble gas temperatures of 2 to 5°C) during ice-age conditions likely contributed to the higher deuterium excess of 16‰ and the ^{18}O depletion. (Modified from Plummer et al. 2012.)

recharge. The concentrations of the noble gases in air-saturated fresh water (i.e., in equilibrium with the atmosphere) are a product of their temperature-dependent solubility (Bunsen coefficient in units of cc_{STP}/cc_{H_2O}/atm, see Table 3.5), which are shown in Figure 8.18 and their atmospheric partial pressure, as shown in Figure 8.19.

From Figure 8.18, the lightest noble gas, He, has the lowest solubility, while the heaviest, Xe, is the most soluble. From Figure 8.19, argon is the most abundant noble gas in air and so has the highest dissolved concentration in air-equilibrated water. Xenon is the least abundant noble gas in air, and, despite its high solubility, it has the lowest concentration in air-saturated water. The two heaviest atmospheric noble gases, Xe and Kr, have the greatest relative change in solubility with temperature (Figure 8.18). For this reason, it is these two gases that provide the most precise determinations of recharge temperatures.

The concentrations of atmospheric noble gas in groundwaters are controlled not only by their atmospheric abundance and temperature. Recharge at higher elevations lowers their concentration through reduced atmospheric pressure, as does high salinity (above a few g/L TDS) (Figure 8.20).

A correction must also be made for additions to the dissolved noble gas concentrations gained by the incorporation of microbubbles of air that can be entrained during a recharge event. When this *excess air* component is carried to greater depth below the water table, it dissolves with the increasing hydrostatic pressure and adds to the air-saturated noble gas concentrations that were dissolved by equilibrium exchange across the gas–water interface. A correction for this excess air-derived noble gas component is made using the neon concentration, which is the atmospheric noble gas that is the least sensitive to temperature and so the best estimate of excess air.

More recently, Aeschbach-Hertig et al. (2000) improved the model for incorporation of excess air during recharge to account for partial dissolution of entrained air bubbles. This excess air component together with salinity and altitude of recharge are incorporated into Matlab programs (Aeschbach-Hertig et al. 1999) that resolve

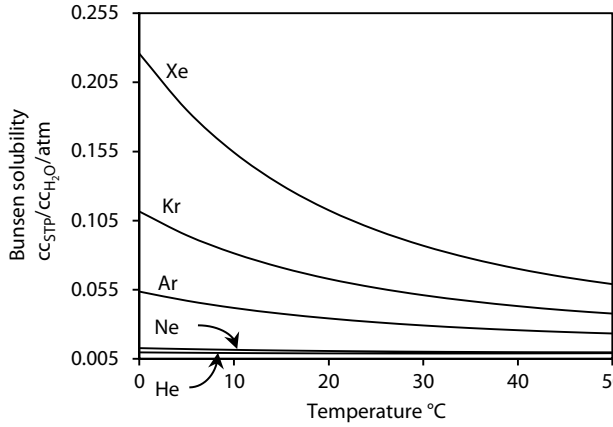

FIGURE 8.18 Solubilities for the noble gases from 0°C to 50°C for 1 atm partial pressure.

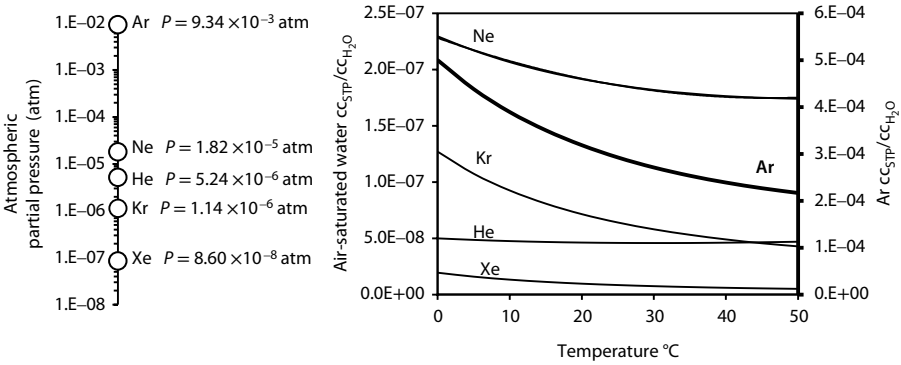

FIGURE 8.19 Noble gas partial pressures in the atmosphere (left) and their concentrations in air-saturated water (right). The temperature–solubility equations for these concentrations are (T in degrees Celsius):

$$\text{He } (cc_{STP}/cc_{H_2O}) = 4.07 \times 10^{-12}\, T^2 - 2.58 \times 10^{-10}\, T + 4.98 \times 10^{-8}$$

$$\text{Ne } (cc_{STP}/cc_{H_2O}) = 2.50 \times 10^{-11}\, T^2 - 2.31 \times 10^{-9}\, T + 2.28 \times 10^{-7}$$

$$\text{Ar } (cc_{STP}/cc_{H_2O}) = 1.05 \times 10^{-7}\, T^2 - 1.06 \times 10^{-5}\, T + 4.91 \times 10^{-4}$$

$$\text{Kr } (cc_{STP}/cc_{H_2O}) = 3.33 \times 10^{-11}\, T^2 - 3.24 \times 10^{-9}\, T + 1.24 \times 10^{-7}$$

$$\text{Xe } (cc_{STP}/cc_{H_2O}) = 6.06 \times 10^{-12}\, T^2 - 5.69 \times 10^{-10}\, T + 1.88 \times 10^{-8}$$

estimates of recharge temperature for each noble gas. The average of these estimates is then used (generally excluding He and Ar if there are geogenic inputs for these gases).

An example of noble gases recording a paleorecharge temperature is that of old groundwaters from New Mexico (Figure 8.21). The lower recharge temperatures calculated from noble gases correlate with depletions in ^{18}O, showing the older groundwaters to have recharged under cooler climate conditions at the last glacial maximum some 20,000 years ago.

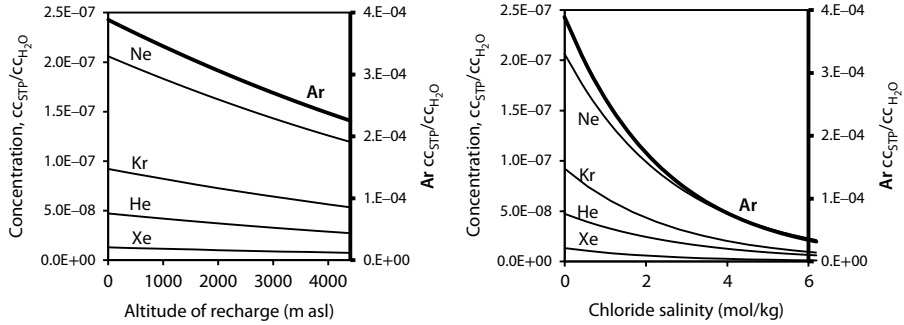

FIGURE 8.20 Noble gas concentrations for air-saturated water at 10°C with (left) altitude and (right) salinity.

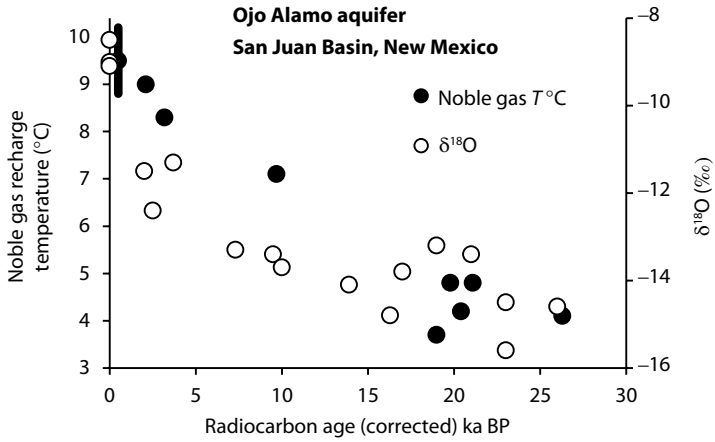

FIGURE 8.21 Noble gas recharge temperatures for Holocene and Pleistocene groundwaters dated with radiocarbon from the San Juan Basin, New Mexico, together with the $\delta^{18}O$ values for these waters, showing an isotope depletion in the older groundwaters, which have lower noble gas recharge temperatures. Range of temperatures for modern groundwaters shown with a black vertical line. (Data from Phillips et al. 1986; Stute et al. 1995.)

DATING VERY OLD GROUNDWATER

It is not usual to find groundwater resources that have recharged longer ago than is possible to date with radiocarbon. This is, however, the case for some important aquifers, which host groundwaters that are older than about 50,000 years and have radiocarbon activities that are below detection. Determining an accurate age is useful for calibrating hydrodynamic models and contributes to resource evaluations. Radiometric tools that can be applied to such groundwaters are limited. Qualitative measures of the age of old groundwaters can be made by the ingrowth of radiogenic isotopes of the noble gases, including ^{4}He, ^{21}Ne, and ^{40}Ar as well as several isotopes of Xe, although uncertainty related to production rates can be considerable. Quantitative measurements can be made by the decay of atmospherically derived radioisotopes (Chapter 4), providing the input function in the recharge environment

can be established. Two such radioisotopes with appropriately long half-lives are ^{36}Cl ($T_{½}$ = 301,000 years) and ^{81}Kr ($T_{½}$ = 229,000 years). Both are conservative solutes and so have less complicated corrections and interpretations than radiocarbon, although their very low atmospheric production rates are an analytical challenge.

Chlorine-36

Decay of cosmogenic radiochlorine, ^{36}Cl, following groundwater recharge, can provide age estimates up to about five half-lives and so over one million years. It is measured in environmental samples as a concentration relative to stable ^{35}Cl, typically with $^{36}Cl/Cl$ ratios on the order of 10^{-15} to 10^{-13} or higher. These very low ratios of ^{36}Cl mean that such samples also have very low concentrations in water and very low radioactivities. It is measured by AMS using total Cl extracted from water or mineral samples, giving an atom ratio of ^{36}Cl to atoms of stable Cl:

$$R^{36}\mathrm{Cl} = \frac{\text{atoms}\,^{36}\mathrm{Cl}}{\mathrm{Cl}}$$

In groundwaters, the concentration of ^{36}Cl as atoms per kilogram or per liter ($A^{36}Cl$) is an important expression, as it is independent of the Cl^- content, and is calculated as

$$A^{36}\mathrm{Cl} = \frac{\text{atoms}\ ^{36}\mathrm{Cl}}{\mathrm{L}} = \frac{^{36}\mathrm{Cl}}{\mathrm{Cl}} \times m_{\mathrm{Cl}^-} \times 6.022 \times 10^{23}$$

where m_{Cl^-} = moles Cl^-/kg or moles/L and $^{36}Cl/Cl = R^{36}Cl$.

Together, these two expressions for ^{36}Cl concentration provide insights into the origin and additions of ^{36}Cl in groundwaters. $R^{36}Cl$ will not change during concentration by evaporation, whereas $A^{36}Cl$ will increase. Conversely, $A^{36}Cl$ will not necessarily change with increases in Cl^- in groundwaters by leaching or evaporite dissolution (^{36}Cl-free additions of Cl^-), whereas $R^{36}Cl$ will decrease proportionally.

Example 8.9: Concentrations and Activities of ^{36}Cl in Groundwater

A sample of groundwater from the Nubian sandstone aquifer at the Dakhla Oasis in the Egyptian Sahara has a $^{36}Cl/Cl$ ratio of 76.5×10^{-15} and a Cl^- concentration of 20 mg/L (Patterson et al. 2005). What is the concentration of ^{36}Cl in groundwater, and what is its activity in Becquerels per liter? Recall from Chapter 4 the concentration–activity relationships, which are used here to convert a ratio (concentration) to activity (in decays per second, or Becquerels).

Concentration

$$^{36}\mathrm{Cl/Cl} = 76.5 \times 10^{-15}$$

$$\mathrm{Cl}^- = 20\ \mathrm{mg/L}$$

$$= 20/35{,}500 = 0.00056\ \mathrm{mol/L}$$

$$^{36}\mathrm{Cl} = 76.5 \times 10^{-15} \times 0.00056 = 4.31 \times 10^{-17}\ \mathrm{mol/L}$$

$$= 4.31 \times 10^{-17} \times 6.02 \times 10^{23} = 25.9 \times 10^{6}\ \mathrm{atoms/L}$$

Activity

$$a = \lambda n$$
$$T_{1/2} = 301{,}000 \text{ years}$$
$$= 9.49 \times 10^{12} \text{ seconds}$$
$$\lambda = \ln 2/T_{1/2}$$
$$= 0.693/9.49 \times 10^{12} = 7.30 \times 10^{-14}$$
$$n^{36}\text{Cl} = 25.9 \times 10^{6} \text{ atoms/L}$$
$$a^{36}\text{Cl} = 7.30 \times 10^{-14} \times 25.9 \times 10^{6} = 1.89 \times 10^{-6} \text{ Bq/L}$$

This very low activity amounts to about six decays per day, and cannot be measured with a scintillation counter. Natural abundance concentrations of ^{36}Cl are measured by AMS.

Both will change through incorporation of ^{36}Cl-active chloride from subsurface sources where ^{36}Cl ingrowth is important.

Radiochloride is used to date groundwaters principally by decay of the initial concentration that accompanies groundwater recharge. The atmospheric production of ^{36}Cl is a function of the geomagnetic latitude, with a maximum in fallout of about 20 atoms/m^2/s at about 45° north or south but falls off to less than 5 atoms/m^2/s near the equator and the poles (Andrews and Fontes 1992). Chloride has a short atmospheric residence time and so ^{36}Cl together with stable Cl^-, is washed to the surface by precipitation (wet fallout) or dry fallout. Ratios for ^{36}Cl/Cl are typically up to 700×10^{-15} in precipitation. However, these ratios drop off at lower and higher latitudes, and in particular with proximity to the coast, where ^{36}Cl-free marine aerosols dilute cosmogenic ^{36}Cl. Bentley et al. (1986) indicate that ^{36}Cl/Cl ratios drop off to values as low as 20×10^{-15} along the U.S. continental margins.

The atmospheric neutron flux impinging on evaporative salts in soils at the surface can activate stable ^{35}Cl (n-γ) to produce ^{36}Cl, which together with minor production from spallation of ^{39}K (n-α) and ^{40}Ca (n-p, α) contribute epigenic ^{36}Cl to recharge waters. This can provide a variable and enriched input function (Andrews and Fontes 1992; Phillips 2000). Accordingly, ^{36}Cl/Cl ratios in recharge waters in temperate latitudes are typically in the range of 300 to 600×10^{-15} and in low latitudes from 100 to 200×10^{-15} (Bentley et al. 1986; Patterson et al. 2005).

Atmospheric and epigenic ^{36}Cl then enters the subsurface with groundwater recharge. If the system remains closed to other sources of ^{36}Cl, losses should be due to radioactive decay to ^{36}Ar and will reflect the subsurface residence time of the groundwater. However, additions from subsurface production must be taken into account. This contribution is illustrated in Figure 8.22, which shows that the loss of cosmogenic ^{36}Cl with time is offset to a minor degree by ingrowth of ^{36}Cl. After about five half-lives, the ^{36}Cl/Cl ratio reaches a steady value of secular equilibrium, where cosmogenic ^{36}Cl has decayed away and in situ production is balanced by decay. After this time, only minimum groundwater ages can be calculated.

The use of ^{36}Cl is also complicated by the potential for the gain of Cl^- during flow by dissolution of salt, diffusion from adjacent aquitards, or by mixing with other

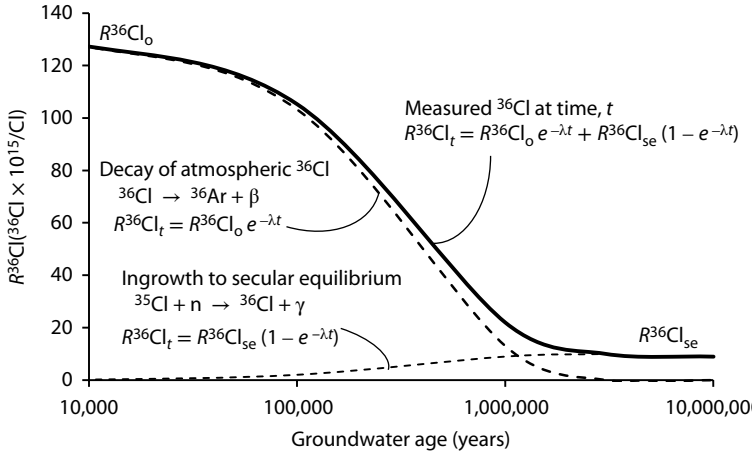

FIGURE 8.22 Decay of atmospheric ^{36}Cl combined with ingrowth toward secular equilibrium, giving total ^{36}Cl in groundwater with age.

TABLE 8.6
$^{36}Cl/Cl$ Ratios at Secular Equilibrium for Various Rock Types

Rock	Secular Equilibrium $^{36}Cl/Cl \times 10^{-15}$
Granite	30.1
Sandstone	4.68
Shale	12.5
Limestone	10.9

Source: Bentley et al. 1986.

groundwater. Such gains of Cl^- will include ^{36}Cl accompanying these sources of Cl^-. Corrections often assume a value for secular equilibrium for ^{36}Cl in the aquitard.

As seen in Figure 8.22, cosmogenic ^{36}Cl gained during recharge is generally the principal source of radiochloride in groundwater, although contributions from subsurface production must be considered. The $^{36}Cl/Cl$ ratio at secular equilibrium depends on the host rock's content of U and Th, which irradiate light elements (O, Na, Mg, Al, Si, and K) through alpha decay to produce an in situ neutron flux (Figure 4.10), J_n. These neutrons activate ^{35}Cl to produce in situ ^{36}Cl (Andrews et al. 1989), which follows an ingrowth function (Figure 8.22) that stabilizes at some value $R^{36}Cl_{se}$ that represents a secular equilibrium between in situ production and decay. Typical values for $R^{36}Cl_{se}$ have been suggested by Bentley et al. (1986), which are considerably lower than typically observed for cosmogenic production of ^{36}Cl (Table 8.6).

Given a fixed initial $R^{36}Cl_0$ in recharge groundwaters, and an established value for secular equilibrium, $R^{36}Cl_{se}$, groundwater age is derived using the ^{36}Cl decay constant $\lambda^{36}Cl = \ln 2/T_{½} = 2.303 \times 10^{-6}\ yr^{-1}$ (Bentley et al. 1986):

$$t = \frac{1}{\lambda^{36}Cl} \ln \frac{(R^{36}Cl_t - R^{36}Cl_{se})}{(R^{36}Cl_0 - R^{36}Cl_{se})}$$

Example 8.10: ^{36}Cl Ages for Groundwaters in the Western Desert of Egypt (Patterson et al. 2005)

The Nubian sandstone underlying much of the northeastern Sahara Desert is one of the world's great aquifers, hosting tens of thousands of cubic kilometers of ancient, low-salinity groundwater. The sandstone is draped over the Precambrian shield, deepening northward from outcrop areas to the southwest. Samples were collected for ^{36}Cl along a transect connecting four oases (Figure 8.23).

The measured chloride and ^{36}Cl values for six wells studied in this basin are given in Table 8.7. Chlorine-36 ratios, R^{36}Cl, and atom concentrations, A^{36}Cl, are plotted in Figure 8.24. Also plotted are the lines for decay (including minor ingrowth, with $R^{36}Cl_{se} = 5 \times 10^{-15}$), showing the decrease in both R^{36}Cl and A^{36}Cl over time from initial values for Cl^- and ^{36}Cl in the recharge area. The range of data for this aquifer suggests variable initial Cl^- concentrations, which account for the variation in A^{36}Cl, but allows for a simple calculation of age from the formula above, incorporating a contribution from in situ production.

Calculated groundwater ages cover a remarkable range from 240,000 years to over 1,000,000 years before present, and fit well with hydrodynamic modeling of the groundwater flow over these distances (Patterson et al. 2005). These ages also fit with paleoclimatic models. Lower and variable Cl^- concentrations in recharge waters as compared with the recharge area today (Figure 8.24(a) and Table 8.7) is consistent with recharge taking place during past pluvial periods. This is supported by the stable isotope data for these groundwaters in Figure 8.24(b), showing that modern recharge is enriched in ^{18}O and D relative to the old groundwaters.

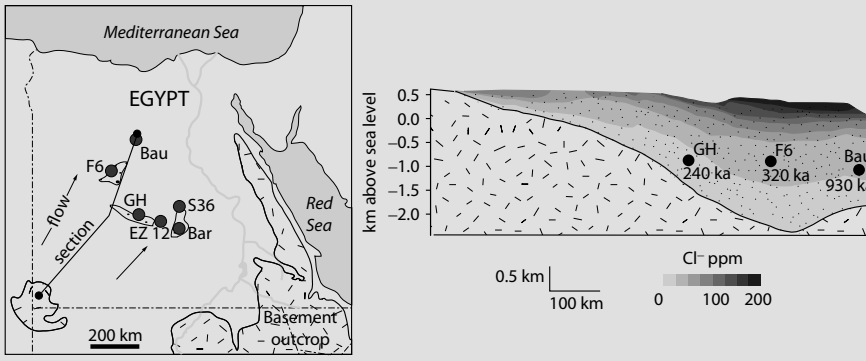

FIGURE 8.23 The Nubian sandstone aquifer overlying the crystalline basement in the Egyptian western desert, showing sample locations and salinity gradient. (Modified from Patterson et al. 2005.)

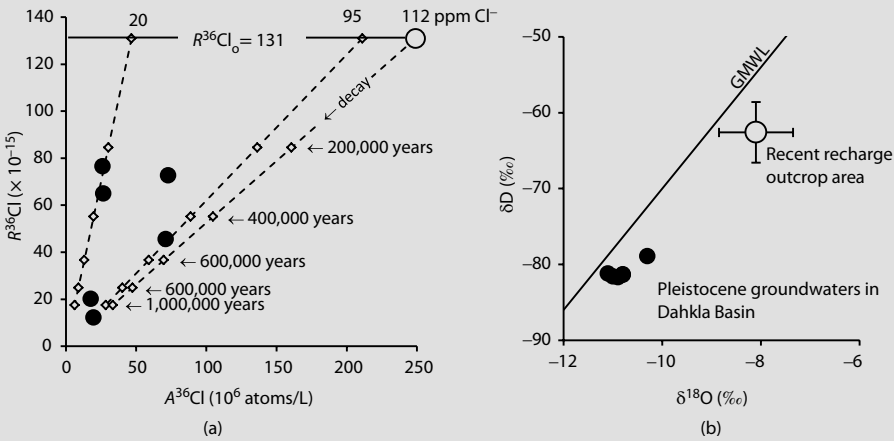

FIGURE 8.24 (a) $R^{36}Cl_t$ versus $A^{36}Cl_t$ showing Pleistocene recharge for groundwaters in the Egyptian Dahkla Basin of the Nubian sandstone aquifer. Dashed lines show decay over 1,000,000 years from varying initial Cl^- concentrations, with open diamonds marking 200,000-year intervals (Patterson et al. 2005). (b) Plot of $\delta^{18}O$ versus δD for Nubian groundwaters. Depletion in the Pleistocene groundwaters is attributed to a continental effect (Chapter 5) with precipitation derived from a vapor source originating over the Atlantic Ocean.

TABLE 8.7
Chloride Concentrations and $^{36}Cl/Cl$ Ratios for Wells in the Dahkla Basin of the Nubian Sandstone Aquifer, Western Egypt

Well	Depth (m)	Cl^- (mg/L)	$R^{36}Cl$ ($\times 10^{-15}$)	$A^{36}Cl$ (10^6 atoms/L)	^{36}Cl Age (ka BP)	$\delta^{18}O$ (‰)	δD (‰)
Recharge area	surface	112	131	249	–	–8.1	–62.6
GH	1200	20	76.5	26.1	240	–11.1	–81.2
EZ 12	720	59	72.7	72.7	270	–10.9	–81.7
F6	800	24	65.0	26.6	320	–10.3	–78.9
Bar	600	92	45.6	71.1	490	–10.8	–81.4
Bau	1200	52	20.2	17.7	930	–10.8	–81.3
S36	750	95	12.2	19.6	1200	–11.0	–81.6

Krypton-81

With its similarly long half-life of 229,000 years, ^{81}Kr is also very suitable for dating groundwaters that were recharged in the Pleistocene. Its discovery is recent (Loosli and Oeschger 1969) and was soon recognized as a potential groundwater dating tool. Unlike ^{36}Cl, it has no complications from subsurface production or dilution with subsurface Kr sources. However, its very low abundance makes analysis a challenge (see Figure 4.7). Until recently, sampling required extraction from cubic meters of

groundwater. ATTA (Jiang et al. 2012) currently requires extraction of Kr from only 100 to 200 L of water, with lower volumes anticipated in the near future. As the sampling requirement decreases, greater deployment of this method can be expected.

Dating with ^{81}Kr is based simply on loss by decay of an initial cosmogenic signal gained during recharge by equilibration with atmospheric Kr. While atmospheric production may have had minor fluctuations over the Pleistocene due to changes in the cosmic ray flux, the atmospheric concentration is believed to have been essentially constant in the past. These data for the abundance and activity of ^{81}Kr in the air and in water come from Jiang et al. (2012) and Aeschbach-Hertig (2014).

Kr atmospheric abundance	1.14 ppmv
^{81}Kr/Kr atmospheric (R^{81}Kr)	5.2×10^{-13}
^{81}Kr atmospheric activity	1.5 μBq/m^3
Activity in air equilibrated water	0.09 nBq/L
Concentration in air-equilibrated water	892 atoms/L
Atmospheric production	$^{80}\text{Kr} + \text{n} \rightarrow {}^{81}\text{Kr}$ plus spallation of other Kr isotopes
Decay	$^{81}\text{Kr} \rightarrow {}^{81}\text{Br} + \beta^+$ (electron capture)
Half-life	229,000 years
Decay constant	$\lambda^{81}\text{Kr} = 3.027 \times 10^{-6}\text{y}^{-1}$

Dating is then based on the simple exponential decay equation using the atmospheric ^{81}Kr/Kr ratio:

$$R^{81}\text{Kr}_t = R^{81}\text{Kr}_0 \times e^{-\lambda t}$$

$$t = -330{,}377 \ln[R^{81}\text{Kr}_t/(5.2 \times 10^{-13})]$$

With the development of the ATTA analytical method, a greater number of field studies have been undertaken. Of interest is the application of ^{81}Kr to the Nubian aquifer for which ^{36}Cl age dating was presented earlier in Example 8.10. In Example 8.11 below, this case study is complemented by the measurement of ^{81}Kr.

Given the constant atmospheric ^{81}Kr/Kr ratio, groundwater ratios can be normalized to the atmospheric ratio (R/R_{air}) and expressed as a percentage of this initial value (Table 8.8).

Example 8.11: ^{81}Kr Ages for Groundwaters in the Western Desert of Egypt (Sturchio et al. 2004)

The ^{36}Cl ages of the Nubian groundwaters were shown earlier to have been recharged during the early to mid-Pleistocene, although with ^{36}Cl dating, there is always a possibility that subsurface contributions to Cl^- and ^{36}Cl in groundwaters bring uncertainty to the estimates. Age dating with ^{81}Kr provides additional certainty. Sturchio et al. (2004) collected Kr from the same pumping wells sampled for ^{36}Cl, with analysis by ATTA at the Argonne National Laboratory.

TABLE 8.8
^{81}Kr Measurements for Groundwaters from the Dahkla Basin of the Nubian Sandstone Aquifer, Egyptian Western Desert

Well	^{81}Kr/Kr ($\times 10^{-12}$)	R/R_{air} (%)	^{81}Kr Age (ka)	^{36}Cl Age (ka)
GH	5.73	52.6 ± 6.1	210	240
EZ 12	3.34	30.6 ± 3.6	390	270
F6	4.00	36.5 ± 4.2	330	320
Bar	2.49	22.8 ± 3.0	490	490
Bau	5.23	4.8 ± 3.8	1000	930
S36	1.40	12.8 ± 3.0	680	1200

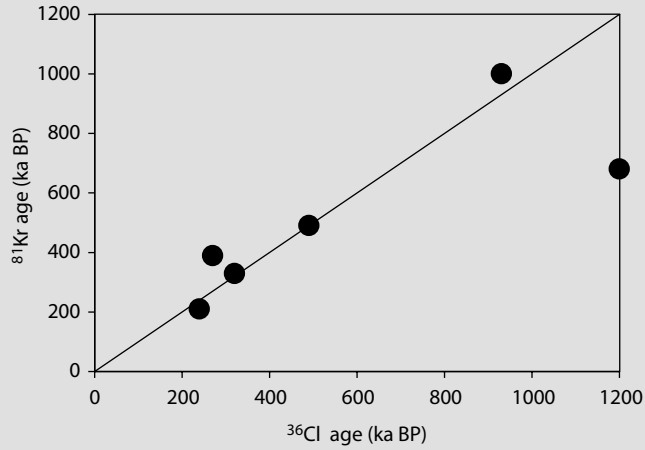

FIGURE 8.25 Comparison of ^{81}Kr groundwater ages with ^{36}Cl groundwater ages for the same wells. (Sturchio et al. 2004; Patterson et al. 2005)

Geogenic Noble Gases

The stable noble gases, He, Ne, Ar, Kr, and Xe, have very well-constrained atmospheric concentrations (Figure 8.18). Each of these gases comprises a range of stable isotopes with well-documented terrestrial atmospheric molar fractions, shown in Figure 8.26. While most were produced during nucleosynthesis at the formation of our solar system, others continue to be produced by nuclear reactions in the subsurface, including radioactive decay, spontaneous uranium fission, and neutron capture. Measuring the increase in abundance of these geogenic noble gases in deep groundwaters provides a measure of time, since the waters were isolated from the atmosphere.

An α particle, 2n2p, is the nucleus of the abundant isotope of helium, ^{4}He, and the principle building block of the elements during nuclear fusion in stars. Alpha-decay of the actinides, mainly along the U and Th decay series, produces ^{4}He nuclides, which

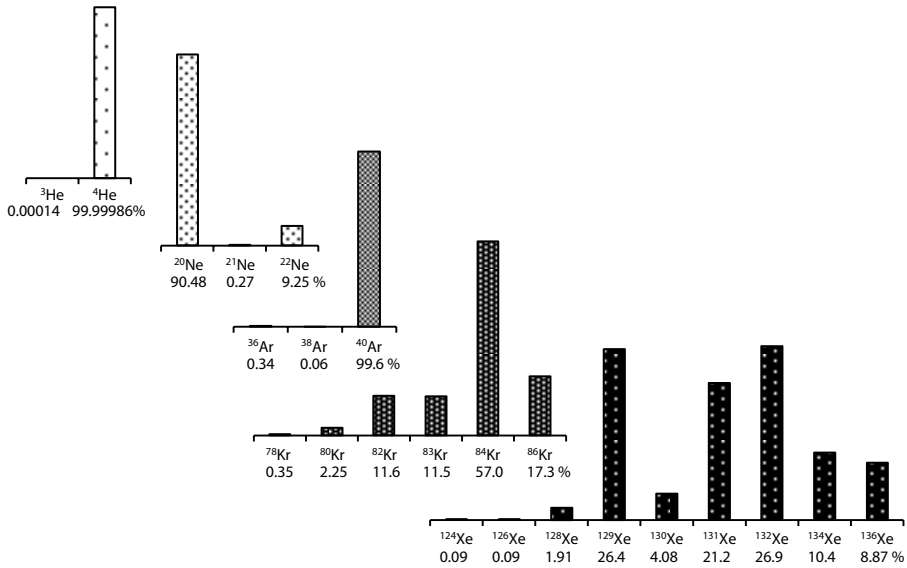

FIGURE 8.26 Stable isotope abundances (percent) of the five stable atmospheric noble gases.

can accumulate within the environment of production. Similarly, beta decay of ^{40}K produces ^{40}Ar, the abundant stable isotope of Ar, which also can accumulate in the subsurface. Providing the release of these radiogenic nuclides into groundwater from their mineral host in the aquifer material is relatively efficient and there are no other gains or losses, their concentration can be considered as an estimate of age. Both ^{4}He and ^{40}Ar are the abundant isotope of atmospheric helium and argon, so these atmospheric contributions in the groundwater must be known and accounted for, according to the temperature–solubility and excess-air considerations discussed earlier.

Helium production is proportional to the concentration of U and Th in the aquifer. Geogenic ^{4}He is mainly produced in the ^{238}U decay chain, which releases eight helium nuclides by the time it decays to stable lead, with lesser contributions from ^{232}Th, which is more abundant but with a much longer half-life, and ^{235}U, which is the most active of the three primordial actinides but with an abundance of only 0.73% of total uranium.

The helium age of groundwater is simply calculated from the ratio of the radiogenic helium concentration, $^{4}He_{radiogenic}$ (essentially all measured ^{4}He with correction for atmospheric He (dissolved and excess, see Example 8.3) incorporated during recharge), to the helium accumulation rate, $^{4}He_{acc\ rate}$, assuming that there are no contributions from a flux of He from a deeper source in the crust.

$$t = \frac{^{4}\mathrm{He}_{\mathrm{radiogenic}}(\mathrm{cc}_{\mathrm{STP}} / \mathrm{cc}_{\mathrm{H_2O}})}{^{4}\mathrm{He}_{\mathrm{acc\ rate}}(\mathrm{cc}_{\mathrm{STP}} / \mathrm{cc}_{\mathrm{H_2O}} / \mathrm{y})}$$

Calculation of the helium accumulation rate, $^{4}He_{acc\ rate}$, in groundwater is based on the concentrations of U and Th in the aquifer matrix, the matrix density and porosity, and the decay factors for these radionuclides (Andrews et al. 1989):

$$^{4}\mathrm{He}_{\mathrm{acc\ rate}} = \mathrm{RF}_{\mathrm{He}} \frac{\rho_r}{\rho_w} \frac{1-n}{n_{\mathrm{eff}}} \left(1.19 \times 10^{-13}[\mathrm{U}] + 2.88 \times 10^{-14}[\mathrm{Th}]\right) \mathrm{cc}_{\mathrm{STP}} / \mathrm{cc}_{\mathrm{H_2O}} / \mathrm{y}$$

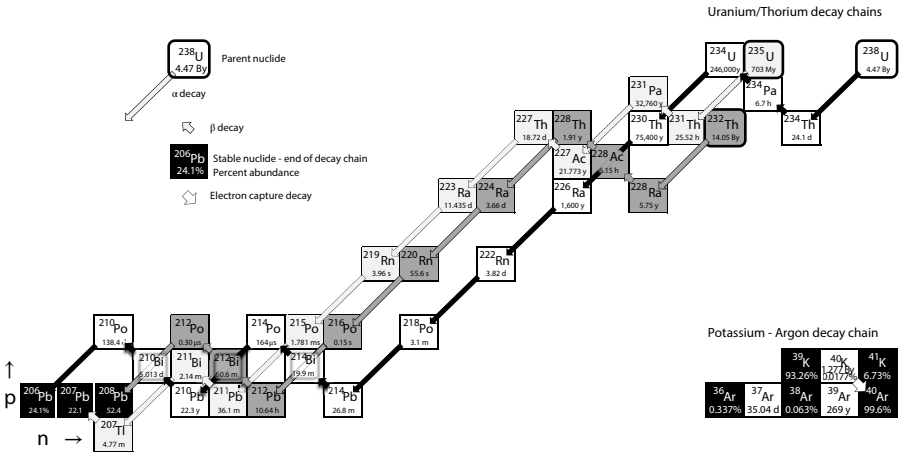

FIGURE 8.27 The U and Th decay series showing alpha and beta decay steps and intermediary radioisotopes. Decay in the ^{238}U series produces 8 ^{4}He nuclides, 7 ^{4}He in the ^{235}U series, and 6 ^{4}He in the ^{232}Th–decay series. Shown also is the ^{40}K decay to ^{40}Ar by electron capture.

where RF_{He} is the helium release factor for diffusion of ^{4}He from the mineral lattice where the α particles are produced from U and Th decay. For long time periods this is generally taken to be 1 (full release of produced He from minerals to groundwater).

ρ_r is the density of the rock, in g cm^{-3}

ρ_w is the density of the water, in g cm^{-3}

n is the total fractional porosity of the rock

n_{eff} is the effective porosity of the rock (connected porosity contributing to flow)

[U] and [Th] are the uranium and thorium contents of the rock matrix in ppm

Example 8.12 Helium Dating of Groundwater

The stable isotope composition and noble gas temperatures of the Patapsco aquifer paleogroundwaters in Maryland were presented above in Figure 8.17b. The low sea level during glacial recharge allows enhanced recharge and flow to the east under Chesapeake Bay (Plummer et al. 2012). The $^{14}C_{DIC}$ activity becomes less than detection within 40 km along the flow path.

The ^{4}He accumulation rate ($^{4}He_{acc\ rate}$) for this aquifer was calculated from the mineral concentrations of U and Th (ppm), according to the equation presented above, and using a helium release factor, RF, of 1 (full release from the mineral matrix to the groundwater).

$$
\begin{aligned}
{}^{4}He_{acc\ rate} &= RF_{He}\frac{\rho_r}{\rho_w}\frac{1-n}{n_{eff}}\left(1.19\times10^{-13}[U] + 2.88\times10^{-14}[Th]\right)\\
&= 1\times\frac{2.6}{1}\times\frac{1-0.39}{0.25}\left(1.19\times10^{-13}[1.9] + 2.88\times10^{-14}[7.5]\right)\\
&= 2.80\times10^{-12}\ cc_{STP}/cc_{H_2O}/y
\end{aligned}
$$

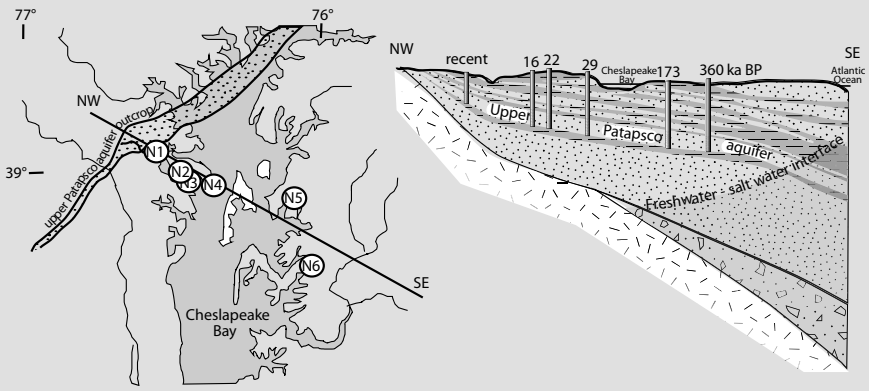

FIGURE 8.28 Location and cross section of the Patapsco aquifer, Maryland, showing the outcrop and subsurface geology. Wells sampled along the northern flow path are identified on the plan view and in section with ^{4}He ages in thousands of years before present (ka BP). (Modified from Plummer et al. 2012.)

TABLE 8.9
Helium and Neon Data (cc_{STP}/cc_{H_2O}) for Wells along the Northern Flow Path, Patapsco Aquifer, Maryland

Well	T_{NG} °C	Ne_{meas}	$Ne_{dissolved}$	$Ne_{excess\ air}$	He_{meas}	$He_{excess\ air}$	$He_{dissolved}$	$He_{recharge}$	$^4He_{radiogenic}$	^{4}He Age Years
N-1	10	2.5E–7	2.1E-07	4.6E-08	5.8E-08	1.3E-08	4.8E-08	6.1E-08	LD	
N-2	3.9	2.8e–7	2.2E-07	6.2E-08	1.1E-07	1.8E-08	4.9E-08	6.7E-08	4.6E-08	16,000
N-3	3.3	2.6E–7	2.2E-07	4.0E-08	1.2E-07	1.2E-08	4.9E-08	6.1E-08	6.2E-08	22,000
N-4	1.5	2.7E–7	2.2E-07	4.6E-08	1.4E-07	1.3E-08	4.9E-08	6.3E-08	8.0E-08	29,000
N-5	5.4	2.6E–7	2.2E-07	4.3E-08	5.5E-07	1.2E-08	4.9E-08	6.1E-08	4.9E-07	175,000
N-6	4.3	2.6E–7	2.2E-07	4.0E-08	1.1E-06	1.2E-08	4.9E-08	6.0E-08	1.0E-06	360,000

Source: Plummer et al. 2012.
Notes:
1. Helium from excess air incorporated during recharge is calculated from measured neon less the neon dissolved from air at the recharge temperature, according to the equation given in Figure 8.19 and calculations in Example 8.3.
2. The ^{4}He age in years is calculated from the radiogenic ^{4}He and the ^{4}He production rate, $^4\text{He age} = He_{radiogenic}/{}^4He_{acc\ rate}$.

The measured radiogenic ^{4}He concentrations, together with the ^{4}He production rate calculated from the U and Th concentrations in the aquifer, provide age estimates that increase from modern groundwater (no measureable radiogenic ^{4}He) in the recharge area to over 360,000 years before present (Figure 8.29). These very old estimates are interpreted to represent recharge during past Pleistocene glaciations when the low sea level stand increased the hydraulic gradient and increased recharge and flow. Refinements of these age estimates were made by using ^{14}C ages in the zone overlapping with

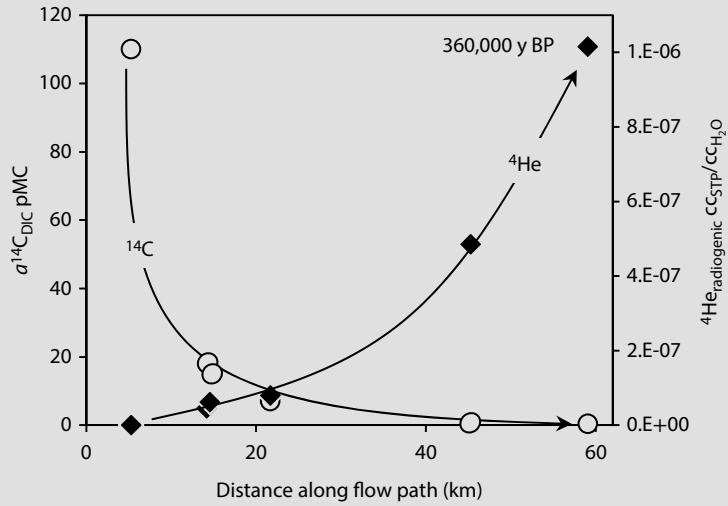

FIGURE 8.29 Increase in ^{4}He with decrease in ^{14}C along northern groundwater flow path in the Patapsco aquifer, Maryland. High ^{4}He concentrations are found beyond 40 km, where ^{14}C activities are near detection. The high radiogenic ^{4}He measurements beyond 40 km provide age estimates up to 360,000 years before present (Plummer et al. 2012.)

measureable ^{4}He (15–25 km) to calibrate the production of radiogenic ^{4}He (Plummer et al. 2012.)

Like ^{4}He, the age from the accumulation of ^{40}Ar (the dominant isotope of argon) is calculated from

$$t = \frac{^{40}\mathrm{Ar}_{\mathrm{radiogenic}}\,(\mathrm{cc}_{\mathrm{STP}}/\mathrm{cc}_{\mathrm{H_2O}})}{^{40}\mathrm{Ar}_{\mathrm{acc\ rate}}\,(\mathrm{cc}_{\mathrm{STP}}/\mathrm{cc}_{\mathrm{H_2O}}/\mathrm{y})}$$

and

$$^{40}\mathrm{Ar}_{\mathrm{radiogenic}} = \mathrm{RF}_{\mathrm{Ar}}\frac{\rho_r}{\rho_w}\frac{1-n}{n_{\mathrm{eff}}}3.887\times10^{-14}\,[\mathrm{K}]\ \mathrm{cc}_{\mathrm{STP}}/\mathrm{cc}_{\mathrm{H_2O}}/\mathrm{y}$$

Here, [K] is the weight percent of potassium in the rock. This formula takes into account that the abundance of radioactive ^{40}K is only 0.0177% of stable potassium (Figure 8.27). The half-life for ^{40}K is also long (1.277 By), but only one daughter ^{40}Ar is produced, while U and Th decay produces 8 and 6 ^{4}He nuclides, respectively, and so total accumulation is considerably less.

Example 8.13 ^{4}He and ^{40}Ar Ages in Crustal Brines

The origin and age of deep crustal brines is of interest for the isolation of waste in the subsurface. Of particular concern is the movement of groundwater near deep geological repositories proposed for the disposal of radioactive waste. Brines encountered at depth in the Con Mine, Yellowknife, NWT, Canada, were studied as part of research on fluids deep within the crystalline terrain of the Canadian Shield (Greene et al. 2008).

The Con Mine follows a gold-bearing shear zone dipping almost 2 km through faulted metavolcanics within the granitic terrain of the Canadian Shield. Shallow groundwaters from Holocene to modern age are underlain by glacial meltwaters that recharged at the end of the Pleistocene along the steep gradients below the melting Laurentide ice sheet. The deepest mine levels have inflows of high salinity Ca^{2+} – Cl^- brine, with TDS up to 290 g/kg.

The deep brines are believed to have been recharged during Devonian time, when the region was covered by highly evaporated epicontinental seas. The highest salinity brine was analyzed for radiogenic ^{4}He and ^{40}Ar in an attempt to constrain their subsurface residence time.

$^4He = 0.0129\ cc_{STP}/cc_{H_2O}$
$^{40}Ar = 0.00495\ cc_{STP}/cc_{H_2O}$
$n = 0.005$
$n_{eff} = 0.005$ (take to be same as n for fracture flow)
$\rho_{brine} = 1.188$ g/mL
$\rho_{rock} = 3.0$ g/mL
$U_{rock} = 0.57$ ppm
$Th_{rock} = 2$ ppm

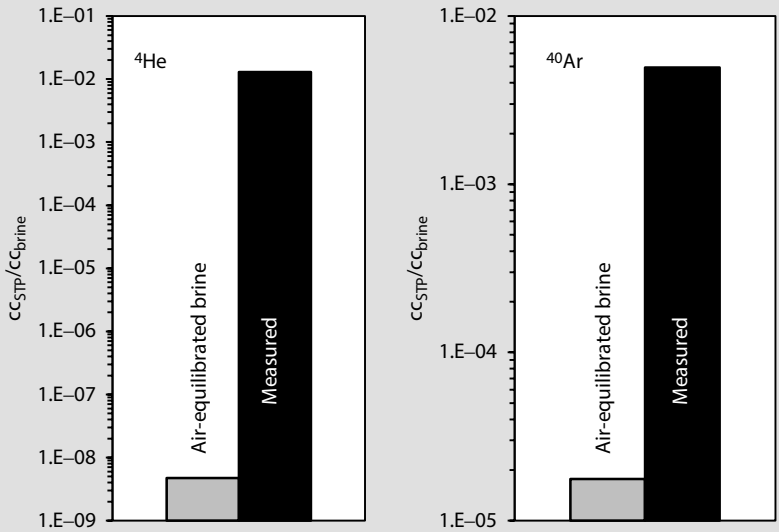

FIGURE 8.30 Concentrations of ^{4}He and ^{40}Ar in Con Mine brines compared with air-saturated water and brine, yielding ages of about 400 million years. (After Greene et al. 2008.)

K_{rock} = 0.86 weight% (^{40}K = 0.0177% of K, with a concentration of 1.5 ppm)

Note that the concentrations of both ^{4}He and ^{40}K are orders of magnitude higher than found in air-equilibrated water or in air-equilibrated brine (Figure 8.30). The greater accumulation of ^{4}He than ^{40}Ar (six orders of magnitude, compared with two orders of magnitude) reflects the high production of ^{4}He from the alpha decay chains for ^{238}U (8 ^{4}He atoms), ^{235}U (7 ^{4}He atoms), and ^{232}Th (6 ^{4}He atoms) (Figure 8.27), despite their similar abundances in these rocks.

Using the dating equation presented earlier in this section and in Example 8.12 for ^{4}He, Greene et al. (2008) determine the He and Ar accumulation ages to be 200 and 300 million years, respectively. Considering some diffusive loss of these gases over this period of time, a late Paleozoic age for the brine was concluded.

Long subsurface residence times can be estimated by ^{129}I, which has a half-life of 15.7 million years. As a halide, it is useful in studies of saline systems, such as marine sediments, and crustal brines. Iodine-129 has an atmospheric source through n-p reaction by cosmic radiation of atmospheric ^{129}Xe. Before anthropogenic inputs to environmental ^{129}I from the reprocessing of spent nuclear fuel, natural fallout provided some 200,000 to 400,000 atoms/L to surface waters. Now surface waters can have upward of 10 million atoms/L. Decay of atmospheric sources is seldom used as an approach to dating. Subsurface production by spontaneous fission of ^{238}U (Figure 4.10) generates greater concentrations of ^{129}I:

$$^{238}U_{SF} \rightarrow {}^{129}I + {}^{107}Pd + 2n$$

^{129}I decays by beta emission to stable ^{129}Xe

$$^{129}I \rightarrow {}^{129}Xe + \beta^{-}$$

Spontaneous fission of ^{238}U is well known for the production of fission-tracks in quartz grains and used for mineral dating. Decay of ^{238}U by spontaneous fission occurs with a half-life ($T_{½\,sf} = 8.15 \times 10^{15}$ y), far longer than that of ^{238}U decay by alpha emission ($T_{½\,\alpha} = 4.47 \times 10^{9}$ y). The fission yield of ^{129}I is only 0.03% but sufficient for significant accumulation over periods of time up to about five half-lives or 80 million years. In situ production of ^{129}I is then solely a function of the concentration of uranium in the host rock and will build up to the point of secular equilibrium, where the rate of production is equal to the rate of decay (for example, as shown for ^{36}Cl in Figure 8.22).

In a study of the deep crustal brines from the Con Mine (Example 8.13), Bottomley et al. (2002) compare a measured ^{129}I concentration of 340 million atoms/L to an in situ secular equilibrium value of 380 million atom/L, calculated using a uranium concentration of 1 ppm, and conclude that the brines have a subsurface resident time in that environment for greater than five half-lives or >80 million years.

Other radiogenic isotopes of noble gases can be used to support long subsurface residence times. Neon has three stable isotopes with well-constrained abundances in the modern atmosphere—^{20}Ne (90.48%), ^{21}Ne (0.27%), and ^{22}Ne (9.25%). The impact of alpha particles from the U and Th decay series on oxygen in the rock produces an enrichment of ^{21}Ne/^{22}Ne ratio:

$$^{17}\mathrm{O} + \alpha \rightarrow {}^{21}\mathrm{Ne} + \mathrm{n}$$

Spontaneous fission of ^{238}U produces stable isotopes of xenon at higher yields than for ^{129}I, and with the greatest yield for ^{136}Xe:

$$^{238}\mathrm{U}_{sf} \rightarrow {}^{136}\mathrm{Xe} + {}^{100}\mathrm{Mo} + 2\mathrm{n}$$

Enrichment of these daughter nuclides above their atmospheric ratios (Figure 8.26) provides a measure of time. A recent study by Holland et al. (2013) used neon and xenon isotopes together with ^{4}He and ^{40}Ar to date groundwater discharges from boreholes in a 2.4-km-deep mine in the Timmins Archean greenstone belt, Ontario, Canada. In such work, the radiogenic isotope is normalized to an isotope that is more representative of an atmospheric input, that is, ^{21}Ne/^{22}Ne and ^{136}Xe/^{130}Xe. Holland found enrichments in ^{21}Ne/^{22}Ne up to 0.396, which is more than 13× the ratio in air (0.029). Similarly, they measure enrichments in ^{136}Xe/^{130}Xe up to 2.71, or 25% greater than the atmospheric ratio of 2.17. On the basis of the concentrations of U, Th, and K in these rocks, they calculate ingrowth times for ^{4}He, ^{21}Ne, ^{40}Ar, and ^{136}Xe, to show that these fracture fluids have been resident in these deep, isolated fractures for perhaps 1.5 billion years, making these brines the oldest free-flowing waters ever dated.

PROBLEMS

1. Give examples of radiometric dating methods involving (1) loss of parent, (2) ingrowth of daughter, and (3) both loss of parent and gain of daughter.
2. The following noble gas concentrations were measured for low-salinity coastal aquifer groundwaters, which were dated with radiocarbon to 22,000 years before present. Correct for excess air with Ne and calculate an estimate for the paleogroundwater recharge temperature.
   a. $\mathrm{Ne} = 3.08 \times 10^{-7}\ \mathrm{cc_{STP}/cc_{H_2O}}$
   b. $\mathrm{Kr} = 1.13 \times 10^{-7}\ \mathrm{cc_{STP}/cc_{H_2O}}$
   c. $\mathrm{Xe} = 1.63 \times 10^{-8}\ \mathrm{cc_{STP}/cc_{H_2O}}$
3. Visit the GNIP site (http://www.iaea.org/water) and download tritium data from Ottawa (Canada), Vienna (Austria), and Kaitoke (New Zealand). Plot these data on a semilogarithmic chart. Account for the similarities and/or differences in the magnitude of the 1963 thermonuclear peaks in these records. Why do all records have strong seasonal variability? Plot decay curves on the chart. What are the two principal factors contributing to the attenuation of the high levels of tritium from 1963 to today? What are the constraints on using this 1963 peak in groundwater as a time horizon for dating?

4. The following CFC and SF_6 measurements were made for 15°C groundwater sampled in a semiconfined sand aquifer in southern Ontario. Calculate the atmospheric concentrations of these compounds and compare with the atmospheric scenarios in Figure 8.3 to determine a mean subsurface residence time for these samples. Concentrations are parts per trillion (10^{-12} or pmol/L) in groundwater.

	CFC-11	CFC-12	CFC-113	SF_6
10 m (pmol/L)	2.73	1.36	0.098	0.0026
30 m (pmol/L)	0.31	0.26	0.015	0.000048
K_H 15°C (pmol/L/atm)	0.016	0.0043	0.0049	0.00032

5. Groundwater was sampled for tritium on June 21, 2009, but not analyzed until November 13, 2013. The measured value was 6.8 TU. What was its tritium concentration on the sampling date?
6. Groundwater from the base of an alluvial aquifer overlying crystalline bedrock had a helium concentration (corrected for excess air) of 1.47×10^{-7} cc_{STP}/cc_{H_2O} and a recharge temperature of 15°C. What is the excess *geogenic* He in this sample? What would be the complications of using this sample for dating by the T–^{3}He method?
7. A series of shallow groundwaters (10°C) were sampled from a confined sandy aquifer from piezometers installed at increasing distances from the unconfined recharge area. Analysis of T and ^{3}He concentrations (^{3}He values corrected for atmospheric ^{3}He) gave the following results:

Sample	Distance from recharge (m)	T (TU)	^{3}He (cc_{STP}/cc_{H_2O})
CJ1	180	7.8	5.97×10^{-15}
CJ2	360	6.3	1.02×10^{-14}
CJ3	650	5.4	2.14×10^{-14}
CJ4	980	4.4	2.89×10^{-14}

Conversion: 1 cc_{STP} ^{3}He/cc_{H_2O} = 4.0177×10^{14} TU (^{3}He equivalent)

Plot the distribution of T and ^{3}He with distance from the recharge area, with ^{3}He both in units of cc_{STP}/cc_{H_2O} and in equivalent TU. Calculate the T–^{3}He age for each sample and from this calculate the average groundwater velocity (note that the calculated ages will be a mean of a range due to hydrodynamic dispersion). What was the initial tritium concentration in each sample at the time of recharge? Plot initial tritium with age for each sample and account for the change through time. (Refer to the charts in Figures 8.5 and 8.10 and suggest possible regions where this aquifer may be located.)

8. Groundwaters were sampled from a Cretaceous limestone aquifer (LMWL: $\delta D = 7.8\ \delta^{18}O + 10$) and produced the following data. What are the age constraints given by the stable isotope data and from the tritium data and from the radiocarbon data?

$\delta^{18}O$	$\delta^{2}H$	^{3}H (TU)	^{14}C (pMC)	$\delta^{18}O$	$\delta^{2}H$	^{3}H (TU)	^{14}C (pMC)
Recharge area				*Down gradient*			
–5.9	–36	9.4	40.1	–5.7	–42	<0.8	14.1
–6.1	–38	6.5	45.3	–6.1	–46	<0.8	12.2
–6.2	–40	2.5	39.6	–5.9	–43	<0.8	9.5
–5.7	–34	6.7	43.9	–6.0	–41	<0.8	8.9
–5.4	–32	8.3	51.1	–6.4	–44	<0.8	9.6
–5.9	–37	9.6	46.4	–6.1	–43	<0.8	7.1
–5.5	–34	5.8	44.7	–6.3	–46	<0.8	12.8
–5.5	–35	6.9	45.8	–5.8	–41	<0.8	10.5
–6.2	–38	8.1	52.2	–6.1	–45	<0.8	10.2
–5.9	–36	7.4	48.3	–5.9	–43	<0.8	7.9
–5.1	–30	8.3	41.8	–6.1	–43	<0.8	6.5
–5.0	–30	4.2	43.6	–6.4	–46	<0.8	8.3

9 Contaminant Geochemistry and Isotopes

INTRODUCTION

The contamination of groundwater resources has generated an industry with hydrogeologists, engineers, and environmental scientists involved in research and studies from environmental assessments through to design and installation of remediation schemes. Geochemistry and isotopes play an important role at all stages. Geochemistry and isotopes are used to trace both the origin and transformation of contaminants in groundwater, as well as predicting their fate and impacts on surface waters and water supplies. In this chapter, the major areas of application are examined, using the background on geochemistry and isotopes developed in the earlier chapters.

NITROGEN SPECIES AND GROUNDWATER CONTAMINATION

> Nitrogen bacteria teach us that Nature, with her sophisticated forms of the chemistry of living matter, still understands and utilizes methods which we do not as yet know how to imitate. Let it suffice that in the meantime improved nitrogen fertilization of the soil brings new nutritive riches to mankind and that the chemical industry comes to the aid of the farmer who, in the good earth, changes stones into bread.
>
> **—Fritz Haber, Nobel Prize acceptance speech, 1919**

Nitrogen is an essential nutrient for life, with a key structural role in protein and plant tissue. Algae, for example, have a chemical composition close to $C_{106}H_{263}O_{110}N_{16}P(S)$. The largest reservoir of nitrogen is atmospheric N_2, but requires transformation to mineralized or *fixed* forms for assimilation by life. The triple covalent bond of N_2 makes this molecule remarkably refractory, and so nitrogen is very difficult to fix in an ionic form that can be incorporated as nucleotides in DNA and as amino groups in protein. Nitrogenase enzymes manage this by transferring electrons to N_2 and producing reduced nitrogen as NH_3. Prokaryotes accomplished this reaction billions of years ago, but these nitrogen-fixers remain restricted to certain cyanobacteria in marine environments and root nodules in the legumes, such as clover, soybeans, and alfalfa. Cycling from NH_3 to organic N and NO_3^- ultimately returns nitrogen back to the atmosphere as N_2. Another pathway for nitrogen fixation includes NO_2 from lightning in the atmosphere, which can oxidize several kilograms of N_2 per strike.

As civilization developed over the Holocene, the importance of N-rich manure for agriculture became recognized. By early in the last millennium, saltpeter (KNO_3) for agriculture and for black powder dominated international trade, with supplies mainly from urea purified from soil in the cattle pens of India. By the late nineteenth century this source was eclipsed by the rich deposits of guano from the arid islands off the coast of Peru and the even richer accumulations of nitrate from Chile's hyperarid Atacama Desert. These deposits supplied NO_3^- not only for agriculture but also for the production of Alfred Nobel's stabilized form of nitroglycerin, which fueled the huge construction projects of the late 1800s, such as the Suez Canal and train tunnels through the Rocky Mountains as well as trinitrophenol for the high explosive artillery that sustained World War I. Competition for these coveted supplies spawned efforts to synthesize nitrate from atmospheric N_2, mainly by arcing, requiring hydroelectric generation and with limited yields. However, in 1909, Fritz Haber managed to reduce N_2 to ammonia at high pressure using H_2 as an electron donor and a hot ferric iron catalyst:

$$N_2 + 3H_2 \rightarrow 2NH_3 \qquad \Delta G_r^\circ = -16.5 \text{ kJ /mol} \qquad \text{Synthesis of ammonia}$$

Brought to full industrial scale by Carl Bosch, the method is responsible for the agricultural revolution of the twentieth century that supported a threefold increase in the human population. Today, nitrogen from the Haber–Bosch process is found in over 90% of the world food supply. However, the widespread use of fixed nitrogen compounds has led to unprecedented contamination of surface waters and groundwaters, making nitrogen perhaps the most pervasive anthropogenic contaminant in the environment today.

Nitrogen Species and Water Quality

Once nitrogen is fixed from atmospheric N_2, it can be transformed between a variety of redox states and species in a complex cycle involving inorganic and bacterially mediated reactions under both aerobic and anaerobic conditions. The principal species and their redox state include the following:

Nitrate	NO_3^-	N^{+V}	Stable oxide of N, highly soluble as an anion
Nitrogen dioxide	NO_2	N^{+IV}	Produced by lightning and combustion
Nitrite	NO_2^-	N^{+III}	Intermediate in conversions between NO_3^- and NH_4^+
Nitrogen oxide	NO	N^{+II}	Produced by lightning and combustion, $NO_2 + NO = NO_x$
Nitrous oxide	N_2O	N^{+I}	Bacterially produced gas, in atmosphere at <1 ppm
Nitrogen	N_2	N	Elemental nitrogen gas
Hydroxylamine	NH_2OH	N^{-I}	Intermediate species during oxidation of NH_4^+
Ammonia	NH_3	N^{-III}	Unionized ammonia gas
Ammonium	NH_4^+	N^{-III}	Ionized ammonia (dominates at pH below 9.23)
Organic N	$-NH_2$	N^{-III}	Reduced N in organic compounds including protein.

Of these nitrogen species it is nitrogen (N_2), ammonium (NH_4^+), nitrate (NO_3^-), and nitrous oxide (N_2O) that represent the largest reservoirs in groundwaters. The cycle

of nitrogen from fixation of atmospheric nitrogen to organic nitrogen in plants and its transformation back to atmospheric nitrogen is shown in Figure 9.1.

The NO_x gases, NO and NO_2, produced by internal combustion engines and thermal power plants, contribute to smog and respiratory problems, although catalytic converters have been effective in reducing NO_x and improving air quality over the past decades (McKitrick 2014; www.yourenvironment.ca). There are, however, two predominant water quality issues with nitrogen species that are largely restricted to agricultural settings. These are elevated NO_3^- (and NO_2^-) in drinking water and elevated NH_3 in surface waters. There is no maximum acceptable concentration (MAC) for ammonia in drinking water, as it is naturally part of our metabolic system, produced through digestion and eliminated as urea. However, unionized ammonia does pose a problem to aquatic life at concentrations exceeding a few micrograms per liter. The concentration of unionized ammonia is calculated from total ammonia for a given temperature and pH. Most jurisdictions place the limit for unionized at some 20 µg/L. At pH 8 and 25°C, this corresponds to a total ammonia concentration of only 0.35 mg/L.

Nitrate affects human health when it is converted to nitrite in the stomach. Nitrite interferes with the blood's capacity to carry oxygen. This leads to methemoglobinemia or *blue baby* syndrome in infants. The MAC for nitrate in drinking water is universally set at 10 mg/L as N, and for NO_2^- at 1 mg N/L. In surface waters, nitrate generally has no limit, although high concentrations promote excessive algae and weed growth.

Oxidation of nitrous oxide and nitrogen dioxide with O_2 produces nitric acid and contributes to soil nitrate via precipitation or dry fallout, but represents a minor contribution to the inventory of fixed nitrogen species in soils and soil water. The cycling

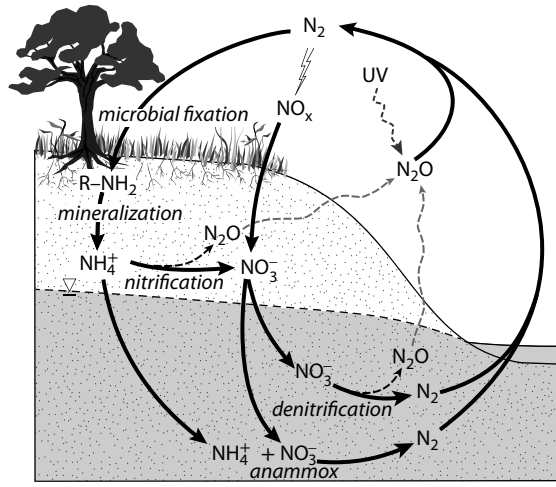

FIGURE 9.1 The nitrogen cycle, showing the principal reservoirs and reactions from the fixation of atmospheric nitrogen by microbial activity to the mineralization of organic carbon and transformation back to atmospheric N_2. N_2O produced during bacterial nitrification and denitrification is photo-dissociated and photo-oxidized in the atmosphere to N_2. Oxidation of N_2 to atmospheric nitrous oxide by lightning also contributes to NO_3^- in soils through wet and dry fallout.

of nitrogen in soils and groundwater involves a number of possible transformations, which occur under a range of redox conditions.

Biological fixation of N_2:

$$N_2 + 8H^+ + 16\,\text{MgATP} + 8e^- \rightarrow 2NH_3 + H_2 + 16\text{MgADP} + 16\text{P}$$

The most common N-fixation reaction is mediated by the molybdenum-dependent nitrogenase enzyme (Seefeldt et al. 2009) common to cyanobacteria and operating for over 3 billion years. It produces ammonia and hydrogen, which are then synthesized into proteins as R–NH_2.

Degradation of organic N: $-NH_2 + H^+ \rightarrow NH_3$

Organically bound nitrogen is a component of all proteins and plant biomass. Aerobic and anaerobic degradation of such carbon compounds releases this reduced nitrogen in the form of ammonia. Where this occurs in unsaturated materials such as soils or manure, the ammonia can volatilize, or dissolve into water.

Decomposition of urea: $CO(NH_2)_2 + H_2O \rightarrow 2NH_3 + CO_2$

Urea is often applied as fertilizer in granulated form, and breaks down by a bacterially mediated reaction (*urease* enzyme) to release ammonia for plants.

Ionization of ammonia: $NH_3 + H^+ \leftrightarrow NH_4^+ \quad K_T = 10^{-9.23}$

Ionization of ammonia to highly soluble ammonium occurs at neutral pH. The two species have equal concentrations at pH 9.23. Analytical reports generally provide a single value of total ammonia that includes both ionized and unionized ammonia.

Volatilization of ammonia: $NH_{3(aq)} \rightarrow NH_{3(g)} \quad K_H = 10^{1.76}$

The relatively high Henry's law constant for ammonia allows an aqueous concentration of 246 mg/L at 25°C for a NH_3 partial pressure of 1 atm. As the partial pressure of NH_3 in the air is negligible, diffusive loss from manure piles or surface applications occurs. Volatilization from groundwater below the water table is greatly minimized by the slow rate of aqueous diffusion.

Sorption of ammonium: $\text{Na–clay} + NH_4^+ \rightarrow NH_4\text{–clay} + Na^+$

Ammonium is sorbed onto clay minerals in soils and aquifers with a selectivity coefficient close to that of K^+. Accordingly, NH_4^+ migration in aquifers is significantly retarded. Erosion of NH_4-bearing soils is one of the major sources of ammonia contamination in surface waters.

Aerobic nitrification of ammonium: $NH_4^+ + 2O_2 \rightarrow NO_3^- + H_2O + 2H^+$
$\Delta G_r^\circ = -266.5\ \text{kJ/mol}$

Both ionized and unionized ammonia can be oxidized to NO_3^- in water by reaction with elemental oxygen (O_2). The significant energy yield makes this favorable for bacteria. It follows a two-step reaction of oxidation to nitrite and then to nitrate by a mixture of species, including *Nitrosomonas*, *Nitrobacter*, and *Nitrosospira*. Dissolved oxygen is required, limiting this reaction to manure piles, soils, and shallow groundwaters. Such losses from farm fields are costly, requiring slow-release fertilizers like urea to allow plants to assimilate it before it is oxidized.

Anaerobic oxidation of ammonium–anammox: $NH_4^+ + NO_2^- \rightarrow N_2 + 2H_2O$
$\Delta G_r^\circ = -362.8$ kJ/mol

This is a recently discovered yet thermodynamically favorable bacterial reaction (Jetten 1999). It is found to operate in anaerobic environments where both ammonium and nitrate species are present, such as in wastewater streams, anoxic marine waters, and contaminated groundwaters. The anammox bacteria use NH_4^+ as an electron donor and NO_2^- generated through partial reduction of NO_3^- as an electron acceptor in a reaction that converts both species to elemental nitrogen, N_2. It is apparently the only known biologically mediated reaction for the conversion of ammonium to N_2 in natural systems. The nitrite for this reaction can be produced by partial denitrification of NO_3^-, giving the overall reaction $3NO_3^- + 5NH_4^+ \rightarrow 4N_2 + 9H_2O + 2H^+$ (Mulder et al. 1995) or through partial oxidation of NH_4^+ under low redox conditions.

Denitrification: $5CH_2O + 4NO_3^- + 4H^+ \rightarrow 2N_2 + 5CO_2 + 7H_2O$
$\Delta G_r^\circ = -252.47$ kJ/mol

Where a low-p*e* electron donor exists, such as carbon or sulfide, nitrate can be used as an electron acceptor with nearly the same energy yield as O_2. *Pseudomonas denitrificans* reduces NO_3^- to N_2 using fixed carbon (biomass) as a source of energy. Chemotrophs such as *Thiobacillus denitrificans* use sulfide (H_2S or pyrite) as a substrate for denitrification. As this reaction requires organic carbon, it generally will not occur in oxygenated waters where aerobic bacteria outcompete denitrifiers for available carbon substrates. In anaerobic waters with low nitrate concentrations (NO_3^--limited), denitrification to N_2 gas may not be complete, resulting in the production of N_2O gas.

The transformations of nitrogen species are strongly redox sensitive, with nitrate stable under oxidizing conditions, and ammonium stable under reducing conditions

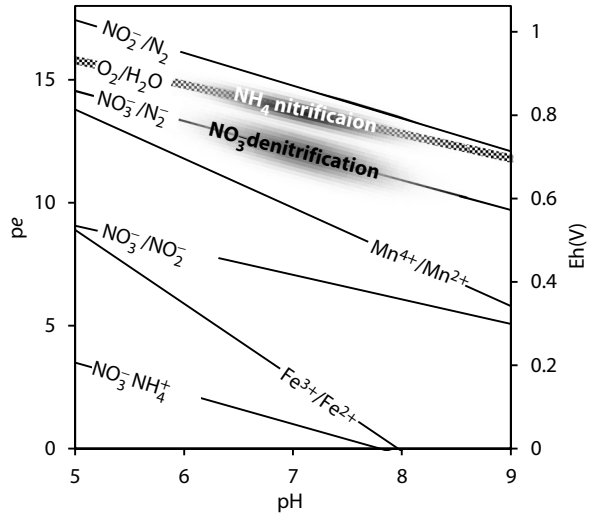

FIGURE 9.2 pH-redox conditions for nitrogen transformation reactions in the environment.

(Figure 9.2). This restricts the settings under which nitrification, denitrification, and anammox can take place.

^{15}N and ^{18}O in the Nitrogen Cycle

The isotope ^{15}N is present in the nitrogen reservoir on the earth at a concentration of about 0.4% of the common nitrogen isotope, ^{14}N, and can be used to trace the origin and the transformations of nitrogen species. As nitrogen transformations are dominantly biologically mediated redox reactions, fractionation tends to be significant, and with Rayleigh distillation as the reactant reservoir is consumed, leads to readily observed enrichment that signifies reaction.

The ^{15}N content of nitrate or ammonium is determined by the ^{15}N of its nitrogen source plus the associated fractionation. Most industrial nitrogen compounds, including ammonium and nitrate, are synthesized from atmospheric N_2, and as the reaction is *quantitative* (i.e., complete conversion of the reactant), these compounds have $\delta^{15}N$-values close to 0‰. The $\delta^{18}O$ of nitrate is established during oxidation or *nitrification* from ammonia. During low-temperature nitrification, the $\delta^{18}O$ of the ambient water plays an important role. In the production of KNO_3 chemical fertilizers, the $\delta^{18}O$ of atmospheric O_2 dominates. The trends in isotope values during the geochemical transformations presented above are as follows:

Ammonium volatilization, NH_4^+ *to* NH_3, $\varepsilon^{15}N_{NH_4-NH_{3(g)}} = 20.5‰$ (Wickens 2003). This reaction involves dissociation of NH_4^+ to $NH_{3(aq)}$ and diffusion of $NH_{3(aq)}$ to $NH_{3(g)}$, both of which favor the light isotope, ^{14}N, with enrichment of ^{15}N in the residual NH_4^+. NH_3 volatilization is minimal under circumneutral pH conditions where the unionized ammonia fraction of the total ammonium pool is less than 1% ($K_{NH_4-NH_3} = 10^{-9.23}$ and so the NH_3 fraction is 50% at pH 9.23, 5% at pH 8.23, but only 0.5% at pH 7.23). Rayleigh enrichment of $\delta^{15}N_{NH_4^+}$ is typically less than 2‰ to 3‰ in the dissolved NH_4^+ pool unless the soils are particularly alkaline (Figure 9.3).

Nitrification of ammonium, NH_4^+ *to* NO_3^-, $\varepsilon^{15}N_{NH_4^+-NO_3} \approx 30‰$ (Kendall and Aravena 2000). The oxidation of ammonium to nitrate favors ^{14}N, resulting in ^{15}N enrichment of the residual ammonium (Figure 9.3). The $\delta^{15}N$ value of the initially produced nitrate should be depleted by about 30‰ below $\delta^{15}N_{NH_4^+}$, but both $\delta^{15}N_{NO_3^-}$ and $\delta^{15}N_{NH_4^+}$ will increase as the NH_4^+ reservoir is converted to NO_3^-, with $\delta^{15}N_{NO_3^-}$ evolving toward the initial $\delta^{15}N_{NH_4^+}$ value (Wassenaar 1995). The nitrification of ammonium can be traced with $\delta^{18}O$, which differentiates the resulting NO_3^- from synthetic KNO_3 fertilizer. Nitrification generally takes one oxygen from the air ($\delta^{18}O_{O_2} = 23‰$) and two oxygen atoms from the ambient soil water (Kendall and Aravena 2000; Anderson and Hooper 1983). For example, water with $\delta^{18}O$ of $-10 \pm 2‰$ would yield a value for $\delta^{18}O_{NO_3^-}$ between $-1‰$ and 2%. This contrasts with synthetic KNO_3, which is produced with only atmospheric O_2 and so has $\delta^{18}O_{KNO_3}$ between about 20‰ and 25‰ (Figure 9.4). As nitrate does not readily exchange ^{18}O with water, this signal can only be modified by denitrification or anammox reaction.

Denitrification, NO_3 to N_2, $\varepsilon^{15}N_{NO_3^- - N_2} \approx 25‰$ to 30‰, and $\varepsilon^{18}O_{NO_3^- - N_2} \approx 10‰$ to 15‰ (Kendall and Aravena 2000). Denitrification is a strongly fractionating process that results in an increase in $\delta^{15}N$ and $\delta^{18}O$ in the residual (unreacted) nitrate in the groundwater (Figure 9.3). This strong enrichment is characteristic of this reaction, and is used to unambiguously distinguish denitrification (reactive loss of NO_3^-) from simple dilution by dispersion in groundwater, which is nonfractionating.

Anammox NH_4^+ + NO_3^- to N_2, $\varepsilon^{15}N_{NH_4^+ - N_2} \approx 4‰$ (Clark et al. 2008). Few studies have looked at isotope fractionation during anammox reaction. As in nitrification and denitrification, the residual ammonium and nitrate in the groundwater will have more positive $\delta^{15}N$ values. Robertson et al. (2012) observed an isotopic enrichment factor from 4.3‰ to 7.7‰ in a field septic system study. The low fractionation in the field studies likely relates to the greater reservoir of ammonium sorbed on the aquifer that buffers the enrichment of $\delta^{15}N_{NH_4^+}$ in dissolved NH_4^+.

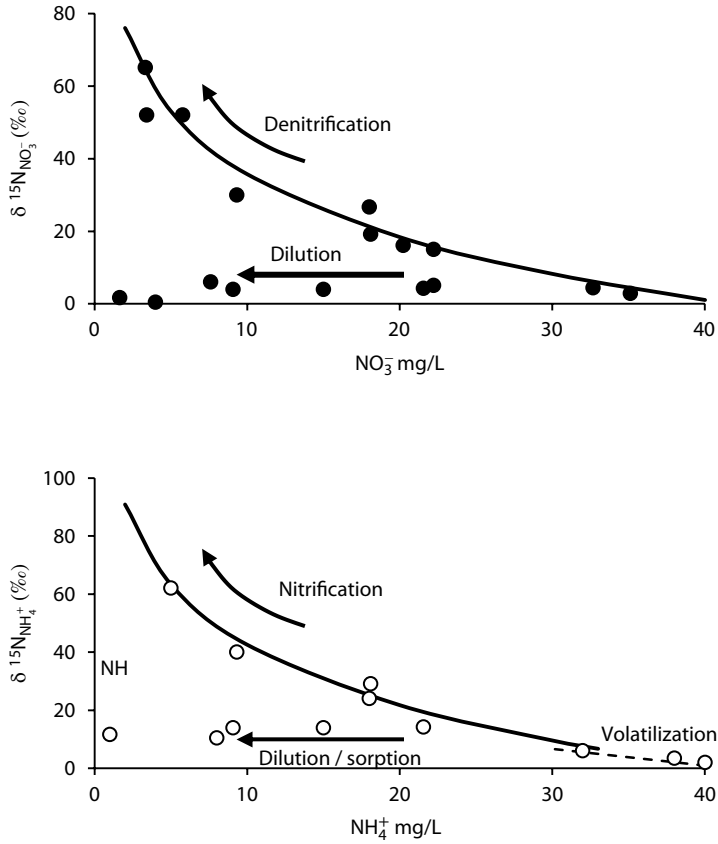

FIGURE 9.3 Trends for ^{15}N during nitrate and ammonium attenuation by reaction and by dilution. Sorption of NH_4^+ can have a minor enrichment, but is seldom observed above background variability.

Nitrogen in Agricultural Settings

Groundwater quality in agricultural regions has become a focal point for geochemical research, given the growing impact of farming activities. Rudolph et al. (1998) show in a province-wide study that over 25% of groundwaters in agricultural areas had NO_3^- levels above drinking water standards, largely attributable to contributions from field applications of manure. Rural regions are also dependent on septic tanks and tile fields for waste disposal. In both settings, concerns include not only NO_3^- and NH_4^+ sources and transformations but also the potential for the transport of pathogenic bacteria into aquifers.

Concentrations of NO_3^- in groundwater in agricultural settings generally decrease with depth, due to dilution of waters recharging through the fields and by denitrification. Rudolph et al. (1998) show NO_3^- concentrations up to three and four times the drinking water limit of 10 mg N/L in the upper 2 m below the water table decreasing to less than 20 mg N/L by 8 m depth. Ammonium concentrations are typically much less, due to nitrification in agricultural soils and to sorption onto the soil and aquifer matrix.

Stable isotopes are useful tracers for the source of nitrogen from agricultural activities (Figure 9.4). Potassium nitrate fertilizer is derived from NH_3 produced by the Haber–Bosch process using atmospheric N_2 ($\delta^{15}N = 0‰$) and oxidized by atmospheric oxygen ($\delta^{18}O = 23‰$). Urea is also produced from atmospheric N_2, but mineralization involves oxygen from the soil water and so the resulting NO_3^- has a more depleted $\delta^{18}O$ value. Subsequent attenuation by dilution during recharge will not affect these signatures, whereas losses through denitrification or anammox will. The associated fractionation and Rayleigh distillation enrich the residual NO_3^- in both isotopes (Figure 9.4).

The Abbotsford aquifer is a transboundary aquifer on the Fraser River in British Columbia and Washington state that has chronic nitrate contamination with levels in water wells routinely exceeding drinking water guidelines. The source was linked

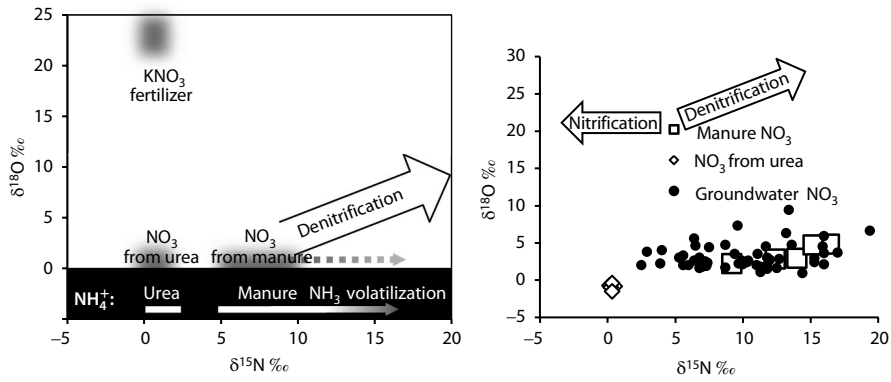

FIGURE 9.4 Left: Sources and approximate isotopic composition of NO_3^- ($\delta^{15}N$ and $\delta^{18}O$ in upper part of chart, in white) and NH_4^+ ($\delta^{15}N$ alone in lower part of chart, in black) in agricultural settings. Right: Case study—Abbotsford aquifer, British Columbia. (After Wassenaar 1995.)

by Wassenaar (1995) to poultry manure stockpiles on the highly permeable gravel sediments. In Figure 9.4 (right-hand chart) the distribution of $\delta^{15}N$ and $\delta^{18}O$ data for NO_3^- shows a clear source in the manure, with a trend of ^{15}N depletion due to nitrification. No contribution from nitrification of urea, which is used on many farms, is observed. Further, the absence of any enrichment trend for $\delta^{15}N$ and $\delta^{18}O$ shows that there is little to no natural attenuation by denitrification, which was anticipated due to the paucity of organic carbon and highly oxidizing redox conditions (Wassenaar 1995). This conclusion led to new best management practices adopted for the handling and storage of manure.

Septic Effluent Infiltration

Infiltration from septic tile beds in rural areas represents a significant input of NO_3^- to groundwaters. Unlike the spatially extensive source area of agricultural fields, these are point sources. Loadings of nitrogen species can be significant, with concentrations well in excess of drinking water standards, such as observed at the seasonal-use campground at Long Point, Ontario (Robertson et al. 2012). Here, multilevel groundwater samplers were used to monitor concentrations (Figure 9.5) and ^{15}N (Figure 9.6) for NH_4^+ and NO_3^- during the infiltration of a plume from the May 24 opening weekend. Concentrations together with ^{15}N data were used to demonstrate three zones of reaction:

Top of plume—nitrification of the NH_4^+ to NO_3^-
Core of plume—anammox oxidation of NH_4^+ using NO_3^- to produce N_2
Below plume—denitrification of NO_3^- to N_2

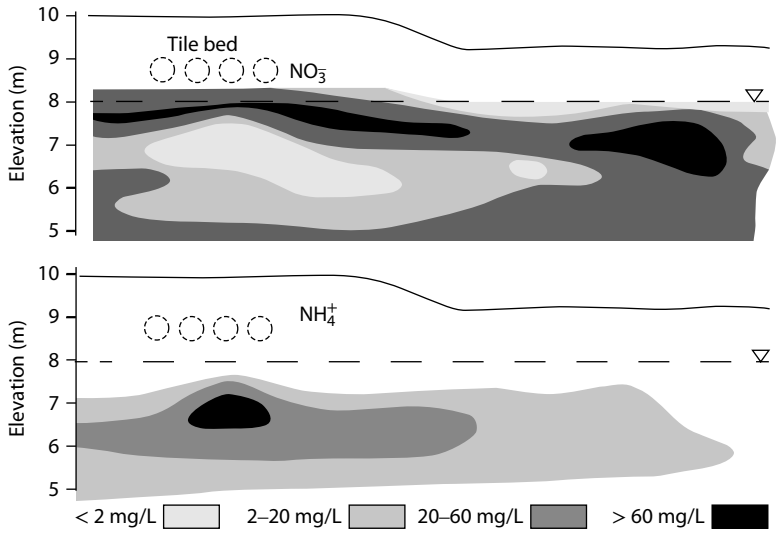

FIGURE 9.5 NO_3^- and NH_4^+ plumes beneath a septic effluent tile bed (Modified from Robertson et al. 2012). Length of section is 30 m.

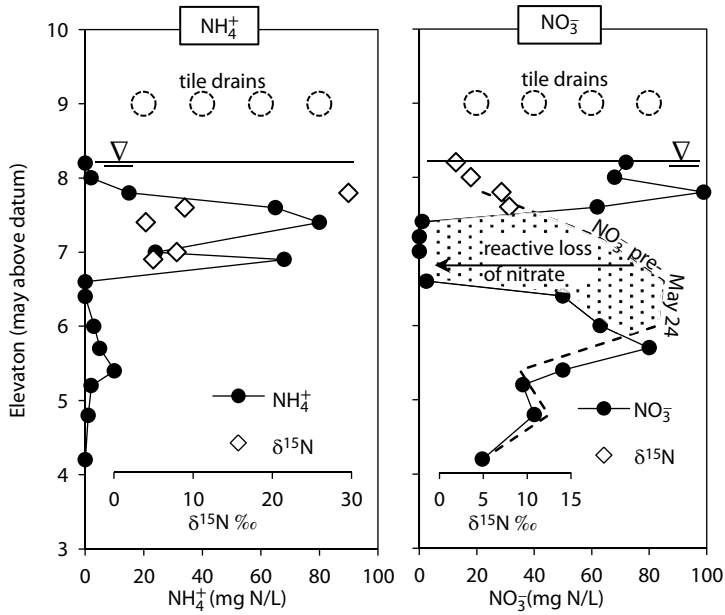

FIGURE 9.6 Concentrations and $\delta^{15}N$ for NO_3^- and NH_4^+ vertically through the plume at a location beneath the tile bed, showing downward movement of the May 24 NH_4^+ plume (After Robertson et al. 2012). The concentration shows the NH_4^+ plume at the 7–8 m elevation and with nitrate occurring at the top of this plume but dropping off with depth. The $\delta^{15}N_{NO_3^-}$ is depleted at the top of the plume, while $\delta^{15}N_{NH_4^+}$ is enriched, signifying nitrification. Below this zone where NH_4^+ and NO_3^- coexist, anammox reaction is enriching both $\delta^{15}N_{NO_3^-}$ and $\delta^{15}N_{NH_4^+}$ above the range of 3‰–6‰ from the tile bed. Below the plume, only NO_3^- remains, which is attenuated by denitrification. Monitoring of this plume over time shows nitrogen loss of over 80% by these reactions.

DNA evidence was then used to identify the strains of anammox bacteria involved in the attenuation of these nitrogen species.

Removal of nitrate from septic effluent can also be achieved with in situ reactive barriers, where favorable conditions for denitrification are established in porous walls or beds through which the effluent passively migrates. Robertson et al. (2000) describe installations at three sites, where waste cellulose from wood chips, sawdust, and leaf litter comprised the carbon source for denitrification in groundwaters flowing through the porous material. Losses of NO_3^- were greatest for the highest initial concentrations, with denitrification of up to 90% for nitrate starting at 60 ppm N and over 50% for initial NO_3^- levels of less than 5 ppm N.

Boron as a Tracer of Nitrogen from Wastewater

In addition to its potential impact on water quality, boron can also serve as a tracer for sources of wastewater contamination. Natural boron concentrations in groundwater are typically only a few ppb, but are significantly enriched in liquid manure

and septic effluents. Natural B in groundwater can be derived from mixing with seawater (B = 4.5 ppm) or from the weathering of sandstones and igneous rocks. Boron is also found naturally in certain evaporites as borax ($Na_2B_4O_5[OH]_4{\cdot}8H_2O$), which is mined for use in detergents due to its strong complexing ability as well as other industrial uses. In water, B^{III} dominates as neutral trigonal borate $B(OH)_3^\circ$ but hydroxylates to tetrahedral $B(OH)_4^-$ above pH 8 (Figure 3.1) with a dissociation constant of $10^{-9.24}$. Transformations between these two species serve to fractionate its two stable isotopes, ^{10}B and ^{11}B, and provide a tool for tracing B and its associated compounds.

Figure 9.7 shows the ranges for the principle natural and contaminant sources of B. Boron from cleaning agents in wastewater systems have $\delta^{11}B$ values close to the boron standard NBS951 with values between 10‰ and −10‰, whereas fertilizers from animal manure are typically enriched with values from 10‰ to as high as 40‰, which is the value for modern marine borate. Widory et al. (2004, 2012) use $\delta^{11}B$ in conjunction with isotopes of nitrate to distinguish nitrate contamination by manure applications from sewage inputs (Figure 9.7). Sorption along groundwater flow paths can enrich the ^{11}B when the pH is above pH 8, when the anion $B(OH)_4^-$ becomes important. In this case, ^{10}B is preferentially sorbed, which imparts an enrichment of ^{11}B in solution. However, Kloppmann et al. (2009) show that B transport is essentially nonfractionating at neutral pH, where $B(OH)_3^\circ$ dominates and is therefore a reliable tracer of source.

Industrial Sources of Ammonium

Sources and degradation pathways of industrial contamination by nitrogen species in the Elmira aquifer in southern Ontario were traced with $\delta^{15}N$ (Clark et al. 2008). At this site, remediation of the aquifer for chlorobenzene by pump and treat was complicated by ammonium contamination from chemical wastewater infiltration ponds and infiltration of both NH_4^+ and NO_3^- from adjacent fertilizer-blending activities (Figure 9.8).

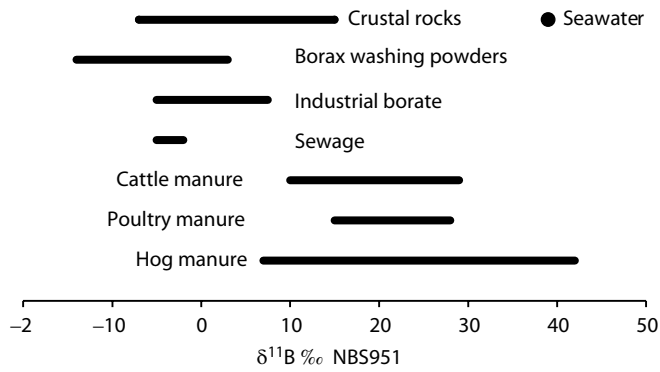

FIGURE 9.7 Ranges for $\delta^{11}B$ in sources of B. (Data sources: Widory et al. 2004; 2012; Kloppmann et al. 2009.)

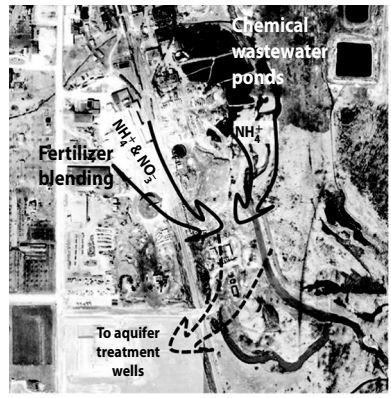

FIGURE 9.8 Industrial site showing sources of ammonium and impacted aquifer at Elmira, Ontario. Solid arrows show flow through surficial aquifer. Dashed arrow shows recharge to deep aquifer and pathway for nitrogen species.

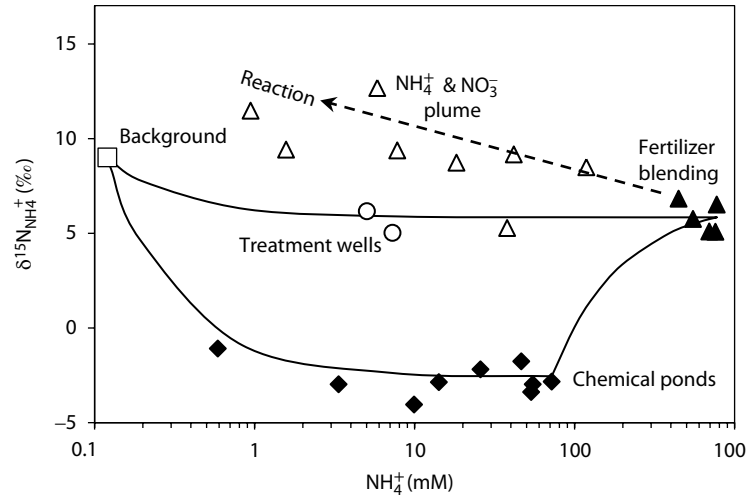

FIGURE 9.9 Three component mixing diagram for NH_4^+ and $\delta^{15}N_{NH_4^+}$ in groundwaters in the source areas and in the deep aquifer. (Modified from Clark et al. 2008.)

Apportioning the sources of ammonium based on $\delta^{15}N_{NH_4^+}$ was complicated by reaction in the subsurface, which modified the source $\delta^{15}N$ values. This is shown in Figure 9.9, where NH_4^+ samples from the chemical wastewater ponds and from the fertilizer blending operations are distinctly different. However, NH_4^+ sampled along the plume from the fertilizer-blending site became progressively enriched in ^{15}N, plotting outside the mixing envelope, and indicating reactive loss of ammonium. Sampling in the subsurface showed that NH_4^+ and NO_3^- were decreasing together along the groundwater plume from the fertilizer-blending site, while both $\delta^{15}N_{NH_4^+}$ and $\delta^{15}N_{NO_3^-}$ as well as N_2 partial pressure increase together Figure 9.10. Anammox was concluded (Figure 9.10), a reaction that was previously unknown in groundwater.

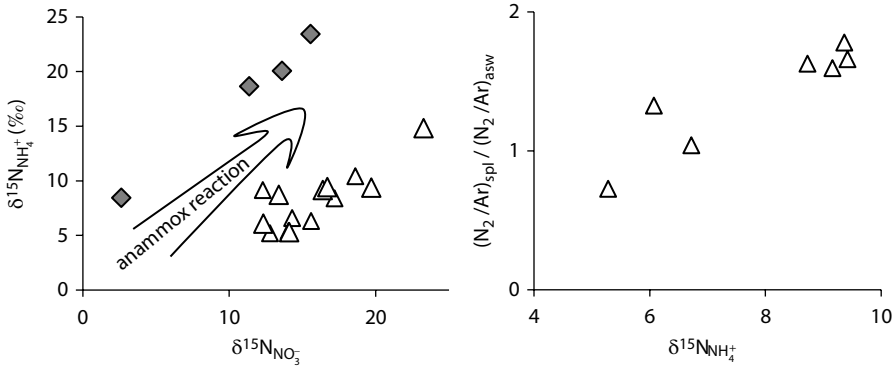

FIGURE 9.10 Left: Enrichment in both $\delta^{15}N_{NH_4^+}$ and $\delta^{15}N_{NO_3^-}$ during anammox reaction of NH_4^+ and NO_3^-. Right: N_2 overpressuring due to anammox activity, measured as N_2/Ar normalized to the N_2/Ar ratio in air-saturated water.

Molecular techniques to amplify and clone DNA in samples from this site identified several anammox strains, including *Candidatus Brocadia* and *Candidatus Scalindua* (Moore et al. 2011). Apportionment calculations concluded that the treatment wells were impacted by NH_4^+ from both sources and that the $\delta^{15}N_{NH_4^+}$ measured in the treatment wells had been enriched from an intermediate value by anammox activity.

Atmospheric Sources of NO_3^- and ClO_4^-

The brine basins or *salar* of the Atacama Desert in northern Chile host rich nitrate deposits that were exploited for decades in the nineteenth century for agriculture and for explosives. Similar accumulations are found in Death Valley of the Mojave Desert in California. Although their accumulation as salts in these hyperarid closed basins was not surprising, the origin of the nitrogen remained a mystery. More recently, these deposits were found to contain significant concentrations of another strong electron acceptor—perchlorate, ClO_4^-. In perchlorate the chlorine atom is oxidized to Cl^{7+}, making it a highly reactive oxidant that is manufactured for solid rocket boosters and for fireworks. It is also toxic to humans where it disrupts the uptake of iodine by the thyroid. The extensive use of Atacama nitrate in the past and industrial perchlorate sources today contribute ClO_4^- to groundwaters, which can have concentrations well above regulatory limits of 1–18 ppb (Sturchio et al. 2009). Distinguishing the origin of these compounds is important to trace the source of contamination. Desert nitrates were believed to originate through leaching of soils and accumulation in arid basins by evaporation until analysis of their stable isotope composition demonstrated an atmospheric source (Böhlke et al. 1997).

The oxidation of atmospheric N_2 by lightning produces NO and NO_2, which oxidize to nitrate with atmospheric ozone according to the following reactions:

$$N_2 + O_2 \rightarrow 2NO$$

$$NO + O_3 \rightarrow NO_2 + O_2$$

$$2NO_2 + O_3 + H_2O \rightarrow 2HNO_3 + O_2$$

Nitrate then accumulates on the surface by dry fallout of nitric acid aerosols or is washed out by precipitation. Price et al. (1997) determined that lightning over the continents contributes some 12 million tons of nitrate to the surface annually, which represents almost 10% of the natural nitrogen fixation that takes place through nitrogenase enzyme activity in the roots of certain plants, such as clover and legumes. In contrast, the Haber–Bosch process produces some 160 million tons of nitrogen fertilizers annually (FAO 2008). Nonetheless, fallout of atmospheric nitrate can accumulate as surface salts in arid regions with closed basins.

Böhlke et al. (1997) use both $\delta^{15}N$ and $\delta^{18}O$ of nitrate to show the involvement of atmospheric N_2 and O_2, showing $\delta^{15}N$ values for the Atacama NO_3^- clustering around 0‰ and $\delta^{18}O$ even greater than the atmospheric value of 23‰. This is diagnostic, considering that bacterially mediated nitrate involves oxygen from local groundwaters and so has $\delta^{18}O$ near −10‰. However, the involvement of O_3 allows another isotope to be used—$\delta^{17}O$. Oxygen-17, present as only 0.038% of all oxygen, fractionates the same as ^{18}O, but with about half of the mass effect. As it brings no additional information, it has not been of interest in hydrological studies. However, recently it has been shown that production of atmospheric ozone involves reaction steps where the input of atmospheric oxygen occurs with little to no mass fractionation, resulting in an enrichment of ^{17}O in O_3. This mass independent fractionation is observed in atmospheric nitrate, which involves O_3 during transformation of NO_x to HNO_3, during the reactions above (Figure 9.11).

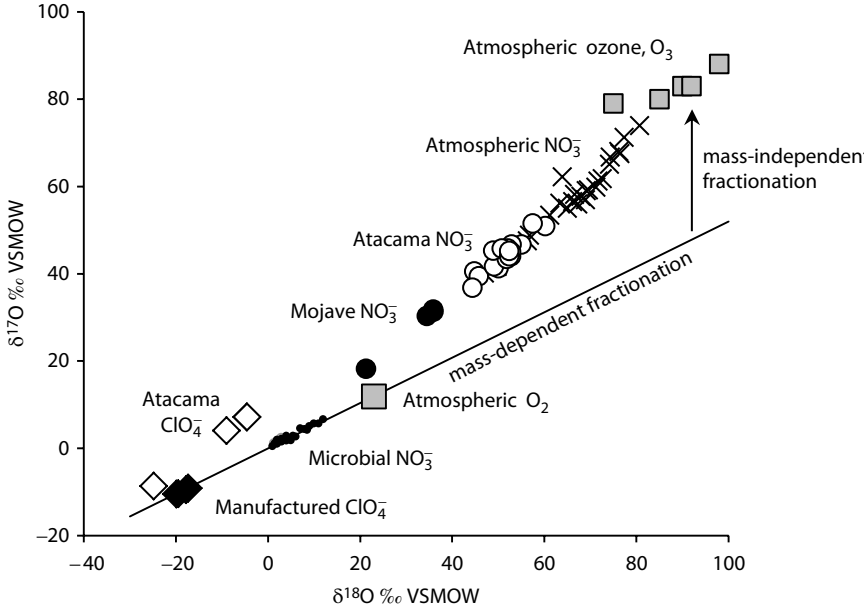

FIGURE 9.11 The oxygen isotope contents of atmospheric nitrate and perchlorate, showing a $\delta^{17}O$ anomaly that indicates formation by atmospheric ozone. Atmospheric NO_3^- from Proemse et al. (2013); Ozone, Atacama, and Mojave NO_3^- from Michalski et al. 2004); Microbial NO_3^- from Kaiser et al. (2007); Atacama and Manufactured ClO_4^- from Bao and Gu (2004).

The production and fallout of atmospheric perchlorate is believed to occur through the photo-oxidation of atmospheric chloride and chlorate ions during the polar sunrise in high latitudes, but in mid and low latitudes, the pathway is unclear. Bao and Gu (2004) use $\delta^{17}O$ together with $\delta^{18}O$ to show that the perchlorate associated with the atmospheric nitrate deposits of the Atacama Desert is derived in part from atmospheric ozone, and not from industrial sources. The origin of perchlorate can be demonstrated by isotopes of Cl as well. Sturchio et al. (2009) use low concentrations of ^{36}Cl (recall from dating in Chapter 8) together with $\delta^{37}Cl$ close to 0‰ as evidence for ClO_4^- contamination in many groundwaters in the United States from manufactured perchlorate.

ORGANIC CARBON COMPOUNDS

Organic debris accumulating in marine sediments over Phanerozoic time, through burial and heating, has been transformed to hydrocarbon, with high energy yield (e.g., 817.78 kJ/mol for combustion of methane). Two-thirds of what we exploit of this resource goes to transportation as gasoline and diesel for internal combustion engines, and paraffins for jet engines, with the balance being used for a range of industrial compounds, solvents, insulators, and polymers. Their inevitable spills and leaks in the environment have spawned research on their mobility and degradation (Figure 9.12). This section presents the use of geochemical and isotopic principles to trace contamination and biodegradation.

Crude oil contains a range of aliphatic (chain-structured hydrocarbon) and aromatic (benzene-ring structures) compounds, most with functional groups attached, including compounds such as methyl $-CH_3$, hydroxyl –OH, carbonyl –CO, carboxyl –COOH, amine $-NH_2$, and sulfanyl –SH. Refined petroleum products generally fall into two groups (Figure 9.13). BTEX is composed of about 11% benzene and the balance as *alkyl*benzene compounds—benzene with an alkane group such as a methyl group (CH_3)—making toluene and xylene, or an ethyl group, $-CH_2-CH_3$, making ethylbenzene. Carbon in the benzene ring is triple-bonded with its two neighbors, with redox state C^{-I}. In the methyl group, the carbon is C^{-III}, providing more energy during combustion. Alkanes (or paraffins) are single-bonded carbon

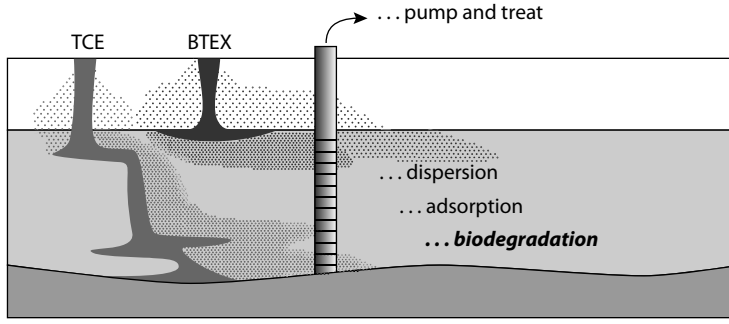

FIGURE 9.12 Pathway for hydrocarbons (e.g., gasoline composed of benzene, toluene, ethylbenzene and xylene, BTEX, with density less than that of water) and chlorinated organics (e.g., trichloroethylene, TCE, with density greater than water) into groundwaters and possible attenuation/mitigation processes.

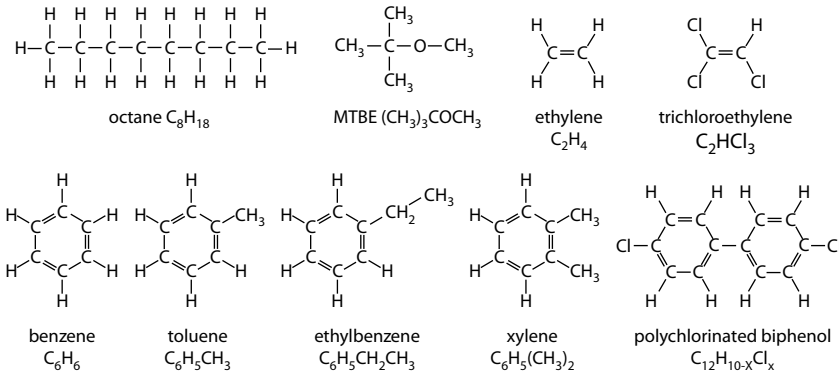

FIGURE 9.13 Aliphatic (upper row) and aromatic (lower row) hydrocarbon and chlorinated hydrocarbon compounds commonly found as contaminants in groundwater.

chains (double-bonded aliphatic HCs are alkenes, and triple-bonded are alkynes). They have the highest energy density because the linked carbons, $–CH_2–$, are in the $C^{–II}$ state, with the methyl groups at the ends in the $C^{–III}$ state. The simplest, of course, is methane, with $C^{–IV}$ covalently bonded with its four H^+ atoms.

BTEX now contains up to some 10% ethanol, C_2H_5OH, as an additive to reduce CO_2 emissions. The addition of ethanol to fuel reduces its energy density (lower mileage), and the roughly equal cost in fossil fuel for production and distribution makes it CO_2 neutral. As an oxygenate it offers an alternative to MTBE to reduce CO emission, although it is found to increase other emissions and poses a greater hazard to water quality than MTBE (Williams et al. 2003).

Diesel fuel (natural petrodiesel) is largely alkane molecules with about 25% aromatics, including alklylbenzenes, which have a high ignition temperature achieved by high compression rather than spark ignition. Biodiesel is similar, but uses vegetable oil with long-chain fatty acids (soluble aliphatic chains of single carbons with a carboxyl group, O–C–OH) like alkanes but transformed with methanol, C_2H_5OH, to a fatty acid methyl ester (FAME).

The solubility of these compounds in groundwater varies greatly from a few milligrams per liter for the aliphatic components to several grams per liter for the hydrophilic oxygenates (Table 9.1). The concentration of these fuel components and additives in groundwater depends not only on their pure phase solubility, S_{pure}, but also on their mass fraction of the product, f_m, that is leaking from a storage tank or a spill. This is the effective solubility, S_{eff}, and is established by Raoult's law:

$$S_{eff} = S_{pure} \times f_m$$

For example, most gasoline (BTEX) has about 11% benzene and 10% MTBE. If the tank beneath the filling station is leaking into the groundwater, then the concentration of these two components would then be as follows:

$$S_{eff\,(benzene)} = S_{benzene} \times f_{benzene}$$
$$= 1{,}780 \times 0.11$$
$$= 196 \text{ mg/L}$$

$$S_{eff\,(MTBE)} = S_{MTBE} \times f_{MTBE}$$
$$= 48{,}000 \times 0.10$$
$$= 4{,}800 \text{ mg/L}$$

Measurement of concentrations near these values in groundwater would be evidence that there is a nearby free-product source that is supporting such high concentrations.

Biodegradation of Hydrocarbons

Hydrocarbon solubility is unique to each compound. Because of their high volatility, they have a Henry's law constant that defines the solubility of the vapor phase (Table 9.1). Accordingly, hydrocarbons can be dissolved in groundwater from a vapor phase present within the unsaturated zone or from a liquid phase pooled on the water table or residually coating grains in the unsaturated zone. Remediation options range from excavation or pumping to in situ degradation that may involve injection of oxidants or passive biodegradation. Biodegradation of hydrocarbons can follow a number of pathways that are typically mediated by aerobic, denitrifying, and sulfate-reducing bacteria, or methanogenic archaea. These involve multistepped enzymatic reactions, resulting ultimately in the production of CO_2 accompanied under anaerobic conditions by N_2, H_2S, and CH_4.

Benzene and alkylbenzene components of BTEX are sparingly soluble in groundwater (Table 9.1). Under oxidizing conditions, BTEX follows a multistep oxidation, as described by Yu et al. (2001), that increases both their solubility and their

TABLE 9.1
Solubilities (EPA) and Henry's Law Constants[a] (Sander, 1999) for Major Fuel Components and Solvents

Compound	K_H (M/atm)	Solubility in Water (mg/L) at 25°C
Benzene	0.18	1,780
Toluene	0.15	535
Xylene	0.12–0.19	130–196
Diesel[b]	0.0002–0.0008	40
MTBE	1.6	48,000
Catechol	4,600	430,000
Ethanol[c]	200	miscible
PCE	0.0054	200
TCE	0.097	1,100
cis-DCE	0.24	3,500
Trichloromethane	0.25	4,000

[a] Note that Henry's law constants for volatile compounds are often expressed as the volatility constant, $K_{H\text{-inv}}$, which is the inverse of the more familiar gas solubility constant, K_H (mol/L/atm, such that $K_{H\text{-inv}} = 1/K_H \times$ Units of $K_{H\text{-inv}}$ are atm/mol/L or atm × L/mol, but are often seen as atm × m3/mol, where K_H (mol/L/atm) = $1/(K_{H\text{-inv}} \cdot 1000)$ (atm × m3/mol).

[b] Grade 1-D for cars, and trucks, and boats, containing kerosenes (alkanes—paraffins and cycloparaffins).

[c] Ethanol is the dominant water-soluble component of biofuels, including biodiesel. Other components of biodiesel include long-chain fatty acid methyl esters that are of very low solubility in water.

bioavailability for further degradation. Benzene, for example, is partially hydrolyzed through an initial step where carbon atoms are oxidized from a C^{-I} state to a C^{+I} state, producing highly soluble dihydroxylbenzene or catechol compounds (Table 9.1). This increases the oxygen content of the product becomes available for further oxidation in groundwaters.

$$C_6H_6 + O_2 \rightarrow C_6H_6O_2 \text{ (hydroxylbenzene or catechol)}$$

Further oxidation ultimately produces CO_2:

$$C_6H_6O_2 + 6\tfrac{1}{3}O_2 \rightarrow 6CO_2 + 3H_2O$$

With an overall reaction and energy yield of

$$C_6H_6 + 7\tfrac{1}{2}O_2 \rightarrow 6CO_2 + 3H_2O \qquad \Delta G^\circ = -3202.32 \text{ kJ/mol}$$

However, groundwaters with high organic carbon loadings can quickly become anoxic, making redox reactions operating lower on the electromotive potential scale more competitive. Unlike the formation of catechols during aerobic oxidation of BTEX, there is no evidence for significant generation of extracellular intermediates under anaerobic conditions. Burland and Edwards (1999) show the degradation of ^{14}C-labeled benzene by nitrate reduction in microcosm studies using soils from a contaminated aquifer. The stoichiometry of the reaction (six moles NO_3^- per mole C_6H_6) is seen in the experimental measurements showing the loss of benzene tracking the loss of nitrate (Figure 9.14).

$$C_6H_6 + 6NO_3^- \rightarrow 6HCO_3^- + 3N_2 \qquad \Delta G^\circ = -2992.86 \text{ kJ/mol}$$

As observed above for nitrate and ammonium reactions, the loss of organic carbon by degradation can be distinguished from simple dilution in the field by the use

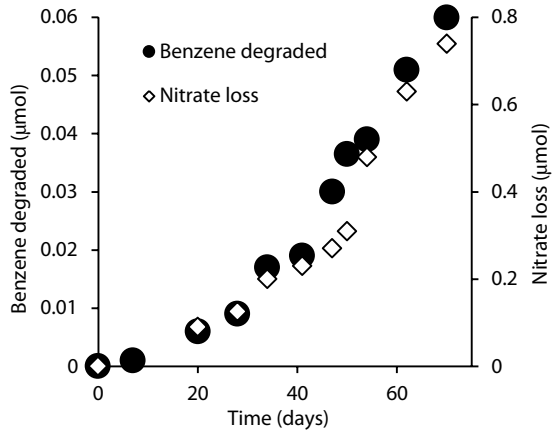

FIGURE 9.14 Biodegradation of benzene by denitrification showing loss of both benzene and nitrate over time in microcosm studies. ^{14}C-labeled benzene was used, and the CO_2 reaction product was sampled. Up to 95% of the ^{14}C activity was recovered as CO_2, with the balance attributed to cell growth. (Modified from Burland and Edwards 1999.)

of isotopes. Recall in Chapter 4 that isotopes undergo a Rayleigh-type enrichment or depletion as a reservoir of the reactant is depleted. This Rayleigh enrichment was observed for the biodegradation of ethylbenzene in microcosm studies using nitrate as the electron acceptor (Meckenstock et al. 2004). The stoichiometry of the oxidation of ethylbenzene is not as simple as that of benzene (above), but also yields bicarbonate and nitrogen gas:

$$C_6H_5CH_2CH_3 + 8\tfrac{2}{5}NO_3^- + \tfrac{2}{5}H^+ \rightarrow 8HCO_3^- + 4\tfrac{1}{5}N_2 + 1\tfrac{1}{5}H_2O$$

Nonetheless, the reaction produced ^{13}C enrichments of up to 8‰ in the residual ethylbezene after 50 days (Figure 9.15).

Further down the electromotive potential scale, benzene degradation can take place by ferric iron reduction, which has an energy yield still in the same range as for aerobic and denitrifying degradation, and by sulfate reduction, which has a significantly lower energy yield per mole of benzene:

$$C_6H_6 + 30Fe(OH)_{3\,fer} + 54H^+ \rightarrow 6HCO_3^- + 30Fe^{2+} + 72H_2O$$
$$\Delta G^\circ = -2443.68 \text{ kJ/mol}$$

$$C_6H_6 + 3\tfrac{3}{4}SO_4^{2-} + 3H_2O + 1\tfrac{1}{2}H^+ \rightarrow 6HCO_3^- + 3\tfrac{3}{4}H_2S$$
$$\Delta G^\circ = -248.24 \text{ kJ/mol}$$

Ferrihydrite as an electron donor is required in high quantities, as it involves only a single electron transfer, making this a poor remediation option. Sulfate reduction, however, involves a six-electron transfer and, as sulfate solutions, can be injected into aquifers; this represents a viable in situ treatment option. Meckenstock et al. (2004) monitored H_2S and toluene together with analysis of $\delta^{13}C$ in residual toluene (CSIA) to demonstrate biodegradation by sulfate reduction (Figure 9.16). By the end of the 11-day experiment, 300 µmol of toluene had been consumed and 1100 µmol of sulfide produced. This gives a stoichiometric ratio of just under 4 mol of sulfate per mole of toluene, which approximates the reaction above for benzene.

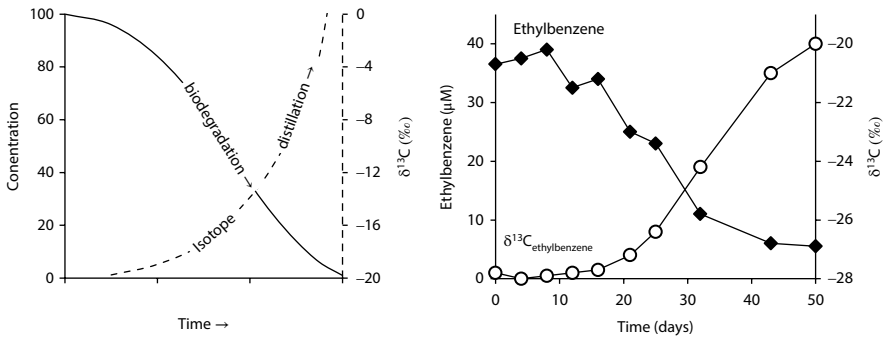

FIGURE 9.15 Isotope enrichment by Rayleigh distillation during biodegradation, theoretical (left) and observed (right) for ^{13}C in ethylbenzene during biodegradation by denitrification. (After Meckenstock et al. 2004.)

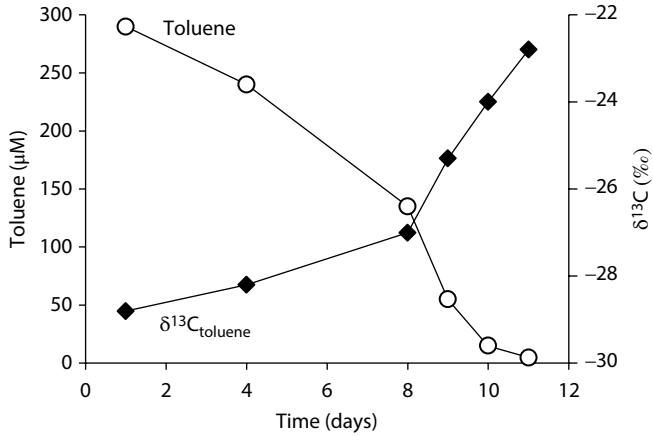

FIGURE 9.16 Biodegradation of toluene by sulfate reduction in a microcosm, with $\delta^{13}C$ enrichment in the residual toluene. (After Meckenstock et al. 2004.)

Neither of these reactions is very favorable from an environmental perspective, given the high production of ferrous iron or hydrogen sulfide. Further, these electron acceptors need to be plentiful in the aquifer for any significant amount of BTEX degradation to take place. In their absence, there is a rapid jump to methanogenic conditions for the degradation of these compounds. Although the energy yield is low, autoclastic methanogenesis is one of the most common pathways for the degradation of aromatics and aliphatic hydrocarbons:

$$C_6H_6 + 6\tfrac{3}{4}H_2O \rightarrow 3\tfrac{3}{4}CH_4 + 2\tfrac{1}{4}HCO_3^- + 2\tfrac{1}{4}H^+ \qquad \Delta G^\circ = -34.23 \text{ kJ/mol}$$

If a substrate of hydrogen gas is available from other fermentative reactions in the aquifer, then it can act as an electron donor for benzene reduction to methane:

$$C_6H_6 + 9H_2 \rightarrow 6CH_4 \quad \Delta G^\circ = -428.7 \text{ kJ/mol}$$

In a series of microcosm experiments under anaerobic conditions, Mancini et al. (2003) demonstrate that very strong Rayleigh enrichments are associated with this low-electromotive potential pathway for benzene biodegradation. Figure 9.17 is adapted from their full data sets to show these enrichments. From these isotope values, the enrichment factor for the reaction can be calculated. Recall from Chapter 4 the formulation of a Rayleigh equation in permil units.

$$\delta_{\text{reactant}} = \delta_{\text{initial reactant}} + \varepsilon_{\text{product-reactant}} \times \ln f_{\text{residual reactant}}$$

Rearranging this equation and using the values given in Table 9.2 for the isotope enrichment trends in Figure 9.17 allows calculation of the enrichment factor for the biodegradation of benzene to CH_4 and dissolved inorganic carbon (DIC):

$$\varepsilon^{13}C_{CH_4/\text{DIC-benzene}} = \frac{(\delta^{13}C_{\text{benzene–initial}} - \delta^{13}C_{\text{benzene-residual}})}{\ln f_{\text{residual benzene}}}$$

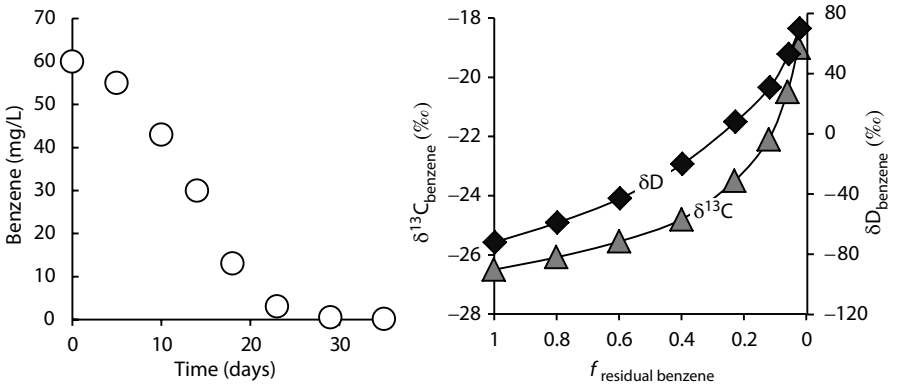

FIGURE 9.17 Compound-specific isotope analysis of benzene during methanogenic biodegradation, showing a decline in benzene to less than detection over a 20-day period that is associated with enrichments in both ^{13}C and D of the residual benzene. (After Mancini et al. 2003.)

TABLE 9.2
Calculation of Isotope Enrichment Factors, $\varepsilon^{13}C$ and εD, for Methanogenic Biodegradation of Benzene

$f_{residual\ benzene}$	$\delta^{13}C_{benzene}$	$\varepsilon^{13}C_{benzene-CH_4/DIC}$	$\delta D_{benzene}$	$\varepsilon D_{benzene-CH_4/DIC}$
1	−26.5		−72	
0.6	−25.6	1.9	−43	57
0.4	−24.8	1.9	−20	57
0.12	−22.1	1.9	31	49
0.025	−19.0	1.9	70	38

Source: Mancini et al. 2003.

Degradation of Fuel Oxygenates: MTBE and Ethanol

The addition of oxygenates to fuel is designed to reduce emissions of CO and ground-level ozone. However, their high solubility (Table 9.2) gives these minor components of BTEX a disproportionately high concentration in groundwaters impacted by leaking storage tanks and spills. Ethanol can be readily attenuated by both aerobic and anaerobic biodegradation, while MTBE is often found to be more recalcitrant (Church et al. 1997). Both are mineralized under oxidizing conditions:

$$C_2H_5OH_{ethanol} + 3O_2 \rightarrow 2CO_2 + 3H_2O \qquad \Delta G^\circ = -1325.32\ kJ/mol$$

$$(CH_3)_3COCH_{3\,MTBE} + 7\tfrac{1}{2}O_2 \rightarrow 5CO_2 + 6H_2O \qquad \Delta G^\circ = -3158.5\ kJ/mol$$

Under anaerobic conditions, biodegradation follows the electrochemical chain of electron acceptors from nitrate to sulfate (Finneran and Lovley 2001):

$$(CH_3)_3COCH_{3\,MTBE} + 6NO_3^- + H^+ \rightarrow 5HCO_3^- + N_2 + 4H_2O$$
$$(CH_3)_3COCH_{3\,MTBE} + 30Fe(OH)_3 + 55H^+ \rightarrow 5HCO_3^- + 30Fe^{2+} + 76H_2O$$
$$(CH_3)_3COCH_{3\,MTBE} + 3\tfrac{3}{4}SO_4^{2-} + 2\tfrac{1}{2}H^+ \rightarrow 5HCO_3^- + 3\tfrac{3}{4}H_2S + H_2O$$

Under methanogenic conditions, evidence suggests that the degradation includes the formation of the intermediary compound *tert*-butyl alcohol (TBA).

$$(CH_3)_3COCH_{3\,MTBE} + H_2 \rightarrow (CH_3)_3COH + CH_4$$
$$(CH_3)_3COH + H_2O \rightarrow 3CH_4 + CO_2$$

Giving an overall reaction as:

$$(CH_3)_3COCH_{3\,MTBE} + 2\tfrac{3}{4}H_2O \rightarrow 3\tfrac{3}{4}CH_4 + 1\tfrac{1}{4}HCO_3^- + 1\tfrac{1}{4}H^+$$

Microbial degradation of MTBE in groundwaters has been recognized as a favorable treatment technology, but recognizing biodegradation from that of dispersive attenuation has been difficult at the field scale. Thornton et al. (2011) used both ^{14}C-labeled MTBE and natural abundance ^{13}C to trace its degradation under both aerobic and anaerobic conditions. Their radiolabeled MTBE was recovered as $^{14}CO_2$ along the aquifer, demonstrating active biodegradation. However, although a 7‰ enrichment was observed in highly aerobic microcosm experiments, their field study found no significant ^{13}C enrichment in MTBE along the groundwater flow path.

Under highly reducing conditions for methanogenic degradation of MTBE where the intermediary TBA is produced, ^{13}C does become a good tool to track the amount of degradation (Figure 9.18).

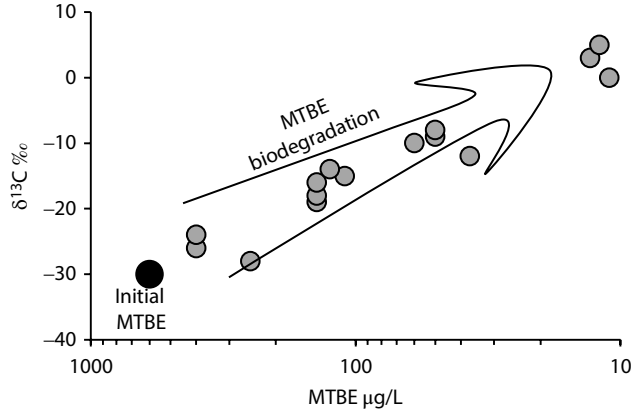

FIGURE 9.18 The Rayleigh enrichment of ^{13}C during the biodegradation of MTBE to TBA and methane in well-stratified sand to clay sediments. Initial value for $\delta^{13}C_{MTBE}$ in gasoline is close to −30‰. (Modified from Kolhatkar et al. 2002.)

Biodegradation of Organohalogens

Of particular concern in hydrogeology are the organohalogens—chlorinated or brominated organic compounds. These dense hydrophobic organic liquids can sink through aquifers, leaving a residual phase that can sustain a chronic contamination of groundwater over many decades. A range of compounds exists, including polychlorinated biphenols used as electrical insulators and chlorinated alkenes such as perchloroethylene (PCE), used as solvents for dry cleaning and degreasers in industry (Figure 9.13). Organobromine compounds such as polybrominated diphenyl ether (PBDE) used as a fire retardant can also be of concern.

Highly chlorinated compounds are found to degrade slowly in aerobic groundwaters, whereas under anaerobic conditions, reductive dechlorination can reduce such compounds to more readily oxidized forms (Fennell et al. 1997; Hunkeler et al. 1999). In such reactions, hydrogen atoms are replaced by chlorine atoms carrying a +I valence state for coordination with carbon. Perchloroethylene is a common example. Perc has been widely used as a solvent in dry cleaning, leading to widespread contamination arising from poor disposal practices. Under anaerobic conditions, it can be sequentially dechlorinated through a series of reductive reaction steps that produce vinyl chloride (VC) and then ethene.

$$C_2Cl_{4\,PCE} + 2e^- \rightarrow C_2HCl_{3\,TCE} + Cl^-$$

$$+ 2e^- \rightarrow cis - C_2H_2Cl_{2\,DCE} + Cl^-$$

$$+ 2e^- \rightarrow C_2H_3Cl_{VC} + Cl^-$$

$$+ 2e^- \rightarrow C_2H_{4\,ethene} + Cl^-$$

Reductive dechlorination requires some organic substrate as the electron donor, which is often provided by labile organic compounds that may accompany such spills, or occur naturally in the aquifer. Tracing these reactions in aquifers by measurement of these reaction products can demonstrate degradation of these compounds and the viability of in situ biodegradation as remediation technique. However, when the source of such chlorinated organics is poorly characterized, evidence for active degradation may be uncertain. As seen above for BTEX degradation, compound-specific isotope analysis provides unambiguous evidence for reactive degradation.

Hunkeler et al. (1999) used compound specific isotope analysis of TCE and its degradation compounds to demonstrate microbial degradation in both microcosms and contaminated groundwaters. Noteworthy in the microcosm experiments were the strong isotope enrichments for *cis*-DCE, VC, and ethane (Figure 9.19). These enrichments are due to a combination of two processes. First, the precursors PCE and TCE experience strong enrichments due to Rayleigh distillation during reaction to *cis*-DCE. These enrichments are passed onto the *cis*-DCE and VC as they accumulate. Second, as the *cis*-DCE are dechlorinated, both experience a Rayleigh

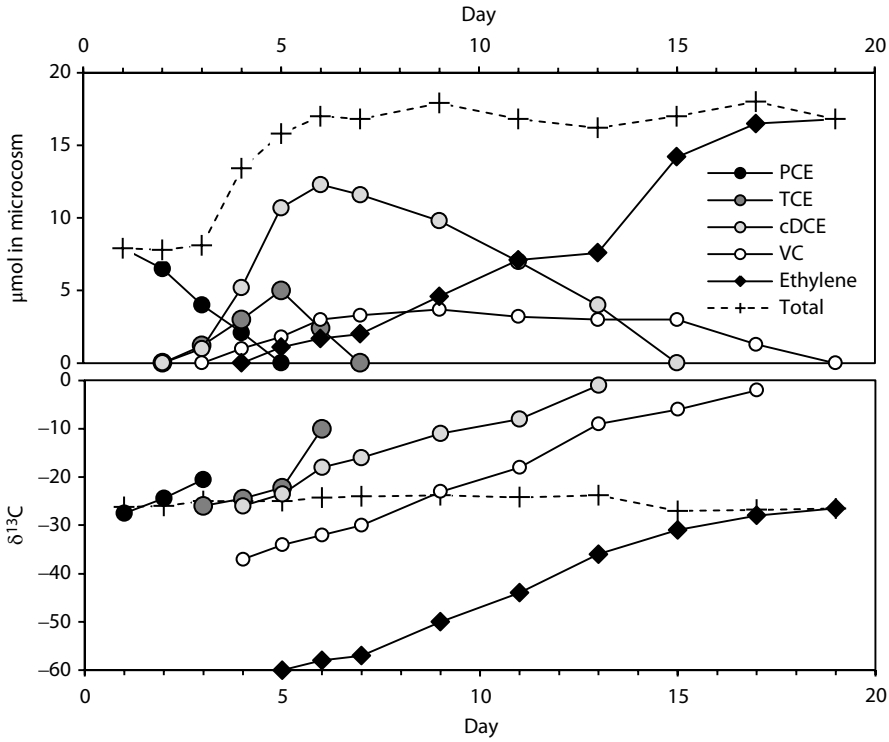

FIGURE 9.19 Concentration and $\delta^{13}C$ of PCE and its degradation products over a 20-day microcosm experiment, and the $\delta^{13}C$ of perchloroethene and degradation products in anaerobic groundwaters from a sandy aquifer. (After Hunkeler et al. 1999.)

enrichment, resulting in very substantial enrichments. Note that the accumulation of *cis*-DCE and its degradation products, VC and ethane, have a higher aqueous concentration than the initial PCE. This is due to desorption of the added PCE from the aquifer material as PCE reaction begins. About half of the PCE added to the microcosm at the outset was sorbed onto the solid material.

The diagnostic capability of stable isotopes for such reactions was then applied in a sandy silt aquifer that had been contaminated in the past by PCE. Here, this study finds the same enrichments in the product compounds, providing unequivocal evidence for bioremediation of these groundwaters.

Abiotic Degradation of Organochlorine Compounds in Permeable Reactive Barriers

Management of groundwaters contaminated by chlorinated organic carbon compounds by pump-and-treat methods, usually involving sorption on reactive carbon, is recognized as expensive remediation in perpetuity (Mackay and Cherry 1989).

In situ degradation of contaminants, often by injecting nutrients and bacterial strains to stimulate biological activity, faces problems of aquifer heterogeneity. Research over the past two decades has focused on the inorganic degradation of chlorinated carbon compounds such as PCE and tetrachloromethane using zero-valence (metallic) iron installed as a geochemically-reactive barrier to intercept the contaminant plume in the aquifer. (Gillham and O'Hannesin 1992; 1994; Gillham et al. 1993). In such reductive dechlorination reactions, the covalently bonded Cl^+ is reduced to Cl^- using Fe^0 as the electron donor. Multiple dechlorination steps take place simultaneously or in rapid succession, with intermediate degradation products present at only low residual concentrations. Dissociation of water accompanies reductive dechlorination, providing H^+ to replace the Cl^+ and forming ethylene or methane.

$$C_2Cl_{4\,PCE} + 4Fe^0 + 4H_2O \rightarrow C_2H_4 + 4Cl^- + 4OH^- + 4Fe^{2+}$$

$$CCl_{4\,CT} + 4Fe^0 + 4H_2O \rightarrow CH_4 + 4Cl^- + 4OH^- + 4Fe^{2+}$$

The hydrocarbon products of reductive dechlorination are considerably more benign than the chlorinated compounds and more susceptible to aerobic or anaerobic biodegradation in the aquifer.

Following the 1991 pilot-scale installation at Base Borden in southern Ontario (O'Hannesin and Gillham 1998), permeable reactive barriers with zero-valence iron have been used worldwide. Henderson and Demond (2007) report that the few underperforming installations were more likely to be compromised by poor hydraulic characterization of the aquifer than by performance of the reactive barrier itself.

Fugitive Gases

The increased production of natural gas from shales by high-pressure fracturing, or fracking, has heightened concern for impacts on shallow groundwater resources. Dissolved methane in groundwater becomes an explosion hazard as it degases in domestic water distribution systems that are under lower pressure than in the aquifer. However, methane can have natural production by microbial methanogenesis in shallow groundwaters, making it difficult to associate methane found in water supplies to shale-gas activities. Aravena et al. (1995) provide a good example of the former, where groundwaters in the Alliston aquifer of Southern Ontario have significant methane accumulations that pose a hazard to rural residents. Osborn et al. (2011) provide a good example of the latter, where high methane in domestic wells is attributed to leaking gas wells. In both cases, the stable isotope composition of methane was used to identify the source of methane. However, in addition to the $\delta^{13}C$ and δD composition of methane, the $C_1/(C_2 + C_3)$ ratio, radiocarbon and He data can discriminate between sources.

Biogenic methane tends to be very depleted in ^{13}C due to preferential selection of ^{12}C during methanogenesis. Depending on the pathway, $\delta^{13}C_{CH_4}$ can range from $-50‰$ to less than $-100‰$. Values for δD_{CH_4} are even more depleted, with a range from about $-150‰$ to less than $-350‰$.

Acetatoclastic $CH_3COOH \rightarrow CH_4 + CO_2$

CO_2 reduction $CO_2 + 4H_2 \rightarrow CH_4 + 2H_2O$

Thermocatalyitic Kerogen $\rightarrow CH_4 + C_2H_6 + C_3H_8 + ... + CO_2$

Thermocatalytic methane forms during the high-temperature decomposition of kerogen in marine sediments. Kerogen is the high-molecular-weight humic material generated during burial of organics (carbohydrate, proteins, etc.) with up to 1000 atomic mass units (daltons). As burial depth increases, kerogen cracks to lighter-weight hydrocarbons, losing oxygen, nitrogen, and sulfur from its structure in the process. The oil window for such reactions is generally from about 60°C to 150°C. Rapid burial of kerogen to greater depths brings it into the gas window, above about 150°C, favoring production of the lighter alkane hydrocarbons found in natural gas—methane (CH_4), ethane (C_2H_6), and propane (C_3H_8) plus minor heavier alkanes or condensates. These are the C_1 to C_3 alkanes. The composition of natural gas from different fields can be characterized by the molar ratio of methane to the higher weight alkanes, determined as:

$$\frac{CH_4}{C_2H_6 + C_3H_8} \quad \text{or} \quad \frac{C_1}{C_2 + C_3}$$

In thermogenic natural gas, the $C_1/(C_2+C_3)$ ratio is generally less than 100 (Prinzhofer and Huc 1995). In contrast, archaeal activity in anaerobic waters, such as groundwaters or bogs, generates almost exclusively methane, and so the $C_1/(C_2+C_3)$ ratio for such gases is typically greater than 1000 (Whiticar et al. 1986).

As discussed in Chapter 7 (Redox Evolution), methane produced by archaeal reduction of CO_2 with H_2 tends to be more depleted in ^{13}C but enriched in D due to the incorporation of hydrogen from water. By comparison, acetoclastic archaea are less discriminating, producing methane that is more enriched in ^{13}C, but more depleted in D because the hydrogen comes from the methyl group in the acetate (Figure 9.20). In contrast to archaeal methanogenesis, thermogenic methane is produced at high temperature by inorganic reaction (cracking) of higher-weight carbon compounds and so experiences less isotope fractionation. The $\delta^{13}C$ ranges from the value for marine kerogen, about −30‰, up to about −50‰.

The two case studies here show that the stable isotope values of methane in groundwater are indicative of its source. However, there can be some overlap due to mixing, and due to methanotrophic activity such as aerobic methane oxidation or sulfate reduction:

$$CH_4 + 2O_2 \rightarrow HCO_3^- + H_2O + H^+ \qquad \Delta G° = -773.24 \text{ kJ/mol}$$

$$CH_4 + SO_4^{2-} \rightarrow HCO_3^- + HS^- + H_2O \qquad \Delta G° = -17.16 \text{ kJ/mol}$$

Both are bacterially mediated and so discriminate against ^{13}C and D, which imparts an enrichment on the residual methane. In the case of sulfate reduction, the residual SO_4^{2-} will also become enriched in ^{34}S. Stempvoort et al. (2005) observe

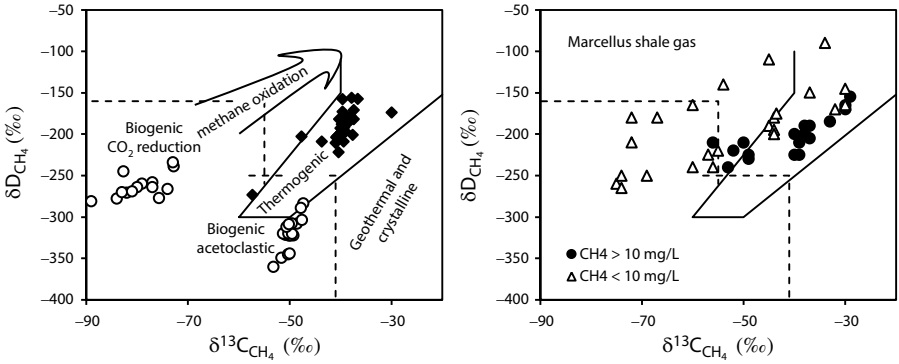

FIGURE 9.20 Ranges for stable isotope composition of methane from bacterial and thermogenic sources (based on Schoell 1980; Osborn et al. 2011). Left: selection of biogenic (open discs) and thermogenic (closed diamonds) from Southern Ontario (Data from Sherwood Lollar et al. 1994; Aravena et al. 1995; Clark et al. 2013). Right: methane from shallow groundwaters in the vicinity of the Marcellus shale gas field showing the high concentrations in water wells to be associated with production from the Marcellus shale. (Data from Osborn et al. 2011.)

depletion in $\delta^{13}C_{DIC}$ together with enrichment in both $\delta^{13}C_{CH_4}$ and $\delta^{34}S_{SO_4^{2-}}$ to demonstrate natural attenuation of fugitive methane from a leaking gas well in groundwaters from a site near Lloydminster, Alberta.

Radiocarbon is an additional tool that can often be used to discriminate between biogenic and thermogenic methane. Biogenic methane in shallow systems is typically generated by degradation of recently buried organics, which will contain ^{14}C. This is the case in the Alliston aquifer, which hosts buried peat horizons from the late Pleistocene and Holocene (Aravena et al. 1995), where measured ^{14}C activities of the methane in the overburden are up to 15 pMC. In contrast, thermogenic methane will have essentially no ^{14}C activity, as it is derived from old marine carbon.

Commercial natural gas sources are not exclusively derived from thermogenic sources. Coalbed methane is generated by bacterial activity within the formations, often stimulated by infiltration of fresh waters during the last deglaciation (McIntosh et al. 2002). Shale gas also has a high proportion generated by microbial activity (Curtis 2002; Martini et al. 2003), which precludes the use of $\delta^{13}C_{CH_4}$ and δD_{CH_4} as tools to distinguish natural shallow methane in groundwaters from fugitive gas from production wells. In such cases, radiocarbon can be used. As before, unlike shallow biogenic methane sources, which have modern radiocarbon activities (Nakagawa and Yoshida 2002; Chanton et al. 1995), methane from coalbeds and marine carbon substrates is radiocarbon-free. Even when the circulating waters contain ^{14}C-active DIC that can contribute to methane production by CO_2 reduction, this component is typically diluted below detection by the in situ degradation of the alkane precursors that produce both CH_4 and CO_2 (Jones et al. 2008).

Fugitive CO_2 from deep injection for carbon capture and storage (CCS) may similarly be traced with radiocarbon. Although the $\delta^{13}C$ of such fossil-fuel-derived CO_2 should be highly depleted, near –30‰, reaction with carbonate in the subsurface can shift this

value into the range commonly found for DIC in shallow groundwaters and soils (−20 to −15‰), and so $\delta^{13}C$ alone is not diagnostic. However, shallow DIC in young groundwaters will have measurable radiocarbon, while CO_2 from CCS will be radiocarbon-free. The $\delta^{13}C$ of CO_2 from CCS would also differ from that of ^{14}C-free geogenic CO_2 originating in metamorphic and volcanogenic terrains, which are generally close to 0‰.

Finally, radiogenic ^4He is a diagnostic tracer of fugitive gases of deep thermogenic origin. Geogenic CH_4 is accompanied by ^4He in a ratio that is characteristic of the source formation and which will differ from shallow biogenic CH_4. Jackson et al. (2013) show that drinking water wells nearest the Marcellus shale-gas field (methane data in Figure 9.20) have $^4He/CH_4$ ratios distinctly lower from that of other potential methane sources.

LANDFILL LEACHATE

Modern landfill design and construction rely upon engineered barriers of clay and geopolymers at the base, together with internal systems to collect leachate and gases and often a cap to reduce infiltration and leachate production. Leachates can then be treated, often in municipal treatment plants, before discharge. Older landfills, by contrast, lack these infrastructures, and so represent a legacy threat to groundwater resources that must be monitored and remediated. Understanding the biodegradation processes during leachate production and interaction with shallow groundwaters is fundamental to assessing impact and planning remediation.

Landfill Waste

The composition of municipal waste is dominated by organic refuse, categorized by the EPA according to waste forms both before and after diversion for recycling and composting (Table 9.3).

TABLE 9.3
Composition of Municipal Solid Waste in United States in 2011

	% of 250 Million Tons before Recycling and Composting	% of 164 Million Tons after Recycling and Composting
Paper and cardboard	28	14.8
Food waste	14.5	21.3
Yard trimmings	13.5	8.8
Plastics	12.7	17.8
Metals	8.8	8.8
Rubber, leather, textiles	8.2	10.6
Wood	6.4	8.4
Glass	4.6	5.1

Source: EPA, Municipal Solid Waste Generation, Recycling, and Disposal in the United States: Facts and Figures for 2011, EPA, Washington, DC, 2013.

Considering that legacy landfills operated largely prior to the increasingly aggressive municipal waste diversion programs of recent decades, their inventory can be considered to be over 70% organic biomass, which can biodegrade. The steel components of the metal stream can oxidize as well, while most plastics and glass will remain relatively inert on the time scales considered for degradation. On top of this is placed the daily cover material, usually derived from local sources of surficial materials, including sand, soils, and till.

Under humid conditions, the degradation reactions in this biomass-dominated inventory quickly evolve to methanogenesis. Eleazer et al. (1997) have documented with microcosm experiments the methane production that can be achieved from the various organic components. CH_4 and CO_2 are the two most significant gases produced.

Biodegradation and Landfill Leachate

Following disposal and compaction, landfilled material typically begins to saturated with meteoric waters. The subsequent series of reactions that then occur include the following:

Salt mobilization	$NaCl \rightarrow Na^+ + Cl^-$
Humification of organics	$CH_2O + O_2 \rightarrow HA + FA + CO_2 + H_2O$
Carbonate weathering	$CaCO_3 + CO_2 + H_2O \rightarrow Ca^{2+} + 2HCO_3^-$
Silicate weathering	$CaAl_2Si_2O_8 + 3H_2O + 2CO_2 \rightarrow Ca^{2+} + 2HCO_3^- + Al_2Si_2O_5(OH)_4$
N_{org} mineralization	$R–NH_2 + H_2O + H^+ \rightarrow NH_4^+ + R–OH$
Cellulose fermentation	$C_6H_{12}O_6 \rightarrow CH_3CH_2CH_2COOH + 2CO_2 + 2H_2$
Acetogenesis	$CH_3CH_2COOH + 2H_2O \rightarrow CH_3COOH + CO_2 + 3H_2$
Iron reduction	$4Fe(OH)_3 + CH_2O + 7H^+ \rightarrow HCO_2^- + 4\,Fe^{2+} + 10H_2O$
Sulfate reduction	$CH_3COOH + SO_4^{2-} \rightarrow H_2S + 2HCO_3^-$
Metallic iron oxidation	$Fe^\circ + 2H_2O \rightarrow Fe^{2+} + H_2 + 2OH^-$
Methanogenesis	$CH_3COOH \rightarrow CH_4 + CO_2$
CO_2 reduction	$CO_2 + 4H_2 \rightarrow CH_4 + 2H_2O$

This series of reactions shows an evolution from the oxidizing conditions at the surface of the landfill, where rainfall infiltrates with oxygen and begins the humification and mineral weathering processes, to anaerobic conditions, where fermentative and methanogenic reactions proceed. Plasterboard or Gyproc® waste is not permitted in municipal landfills, as the gypsum ($CaSO_4{\cdot}2H_2O$) supports sulfate reduction and production of toxic H_2S. In addition to these primary products of aerobic and anaerobic biodegradation of the organic material, Christensen et al. (2001) note the trace (<ppm) concentration of heavy metals, Cd, Cr, Cu, Pb, Ni, and Zn, likely released during reduction of ferrihydrite and other oxyhydroxides, and the presence of xenoorganics, such as BTEX components, pesticides, and solvents.

The leachate generated by these reactions is represented for a series of landfills evaluated by Christensen et al. (2001), together with a specific example from the Trail Road Landfill, near Ottawa, Canada (Figure 9.21), which has a significant mineral component (TDS > 10 g/L) and a pH of 7.4. The very high HCO_3^- is derived

from both the aerobic and anaerobic biodegradation reactions and acetoclastic methanogenesis. Carbonic acid from CO_2 produced in these reactions is consumed by mineral weathering, contributing to Ca^{2+} and Mg^{2+} concentrations. Na^+ and Cl^- are common in leachate from food waste. The redox-sensitive species all demonstrate an evolution driven by the high dissolved organic carbon (DOC). The system has exhausted any high-electromotive-potential electron acceptors, such as NO_3^- and SO_4^{2-}, which are negligible in these waters. The high concentrations of Mn and Fe exceed the solubility limits for their oxidized species (Figure 7.14), and so have been reduced to Mn^{2+} and Fe^{2+}. Similarly, the high concentration of sulfide and the presence of CH_4 indicate that the redox evolution has dropped to methanogenesis, which is the final step in the redox evolution driven by organic carbon.

Tracing Leachate Biodegradation with ^{13}C

The biodegradation reactions given earlier can be traced through analysis of isotopes in the different compounds of leachate. Notably, ^{13}C is useful to trace the role of DIC, bulk DOC, and specific DOC compounds during leachate generation. The bulk DOC from the Trail Road Landfill, shown in Figure 9.21, was separated into specific components for their concentration and $\delta^{13}C$ (Mohammadzadeh et al. 2005). Here the major compounds of the DOC show the pattern for ^{13}C partitioning during degradation and methanogenesis:

Primary organics	→	Humic acid	→	Fulvic acid	→	Acetate	→	CH_4	+	CO_2
–28.1‰		–28.1‰		–20.3‰		–12.0‰		–68.4‰		+10.7‰

Bacteria preferentially degrade the ^{12}C-fraction of a particular substrate (fulvic acid [FA], acetate), and discriminate against the ^{13}C-enriched fraction. The distribution of ^{13}C then reflects the rate of production and consumption of a given compound, according to the Rayleigh distillation function. As a particular substrate compound is consumed, it will become enriched in ^{13}C. The significant enrichments of ^{13}C in FA and acetate show that these components have been significantly

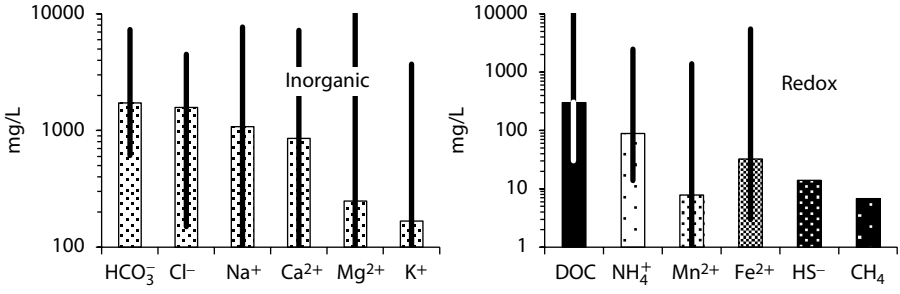

FIGURE 9.21 Geochemistry of municipal landfill leachate with an example (histograms) from the Trail Road Landfill, Ottawa, Canada (Mohammadzadeh and Clark 2008) and ranges (lines) for a series of landfills. (Data from Christensen et al. 2001.)

consumed to produce methane and CO_2. The distribution of ^{13}C between these two terminal products of biodegradation in the leachate shows that a mass balance is preserved:

$$2CH_2O_{\text{primary organics}} \rightarrow CH_4 + CO_2$$

$$-28.1‰ \approx (-68.4 + 10.7)/2$$

$$\approx -28.8‰$$

Methanogenesis and δD

Another important isotope effect is observed for δD, which is enriched in leachate by about 15‰ (Figure 9.22) due to exchange during methanogenesis and through anaerobic oxidation of iron. In the following reactions, the production of H_2, and ultimately CH_4, is associated with strong fractionation for deuterium, which is partitioned into the water directly or through exchange with H^+ in the fatty acids (with deuterium, D noted):

$$C_6H_{11}DO_6 \rightarrow CH_3CH_2CH_2COO^- + D^+ + 2CO_2 + 2H_2 \quad \textit{Fermentation}$$

$$Fe^\circ + 2HDO \rightarrow Fe^{2+} + H_2 + 2OD^- \quad \textit{Iron reduction}$$

The fractionation factor $\alpha D_{H_2O-H_2} = 3.76$, and so hydrogen gas in equilibrium with water will be depleted in D by over 700‰ (recall from fractionation in Chapter 4). The fractionation factor for methane–water exchange, $\alpha D_{H_2O-CH_4} = 1.027$, is minor by comparison, but would also act to partition D into the water. The deuterium depletion is transferred into methane, leaving a residual enrichment in the water. Recalling that Rayleigh distillation requires substantial reaction to have a measurable isotope shift, modification of δD_{H_2O} by the overall process of H_2 production and

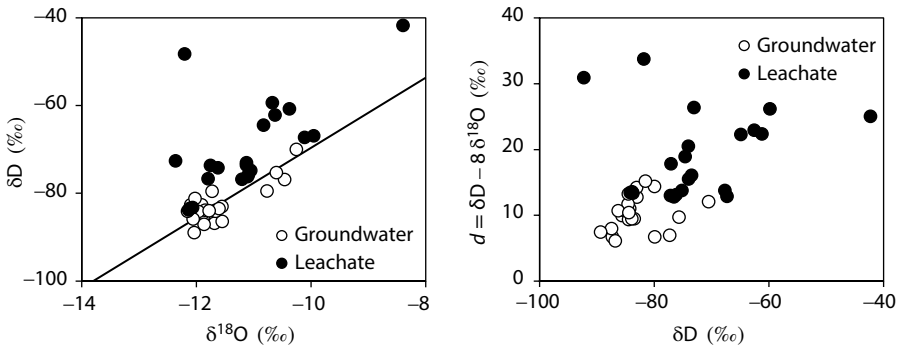

FIGURE 9.22 Deuterium enrichment in landfill leachate due to hydrogen exchange with water during H_2 generation for methanogenesis. Right diagram shows the deuterium enrichment relative to the local meteoric water line, while the left shows the variability of *d* with δD. Most groundwaters plot near the meteoric water line with *d* close to 10, while some exhibit minor deuterium enrichment due to leachate contamination.

methanogenesis would then require production of several moles of methane per L leachate. Using an enrichment factor for deuterium fractionation between H_2 and H_2O of 700‰, the amount of methane produced per liter of leachate can be estimated from the deuterium enrichment in the leachate, according to methanogenesis from H_2 and CO_2:

$$\delta D_{H_2O(\text{leachate})} - \delta D_{H_2O(\text{precipitation})} = 10‰$$

Rayleigh distillation: $\delta_f = \delta_o + \varepsilon D_{H_2O-H_2} \times \ln f$

$$10‰ = -700‰ \times \ln f$$

And so $f = 0.986$ and so 0.014 L/L or 14 mL/L or 1.4% of the water has reacted.

This amounts to 0.014 L × 55.6 mol H_2O/L = 0.8 mol H_2O. Considering the 2 H per H_2O and 4 H per CH_4, this would amount to a production of 0.4 moles or 9 L of $CH_{4(STP)}$ per liter of leachate. These calculations are of course not well constrained but demonstrate that a tremendous production of gas is required to affect the isotopic composition of water and that the conditions within the landfill must remain unsaturated to have this volume of gas generated from this volume of water. It further shows that monitoring the D and ^{18}O contents of leachate could be used as a measure of methane production in the landfill.

ACID MINE DRAINAGE

The juxtaposition of highly reduced minerals, including pyrite and other base metal sulfides, from deep crustal environments with the humid, aerobic exogene setting where waste rock and mine tailings are dumped fosters a host of oxidation reactions. The energy released converting sulfide to sulfate and ferrous iron to ferric iron is used by various bacteria to fix CO_2 for cell construction and for their fuel. In the process, metals and H^+ are released in abundance to solution. The consequences for the immediate landscape as well as for local water bodies are tremendous, with dieback of vegetation, fish kills, and landscape destruction. This legacy exists for many mining camps throughout the world.

Mitigation strategies are generally based on minimizing oxidation pathways. Engineered wetlands can buffer metal transport to runoff. Permeable reactive barriers can be designed to attenuate a particular geochemical parameter or solute. Finally, conversion of the source of acid mine drainage to anaerobic conditions by saturating them to exclude O_2 has become a part of remediation efforts in mine closure plans.

Generation of Acid Mine Drainage

Oxidation reactions generate acid. Oxidation of sulfide to sulfate involves the transfer of eight electrons, and so is a particularly acidic reaction. These reactions have been presented in Chapter 7, on redox evolution. The chain of reactions begins as a near surface reaction by O_2 on sulfide minerals, usually ubiquitous pyrite found in abundant

association with base metal sulfides. O_2 diffusion through water is slow and impedes the reaction, and so oxidation reactions are greatly favored by unsaturated conditions.

$$FeS_2 + 3\tfrac{1}{2}O_2 + H_2O \rightarrow Fe^{2+} + 2SO_4^{2-} + 2H^+ \qquad \textit{Thiobacillus thiooxidans}$$

The ferrous iron released by sulfide oxidation is also oxidized by O_2, producing Fe^{3+} and ferrihydrite:

$$Fe^{2+} + \tfrac{1}{4}O_2 + 2\tfrac{1}{2}H_2O \rightarrow Fe(OH)_{3(fer)} + 2H^+ \qquad \textit{Thiobacillus ferrooxidans}$$

The low solubility of ferric hydroxide or ferrihydrite ($Fe[OH]_{3(fer)}$) allows it to precipitate from solution at circumneutral pH. As acidity is generated, the pH of the aqueous setting drops and Fe^{3+} is released to solution. Sulfide oxidation is then greatly accelerated by a second, abiotic oxidation pathway, where ferric and ferrous iron cycle under aerobic conditions:

$$FeS_2 + 14Fe^{3+} + 8H_2O \rightarrow 15Fe^{2+} + 2SO_4^{2-} + 16H^+$$

and

$$Fe^{2+} + \tfrac{1}{4}O_2 + H^+ \rightarrow Fe^{3+} + \tfrac{1}{2}H_2O$$

The result is a jump to pH levels as low as 1–2. Negative pH values have even been observed in some extreme cases. Sulfate concentrations increase from the ppm to the parts per thousand (permil) and even percent range. The transition metals, including Fe, Mn, Ni, Cu, and Zn, also become soluble at low pH and rise to high concentrations.

The high acidity of acid mine drainage accelerates the weathering of aluminosilicate minerals. However, unlike natural weathering reactions driven by carbonic acid at pH levels of 5–7, weathering by AMD precludes significant formation of kaolinite and other clays due to the high solubility of Al^{3+} at low pH.

Secondary Mineral Precipitates

The high acidity and elevated sulfate and metal concentrations in acid mine drainage evolve by mixing with natural watershed drainage. The most important initial reaction is dilution, which has an immediate effect on pH. However, each unit increase of pH requires a tenfold dilution of the acid drainage unless the receiving waters are highly buffered with bicarbonate.

An increase in pH affects pH-sensitive solutes, such as Fe and Al, which move into the stability fields of their less soluble hydroxides. The response is a precipitation of ferrihydrite and gibbsite. Ferrihydrite, with high surface area and charge, sorbs other metals from solution.

In the unsaturated environment of tailings and pyritic waste rock where AMD is generated, seasonal dry periods allow desiccation of acidic pore waters and the accumulation of sulfate salts. These evaporite minerals also form along the borders of AMD channels and surface water accumulations. However, rather than representing a mineralogical control or sink for metals and sulfate in the environment, they act only as a storage term in the watershed. Their dissolution following renewed precipitation is accompanied by high solute and acidity loading to runoff.

Soluble ferric iron and aluminum sulfates, such as jarosite ($KFe_3[SO_4]_2[OH]_6$), rhomboclase ($HFe[SO_4]_2 \cdot 4[H_2O]$), and alunogen ($Al_2[SO_4]_3 \cdot 17H_2O$), contribute high concentrations of SO_4^{2-} as well as $Fe^{3+}$and Al^{3+}. Hydration and dissociation of these trivalent cations also lowers the pH. Rhomboclase contributes H^+ directly to solution.

Remediation

A legacy of mining over the past 200 years can be observed as stockpiles of reactive waste rock and tailings sitting on the surface. Long-term solutions to the generation of acid mine drainage at these sites are expensive, and focus on the isolation of the source materials under saturated conditions. This cuts the supply of oxygen and greatly reduces the rate of sulfide oxidation. Allowing vegetation to reestablish over the site as a wetland or soil provides the added security of an organic carbon loading, which reverses the oxidation reactions and raises pH. Bacterial iron and sulfate reduction during oxidation of organic carbon are key reactions. They can result in the neutralization of pH and the precipitation of sulfide minerals:

$$CH_2O + 4Fe(OH)_3 + 7H^+ \rightarrow 4Fe^{2+} + HCO_3^- + 10H_2O$$

$$2CH_2O + SO_4^{2-} + Fe^{2+} \rightarrow FeS_{\text{mackinawite}} + 2HCO_3^- + 2H^+$$

The reduction of ferric iron occurs under higher Eh conditions than sulfate reduction (see Chapter 7) and results in the mobility of iron and other metals, which may have been adsorbed onto ferric iron hydroxide precipitates in tailings or acidic waste rock. However, subsequent sulfate reduction will greatly lower their solubility as sulfide minerals. In neutral-pH waters, a black amorphous iron sulfide or mackinawite forms, whereas at lower pH, fine-grained biogenic pyrite (FeS_2) may also precipitate. The overall reaction is acid consuming, and the pH is buffered by the bicarbonate produced.

Engineered wetlands are not possible where topography, precipitation and bedrock drainage are constraints. Seasonal desiccation and remobilization of metal-laden dust is also a concern.

Short-term solutions include treating the effluent with lime (CaO) or hydrated (slaked) lime ($Ca[OH]_2$), or limestone ($CaCO_3$). These buffer the acidity at neutral pH and precipitate most of the metals as hydroxides. However, this presents the problem of isolating the metal-laden precipitates so that subsequent leaching or wind erosion does not remobilize the metals.

$$CaO + H_2O + 2H^+ \rightarrow Ca^{2+} + 2H_2O$$

$$CaCO_3 + H^+ \rightarrow Ca^{2+} + HCO_3^-$$

The following two examples represent drainage from mine environments with differing levels of acidity. The Iron Mountain site in northern California represents perhaps the most acidic drainage ever recorded, with subsequent mineralization by a suite of unusual iron sulfate salts. By contrast, acid drainage from Nordic Mine in

Elliot Lake, Ontario, shows the important role of carbonates for the attenuation of acid drainage.

Hyperacid Drainage at Iron Mountain, California

Mining of the Iron Mountain massive sulfide deposit in northern California began in the 1860s, with underground workings producing copper plus silver, gold, iron, and zinc in addition to sulfur for sulfuric acid. Mining activities ended in 1962, and remediation efforts were implemented following its designation as a superfund environmental cleanup site. Until that time, several thousand tons of pyrite per year were being oxidized and contributing to acid drainage from the site. Along with the discharge of this acidity to the Sacramento River went hundreds of tons per year of dissolved Cd, Cu, and Zn.

The drainage from the old mines at Iron Mountain provides a good example of weathering, metal loading, and pH under extremely acidic conditions (Nordstrom and Alper 1999). At this site, phreatic drainage through fractures in the host rock and ore body (Figure 9.23) creates a highly oxygenated environment for pyrite oxidation. Heat liberated from these exothermic reactions raises the local groundwater temperatures to around 40°C, enhancing reaction. The sulfide oxidation reactions follow the reactions shown above, including the abiotic reaction based on reduction of Fe^{3+} to Fe^{2+}, which is immediately recycled by atmospheric oxygen back to Fe^{3+}. The net product is sulfuric acid, with few mineralogical controls under these extremely acid conditions to limit the pyrite oxidation reaction.

The generation of sulfuric acid and dissolved iron from pyrite oxidation in this environment is illustrated in Figure 9.24. Using pH electrodes calibrated with sulfuric acid buffers, Nordstrom et al. (2000) measure pH values as low as −3.6, with sulfate concentrations at that pH of close to 800 g/L (800,000 mg/L) and total dissolved iron concentrations of 140 g/L (140,000 mg/L). The high sulfate and metal loadings give rise to some interesting and colorful mineralization. However, equally interesting are the negative pH values.

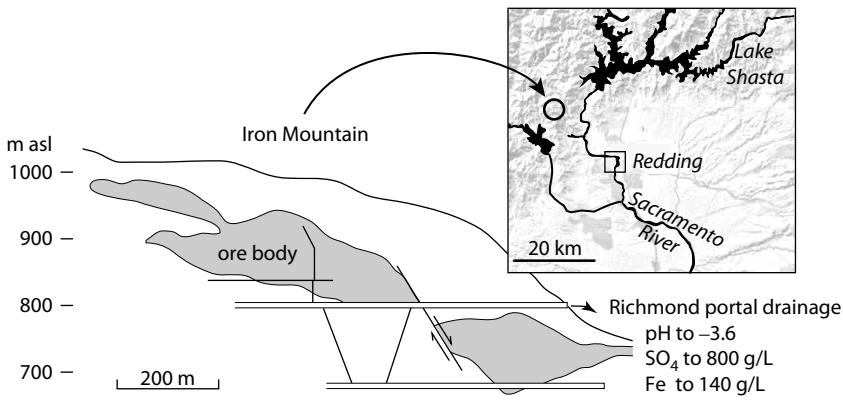

FIGURE 9.23 Iron Mountain acid mine drainage superfund site, location and cross section showing sites of drainage from Richmond Mine portal. Host rock is fractured rhyolite encompassing the massive sulfide body. (Modified from Nordstrom and Alper 1999.)

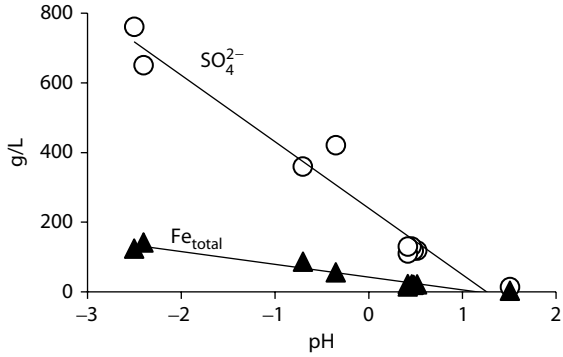

FIGURE 9.24 Plot of dissolved sulfate and iron in drainage from the Richmond Mine with measured pH. Negative pH values signify activities for H^- that are greater than 1. (After Nordstrom et al. 2000.)

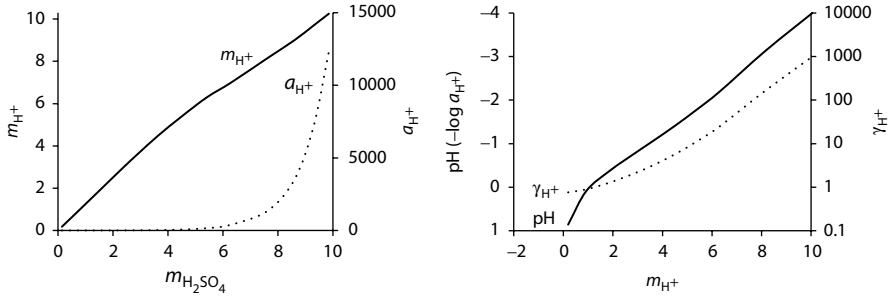

FIGURE 9.25 Activity–concentration behavior for H^+ in sulfuric acid solutions. Left: H^+ concentration (m_{H^+}) increases uniformly with sulfuric acid concentration ($m_{H_2SO_4}$) from the dissociation reaction ($H_2SO_4 \rightarrow H^+ + HSO_4^-$), but H^+ activity (a_{H^+}) increases logarithmically. This is due to the logarithmic rise in the H^+ activity coefficient (γ_{H^+}) in high-ionic-strength solutions, such as sulfuric acid. In low ionic strength solutions, γ is less than 1, but in strong electrolyte solutions (brines, acids) it increases exponentially (see Figure 2.4). Right: the strong increase in pH ($-\log a_{H^+}$) correlates with γ_{H^+} (both on log scales).

Because pH is a logarithmic expression, a pH value as low as –3.6 would suggest that, assuming $a_{H^+} \approx m_{H^+}$, some 390 kg sulfuric acid was dissolved per kg of this acid mine drainage ($10^{-pH} = 3981$ mol/kg), which is clearly wrong. To understand what these negative pH values represent, one needs to consider the activity–concentration relationship for hydrogen ions in these highly acidic conditions. To do this, these researchers calculate the hydrogen ion activities for sulfuric acid at different concentrations, using the Pitzer (1973) equations incorporated in PHRQPITZ (Plummer et al. 1988). These equations represent ion activities in strong electrolyte solutions, showing that the activity coefficient, γ_{H^+}, reverses exponentially from a fractional value less than 1 in lower salinity solutions ($m_{H_2SO_4}$ <1 mol/kg) to 10,000 in 10 molal solutions (Figure 9.25). For this reason, the measured H^+ activity is much

greater than the associated concentration of H^+ ions based on the dissociation of the sulfuric acid at its given concentration ($m_{H_2SO_4}$):

$$H_2SO_4 \rightarrow H^+ + HSO_4^-$$

$$a_{H^+} = m_{H^+} \times \gamma_{H^+}$$

The sulfide mineralization at Iron Mountain is hosted by rhyolitic volcanic sequences dominated by albite plus phyllosilicates (chlinochlore and muscovite), quartz, and only minor calcite. The weathering of albite was shown in Chapter 6 to consume acidity and produce low-temperature clay minerals. However, under conditions of hyperacidity, these clays are no longer stable due to the high solubility of aluminum (Figure 3.4). Iron and other metals all become highly soluble at low pH, where hydroxide species ($Al[OH]_3$, $Fe[OH]_3$, $Cu[OH]_2$, etc.) are unstable. Only the silicate minerals, such as amorphous silica, opal, and chalcedony, are stable at low pH (Figures 3.5 and 6.8).

$$NaAlSi_3O_{8\ albite} + 4H_2O + 4H^+ \rightarrow Na^+ + Al^{3+} + 3H_4SiO_4$$

$$Al_2Si_2O_5(OH)_{4\ kaolinite} + 6H^+ \rightarrow 2Al^{3+} + 2H_4SiO_4 + H_2O$$

$$(Mg_5Al)AlSi_3O_{10}(OH)_{8\ clinochlore} + 16H^+ \rightarrow 5Mg^{2+} + 2Al^{3+} + 3H_4SiO_4 + 6H_2O$$

$$KAl_2(AlSi_3O_{10})(OH)_{2\ muscovite} + 10H^+ \rightarrow K^+ + 3Al^{3+} + 3H_4SiO_4$$

This series of acid-consuming mineral dissolution reactions can then be compared with the geochemistry of the acid discharge from Iron Mountain. Figure 9.26 shows the high concentrations produced by the sulfide (mainly pyrite) oxidation reactions, which release base metals and sulfuric acid (pH = −2.5) into solution. The base metal concentrations reflect their abundance in the sulfide ore,

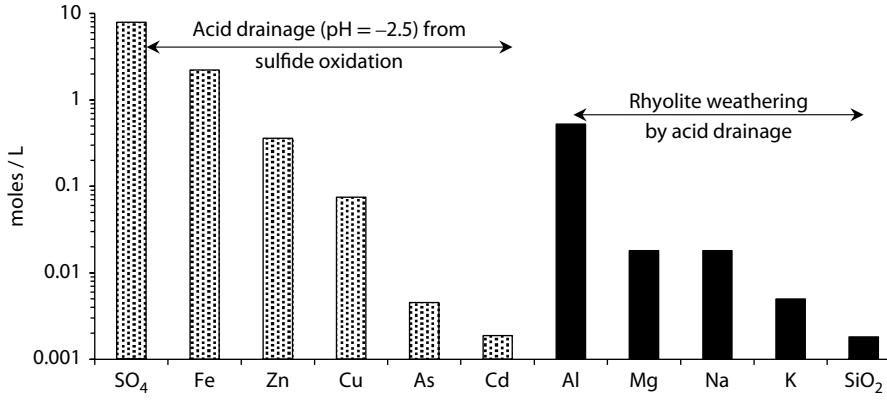

FIGURE 9.26 Geochemistry of the acid drainage waters with pH −2.5 from Iron Mountain. (Data from Nordstrom et al. 2000.)

which is mainly pyrite (FeS_2). The acid produced by sulfide oxidation is then consumed by mineral weathering, producing Al^{3+}, Mg^{2+}, and the alkali cations, Na^+ and K^+, found in the rhyolite. The relative abundances of these cations in the acid drainage reflect their relative abundances in the minerals above. Only silicic acid is anomalously low, due to precipitation of amorphous silica and its polymorphs.

The extreme geochemistry of the Iron Mountain discharge generates a range of rare efflorescent (evaporative) salts formed by evaporative concentration of the acid drainage at seepage points in the mine. Nordstrom and Alpers (1999) analyzed such precipitates collected at drips and seepage faces, showing them to be sulfate minerals with variable metal and water contents. Most were iron sulfates, including the following:

- Ferrous iron sulfates, such as melanterite ($FeSO_4 \cdot 7H_2O$) and rozenite ($FeSO_4 \cdot 4H_2O$)
- Ferrous-ferric sulfates, including copiapite ($Fe^{II}Fe^{III}_4[SO_4]_6[OH]_2 \cdot 20H_2O$) and voltaite ($K_2Fe^{II}_5Fe^{III}_4[SO_4]_{12} \cdot 18H_2O$)
- Ferric iron sulfates kornelite ($Fe_2[SO_4]_3 \cdot 7H_2O$) and rhomboclase ($HFe[SO_4]_2 \cdot 4H_2O$)

The ferrous iron sites in these minerals are readily substituted with divalent Cu^{2+} and Zn^{2+}, and the ferric iron sites with Al^{3+}. Dissolution of these minerals generates significant acidity, not only due to the release of H^+ in the structure of minerals such as rhomboclase, but also by the hydrolysis of Fe^{3+} and Al^{3+} in solution. The result from the dissolution of these efflorescent salts is the heavy loading of acidity and metals during early stream discharge following rainfall.

Nordic Mine Uranium-Tailings Impoundment, Elliot Lake, Ontario

This study by Morin et al. (1988) provides a great example of the acid generation and subsequent buffering reactions as the acid drainage moves through the subsurface. In this case, there is some acid-buffering capacity in the sandy aquifer, which contains a few percent calcite and dolomite. The acid plume movement and reaction in the aquifer is shown in cross section in Figure 9.27, together with the multilevel piezometer-monitoring network.

The core of the plume in the tailings was determined to be generated according to the classic reactions on residual pyrite:

$$FeS_2 + 3\tfrac{1}{2}O_2 + H_2O \rightarrow Fe^{2+} + 2SO_4^{2-} + 2H^+ \qquad \textit{Thiobacillus thiooxidans}$$

$$Fe^{2+} + \tfrac{1}{4}O_2 + 2\tfrac{1}{2}H_2O \rightarrow Fe(OH)_3 + 2H^+ \qquad \textit{Thiobacillus ferrooxidans}$$

$$Fe(OH)_{3(fer)} + 3H^+ \rightarrow Fe^{3+} + 3H_2O \qquad \textit{abiotic}$$

The tailings themselves are carbonate-free, and pH values below 3 are generated. At this pH, metals, including Fe, Cu, Pb, Zn, and U, are very soluble and are mobilized from the tailings. The low pH also reduced the cation exchange capacity of the substrate, precluding sorption as a mechanism to slow contaminant migration. This allows high mobility for radium, which as a divalent base cation (Ra^{2+}, like

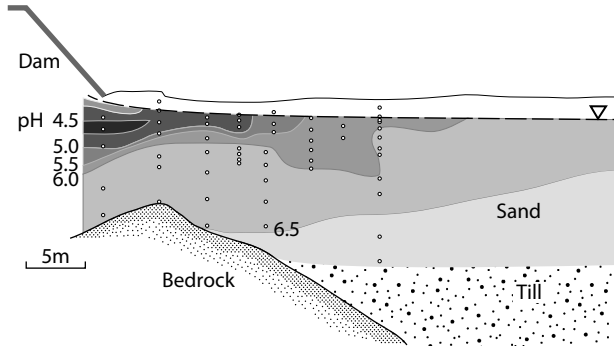

FIGURE 9.27 pH of acid drainage migrating below a tailings dam at the Nordic Mine, Elliot Lake, Ontario. pH values increase by reaction during flow through the carbonate-bearing sand. Multilevel piezometer tips shown. (After Morin et al. 1988.)

Sr^{2+}) would normally have a high retardation factor. This allows the high activity of 5 Bq/L that was measured. Along with these metals is a high concentration of SO_4^{2-} from sulfide oxidation. Note that the high con centration of SO_4^{2-} is also favored at low pH, as the second dissociation constant for sulfuric acid is 10^{-2}. At pH 2.7, over 20% of the dissolved sulfate is as bisulfate, HSO_4^-, and as pH decreases, the solubility of gypsum increases.

As this plume migrates in the subsurface, its velocity is retarded by reactions with native minerals in the aquifer. The principle attenuation process is the dissolution of carbonate minerals in the aquifer. At lower pH, this generates carbonic acid,

$$2H^+ + CaCO_{3(cal)} \rightarrow Ca^{2+} + H_2CO_3 \qquad \text{below pH 6.4}$$

As the pH rises by consuming H^+ in the plume, the carbonic acid will dissociate, and so attenuation reactions at higher pH produce bicarbonate:

$$H^+ + CaCO_{3(cal)} \rightarrow Ca^{2+} + HCO_3^- \qquad \text{above pH 6.4}$$

The production of bicarbonate and increase in pH begin to increase the activity of dissolved carbonate:

$$HCO_3^- \rightarrow CO_3^{2-} + H^+$$

which acts to attenuate the concentration of ferrous iron through precipitation of siderite:

$$Fe^{2+} + CO_3^{2-} \rightarrow FeCO_{3(sid)}$$

Siderite is less soluble than calcite, so ferrous iron is also attenuated by the incongruent dissolution of calcite:

$$Fe^{2+} + CaCO_{3(cal)} \rightarrow FeCO_{3(sid)} + Ca^{2+}$$

As these reactions raise the pH, ferric iron species in the plume becomes insoluble as ferrihydrite and precipitates as an additional reactive substrate for sorption of other metals:

$$Fe(OH)_2^+ + H_2O \rightarrow Fe(OH)_{3(fer)} + H^+$$

The release of Ca^{2+} from calcite dissolution and siderite formation, together with the high sulfate concentration from the tailings generate supersaturated conditions for gypsum, and so reduce the very high dissolved SO_4^{2-}:

$$Ca^{2+} + SO_4^{2-} + 2H_2O \rightarrow CaSO_4 \cdot 2H_2O_{(gyp)}$$

Finally, the increased pH also greatly reduces the solubility of aluminum. Toward circumneutral pH values, Al^{3+} is stable as hydroxide and precipitates as amorphous aluminum hydroxide, gibbsite.

$$Al^{3+} + 3H_2O \rightarrow Al(OH)_{3\,(gib)} + 3H^+$$

These reactions will proceed until the buffering capacity of the aquifer is depleted. With measurements of the calcite content in the aquifer, mass balance calculations of the long-term acid generation capacity of the tailings versus the acid and metal buffering capacity of the aquifer can be made. If there is insufficient buffering in the subsurface for the long-term loading from the tailings, other remedial measures must be considered. In the case of the Nordic mine, reducing conditions in the tailings were established to limit the production of acid drainage. This was accomplished with a low-permeability cap and soil over the top, and monitoring since that time shows decreasing levels of acidity, iron, and other solutes.

Surface discharges from the tailings impoundment are treated differently at this mine, by diversion and treatment. In particular, the acidity and potential for ^{226}Ra contamination of the local surface waters is prevented by treatment with soluble barium chloride and lime (CaO):

$$CaO + H_2O \rightarrow Ca^{2+} + 2OH^-$$

$$OH^- + H^+ \rightarrow H_2O$$

$$^{226}Ra^{2+} + Ba^{2+} + SO_4^{2-} \rightarrow Ba_{(1-x)}{}^{226}Ra_xSO_4$$

Subsequent flow through a settling pond prior to discharge into natural drainage waters allows the insoluble barium sulfate to precipitate and settle out, sequestering with it the trace concentrations of highly radioactive ^{226}Ra. The neutral pH also then sequesters ferric hydroxides (ferrihydrite) and other metals along with it.

BASE METALS IN GROUNDWATER

The first series transition metals include the important base metals, such as copper, iron, nickel, and zinc, which are found as contaminants in mining camps and industrial settings. Iron, the fourth most abundant element in the earth's crust and the most abundant of the transition metals is discussed in Chapter 7. Like iron, most of the transition metals, are multivalent cations that form hydroxide species over the range of pH of natural waters, and have low solubilities at neutral pH. In circumneutral waters under oxidizing conditions, these metals are readily adsorbed onto Fe oxyhydroxides, complexed with organics, or precipitated as hydroxides or carbonates at elevated pH. All form sulfide or oxide minerals, and with the exception of

Fe and Cu are not found in their native state. Despite these similarities, variations in their oxidation states and their crustal abundances allow differences in their geochemical behavior in the environment.

Chromium (Cr)

Chromium is a trace element in the natural environment, occurring mainly as trivalent Cr^{III}, and readily substituting for Fe^{III} in oxides and hydroxides. Toxic hexavalent Cr^{VI} is found only under highly oxidizing conditions, usually from anthropogenic activities. Commonly mined as chromite ($FeCr_2O_4$) a refractory mineral associated mainly with ultramafic rocks and used to line blast furnaces. It is used for its corrosion resistance in chromium steel and metal plating, for its chromatographic characteristics in paints and dyes, in explosives, pesticides, and drilling mud, as well as in pressure-treated wood as chromated copper arsenate. Although trivalent Cr^{III} is an essential micronutrient, hexavalent Cr^{VI} is a neurotoxin and carcinogen at levels as low as 50 ppb. It gained public attention following the lethal contamination of Baechtel Creek in California by the dumping of plating liquids up to 1995.

Concentrations in natural waters are typically in the range of 1 to 20 ppb, and average only generally below the WHO guideline of 50 ppb in drinking water. Seawater contains less than 1 ppb Cr. Cr^{III} has very low solubility in natural waters, where it exists in sixfold coordination with H_2O as $Cr(H_2O)_6^{3+}$) below pH 3.8, and as the hydroxide $Cr(OH)^{2+}$ up to neutral pH (Figure 9.28). Under alkaline conditions, $Cr(OH)_3$dominates. Only above pH 11.5 does Cr^{III} dominate as an anion, $Cr(OH)_4^-$. Under neutral pH conditions, solid chromium hydroxide ($Cr[OH]_{3(s)}$) maintains $Cr(OH)_3^o$ concentrations at less than about 5 ppb. In lower pH waters, the cation forms are readily sorbed onto clays or precipitate with iron oxyhydroxides.

Cr^{III} can be oxidized to Cr^{VI} under natural conditions by O_2 or other electron acceptors, including NO_3^- and Mn^{4+}. Unlike Cr^{III}, hexavalent Cr^{VI} forms chromic acid (H_2CrO_4). Dichromate ($Cr_2O_7^{2-}$) dominates in natural waters up to pH 6.5 where

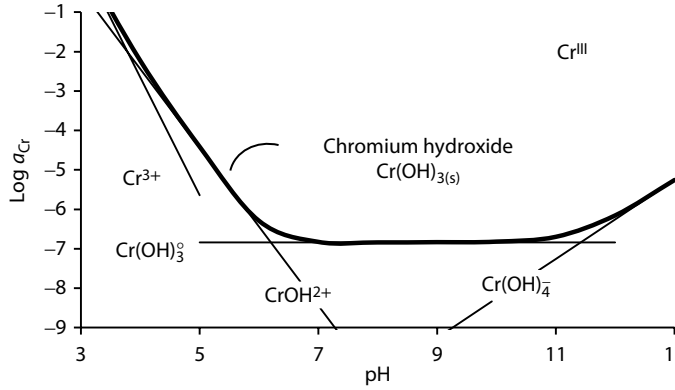

FIGURE 9.28 Cr^{III} speciation and solubility. (Based on Rai et al. 1987; Palmer and Wittbrodt 1991; Wu et al. 2008.)

it dissociates to chromate (CrO_4^{2-}) (Figure 9.29). These anions are highly soluble but are readily reduced back to Cr^{III} by organic carbon and other elements of lower redox potential, including ferrous iron (Fe^{II}) and sulfide. Seldom do chromate concentrations exceed a few ppb in natural waters. Hem (1985) cites pH 9 groundwaters with up to 200 ppb Cr as CrO_4^{2-}. The hyperalkaline groundwaters in northern Jordan (see Example 6.11) that discharge at pH 12.5 are pale green with 7.02 ppm Cr (Khoury et al. 1992).

Trivalent Cr^{III} dominates in groundwater as it is slow to oxidize, and does so only at a high electromotive potential (Figure 9.30). From this diagram, only manganese, nitrate, or oxygen can be used to oxidize trivalent chromium to soluble hexavalent Cr^{VI}.

The release of hexavalent chromate from industrial activities has led to reactive barrier technologies to mitigate its mobility (Blowes and Ptacek 1992). These make use of the low solubility of trivalent chromium hydroxide, providing it can be reduced to this form. From Figure 9.30, any electron donor below the Cr^{VI}/Cr^{III} line can potentially reduce chromate to precipitate trivalent chromium hydroxide ($Cr[OH]_{3(s)}$). Examples are reduction with ferrous iron and with carbon, although the most effective reduction rates were observed when using zero-valence iron as the electron donor with precipitation of ferric chromium oxyhydroxide $CrFe(OOH)_2$:

$$CrO_4^{2-} + 3Fe^{2+} + 5H_2O \rightarrow Cr(OH)_3 + 3Fe(OH)_2^+ + H^+$$

$$2Cr_2O_7^{2-} + 3CH_2O + 4H^+ + H_2O \rightarrow 4Cr(OH)_3 + 3CO_2$$

$$CrO_4^{2-} + Fe^0{}_{(s)} + 2H^+ \rightarrow CrFe(OOH)_{2(s)}$$

These reactions were traced using chromium isotopes in batch experiments to monitor the reduction of chromate to chromium hydroxide using fixed carbon (Jamieson-Hanes et al. 2012) and using ferrous iron (Kitchen et al. 2012) as the electron donor. As discussed for other systems, isotopes resolve reactive loss of a contaminant from attenuation by dispersion and mixing, which are not fractionating. Chromium has four stable isotopes, ^{50}Cr (4.35%), ^{52}Cr (83.8%), ^{53}Cr (9.5%), and ^{54}Cr (2.37%). The ^{53}Cr to ^{52}Cr ratio is typically measured, using a multicollector ICP-MS,

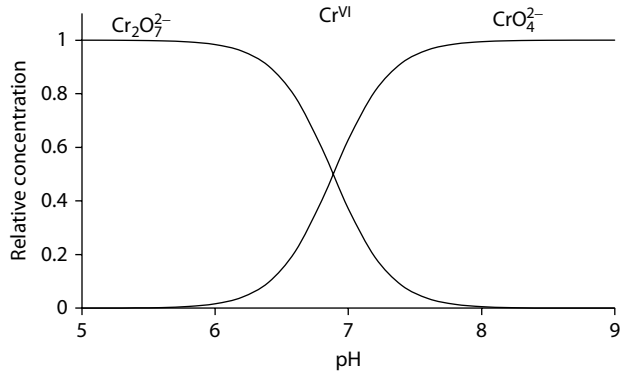

FIGURE 9.29 Cr^{VI} speciation with pH. Toxic chromate ions are highly soluble.

and is referenced to a National Institute of Standards and Technology chromium nitrate solid (NIST SRM 979) and expressed in the standard delta-permil fashion as $\delta^{53}Cr‰$ SRM 979. The experimental data for chromate reduction by ferrous iron and organic carbon are shown in Figure 9.31. Both impart an enrichment on the residual chromate, suggesting that $\delta^{53}Cr$ can be a useful tool to track chromate reduction and attenuation in field sites of hexavalent chromium contamination.

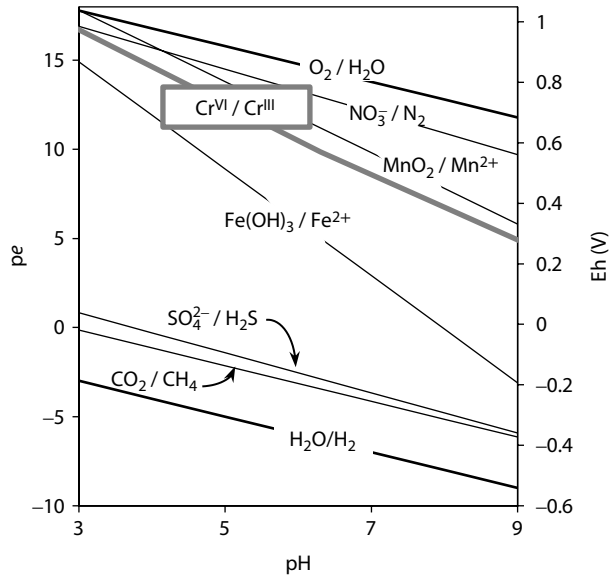

FIGURE 9.30 Electromotive potential for the Cr^{VI}/Cr^{III} redox reaction.

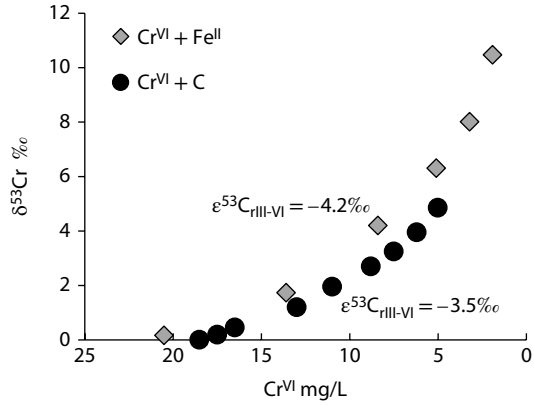

FIGURE 9.31 $\delta^{53}Cr$ fractionation and Rayleigh distillation during reduction of Cr^{VI} chromate to Cr^{III} using ferrous iron at pH 5 (gray diamonds; Kitchen et al. 2012) and with organic carbon (black discs; Jamieson-Hanes et al. 2012). Both reduction reactions show Rayleigh-type enrichments in ^{53}Cr, with enrichment factors of $\varepsilon^{53}Cr_{VI\text{-}III} = -4.2‰$ for Cr^{VI} reduction with ferrous iron, and $\varepsilon^{53}Cr_{VI\text{-}III} = -3.5‰$ for reduction on carbon.

Manganese (Mn)

Manganese has a crustal abundance of 950 ppm and is the second most abundant transition metal, after Fe at 5%. It is used extensively in the steel industry alloyed with iron to improve strength and durability. Its distinctive pink color is used in paints, glass, and ceramics. As Mn^{VII} in permanganate, MnO_4^-, its high electromotive potential makes it a strong oxidant for matches, fireworks, and as a laboratory reagent (e.g., potassium permanganate ($KMnO_4$). Mn is an essential nutrient for life, and is often added as a component of fertilizers.

Manganese behaves very much like iron in natural waters, with high solubility in its reduced, Mn^{2+} state, but highly insoluble in its oxidized states, Mn^{3+} and Mn^{4+}. It has only one stable isotope, ^{55}Mn. Divalent Mn^{II} substitutes for ferrous iron (Fe^{II}) as well as for Mg and Ca in mafic minerals as well as limestone and dolomite. Mn^{II} minerals are pink, such as rhodochrosite ($MnCO_3$), and rhodonite ($[Mn,Fe,Ca]SiO_3$), and gives amethyst quartz its mauve hue. Weathering of mafic rocks liberates soluble Mn^{II} into solution, although under aerobic conditions it is rapidly oxidized to Mn^{III} and Mn^{IV} and precipitates in fractures and soils as various low-temperature phases, including amorphous β–MnO_2, Mn_2O_3, and Mn_3O_4.

Mn^{IV} has a redox potential lower than NO_3^- but above ferric iron. MnO_2 is an important electron acceptor that participates in the oxidation of dissolved organics, methane, sulfides, ferrous iron, trivalent arsenic, and other lower redox potential species. Problematic in many groundwaters are high levels of Mn^{2+} and Fe^{2+} released to solution through reduction of $Fe(OH)_3$ and MnO_2 in aquifers by oxidation of dissolved organics. Dissolved Fe and Mn are then reoxidized in the oxygenated zone near well screens by bacteria, biofouling wells and reducing yield.

Mn^{III} and Mn^{IV} oxides maintain dissolved Mn concentrations at less than 50 ppb in aerobic groundwaters, usually coprecipitated with ferrihydrite ($Fe[OH]_3$). In the anaerobic environment, Mn-oxides react with organics, reducing manganese to the more soluble Mn^{II}. Here, the strongest mineralogical control on solubility is the carbonate form. Neutral pH waters with total DIC of 10 ppm C will support a dissolved Mn^{2+} concentration of over 3 ppm, but only 0.3 ppm at pH 8. Higher DIC concentrations reduce Mn^{2+} proportionally.

Manganese is not considered to be a contaminant. It is an essential nutrient for plants and animals, and has not been shown to be toxic or carcinogenic except under extreme doses potentially encountered under some mining situations. Water quality limits are set at 0.5 ppm for aesthetic purposes, as it produces black staining.

Cobalt (Co)

Cobalt is a trace metal with a crustal abundance of only 25 ppm. Like iron, it can be magnetized, but its major use is to improve strength and corrosion resistance of steel when alloyed with iron and nickel. A Co–Cr alloy is used for hip and knee joint replacements. Co-oxides provide blue tints in glass and ceramics. As a structural component of vitamin B-12, cobalt is an essential micronutrient for plants and animals, and can be added as sulfate to phosphate fertilizers. It has one stable isotope, ^{59}Co, and one long-lived radionuclide, ^{60}Co, produced by neutron activation of ^{59}Co

in nuclear reactors. It decays to ^{60}Ni by beta emission ($T_{½} = 5.27$ years), with strong gamma radiation that is used in nuclear medicine. Stable cobalt is generally coproduced from copper–nickel deposits, where it occurs in a variety of sulfides and arsenides, with releases to the environment through smelting operations and coal-fired generating plants. Cobalt is soluble under lower pH conditions, and generally follows Fe and Mn oxyhydroxides.

Freshwaters seldom exceed 1 ppb except where anthropogenic sources exist. Both divalent Co^{II} and trivalent Co^{III} exist in natural waters, although $Co^{III}$is a strong oxidant and readily converted to soluble divalent cobalt. Uncomplexed Co^{2+} and inorganic complexes such as $CoCO_3^0$ dominate in freshwaters. However, transport is dominantly in colloidal form complexed with organics or adsorbed to Mn and Fe oxyhydroxides. Like most transition metals, higher concentrations are favored at lower pH. Under anoxic conditions, cobalt sulfides are highly insoluble.

Cobalt is not biomagnified in ecosystems, although it is accumulated by both plants and organisms. It is not identified as a contaminant by either WHO or US EPA and has no drinking water limit. Environmental regulations for surface water quality limit Co to 0.1 ppm.

Nickel (Ni)

Like Co, nickel has similar geochemical characteristics to iron, with which it is alloyed in the core of the terrestrial planets and in iron meteorites. Its concentration is lower in the mantle, and only 75 ppm in the crust, associated preferentially with mafic and ultramafic rocks, where it substitutes for Fe^{2+} and Mg^{2+}. Nickel is found in economic concentrations as pentlandite ($[Fe,Ni]_9S_8$) associated with copper sulfide, but also as iron–nickel oxyhydroxides and nickel arsenides, such as niccolite (NiAs). It is used primarily for its anticorrosion and high strength characteristics in the production of stainless steel and in nickel plating.

Like Co, divalent Ni^{II} dominates in minerals and waters. It is essentially insoluble as a sulfide. Under aerobic conditions, nickel tends to be relatively mobile. It becomes increasingly soluble as Ni^{2+} below pH 6. At higher pH, nickel is readily transported as inorganic and organic chelates, or is adsorbed onto Fe and Mn oxyhydroxides. Above pH 9, solubility is limited by its hydroxide ($Ni[OH]_2$) ($K = 10^{-15.26}$) to less than 1 ppm. Although nickel has five stable isotopes, little development as tracers exists, given the relatively low reactivity and redox of nickel in the environment.

Natural surface waters typically carry low to sub-ppb concentrations of Ni, although values over 100 ppb–10 ppm can be found in high source-term regions and mining camps. As nickel partitions onto solid phases, freshwater sediments have concentrations averaging 25 ppm in background regions. Seawater has less than 1 ppb Ni, where scavenging by particulates and organics control solubility. Similarly, groundwaters seldom have concentrations over 10 ppb. Drinking waters have typically less than 10 ppb Ni. The WHO provides a drinking water limit of 20 ppb, although no adverse health effects in humans from ingested nickel have been demonstrated.

Copper (Cu)

Copper has a crustal abundance of only 55 ppm and is one of the least abundant transition metals. Nonetheless, it is significantly concentrated during magmatic and hydrothermal activity as insoluble sulfides. Chalcopyrite ($CuFeS_2$) is the most common ore mineral, although Cu forms other sulfide minerals as well as a host of oxides, such as cuprite (Cu_2O) and carbonates including azurite ($2CuCO_3{\cdot}Cu[OH]_2$) and malachite ($CuCO_3{\cdot}Cu[OH]_2$). It is also one of the few metals to be found and mined in its elemental state, as native Cu^0. It is an essential trace element for metabolism in plants and animals, but at higher concentrations becomes toxic to microorganisms and so is used in pesticides, in antifouling paints for marine boat hulls, and in pressure-treated wood as chromated copper. Copper has two stable isotopes, ^{63}Cu (69.17%) and ^{65}Cu (30.83%), expressed as $\delta^{65}Cu$ referenced to the NIST 976 Cu standard, which have been shown to fractionate between Cu^I and Cu^{II} redox states during copper mineralization (Braxton and Mathur 2011). Partitioning during aqueous complexation and transport suggests species-dominated fractionation (Maréchal and Albarède 2002) although only minor in natural aqueous systems (Bigalke et al. 2010).

Weathering of copper mineralization is the dominant natural source of Cu in aquatic systems above background levels of several ppb. Runoff from mining camps and tailings, particularly if acidic, and fallout from smelting are sources of much higher concentrations in the environment. In minerals and waters, cupric Cu^{II} predominates. Monovalent or cuprous Cu^I is unstable under most pH conditions, and rarely found. Like other transition metals, copper has a strong affinity for adsorption onto organic and inorganic substrates, including ferric oxyhydroxides and clays. Accordingly, its solubility as Cu^{2+} is favored only at low pH, allowing concentrations in the range of 100–1000 ppm in acid mine drainage.

Copper hydroxide ($Cu[OH]_2$) limits Cu^{2+} solubility to less than 1 ppm at circumneutral pH and in the low ppb range at higher pH (Figure 9.32). DIC further reduces copper solubility by precipitation of malachite ($Cu_2[OH]_2CO_3$). Copper can be concentrated in reducing environments by reduction to monovalent Cu^I and precipitation as chalcosite (Cu_2S).

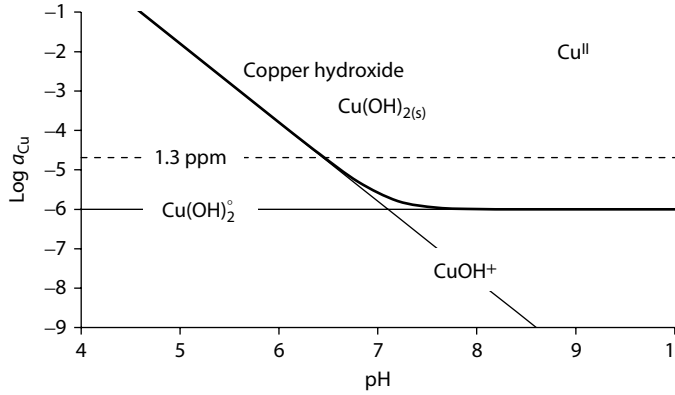

FIGURE 9.32 Solubility of copper hydroxide ($Cu[OH]_2$), with pH. (After Cravotta 2008.)

Natural surface waters have less than 0.1 ppm dissolved Cu. Similarly, groundwater concentrations are limited by sorption to less than 1 ppm. In natural waters, sorption seems to limit dissolved copper to concentrations below those predicted by pH-mineral stability calculations. The WHO recommends an upper limit of 2 ppm for copper in drinking water, based on potential gastrointestinal irritation at higher levels, and aesthetic qualities of taste and staining. The US EPA sets a limit for drinking water at 1.3 ppm. The Canadian water quality guideline for aquatic life is 4 ppb and for irrigation waters is 200 ppb.

Zinc (Zn)

Zinc has a crustal abundance of 70 ppm, but is concentrated by hydrothermal solutions. Sphalerite (ZnS) is the principal ore-forming mineral, most commonly found in association with galena (PbS) filling dissolution voids in carbonate rocks. Zn replaces Fe and other divalent metals in a host of minerals including magnetite and ferromagnesian silicates. The greatest industrial use of zinc is in galvanization of steel to reduce corrosion by Zn-electroplating or hot dipping into molten zinc. It is also used in alloys, particularly with copper to produce brass. Metallic zinc is rolled as malleable sheeting for batteries, roofing, and other applications requiring low-corrosion seals.

In the weathering environment, Zn retains its divalent state and is soluble under acidic conditions where Zn^{2+} is stable. Zn^{2+} is the dominant dissolved species below pH 7, whereas under alkaline conditions, $ZnHCO_3^+$ and $Zn(OH)^+$ become the important dissolved phases. At higher pH, zinc hydroxide ($Zn[OH]_2$) limits solubility (2 ppm at pH 8). Dissolved Zn^{2+} is also very sensitive to DIC, as smithsonite ($ZnCO_3$) ($K = 10^{-10}$) is a significant control when DIC exceeds about 10 ppm. At very high pH, anionic Zn hydroxides such as $Zn(OH)_4^{2-}$ enhance solubility, although such environments are restricted to cement pore waters, coal fly-ash deposits, and slags where Na and Ca hydroxides may leach.

Like other transition metals, Zn is preferentially sorbed onto humic substances and iron hydroxides in water. Under circumneutral to high pH conditions, this is the dominant control on Zn solubility, and is responsible for the low concentration in most natural waters. Concentrations in natural groundwater seldom exceed 100 ppb, and less than 50 ppb in lakes, where sorption onto organics and uptake by microorganisms occur. Higher concentrations are commonly associated with wastewater discharges, particularly from sewage plants. Acid mine drainage can be very significant point sources of Zn^{2+} in aquatic systems (Figure 9.33).

Accumulation by sorption onto particulates and solid organic carbon is reflected by the concentration of Zn in sediments, which averages about two times its crustal abundance. Zn has four stable isotopes, ^{64}Zn (48.6%), ^{66}Zn (27.9%), ^{67}Zn (4.1%), and ^{68}Zn (18.8%), and measurements are made of the ^{66}Zn to ^{64}Zn ratio, expressed as $\delta^{66}Zn$. The sorption and cycling of Zn in these aqueous systems suggest that isotope fractionation could be significant (Maréchal and Albarède 2002).

Zinc is an essential nutrient, required in biological systems for the synthesis of nucleic acids and enzymes. Drinking water standards have a relatively high limit of 3–5 ppm based on aesthetic considerations. Humans require about 10–20 mg Zn daily. In aquatic systems, standards are more severe, due to high bioaccumulation

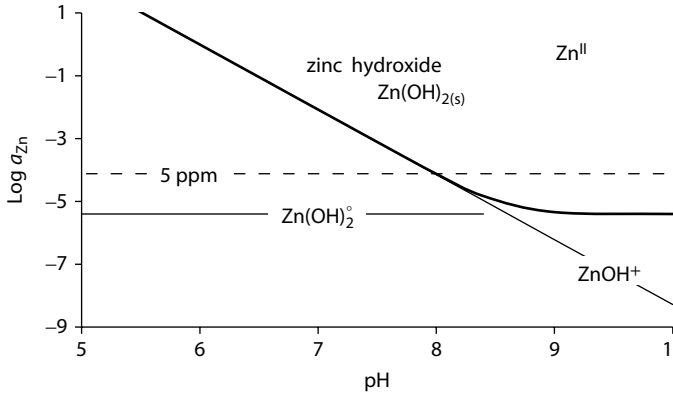

FIGURE 9.33 Zinc hydroxide speciation and solubility with pH.

factors in biota. Maximum allowable concentrations of dissolve Zn are set in the low ppb range (EPA indicates 17 ppb), although this limit rises progressively to over 300 ppb in high DIC waters due to complexation with carbonate.

SALINITY IN GROUNDWATER

Groundwater salinization can represent a considerable threat to freshwater resources. Salinity increases can be due to overexploitation and induced intrusion of saline waters or to anthropogenic inputs from surface or injection wells. In either case, tracing the source is important to establish the pathway and possible approaches to remediation. Figure 9.34 provides typical sources and ranges of salinity impacts on groundwater resources.

Seawater Evaporation and Bedrock Brines

Ultimately, most of the Cl^- in saline groundwaters is derived from marine sources, whether as evaporite minerals in sedimentary strata or through infiltration of seawater and evaporated basin brines into the subsurface. Modern seawater has a Na–Cl facies, with a minor Mg–SO_4 component and trace Ca–HCO_3 (Table 9.4). Although the overall salinity of seawater has been fairly constant over the Phanerozoic, the Ca and Mg composition has varied to a certain extent, which has an impact on the minerals that precipitate from evaporite basins in the past (Lowenstein et al. 2003). Evaporation of modern seawater follows a geochemical evolution that is generated by the solubility of the carbonates, sulfates, and chloride minerals. The reaction series was determined empirically by McCaffey et al. (1987) through measurements from brine evaporation ponds. They found the sequence of mineral controls to be first the calcium carbonates (calcite and aragonite) followed closely by gypsum, such that by 4× seawater concentration, Ca begins to drop out of solution. By 10.6× seawater, halite begins precipitating, which holds the Cl^- concentration constant for most of the balance of evaporative enrichment, and Na^+ begins to drop, such that by 50× seawater, the geochemical facies has shifted from Na–Cl to Mg–Cl. By 70× seawater

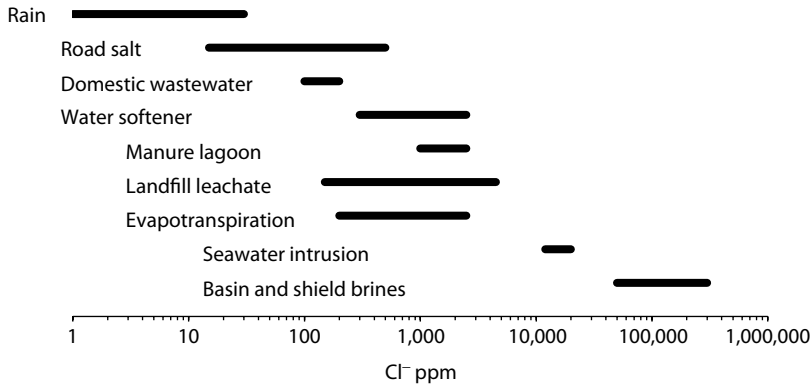

FIGURE 9.34 Sources and ranges for chloride in groundwaters. (Data from Eriksson 1952; Howard and Haynes 1993; Krapac et al. 2002; Kinsley et al. 2005; Christensen et al. 2001; Clark et al. 2013.)

TABLE 9.4
Geochemistry and Isotopes of Seawater

Anions	ppm	mmolal	Cations	ppm	mmolal
Cl^-	19,350	546	Na^+	10,760	468
SO_4^{2-}	2,710	28.3	Mg^{2+}	1,290	53.1
HCO_3^-	142	2.33	Ca^{2+}	411	10.3
Br^-	67	0.84	K^+	399	10.2
F^-	1.3	0.068	Sr^{2+}	8	0.091
I (I^- and IO_4^-)	0.045	0.00035	Li^+	0.18	0.026
NO_3^- (as N)	0.005–2	$0.8–300 \times 10^{-4}$	Ba^{2+}	0.02	0.00015
$H_3PO_{4(total)}$ (as P)	0.001–0.05	$1–50 \times 10^{-5}$	$H_4SiO_4^\circ$ (as Si)	0.03–10	0.001–0.3
$H_3BO_{3(total)}$ (as B)	4.5	0.42	DOC	0.3–2 as C	0.02–0.2

Isotopes

$\delta^{18}O$	0‰ VSMOW	$\delta^{13}C_{DIC}$	0‰ PDB	$\delta^{34}S_{SO4}$	21‰ CDT
δD	0‰ VSMOW	$\delta^{13}C_{DOC}$	–27‰ PDB	$\delta^{18}O_{SO4}$	9.5‰ VSMOW
δ^6Li	–32.3‰ LSVEC	$\delta^{18}O_{PO4}$	19.7‰ VSMOW	$\delta^{37}Cl$	0‰ SMOC
$\delta^{11}B$	40.4‰ NBS 951	$^{87}Sr/^{86}Sr$	0.707924	$\delta^{81}Br$	0‰ SMOB

Sources: Bernat et al. 1972; Drever 1997; Tsunogai and Henmi 1971.

concentration, Mg^{2+} and SO_4^{2-} begin to coprecipitate as epsomite ($MgSO_4 \cdot 2H_2O$). The final phase of mineral precipitation is potassium chloride, sylvite, although K^+ losses by coprecipitation with halite along the way have attenuated its enrichment during evaporation.

The strong evaporative effect on seawater in restricted seas such as the Dead Sea and the Red Sea has generated salinity-enriched brines. From the sequence of reactions in Figure 9.35, the geochemical facies of the evaporating seawater shifts

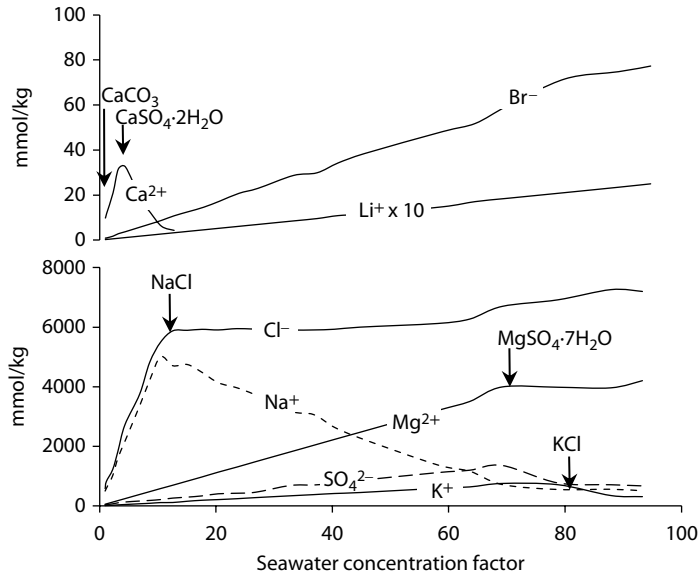

FIGURE 9.35 Evolution of seawater chemistry during evaporation and salt formation, in the order of calcium carbonate ($CaCO_3$), gypsum ($CaSO_4{\cdot}2H_2O$), halite (NaCl), epsomite ($MgSO_4{\cdot}7H_2O$), and sylvite (KCl). (Data from McCaffrey et al. 1987.)

from Na–Cl to Mg–Cl through the precipitation of halite. This is observed for the Dead Sea, which has some 400 m of halite deposited as deep sediments and along the shoreline as a coating on coastal rocks. Brines also exist in the deep subsurface. Early drilling for oil and gas showed that deep sedimentary formations also host brines, typically accompanied by a Na–Cl facies. Early mining reports were the first to document hypersaline brines deep in crystalline basement rocks such as the Canadian Shield. In the ensuing decades since Chebotarev, a greater understanding of the origin of subsurface brines has been developed. New geochemical and isotopic tools show that these brines have not been generated simply through extensive water–rock interaction, but likely originated as highly evaporated seawater in epicontinental seas. Their high density allowed infiltration into the subsurface, displacing preexisting seawater in the fractures and porosity of the underlying bedrock. In the past, such evaporitic seas generated the thick evaporite beds now mined for salt.

Infiltration of these high-density, high-chloride brines into the subsurface led to a sequence of reactions that altered their geochemical facies. The starting brines would have been close to that of the Dead Sea, with a Mg–Cl facies. Penetration through carbonate strata consumed Mg, with release of Ca engendered geochemical evolution toward that of the Basin brine. Further evolution through smectite shales into the basement crystalline rocks consumed K^+ by illitization and exchanged Na^+ for Ca^{2+} by albitization of anorthite feldspar under conditions of very low water-to-rock ratios over long periods of time and elevated temperature (Figure 9.36).

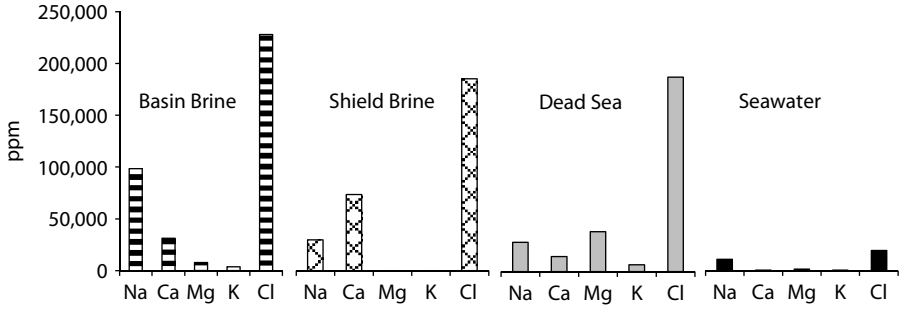

FIGURE 9.36 Major ion geochemistry of highly evaporated basin brine (Intera 2011), crystalline shield brine (Douglas et al. 2000), Dead Sea water, and modern seawater.

Dolomitization $2CaCO_3 + Mg^{2+} \rightarrow MgCa(CO_3)_2 + Ca^{2+}$

Illitization of smectite $NaAl_2Si_4O_{10}(OH)_2 + K^+ \rightarrow KAl_2Si_4O_{10}(OH)_2 + Na^+$

Albitization $CaAl_2Si_2O_8 + 2Na^+ + 4H_4SiO_4 \rightarrow 2NaAlSi_3O_8 + 8H_2O + Ca^{2+}$

Stable Isotopes and Sources of Salinity

The origin of salinity in groundwaters can often be determined from the hydrogeological context, including groundwater flow directions and candidate sources of salinity. Geochemical facies are important in such evaluations, but can be ambiguous due to subsurface processes, such as cation exchange. Chloride is a conservative tracer of salinity that can be complemented by stable isotopes, which also behave conservatively in most cases.

If salinity in groundwater is gained by mixing in the subsurface, whether from seawater intrusion or deeper crustal brine from bedrock, the isotope signature of the saline water will be conservative during mixing and can be diagnostic. Salinity gained through dissolution of evaporite minerals will not have a measurable effect on the stable isotope contents of the impacted groundwaters. Two case studies in Figure 9.37 illustrate these two scenarios.

Sources of salinity can also be traced on the basis of the $\delta^{37}Cl$ and to a lesser extent with $\delta^{81}Br$ in dissolved halides. These halides do not participate in any redox reactions in groundwaters, which are responsible for the strong fractionations observed in the N, C, and S cycles. Halide isotope fractionation is then limited to mineral reactions, such as evaporite dissolution and precipitation, and diffusion through low permeability materials. Further limiting fractionation are the lower mass effects provided by these isotopes. For $^{37}Cl/^{35}Cl$ this is less than 6% compared with 12.5% for $^{18}O/^{16}O$, and is only 2.5% for $^{81}Br/^{79}Br$. Consequently, $\delta^{37}C$ varies typically within a range of only a few permil, and $\delta^{81}Br$ less. Stotler et al. (2010) show that $\delta^{37}C$ for Shield brines in Canada and Scandinavia vary within a range of −1‰ and +2‰ SMOC (standard mean ocean chloride). Values for $\delta^{81}Br$ fall within a range of 0‰–2‰ SMOB (standard marine ocean bromide). Measurements of Cl^- in

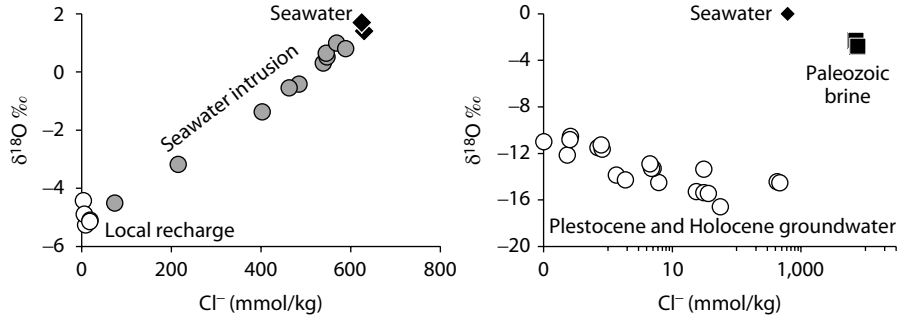

FIGURE 9.37 Salinization by seawater intrusion (left: modified from Sivan et al. 2005) is clearly identified by the mixing line between local seawater and locally recharged groundwater. In contrast, groundwater circulation to as deep as 330 m shows no mixing with deeper brine (380 m) in carbonate strata from the Michigan Basin and has gained salinity from evaporite dissolution (right; Clark et al. 2013), which has no effect on $\delta^{18}O$ or δD. The variation in $\delta^{18}O$ of the groundwaters is due to variable contributions from residual glacial meltwater with depleted $\delta^{18}O$ and δD resident in the subsurface since deglaciation some 12,000 years ago.

basin brines are more depleted in ^{37}Cl. In contrast, marine halite from evaporite deposits spanning the Phanerozoic (Cambrian to Tertiary) have marginally positive $\delta^{37}Cl$ values ranging from 0.0‰ to 0.9‰ SMOC (Eastoe et al. 2007) due largely to fractionation during crystallization.

Road Salt in Urban Aquifers

Urban hydrogeology has become an important field in view of the rapid pace of development in rural regions. Considerable focus has been made on the use of deicing chemicals, which are greatly dominated by halite. Infiltration into the subsurface is of course aggravated by the capacity of the chloride brine runoff to penetrate frozen soil and represents perhaps the most significant single threat to groundwater quality in urban regions (Howard et al. 1993). The increases in Na^+ and Cl^- are not the only threats to water quality. Bäckström et al. (2004) show releases of sorbed Cd, Cu, Pb, and Zn due to cation exchange in soil water following road salting.

A good example of road salt impact is the Waterloo moraine, which supplies the twin cities of Kitchener and Waterloo, Ontario, with groundwater from a series of well fields. Monitoring of groundwater quality at the Greenbrook well field over the past several decades shows a steady increase in Cl^- from levels below 50 mg/L back in the early 1970s to levels above the drinking water limit by 2000 (Bester et al. 2006; Figure 9.38). Further, the steady increase in Cl^- correlates with increased urbanization, including the addition of new local and arterial roads that are salted in winter months. The impact of these increased road-salt loadings on the aquifer was modeled in a three-dimensional grid that captured the complex architecture of the glacial outwash sediments (Bester et al. 2006), using the measured increases of Cl^- from a series of wells for calibration. Figure 9.38 shows infiltration of Cl^- from the main arterial network. Projections from the study allowed testing of mitigation strategies and a modification of the protocols for road-salt applications.

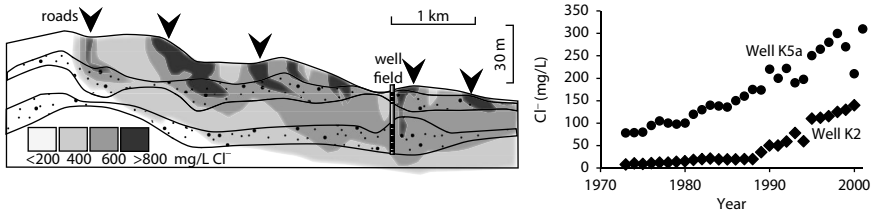

FIGURE 9.38 Increased Cl^- in urban water supply well and modeled inputs from regional road deicing salt (after Bester et al. 2006). Road crossings on section are shown with downward arrowheads.

Mitigation of the impacts of salinity buildup in urban aquifers requires reliable identification of the source of salinity. An increase in Cl^- in groundwaters cannot necessarily be attributed to road salt. Domestic septic infiltration beds are typically a source of Na^+ and Cl^-, largely from the prevalence of salt in food. Landfill leachate (above) is also enriched in Na^+ and Cl^- from domestic waste. Finally, deep crystalline and sedimentary basin settings typically host hypersaline brines mixed to varying degrees with meteoric waters. However, each of these sources has additional geochemical components that can be useful in discriminating the source of salinity. Although Na–Cl ratios can be distorted by cation exchange along the flow path, Br^- and I^- are good complements to Cl^-. These heavier halides are generally enriched in bedrock brine, which is derived from evaporated seawater but depleted in road salt. Nitrogen species and DOC are useful in identifying domestic wastewater and landfill leachate (Panno et al. 2006), as they have significant enrichments in these sources (Figure 9.39).

Sources of Sulfate in Groundwater

The Chebotarev model for the evolution of geochemical facies in groundwater (Chapter 7) shows that between the shallow low-salinity bicarbonate groundwaters and the deep chloride brines is an intermediate facies dominated by the solubility of sulfate minerals like gypsum, which provide salinities over 2000 ppm TDS and has an impact on water quality. The availability of SO_4^{2-} in anoxic aquifers with organic carbon stimulates sulfate reduction, and production of toxic H_2S. Hydrogen sulfide can be detected by odor at less than 0.01 ppmv in air and is an irritant at 20 ppmv. Above 100 ppmv it neutralizes the olfactory nerve so is no longer detected by scent and becomes lethal at 300 ppmv. Hydrogen sulfide is a weak acid in water, with a dissociation constant of 10^{-7}, and so at pH 7, it is 50% dissociated into ionized HS^-. At low pH, unionized H_2S dominates. Sulfate, by contrast, is a strong acid and so only below pH 2 does the first dissociation species, HSO_4^-, become important in increasing solubility.

Sulfate in groundwater has the capacity to compromise water quality both by the elevated salinity it can contribute (drinking water limit is 250 ppm), and by the potential for reduction to toxic H_2S. Sources of sulfate in groundwater include the dissolution of gypsum and anhydrite:

$$CaSO_4 \cdot 2H_2O \rightarrow Ca^{2+} + SO_4^{2-} + 2H_2O \qquad K_{gyp} = 10^{-4.58}$$

$$CaSO_4 \rightarrow Ca^{2+} + SO_4^{2-} \qquad K_{anh} = 10^{-4.36}$$

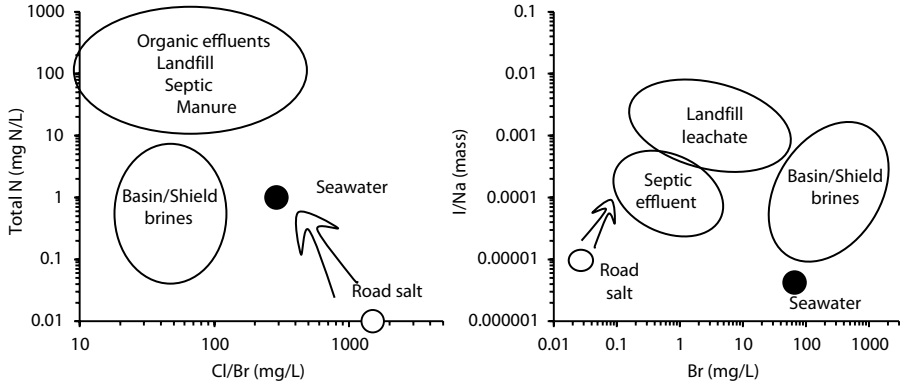

FIGURE 9.39 Distinguishing sources of salinity in groundwater with halides and nitrogen species. (Modified from Panno et al., 2006, with data from Bottomley et al. 2002 and 2005.)

Gypsum dissolution can generate some 1500 ppm SO_4^{2-} in solution. Without the solubility control of Ca^{2+} in, for example, acid mine drainage, SO_4^{2-} concentrations can increase to the g/L range. Other sulfate minerals, such as celestite ($SrSO_4$; $K_{cel} = 10^{-6.63}$) and barite ($BaSO_4$; $K_{bar} = 10^{-9.97}$) are highly insoluble and maintain SO_4^{2-} concentrations below 100 ppm. The other principle source of sulfate in groundwater is from the oxidation of pyrite:

$$FeS_2 + 3\frac{1}{2}O_2 + H_2O \rightarrow Fe^{2+} + 2SO_4^{2-} + 2H^+$$

This proceeds naturally in soils developed on newly exposed materials, such as glacial till which may have a component of pyrite that can be oxidized and contribute sulfate to the recharging groundwaters. This also takes place, although perhaps more slowly, during the weathering of sulfide-bearing bedrock, such as black shales and ore bodies. Exposure of such materials to atmospheric oxygen as a consequence of mining or road construction, as discussed above, is a mechanism to release sulfate to the environment.

In the past, industrial sources from sulfide ore smelting and coal-fired thermal generating stations contributed to sulfate in groundwaters and surface waters through oxidation of SO_2 emissions. Strict controls on these atmospheric releases have greatly reduced this source of sulfate in groundwaters recharged in recent decades.

Determining the sources of sulfate and sulfide in groundwater is helped by measuring their isotopes, $\delta^{34}S_{SO_4^{2-}}$, $\delta^{34}S_{H_2S}$, and $\delta^{18}O_{SO_4^{2-}}$. The $\delta^{34}S$ of sulfate can be simplified into that originating from marine sulfate, which is enriched in ^{34}S and that originating from oxidation of sulfide and other reduced sources such as mantle and volcanic sulfur, which are depleted in ^{34}S. Today, seawater sulfate has a $\delta^{34}S$ value of 21‰ CDT and a $\delta^{18}O$ value of 9.5‰ VSMOW. In the past, $\delta^{34}S_{seawater}$ varied between about 10‰ and 30‰, essentially controlled by the relative fluxes of carbon and sulfur through oxidation and reduction (Veizer et al. 1980). Oxygen-18 followed a more constrained range averaging close to 15‰ during most of the Phanerozoic with excursions up to 16‰ during the Carboniferous and down to 10‰ during the Permian (Figure 9.40). Values for marine $\delta^{18}O_{SO_4^{2-}}$ are largely controlled

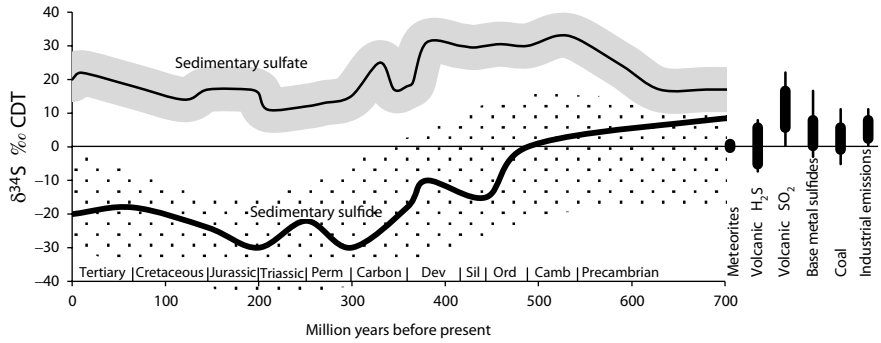

FIGURE 9.40 Ranges in $\delta^{34}S$ in sedimentary (marine) sulfate and diagenetic sulfide over the Phanerozoic era. The $\delta^{18}O$ of marine sulfate was close to 15‰ VSMOW over the Phanerozoic. (Data from: Claypool et al. 1980; Veizer et al. 1980; Turchyn and Schrag 2006; Seal 2006.)

by continental oxidation of sulfides with varying contributions of ^{18}O from the water ($\delta^{18}O \approx -5$ to -20‰) and from atmospheric O_2 ($\delta^{18}O = +23.5$‰).

Sulfate derived from dissolution of marine gypsum or anhydrite will then be enriched in ^{34}S, while sulfate derived from sulfide oxidation will be depleted, allowing some insight to the source of sulfate in groundwater. The difference between the two forms is largely due to the fractionation that accompanies sulfate reduction. Bacterial reduction of sulfate in marine sediments is accompanied by a fractionation, $\varepsilon^{34}S_{SO_4^{2-}-H_2S}$, between about 20‰ and 30‰, and so sedimentary pyrite has the low values seen in Figure 9.40. Sulfide in coal and sulfide ore is similarly depleted, with $\delta^{34}S$ values less than 10‰. Mantle-derived sulfide (volcanic H_2S) and meteorites also have $\delta^{34}S$ values near or less than 0‰.

Rayleigh distillation during sulfate reduction to H_2S has strong impact on the $\delta^{34}S$ (and $\delta^{18}O$) of sulfate, which can be useful to identify reactions and sulfate loss. As discussed in Chapter 7, both isotopes become enriched during bacterial sulfate reduction, with $\delta^{34}S$ values reaching 40‰ and higher.

Both ^{34}S and ^{18}O Isotopes of sulfate are also diagnostic of atmospheric deposition from industrial emissions associated with energy production. These sources are characterized by low $\delta^{34}S$ below about 10‰ (Figure 9.40) and an elevated $\delta^{18}O$ from atmospheric O_2 in groundwater. Proemse et al. (2012) use this co-isotope signature to trace fallout from the oil sands in western Canada. Einsiedl and Mayer (2005), identify industrial fallout as being the dominant source of SO_4^{2-} in karst groundwaters in southern Germany, where concentrations are attenuated in older groundwaters by sulfate reduction, a process that can contribute to the degradation of organic contaminants accompanying this anthropogenic source.

Strontium Isotopes and Salinity

Strontium isotopes have proven useful for tracing the source of salinity. Sr^{2+} is more precisely a tracer for Ca^{2+}, with which it can substitute in carbonates, sulfates, feldspars, and other rock-forming minerals (introduced with weathering in Chapter 6). However, different sources of chloride salinity will often have

characteristic sources of Ca^{2+} and therefore Sr^{2+}, which can often be distinguished by the $^{87}Sr/^{86}Sr$ ratio.

The basis for variations in this ratio is due to the contributions of ^{87}Sr generated by the β-decay of ^{87}Rb, which has a half-life of 47.5 billion years. Contributions of ^{87}Sr from ^{87}Rb decay in the K-rich rocks have increased the $^{87}Sr/^{86}Sr$ ratio of the continental cratons from the primordial $^{87}Sr/^{86}Sr$ ratio of 0.699 to between 0.71 and 0.74. Seawater and marine carbonates and sulfate, in contrast, have lower ratios due to weathering of K-poor basalts along the midoceanic ridges. Today, seawater has $^{87}Sr/^{86}Sr = 0.709$ (Veizer 1989), although different rates of continental weathering versus rates of ocean spreading and tectonics have altered this ratio through time. Marine sediments have recorded these variations over Phanerozoic time (Figure 9.41).

The $^{87}Sr/^{86}Sr$ ratio in groundwaters then reflects the source of strontium, which is usually associated with the weathering source in either sedimentary or crystalline rocks. This ratio can be used to identify mixing sources. An example is in oil-producing regions, where deep brines may impact shallow groundwaters through surface disposal activities and by improperly abandoned legacy wells that may leak deep brines into shallow aquifers. Peterman et al. (2010) use $^{87}Sr/^{86}Sr$ to calculate the amount of oil field brine from deep wells impacting shallow groundwater in the Williston Basin of northeastern Montana (Figure 9.42). Shallow meteoric waters have Sr^{2+} with radiogenic $^{87}Sr/^{86}Sr$ signature from weathering of the Canadian

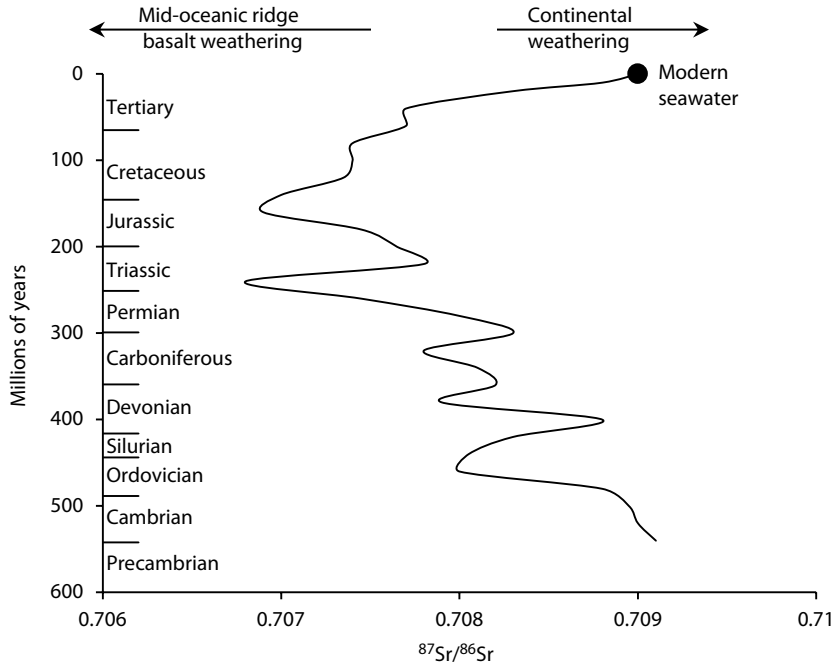

FIGURE 9.41 Strontium isotopes in sedimentary rocks throughout Phanerozoic time. (Modified from Veizer 1989.)

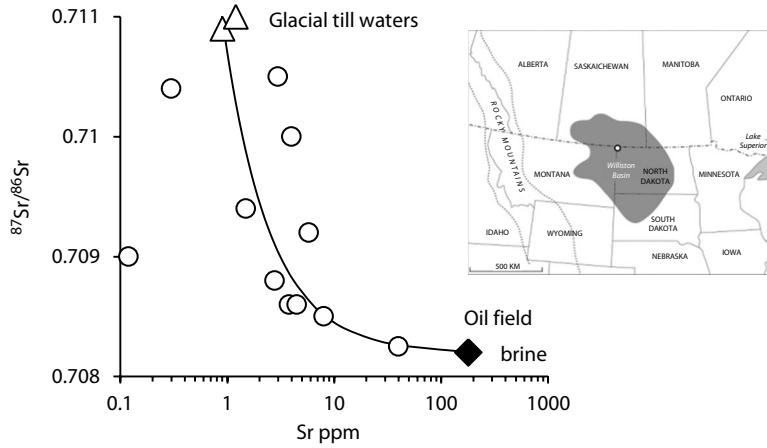

FIGURE 9.42 Use of $^{87}Sr/^{86}Sr$ to quantify salinity contributions from deep brines (black diamond) to shallow groundwaters (open discs) in the Williston Basin, Montana. (Modified from Peterman et al. 2010.)

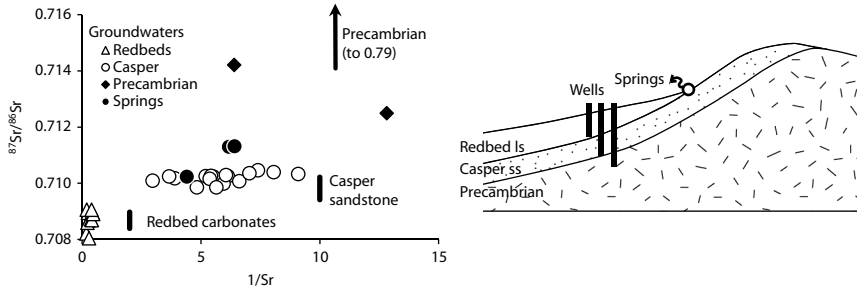

FIGURE 9.43 Groundwater from wells completed in the three main aquifers have $^{87}Sr/^{86}Sr$ ratios that closely associate with those of the host aquifer materials in the Laramie Basin, Wyoming. (Modified from Frost and Toner 2004.)

Shield–derived glacial till, whereas the basin brines have a Paleozoic marine ratio (Figure 9.41). Their measurements show a range of mixtures of these two sources. The Sr^{2+} concentration can be affected by sorption and exchange reactions, while the $^{87}Sr/^{86}Sr$ ratio is conservative. However, calculating mixing fractions with isotope ratios requires that the ratio is weighted with the concentration of strontium in the sample. Mixing calculations and equations are presented in Chapter 5.

In a study to identify groundwater flow paths, Frost and Toner (2004) measured $^{87}Sr/^{86}Sr$ and Sr^{2+} concentrations in wells completed within carbonate-cemented Casper sandstone and overlying carbonate and evaporite Redbeds of the Mesozoic Laramie Basin, and underlying Precambrian crystalline basement (Figure 9.43). Measurements of strontium isotopes in the aquifer materials show well-defined ranges. The $^{87}Sr/^{86}Sr$ measurements for groundwaters suggest that they are recharged in their respective aquifer outcrop regions, where they gain their strontium isotopic

signature from weathering. The springs in this basin are shown to be flowing from both the Casper sandstones and the Precambrian basement aquifer.

Lithium, δ^6Li, and Salinity

The lightest alkali element and number 3 on the periodic table after helium, Li^+ is a lithophilic and highly soluble cation. Its high solubility comes from its high hydration number of 6, which gives it a hydrated diameter over three times larger than its crystallographic diameter of 1 angstrom. Lithium also does not participate in redox or biological reactions. These characteristics make it a relatively conservative solute. Lithium is found in igneous rocks, particularly pegmatites, and in minerals such as lepidolite ($K[Li,Al,Rb]_3[Al,Si]_4O_{10}[F,OH]_2$) and spodumene ($LiAl[SiO_3]_2$), but more abundantly in brines associated with evaporite deposits (playas and salars). Its broad range in isotope distribution between seawater and igneous rocks makes it a good tracer of origin.

Li^+ concentration in seawater is only 0.18 ppm, with δ^6Li of −32.3‰. Studies show that through evaporation its isotope ratio r is conservative. In contrast, igneous rocks have δ^6Li values close to the LSVEC standard. The dominantly Na–Cl brines of the groundwater-fed Salar or brine lakes in the Atacama Desert of northern Chile, for example, contain up to 4 g/L Li^+ (Bradley et al. 2013) originating from hydrothermal alteration of the andesite rocks of the Andes. These high concentrations are augmented by further evaporation in surface lagoons and the highly concentrated Li^+ then recovered for commercial uses, principally Li-batteries, by alkaline precipitation as Li_2CO_3. Strong evaporation of brines in playas and salars can precipitate Li^+ in a range of phosphate and sulfate evaporite minerals. In contrast to these igneous origins for lithium are brines derived from the evaporation of seawater (Figure 9.35), such as the Dead Sea brine, which has concentrated Li^+ to 18 ppm representing a tenfold increase over seawater (Epstein et al. 1981). Brines derived from seawater evaporation can then be identified on the basis of δ^6Li, which is conservative during simple concentration. Bottomley (1999, 2003) uses δ^6Li to trace the source of deep crustal brines to an evaporated seawater source.

Weathering of granitic bedrock is a source of Li^+ in groundwaters, although fractionation by sorption can occur along the flow path. Lemarchand et al. (2010) show this for drainage in granitic terrain with a highly weathered saprolite developed at the surface (Figure 9.44).

ARSENIC

Arsenic has gained considerable interest over the past decades, as concentrations increase in a number of groundwater systems and its impact on human health becomes more prevalent, and the impacts of chronic ingestion of arsenic at low concentrations become more evident (Kapaj et al. 2006). For this reason, the WHO has recommended a safe drinking water limit of 10 µg/L. However, the redox chemistry of arsenic and its behavior in natural groundwater flow systems makes this limit often difficult to achieve. It also makes it difficult to manage in legacy mine-tailings sites.

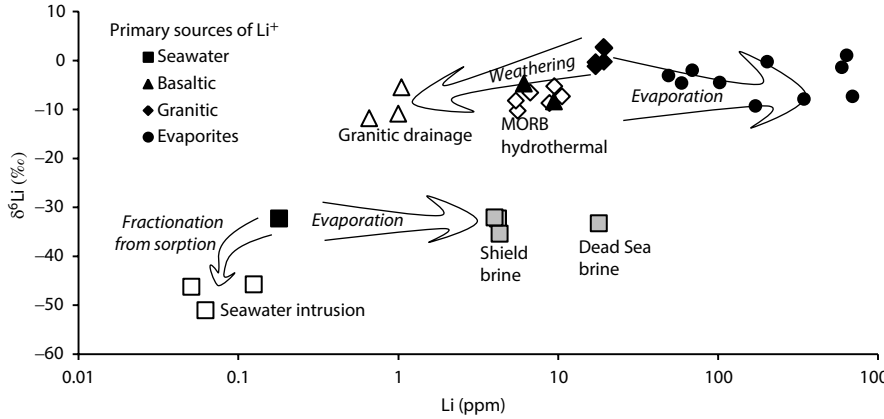

FIGURE 9.44 Lithium and δ^6Li in various fresh and saline waters and in rocks (MORB—midoceanic ridge basalt). (Sources of data: Svec and Anderson 1965; Chan and Edmond 1988; Bottomley et al. 1999; Bottomley et al. 2003; Hogan and Blum 2003; Lemarchand et al. 2010; Araoka et al. 2013.)

Arsenic Sources and Solubility

Arsenic, sits in the fourth row of the periodic table, at atomic number 33 as a metalloid between germanium and selenium, and so has a variety of valences, including arsenide (As^{-III}), elemental (As^0), arsenite (As^{III}), and arsenate (As^V). As elemental arsenic, it has metallic properties and can be alloyed to strengthen metals, for example, lead in car batteries. In its reduced valence state, it can form metallic arsenides, such as GaAs semiconductors in the electronics industry. Arsenic trioxide (As_2O_3) is highly soluble (>10 g/L) and very toxic.

Its greatest use is perhaps the antibacterial properties of arsenate compounds with applications from fungicides and pesticides like sodium methyl arsenate to pressure-treated wood preservatives such as chromated copper arsenate, which is now restricted due to As-exposure and replaced for many applications by cupric ammonium and cupric chromium compounds.

Natural As minerals include the arsenite sulfide orpiment (As_2S_3) and realgar (As_4S_4) with As covalent bonding, but formally as As^{II}. Both are associated with hydrothermal deposits as low-temperature mineralization. Another substantial natural occurrence is as an arsenide replacing S in iron sulfides—arsenopyrite (FeAsS). Weathering of arsenopyrite and other As minerals oxidizes and releases arsenic to the environment. This has led to some regions, such as Bangladesh, with significant concentrations in the drinking water. Arsenopyrite can host economic grades of gold, as microinclusions. However, it cannot be routinely recovered by crushing and floatation with CN^- complexation and must be roasted, releasing As oxide gases that are recovered as arsenic trioxide (As_2O_3) powder. Past mining practices have led to significant As contamination of soils and tailings in some gold-mining camps.

In the aqueous environment, arsenic is generally found as either As^V, arsenate, or As^{III}, arsenite, with the speciation of either redox state a function of pH. Arsenate, like P^V sitting just above in column 15 of the periodic table, forms a weak acid

as a hydroxide. Arsenate hydroxide species and their dissociation constants are as follows (from Nordstrom and Archer 2003):

$$H_3AsO_4^\circ \rightarrow H_2AsO_4^- + H^+ \qquad K_{H_3AsO_4} = 10^{-2.3}$$

$$H_2AsO_4^- \rightarrow HAsO_4^{2-} + H^+ \qquad K_{H_2AsO_4^-} = 10^{-6.99}$$

$$HAsO_4^{2-} \rightarrow AsO_4^{3-} + H^+ \qquad K_{HAsO_4^{2-}} = 10^{-11.8}$$

While As^{III} has only two stable hydroxides within the pH range of natural waters:

$$H_3AsO_3 \rightarrow H_2AsO_3^- + H^+ \qquad K_{H_2AsO_3} = 10^{-9.17}$$

The speciation of the arsenate and arsenite hydroxides is shown in the left-hand chart of Figure 9.45.

The As^V hydroxide species $H_2AsO_4^-$ dominates below pH 7, and $HAsO_4^{2-}$ dominates above pH 7, while reduced As^{III} as the neutral species H_3AsO_3 dominates over the pH range of most natural waters. The reduction of arsenate, As^V, to arsenite, As^{III}, occurs at a relatively low p*e*, well below NO_3^- and even after ferric iron (Figure 9.45; right chart).

Under oxidizing conditions, where both ferrihydrite ($Fe[OH]_3$) and As^V exist, arsenate is strongly sorbed onto this ubiquitous solid iron hydroxide phase, particularly at low pH, and dissolved arsenic concentrations are well below the drinking water standard of 10 ppb. As the speciation shifts to the $HAsO_4^{2-}$ field with increasing pH, As sorption decreases (Figure 9.46). As^{III} is also sorbed onto ferrihydrite, less so at low pH but significantly under alkaline conditions. Under strongly reducing conditions, where sulfate reduction produces hydrogen sulfide (H_2S and HS^-), As^{III} is highly insoluble as the arsenite sulfide, orpiment (As_2S_3).

Arsenate reduction occurs above sulfate reduction and below iron reduction, which provides a window in the redox ladder where arsenic has very high solubility.

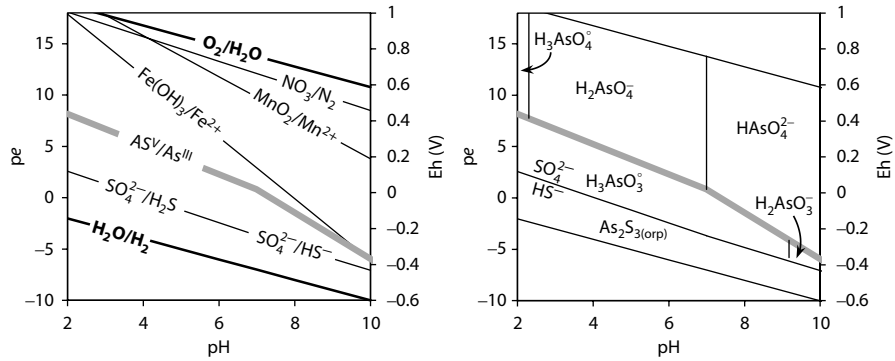

FIGURE 9.45 pH–redox stability fields for arsenic hydroxides and sulfides. Left: the As^V/As^{III} redox line with respect to other major redox pairs. Right: stability fields for arsenate and arsenite hydroxides and arsenic sulfide. The redox line for conversion of $H_3AsO_3^\circ$ to orpiment, $As_2S_{3(orp)}$, is calculated for a total sulfur ($SO_4^{2-} + H_2S + HS^-$) concentration of 3.2 ppm or 10^{-4} mol/kg, and coincides with that for sulfate reduction to hydrogen sulfide, SO_4^{2-}/HS^-.

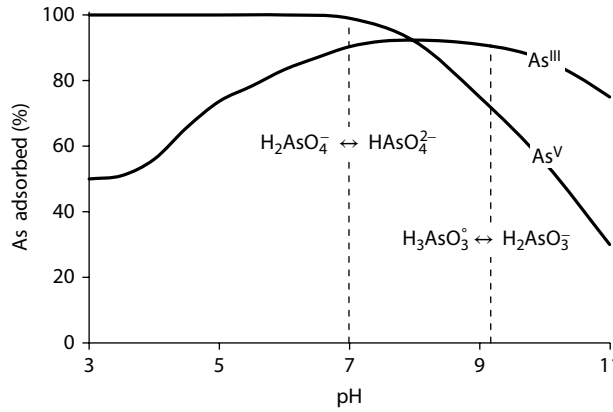

FIGURE 9.46 Sorption of arsenate (As^V) and arsenite (As^{III}) on ferric hydroxide, $Fe(OH)_3$, over a range of pH (modified from Masue et al. 2007). The pH boundaries for the dominant arsenate and arsenite hydroxide species are shown with vertical lines. A reduction in sorption for both As^{III} and As^V occurs as these species become more anionic.

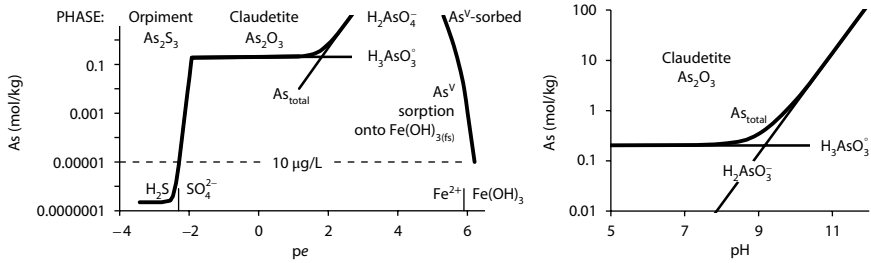

FIGURE 9.47 Mineral controls on arsenic solubility. Left: Redox control on arsenic solubility, constructed for pH 6, assuming 10^{-4} molar total sulfur as SO_4^{2-} and H_2S. At p*e* above about 1.5, mineralogical control of As can be achieved by As^V ($H_2AsO_4^-$) sorption onto ferric oxyhydroxides. Right: solubility of Claudetite (As_2O_3) with pH.

Above the ferric/ferrous iron line, As solubility is limited by sorption onto ferrihydrite; and below the sulfate reduction line, by orpiment solubility. Between, only claudetite can exert any solubility control, and with an equilibrium arsenite concentration of over 10,000 ppm (Figure 9.47).

Although arsenic pentoxide (As_2O_5) can be synthesized under highly oxidizing conditions, arsenic trioxide (As_2O_3) is the only stable arsenic oxide, with two polymorphs—cubic arsenolite and the more stable monoclinic claudetite, which dissolve with very high solubilities:

$$As_2O_{3(claud)} + 3H_2O \rightarrow 2H_3AsO_{3(aq)} \qquad K_{claud} = a^2_{H_3AsO_3} = 10^{-1.34}$$

This provides an arsenic activity of $10^{-0.67}$. Not accounting for ionic strength, this is a dissolved concentration greater than 0.2 mol/kg or 15,000 ppm (Figure 9.47, right-hand chart).

Bangladesh

Perhaps one of the most serious examples of natural arsenic contamination of groundwater is that of the Ganges delta in Bangladesh, which supplies millions of people with drinking water. Wells have been installed to replace surface water supplies that are typically contaminated with nitrate and bacteria. However, the groundwaters have As concentrations up to and exceeding 300 µg/L (von Brömssen et al. 2007; Figure 9.48). The source and mobility in this case represent a good example of the solubility of arsenic under different redox conditions. Nickson et al. (1998) show that these deltas build from sediments, with over 10 ppm As sorbed on the solid iron hydroxides derived from oxidation of base metal sulfides in the Himalayas. In the subsurface, organic material generates reducing conditions using the ferric iron hydroxide as an electron acceptor:

$$CH_2O + As^{V}{-}2Fe(OH)_3 \rightarrow 2Fe^{2+} + H_3AsO_3^{\circ} + HCO_3^{-} + H_2O + 2H^{+}$$

The system then releases sorbed As into groundwater as ferric hydroxide is transformed to ferrous iron. Perturbation of the system by deep groundwater pumping then draws down these shallow, reducing groundwater with high dissolved arsenite into the exploited aquifer. Neumann et al. (2010) show that the labile organic carbon involved in the release of As comes with infiltration of water from constructed ponds, which are the major source of recharge to much of the agricultural area. Thus, the geochemical signatures of this process are the elevated As itself but also highly dissolved (ferrous) iron and increased bicarbonate.

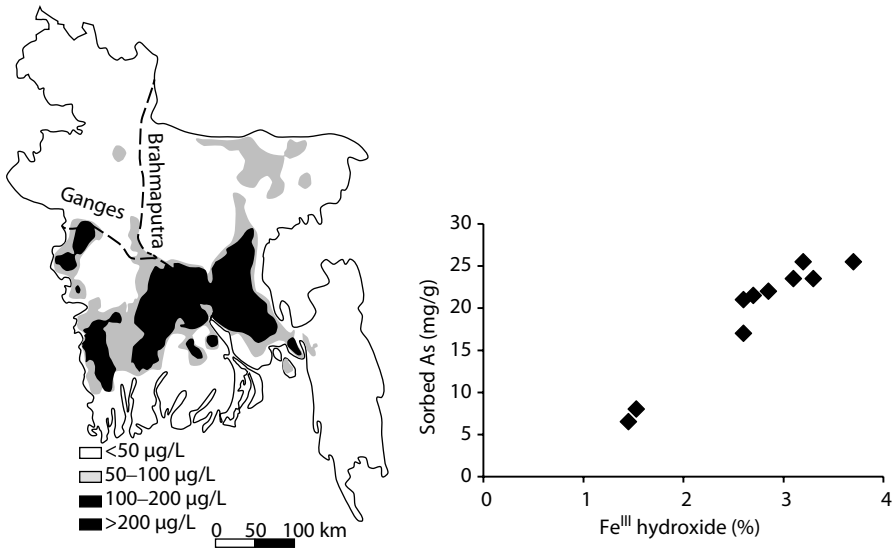

FIGURE 9.48 As in groundwater in the Ganges river delta of Bangladesh (left; von Brömssen et al. 2007). As sorbed on ferrihydrite in the sediments (right; Nickson et al. 1998) is released to groundwaters under reducing conditions.

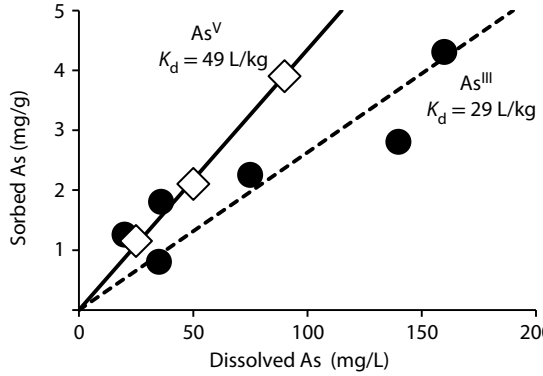

FIGURE 9.49 Sorption isotherms for As^V (as $H_2AsO_4^-$) and As^{III} (as H_3AsO_3) on deep (58 m) sands with ferric iron hydroxide, below the zone of As-contaminated groundwaters (Radloff et al. 2011), showing greater sorption for the more oxidized As^V than the more soluble As^{III}.

The widespread contamination has been somewhat mitigated by drilling deeper wells that are exclusively for drinking water, although the downward infiltration of the high As groundwaters from the overlying reducing zones remains a threat. Radloff et al. (2011) have measured the sorption of As^{III} and As^V onto the brown, ferric iron hydroxide-bearing sands, which today host groundwaters with less than 2 μg/L As. They show high sorption for arsenite, As^{III}, but even greater sorption for As^V (Figure 9.49), which will retard the migration of As from above due to groundwater pumping from the deeper sands.

Arsenic in Mine Waters

Arsenic in mine drainage is common in gold camps working ore hosted with arsenopyrite. Determining its origin is important for remediation. At the Giant Mine gold mining camp in Yellowknife in the Canadian arctic, arsenic emissions from roasting of the arsenopyrite ore in the past have impacted the regional landscape. More modern procedures condensed arsenic gases and stockpiled the arsenic trioxide (As_2O_3) powder in underground chambers. Leaching of this has raised As concentrations in some mine waters to over 4 g/L. Mine tailings backfilled in the underground workings also host residual arsenopyrite in tailings from which low temperature oxidation releases both SO_4^{2-} and As. Here, sulfate isotopes distinguish between these two sources of SO_4^{2-} and As in the mine waters. The high roasting temperature and exclusive involvement of atmospheric O_2 ($\delta^{18}O_{O_2}$ = 23.5‰) in combustion is evident in the sulfate from the arsenic trioxide chambers, as well as in the regional sulfate from ore-roasting emissions in the past and in the tailings mine water that comes from mine-water discharge. By contrast, the local groundwaters, which have As from 100 ppb to 1 ppm, derived their arsenic and sulfate from the aqueous (low temperature) oxidation of sulfides in the underground (Figure 9.50).

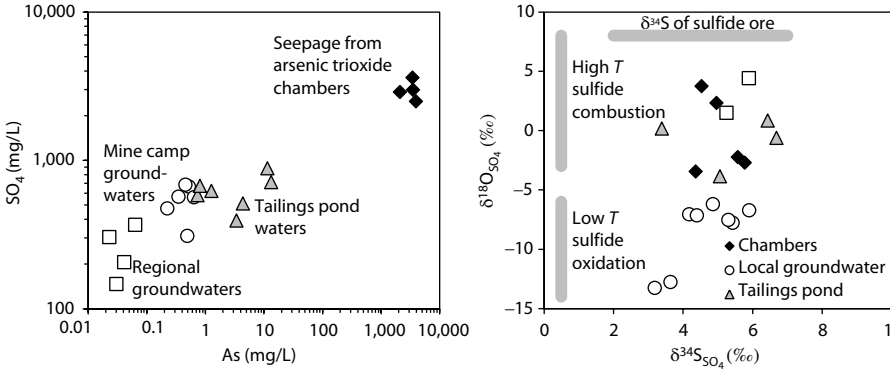

FIGURE 9.50 Arsenic and sulfate in Giant Mine, Yellowknife, mine waters (Clark and Raven 2003). The association between SO_4^{2-} and As (left) allows sulfate isotopes to be used as a proxy for the source of As at this mine (right), showing contributions from both high-temperature roasting of the ore (chambers, tailings, and regional groundwaters) and low-temperature oxidation of arsenopyrite in the mining camp (local groundwaters).

NUCLEAR WASTE

Uranium, the heaviest of all naturally occurring elements, was first identified in pitchblende (UO_2) in 1789 by Martin Klaproth. Just over a century later the development of photography led to Antoine Becquerel's discovery of radioactivity from observations that uranium salts would expose photographic plates. By the turn of the century, Marie Curie had isolated polonium and radium from uranium ore, demonstrating the occurrence of radioactive daughter elements neighboring U on the periodic table. Lord Rutherford showed that this decay occurred with a constant half-life, providing geologists with the basis for geochronology. However, fission was not discovered until 1938, when Hahn and Meitner exposed uranium to neutrons and found that they produced barium, an element with atomic number 56 and far from uranium on the periodic table. This rapidly led to the dramatic effort to exploit the associated energy release from conversion of a small amount of mass to energy, as predicted by Einstein in 1905.

Initial efforts to developed fission as a weapon led to later efforts to harness it as an energy source. Both have left a considerable environmental legacy from the mining, refining and enrichment of uranium to the radioactive fission products of nuclear waste. Understanding the mobility of these radionuclides in the environment and finding sites for their long-term isolation present some of the most compelling hydrogeologiical challenges we face.

Uranium Geochemistry

Uranium has a very effective geochemical mechanism for accumulation, based on its high solubility as oxidized hexavalent U^{VI} but almost insoluble nature as tetravalent U^{IV}. Most uranium ores form at a redox interface in groundwater or hydrothermal systems (Figure 9.51).

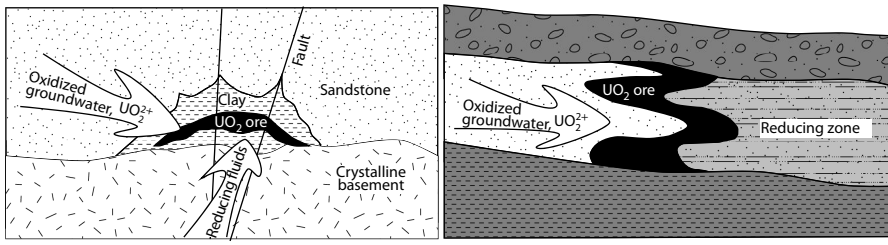

FIGURE 9.51 Typical redox *traps* for the formation of uranium deposits. Left: Cigar Lake (after Cramer 1994), Canada, mixing between reducing hydrothermal fluids and U-bearing oxidizing groundwaters. Right: South Australia, flow of oxidizing, U-bearing groundwaters into an aquifer zone with reduced compounds such as sulfides and organics.

Oxidizing waters leach uranium from primary materials, such as granite or granitic sediments. Oxidation to hexavalent U^{VI} makes uranium soluble as the uranyl cation UO_2^{2+} or as a carbonate-complexed species, such as $UO_2CO_3^o$ and $UO_2(CO_3)_2^{2-}$. When uraniferous groundwaters encounter reducing zones in the aquifer, the uranium is reduced back to the tetravalent state and precipitated from solution as insoluble uraninite (UO_2) and pitchblende, which can have forms ranging from UO_2 to U_3O_7. Such *roll front* deposits, so-called for their slow forward migration, occur where reduced species, such as organic carbon, graphite, and sulfides, are found with in the aquifer, or at a zone of mixing with reduced hydrothermal fluids. As such settings are typically found with in clastic sediments, porosity is high and accumulations of UO_2 ore can reach high percentages. Major uranium ore-producing regions are often found on the periphery of sedimentary basins in shield terrain.

Uranium is the heaviest of the naturally occurring elements and has no stable isotopes. It is dominantly ^{238}U with a half-life of 4.5 billion years. The fissionable isotope ^{235}U ($T_{½}$ = 704 My) makes up only 0.72% of natural uranium—insufficient for sustained fission in light water and graphite reactors. Decay of ^{238}U by release of α particles (2p2n which is a ^4He nucleus) generates a series of daughters, including ^{230}U, ^{230}Th, ^{226}Ra, and ^{222}Rn, eventually ending with stable lead, ^{206}Pb (Figure 7.28). It is a lithophilic element that is enriched in granitic rocks. Its average crustal abundance of about 2 ppm varies up to 10 ppm in U-rich granites, and to less than 50 ppb in mafic rocks.

Uranium is found as tetravalent U^{IV} and hexavalent U^{VI} redox states. In the reduced state, uranium solubility is limited by uraninite (UO_2) and its microcrystalline form, pitchblende, which are the principal U-ore forming minerals (Figure 9.52). Only below pH 3.5 will UO_2 support dissolved U concentrations above 100 ppb (as $U[OH]^{3+}$). At neutral pH, uraninite limits U solubility to less than 1 ppb.

Hexavalent uranium is soluble as the uranyl ion, UO_2^{2+}, up to pH 5.8, at which point the uranium hydroxide $UO_2(OH)^+$ becomes the dominant species (Figure 9.52). The low solubility of $UO_2(OH)_2$ maintains dissolved uranium concentrations at less than 10 ppb at pH 6 and less than 1 ppb at pH 7 (Figure 9.53). The uranyl ion, however, readily complexes with the carbonate anion, greatly enhancing uranium solubility as $UO_2(CO_3)_2^{2-}$ and making uranium carbonate, Rutherfordine (UO_2CO_3) one

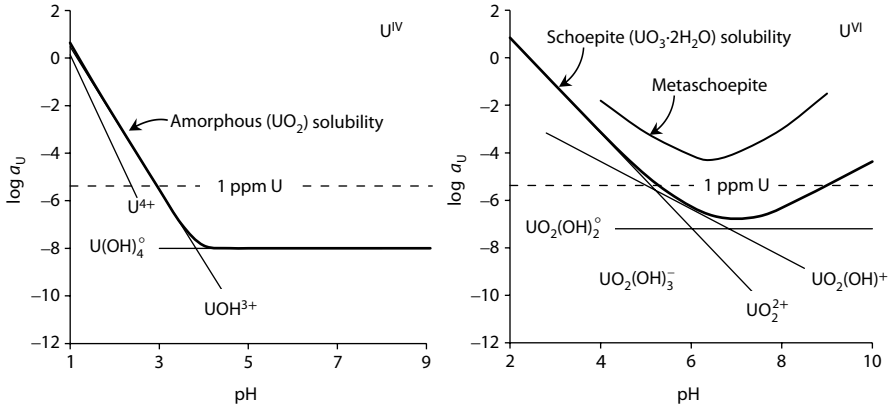

FIGURE 9.52 Solubility of reduced (U^{IV}) uranium oxide (amorphous) (UO_2) (left) and oxidized (U^{VI}) uranium oxyhydroxides, schoepite, (β $UO_3{\cdot}2H_2O$) (right). Also shown is the solubility of metaschoepite (Gorman-Lewis et al. 2008). Crystalline uranium oxide, uraninite, has a solubility some eight orders of magnitude lower than amorphous UO_2. Lines drawn using ΔG° values compiled by Langmuir (1997) from various sources.

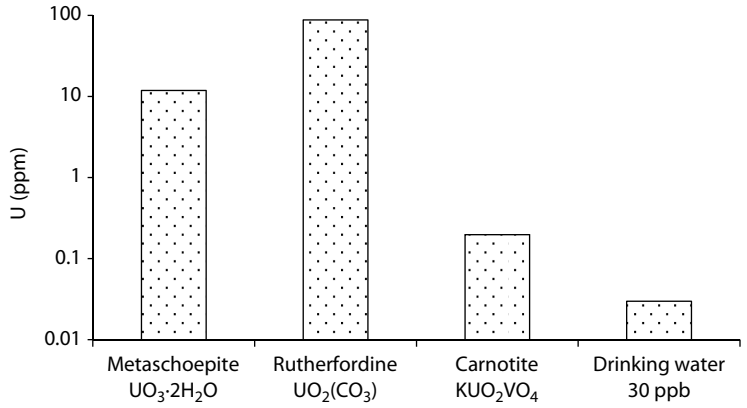

FIGURE 9.53 Solubility of U^{VI} minerals in fresh water showing the importance of carbonate complexed uranium, $UO_2(CO_3)_2^{2-}$, to increase the solubility of the uranyl ion, UO_2^{2+}, and vanadium, V^V as vanadate, $H_2VO_4^-$, to decrease UO_2^{2+} solubility in fresh water.

of the most soluble uranium minerals in low-ionic-strength water. By contrast, vanadium, V, complexes the uranyl ion, limiting uranium solubility to less than 1 ppm with the uranium vanadate mineral carnotite (KUO_2VO_4).

Surface waters and groundwaters have on average less than 1 ppb, although concentrations of several ppb can be observed. Low concentrations of soluble U^{VI} species in natural waters are due to its low crustal abundance and sorption of the uranyl ion on clays. It is also limited by reaction with iron oxyhydroxide at higher pH. The US EPA places a maximum concentration limit of 30 ppb for total U in drinking water. The WHO uses a radiologically derived limit of 130 ppb.

The long half-life of ^{238}U gives it only a minimal radiological hazard. However, it is a toxic heavy metal that accumulates in the kidneys, creating long-term health problems. Important sources of uranium in the environment are from the uranium enrichment process used to increase the $^{235}U/^{238}U$ ratio for light-water nuclear reactors and for nuclear weapons (uranium depleted in ^{235}U or DU being the waste product). The use of depleted uranium for armor and armor-piercing shells has also increased environmental exposure.

Nuclear Fuel and Radioactive Waste

Most reactors *burn* purified uranium dioxide (UO_2) that has been fired to produce a fine-grain porcelain structure. Light-water reactors require enriched fuel, where the ratio of fissionable ^{235}U to common ^{238}U is increased from the natural level of 0.72% to over 3% in the fuel. This is done by the gaseous diffusion of uranium hexafluoride UF_6, which generates large quantities of ^{235}U-depleted uranium hexafluoride or DUF_6. A solid at room temperature, UF_6 readily hydrates to produce soluble uranium oxyfluoride (UO_2F_2) and highly corrosive hydrofluoric acid (HF), both of which are toxic. Spent uranium fuel, can also be reprocessed to re-enrich the ^{235}U content, recover plutonium for fuel and reduce the mass of radioactive waste. Reprocessing, however, is accompanied by the release of short-lived noble gas radioisotopes, as well as volatile radionuclides, including ^{129}I and tritium.

The natural radioactivity in uranium fuel generates a neutron flux that propagates fission of ^{235}U, producing new high-energy neutrons and two lighter-weight nuclides. In a nuclear weapon, a super critical mass of pure ^{235}U, the fission neutrons released propagate an uncontrolled chain reaction. In a nuclear reactor, the much lower ^{235}U to ^{238}U ratio sustains a lower neutron flux that is controlled by rods of neutron-absorbing elements, usually boron. A moderator is also used to slow the high-energy neutrons (by multiple neutron-hydrogen impacts) to thermal range, where they are more likely to be captured by other ^{235}U nuclides to sustain fission. Reactors burning enriched uranium fuel use light water as a moderator, although H_2O will capture neutrons and so is an inefficient moderator. The deuterium in heavy water (D_2O) has a small neutron capture cross section and so is more efficient at slowing neutrons, allowing nonenriched fuel to be used. This is the basis for the Canadian Deuterium Uranium or CanDU reactor design launched in 1944 by C.J. Mackenzie as director of the Canadian National Research Council.

Fission generates one to two fast neutrons and two lighter nuclides or fission products, with masses of about 90 and 140. The kinetic energy of these products accounts for over 80% of the total energy release and is harnessed as heat by the cooling water to drive steam turbines. Subsequent β and γ decay of the daughter nuclides accounts for the remainder of the energy released. Examples of possible decay schemes are as follows:

$$^{235}_{92}U_{143} + n \rightarrow {}^{90}_{38}Sr_{52} + {}^{143}_{60}Nd_{83} + 2n$$

$$^{235}_{92}U_{143} + n \rightarrow {}^{96}_{40}Zr_{56} + {}^{137}_{55}Cs_{82} + 2n$$

$$^{235}_{92}U_{143} + n \rightarrow {}^{104}_{44}Ru_{60} + {}^{129}_{53}I_{76} + 2n$$

Excess neutrons in the fission products convert to protons by β decay. This produces elements of higher atomic number and lower neutron number, but with essentially the same mass. There is no loss of nucleons (one neutron with mass 1.6749×10^{-24} g decays to one proton with mass 1.6726×10^{-24} g, with the difference of 2.3×10^{-27} g or 0.14% attributed to the β particle and energy), and so the decay chains are essentially isobaric, stepping left to right from element to element along the rows of the periodic table until a stable or long-lived radionuclide is reached. Some fission products decay rapidly to stable nuclides and are not of concern:

$$^{140}\mathrm{Xe}_{(13.6\ \mathrm{s})} \rightarrow ^{140}\mathrm{Cs}_{(63.7\ \mathrm{s})} \rightarrow ^{140}\mathrm{Ba}_{(12.8\ \mathrm{d})} \rightarrow ^{140}\mathrm{La}_{(1.68\ \mathrm{d})} \rightarrow ^{140}\mathrm{Ce}_{(\mathrm{stable})}$$

Others decay by β emission to long-lived radionuclides that pose a long radiohazard:

$$^{90}\mathrm{Se}_{(140\ \mathrm{ms})} \xrightarrow{\beta} ^{90}\mathrm{Br}_{(1.92\ \mathrm{s})} \xrightarrow{\beta} ^{90}\mathrm{Kr}_{(32\ \mathrm{s})} \xrightarrow{\beta} ^{90}\mathrm{Rb}_{(158\ \mathrm{s})} \xrightarrow{\beta} ^{90}\mathrm{Sr}_{(28.78\ \mathrm{y})}$$

$$^{129}\mathrm{In}_{(0.61\ \mathrm{s})} \xrightarrow{\beta} ^{129}\mathrm{Sn}_{(2.23\ \mathrm{m})} \xrightarrow{\beta} ^{129}\mathrm{Sb}_{(4.4\ \mathrm{h})} \xrightarrow{\beta} ^{129}\mathrm{Te}_{(69.6\ \mathrm{m})} \xrightarrow{\beta} ^{129}\mathrm{I}_{(15.7\ \mathrm{My})}$$

In addition to the suite of fission products in spent uranium fuel is a second group of radionuclides produced by neutron activation of other elements in the reactor core. Tritium and radiocarbon are both produced by neutron impacts on nitrogen, present as ubiquitous N_2 gas in the fuel rods, the coolant water, and the moderator water.

$$^{14}_{7}\mathrm{N}_7 + \mathrm{n} \rightarrow ^{3}_{1}\mathrm{H}_2 + ^{12}_{6}\mathrm{C}_6$$

$$^{14}_{7}\mathrm{N}_7 + \mathrm{n} \rightarrow ^{14}_{6}\mathrm{C}_8 + \mathrm{p}$$

Trace amounts of chloride in the fuel and water are also neutron-activated:

$$^{35}_{17}\mathrm{Cl}_{18} + \mathrm{n} \rightarrow ^{36}_{17}\mathrm{Cl}_{19} + \gamma$$

Finally, the tremendous neutron flux in the fuel also activates ^{238}U to form the transuranic or superheavy elements. Activation of abundant ^{238}U produces ^{239}Np, an isotope of the first transuranic element neptunium. This decays with half-life of 2.4 days to more stable plutonium, ^{239}Pu:

$$^{238}_{92}\mathrm{U} + \mathrm{n} \rightarrow ^{239}_{92}\mathrm{U}_{147(24\,\mathrm{m})} \xrightarrow{\beta} ^{239}_{93}\mathrm{Np}_{146(2.4\ \mathrm{d})} \xrightarrow{\beta} ^{239}_{94}\mathrm{Pu}_{146(24{,}100\ \mathrm{y})}$$

The long half-life of ^{239}Pu allows it to accumulate in the fuel rods, where further activation produces other long-lived radionuclides of the actinides, including $^{240}\mathrm{Pu}_{(6{,}570\ \mathrm{y})}$, $^{242}\mathrm{Pu}_{(376{,}000\ \mathrm{y})}$, $^{241}\mathrm{Am}_{(432\ \mathrm{y})}$, $^{243}\mathrm{Am}_{(7{,}370\ \mathrm{y})}$, and $^{244}\mathrm{Cm}_{(18.1\ \mathrm{y})}$.

The radioactivities contributed by the main radionuclides in spent fuel are listed in Table 9.5, together with their half-life, their final stable decay product, and the geochemical form. Also calculated here are their contribution to the mass (based on $A = \lambda N$) of spent fuel. It is noteworthy that the most radioactive constituents, ^{90}Sr and ^{137}Cs, represent only 100 mg and 240 mg, respectively, in 1 kg of spent fuel (i.e., 100 and 240 ppm).

Spent fuel consists of fission-microfractured, porcelain-like UO_2 pellets in corrosion-resistant zircaloy tubes (98% zirconium with ~1.5% tin and minor iron). Radionuclides mobile as anions or gas, including T, ^{14}C, ^{36}Cl, and ^{129}I, represent the early release group, followed by the soluble alkali, Cs^+, and the alkaline earth, Sr^{2+}. The long-term release group is essentially the actinides present as insoluble tetravalent oxides. Only extensive oxidation of the uranium fuel pellets will release them to groundwater.

With the high radioactivity of these fission and activation products, spent fuel is considered *high level waste* (HLW). Once removed from the reactor, it is stored in pools to dissipate the heat from β decay of the early fission products. However, long-term isolation is required for the decay of nuclides in Table 9.5. In addition to HLW is the class of *low and intermediate level waste* (LILW), consisting of ^{14}C extracted onto resin columns from reactor moderator water plus irradiated equipment, decommissioning waste and materials associated with the handling of nuclear compounds, laboratory clothing and liquids, and wastes from hospitals and industries using nuclear radiation in specific applications. Although low in overall radioactivity, LILW generally has high volume and, with the long half-life of some radionuclides like ^{14}C, requires a long-term disposal solution.

TABLE 9.5
The Long-lived Radionuclides of Concern in Spent Uranium Fuel Waste

Nuclide	Half-life (years)	Radioactivity (million Bq per kg spent UO_2 fuel)	Mass (g per kg spent UO_2 fuel)	Stable decay product	Geochemical species
Activation products					
^{3}H (or T)	12.43	0.16	4.5E-10	^{3}He	H_2O, H_2
^{14}C	5,730	42.6	0.00026	^{14}N	CO_2, CH_4
^{36}Cl	301,000	0.46	0.00038	^{36}Ar	Cl^-
Fission products					
^{90}Sr	28.78	514,000	0.10	^{90}Zr	Sr^{2+}
^{99}Tc	211,100	128.4	0.20	^{99}Ru	TcO_2
^{93}Zr	1,530,000	15.6	0.17	^{93}Nb	ZrO_2
^{129}I	15,700,000	5.18	0.79	^{129}Xe	I^-
^{135}Cs	2,300,000	1.01	0.024	^{135}Ba	Cs^+
^{137}Cs	30.07	766,000	0.24	^{137}Ba	Cs^+
Actinides					
^{238}U	4,500 My	12.2	987	^{206}Pb	UO_2
^{239}Pu	24,100	6,360	2.8	^{207}Pb	PuO_2
^{240}Pu	6,570	8,700	1.0	^{208}Pb	PuO_2
^{242}Pu	376,000	8.81	0.061	^{206}Pb	PuO_2
^{241}Am	432	11,100	0.087	^{209}B	AmO_2
^{243}Am	7,370	19.4	0.0026	^{207}Bi	AmO_2
^{244}Cm	18.10	448	0.00015	^{208}Pb	CmO_2

Radioactive Waste Disposal

Burial of nuclear waste in deep geological repositories (DGR) is considered by most countries to be the most favorable option to provide secure isolation for the period of time required decay to low levels of radioactivity. Figure 9.54 shows rate of decay for the radionuclides in spent fuel listed in Table 9.5. The time periods for decay range from decades for tritium to millions of years for ^{129}I. Both HLW and LILW require isolation on a time scale of 10,000 years or longer to allow decay of highly radioactive and soluble ^{90}Sr and ^{137}Cs, and of very mobile ^{14}C. Beyond this time frame, only ^{129}I, mobile as an anion, is considered of concern.

DGRs include packaging of the waste in copper canisters emplaced in holes drilled in adit floors and packed with dry bentonite clay buffer. Adits and shafts are then backfilled with clay and sand, and/or cement. This engineered barrier, or *near field*, provides security over a long period of time, but conservative models accept that it will at one point be breeched. Containment of the radionuclides in Table 9.5 after this time relies on the integrity of the *far field*—the hydrogeological and geochemical environment.

Migration through the far field to surface could occur by advection with groundwater along fractures and permeable horizons or by diffusion through porewater. In either case, mobility will be affected by geochemical reaction with the surfaces of

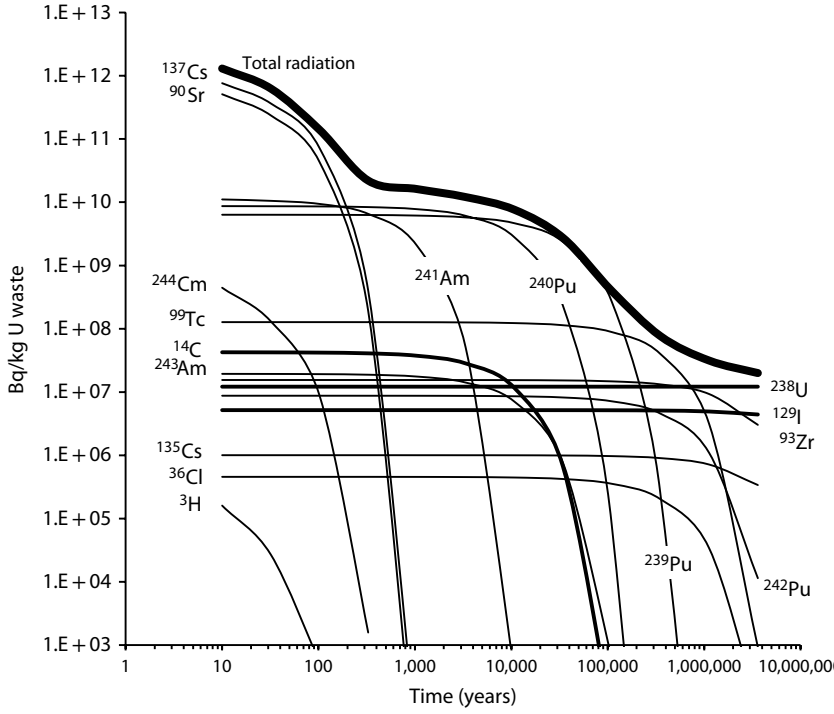

FIGURE 9.54 Contribution of major radionuclides to overall radiation of spent uranium fuel and their decay over time. Both ^{14}C and ^{129}I (in bold) are of concern as C and I are mobile as anions (HCO_3^-, I^-, and IO_4^-) and gases (CO_2, CH_4, and CH_3I) and are biophylic.

minerals and organics along the pathway. Redox and pH, of course, play significant roles. The following discusses the important geochemical consideration for migration of the radionuclides of concern.

^{3}H or T—Hydrogen is highly mobile as H_2O. However, the risk posed by tritium is not from its presence in high-level waste but in releases from power plants during operation. Releases occur as water, HTO, and hydrogen gas, HT. Most tritium produced by neutron activation of H and D in moderator water is stripped and stored as solid titanium hydride (TiT_2) to decay. Some is sealed as T_2 gas in glass tubes with a phosphor coating that emits light by radioluminescence for emergency lighting, gun sights, and other applications that demand nonelectrical lighting. The high volatility of HTO and its accumulation in vegetation as organically bound tritium creates halos around nuclear generating facilities that are up to about 30 Bq/L compared to regional backgrounds of about 3 Bq/L. Nonetheless, levels are well below those posing a radio-hazard.

^{14}C—Carbon in natural groundwaters is largely present as DIC, and usually bicarbonate, HCO_3^-, but is particularly mobile in its reduced form as CH_4. Organic resins used to strip ^{14}C from moderator water represent most of the radiocarbon inventory of LILW. Conservative models consider that the organic wastes with ^{14}C will decompose to $^{14}CO_2$ and, with H_2 from corrosion of steel containers in the vaults, would produce highly mobile $^{14}CH_4$ by CO_2 reduction. Methane in the far field may then be oxidized by methanotrophic bacteria in the near surface, representing a potential loss of ^{14}C to the biosphere. Radiocarbon transported as DIC would experience some attenuation by precipitation and exchange with carbonate minerals along fractures. Radiocarbon as DIC would also be retained by reaction with any concrete used as backfill material and bulkheads in the decommissioned repository, as well as cement grout to fill fractures and fault zones. Reardon and Dewaele (1990) and Dayal and Reardon (1994) show that DIC species react strongly with the calcium–silica–hydrate minerals in cement, producing more stable calcite.

^{36}Cl—Chloride is ubiquitous in natural waters as the conservative anion, Cl^-, and particularly in groundwaters, where it can originate from saline sources such as crustal brines, seawater and accumulated salts. Almost always present as an anion, $^{36}Cl^-$ is very conservative and does not adsorb onto minerals or organics.

^{90}Sr—Strontium is always present as a divalent alkaline earth cation, Sr^{2+}. It is not redox sensitive, and replaces Ca^{2+} in feldspars and carbonate minerals. Sr^{2+} is retarded by adsorption on clay minerals. The bentonite buffer around the canisters, while creating a very low permeability barrier after hydration, would also retain strontium by cation exchange.

^{99}Tc—Technetium is a most interesting element in that it has no stable isotope and is not found in nature. Its longest-lived isotope, ^{98}Tc, has a half-life of only 4.2 million years, and so any technetium generated during nucleosynthesis at the creation of our solar system some 4.5 billion years ago has long since decayed away. This makes understanding its geochemical behavior somewhat problematic, and we must rely on close analogues, such as its heavier Group VIIA neighbor, rhenium, Re. Under reducing conditions in the spent fuel repository, tetravalent TcO_2 should be stable, but, like ReO_2, is weakly soluble, with concentrations greater than 40–100 ppb. If oxidized to Tc^{VII}, it is highly mobile as the TcO_4^- anion (Kim and Boulègue 2003).

^{135}Cs and ^{137}Cs—Cesium is an alkali metal, found exclusively in the hydrosphere as Cs^+. Like K^+, it is soluble in water, but in aquifers is highly retarded by cation exchange on clays. Some 50 to 100 × 10^{15} Bq of ^{137}Cs (about 25 kg) out of a total of 1 to 2 × 10^{18} Bq of radioactivity (4% to 8%) was released from the Chernobyl reactor 4 following the steam explosions and ignition of the graphite core in April 1986 (NEA 2002). ^{137}Cs remains today the radionuclide of greatest concern, although monitoring shows that local deposition was largely retained on clays within the upper soil horizon.

^{129}I—Iodine is a halogen and is stable in the environment as the reduced form, iodide, I^-, and also as the oxidized species, iodate, IO_3^- (Figure 9.55). As an anion, it has higher potential for mobility from nuclear waste than the cations, Cs^+, Sr^{2+}, and the actinides. However, it can be readily complexed by organics and so has a strong potential for adsorption in soils (Alvarado et al. 2002) and on ferric iron oxides (Kennedy et al. 2011). It has high volatility as methyl iodide, ICH_3. The risk from ^{129}I is its uptake by the thyroid gland, coupled with its high mobility and long half-life. The short-lived isotope (^{131}I, $T_{½}$ = 8 days) is a hazard from immediate releases from accidents, but is not considered in the waste inventory.

^{239}Pu, ^{240}Pu,^{242}Pu, ^{241}Am, ^{243}Am, and ^{244}Cm—The transuranic radionuclides produced in the fuel by neutron capture with ^{238}U are all stable as tetravalent oxides, PuO_2, AmO_2, and CmO_2. Like UO_2, they will be essentially immobile under reducing conditions. Under oxidizing conditions, they can gain mobility with higher valence states as anions, such as PuO_4^{2-}. However, unlike hexavalent uranium, these actinides are readily reduced back to their insoluble tetravalent state.

Radionuclide Releases to Groundwater: Two Case Studies

In November 1954, the accidental loss of process solutions from an experimental spent fuel reprocessing plant at the Chalk River Nuclear Laboratories released some 26 TBq (26 × 10^{12} Bq) of ^{90}Sr and 37 TBq ^{137}Cs into a shallow sand aquifer, along with much lower activities of other fission products, ^{154}Eu ($T_{½}$ = 8.6 years), ^{106}Ru ($T_{½}$ = 374 days), and ^{144}Ce ($T_{½}$ = 285 days). Some 35 years later, it was found that the undecayed ^{137}Cs and ^{154}Eu remained sorbed within the unsaturated zone

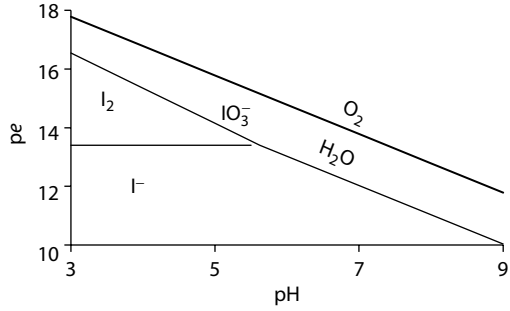

FIGURE 9.55 Aqueous speciation of iodine with redox and pH, showing the dominant species and the upper stability field of water. Iodide can also form methyl iodide, ICH_3 at low p*e* and with available organic matter.

and that the short-lived ^{106}Ru and ^{144}Ce radionuclides had decayed to background. However, the ^{90}Sr had generated a plume extending up to 350 m from the source (Killey and Munch 1987), with potential discharge into a wetland before the ^{90}Sr activity had decayed to below the standard of 5 Bq/L.

The sand aquifer has an average linear groundwater velocity of about 70 m/y, giving a circulation time for groundwater along the 350 m flow path of about 10 years. The ^{90}Sr plume, however, was found to be moving at a rate of only about 10 m/y due to sorption onto ferric iron oxyhydroxides coatings on the sand (Killey and Munch 1987). Distribution coefficients for ^{90}Sr in the core of the plume were calculated from concentrations in the porewater compared with the sorbed fraction and found to be high, at 12.9 mL/g. However, the K_d measured at the leading edge of the plume is much lower, 1.6 mL/g, due to the existence of preferential pathways with less ferric iron substrate for sorption. Using the calculation for a retardation factor discussed in Chapter 7, and values for porosity, $\theta = 0.33$, and bulk density, $\rho = 2$ g/cm^3, velocities for the core of the plume and for the leading edge can be made. Both are important, as the latter determines when the receptor wetland will be impacted and the former will determine whether decay to background will occur before the bulk of the ^{90}Sr reaches the wetland.

Core	*Leading edge*
$R = 1 + \frac{\rho}{\theta} \times K_d$	$R = 1 + \frac{\rho}{\theta} \times K_d$
$= 1 + \frac{2}{0.33} \times 12.9$	$= 1 + \frac{2}{0.33} \times 0.8$
$= 79$	$= 5.8$

Using the relationship for $v_{Sr} = \frac{v_{gw}}{R}$ and groundwater velocity of 70 m/y allows calculation of the plume:

$v_{Sr} = \frac{v_{gw}}{R}$	$v_{Sr} = \frac{v_{gw}}{R}$
$= 73/79$	$= 73/5.8$
$= 0.92$ m/y	$= 12.5$ m/y
Time to wetland: 28 years	360 years

The velocity of the leading edge of the plume predicts arrival at the wetland from the source 350 m up-gradient within about one half-life, while the core of the plume would not arrive before 12 half-lives elapsed, bringing ^{90}Sr activities to background levels. Accordingly, an in situ wall-and-curtain permeable reactive barrier was designed to remove ^{90}Sr as the leading edge reached the wetland, but not for the full load of ^{90}Sr in the aquifer (Lee et al. 1998). A sheet piling wall was driven to the base of the aquifer and a permeable curtain in front filled with a zeolite, clinoptilolite ($K_3Al_3[Al,Si]_2Si_{13}O_{36}{\cdot}12H_2O$) with high surface area and high cation exchange capacity. The groundwaters have a Ca^{2+} concentration of only 10 mg/L, whereas higher ionic strength water would decrease ^{90}Sr sorption due to competition from other cations (Hull and Schafer 2008).

The K_d for $^{90}Sr^{2+}$ sorption on clinoptilolite is reported to be as high as 2600 mL/g, providing sorption for several decades (Lee et al. 1998). Lee and Hartwig (2005) report the following performance of the wall and curtain:

Contaminated groundwater treated: 15 million L/y (15,000 m^3/y)
Uncontaminated groundwater diverted: 10 million L/y (10,000 m^3/y)
^{90}Sr activity of contaminated groundwater: 85 Bq/L
^{90}Sr activity of treated groundwater: <0.6 Bq/L
^{90}Sr removed from groundwater: 850 million Bq/y or 99.5%

The magnitude 9.0 Tōhoku earthquake of March 11, 2011, released a tsunami that killed over 15,000 people and displaced 4.4 million households. The tsunami also breached the seawall at the Fukushima Dai'ichi nuclear power plant, leading to meltdowns and releases of radionuclides to the atmosphere. Extensive monitoring of short- and long-lived radionuclides has been undertaken in air, soils, surface waters, and groundwaters (MEXT 2012; Kinoshita et al. 2011). The greatest activities measured were contributed by short-lived ^{131}I ($T_{½}$ = 8 days), with levels exceeding 10^6 Bq/m^2 along a northwest trajectory generated by the prevailing winds at that time from the power plant to the 30 km perimeter and beyond into the extended evacuation zone (Kinoshita et al. 2011). However, more emphasis was placed on ^{137}Cs and ^{90}Sr as long-lived radioisotopes that contribute the greatest amount to the long-term effective radiation dose. Figure 9.56 shows that ^{137}Cs activities were over 1 million Bq/m^2 along the northwest trajectory and over 500,000 Bq/m^2 within the extended evacuation zone, whereas ^{90}Sr activities were largely below 10,000 Bq/m^2.

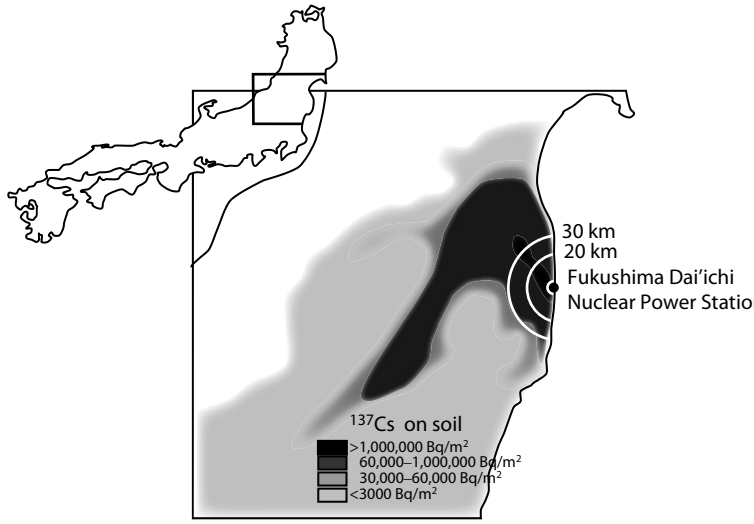

FIGURE 9.56 ^{137}Cs fallout on soils of the Fukushima region (after MEXT 2012) in northeastern Japan (inset).

Contributions of these long-lived radionuclides to soil and groundwater remain as on-going questions. Subsequent monitoring of well water in the region, however, found activities for ^{137}Cs below 0.72 Bq/kg in groundwater and one detectable level of ^{90}Sr at 0.0014 Bq/kg (Iijima 2013). Surface waters draining the high activity corridor had ^{137}Cs activities on the order of 1–2 Bq/kg and ^{90}Sr less than 0.02 Bq/kg. The disparity between the high levels found in soils and those found in runoff and infiltrating waters is attributed to sorption. The distribution coefficients measured for highly organic paddy and upland soils in Japan are on the order of 100–1000 mL/g for ^{90}Sr and an order of magnitude greater for ^{137}Cs (Kamei-Ishikawa et al. 2008). The associated retardation factors, R, and velocities (v_{Sr} and v_{Cs}) then make ^{137}Cs essentially immobile and ^{90}Sr highly retarded in the soils and aquifers of the Fukushima region.

Aquitards and Nuclear Waste Isolation

Most countries with a nuclear power generation capability are now looking for appropriate aquitards in which to bury their LILW and the spent fuel that constitutes HLW in a DGR. Safety assessment of a DGR considers that the engineered barrier will fail at some point and release radionuclides into the groundwater. The hydrogeological *far-field* beyond the repository then becomes the long-term barrier to the migration of radionuclides. Site investigations must demonstrate that groundwaters in the far-field are ancient and that solute transport is by diffusion only.

Geological settings that satisfy these two conditions fall into two categories, crystalline bedrock and argillaceous sedimentary formations. Crystalline terrains, generally granites, have very low hydraulic conductivities, providing the rock mass has no significant fracturing. However, finding a sufficiently large volume of unfractured crystalline rock is a challenge. In contrast, sedimentary formations in undeformed basins have predictable geology with few fractures. Clay minerals in shales, argillaceous carbonates, and unlithified clay units reduce permeability and preclude advective transport. Both the advective and diffusive regimes can be assessed with geochemistry and isotopes in the porewaters. Advective flow in permeable formations represents the boundaries to the site, and diffusive regime is the geological environment being evaluated for its barrier properties.

Solute transport by diffusion in aquitards is most clearly demonstrated by the porewater profiles for naturally occurring conservative tracers, such as ^{18}O, D, and Cl^-, as well as highly diffusive species like helium (Mazurek et al. 2009). Sampling porewaters for analysis of these natural tracers can be challenging, with methods ranging from slowly responding piezometers to extraction from core samples by squeezing, direct equilibration, or vacuum distillation. The shape of the profile that these tracers establish is a function of (1) their initial concentrations at the aquitard boundaries and in the aquitard porewaters, (2) their rate of diffusion, and (3) time. Using measurements of effective diffusion coefficients in the aquitard (see Chapter 5 in the section on diffusive mixing in aquitards) together with an understanding of the initial boundary conditions, the time to establish the observed profile can be determined. This provides an estimate of the time afforded by the aquitard to retain radionuclides migrating from the DGR.

Hendry and Wassennaar (1999) use δD measured in porewaters collected from piezometer nests installed through an 80 m thick glacial clay till aquitard overlying a 76 m thick Cretaceous marine clay. This profile is shown in Figure 5.39 as an example of diffusive mixing of groundwater. The profile was used to calibrate a 1-D groundwater flow and transport model to constrain the time to establish the δD profile (Figure 9.57). The lower profile is considered to have developed over the last 30,000 years, following emplacement of the till during the last advance of the Laurentide Ice Sheet, while the upper profile developed over the Holocene after the glacier retreated some 10,000 years ago.

A diffusional profile developed over a longer period of time was studied in porewater of the Opalinus Clay at Benken, Switzerland (Gimmi et al. 2007). Here the aquitard has two bounding aquifers, with well-established timing for meteoric groundwaters replacing initially marine water. Diffusional modeling indicates that the initially marine porewaters evolved to the observed profile over some 700,000 years (Figure 9.57).

A final example comes from a site in the Ordovician shales and limestones on the eastern flank of the Michigan Basin in central North America under consideration for a DGR for LILW in southern Ontario. In the section under consideration, hypersaline porewaters from Silurian seawater in the shales are bounded above and below by basin brines (Intera 2011; Clark et al. 2013). The $\delta^{18}O$ profile (Figure 9.57) shows diffusional profiles above and below the argillaceous formations, but remains

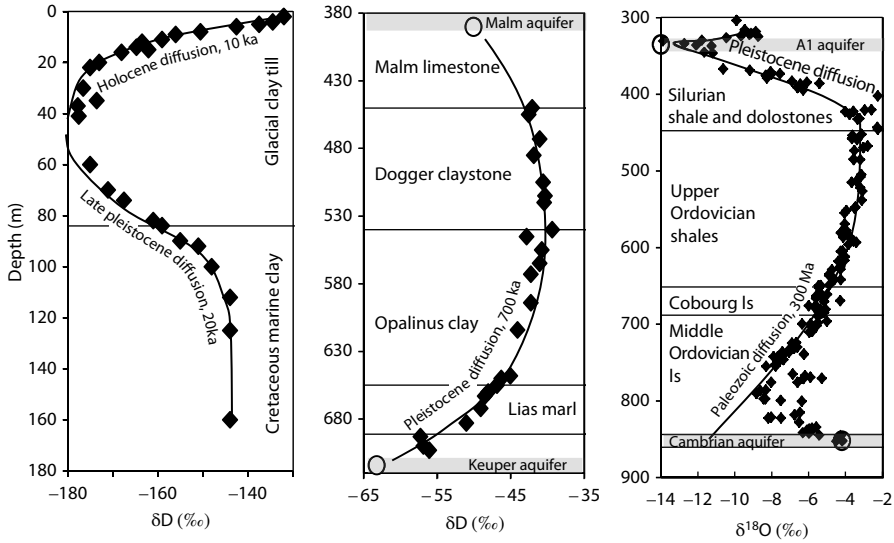

FIGURE 9.57 Isotope profiles and 1-D diffusional modeling in aquitards. Left: δD profile in porewaters from the Pleistocene Battleford till and underlying Cretaceous Bearpaw marine clay, southern Saskatchewan (after Hendry and Wassenaar 1999), center: $\delta^{18}O$ profile through the Opalinus Clay in Switzerland (after Gimmi et al. 2007), and right: $\delta^{18}O$ profile through Ordovician to lower Silurian shales and carbonates of the Michigan Basin. Aquifer groundwaters shown in open discs. (After Clark et al. 2013.)

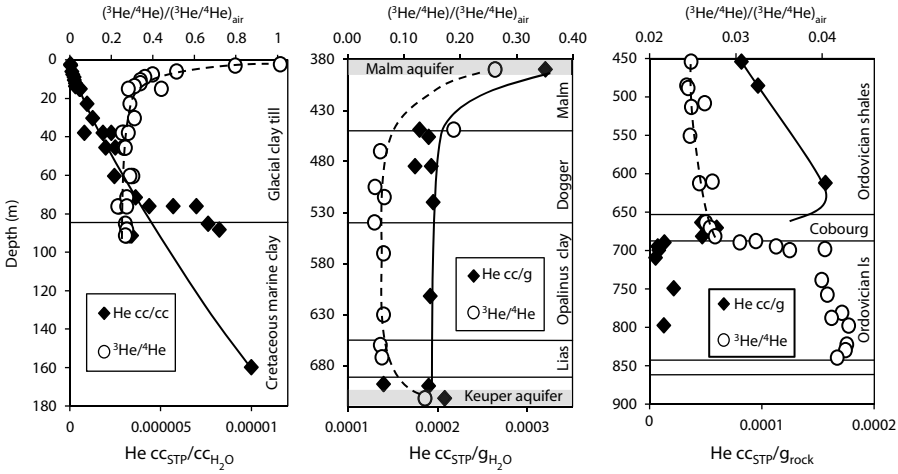

FIGURE 9.58 Helium concentration and isotope profiles in aquitards. Left: clay till, southern Saskatchewan with diffusion trend toward atmospheric concentration and isotope ratio at surface (after Hendry et al. 2005); Opalinus clay, Switzerland, with linear distribution for concentration and isotopes from in situ production in Opalinus and Dogger clays (after Mazurek et al. 2009); and Ordovician shales and carbonates, Michigan basin, southern Ontario, with upward diffusion from in situ production in the shales but isolated below the Cobourg Formation from basin-derived helium (Intera 2011; Clark et al. 2013).

essentially uniform through them. In this case, this profile shows little diffusion over some 300 million years.

An additional perspective on the dominance of diffusive transport in aquitards is given by the analysis of helium concentrations and isotopes in porewaters. Sampling this highly diffusive gas can be done from piezometers but more often requires encapsulation of core samples immediately following recovery followed by outgassing and analysis under high vacuum. The resulting profiles of the $^3He/^4He$ ratio give insights to the source of the geogenic component, and the helium concentration in the porewaters allows calculation of diffusion rates and time.

Helium profiles for the three sites discussed above in Figure 9.57 are shown in Figure 9.58. For the southern Saskatchewan clay till site, Hendry et al. (2005) use the $^3He/^4He$ ratio to show radiogenic production below the profile and the concentration profile to show upward diffusion toward the surface over the past 15,000–25,000 years. By contrast, helium in the Opalinus Clay in Switzerland (Mazurek et al. 2009) originates largely within the aquitard by in situ radiogenic production over a 17-million-year period with a minor component of deep (mantle) He with enriched $^3He/^4He$. The helium isotope profile from the Ordovician strata of the Michigan Basin shows a zone of in situ He production in the Ordovician shales, which is isolated at the base of the Cobourg Formation from a deeper zone of regionally sourced helium with a much more enriched $^3He/^4He$ signature. The concentrations of helium in this aquiclude proposed for a DGR suggest an age for the porewaters of some 260 million years.

This page intentionally left blank

10 Sampling and Analysis

INTRODUCTION

The use of geochemistry and isotope methods in hydrogeology usually involves a well-planned sampling and analytical program. The following is provided as a guide for students and professionals taking water samples for geochemistry and isotope analysis. Table 10.1 provides a summary of the basic requirements to be met in terms of sample size and storage. Much of this chapter presents routine sampling and analytical methods. Sampling for some analyses may be more complicated, and the sampling containers, volumes, and methods should be discussed in advance with the laboratory involved.

FIELD MEASUREMENTS

Geochemical and isotope sampling requires measurement of a number of field parameters that are sensitive to change during sample transport and storage. Some provide useful information that can help decide on the size and type of samples to be taken.

Temperature

The temperature of groundwater is fundamental to all thermodynamic calculations. It is also needed to correct EC measurements and for calibrating the pH meter. It must be measured as close to in situ conditions as possible. Use a standard glass thermometer or the temperature probe that is a component of most pH meters.

Electrical Conductivity

Electrical conductivity (EC) is measured in units of µS/cm using a field-portable meter with a probe consisting of two electrodes with a calibrated spacing. EC is proportional to the concentration of dissolved ions present in a solution and can provide a rough idea of the total dissolved solids (TDS), which may help with selecting sample volumes and other analyses. For most groundwaters, the EC value corrected to 25°C is about 50% greater than the TDS expressed as milligrams per liter, and can be estimated according to the following:

$$\begin{aligned} \text{TDS} &= A \times \text{EC}\ (\mu\text{S/cm}) \\ A &\cong 0.55 \text{ in bicarbonate waters} \\ &\cong 0.75 \text{ in high-sulfate waters} \\ &\cong 0.9 \text{ in high-chloride waters} \end{aligned}$$

TABLE 10.1
Guide to Sample Size and Sampling Protocol.

Analysis	Method of Analysis	Sample	Field Sampling Protocol
		Geochemistry	
Cations	ICP-AES or MP-AES	25 mL	Filter, acidify to pH 2
Anions	LC	25 mL	Filter, not acidified
Trace metals	ICP-MS	25 mL	Filter, acidify to pH 2
NH_4^+	FIA-SP	50 mL	Filter, keep cool or freeze
PO_4	FIA-SP	50 mL	Keep cool or freeze
H_2S	Colorimetric	20 mL	Field kit
		Isotopes of water	
$^{18}O/D$	IRMS (CO_2/H_2)	1 mL	Minimize headspace
$^{18}O/D$	CRDS (H_2O)	2 mL septum vial	Avoid evaporation
T	Direct counting (±8 TU)	25 mL	Plastic or glass
	Enriched LSC (±0.8 TU)	500 mL	Plastic or glass
	^{3}He-ingrowth (±0.1 TU)	50 mL	Plastic or glass
		Dissolved carbon isotopes	
DIC ^{13}C	TC-IRMS (CO_2)	40 mL glass	Filter, butyl septum, keep cool
DIC ^{14}C	AMS (C)	500 mL glass	Filter, butyl septum, keep cool
DOC ^{13}C	TC or LC-IRMS (CO_2)	40 mL glass	Filter, butyl septum, keep cool
DOC ^{14}C	AMS (C)	1 L, glass	Filter, keep cool
		Nitrogen species isotopes	
NO_3^- $^{15}N/^{18}O$	IRMS (N_2/CO_2)	100 mL	Filter or freeze
NH_4^+ ^{15}N	EA-IRMS (N_2)	1L	Freeze
		Sulfur species isotopes	
SO_4^{2-} ^{34}S	EA-IRMS (SO_2/CO)	Sufficient for 0.1 mg S	Filter, remove sulfide
H_2S ^{34}S	EA-IRMS (SO_2)	0.1 mg S	Cd or Zn-Acetate
SO_4^{2-} ^{18}O	TC-EA-IRMS (CO)	1 mg SO_4	Filter, remove sulfide
		Isotopes of the halides	
^{37}Cl	IRMS (CH_3Cl)	100 mL (0.1 mg Cl^-)	Filter
^{36}Cl	AMS (AgCl)	100 mL (1 mg Cl^-)	Filter
^{81}Br	IRMS (CH_3Br)	500 mL (0.1 mg Br^-)	Filter
^{129}I	AMS (AgI)	500 mL (1µg I^-)	Filter
		Minor elements	
^6Li	TIMS (MC-ICP-MS)	100 mL (3µg Li)	Filter
^{11}B	TIMS (MC-ICP-MS)	100 mL (1µg B)	Filter
$^{87}Sr/^{86}Sr$	TIMS	25 mL (0.1µg Sr)	Filter
		Gas concentration and isotopes	
Free gas	GC and GCC or GC-TC-IRMS, CRDS for ^{13}C and ^{15}N in CO_2, CH_4 and N_2O	Glass bottle with butyl rubber septum, <10 mL needed	

(*Continued*)

TABLE 10.1 (*Continued*)
Guide to Sample Size and Sampling Protocol.

Analysis	Method of Analysis	Sample	Field Sampling Protocol
Dissolved gas	GC and GCC or GC-TC-IRMS	Glass bottle with butyl rubber septum, 100 mL, no headspace	
		Noble gases	
Free gas	NGMS and QMS	10 cm soft copper diffusion sampler, field-crimped or clamped	
Dissolved	NGMS and QMS	20 cm soft copper tube, flushed and filled at formation pressure, clamped	

ICP-AES—inductively coupled (induction furnace with argon gas flux) plasma with an atomic emission spectroscopy (wavelength) detector, sometimes expressed as ICP-OES for optical emission spectroscopy.

MP-AES—a microwave source is used to generate an N_2 plasma at a lower temperature than ICP, but produces atomic emission lines for most cations of interest. This is a robust instrument that is less expensive and reliable for student use and training.

ICP-MS—inductively coupled (argon) plasma with quadrupole mass spectrometer for analysis of minor and trace elements, including heavy metals and halides (Br and I). ICP-MS is less suitable for high concentrations of major ions.

FIA-SP—flow injection analysis by spectrophotometry, where the water sample is injected into a carrier solution to the spectrophotometer. Samples are chemically pretreated to complex the analyte (e.g., ammonium) to provide a diagnostic color. Color density is measured by light absorption at a particular wavelength.

IRMS—isotope ratio mass spectrometry. IRMS analysis by continuous-flow technology involves the injection of a nano-mole aliquot of the sample gas into a helium gas stream which carries the sample into into the ion source where it is ionized to form an ion beam focused along a flight path and through a magnetic field that deflects the ions according to their momentum into a spectrum of masses that are measured with faraday cup collectors. Dual inlet instruments require millimole sample sizes and longer analysis time for higher-precision measurements.

CRDS—cavity ring-down spectroscopy (laser attenuation) is the basis of a new generation of instruments for analysis of stable isotopes (D, ^{13}C, ^{18}O, ^{15}N) in water, water vapor, and gases (including CO_2, CH_4, and N_2O). Analytical precision rivals IRMS, but the range of sample types and interfaces is more limited. Measurements are made by the degree of absorbance of pulsed laser light.

TC-IRMS—total carbon analyzer interfaced with IRMS. Total carbon analyzers have recently been designed to operate with a He carrier that allows them to sequentially convert DIC to CO_2 by acidification and DOC by wet oxidation. CO_2 is sparged by the He carrier and analyzed by IRMS (St.-Jean, 2003).

LC-IRMS—liquid chromatography with IRMS for compound-specific ^{13}C analysis, by chromatographic separation of organic compounds and advection with the He carrier to a combustion zone (TC) and as CO_2 to the IRMS.

EA-IRMS—elemental analyzer interfaced with IRMS, to combust solid or liquid samples to gases at high temperature, followed by gas separation (CO_2, SO_2, N_2) and IRMS analysis, using a He carrier gas.

TC-EA-IRMS—high-temperature (pyrolysis) conversion of solid samples followed by gas separation (CO, H_2) for elemental analysis and IRMS, using a He carrier gas.

(*Continued*)

TABLE 10.1 (*Continued*)
Guide to Sample Size and Sampling Protocol.

GCC-IRMS—combustion gas chromatography interfaced with IRMS for separation of CO_2, CH_4, and higher C hydrocarbon gases followed by combustion for sequential analysis of $\delta^{13}C$ on single-injection samples. Used without combustion for H_2, O_2, N_2, N_2O, SO_2, and other gases.

GC-TC-IRMS—high-temperature (pyrolysis) conversion of compounds to reduced gases (H_2 and CO) for analysis of δD and $\delta^{18}O$ in hydrocarbons and organics.

NGMS—noble gas mass spectrometer with high-sensitivity source and magnetic field separation into major and minor isotopes, with detection by both faraday and electron multiplier detectors.

QMS—quadrupole mass spectrometer, or residual gas analyzer (RGA) uses a radio frequency through the four rods to generate a magnetic field that guides selected mass from the source to the faraday collector. Inexpensive and versatile for major isotopes of noble gases.

AMS—accelerator mass spectrometry. Samples of organic and inorganic carbon are converted to CO_2 and then to graphite for analysis. In the source, a cesium ion beam sputters the sample to produce carbon anions that are accelerated to high velocity for greater mass resolution needed for the very low abundance of ^{14}C.

LSC—liquid scintillation counting. Photomultipliers are used to count photon emissions generated by decay events in the sample.

TIMS—thermal ionization mass spectrometer. Solid-source IRMS where samples are prepared as coatings on the source filament and ionized by resistance heating of the filament.

Note: For detailed requirements, review with analytical facility. If not specified, bottles should be high density polypropylene (HDPP) or polyethylene (HDPE)

pH

A reliable pH measurement is one of the most important field parameters to be measured, and must be made with care and patience. In natural waters, pH is generally between about 6.5 and 8. Measurement at a sampling site requires calibration of the meter with buffer solutions of known pH. Two buffers are required to bracket the pH of the groundwater (i.e., pH 4 and 7, or 7 and 10) and should be equilibrated to the temperature of the sample water, using the following pH values for the measurement temperature:

The electrode must be rinsed with deionized water (DI) between measurements in buffers and the sample. When taking a measurement, move the electrode slowly to prevent buildup of voltage potentials. Poorly buffered waters (low TDS, low-alkalinity waters) may have some drift. Follow the manufacturer's instruction for storing the electrode.

***T* (°C)**	**0**	**5**	**10**	**15**	**20**	**25**	**30**
Buffer pH 4	4.00	4.00	4.00	4.00	4.00	4.01	4.02
Buffer pH 7	7.12	7.09	7.06	7.04	7.02	7.00	6.99
Buffer pH 10	10.20	10.18	10.15	10.12	10.05	10.00	9.96

It is not always critical to measure pH in a flow-through cell, although recommended if CO_2 degassing or ferrous iron and/or hydrogen sulfide oxidation is a concern (low redox waters). A flow-through cell can be constructed or purchased, and consists of

an enclosed cylinder, typically of Plexiglas, with an inlet and outlet for sample water to flow through out of contact with air. Electrode ports with O-ring gasket seals are installed through the cell wall to insert calibrated pH, Eh, and DO (dissolved oxygen) electrodes. These measurements are then taken without the influence of degassing or atmospheric gas uptake, which can change pH, Eh, and DO.

Redox Potential

Redox measurements provide a measure of the electromotive force of water, or the relative dominance of oxidized versus reduced species in solution. Electromotive potential (E) is expressed in volts, relative to the standard hydrogen electrode (Eh), which by this convention has zero potential (Eh = 0 V). It is generally measured with a platinum electrode with a silver–silver chloride redox junction, which has its own standard potential.

As electrodes are simply measuring an electromotive force, there is no calibration. The electrode can, however, be checked against a solution of fixed Eh to determine whether it is functioning. Two solutions with fixed Eh are Zobell's (ferric-ferrous cyanide solution) and quinhydrone (pH 4 and 7 buffers saturated with quinhydrone powder [~0.2 g/100 mL]):

Zobell's Solution (Eh = 0.430 V at 25°C)	**Quinhydrone Solution**
0.0033 M K^+–Fe^{2+}–CN^- solution	pH 7 solution = 86 ± 20 mV
0.0033 M K^+–Fe^{3+}–CN^- solution	pH 4 solution = 263 ± 20 mV
0.01 M K^+/Cl^- solution	Δ3 pH (difference between the two solutions) = 177 ± 4 mV

When making a measurement, stir sample gently to prevent buildup of a static potential on the electrode and wait a few minutes for a stable reading. If readings are dropping and begin to rise, record lowest reading as atmospheric O_2; contamination may be occurring. Correct the measured E to Eh by adding the electrode's standard potential, E_R, to the measured value, according to the following equation:

$$Eh = E_{measured} + E_R .$$

The following are the standard potentials for a Ag-AgCl electrode with 3.8 N KCl filling solution (according to the equation $E_R = -1.39T\,(°C) + 305$):

T **(°C)**	0	5	10	15	25	35	50
$\mathbf{E_R}$	220	216	213	209	202	195	184

Clean the electrode if there are problems with reference readings or time for stabilization. Use liquid hand soap and a soft brush. Do not use the Eh aliquot as a sample due to K^+ and Cl^- contamination. Store the electrode in a soaker bottle (bottle with O-ring seal) filled with 2 N KCl.

A caution is warranted regarding Eh measurements with platinum electrodes in solutions with multiple redox species. The electrode may preferentially respond to one redox pair over another. Jackson and Patterson (1982) make the case that the most accurate Eh is that calculated from precise measurements of the activities of the redox couple at the lowest potential. In a study of groundwaters containing detectable H_2S

and up to 16 ppm Fe_{total}, they show that Eh measured by platinum electrode were in the range of 0.1–0.2 V, whereas Eh calculated from the SO_4^{2-}/H_2S redox pair gave values of –0.2 to –0.3. Using these Eh values to distribute dissolved iron between Fe^{2+} and Fe^{3+}, the resulting saturation indices for ferrihydrite, $SI_{Fe(OH)_3}$, greatly differed, showing ferrihydrite to be an order of magnitude oversaturated using Eh_{Pt} (log $SI_{Fe(OH)_3} = 1$ to 3) while the more accurate results using the calculated Eh_{SO_4/H_2S} showed ferrihydrite to be undersaturated in these waters, with log $SI_{Fe(OH)_3} = -3$ to –5.

Field Filtering

Geochemical interpretations and thermodynamic modeling are based on the dissolved constituents in water. Particulates from the aquifer, such as clay particles, grains of carbonate or silicate, and metal hydroxides, particularly in newly developed wells, would contribute to the concentration of many components if not removed in the field. However, the filter pore size below which components are considered dissolved is a mechanical division designed to exclude the larger particles that make up the suspended load. Table 1.1 shows the size of many of the components of water. Filtering is best done in the field to prevent geochemical reactions during shipment and storage.

The standard filter size of 0.45 μm is designed to remove particulates. It will also remove most bacteria, suspended clays, and a proportion of iron and manganese oxyhydroxides, but will not retain viruses or some organic molecules, such as fulvic and humic acids. For colloid studies, it is important to use a range of filter sizes down to 0.1μm.

The simplest filtering mechanism is a 25 mm syringe-tip filter, which can be used to filter several hundred milliliters, depending on turbidity. These can be disposable or cartridges with replacement filter discs. Larger formats can be acquired for higher volumes and faster filtering. It is preferable to use positive-pressure filtration systems, as vacuum systems can degas CO_2 and cause shifts in pH and the carbonate system.

Alkalinity Titrations

Analysis of dissolved inorganic carbon (DIC) species (see Chapter 3) is fundamental to the geochemical characterization of water, and is typically accompanied by analysis of dissolved organic carbon (DOC). Measurement of DIC together with pH allows calculation of all DIC species, including the major one, HCO_3^-. DIC and DOC analyses are fully automated, providing both concentration and $\delta^{13}C$ measurements. Sampling for DIC and DOC is discussed later with the isotopes of water and solutes. However, a DIC measurement is done only in the laboratory. A field titration for alkalinity in most near-neutral pH waters provides a measurement of bicarbonate, HCO_3^-, and together with pH allows calculation of all the DIC species.

Alkalinity is a useful field measurement to have. When sampling for ^{14}C it ensures that sufficient water is collected. It is also essential to complement anion analysis by liquid chromatography (LC), which uses a carbonate carrier liquid and does not provide a measure of HCO_3^-. Analysis of $\delta^{13}C_{DIC}$ is now typically done on a total carbon analyzer (TC) interfaced with an isotope ratio mass spectrometry (IRMS) and provides a measure of DIC concentration. Chapter 3 reviews the calculation of CO_2, H_2CO_3, HCO_3^-, and CO_3^{2-} from a DIC or alkalinity measurement.

The alkalinity of a solution is a measure of its capacity to buffer acidity, and is equal to the sum of anions that can act as proton acceptors at the pH range of water. Alkalinity is expressed in units of equivalence, that is, meq/L, and for most natural waters is determined as follows:

$$\text{Total alkalinity, alk}_T = m_{HCO_3^-} + 2m_{CO_3^{2-}} + m_{H_3SiO_4^-} + m_{H_2BO_3^-} + m_{HS^-} + m_{OH^-}$$

In most natural groundwaters, HCO_3^- is the major contributor to alkalinity. Under high pH conditions (above ~8.5), CO_3^{2-} can also make a significant contribution. Both contribute to carbonate alkalinity.

$$\text{alk}_c = m_{HCO_3^-} + 2m_{CO_3^{2-}} \left(\text{meq/kg}\right)$$

Carbonate alkalinity is routinely measured by titrating the solution with a strong acid, usually H_2SO_4, to an end point at pH ~4.3. Calibrated micropipettes with acid cartridges, such as available from Hach®, greatly simplify measurement in the field. The end point can be determined with a colorimetric method using bromocresol/methyl red color indicator. Better is the use of a pH meter as the pH response curve provides a measure of the concentrations of both HCO_3^- and CO_3^{2-}. The titration end point is the pH at which all the alkaline species (i.e., HCO_3^- and CO_3^{2-}) have been converted to carbonic acid, H_2CO_3. This occurs below pH ~4.5, and is observed by an inflection in the pH–acid titration curve. In many waters, this point is difficult to observe with any precision, and so a better graphical solution is to use a Gran plot of milliliter acid versus hydrogen ion activity a_{H^+} (i.e., 10^{-pH}).

The following is an example titration, using a shallow groundwater sampled from dolomite sands. It has no sulfide (HS^-), and at the measured pH there is no significant concentration of dissociated silicic or phosphoric acid (i.e., total alkalinity, alk_T, is equal to carbonate alkalinity, alk_C). It was also filtered with 0.45 μm filter paper to remove particulate carbonate matter that would erroneously contribute to alkalinity.

The data below were generated by titration of a 50 mL sample with 1.6 N H_2SO_4, using a Hach digital titrator (0.00125 mL acid per digit on the readout). The measured pH and associated digital readout have been converted to hydrogen ion activity and millilters of acid, respectively.

pH	Digits	(H^+)	mL acid	pH	Digits	(H^+)	mL acid
8.36	0	2.75E-09	0	5.15	95	4.47E-06	0.11875
7.55	20	2.82E-08	0.025	4.65	100	2.24E-05	0.125
6.86	40	1.38E-07	0.05	4.15	105	7.08E-05	0.13125
6.54	60	2.88E-07	0.075	3.74	110	0.000178	0.1375
6.02	80	8.32E-07	0.1	3.51	115	0.000354	0.14375
5.55	90	1.78E-06	0.113	3.35	120	0.000550	0.15

These data are plotted to find the titration end point where all the alkaline carbonate species have been converted to carbonic acid (Figure 10.1). Locating the titration end point on the plot of pH versus milliliters of acid is complicated by the exponential rise of the graph at low pH, because it is a log-normal plot. This is

an artifact of plotting mL of acid in a linear manner while plotting the response logarithmically as pH. The end point is more easily read from a Gran titration plot (Drever 1997) of acid concentration as a_{H^+} (i.e., 10^{-pH}) (plot on the left). Here, one can observe the considerable addition of acid before there is an observed increase in a_{H^+}. At this point, further addition of acid generates a linear increase in a_{H^+}. Back extrapolation to zero gives the amount of acid added to the solution that has been neutralized by the alkalinity of the solution (i.e., acidity of the solution or a change in pH). This amount of acid is equal to the concentration of alkaline species. If there were no alkaline species, then this line would pass through the origin at 0 mL acid.

In this example, the titration result indicates 0.128 mL acid at the titration end point. This is converted to a measure of alkalinity using the sample volume and the concentration of the titration acid, according to the relationship:

$$\text{alk}_T\left(\text{eq/kg}\right) = \frac{V_{\text{acid}}\ (\text{mL}) \times N_{\text{acid}}\ (\text{eq/kg})}{V_{\text{sample}}\ (\text{mL})} = \frac{0.128 \times 1.6}{50} = 0.0041\ \text{eq/kg}$$
$$= 4.1\ \text{meq/kg}$$

As alk_T is equal to alk_C, and as the water is in a pH range dominated by HCO_3^- (less than 1% CO_3^{2-}), the concentration of HCO_3^- can be calculated:

$$m_{HCO_3^-} = \text{alk}_C/z = 0.0041/1 = 0.0041\ \text{mol/kg}$$

and $$HCO_3^-\left(\text{ppm}\right) = m_{HCO_3^-} \times \text{gfw} \times 1000 = 0.0041 \times 61000 = 250\ \text{ppm}$$

Commercial alkalinity test kits include bromocresol/methyl red powder as a color indicator for pH 4.3. However, detecting the subtle color change can introduce some error in the titration.

It is recommended to perform an alkalinity titration in the field, to minimize changes during transport, and if necessary out of contact with the atmosphere, as reactions such as oxidation of Fe^{2+}, degassing of H_2S, and equilibration with atmospheric CO_2 can have an effect.

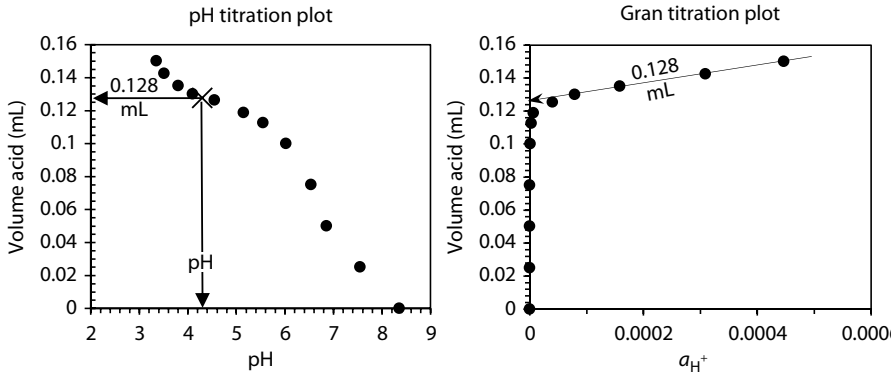

FIGURE 10.1 Alkalinity titration curves as milliliters of acid plotted with pH (left) and 10^{-pH} (right).

MAJOR ION GEOCHEMISTRY

Major Anions (Cl^-, F^-, SO_4^-, NO_3^-, Br^-)

Analyses of most anions are normally done in a laboratory by LC, although field kits and ion-specific electrodes exist for most anions of interest. HCO_3^- and CO_3^{2-} are determined by alkalinity titration (above). Less than 5 mL of sample can be analyzed for most major anions, although using 25-mL samples allows repeat measurements. Use HDPE or PP bottles rinsed a few times with the sample water. Samples should be filtered (0.45 μm) but not acidified. Store cool to prevent microbial activity and carbonate precipitation.

Major Cations, Minor and Trace Metals

All geochemical analyses require measurement of major metals or cations (Ca^{2+}, Mg^{2+}, Na^+, K^+, and SiO_2). Minor (Fe, Mn, Sr, and Ba) and trace metals may be required as well. Cations are usually analyzed by routine methods, including ICP-AES (inductively coupled plasma-atomic emission spectrometry), Microwave Plasma MP-AES, and ICP-MS (ICP-mass spectrometry). Only a few milliliters of sample are required for ICP instruments that measure multiple wavelengths or masses simultaneously. A typical size is 25 mL.

Carbonates and oxides can precipitate after sampling, and so samples are acidified to keep metals in solution. To ensure that only dissolved species are analyzed, the solution must be filtered first. Ultrapure nitric acid is used to acidify to below pH 2. Reagent grade is adequate for major and minor cations only. HCl should be used for brines, as it releases hydrogen ions more quickly. The filtered and acidified sample should be stored in fresh HDPE or PP bottles. Refrigeration is not required.

Nutrients

Nitrogen and phosphate species are important components of a water quality analysis. The basic analytical program includes the following:

a. Nitrate (NO_3^-) and nitrite (NO_2^-) that are routinely analyzed by LC with the full anion suite. Concentrations are routinely expressed as mass of nitrogen (gram formula weight [gfw] of 14), not nitrate (gfw of 62) or nitrite (gfw of 46) for ease of comparison with other nitrogen species, thus mg-N/L or ppm-N.
b. Ammonium (NH_4^+) with pH can provide the concentration of unionized ammonia (NH_3) that is highly toxic to fish at sub ppm-N concentrations. Total ammonium and ammonia are measured by flow-injection analysis with spectrophotometer detector. (FIA-SP) ammonium is highly sorbed onto soils, and so any concentration in groundwater is generally supported by a higher-sorbed concentration. This can be sampled from soils by extraction into a 2 M KCl solution followed by FIA-SP or colorimetric methods.

c. Phosphorus is an essential nutrient but in ecosystems can be the limiting nutrient for excessive algal growth, even at concentrations as low as 0.01 mg-P/L. It is typically measured in surface waters, but in groundwaters is typically below detection due to strong sorption onto clays in soil. It exists as mineralized orthophosphate, oPO_4, or as organically complexed phosphorus derived from biomass. At pH 7.2, orthophosphate has equal concentrations of $H_2PO_3^-$ and HPO_3^{2-}, which readily sorb onto clays, organics, and ferrihydrite. It is measured as dissolved oPO_4 (filtered) or total oPO_4 (unfiltered) by spectrophotometry as a colored molybdate complex. Total phosphate is measured by sample oxidation with hot nitric acid to convert organic phosphorus to oPO_4 followed by FIA spectrophotometric analysis.

Sulfate and Hydrogen Sulfide

Hydrogen sulfide is a highly toxic gas produced by sulfate reduction in many anaerobic aquifers. It is highly soluble as the ionized species HS^- in groundwaters above pH 7 (first dissociation constant for H_2S is $10^{-6.99}$) and below pH 7 as H_2S, which has a characteristic rotten-egg smell. It can be detected in high-pH waters by acidification to produce H_2S, as its odor can be detected at the ppb level in air. If present, care must be taken to measure its concentration and to separate it from dissolved sulfate, SO_4^{2-}. It is highly unstable in the presence of atmospheric O_2 and will rapidly oxidize to SO_4^{2-}. Diffusion of O_2 through plastic bottles will oxidize H_2S and HS^- during storage, so it must be measured or stabilized in the field. Field kits use methylene blue to complex the sulfides for analysis with color charts in the field or with a spectrophotometer.

Sulfate analyses on water that contains sulfide (H_2S or HS^-) will be erroneous due to contributions as it oxidizes. It is mandatory to remove dissolved sulfide, preferably with highly soluble cadmium acetate, as CdS has a diagnostic yellow color indicative of the presence of reduced S-species. Zinc acetate is less toxic and forms a white precipitate. Filter the water sample out of contact with air into a 100 mL plastic bottle with 10–20 mg of Cd-acetate or Zn-acetate powder at the bottom. CdS or ZnS will precipitate immediately and stabilize the sample. Cap and filter in the laboratory to separate the CdS or ZnS from the filtered sample with dissolved SO_4^{2-}. The lab may not want to analyze water with high residual Cd^{2+} or Zn^{2+} by LC. To measure sulfate concentration, take a second sample, filter, and preserve with 0.5 mL of 30% H_2O_2 for total sulfur as SO_4^{2-}. Then subtract the measurement for dissolved sulfide. Sulfate can also be measured in the field with reagent test kits.

ISOTOPES IN WATER

$\delta^{18}O$ and δD in Water

Sampling for ^2H and ^{18}O in water is simple, as neither is significantly affected by chemical and biological processes. Considering the high concentration of these isotopes in water (56 mol/L for O and 111 mol/L for H), there would have to be abundant exchange or dilution with other sources of isotopes to measurably affect their isotope ratios. Evaporation

from large bottles with large headspace can enrich the residual water, but a minor headspace (e.g., 50% or less of sample volume) in a tightly capped bottle is not a problem.

No filtering is required to stabilize the sample. Samples must be kept sealed to avoid evaporation; storing cool is recommended but not critical. Analysis by IRMS requires that the water is equilibrated with a gas. For $\delta^{18}O$, a 200 µL aliquot of water is equilibrated with 2% CO_2 in He-flushed, 12 mL Exetainer®—a septum-capped glass tube. For δD, the 200 µL aliquot equilibrates with 2% H_2 in He, catalyzed by platinum Hoko beads on a short baton placed in the Exetainer.

CRDS analysis is simpler, requiring only a 2 mL serum vial filled with the water sample. These are placed in a 100-sample tray on the automated instrument inlet system. The analysis is made on a 2 µL aliquot injected through a heated block to vaporize the sample into the laser cavity. Analysis of δD can be affected by small concentrations of CH_4 or higher-weight hydrocarbons. The instrument can detect so-affected samples and screen them, but corrections induce significant error. These instruments are also affected by salinity, although manufacturers are making improvements for these more complex analyses. Turbid samples should be filtered to extend syringe life.

CRDS instruments for vapor samples are available, which allow headspace analysis of water. This is particularly useful for porewater analysis in aquitard research (Wassenaar et al. 2008), where porewater in the core or sediment produces a vapor headspace that can be sampled and rapidly analyzed by the CRDS, eliminating the need to extract the porewater.

Tritium

Tritium is typically measured in precipitation and groundwaters although organically-bound tritium or OBT can be important, particularly in tracking this radionuclide in the vicinity of nuclear power plants and nuclear fuel processing sites. Tritium measurements can be made by one of three methods, including decay counting of enriched or non-enriched samples, ingrowth of the ^3He daughter and by accelerator mass spectrometrry (AMS). Sampling is constrained to some degree by the method used. Analysis of tritium by direct decay counting requires only a 25 mL sample. No field filtering or special preservation or storage is required. Even contamination by atmospheric water vapor is considered to be negligible, considering the concentration of H_2O vapor in air (e.g., 25 g vapor/m^3 of humid air, or $2.5 \cdot 10^{-5}$ g/cc, compared to 1 g/cc for water). Electrolytic enrichment of tritium in water requires 250 mL.

Tritium in modern waters today is in the range of 2–20 TU (recall that 1 TU represents a T/H ratio of 10^{-18}). Direct counting has an analytical detection of about 8 ± 8 TU, making this a reasonable method only for high background measurements, such as near nuclear facilities. The very high fractionation for tritium during electrolytic enrichment partitions tritium into the residual water:

$$H_2O + HTO \rightarrow \tfrac{1}{2}O_2 + H_2 + HTO \qquad \alpha T_{H_2O-H_2} > 7$$

This results in close to 100% concentration of tritium in the residual water, allowing a ten fold increase in its concentration with hydrolysis of 100 mL to 10 mL. This reduces the analytical detection to about 0.8 ± 0.8 TU (10^{-18}) or better. For decay counting OBT samples, the material is first combusted to water and CO_2.

Analysis by ingrowth of the daughter isotope, ^{3}He, allows another order of magnitude to be achieved. Noble gas mass spectrometers can analyze as few as about 10,000 atoms of ^{3}He, which reduces the analytical detection limit to very low values. Consider a water sample with 1 TU sealed in a helium-tight container for 30 days:

Tritium content:		$1\text{TU} = 10^{-18}$ T per H
Tritium atoms in 100 mL	100 mL	$= 100$ g H_2O
		$= 100/18 \times 2 = 11.1$ mol H
		$= 11.1 \times 6.02 \times 10^{23}$
		$= 6.7 \times 10^{24}$ atoms H
		$= 6.7 \times 10^{24} \times 10^{-18}$
		$= 6.7 \times 10^{6}$ atoms T
T decays to ^{3}He per second		$a_T = \lambda_T n_T$
		$= \left[\ln(2)/T_{½}\right] \times n_T$
		$= 1.784 \times 10^{-9} \times 6.7 \times 10^{6}$
		$= 0.012$ decays to ^{3}He per second
Ingrowth of ^{3}He	30 days	$= 2{,}592{,}000$ seconds
		$= 2{,}592{,}000 \times 0.012 = 30{,}982$ atoms of ^{3}He

In cc of gas, this becomes: $30{,}982/6.02{\cdot}10^{23} \times 22404\ (cc_{STP}/mol) = 1.15 \times 10^{-15}\ cc_{STP}$ ^{3}He

With larger samples and longer ingrowth times, detection limits better than 0.1 TU are readily achieved. Helium-3 ingrowth is also used for OBT samples, where combustion to water is not required.

Tritium analysis by AMS provides the advantage of very small sample sizes, as less than a milligram of water or organic material can be analyzed. However, the detection limit is in the range of 10^{-15} and so only samples from contaminated sites near nuclear activities can be considered. For AMS, samples are converted to titanium hydride, TiH_2, prepared as a solid target for mounting in the cesium ion source carousel. AMS analysis is described below for radiocarbon.

DISSOLVED CARBON

Dissolved Inorganic Carbon and Dissolved Organic Carbon Concentration and ^{13}C

Sampling for dissolve inorganic and organic carbon (DIC and DOC) is recommended for any study where redox processes and the carbon system are important. Carbon-13 analyses on DIC and DOC are a requirement for the interpretation of radiocarbon data but are also important for the interpretation of geochemical and microbiological processes in groundwater. Traditional analysis of DIC by acidification of water under

vacuum has been replaced by total carbon analyzers that use a two-step process for conversion of DIC and DOC to CO_2, interfaced with an IRMS (St-Jean 2003).

Samples are collected in 40 mL amber glass septum vials, and often now in 12 mL exetainer septum tubes. Sampling requires field filtering to 0.45 μm to remove particulates and bacteria, which can alter the DIC and DOC during sample storage. These are placed in a sample rack for automated analysis on the TC followed by IRMS. The sample is injected and acidified to convert DIC species to CO_2, which is sparged using a He carrier gas to carry the sample to the detector for measurement of concentration. The CO_2 sample in the He stream is then carried to the IRMS to measure $\delta^{13}C_{DIC}$. The residual water sample is then wet-oxidized using sodium persulfate ($Na_2S_2O_8$) to convert organic carbon to CO_2, which is again sparged with the carrier gas and analyzed for both concentration and $\delta^{13}C_{DOC}$.

In addition to bulk DOC analysis, compound-specific analysis has gained considerable attention. This is the identification and separation of carbon compounds for isotope analysis of specific compounds. These can include humic and fulvic acids, as well as fatty acids, such as acetate (CH_3COOH) and ethanol (C_2H_5OH). New interfaces involving LC to separate organic compounds followed by TC oxidation and trapping of the fraction converted to CO_2. Few laboratories are able to offer this new interface.

Radiocarbon

Radiocarbon measurements are expressed as activity, $a^{14}C$ relative to the standard Modern Carbon (MC). The activity of MC is equal to the initial ^{14}C activity of wood grown in 1890. The Modern Carbon standard is the National Institute of Standards and Technology oxalic acid SRM 4990 C. MC has an activity of 0.226 Bq/g C, and its abundance relative to ^{12}C in atmospheric CO_2 is 1.17×10^{-12}. Measurements are expressed as percent MC and are normalized to a $\delta^{13}C$ value of –25‰ to account for fractionation in the environment and during analysis.

The low abundance of ^{14}C and low radioactivity of only 0.226 Bq/g means that for radiometric analysis (counting decay events), one must either have a lot of sample or count β-decay events for a long time. Limitations to decay counting come from the background interference generated by cosmic rays impinging on the detector. While radiometric methods, such as gas proportional counting with anticoincidence and shielding, greatly improved detection limits, large sample sizes and long counting time remain impediments to laboratory throughput. Although the number of decays per second in a gram of carbon is low, the number of atoms, $n^{14}C$, in that 1 g of carbon is rather substantial:

$$\begin{aligned}
\text{modern carbon} &= 0.226\ \text{Bq/g} \\
a^{14}C(\text{Bq}) &= \lambda^{14}C \times n^{14}C(\text{atoms}) \\
\lambda^{14}C &= \ln(2)/T_{1/2} = 3.84 \times 10^{-12}\,(\text{s}^{-1}) \\
n^{14}C &= 0.226/3.84 \times 10^{-12} = 58.9\ \text{billion atoms } ^{14}C
\end{aligned}$$

Traditional radiocarbon dating of groundwaters required stripping DIC from approximately 50 L of groundwater made alkaline with NaOH and precipitated as $BaCO_3$

or $SrCO_3$ by adding barium or strontium chloride. However, the highly alkaline precipitates are highly reactive with atmospheric $^{14}CO_2$ and so contamination is very difficult to avoid.

Traditional decay counting methods are now replaced with atom counting by mass spectrometry. However, the low natural abundance of radiocarbon at 10^{-12} or less requires very high energies of accelerator mass spectrometry (AMS) to resolve the trace ^{14}C ion beam from abundant ^{12}C. AMS analysis for groundwater involves stripping DIC from solution under vacuum by acidification. For DOC, a wet oxidation step is included. The DIC or DOC collected as CO_2 is reacted with H_2 at 600°C on zero-valence iron to produce graphite. This is pressed into a small aluminum "target" holder and mounted in the source of the AMS.

AMS has greatly reduced sample requirements. Samples of 1 mg C can be routinely analyzed. The high precision of atom counting allows greater ages to be measured than was possible by decay-counting methods. The very low background allows measurement down to less than 0.1 pMC or about 10 half-lives (57,300 years).

The sample volume for typical groundwaters has reduced from 50 L for decay counting to less than 500 mL for AMS.

Targets are loaded (up to 100 or more) in a source carousel on the AMS. A cesium ion beam sputters this target, producing negatively charged carbon ions that are accelerated toward the positive high-voltage terminal in the accelerator, passing through a charge-stripping canal of Ar gas to produce cations that are repelled with increasing acceleration out along the flight tube and through the analyzing magnet where the ion beam is separated into a spectrum of masses. The ^{14}C ions continue into the gas ionization chamber to be counted, while the abundant isotopes, ^{12}C and ^{13}C, are analyzed by faraday cups.

The ^{14}C activity of DOC has gained interest in hydrogeological studies because of its importance in the geochemical evolution of groundwater and because DOC from the soil zone can be used for groundwater dating. It is also an important tracer of carbon sources in carbon cycling research. Sampling and preparation of DOC for ^{14}C can be complicated if specific components of DOC are required. This involves column separation and concentration (Wassenaar et al. 1991; Artinger et al. 1996). Humic acid (HA) can be precipitated from a water sample by acidification with HCl to pH 2, whereas the residual fulvic acid (FA)—still in solution—can be separated on an XAD-8 resin followed online by a silicalite column to trap at least a portion of the low-molecular-weight DOC (LMW-DOC). As DOC concentrations in groundwater in general are <5 mg/L, up to 1 L of water is required. Samples should be filtered to remove bacteria and particulate carbon and stored cool in amber glass bottles. Alternatively, they can be stored in Nalgene plastic bottles and frozen to prevent sorption of organics onto the walls.

NITROGEN SPECIES ISOTOPES

Nitrogen species in water and soils, including nitrate, ammonium, and organic nitrogen, are important redox species as well as potential contaminants. Routine analysis of their concentrations and isotopes are important to observe nitrogen transport and

reaction. A variety of methods are available for isotopes of these species, and so the laboratory protocols and minimum sampling requirements should be discussed in advance of sampling.

NO_3^-–^{15}N AND ^{18}O

Measurement of $\delta^{15}N_{NO_3^-}$ alone provides much of the evidence required for denitrification or anammox reaction in groundwater. However, $\delta^{18}O_{NO_3^-}$ is diagnostic of the origin of nitrate as well as providing evidence for denitrification. Nitrate can be analyzed for ^{15}N and ^{18}O by bacterial reduction to N_2O (Sigman et al. 2001). The denitrifier method requires strict laboratory protocols for growth of the *Pseudomonas aureofaciens* bacteria and incubation during conversion of NO_3^- to N_2O for IRMS analysis, and few laboratories offer the method. Inorganic methods are based on chemical conversions and separation. For $^{15}N_{NO_3}$, a common method is reduction to NH_4^+ using Devarda's alloy, a Cu–Al alloy with about 5% Zn followed by precipitation as ammonium sulfate or without the ammonium step by precipitation as $AgNO_3$. For ^{18}O, NO_3^- is stripped from the water by column separation and precipitation as dried nitric acid, and then baked with mercuric cyanide to produce CO_2 for IRMS. Minimum amounts are generally about 1 mg/L.

NH_4^+–^{15}N

The analysis of $\delta^{15}N_{NH_4^+}$ is carried out by precipitation of dissolved ammonium as ammonium sulfate. The ammonium sulfate is then analyzed by combustion and reduction to N_2 gas in an elemental analyzer interfaced with an IRMS (EA-IRMS) (Sebilo et al. 2004; Schleppi et al. 2006). About 100 μg of dissolved NH_4^+–N is converted to NH_3 by raising the solution pH above 10. Ammonia diffuses from the solution and is trapped with sulfuric acid.

Groundwater samples are generally collected as bulk water samples. The typically low concentration of ammonium in groundwater generally requires that 1 L be collected. It does not need to be filtered, but should be frozen to stop bacterial activity. Nitrate concentrations are usually higher, and as little as 50 mL can be taken. Again, filtering is not required if it is kept frozen. In low-nitrate waters, ion exchange resins can be used.

SULFUR SPECIES ISOTOPES

Isotopes of dissolved, mineral, and organic sulfur compounds are helpful in tracing sulfur origins and cycling, as well as tracing the origin of salinity. Sulfur in reduced form (S^{2-}) can be complexed with carbon as organically bound sulfur in a range of substrates from marine sediments to landfill leachates. It is also complexed with metals as sulfides. In its oxidized state, S^{6+}, it forms the sulfate anion that precipitates as gypsum ($CaSO_4{\cdot}2H_2O$) or as anhydrite ($CaSO_4$) above about 50°C. Aqueous forms, discussed earlier for concentration analysis, include principally dissolved SO_4^{2-} and the sulfide species, H_2S and HS^-.

SO_4^{2-}–^{34}S AND ^{18}O

Sampling sulfate for analysis of ^{34}S in water with no sulfide (H_2S and HS^-) is straightforward. However, where dissolved sulfide is present (it can be detected by smell), sampling is complicated because oxidation by O_2 from the air will convert the sulfide to SO_4^{2-} and neither component will then be representative of in situ conditions. In this case, they must be separated in the field, or at least stabilized using Cd-acetate or Zn-acetate to precipitate the sulfide (see earlier for concentration analysis).

Isotopes of sulfate are measured on $BaSO_4$ or $SrSO_4$, which is precipitated from a filtered sample by the addition of $BaCl_2$ or $SrCl_2$. The sample is brought to a pH between 4 and 5 to prevent coprecipitation of carbonate. The sulfate concentration should be measured to calculate the amount of barium chloride needed to fully precipitate the sulfate. For example, 10 mg/L SO_4^{2-}, extraction from 100 mL will provide sufficient sulfate for an analysis.

For this purpose, a field kit can be used. Alternatively, a simple test for sulfate is to add barium chloride to an aliquot of sample water; adjusted to pH 5 to prevent carbonate precipitate from forming. The solution will turn cloudy if SO_4^{2-} is present. Pour slowly into a graduated cylinder (100 mL will do) with a black X on the bottom until the X is no longer visible. The sulfate concentration is roughly determined from the height of water in the cylinder (in cm), using the following equation:

$$\text{Concentration } SO_4^{2-} = -130 \times \log(\text{cm}) + 190 \text{ mg/L}$$

Only a few milligrams of $BaSO_4$ are required for an isotope analysis. For ^{34}S, this is done with an elemental analyzer interfaced with an EA-IRMS. The high-temperature reaction releases the sulfur as SO_2 gas. The ^{18}O content of the sulfate is measured by pyrolysis conversion to CO using a glassy-carbon reaction tube with gas chromatography (GC) separation of the gases (TC-EA-IRMS).

H_2S–^{34}S

Hydrogen sulfide must be immediately removed in the field from groundwater collected for sulfate concentration and isotopes, as sulfide is rapidly oxidized to SO_4^{2-} by O_2. This can be done by adding a few milligrams (tip of a spatula) of cadmium or zinc acetate to the sampling bottle before filling. Filter the water in-line out of contact with air as the bottle is filled. The precipitated ZnS (white) or CdS (yellow) can be filtered from the water in the laboratory, dried, and weighed for analysis of $\delta^{34}S$. Sulfate can then be precipitated from the sulfide-free water for analysis. Isotope analysis is carried out by combustion in an elemental analyzer to SO_2. Less than 0.1 mg sulfide is required.

ISOTOPES OF THE HALIDES

Other nonmetal elements with isotopes of interest in hydrogeology include the halides, which as anions are important tracers of salinity. The lightest, fluoride, has only one isotope, ^{19}F, which precludes it as a tracer, but has one important feature.

Coordinated with sulfur as SF_6 allows analysis of both $\delta^{34}S$ and $\delta^{33}S$ without any isobaric interference, unlike analysis as SO_2, which has interferences from both ^{18}O and ^{17}O. Chlorine has ^{37}Cl and ^{35}Cl as well as the important radioisotope, ^{36}Cl. Bromine has two stable isotopes, ^{79}Br and ^{81}Br, with almost equal abundances, but its radioisotopes are too short-lived to be of use in hydrogeology. Finally, iodine, like fluorine, has one stable isotope, ^{127}I, and two radioisotopes relevant to environmental science. ^{131}I has an 8-day half-life and is an important uranium fission product that is monitored globally for evidence of releases from nuclear incidents. ^{129}I has a 15.8 million year half-life and is important as a tracer of releases from spent fuel, but also for dating age and movement of brines.

^{37}Cl

The measurement of stable chlorine isotopes ($^{37}Cl/^{35}Cl$) is carried out by IRMS of methyl chloride gas (CH_3Cl). For water samples, less than 1 mg of Cl^- is required, and water samples require only filtration in the field or laboratory. Laboratory analysis involves precipitation of Cl^- as AgCl by the addition of $AgNO_3$. This is converted to CH_3Cl by the reaction of methyl iodide (CH_3I).

Analysis of ^{37}Cl in organochlorine compounds, such as PCE and C_2Cl_4, requires more complicated sampling and preparation techniques. While such analyses are now more routinely deployed for tracing the origin and biodegradation of these compounds, their application requires collaboration with the laboratory facility that will undertake the analysis.

^{36}Cl

The importance of ^{36}Cl as a dating tool is presented in Chapter 8. It is present in the natural environment with an abundance ratio on the order of 10^{-13}. This makes measurement by radiometric methods impractical (Figure 4.7). This low abundance is readily measured by AMS, although the high acceleration energy required to eliminate the ubiquitous ^{36}S isobar is available at a very few AMS facilities worldwide. Gas collision cells have now been developed as an isobar separator to neutralize SO_2 and remove it from the Cl^- ion beam (Kieser et al. 2011), which makes ^{36}Cl analysis possible at the more common medium-energy AMS facilities. Targets are prepared as AgCl. Only a milligram is required, allowing precipitation in the laboratory typically from less than 500 mL of water. Filtering is the only requirement, with no particular constraints on storage.

^{81}Br

Similar to ^{37}Cl, ^{81}Br can be used to trace sources of this halide, and also brominated hydrocarbons and industrial compounds. Shouakar-Stash et al. (2005) developed the method currently adopted for $\delta^{81}Br$ for inorganic samples, based on that of $\delta^{37}Cl$. As little as 0.1 mg (1 μmol) of Br^- is precipitated as AgBr by the addition of $AgNO_3$ and converted to CH_3Br. Also like Cl^-, the sample is very stable and nonreactive,

requiring only filtering before precipitation. Sampling for brominated hydrocarbons should be discussed with the analytical facility.

^{129}I

Both stable ^{127}I and the long-lived radioisotope, ^{129}I, are of interest for water quality. Iodine is an essential nutrient for thyroid function that is supplemented as iodized salt in most countries, precluding a need for I from water supplies. Its biophilic nature makes radioiodine a hazardous product of uranium fission. The short-lived radioisotope, ^{131}I with half-life of only 8 days, is of little concern in groundwaters, while ^{129}I ($T_{½}$ = 15.8 million years) is persistent and mobile. It is also formed naturally from spontaneous fission of ^{238}U and can be used as a dating tool (see Chapter 8), making iodine an element of interest in hydrogeology.

Unlike chlorine and bromine, which are present in groundwaters in reduced forms as Cl^- and Br^-, iodine has two common valence states, as reduced iodide, I^-, with a valence of –I or as iodate, IO_3^-, with a valence of +V. Under low pH conditions, it can also be present as elemental I_2 as crystalline iodine and I_2 gas with low solubility in polar liquids, like water. Figure 9.55 shows the redox and pH controls on iodine speciation. As iodine is very stable in groundwater as either I^- or IO_3^-, sampling is very straightforward, with only 25 mL of filtered water required for stable iodine concentration and 200 mL for ^{129}I. Stable I is typically present in groundwaters at the ppb level, which is not possible with routine LC as used for the major anions. ICP-MS provides a limit of detection below 1 ppb and is the commonly used method of analysis for total I. Lower concentrations can be measured by extraction of iodine as an iodopentanone complex into hexane for GC analysis (Marchetti et al. 1997). For iodine speciation, iodide can be separated from iodate through pretreatment with anion-specific columns.

The concentration of ^{129}I in groundwaters is typically 10–100 million atoms per liter, with an abundance relative to stable ^{127}I of about 10^{-8}. This allows routine analysis by AMS. It is extracted from water by adding a carrier of stable ^{127}I and conversion to iodide, which can be precipitated from solution as AgI. As chloride would coprecipitate, it is removed by converting I^- to I_2 at low pH, partitioning into a nonpolar liquid—hexane—and then reducing back to I^- and into DI.

Radioiodine in solids (organics, soils, rock) can be analyzed by extraction using caustic fusion, involving a high-temperature treatment of the powdered sample mixed with solid sodium hydroxide followed by leaching and hexane extraction as for waters. A newly developed carrier-free method involves high-temperature combustion in a stream of O_2 with and trapping in an alkaline solution (Yi et al. 2011).

ISOTOPES OF MINOR ELEMENTS

While less routinely considered in hydrogeological studies, stable isotopes of some minor elements can be readily analyzed and provide useful information for tracing groundwaters and brines. A few of the isotope ratios that can be considered include ^{6}Li/^{7}Li, ^{11}B/^{10}B, and ^{87}Sr/^{86}Sr. Ratios are expressed in delta-permil format for δ^6Li

and $\delta^{11}B$, but in ratio format, $^{87}Sr/^{86}Sr$, for strontium. All three are analyzed by thermal ionization mass spectrometry (TIMS), where the element is concentrated from water with ion-exchange columns and coated onto a tungsten filament. The sample-coated filament is mounted in the high vacuum source of a TIMS instrument and heated to produce an ion current that is measured by magnetic sector mass spectrometry. Lithium and boron isotopes can also be measured by multicollector ICP-MS (MC-ICP-MS) directly from prepared solutions.

GASES

Gases are an integral part of most geochemical systems, and are particularly important in redox reactions. Both concentrations and isotopes of gases provide valuable information, and are included in most geochemical programs such as PHREEQC.

Both dissolved and effervescing gas phases can be sampled. In a natural spring discharge or with pumping of deep groundwaters, as the water approaches surface pressure, degassing can occur, and this separate gas phase can be sampled. In most confined aquifers, a gas phase does not naturally exist, although degassing can occur after drilling and pumping. If gases are bubbling from groundwaters at discharge, their aqueous concentrations (mg/kg or cc_{STP}/cc_{H_2O}) can only be approximated. However, molar ratios of the gases (relative abundances) and isotopes of these gases can be measured.

Routinely sampled and analyzed gases include CO_2, N_2, N_2O, O_2, and CH_4 as tracers of biological activity. Measurement of inert Ar is helpful to normalize to atmospheric concentrations in shallow groundwater systems where no significant geogenic ^{40}Ar is produced. Higher-weight alkanes (ethane, C_2H_6, propane, C_3H_8, etc.) are important in the studies of deep gas and hydrocarbon contamination.

Effervescing Gases

Sampling a separate gas phase in a spring or well discharge is most effectively done by inverting a glass bottle (plastic is diffusive to some gases) filled with sample water over the bubble stream, or have the pump discharge line placed into the neck of the bottle for full capture of gas bubbles. Use a funnel in the neck of the bottle to collect the rising gas bubbles. After displacing at least 50% of the volume with gas, remove the funnel and place a septum cap on the bottle under water. Solid caps require reversing the procedure in the laboratory in a container of boiled or gas-flushed water.

Dissolved Gases

Dissolved gas samples are required for molar concentration in water. They are simply collected from noneffervescing groundwater by completely filling a 12–250 mL glass septum bottle (depending on the number of analyses) and capping it. To

minimize atmospheric contamination, this can be done in a larger container of the groundwater with capping under water. No filtering should be done unless an inline system is used that precludes air contamination.

A note about the discharge line used between the well or spring and the sampling point is important. Many types of plastic, particularly silicon tubing, are diffusive to gas and will inevitably allow contamination by atmospheric O_2, noble gases, and other gases. For critical samples, consider using soft copper tubing available at any hardware store.

Gas diffusion samplers can be used to collect water-free gas samples in the field. These are described later for sampling noble gases, but are equally useful for dissolved reactive gases in groundwater. Simple devices as shown here are useful for shallow deployments in groundwaters with total gas pressures close to 1 atm.

Analysis

Concentration analysis by GC requires milliliter to microliter volumes, so very little gas at standard pressure and temperature is required. GC analysis uses a carrier gas (usually He) that carries the sample gases by advection along a coated capillary tube, where they are separated and then measured with one of several detectors, including a flame ionization detector for combustible gases (H_2, CH_4, C_2H_6, C_3H_8, etc.), and a thermal conductivity detector for CO_2, N_2, N_2O, O_2, Ar, and He. Gas standards are used to calibrate the sample gases for their range of concentration.

Gas phase samples are directly injected into the GC, whereas dissolved gases must first be extracted from solution. This is achieved by injecting a volume (usually 20 mL) of helium into the sample septum bottle with simultaneous extraction of an equivalent volume of water to create a headspace of known volume at atmospheric pressure. This is agitated to reach equilibrium between the dissolved gases and the created headspace, and then the headspace gas (He and sample gases of interest) can be sampled and analyzed. Henry's law constants for laboratory temperature allow calculation of dissolved concentrations.

Carbon, oxygen, nitrogen, argon, and hydrogen isotope analyses are routinely done by continuous-flow IRMS. Gases, including O_2, N_2, CO_2, and N_2O mixtures, are injected into a GC interface to separate before advection to the mass spectrometer in a He carrier. The GC interface can be followed by either (1) a combustion step (GCC) to sequentially convert hydrocarbon gases (CH_4, C_2H_6, C_3H_8, etc.) in the sample to CO_2 for $\delta^{13}C$ analysis; or (2) a pyrolysis interface (GC-TC) to reduce hydrocarbon gases to H_2 and CO for analysis of δD, and $\delta^{18}O$ in certain samples, such as nano-sized water samples. The sample peak intensity measured on the IRMS can be used, with calibration standards, to quantify concentration, but with greater uncertainty than by traditional GC, as described earlier.

Cavity ring-down laser attenuation spectrometers are now available (Los Gatos Research, Picarro Inc.) for direct, routine analysis of $\delta^{13}C_{CO_2}$, $\delta^{13}C_{CH_4}$, and $\delta^{15}N_{N_2O}$. These instruments are field portable and require only stable temperature and AC current for operation. Analytical uncertainties continue to improve and now rival those of IRMS, when interferences are not present.

NOBLE GASES

Noble gases and their isotopes are important geochemical tools for many hydrogeological systems. All five stable noble gases (He, Ne, Ar, Kr, and Xe) have different temperature–solubility relationships used for recharge temperature reconstructions. They are mostly derived from atmospheric equilibrium, but are also contributed to groundwaters from subsurface production. Measurements of ^{3}He with tritium provide a precise groundwater dating tool for modern flow systems, whereas ^{4}He, ^{40}Ar, and other geogenic isotopes of noble gases can date very old groundwaters.

Concentrations of the noble gases in the atmosphere are expressed as a percent of the total atmosphere, or as parts per million by volume (ppmv). In water, concentrations are generally expressed as the volume of gas (at STP, standard temperature, 273.16 K, and pressure, 1 atm) per volume of water, that is, cc_{STP}/cc_{H_2O}. Their low concentrations in groundwater make it a challenge to sample without incorporating air.

Water Samples

With the exception of strong He and Ar enrichments from geogenic sources in old samples, noble gases are close to atmospheric equilibrium, and so air contamination during sampling must be avoided. Further, diffusion in and out of the sample container during storage can impact the lighter noble gases. For this reason, 3/8th inch OD (outside diameter) (9.5 mm) thick-walled soft copper tubing (annealed refrigeration tubing) is used.

For water samples, a 20-cm Cu tube is filled directly in the field, although care must be taken that all air bubbles are removed from the copper tube before sealing. Running excessive sample water through the tubing, at formation pressure, to avoid effervescence, is critical to exclude air from the sample. The tube is clamped with two refrigerator clamps, each placed square to the tube axis 3 cm from each end; tightened together but with the discharge end clamp leading and fully tightened first to prevent a decrease in pressure and degassing in the tube. Stabilize the clamp in a bed or vice and tighten with a socket wrench until the ends of the clamp touch. This creates a cold weld in the copper at the pinch point, which can hold even He gas indefinitely. The ends should be rinsed with DI, particularly when brines are sampled.

Passive Gas Diffusion Samplers

Gas diffusion samplers are largely replacing water samples for noble gases (Sanford et al. 1996; Gardner and Soloman 2009; Matsumoto et al. 2012). Figure 3.9 demonstrates the principle of the partial pressure of dissolved gases using a diffusion sampler, which is a gas-permeable membrane sealing a copper tube that is immersed in the groundwater. Water, being a polar liquid, cannot diffuse through the membrane, but gases will. Over time, gas contents of the tube equilibrate with those present as dissolved gases in the adjacent groundwater, each to their respective partial pressure ($cc_{STP}/cc_{copper\text{-}tube}$). The distribution of gases between the sampler and the groundwater is established by the Henry's constant for that gas (Table 3.5) and the ambient

temperature of the groundwater. As gases preferentially partition into the gas phase, they have a much higher concentration (moles or cc_{STP} per volume) in the diffusion sampler tube than in the groundwater. This also means that a given diffusion sampler volume will be equilibrated with a much larger volume of water in the aquifer. The time to achieve equilibrium can be short for small-volume samplers, but may vary up to days, depending on the rate of groundwater movement around the sampler. Once equilibrated, the samplers are retrieved and immediately clamped (refrigeration clamp, as for water samples) or crimped with a tool to shear the end of the tube closed in a cold weld. For groundwaters with dissolved gas pressures much greater than 1 atm, as found in deep deployments with excess He or CH_4, volume changes due to gas expansion when recovered will lower the measured gas partial pressure. A self-sealing diffusion sampler developed by Gardner and Solomon (2009) for noble gases precludes this artifact.

Sampling rare radioisotopes of noble gases, including ^{39}Ar and ^{81}Kr, requires several liters of water to be collected and stripped of Ar and/or Kr under atmosphere-free conditions. The use of these rare atmospheric isotopes for dating submodern groundwater (^{39}Ar, $T_{½}$ = 269 years) or very old groundwater (^{81}Kr, $T_{½}$ = 229,000 years) and their analysis by laser atom trapping (Jiang et al. 2012) are discussed in Chapter 9.

Analysis

In the case of the water-filled copper tube samples, analysis requires an initial separation of the gases from the water under vacuum. Diffusion samplers are water-free and do not require this step. Noble gases are separated from the reactive gases (N_2, O_2, CO_2, etc.) with getter pumps (reactive metal alloys at elevated temperature). The noble gases themselves can be separated cryogenically and are analyzed for concentration and isotopes on a magnetic-sector noble gas mass spectrometer, calibrated with volumetrically pipetted air standards that are temperature- and pressure-corrected to STP. Quadrupole mass spectrometers can also be used to measure the concentration of the more abundant isotopes or for quantitative analysis by spike dilution (Poole et al. 1997).

References

Aeschbach-Hertig, W., 2014. Radiokrypton dating finally takes off. *PNAS*, 111: 6856–6857.

Aeschbach-Hertig, W., Peeters, F., Beyerle, U., and Kipfer, R., 1999. Interpretation of dissolved atmospheric noble gases in natural waters. *Water Resources Research*, 35: 2779–2792.

Aeschbach-Hertig, W., Peeters, F., Beyerle, U., and Kipfer, R., 2000. Palaeotemperature reconstruction from noble gases in ground water taking into account equilibration with entrapped air. *Nature*, 405: 1040–1044.

Aggarwal, P. K., Alduchov, O. A, Froehlich, K. O., Araguas-Araguas, L. J., Sturchio, N. C., and Kurita, N., 2012. Stable isotopes in global precipitation: A unified interpretation based on atmospheric moisture residence time. *Geophysical Research Letters*, 39, L11705.

Alvaredo Quiroz, N. G., Kotzer, T. G., Milton, G., Clark, I. D., and Bottomley, D., 2002. Partitioning of ^{127}I and ^{129}I in an unconfined glaciofluvial aquifer on the Canadian Shield. *Radiochimica Acta*, 90: 469–478.

Anderson, K. K. and Hooper, A. B., 1983. O_2 and H_2O are each the source of one O in NO_2^- produced from NH3 by nitrosomas: ^{15}N–NMR evidence. *FEBS Letters,* 64: 236–240.

Andrews, J. N., Davis, S. N., Fabryka-Martin, J., Fontes, J.-Ch., Lehmann, B. E., Loosli, H. H., Michelot, J-L., Moser, H., Smith, B., and Wolf, M., 1989. The in situ production of radioisotopes in rock matrices with particular reference to the Stripa granite. *Geochimica et Cosmochimica Acta*, 53: 1803–1815.

Andrews, J.A. and Fontes, J.-Ch., 1992. Importance of the in situ production of ^{36}Cl, ^{36}Ar and ^{14}C in hydrology and hydrogeochemistry. In *Isotope Techniques in Water Resources Development 1991*, IAEA Symposium 319, March 1991, Vienna: 245–269.

Araoka, D., Kawahata, H., Takagi, T., Watanabe, Y., Nishimura, K., and Nishio, Y., 2013. Lithium and strontium isotopic systematics in playas in Nevada, USA: Constraints on the origin of lithium. *Mineralium Deposita*, 49: 371–379.

Aravena, R. and Wassenaar, L. I., 1993. Dissolved organic carbon and methane in a regional confined aquifer: Evidence for associated subsurface sources. *Applied Geochemistry,* 8: 483–493.

Aravena, R., Wassenaar, L. I., and Barker, J. F., 1995. Distribution and isotopic characterization of methane in a confined aquifer in southern Ontario. Canada. *Journal of Hydrology*, 173: 51–70.

Aravena, R., Wassenaar, L. I., and Plummer, L. N., 1995. Estimating ^{14}C groundwater ages in a methanogenic aquifer. *Water Resources Research*, 31: 2307–2317.

Artinger, R., Buckau, G., Kim, J. I., Geyer, S., and Wolf, M., 1996. Influence of sedimentary organic matter on dissolved fulvic acids in groundwater: Significance for groundwater dating with 14C in dissolved organic matter. In *Isotopes in Water Resources Management*, vol. 1, IAEA Symposium 336, March 1995, Vienna, pp. 57–72.

Bäckström, M., Karlsson. S., Bäckman. L., Folkeson, L., and Lind, B., 2004. Mobilisation of heavy metals by deicing salts in a roadside environment. *Water Research*, 38: 720–732.

Bajjali, W., Clark, I. D., and Fritz, P., 1997. The artesian thermal groundwaters of northern Jordan: Insights to their recharge history and age. *Journal of Hydrology*, 192: 355–382.

Bao, H. and Gu, B., 2004. Natural perchlorate has a unique oxygen isotope signature. *Environmental Science and Technology*, 38: 5073–5077.

Barker, J. F. and Pollock, S. J., 1984. The geochemistry and origin of natural gases in southern Ontario. *Bulletin of Canadian Petroleum Geology*, 32: 313–326.

Barnes, I. and O'Neil, J.R., 1978. Present day serpentinization in New Caledonia, Oman and Yugoslavia. *Geochimica Cosmochimica Acta,* 42: 144–145.

Bayari, S., 2002. TRACER: An EXCEL workbook to calculate mean residence time in ground water by use of tracers CFC-11, CFC-12 and tritium. *Computers & Geosciences*, 28: 621–630.

Benetti, P., Calaprice, F., Calligarich, E., Cambiaghi, M., Carbonara, F., Cavanna, F., Cocco, A. G. et al., 2007. Measurement of the specific activity of ^{39}Ar in natural argon. *Nuclear Instruments and Methods in Physics Research A*, 574: 83–88.

Bentley, H. W., Phillips, F. M., and Davis, S. N., 1986. Chlorine-36 in the terrestrial environment. In *Handbook of Environmental Isotope Geochemistry, Volume 2, The Terrestrial Environment, B*, edited by P. Fritz and J.-Ch. Fontes, Elsevier, Amsterdam, the Netherlands: 427–480.

Bernat, M., Church, T., and Allegre, C. J., 1972. Barium and strontium concentrations in Pacific and Mediterranean sea water profiles by direct isotope dilution mass spectrometry. *Earth and Planetary Science Letters*, 16: 75–80.

Bester, M. L., Frind, E. O., Molson, J. W., Rudolph, D. L., Numerical investigation of road salt impact on an urban wellfield. *Ground Water*, 44: 165–175.

Bieringer, J., Schlosser, C., Sartorius, H., and Schmid, S., 2009. Trace analysis of aerosol bound particulates and noble gases at the BfS in Germany. *Applied Radiation and Isotopes*, 67: 672–677.

Bigalke, M., Weyer, S., and Wilcke, W., 2010. Copper isotope fractionation during complexation with insolubilized humic acid. *Environmental Science & Technology*, 44: 5496–5502.

Birkham, T. K., Hendry, M. J., Wassenaar, L. I., and Mendoza, C. A., 2007. A transient model of vadose zone reaction rates using oxygen isotopes and carbon dioxide. *Vadose Zone Journal*, 6: 67–76

Blowes, D. W. and Ptacek, C. J., 1992. Geochemical remediation of groundwater by permeable reactive walls: Removal of chromate by reaction with iron-bearing solids. *Proceedings of the Subsurface Restoration Conference, 3*rd *International Conference on Ground Water Quality Research* Dallas, TX, June 21–24, 1992, pp. 214–216.

Böhlke, J. K., Ericksen, G. E., and Revesz, K. M., 1997. Stable isotope evidence for an atmospheric origin of desert nitrate deposits in northern Chile and Southern California, USA. *Chemical Geology*, 136: 135–152.

Böhlke, J. K., Smith, R. L., and Miller, D. N., 2006. Ammonium transport and reaction in contaminated groundwater: Application of isotope tracers and isotope fractionation studies. *Water Resources Research*, 42. doi:10.1029/2005WR004349.

Bortolami, G. C., Ricci, B., Susella, G. F., and Zuppi, G. M., 1979. Isotope hydrology of the Val Corsaglia, Maritime Alps, Piedmont, Italy. In *Isotope Hydrology 1978*, vol. 1, IAEA Symposium 228, Neuherberg, Germany, June 1978, pp. 327–350.

Bottomley, D. J., Chan, L. H., Katz, A., Starinsky, A., and Clark, I. D., 2003. Lithium isotope geochemistry and origin of Canadian Shield Brines. *Ground Water*, 41: 847–856.

Bottomley, D. J., Clark, I. D., Batty, N., and Kotzer, T., 2005. Geochemical and isotopic evidence for a genetic link between Canadian Shield brines, dolomitization in the Western Canada Sedimentary Basin, and Devonian calcium-chloridic seawater. *Canadian Journal of Earth Sciences*, 42: 2059–2071.

Bottomley, D. J., Gregoire, D. C., Raven, K. G., 1994. Saline groundwater and brines in the Canadian Shield: geochemical and isotopic evidence for a residual evaporite brine component. *Geochimica et Cosmochimica Acta*, 54: 1483–1498.

Bottomley, D. J., Katz, A., Chan, L. H., Starinsky, A., Douglas, M., Clark, I. D., and Raven, K. G., 1999. The origin and evolution of Canadian Shield brines: Evaporation or freezing of seawater? New lithium isotope and geochemical evidence from the Slave craton. *Chemical Geology*, 155: 295–320.

Bottomley, D. J., Renaud, R., Kotzer, T., and Clark, I. D., 2002. Iodine-129 constraints on residence times of deep marine brines in the Canadian Shield. *Geology*, 30: 587–590.

Bottomley, D. J., Ross, J. D., and Clarke, W. B., 1984. Helium and neon isotope geochemistry of some groundwaters from the Canadian Precambrian Shield. *Geochimica et Cosmochimica Acta* 48: 1973–1985.

Boyle, D. R. and Chagnon, M., 1995. An incidence of skeletal fluorosis associated with groundwaters of the maritime carboniferous basin, Gaspé region, Quebec, Canada. *Environmental Geochemistry and Health*, 17: 5–12.

Braxton, D. and Mathur, R., 2011. Exploration applications of copper isotopes in the supergene environment: A case study of the Bayugo porphyry copper-gold deposit, southern Philippines. *Economic Geology*, 106: 1447–1463.

Brown, D. J., Helmke, P. A., and Clayton, M. K., 2003. Robust geochemical indices for redox and weathering on a granitic laterite landscape, in Central Uganda. *Geochimica et Cosmochimica Acta*, 67: 2711–2723.

Brown, R. M., 1961. Hydrology of tritium in the Ottawa Valley. *Geochimica et Cosmochimica Acta*, 21: 199–216.

Buffle, J., 1977. Les substances humiques et leurs interactions avec les ions minéraux. In Conference Proceedings, La Commission d´Hydrologie Appliquée de l´A. G. H. T. M., L´Université de Paris-Sud, Orsay, France, pp. 3–10.

Burland, S. M. and Edwards, E. A., 1999. Anaerobic benzene biodegradation linked to nitrate reduction. *Applied and Environmental Microbiology*, 65: 529–533.

Burns, R. C., and Hardy, R. W. F., 1975. *Nitrogen Fixation in Bacteria and Higher Plants*, Springer, New York.

Chan, L. H., 1987. Lithium isotope analysis by thermal ionization mass spectrometry of lithium tetraborate. *Analytical Chemistry*, 59: 2662–2665.

Chan, L.-H., and Edmond, J. M., 1988. Variation of lithium isotope composition in the marine environment: A preliminary report. *Geochimica et Cosmochimica Acta*, 52: 1711–1717.

Chanton, J. P., Bauer, J. E., Glaser, P. A., Siegel, D. I., Kelley, C. A., Tyler, S. C., Romanowicz, E. H. and Lazrus, A., 1995. Radiocarbon evidence for the substrates supporting methane formation within northern Minnesota peatlands. *Geochimica et Cosmochimica Acta*, 59: 3663–3668.

Chapelle, F. H. and Lovely, D. R., 1992. Competitive exclusion of sulfate reduction by Fe(III)-reducing bacteria: A mechanism for producing discrete zones of high-iron ground water. *Ground Water*, 30: 29–36.

Chebotarev, I. I., 1955. Metamorphism of natural waters in the crust of weathering. *Geochimica et Cosmochimica Acta*, 8, Part 1 22–48; Part II 137–170; Part III 198–212.

Christensen, T. H., Kjeldsen, P., Bjerg, P. L., Jensen, D. L., Christensen, J. B., Baun, A., Albrechtsen, H-J., and Heron, G., 2001. Biogeochemistry of landfill leachate plumes. *Applied Geochemistry*, 16: 659–718.

Church, C. D., Isabelle, L. M., Pankow, J. F., Rose, D. L., and Tratnyek, P. G., 1997. Method for determination of methyl-tert-butyl ether (MTBE) and its degradation products in water. *Environmental Science & Technology*, 31: 3723–3726.

Clark I. D., Fritz, P., Quinn O. P., Rippon P. W., Nash H., Bin Ghalib Sayyid Barghash, Al Said, 1987. Modern and fossil groundwater in an arid environment: A look at the hydrogeology of Oman. In: *Isotope Techniques in Water Resources Development*. International Atomic Energy Agency, Vienna, pp. 167–187.

Clark, I. D. and Fritz, P., 1997. *Environmental Isotopes in Hydrogeology*, Lewis Publishers, Boca Raton, FL, 328 pp.

Clark, I. D. and Raven, K. G., 2003. Arsenic sources in Giant Mine groundwaters, Yellowknife, NWT, Canada. *Isotopes in Environmental and Health Studies*, 40: 115–128.

Clark, I. D., Al, T., Jensen, M., Kennell, L., Mazurek, M., Mohapatra, R., Raven, K. G., 2013. Paleozoic-aged brine and authigenic helium preserved in an Ordovician shale aquiclude. *Geology*, 41: 951–954.

Clark, I. D., Douglas, M., Raven, K., and Bottomley, D. J., 2000. Recharge and preservation of glacial meltwater in the Canadian Shield. *Ground Water*, 38: 735–742.

Clark, I. D. and Fontes, J-Ch., 1990. Palaeoclimatic reconstruction in northern Oman based on carbonates from hyperalkaline groundwaters. *Quaternary Research*, 33, 320–336.

Clark, I. D., Fontes, J.-Ch., and Fritz, P., 1992. Stable isotope disequilibria in travertine from high pH waters: Laboratory investigations and field observations from Oman. *Geochimica Cosmochimica Acta*, 56: 2041–2050.

Clark, I. D., Fritz, P., and Souther, J. G., 1989. Geochemistry and isotope hydrogeology of the Mount Edziza–Mess Creek geothermal area. *Canadian Journal of Earth Sciences*, 26: 1160–1171.

Clark, I. D., Fritz, P., Seidlitz, H. K., Trimborn, P., Milodowski, A. E., Pearce, J. M., and Khoury, H. N., 1993. Recarbonation of metamorphosed marls in Jordan. *Applied Geochemistry*, 8: 473–481.

Clark, I. D., Henderson, L., Chappellaz, J., Fisher, D. A., Koerner, R., Worthy, D. E. J., Kotzer, T., Norman, A.-L., and Barnola, J.-M., 2007. CO_2 isotopes as tracers of firn air diffusion and age in an Arctic ice cap with summer melting, Devon Island, Canada. *Journal of Geophysical Research*, 112, D01301. doi:10.1029/2006jD007471.

Clark, I. D., Lauriol, B., Marschner, M., Sabourin, N., Chauret, Y., and Desrochers, A., 2004. Endostromatolites from permafrost karst, Yukon, Canada: Paleoclimatic proxies for the Holocene hypsithermal, *Canadian Journal of Earth Sciences*, 41: 387–399.

Clark, I. D., Timlin, R., Bourbonnais, A., Jones, K., Lafleur, D., and Wickens, K., 2008. Origin and fate of industrial ammonia in municipal groundwaters: Tracing anaerobic oxidation (anammox) and apportionment with $^{15}N_{NH_4^+}$. *Ground Water Monitoring and Remediation*, 28: 73–82.

Claypool, G. E., Holser, W. T., Kaplan, I. R., Sakai, H., and Zak, I., 1980. The age curves of sulfur and oxygen isotopes in marine sulphate and their mutual interpretation. *Chemical Geology*, 28: 199–260.

Clayton, R. N., Friedman, I., Graff, D. L., Mayeda, T. K., Meents, W. F., and Shimp, N. F., 1966. The origin of saline formation waters, 1. Isotopic composition. *Journal of Geophysical Research*, 71: 3869–3882.

Coleman, D. D., Liu, C.-L., and Riley, K. M., 1988. Microbial methane in the shallow Paleozoic sediments and glacial deposits of Illinois, U.S.A. *Chemical Geology*, 71: 23–40.

Coplen, T. B., 2011. Report of Stable Isotopic Composition, Reference Material LSVEC (Carbon and Lithium isotopes in Lithium Carbonate). United States Geological Survey, Reston Stable Isotope Laboratory, Reston Virginia 20192, September 22, 2011.

Coplen, T. B., Brand, W. A., Gehre, M., Gröning, M., Meijer, H. A. J., Toman, B., and Verkouteren, R. M., 2006. New guidelines for ^{13}C measurements. *Analytical Chemistry*, 78: 2439–2441.

Cornett, R. J., Cramer, J., Andrews, H. R., Chant, L. A., Davies, W., Greiner, B. F., Imahori, Y. et al., 1996. In situ production of ^{36}Cl in uranium ore: A hydrogeological assessment tool. *Water Resources Research*, 32: 1511–1518.

Cox, K. G. and Hawkesworth, C. J., 1985. Geochemical stratigraphy of the Deccan traps at Mahabaleshwar, Western Ghats, India, with implications for open system magmatic processes. *Journal of Petrology*, 26: 355–377.

Craig, H., 1961. Isotopic variations in meteoric waters. *Science*, 133: 1702–1703.

Craig, H., 1963. The isotopic geochemistry of water and carbon in geothermal areas. In *Nuclear Geology on Geothermal Areas,* edited by E. Tongiorgi, Spoleto, 1963, Consiglio Nazionale delle Ricerche, Laboratorio di Geologia Nucleare, Pisa, pp. 17–53.

Cramer, J. J., and Whiteshell Laboratories, 1994. Final Report of the AECL/SKB Cigar Lake Analog Study, Whiteshell Laboratories, Pinawa, Canada.

Cravotta III, Ch. A., 2008. Dissolved metals and associated constituents in abandoned coal-mine discharges, Pennsylvania, USA. Part 2: Geochemical controls on constituent concentrations. *Applied Geochemistry*, 23: 203–226.

Cruz-san, J., Araguas, L, Rozanski, K, Cardenal, J., Hidalgo, M.C., Garcia-Lopez, S., Martinez-Garrido, J. C., Moral, F., Olias, M., 1992. Sources of precipitation over south-eastern Spain and groundwater recharge. An isotopic study. *Tellus*, 44: 226–236.

Curtis, J., 2002. Fractured shale-gas systems. *American Association of Petroleum Geologists Bulletin*, 86: 1921–1938.

Dansgaard, W., 1964. Stable isotopes in precipitation. *Tellus*, 16: 436–468.

Darling, W. G. and Gooddy, D. C., 2007. Assessing the applicability of global CFC and SF_6 input functions to groundwater dating in the UK. *Science of the Total Environment*, 387: 353–362

Darling, W. G., Gooddy, D. C., MacDonald, A. M., and Morris, B. L., 2012. The practicalities of using CFCs and SF_6 for groundwater dating and tracing. *Applied Geochemistry*, 27: 1688–1697.

Das, A., Krishnaswami, S., Sarin, M. M., and Pande, K., 2005. Chemical weathering in the Krishna Basin and Western Ghats of the Deccan Traps, India: Rates of basalt weathering and their controls. *Geochimica et Cosmochimica Acta*, 69: 2067–2084.

Dayal, R. and Reardon, E. J., 1994. Carbon-14 behaviour in a cement-dominated environment: Implications for spend CANDU resin waste disposal. *Waste Management*, 14: 457–466.

Desaulniers, D. E., Kaufmann, R. S., Cherry, J. A., and Bentley, H. W., 1986. ^{35}Cl-^{37}Cl variations in a diffusion-controlled groundwater system. *Geochimica et Cosmochimica Acta*, 50: 1757–1746.

Dimitrakopoulos, R., and Muehlenbachs, K., 1987. Biodegradation of petroleum as a source of ^{13}C-enriched carbon dioxide in the formation of carbonate cement. *Chemical Geology (Isotope Geoscience Section)*, 65: 283–29.

Domenico, P. A. and Schwartz, F. W., 1998. *Physical and Chemical Hydrogeology*. Wiley, New York, NY, p. 506.

Doney, S. C., Glover, D. M., Jenkins, W. J., 1992. A model function of the global bomb tritium distribution in precipitation, 1960–1986. *Journal of Geophysical Research-Oceans*, 97(C4): 5481–5492.

Douglas, M., Clark, I. D., Raven, K., and Bottomley, D., 2000. Groundwater mixing dynamics at a Canadian Shield mine. *Journal of Hydrology*, 235: 88–103.

Drever, J. I., 1997. *The Geochemistry of Natural Waters, Surface and Groundwater Environments*, third edition, Prentice Hall, Upper Saddle River, NJ, 436 pp.

Drever, J. I, 1997. The carbonate system and pH control. In *The Geochemistry of Natural Waters*, Prentice Hall, Upper Saddle River, NJ, p. 436.

Dwight, B., LeeAnn, M., Hillary, J., Scott, H., and Keith, L., 2013. A Preliminary Deposit Model for Lithium Brines, U. S. Geological Survey Open-File Report 2013–1006, p. 6.

Eastoe, C. J., Peryt, T. M., Petrychenko, O. Y., and Geisler-Cussey, S., 2007. Stable chlorine isotopes in Phanerozoic evaporites. *Applied Geochemistry*, 22: 575–588.

Edmunds, W. M. and Bogush, A. A., 2012. Geochemistry of natural waters: The legacy of V. I. Vernadsky and his students. *Applied Geochemistry*, 27: 1871–1886.

Edwards, T. W. D., Aravena, R. O., Fritz, P., and Morgan, A. V., 1985. Interpreting paleoclimate from ^{18}O and ^{2}H in plant cellulose: Comparison with evidence from fossil insects and relict permafrost in southwestern Ontario. *Canadian Journal of Earth Sciences*, 22: 1720–1726.

Einsiedl, F. and Mayer, B., 2005. Sources and processes affecting sulfate in a karstic groundwater system of the Franconian Alb, Southern Germany. *Environmental Science and Technology*, 39: 7118–7125.

Eleazer, W. E., Odle III, W. S., Wang, Y-S., and Barlaz, M. A., 1997. Biodegradability of municipal solid waste components in laboratory-scale landfills. *Environmental Science and Technology*, 31: 911–917.

Emblanch, C., Zuppi, G. M., Mudry, J., Blavoux, B., and Batiot, C., 2003. Carbon 13 of TDIC to quantify the role of the unsaturated zone: The example of the Vaucluse karst systems (Southeastern France). *Journal of Hydrology*, 279: 262–274.

EPA, 2013. Municipal Solid Waste Generation, Recycling, and Disposal in the United States: Facts and Figures for 2011. EPA530-F-13-001 Solid Waste and Emergency Response (5306P) Washington, DC 20460. www.epa.gov/wastes.

EPICA Community Members, 2004. Eight glacial cycles from an Antarctic ice core. *Nature*, 429(6992): 623–628.

Epstein, J. A., Feist, E. M., Zmora, J., and Marcus, Y., 1981. Extractions of lithium from the Dead Sea. *Hydrometallurgy*, 6: 269–275.

Erda, L., Wei, X., Hui, J., Yinlong, X., Yue, L., Liping, B., and Liyong, X., 2005. Climate change impacts on crop yield and quality with CO_2 fertilization in China. *Philosophical Transactions of the Royal Society Biological Sciences*, 360: 2149–2154.

Eriksson, E., 1952. Composition of atmospheric precipitation. II Sulfur, chloride, iodine compounds. *Tellus*, 4: 280–303.

FAO, 2008. Current World Fertilizer Trends and Outlook to 2011/12, Food and Agriculture Organization of the United Nations, Viale delle Terme di Caracalla, 00153 Rome. www.fao.org.

Faure, G., 1998. *Principles and Applications of Geochemistry*, second edition, Prentice Hall, Upper Saddle River, NJ, 600 pp.

Fennell, D. E. and Gossett, J. M, 1997. Comparison of butyric acid, ethanol, lactic acid, and propionic acid as hydrogen donors for the reductive dechlorination of tetrachloroethene. *Environmental Science & Technology*, 31: 918–926.

Ferguson, P. and Veizer, J., 2007. Coupling of water and carbon fluxes via the terrestrial biosphere and its significance to the Earth's climate system. *Journal of Geophysical Research*, 112, D24S06. doi:10.1029/2007JD008431.

Fetter, Ch. W., 2001. *Applied Hydrogeology*, Prentice Hall, Upper Saddle River, NJ, 598 pp.

Feurdean, V., Feurdean, L., and Lari, I., 1997. Deuterium distribution in crude oil. *Isotopes in Environmental and Health Studies*, 33: 389–398.

Field, C. B.; Behrenfeld, M. J., Randerson, J. T., and Falkowski, P., 1998. Primary production of the biosphere: Integrating terrestrial and oceanic components. *Science*, 281: 237–240. doi:10.1126/science.281.5374.237.

Finneran, K. T. and Lovley, D. R., 2001. Anaerobic degradation of methyl tert-butyl ether (MTBE) and tert-butyl alcohol (TBA). *Environmental Science & Technology*, 35: 1785–1790.

Flesch, G. D., Anderson, A. R. Jr., and Svec, H. J., 1973. A secondary isotopic standard for $^{6}Li/^{7}Li$ determinations. *International Journal of Mass Spectrometry and Ion Physics*, 12: 265–272.

Fontes, J.-Ch. and Garnier, J-M., 1979. Determination of the initial ^{14}C activity of total dissolved carbon: A review of existing models and a new approach. *Water Resources Research*, 15: 399–413.

Fortin, D., Roy, M., Rioux, J. -P., and Thibault, P. -J., 2000. Occurrence of sulfate-reducing bacteria under a wide range of physico-chemical conditions in sulfidic mine tailings. *FEMS Microbiological Ecology*, 33, 197–208.

Freeze, R. A. and Cherry, J. A., 1979. *Groundwater*, Prentice Hall, Upper Saddle River, NJ, 604 pp.

Fritz, P. and Fontes, J.-Ch., 1980. *Handbook of Environmental Isotope Geochemistry, Volume 1, The Terrestrial Environment, A*, Elsevier, Amsterdam, The Netherlands, 558 pp.

Fritz, P., Basharmal, G. M., Drimmie, R.J., Ibsen, J., Qureshi, R. M., 1989. Oxygen isotope exchange between sulphate and water during bacterial reduction of sulphate. *Chemical Geology (Isotope Geoscience Section)*, 79: 99–105.

Fritz, P., Clark, I. D., Fontes, J.-Ch. Whiticar, M. J. Faber, E. 1992. Deuterium and ^{13}C evidence for low temperature *production of hydrogen and methane in a highly alkaline groundwater environment in Oman.* In *Proceedings of the 7th International Symposium on Water–Rock Interaction*, Park City, Utah, 13–18 July, 1992, eds. Y. Kharaka and A.S. Maest, p. 793–796.

Fritz, P., Drimmie, R. J., Frape, S. K., and O'Shea, O., 1987a. The isotopic composition of precipitation and groundwater in Canada. In *Isotope Techniques in Water Resources Development*, IAEA Symposium 299, March 1987, Vienna, pp. 539–550.

Fritz, P., Drimmie, R. J., Frape, S. K., O'Shea, O., 1987. The isotopic composition of precipitation and groundwater in Canada. In *Isotope Techniques in Water Resources Development*, IAEA Symposium 299, March 1987, Vienna: 539–550.

Frost, C. D. and Toner, R. N., 2004. Strontium isotopic identification of water-rock interaction and groundwater mixing. *Ground Water*, 42: 418–432.

Gaillardet, J., Dupre, B., Louvat, P., and Allegre C. J., 1999. Global silicate weathering and CO_2 consumption rates deduced from the chemistry of large rivers. *Chemical Geology*, 159: 3–30.

Gardner, P. and Solomon, D. K., 2009. An advanced passive diffusion sampler for the determination of dissolved gas concentrations. *Water Resources Research*, 45, W06423. doi: 10.1029/2008WR007399.

Garrels, R. M. and Christ, C. L., 1965. Carbonate equilibria. In *Solutions, Minerals and Equilibria*. Freeman, Cooper & Company, San Francisco, CA, p. 450.

Gat, J. R. and Carmi, I., 1970. Evolution of the isotopic composition of atmospheric waters in the Mediterranean Sea area. *Journal of Geophysical Research*, 75: 3039–3048.

General Electric Co. and KAPL Inc., 2002. *Chart of the Isotopes*, 16th ed., General Electric Co., Knolls Atomic Power Laboratory, Inc., Schenectady, NY.

Gillham, R. W. and O'Hannesin, S. F., 1992. Metal-catalyzed abiotic degradation of halogenated organic compounds. In *Proceedings of the IAH Conference: Modern Trends in Hydrogeology*, Ontario, Canada, 10–13 May, 1992, p. 94.

Gillham, R. W. and O'Hannesin, S. F., 1994. Enhanced degradation of halogenated aliphatics by zero-valent iron. *Ground Water*, 32: 958.

Gillham, R. W., O'Hannesin, S. F., and Orth, W. S., 1993. Metal enhanced abiotic degradation of halogenated aliphatics: Laboratory tests and field trials. In *Proceedings of the Sixth Annual Environmental Management and Technology Conference*, edited by W. R. Bunner, Advanstar Expositions, Glen Ellyn, IL, p. 440.

Gillon, M., Barbecot, F., Gilbert, E., Corcho Alvarado, J. A., Marlin, C., and Massault, M., 2009. Open to closed system transition traced through TDIC isotopic signature at the aquifer recharge stage, implications for groundwater ^{14}C dating. *Geochimica Cosmochimica Acta*, 73: 6488–6501.

Gimmi, T., Waber, H. N., Gautschi, A., and Rübel, A., 2007. Stable water isotopes in pore water of Jurassic argillaceous rocks as tracers for solute transport over large spatial and temporal scales. *Water Resources Research*, 43, W04410. doi: 10.1029/2005WR004774.

Goldschmidt, V. M., 1954. *Geochemistry*, edited posthumously by A. Muir, Oxford University Press, London.

Gonfiantini, R., 1965. Effetti isotopici nell'evaporazione di acque salate. *Atti Soc. Toscana Sci. Nat. Pisa, Ser. A*, 72: 550–569.

Gonfiantini, R., 1986. Environmental isotopes in lake studies. In P. Fritz and J.-Ch. Fontes (eds.) *Handbook of Environmental Isotope Geochemistry, Vol. 2, The Terrestrial Environment., B*. Elsevier, Amsterdam, The Netherlands: 113–168.

Gori, Y., Wehrens, R., Greule, M., Keppler, F., Ziller, L., La Porta, N., and Camin, F., 2013. Carbon, hydrogen and oxygen stable isotope ratios of whole wood, cellulose and lignin methoxyl groups of *Picea abies* as climate proxies. *Rapid Communications in Mass Spectrometry*, 27: 265–275.

Gorman-Lewis, D., Fein, J. B., Burns, P. C., Szymanowski, J. E. S., and Converse, J., 2008. Solubility measurements of the uranyl oxide hydrate phases metaschoepite, compreignacite, Na–compreignacite, becquerelite, and clarkeite. *Journal of Chemical Thermodynamics*, 40: 980–990.

Gosse, J. C., Lal, D., Schaeffer, J., Ivy-Ochs, S., Granger, D., 2006. Terrestrial cosmogenic nuclide exposure methods. In *The Encyclopedia of Quaternary Science*, edited by S. Elias, Blackwell Publishers, Oxford, UK, p. 3460.

Grasby, S. E. and Chen, Z., 2005. Subglacial recharge into the Western Canada Sedimentary Basin: Impact of Pleistocene glaciation on basin hydrodynamics. *Geological Society of America Bulletin*, 117: 500–514.

Greene, S., Battye, N., Clark, I. D., Kotzer, T., and Bottomley, D., 2008. Canadian Shield brine from the Con Mine, Yellowknife, NT, Canada: Noble gas evidence for an evaporated Palaeozoic seawater origin mixed with glacial meltwater and Holocene recharge. *Geochimica et Cosmochimica Acta*, 72: 4008–4019.

Gu, L., Post, W. M., and King, A. W., 2004. Fast labile carbon turnover obscures sensitivity of heterotrophic respiration from soil to temperature: A model analysis. *Global Biogeochemical Cycles*, 18, GB1022. doi:10.1029/2003GB002119.

Hackley, K. C., Liu, C. L., and Coleman, D. D., 1996. Environmental isotope characteristics of landfill leachates and gases. *Ground Water*, 34: 827–836.

Hardie, L. A. and Eugster, H. P., 1980. Evaporation of seawater: calculated mineral sequences. *Science*, 208: 498–500.

Harper, D. A., Longstaffe, F. J., Wadleigh, M. A., and McNutt, R. H., 1995. Secondary K-feldspar at the Precambrian-Paleozoic unconformity, southwestern Ontario. *Canadian Journal of Earth Science*, 32: 1432–1450.

Hem, J. D., 1985. *Study and Interpretation of the Chemical Characteristics of Natural Water*. U.S. Geological Survey Water-Supply Paper 2254. U.S. Department of the Interior, Washington, DC.

Henderson, A. D. and Demond, A. H., 2007. Long-term performance of zero-valence iron permeable reactive barriers: A critical review. *Environmental Engineering Science*, 24: 401–424.

Hendry, M. J. and Wassenaar, L. I., 1999. Implications of the distribution of δD in pore waters for groundwater flow and the timing of geologic events in a thick aquitard system. *Water Resources Research*, 35: 1751–1760.

Hendry, M. J., Kotzer, T. G., and Solomon, D. K., 2005. Sources of radiogenic helium in a clay till aquitard and its use to evaluate the timing of geologic events. *Geochimica et Cosmochimica Acta*, 69: 475–483.

Hill, R. D., Rinker, R. G., and Dale Wilson, H., 1980. Atmospheric nitrogen fixation by lightning. *Journal of the Atmospheric Sciences*, 37: 179–192.

Hogan, J. F and Blum, J. D., 2003. Boron and lithium isotopes as groundwater tracers: A study at the Fresh Kills Landfill, Staten Island, New York, USA. *Applied Geochemistry*, 18: 615–627.

Holland, G., Sherwood Lollar, B., Li, L., Lacrampe-Couloume, G., Slater, G. F., and Ballentine, C. J., 2013. Deep fracture fluids isolated in the crust since the Precambrian era. *Nature*, 497: 357–362.

Howard, K. W. F. and Haynes, J., 1993. Urban Geology 3. Groundwater contamination due to road de-icing chemicals: Salt balance implications. *Geoscience Canada*, 20: 1–8.

Howard, K. W. F., Boyce, J. I., Livingston, S. J., and Salvatori, S. L., 1993. Road salt impacts on ground water quality—The worst is still to come! *GSA Today*, 3: 319–321.

Hughes, C. E. and Crawford, J., 2012. A new precipitation weighted method for determining the meteoric water line for hydrological applications demonstrated using Australian and global GNIP data. *Journal of Hydrology*, 464: 344–351.

Hull, L. and Schafer, A. L., 2008. Accelerated transport of ^{90}Sr following a release of high ionic strength solution in vadose zone sediments. *Journal of Contaminant Hydrology*, 97: 135–157.

Humlum, O., Stordahl, K., and Solheim, J.-E., 2013. The phase relation between atmospheric carbon dioxide and global temperature. *Global and Planetary Change*, 100: 51–69.

Hunkeler, D., Aravena, R., and Butler, B. J., 1999. Monitoring microbial dechlorination of tetrachloroethene (PCE) in groundwater using compound-specific stable carbon isotope radios: Microcosm and field studies. *Environmental Science and Technology*, 33: 2733–2738.

Hyvönen, R., Ågren, G. I., Linder, S., Persson, T., Cotrufo, M. F., Ekblad, A., Freeman, M. et al., 2007. The likely impact of elevated [CO_2], nitrogen deposition, increased temperature and management on carbon sequestration in temperate and boreal forest ecosystems: A literature review. *New Phytologist*, 173: 463–480.

IAEA, 1981. *Stable Isotope Hydrology: Deuterium and Oxygen-18 in the Water Cycle*, edited by J. R. Gat and R. Gonfiantini, Technical Report Series No. 210, International Atomic Energy Agency, Vienna.

IAEA, 2006. Use of Chlorofluorocarbons in Hydrology: A Guidebook, Atomic Energy Agency STI/PUB/1238. http://www-pub.iaea.org/MTCD/publications/PDF/Pub1238_web.pdf.

IAEA/WMO, 2001. Global Network of Isotopes in Precipitation. *The GNIP Database* http://isohis.iaea.org

IAEA/WMO, 2013. Global Network of Isotopes in Precipitation. The GNIP Database. http://www.iaea.org/water.

Iijima, K., 2013. Background and current status of understanding at both local (Fukushima NPP) and regional (Fukushima Predecture). International Atomic Energy Agency Workshop on Evaluating Groundwater Pathways and Residence Times as part of Site Investigations and Post-Closure Safety Assessments for Geological Repositories, Trieste, Italy, June 17–21, 2013.

Intera Engineering Ltd., 2011. *Descriptive Geosphere Site Model*, Intera Engineering Ltd. report for the Nuclear Waste Management Organization NWMO DGR-TR-2011-24 R000, Toronto, Canada.

IPCC, 2007. Climate Change 2007: The Physical Science Basis. Contribution of Working Group I to the Fourth Assessment Report of the Intergovernmental Panel on Climate Change, edited by Solomon, S., D. Qin, M. Manning, Z. Chen, M. Marquis, K. B. Averyt, M. Tignor and H. L. Miller. Cambridge University Press, Cambridge, United Kingdom and New York, NY.

Jackson, R. E. and Patterson, R. J., 1982. Interpretation of pH and Eh trends in a fluvial-sand aquifer system. *Water Resources Research,* 18: 1255–1268.

Jackson, R.B., Vengosh, A., Darrah, T.H., Warner, N.R., Down, A., Poreda, R.J., Osborn, S.G., Zhao, K. and Karr, J.D., 2013. Increased stray gas abundance in a subset of drinking water wells near Marcellus shale gas extraction. *Proceedings National Academy of Science*, www.pnas.org/cgi/doi/10.1073/pnas.1221635110.

Jamieson-Hanes, J. H., Gibson, B. D., Lindsay, M. B. J., Kim, Y. Ptacek, C. J., and Blowes, D. W., 2012. Chromium isotope fractionation during reduction of Cr(VI) under saturated flow conditions. *Environmental Science & Technology*, 46: 6783–6789.

Jetten, M. S. M., 1999. New pathways for ammonia conversion in soil and aquatic systems. *Plant and Soil*, 230: 9–19.

Jiang, W., Bailey, K., Lu, Z.-T., Mueller, P., O´Connor a, T. P., Cheng, C.-F., Huc, S.-M. et al., 2012. An atom counter for measuring ^{81}Kr and ^{85}Kr in environmental samples. *Geochimica et Cosmochimica Acta*, 91: 1–6.

Jiang, W., Williams, W., Bailey, K., Davis, A. M., Hu, S.-M., Lu, Z.-T., O'Connor, T. P. et al., 2011. ^{39}Ar detection at the 10^{-16} isotope abundance level with atom trap trace analysis. *Physical Review Letters*. 106: 103001.

Jiao, J. J., 2007. A 5,600-year-old wooden well in Zhejiang Province, China. *Hydrogeology Journal*, 15: 1021–1029.

Jones, C. D., Cox, P., and Huntingford, C., 2003. Uncertainty in climate–carbon-cycle projections associated with the sensitivity of soil respiration to temperature. *Tellus B*, 55, 642–648

Jones, D. M., Head, I. M., Gray, N. D., Adams, J. J., Rowan, A. K., Aitken, C. M., Bennett, B. et al., 2008. Crude-oil biodegradation via methanogenesis in subsurface petroleum reservoirs. *Nature*, 451: 176–180.

Jurgens, B. C., Böhlke, J. K., and Eberts, S. M., 2012, Tracer LPM (Version 1): An Excel® Workbook for Interpreting Groundwater Age Distributions from Environmental Tracer Data. U. S. Geological Survey Techniques and Methods Report 4-F3, p. 60.

Kaiser, J., Hastings, M. G., Houlton, B. Z., Röckmann, T., and Sigman, D. M., 2007. Triple oxygen isotope analysis of nitrate using the denitrifier method and thermal decomposition of N_2O. *Analytical Chemistry*, 79: 599–607.

Kamei-Ishikawa, N., Uchida, S., and Tagami,K., 2008. Distribution coefficients for ^{85}Sr and ^{137}Cs in Japanese agricultural soils and their correlations with soil properties. *Journal of Radioanalytical and Nuclear Chemistry*, 277: 433–439.

Kapaj, S., Peterson, H., Liber, K., and Phattacharya, P., 2006. Human health effects from chronic arsenic poisoning: A review. *Journal of Science and Health Part A.*, 41: 2399–2428.

Kendall, C. and Aravena, R., 2000. Nitrate isotopes in groundwater systems. In *Environmental Tracers in Subsurface Hydrology*, edited by Peter Cook and Andrew L. Herczeg, Springer Science+Business Media, New York, NY, pp. 261–297.

Kendall, C. and Caldwell, E. A., 1998. *Isotope Tracers in Catchment Hydrology*, edited by C. Kendall and J. J. McDonnell, Elsevier, Amsterdam, the Netherlands, 839 pp.

Kennedy, C. B., Gault, A. G., Clark, I. D., Fortin, D. and Ferris, F. G., 2011. Retention of Iodide by Bacteriogenic Iron Oxides. *Geomicrobiology Journal*. 28: 387–395.

Kharaka, Y. K., Gunter, W. D., Aggarwal, P. K., Perkins, E. H., DeBraal, J. D., 1988. SOLMINEQ.88: A computer program for geochemical modeling of water–rock interactions. *USGS Water-Resources Investigations Report*: 88–4227.

Khoury, H. N., Salameh, E., Clark, I. D., Fritz, P., Bajjali, W., Milodowski, A. E., Cave, M. R., and Alexander, W. R., 1992. A natural analogue of high pH cement pore waters from the Maqarin site of northern Jordan, 1: Introduction to the site. *Journal of Geochemical Exploration*, 46: 117–132.

Kieser, W. E., Zhao, X-L., Clark, I. D., Kotzer, T., and Litherland, A. E., 2011. The New Accelerator Mass Spectrometry Facility at the University Of Ottawa. Applications of Accelerators in Research and Industry, AIP Conference Proceedings, vol. 1336, pp. 60–66. doi: 10.1063/1.3586057.

Killey, R. W. D. and Munch, J. H., 1987. Radiostrontium migration from a 1953–54 liquid release to a sand aquifer. *Water Pollution Research Journal of Canada*, 22: 107–128.

Kim, E. and Boulègue, J., 2003. Chemistry of rhenium as an analogue of technetium: Experimental studies of the dissolution of rhenium oxides in aqueous solutions, *Radiochimica Acta*, 91: 211–216.

Kinoshita, N., Sueki, K., Sasa, K., Kitagawa, J., Ikarashi, S., Nishimura, T., Wong, Y-S. et al., 2012. Assessment of individual radionuclide distributions from the Fukushima nuclear accident covering central-east Japan. *Proceedings of the National Academy of Sciences* 108.www.pnas.org/cgi/doi/10.1073/pnas.1111724108.

Kinsley, C., Crolla, A., and Joy, D., 2005. Impact of Water Softeners on Septic Tanks Field Evaluation Study. Final Report to Canadian Mortgage and Housing Corporation by Ontario Rural Wastewater Centre, University of Guelph, pp. 19 + appendices.

Kipfer, R., Aeschbach-Hertig, W., Peeters, F., and Stute, M., 2002. Noble gases in lakes and ground waters (in Noble gases in geochemistry and cosmochemistry). *Reviews in Mineralogy and Geochemistry*, 47: 615–700.

Kitchen, J. W., Johnson, T. M., Bullen, T. D., Zhu, J., and Raddatz, A. L., 2012. Chromium isotope fractionation factors for reduction of Cr (VI) by aqueous Fe (II) and organic molecules. *Geochimica et Cosmichimica Acta*, 89, 190–201.

Klass, D. L., 1984. Methane from anaerobic fermentation. *Science*, 223: 1021–1028.

Kloppmann, W., Chikurel, H., Picot, G., Guttman, J., Pettenati, M., Aharoni, A., Guerrot, C. et al., 2009. B and Li isotopes as intrinsic tracers for injection tests in aquifer storage and recovery systems. *Applied Geochemistry*, 24: 1214–1223

Kokelj, S. V., Lacelle, D., Lantz, T. C., Tunnicliffe, J., Malone, L., Clark, I. D., and Chin, K. S., 2013. Thawing of massive ground ice in mega slumps drives increases in stream sediment and solute flux across a range of watershed scales. *Journal of Geophysical Research: Earth Surface*, 118: 1–12.

Kolhatkar, R., Kuder, T., Philp, P., Allen, J., and Wilson, J. T., 2002. Use of compound-specific stable carbon isotope analyses to demonstrate anaerobic biodegradation of MTBE in groundwater at gasoline release site. *Environmental Science & Technology*, 26: 5139–5146.

Krapac, I. G., Dey, W. S., Roy, W. R., Smyth, C. A., Storment, E., Sargent, S. L., and Steele, J. D., 2002. Impacts of swine manure pits on groundwater quality. *Environmental Pollution*, 120: 475–492

Krauskopf, K. and Bird, D. K., 1995. *Introduction to Geochemistry*, third edition, McGraw Hill, Inc., New York, NY, 647 pp.

Lacelle, D., Bjornnson, J., Lauriol, B., Clark, I. D., and Troutet, Y., 2004. Segregated-intrusive ice of subglacial meltwater origin in retrogressive thaw flow headwalls, Richardson Mountains, N. W. T., Canada. *Quaternary Science Reviews*, 23: 681–696.

Langmuir, D., 1997. *Aqueous Environmental Geochemistry*, Prentice Hall, Upper Saddle River, NJ, p. 600.

Langmuir, D., 1997. Carbonate chemistry. In: *Aqueous Environmental Geochemistry*, Prentice Hall, Upper Saddle River, NJ, pp. 193–230.

Lee, D. R. and Hartwig, D. S., 2005. Zeolite prevents discharge of strontium-90-contaminated groundwater. *Canadian Nuclear Society, Waste Management Decommissioning and Environmental Restoration for Canada´s Nuclear Activities: Current Practices and Future Needs*. Ottawa, Ontario, Canada, May 8–11, 2005.

Lee, D. R., Smyth, D. J. A., Shikaze, S. G., Jowett, R., Hartwig, D. S., and Milloy, C., 1998. Wall-and-curtain for passive collection/treatment of contaminant plumes. In *Designing and Applying Treatment Technologies: Remediation of Chlorinated and Recalcitrant Compounds*, edited by G. B. Wickramanayake and R. E. Hinchee, ISBN-13: 9781574770612, Battelle Press, Columbus, OH, pp. 77–84.

Lee, K. Y., Syakir, M. I., Clark, I. D., and Veizer, J., 2013. Isotope constraints on the aquatic carbon budget: Langat watershed, Malaysia. *Aquatic Geochemistry*, 19: 443–475. doi:10.1007/s10498-013-9198-3.

Lemarchand, E., Chabaux, F., Vigier, N., Millot, R., Pierret, M. C., 2010. Lithium isotope systematics in a forested granitic catchment (Strengbach, Vosges Mountains, France). *Geochimica et Cosmochimica Acta*, 74: 4612–4628.

Leybourne, M. I. and Goodfellow, W. D., 2010. Geochemistry of surface waters associated with an undisturbed Zn-Pb massive sulfide deposit: Water-rock reaction, solute sources and the role of trace carbonate. *Chemical Geology*, 279: 40–54.

Li, T., 2013. Geochemistry and runoff processes in Wolf Creek, Whitehorse, Yukon. M.Sc. Thesis, Department of Earth Sciences, University of Ottawa, Ontario, Canada, p. 100.

Liaw, Y. P., 1990. Comparison of field, laboratory and theoretical estimates of global nitrogen fixation by lightning. *Journal of Geophysical Research*, 95: 489–494

Loosli H. H. and Oeschger, H., 1969. ^{37}Ar and ^{81}Kr in the atmosphere. *Earth Planetary Science Letters*, 7: 67–71.

Loosli H. H., Lehmann B. E., and Smethie, W. M. Jr., 2000. Noble gas radioisotopes: ^{37}Ar, ^{85}Kr, ^{39}Ar, ^{81}Kr. In *Environmental Tracers in Subsurface Hydrology*, edited by P. Cook and A. L. Herczeg, Kluwer Academic, Dordrecht, the Netherlands, pp. 379–396.

Loosli, H. H. and Oeschger, H., 1980. Use of ^{39}Ar and ^{14}C for groundwater dating. *Radiocarbon*, 22: 863–870.

Lowenstein, T. K., Hardie, L. A., Timofeeff, M. N., and Demicco, R. V., 2003. Secular variation in seawater chemistry and the origin of calcium chloride basinal brines. *Geology*, 31: 857–860.

Lu, Z.-T., Schlosser, P., Smethie Jr., W. M., Sturchio, N. C., Fischer, T. P., Kennedy, B. M., Purtschert, R.et al., 2013. Tracer applications of noble gas radionuclides in the geosciences. *Earth Science Reviews* http://dx.doi.org/10.1016/j.earscirev.2013.09.002.

Lucas, L. L. and Unterweger, M. P., 2000. Comprehensible review and critical evaluation of the half-life of tritium. *Journal of Research of the National Institute of Standards and Technology*, 105: 541–549.

Mackay, D. M. and Cherry, J. A., 1989. Groundwater contamination: Pump-and-treat remediation. *Environmental Science and Technology*, 23: 630–636.

Majoube, M., 1971. Fractionnement en oxygène–18 et en deutérium entre l'eau et sa vapeur. *Journal of Chemical Physics*, 197: 1423–1436.

Maloszewski, P. and Zuber, A., 1982. Determining turnover time of groundwater systems with the aid of environmental tracers. I. Models and their applicability. *Journal of Hydrology*, 57: 207–231.

Maloszewski, P. and Zuber, A., 1996. Lumped parameter models for interpretation of environmental tracer data (Supplementary Annex). In Manual on Mathematical Models in Isotope Hydrogeology, IAEA-TECHDOC-210, IAEA, Vienna.

Mancini, S. A., Ulrich, A. C., Lacrampe-Couloume, G., Sleep, B., Edwards, E. A., and Sherwood-Lollar, B., 2003. Carbon and hydrogen isotopic fractionation during anaerobic biodegradation of benzene. *Applied Environmental Microbiology*, 69: 191–198.

Marchetti, A. A., Gu, F., Robl, R., and Straume, T., 1997. Determination of total iodine and sample preparation for AMS measurement of ^{129}I in environmental matrices. *Nuclear Instrumentation and Methods in Physics Research B*, 123: 352–355.

Maréchal, C. and Albarède, F., 2002. Ion-exchange fractionation of copper and zinc isotopes. *Geochimica Cosmochimica Acta*, 66: 1499–1509.

Martini, A. M., Walter, L. M., Ku, T. C. W., Budai, J. M., McIntosh, J. C., and Schoell, M., 2003. Microbial production and modification of gases in sedimentary basins: A geochemical case study from a Devonian shale gas play, Michigan basin. *AAPG Bulletin*, 87: 1355–1375.

Marty, B., Torgersen, T., and Meynier, V., 1993. Helium isotope fluxes and groundwater ages in the Dogger Aquifer, Paris Basin. *Water Resources Research*, 29: 1025–1035.

Masue, Y., Loeppert, R. H., and Kramer, T. A., 2007. Arsenate and arsenite adsorption and desorption behavior on coprecipitated aluminum: Iron hydroxides. *Environmental Science and Technology*, 41: 837–842.

Matsumoto, T., Han, L-F., Jaklitsch, M., and Aggarwal, P. K., 2012. A portable membrane contractor sampler for analysis of noble gases in groundwater. *Ground Water*. doi: 10.1111/j.1745-6584.2012.00983.

Mazurek, M., Alt-Epping, P., Bath, A., Gimmi, T., and Waber, H. N., 2009. Natural Tracer Profiles Across Argillaceous Formations: The CLAYTRAC Project. Organization for Economic Cooperation and Development, Nuclear Energy Agency, NEA No. 6253. http://www.oecd-nea.org/rwm/pubs/2009/6253-claytract-project-2009.pdf.

McCaffrey, M. A., Lazar, B., and Holland, H. D., 1987. The evaporation path of seawater and the coprecipitation of Br^- and K^+ with halite. *Journal of Sedimentary Petrology*, 57: 928–937.

McDonald, J. D., 2012. *Electric Power Substations Engineering The Electric Power Engineering Handbook*, third edition. CRC Press, Boca Raton, FL.

McIntosh, J., Walter, L., and Martini, A., 2002. Pleistocene recharge to midcontinent basins: Effects on salinity structure and microbial gas generation. *Geochimica et Cosmochimica Acta*, 66: 1681–1700.

McKitrick, R., 2014. Your Environment: The complete record of air and water pollution levels in Canada. www.yourenvironment.ca

Meckenstock, R. U., Morasch, B., Griebler, C., and Richnow, H. H., 2004. Stable isotope fractionation analysis as a tool to monitor biodegradation in contaminated acquifers. *Journal of Contaminant Hydrology*, 75: 215–255.

MEXT, 2012. Analysis Results Concerning (i) Gamma-Emitting Nuclides and (ii) Sr-89 and Sr-90 (Second distribution survey) by MEXT. Ministry of Education, Culture, Sports, Science and Technology Japan. http://radioactivity.nsr.go.jp/en/contents/6000/5636/24/338_Sr_0912018_e.pdf.

Michalski, G., Böhlke, J. K., and Thiemens, M., 2004. Long term atmospheric deposition as the source of nitrate and other salts in the Atacama Desert, Chile: New evidence from mass-independent oxygen isotopic compositions. *Geochimica et Cosmochimica Acta*, 68: 4023–4038.

Mohammadzadeh, H. and Clark, I. D., 2008. Degradation Pathways of Dissolved Carbon in Landfill Leachate traced with compound-specific ^{13}C analysis of DOC. *Journal of Isotopes in Environmental and Health Studies*, 44: 1–28.

Mohammadzadeh, H., Clark, I. D., Marschner, M., St-Jean, G., 2005. Compound specific isotopic analysis (CSIA) of landfill leachate DOC components. *Chemical Geology*, 218: 3–13.

Momoshima N., Inoue F., Ohta T., Mahara Y., Shimada J., Ikawa R., Kagabu M. et al., 2011. Application of ^{85}Kr dating to groundwater in volcanic aquifer of Kumamoto Area, Japan. *Radioanal Nuclear Chemistry*, 287: 761–767.

Moore, T., Xing, Y., Lazenby, B., Lynch, M., Schiff, S., Robertson, W., Timlin, R. et al., 2011. Prevalence of anaerobic ammonium-oxidizing bacteria in contaminated groundwater. *Environmental Science & Technology*, 45: 7217–7225.

Morgenstern U., 2000. Silicon-32. In *Environmental Tracers in Subsurface Hydrology*, edited by P. G. Cook and A. L. Herczeg, Kluwer Academic, Boston, pp. 499–502.

Morin, K. A., and N. M. Hutt., 1997. *Environmental Geochemistry of Minesite Drainage: Practical Theory and Case Studies*, MDAG Publishing, Vancouver, Canada.

Morin, K. A., Cherry, J. A., Dave, N. A., Lim, T. P., and Vivyurka, A. J., 1988. Migration of acidic groundwater seepage from uranium-tailings impoundments, 1. Field study and conceptual hydrogeochemical model. *Journal of Contaminant Hydrology*, 2: 271–303.

Moser, H. and Stichler, W., 1970. Deuterium measurements on snow samples from the Alps. *Isotope Hydrology 1970*, IAEA Symposium 129, March, 1970, Vienna, pp. 43–57.

Moses, C. O., 1999. Water. In *Encyclopedia of Geochemistry*, edited by C. Marshall and R. W. Fairbridge, Encyclopedia of Earth Sciences Series, Kluwer Academic, Boston, MA, pp. 661–666.

Mulder, A., Van de Graaf, A. A., Robertson, L. A., and Kuenen, J. G., 1995. Anaerobic ammonium oxidation discovered in a denitrifying fluidized bed reactor. *FEMS Microbiology and Ecology*, 16: 177–183.

Murphy, S., Ouellon, T., Ballard, J-M., Lefebvre, R., and Clark, I. D., 2010. Tritium-helium groundwater age used to constrain a groundwater flow model of a valley-fill aquifer contaminated with trichloroethylene (Quebec, Canada). *Hydrogeology Journal*, 19: 195–207.

Nakagawa, F. and Yoshida, N., 2002. Production of methane from alasses in eastern Siberia: Implications from its ^{14}C and stable isotopic compositions. *Global Biogeochemical Cycles*, 16: 1041. doi: 10.1029/2000GB001384.

NEA, 2002. The release, dispersion and deposition of radionuclides. In *Chernobyl: Assessment of Radiological and Health Impact 2002 Update of Chernobyl: Ten Years On.* Nuclear Energy Agency. https://www.oecd-nea.org/rp/chernobyl/c02.html.

Neal, C. and Stanger, G., 1983. Hydrogen generation from mantle source rocks in Oman. *Earth and Planetary Science Letters*, 66: 315–320.

Nemani, R. R., Keeling, C. D., Hashimoto, H., Jolly, W. M., Piper, S. C., Tucker, C. J., Myneni, R. B., and Running. S. W., 2003. Climate-driven increases in global terrestrial net primary production from 1982 to 1999. *Science*, 300: 1560–1563.

Neumann, R. B., Ashfaque, K. N., Badruzzaman, A. B. M., Ashraf Ali, M., Shoemaker, J. K., and Harvey, C. F., 2010. Anthropogenic influences on groundwater arsenic concentrations in Bangladesh. *Nature Geoscience*, 3: 46–52.

Nickson, R., McArthur, J., Burgess, W., Ahmed, K. M., Ravenscroft, P., and Rahmann, M., 1998. Arsenic poisoning of Bangladesh groundwater. *Nature*, 395: 338.

NOAA 2014. U.S. National Oceanographic and Atmospheric Administration. Earth Systems Research Laboratory, Global Monitoring Division. http://www.esrl.noaa.gov/

Nordstrom, D. K. and Alpers, C. N., 1999. Negative pH, efflorescent mineralogy, and consequences for environmental restoration at the Iron Mountain Superfund site, California. *Proceedings of the National Academy of Sciences of the United States of America*, 96: 3455–3462.

Nordstrom, D. K. and Archer, D. G., 2003. Arsenic thermodynamic data and environmental geochemistry: An evaluation of thermodynamic data and environmental geochemistry. In *Arsenic in Ground Water: Geochemistry and Occurrence*, A.H. Welch and K.G. Stollenwerk, eds. Springer, New York, 475 pp.

Nordstrom, D. K., Alpers, C. N., Ptacek, C. J., and Blowes, D. W., 2000. Negative pH and extremely acidic mine waters from Iron Mountain, California. *Environmental Science & Technology*, 34: 254–258.

Noxon, J. F., 1976. Atmospheric nitrogen fixation by lightning. *Geophysical Research Letters*, 3: 463–465.

Nydal, R., and Lövseth, K., 1983. Tracing bomb ^{14}C in the atmosphere 1962–1980. *Journal of Geophysical Research*, 88: 3621–3642.

O´Leary, M. H., 1988. Carbon isotopes in photosynthesis. *Bioscience*, 38: 328–336.

O'Neil, J.R., 1968. Hydrogen and oxygen isotope fractionation between ice and water. *Journal of Physical Chemistry*, 72: 3683–3684.

O'Hannesin, S. F., and Gillham, R. W., 1998. Long-term performance of an in situ "iron wall" for remediation of VOCs. *Ground Water*, 36: 164.

Osborn, S. G., Vengosh, A., Warner, N. A., and Jackson, R. B., 2011. Methane contamination of drinking water accompanying gas-well drilling and hydraulic fracturing. *Proceeding of the National Academy of Sciences*, 108: 8172–8176.

Palmer, C. D. and Wittbrodt, P. R., 1991. Processes affecting the remediation of chromium-contaminated sites. *Environmental Health Perspectives*, 92: 25–40

Panno, S. V., Hackey, K. C., Hwang, H. H., Greenberg, S. E., Krapac, I. G., Landsberger, S., O'Kelly, D. J., 2006. Characterization and identification of NaCl sources in ground water. *Ground Water*, 144: 176–187.

Parkhurst, D. L., 1995, User's guide to PHREEQC—A computer program for speciation, reaction-path, advective-transport, and inverse geochemical calculations: *U.S. Geological Survey Water-Resources Investigations Report 95-4227*, USGS, Washington, DC,143 pp.

Parkhust, D. L. and Appelo, C. A. J., 1999. User's guide to PHREEQC (Version 2): A Computer Program for Speciation, Batch-Reaction, One-Dimensional Transport, and Inverse Geochemical Calculations. Water-Resources Investigations Report 99-4259, U. S. Geological Survey, pp. 312.

Patterson, L. J., Sturchio, N. C., Kennedy, B. M., van Soest, M. C., Sultan, M., Lu, Z.-T., Lehmann, B. et al., 2005. Cosmogenic, radiogenic, and stable isotopic constraints on groundwater residence time in the Nubian Aquifer, Western Desert of Egypt. *Geochemistry, Geophysics, Geosystems G3*, 6, Q01005. doi:10.1029/2004GC000779.

Pauling, L., 1960. *The Nature of the Chemical Bond*, third edition, Cornell University Press, Ithaca, NY.

Pearson, F. J. and Hanshaw, B. B., 1970. Sources of dissolved carbonate species in groundwater and their effects on carbon-14 dating. In *Isotope Hydrology 1970*, IAEA Symposium 129, March 1970, Vienna, pp. 271–286.

Pearson, F. J., 1965. Use of C-13/C-12 ratios to correct radiocarbon ages of material initially diluted by limestone. In *Proceedings of the 6th International Conference on Radiocarbon and Tritium Dating*, Pulman, Washington, p. 357.

Pearson, F. J., 1987, Models of mineral controls on the composition of saline groundwaters of the Canadian Shield. In *Saline Water and Gases in Crystalline Rocks: Geological Association of Canada Special Paper 33*, edited by Fritz, P., and Frape, S. K., pp. 39–51.

Peterman, Z. E., Thamke, J., and Futa, K., 2010. Use of strontium isotopes to detect produced-water contamination in surface water and groundwater in the Williston Basin, Northeastern Montana. In Proceedings, GeoCanada, Calgary, Alberta, May 10–14, 2010.

Phillips, F. M. and Castro, M. C., 2003. Groundwater dating and residence-time measurements. In *Treatise on Geochemistry*, vol. 5, edited by James I. Drever, Heinrich D. Holland, and Karl K. Turekian, ISBN 0-08-043751-6, Elsevier, Amsterdam, the Netherlands, pp. 451–497.

Phillips, F. M., 2000. Chlorine-36. In: *Environmental Tracers in Subsurface Hydrology*, edited by P. Cook and A. L. Herczeg, Kluwer Academic, Norwell, Mass, pp. 299–348.

Phillips, F. M., Peeters, L., Tansey, M. K., and Davis, S. N., 1986. Paleoclimate inferences from an isotopic investigation of groundwater in the central San Juan Basin, New Mexico. *Quaternary Research*, 26: 179–193.

Piper, A.M., 1944. A graphic procedure in the geochemical interpretation of water-analyses. transactions, American Geophysical Union 25: doi: 10.1029/TR025i006p00914. ISSN: 0002–8606.

Pitzer, K. S., 1973, Thermodynamics of electrolytes. I. Theoretical basis and general equations. *Journal Physical Chemistry*, 77: 268–277.

Plummer, L. N., Eggleston, J. R., Andreasen, D. C., Raffensperger, J. P., Hunt, A. G. Casile, G. C., 2012. Old groundwater in parts of the upper Patapsco aquifer, Atlantic Coastal Plain, Maryland, USA: Evidence from radiocarbon, chlorine-36 and helium-4. *Hydrogeology Journal*, 20: 1269–1294.

Plummer, L. N., Parkhurst, D. L., Fleming, G. W., and Dunkle, S. A., 1988. A Computer Program Incorporating Pitzer´s Equations for Calculation of Geochemical Reactions in Brines. U. S. Geological Survey Water-Resources Investigations Report 88-4153, p. 310.

Plummer, N. L., Prestemon, E. C., and Parkhurst, D. L., 1994. An Interactive Code (NETPATH) for Modeling Net Geochemical Reactions along a Flow Path, Version 2.0. U. S. Geological Survey Water Resources Investigations Report 94-4169, U. S. G. S., Reston, VA.

Poole, J. C., McNeill, G. W., Langman, S. R., and Dennis, F., 1997. Analysis of noble gases in water using a quadrupole mass spectrometer in static mode. *Applied Geochemistry*, 12: 707–714.

Price, C., Penner, J., and Prather, M., 1997. NO_x from lightning, 1. Global distribution based on lightning physics. *Journal of Geophysical Research*, 102: 5929–5941.

Prinzhofer, A. A. and Huc, A. Y., 1995. Genetic and post-genetic molecular and isotopic fractionations in natural gases. *Chemical Geology*, 126: 281–290.

Proemse, B. C., Mayer, B., Fenn, M. E., and Ross, C. S., 2013. A multi-isotope approach for estimating industrial contributions to atmospheric nitrogen deposition in the Athabasca oil sands region in Alberta, Canada. *Environmental Pollution*, 182: 80–91.

Quay, P. D., King, S. L., Stutsman, J., Wilbur, D. O., Steele, L. P., Fung, I., Gammon, R. et al., 1991. Carbon isotopic composition of atmospheric CH_4: Fossil fuel and biomass burning source strengths. *Global Biogeochemical Cycles*, 5: 25–47.

Radloff, K. A., Zheng, Y., Michael, H. A., Stute, M., Bostick, B. C., Mihajlov, I., Bounds, M. et al., 2011. Arsenic migration to deep groundwater in Bangladesh influenced by adsorption and water demand. *Nature Geoscience*, 4: 793–798.

Rai, D., Sass, B. M., and Moore, D. A., 1987. Chromium (III) hydrolysis constants and solubility of chromium (III) hydroxide. *Inorganic Chemistry*, 26: 345–349.

Raidlaa, V., Kirsimäea, K., Vaikmäeb, R., Jõelehta, A., Karroa, E., Marandia, A., and Savitskajac, L., 2009. Geochemical evolution of groundwater in the Cambrian–Vendian aquifer system of the Baltic Basin. *Chemical Geology*, 258: 219–231.

Rayleigh, J. W. S., 1896. Theoretical considerations respecting the separation of gases by diffusion and similar processes. *Philosophical Magazine*, 42: 493–498.

Reardon, E. J. and Dewaele, P., 1990. Chemical model for the carbonation of a grout/water slurry. *Journal of the American Ceramic Society*, 73: 1681–1690.

Reardon, E. J., Allison, G. B., and Fritz, P., 1979. Seasonal chemical and isotopic variations of soil CO_2 at Trout Creek, Ontario. *Journal of Hydrology*, 43: 355–371.

Reichel, T., Kersting, A., Ritterbusch, F., Ebser, S., Bender, K., Purtschert, R., Oberthaler, M., Aeschbach-Hertig,W., 2013. First Dating of Groundwater with Atom Trap Trace Analysis of ^{39}Ar: Application. EGU General Assembly 2013, held on April 7–12, 2013, Vienna, Austria, id. EGU2013-10901.

Reimer, P. J., Baillie, M. G. L., Bard, E., Bayliss, A., Beck, J. W., Blackwell, P. G., Bronk Ramsey, C. et al., 2009. IntCal09 and Marine09 radiocarbon age calibration curves, 0–50,000 years cal BP. *Radiocarbon*, 51: 1111–1150.

Renaud, R., Clark, I. D., Kotzer, T. G., Milton, G. M., and Bottomley, D. J., 2005. The mobility of anthropogenic ^{129}I in a shallow sand aquifer at Sturgeon Falls, Ontario, Canada. *Radiochimica Acta*, 93: 363–371.

Robertson, D. E., Perkins, R. W., Lepel, E. L., and Thomas, C. W., 1992. Radionuclide concentrations in environmental samples collected around Chernobyl during the International Chernobyl Project—analyses conducted by Battelle, Pacific Northwest Laboratory. *Journal of Environmental Radioactivity*, 17: 159–182.

Robertson, W. D., Blowes, D. W., Ptacek, C. J., Cherry, J. A., 2000. Long-term performance of in-situ reactive barriers for nitrate remediation. *Ground Water*, 38: 689–695.

Robertson, W. D., Moore, T. A., Spoelstra, J., Li, L., Elgood, R. J., Clark, I. D., Schiff, S. L., Aravena, R., and Neufeld, J. D., 2012. Natural attenuation of septic system nitrogen by anammox. *Ground Water*, 50: 541–553. doi: 10.1111/j.1745-6584.2011.00857.

Robertson,W. D. and Cherry, J. A., 1989. Tritium as an indicator of recharge and dispersion in a groundwater system in Central Ontario. *Water Resource Research*, 25: 1097–1109.

Rudolph, D. L., Barry, D. A. J., and Goss, M. J., 1998. Contamination in Ontario farmstead domestic wells and its association with agriculture: 2. Results from multilevel monitoring well installations. *Journal of Contaminant Hydrology*, 32: 295–311.

Sander, R., 1999. Compilation of Henry´s Law Constants for Inorganic and Organic Species of Potential Importance in Environmental Chemistry. Max-Planck Institute of Chemistry, Mainz, Germany. http://www.mpch-mainz.mpg.de/~sander/res/henry.html.

Sanford, W. E., Shropshire, R. G., and Solomon, D. K., 1996. Dissolved gas tracers: Simplified injection, sampling and analysis. *Water Resources Research*, 32: 1635–1642.

Santella, N., Ho, D. T., Schlosser, P., and Stute, M., 2008. Widespread elevated atmospheric SF6 mixing ratios in the Northeastern United States: Implications for groundwater dating. *Journal of Hydrology*, 349: 139–146.

Sarmiento, J. L. and Gruber, N., 2002. Sinks for anthropogenic carbon. *Physics Today*, August 2002, pp. 30–36.

Savin, S. M. and Epstein, S., 1970. The oxygen and hydrogen isotope geochemistry of clay minerals. *Geochimica et Cosmochimica Acta*, 34: 25–42.

Schleppi, P., Bucher-Wallin, I., Saurer, M., Jäggi, M., and Landolt, W., 2006. Citric acid traps to replace sulphuric acid in the ammonia diffusion of dilute water samples for 15N analysis. *Rapid Communications in Mass Spectrometry*, 20, 629–634.

Schoell, M., 1980. The hydrogen and carbon isotopic composition of methane from natural gas of various origins. *Geochimica et Cosmochimica Acta*, 44: 649–662.

Seal, R. R. II, 2006. Sulfur isotope geochemistry of sulfide minerals. *Reviews in Mineralogy and Geochemistry*, 61: 633–677.

Sebilo, M., Mayer, B., Grably, M., Billious, D., and Mariotti, A., 2004. The use of the ammonium diffusion method for ä^{15}N-NH_4^+ and ä^{15}N-NO_3^- measurements comparison with other techniques. *Environmental Chemistry*, 1: 99–103.

Seefeldt, L. C., Hoffman, B M., and Dean, D. R., 2009. Mechanism of Mo-dependent nitrogenase. *Annual Review of Biochemistry*, 78: 701–722. doi: 10.1146/annurev.biochem.78.070907.103812.

Self, S., Widdowson, M., Thordarson, T., and Jay, A. E., 2005. Volatile fluxes during flood basalt eruptions and potential effects on the global environment: A Deccan perspective. *Earth and Planetary Science Letters*, 248: 518–532.

Shannon, R.D., 1976. Revised effective ionic radii and systematic studies of interatomic distances in halides and chalcogenides. *Acta Crystallographica* A32: 751–767.

Sherwood Lollar, B., Weisse, S. M., Frape, S. K., and Barker, J. F., 1994. Isotopic constraints on the migration of hydrocarbon and helium gases of southwestern Ontario. *Bulletin of Canadian Petroleum Geology*, 42: 283–295.

Shouakar-Stash, O., Frape, S. K., and Drimmie, R. J., 2005. Determination of bromine stable isotopes using continuous-flow isotope ratio mass spectrometry. *Analytical Chemistry*, 77: 4027–4033.

Siegel, D. I. and Mandle, R. J., 1984. Isotopic evidence for glacial meltwater recharge to the Cambrian-Ordovician aquifer, north-central United States. *Quaternary Research*, 22: 328–335.

Sigman, D. M., Casciotti, K. L., Andreani, C., Barford, C., Galanter, M., and Böhlke, J. K., 2001. A bacterial method for the nitrogen isotopic analysis of nitrate in seawater and freshwater. *Analytical Chemistry*, 73, 4145–4153.

Sivan, O., Yechieli, Y., Herut, B., and Lazar, B., 2005. Geochemical evolution and timescale of seawater intrusion into the coastal aquifer of Israel. *Geochimica et Cosmochimica Acta*, 69: 579–592.

Smith, S. P. and Kennedy, B. M., 1983. The solubility of noble gases in water and in NaCl brine. *Geochimica et Cosmochimica Acta*, 47: 503–515.

Solanki, S. K., Usoskin, I. G., Kromer, B., Schussler, M., and Beer, J., 2004. Unusual activity of the Sun during recent decades compared to the previous 11,000 years. *Nature*, 431: 1048–1087.

Squeo, F. A., Aravena, R., Aguirre, E., Pollastri, A., Jorquera, C. B., and Ehleringer, J. R., 2006. Groundwater dynamics in a coastal aquifer in north-central Chile: Implications for groundwater recharge in an arid ecosystem. *Journal of Arid Environments*, 67: 240–254.

Stevenson, F. J., 1985. Geochemistry of soil humic substances. In *Humic Substances in Soil, Sediment, and Water*, edited by G. R. Aiken, D. M. McKnight, R. L. Wershaw, and P. MacCarthy, Wiley, New York, pp. 13–52.

St-Jean, G., 2003. Automated quantitative and isotopic (^{13}C) analysis of dissolved inorganic carbon and dissolved organic carbon in continuous-flow using a total organic carbon analyser. *Rapid Communications in Mass Spectrometry*, 17: 419–428.

Stotler, R. L., Frape, S. K., and Shouakar-Stash, O., 2010. An isotopic survey of δ^{81}Br and δ^{37}Cl of dissolved halides in the Canadian and Fennoscandian Shields. *Chemical Geology*, 274: 38–55.

Sturchio, N. C., Caffee, M., Beloso, A. D. Jr., Heraty, L. J., Böhlke, J. K., Hatzinger, P. B., Jackson, W. A., Gu, B., Heikoop, J. M., Dale, M., 2009. Chlorine-36 as a tracer of perchlorate origin. *Environmental Science & Technology*, 43: 6934–6938.

Sturchio, N. C., Du, X., Purtschert, R., Lehmann, B. E., Sultan, M., Patterson, M. J., Lu, Z.-T et al., 2004. One million year old groundwater in the Sahara revealed by krypton-81 and chlorine-36, *Geophysical Research Letters*, 31, L05503. doi: 10.1029/2003GL019234.

Stute, M., Clark, J. F., Schlosser, P., Broecker, W. S., Bonani, G., 1995. A 30,000 yr continental paleotemperature record derived from noble gases dissolved in groundwater from the San Juan Basin, New Mexico. *Quaternary Research*, 43: 209–220.

Stute, M., Forster, M., Frischkorn, A., Serejo, A., Clark, J. F., Schlosser, P., Broecker, W. S., and Bonani, G., 1995. Cooling of tropical Brazil (5 degrees C) during the last glacial maximum. *Science*, 269: 379–383.

Suchy, M., 2008. Nitrate and ammonium transformation and fate in groundwater of an agricultural watershed: An isotope and geochemistry approach. M.Sc. thesis, Department of Earth Sciences, University of Ottawa, Ontario, Canada. 256 pp.

Suecker J. K., Turk J. T., and Michel, R. L., 1999. Use of cosmogenic sulfur-35 for comparing ages of water from three alpine–subalpine basins in the Colorado Front Range. *Geomorphology*, 27: 61–74.

Suzuoki, T. and Kumura, T., 1973. D/H and $^{18}O/^{16}O$ fractionation in ice-water systems. *Mass Spectroscopy*, 21: 229–233.

Svec, H. J. and Anderson, A. R. Jr., 1965. The absolute abundance of the lithium isotopes in natural sources. *Geochimica et Cosmochimica Acta*, 29: 633–641.

Synal, H. A., Beer, J., Bonani, G., Suter, M., Wölfli, W., 1990. Atmospheric transport of bomb-produced ^{36}Cl. *Nuclear Instruments and Methods in Physics Research Section B: Beam Interactions with Materials and Atoms*, 52: 483–488.

Thornton, S. F., Bottrell, S. H., Spence K. H., Pickup, R., Spence, M. J., Shah, N., Mallinson, H. E. H., and Richnow, H. H., 2011. Assessment of MTBE biodegradation in contaminated groundwater using ^{13}C and ^{14}C analysis: Field and laboratory microcosm studies. *Applied Geochemistry*, 26: 828–837.

Tsunogai, S. and Henmi, T., 1971. Iodine in the surface water of the ocean. *Journal of the Oceanographical Society of Japan*, 27: 67–72.

Turchyn, A. V. and Schrag, D. P., 2006. Cenozoic evolution of the sulfur cycle: Insight from oxygen isotopes in marine sulfate. *Earth and Planetary Science Letters*, 241: 763–779.

Utting, N., Clark, I. D., Lauriol, B., Wieser, M., and Aeschbach-Hertig, W., 2012. Origin and flow dynamics of perennial groundwater in continuous Permafrost Terrain using isotopes and noble gases: Case study of the fishing branch river, Northern Yukon, Canada. *Permafrost and Periglacial Processes*, 23: 91–106.

Van Stempvoort, D., Maathuis, H., Jaworski, E., Mayer, B., and Rich, K., 2005. Oxidation of fugitive methane in ground water linked to bacterial sulfate reduction. *Ground Water*, 43: 187–199.

Veizer, J., 1989. Strontium isotopes in seawater through time. *Annual Review of Earth and Planetary Science,* 17: 141–167.

Veizer, J., Holser, T., and Wilgus, C. K., 1980. Correlation of $^{13}C/^{12}C$ and $^{34}S/^{32}S$ secular variations. *Geochimica et Cosmochimica Acta*, 44: 579–587.

Vernadsky, V. I., 1933. History of minerals of the earth´s crust, vol. 2. *History of Natural Waters. Part 1*, Goshimtehizdat, Leningrad (in Russian).

Vernadsky, V. I., 1934. History of Minerals of the Earth´s Crust, vol. 2. *History of Natural Waters. Part 2*, Onti Himteoret, Leningrad (in Russian).

Vernadsky, V. I., 1936. History of Minerals of the Earth´s Crust, vol. 2. *History of Natural Waters. Part 3*, Onti Himteoret, Leningrad (in Russian).

Vogel, J. C., 1970. Carbon-14 dating of groundwater. In *Isotope Hydrology 1970*, IAEA Symposium 129, March 1970, Vienna, pp. 225–239.

von Brömssen, M., Jakariya, M., Bhattacharya, P., Ahmed, K. M., Hasan, M. A., Sracek, O., Jonsson, L., Lundell, L., and Jacks, G., 2007. Targeting low-arsenic aquifers in Matlab Upazila, Southeastern Bangladesh. *Science of the Total Environment*, 379: 121–132.

Warner, M. J. and Weiss, R. F., 1985. Solubilities of chlorofluorocarbons 11 and 12 in water and seawater. *Deep Sea Research*, 32: 485–497.

Wassenaar, L. I., 1995. Evaluation of the origin and fate of nitrate in the Abbotsford Aquifer using the isotopes of ^{15}N and ^{18}O in NO_3^-. *Applied Geochemistry*, 10: 391–405.

Wassenaar, L. I., Hendry, M. J., Chostner, L. V., and Lis, G. P., 2008. High resolution pore water δ^2H and $\delta^{18}O$ measurements by H_2O (liquid)-H_2O (vapor) equilibration laser spectroscopy. *Environmental Science and Technology*, 42: 9262–9267.

Wassenaar, L., Aravena, R., Hendry, J., and Fritz, P., 1991. Radiocarbon in dissolved organic carbon, a possible groundwater dating method: Case studies from western Canada. *Water Resources Research*, 27: 1975–1986.

Webb, E. and Longstaffe, F. J., 2000. The oxygen isotopic compositions of silica phytoliths and plant water in grasses: Implications for the study of paleoclimate *Geochimica et Cosmochimica Acta*, 64: 767–780.

Welte, J., Ritterbusch, F., Steinke, I., Henrich, M., Aeschbach-Hertig, W., and Oberthaler, M. K., 2010. Towards the realization of atom trap trace analysis for ^{39}Ar. *New Journal of Physics*, 12. 0650311367-2630/10/065031+14$30.00.

Whiticar, M. J., Faber, E., and Schoell, M., 1986. Biogenic methane formation in marine and freshwater environments: CO_2 reduction vs. acetate fermentation—isotope evidence. *Geochimica et Cosmochimica Acta*, 50: 693–709.

Wickens, K., 2003. Determination of isotope enrichment factors for ^{15}N-NH_4 during volatilization and oxidation. Unpublished Honours Degree Thesis, Department of Earth Sciences, University of Ottawa, Ottawa, Canada, K1N 6N5. pp. 21.

Widory, D., Kloppmann, W., Chery, L., Bonnin, J., Rochdi, H., and Guinamant, J.-L., 2004. Nitrate in groundwater: An isotopic multi-tracer approach. *Journal of Contaminant Hydrology*, 72: 165–188.

Widory, D., Petelet-Giraud, E., Bregnot, A., Bronders, J., Tirez, K., Boeckx, P, 2013. Improving the management of nitrate pollution in water by the use of isotope monitoring: The $\delta^{15}N$, $\delta^{18}O$ & $\delta^{11}B$ triptych. *Isotopes in Environmental and Health Studies*. 49: 29–47.

Wiles, D. R., 2002. *The Chemistry of Nuclear Fuel Waste Disposal*. Polytechnic International Press, Montreal, Canada, p. 182.

Williams, P. R. D., Cushing, C. A., and Sheehan, P. J., 2003. Data available for evaluating the risks and benefits of MTBE and ethanol as alternative fuel oxygenates. *Risk Analysis,* 23: 1085–1115.

Winograd, I. J., Coplen, T. B., Landwehr, J. M., Riggs, A. C., Ludwig, K. R., Szabo, B. J., Kolesar, P. T., and Revesz, K. M., 1992. Continuous 500,000 year climate record from vein calcite in Devils Hole, Nevada. *Science*, New Series, 258: 255–260.

Wood, S. and Samson, I. M., 2006. The aqueous geochemistry of gallium, germanium, indium and scandium. *Ore Geology Reviews*, 28: 57–102.

Wu, D., Sui, Y., He, S., Wang, X., Li, C., and Kong, H., 2008. Removal of trivalent chromium from aqueous solution by zeolite synthesized from coal fly ash. *Journal of Hazardous Materials*, 155: 415–423.

Yi, L. M., Zhou, W-J., Hou, X-L., Chen, N., Zhang, L-Y., Liu, Q., He, C-H. et al., 2011. Determination of low level ^{129}I in soil samples using coprecipitation separation of carrier-free iodine and accelerator mass spectrometry measurement. *Chinese Journal of Analytical Chemistry*, 39: 193–197.

Yokochi, R., Sturchio, N. C., and Purtschert R., 2012. Determination of crustal fluid residence times using nucleogenic ^{39}Ar. *Geochimica et Cosmochimica Acta*, 88: 19–26.

Yu, H., Kim, B. J., and Rittmann, B. E., 2001. A two-step model for the kinetics of BTX degradation and intermediate formation by *Pseudomonas putida* F1. *Biodegradation*, 12: 465–475.

This page intentionally left blank

Groundwater Geochemistry and Isotopes

"The book is very clearly written, and each chapter provides students and long-time practitioners with practical examples and essential information needed for understanding and applying isotopic and geochemical principles to their research. ***Groundwater Geochemistry and Isotopes*** will be an essential resource for all students of isotopes and aqueous geochemistry."

—Dr. Leonard Wassenaar, International Atomic Energy Agency

"The author combines geochemistry and environmental isotopes quite nicely.He uses short and rather simple explanations (not an easy task) with many practical examples. …I am sure this new book will become a standard reference on groundwater geochemistry and isotopes as a basis for solving problems of groundwater quality and will meet expectations for use by graduate students and scientists on groundwater conditions."

—Dr. Alfonso Rivera, Geological Survey of Canada

The integration of environmental isotopes with geochemical studies is now recognized as a routine approach to solving problems of natural and contaminated groundwater quality. Advanced sampling and analytical methods are readily accessible and affordable, providing abundant geochemical and isotope data for high spatial resolution and high frequency time series. ***Groundwater Geochemistry and Isotopes*** provides the theoretical understanding and interpretive methods needed by students, researchers, and practitioners to apply isotopes and geochemistry in groundwater studies and contains a useful chapter presenting the basics of sampling and analysis.

This text teaches the thermodynamic basis and principal reactions involving the major ions, gases, and isotopes during groundwater recharge, weathering and redox evolution. Subsequent chapters apply these principles in hands-on training for dating young groundwaters with tritium and helium and ancient systems with radiocarbon, radiohalides and noble gases, and for tracing reactions of the major contaminants of concern in groundwaters.

Groundwater Geochemistry and Isotopes presents the basics of environmental isotopes and geochemistry and provides readers with a full understanding of their use in natural and contaminated groundwater.

K20528

ISBN: 978-1-4665-9173-8

90000

9 781466 591738

www.crcpress.com

CRC Press
Taylor & Francis Group
an **informa** business

www.crcpress.com

6000 Broken Sound Parkway, NW
Suite 300, Boca Raton, FL 33487
711 Third Avenue
New York, NY 10017
2 Park Square, Milton Park
Abingdon, Oxon OX14 4RN, UK